Engineering and validation of an integrated lab on a chip platform for platelet research and clinical diagnostics

Rose Brazilek

A thesis submitted for the degree of Doctor of Philosophy at
Monash University in 2019
Faculty of Medicine, Nursing and Health Sciences
Australian Centre for Blood Diseases

Copyright notice

I certify that I have made all reasonable efforts to secure copyright permissions for third-party content included in this thesis and have not knowingly added copyright content to my work without the owner's permission.

Abstract

Current platelet function diagnostics require long turnaround times, large blood volumes, trained operators, have low throughput and fail to accurately mimic vascular haemodynamics. This results in poor sensitivity and specificity, and impacts diagnostic outcomes. In this thesis, a microfluidic system was developed to provide an alternative platelet function diagnostic through mimicry of the *in vivo* haemodynamic environment. Automation of the device was achieved through development of a haemocompatible microvalve, micropump and micromixer which offered improvement in fluidic control and isolation without impacting blood components. Specifically, these systems were characterised by a comprehensive battery of assays to assess their impact on platelet activation and aggregation, red cell function, and plasma protein composition and quantity. Findings suggested the haemodynamic profile of microfluidic vessels can significantly modulate cellular and protein function, and this quality can be manipulated to improve haemocompatibility. The diagnostic element of the device consisted of channels with micro-contractions that harnessed well-defined haemodynamic shear gradients to initiate platelet aggregation in human whole blood in real time. Platelet function was assessed through examination of resulting aggregate size in the microcontraction. The system was validated in subjects with von Willebrand Disease, a shear-sensitive platelet function disorder, and found to have direct correlation with standard pathology-based testing. This microfluidic system offers a novel approach to understanding platelet function in high-shear environments and has the potential to be a rapid, high-throughput tool for drug screening and shear-based platelet function disorders.

Declaration

This thesis contains no material which has been accepted for the award of any other degree or diploma at any university or equivalent institution and that, to the best of my knowledge and belief, this thesis contains no material previously published or written by another person, except where due reference is made in the text of the thesis.

Signature:

Print Name: Rose Brazilek

Date: 3rd January 2018

Publications during enrolment

1. ***Brazilek RJ,*** *Szydzik C, Khoshmanesh K, Akbaridoust F, Knoerzer M, Thurgood P, Muir I, Marusic I, Nandurkar H, Mitchell A, Nesbitt W. Elastomeric microvalve geometry affects haemocompatibility. Lab Chip. 2018;18(12):1778-92.*
2. ***Brazilek RJ****, Tovar-Lopez FJ, Wong AK, Tran H, Davis AS, McFadyen JD, Kaplan Z, Chunilal S, Jackson S, Nandurkar H, Mitchell A, Nesbitt W. Application of a strain rate gradient microfluidic device to von Willebrand's disease screening. Lab Chip. 2017;17(15):2595-608.*
3. *Akbaridoust F, Silva CMd,* ***Brazilek RJ****, Chen X, Poon E, Ooi A, Mitchell A, Nandurkar H, Tovar-Lopez FJ, Nesbitt W, Marusic I. Examining flow dynamics of platelet function in micro-contractions using micro-PIV. Australasian Fluid Mechanics Conference; Adelaide, Australia 2018.*
4. *Selvadurai MV,* ***Brazilek RJ****, Moon MJ, Rinckel J-Y, Eckly A, Gachet C, Meikle PJ, Nandurkar H, Nesbitt W, Hamilton J. The PI 3-kinase PI3KC2α regulates mouse platelet membrane structure and function independently of membrane lipid composition. FEBS Letters. 2019;593(1):88-96.*
5. *Selvadurai MV, Moon MJ, Zheng Z, Mountford SJ,* ***Brazilek RJ****, Iman RP, Rinckel J-Y, Eckly A, Gachet C, Nesbitt W, Jennings IG, Thompson PE, Hamilton J. Disrupting the platelet internal membrane via PI3KC2α inhibition impairs thrombosis independently of canonical platelet activation. Manuscript submitted to Science Translational Medicine. 2018.*

Thesis including published works declaration

I hereby declare that this thesis contains no material which has been accepted for the award of any other degree or diploma at any university or equivalent institution and that, to the best of my knowledge and belief, this thesis contains no material previously published or written by another person, except where due reference is made in the text of the thesis.

This thesis includes 4 original papers published in peer reviewed journals and 1 submitted publication. The core theme of the thesis is haemocompatibility in blood-handling microfluidics. The ideas, development and writing up of all the papers in the thesis were the principal responsibility of myself, the student, working within the Australian Centre for Blood Diseases under the supervision of Dr. Warwick Nesbitt, Professor Harshal Nandurkar and Professor Arnan Mitchell.

In the case of chapters 3 and 5 my contribution to the work involved the following:

Thesis Chapter	Publication Title	Status	Nature and % of student contribution	Co-author name(s) Nature and % of Co-author's contribution*	Co-author(s) Monash student Y/N
3	Elastomeric microvalve geometry affects haemocompatibility	Published	50%. Carried out biological experiments and co-wrote the manuscript.	CS: 34%. Designed, fabricated, and ran mechanical testing of the microfluidic device and co-wrote the manuscript KK: 2%. Developed and ran the CFD simulations. FA: 2%. Developed and ran the µPIV experiments. MK: 1%. Developed and built the ancillary valve drivers and carried out mechanical testing. PT: 1%. Contributed to the design of the test manifolds. IM: 1%. Carried out VWF	No

				experiments and multimer analysis. IM: 1%. Developed the μPIV experiments and imaging system. HN: 1%. Contributed to biological experimental design. AM: 2%. Designed the microfluidic device and fabrication methods and contributed to experimental design. WSN: 5%. Developed the experimental design, supervised the study and wrote the manuscript.	
5	Application of a strain rate gradient microfluidic device to von Willebrand's disease screening	Published	60%. Carried out biological experiments and co-wrote the manuscript.	FT-V: 10%. Developed and ran the CFD simulations. AW: 7%. Carrie out preliminary biological experiments. HT: 3%. Assisted with patient recruitment and biological experimental design. AD: 3%. Assisted with patient recruitment. JM: 3%. Assisted with patient recruitment.	No

				ZK: 3%. Assisted with patient recruitment. SC: 1%. Assisted with patient recruitment. SJ: 1%. Contributed to biological experimental design. HN: 2%. Contributed to biological experimental design. AM: 2%. Designed fabrication methods and contributed to experimental design. WN: 5%. Developed the experimental design, supervised the study and wrote the manuscript.	

Student signature: **Date:** 3rd January 2019

The undersigned hereby certify that the above declaration correctly reflects the nature and extent of the student's and co-authors' contributions to this work. In instances where I am not the responsible author I have consulted with the responsible author to agree on the respective contributions of the authors.

Main Supervisor signature: **Date:** 3rd January 2019

Acknowledgements

This project would not have come to fruition without the hard work and patience of my supervisors, Dr, Warwick Nesbitt and Professor Harshal Nandurkar. Warwick, your wisdom and fortitude, despite my utter lack of laboratory nous, was very much appreciated. Thank you for your tireless efforts in getting this project up and running. Professor Nandurkar, your constructive criticism at laboratory meetings was very helpful, and I appreciate your patience with my endless pathology form requests.

I would also like to thank the RMIT Microfluidics and Bio-Micro-Electromechanical Systems team, without whom I would not have had a device to test, nor the knowledge nor facilities to fabricate it.

The Ronald Sawyer team were also of invaluable assistance. Thanks must go to Dr. James McFadyen, Dr. Mandy Davis, Dr. Huyen Tran, Penny, Debra, Susan and Megan for their tireless efforts to recognise and recruit suitable patients.

Within the lab, I would like to thank the Nandurkar and Hamilton labs, particularly for accommodating for the relentless venipuncture requests on my part. Additionally, I would like to thank Erica Malan from the Monash Medical Centre Pathology Service for providing invaluable assistance in the collection of PFA-100 data.

Finally, thanks go to my wonderful friends and family, who have supported my decision to stray from the path of clinical medicine and explore the underlying principles of it all. Without the support and encouragement of everyone mentioned, and many others, this thesis would not have been possible.

This research was supported by an Australian Government Research Training Program (RTP) Scholarship.

Table of Contents

List of Equations 11
List of Tables 11
List of Abbreviations 12
Chapter one: Introduction 16
Chapter two: Methods 149
Chapter three: Development and characterisation of haemocompatible microvalves 192
Chapter four: Design of elastomeric reciprocating micropumps 220
Chapter five: Investigation of the impact of spatial haemodynamic gradients on platelet function 282
Chapter six: Discussion 321
Appendices 346
Appendix one: Materials 347
Appendix two: Project ethics approval 354
Appendix three: Patient consent form 356
Appendix four: 'Disrupting the platelet internal membrane via PI3KC2α inhibition impairs thrombosis independently of canonical platelet activation' 361
Appendix five: 'The PI 3-kinase PI3KC2α regulates mouse platelet membrane structure and function independently of membrane lipid composition' 398
Appendix six: 'Examining flow dynamics of platelet function in micro-contractions using micro-PIV' 408

List of Figures

Figure 1. 1 Platelet cytoplasmic organisation 22
Figure 1. 2 Platelet adhesion and aggregation 26
Figure 1. 3 vWF genetic domains 29
Figure 1. 4 von Willebrand Factor 32
Figure 1. 5 Calcium signalling pathways 39
Figure 1. 6 Laminar parabolic fluid velocity profile 53
Figure 1. 7 Simplified stenotic geometry parameters 55
Figure 1. 8 Pneumatically-actuated elastomeric microvalves 95
Figure 1. 9 Reciprocating diaphragm pump 101
Figure 1. 10 Automated haematology cartridge 110

List of Equations

Equation 1. 1 Reynold's number 47
Equation 1. 2 Shear stress calculation 49
Equation 1. 3 Péclet number 50
Equation 1. 4 Navier Stokes Equation 51

List of Tables

Table 1. 1 Platelet receptors 37
Table 1. 2 vWD classification 60
Table 1. 3 vWD-specific testing 63
Table 1. 4 Clinical and pre-clinical platelet analysis methods 70

List of Abbreviations

Abbreviation	
µL	Microlitres
µM	Micrometres
µTAS	Micro total analysis systems
5-HT	Serotonin
AC	Adenyl Cyclase
ACD	Anticoagulant Citrate Dextrose Solution
ADAMTS-13	A metalloproteinase and disintegrin with a type 1 thrombospondin motif
ADH	Anti-diuretic hormone
ADP	Adenosine diphosphate
Akt	Protein kinase B
APT	Antiplatelet Therapy
ATP	Adenosine triphosphate
Ca^{2+}	Calcium ion
CalDAG-GEF1	Calcium and diacylglycerol-regulated guanine exchange factor 1
cAMP	Cyclic adenosine monophosphate
DNA	Deoxyribonucleic acid
COX	Cyclooxygenase
DAG	Diacylglycerol
DDAVP	1-desamino-8-D-arginine vasopressin
DTS	Dense tubular system
EDTA	Ethylenediaminetetraacetic acid

ELISA	Enzyme-linked immunosorbent assay
ER	Endoplasmic reticulum
FBE	Full blood examination
FcRγ	Fc receptor γ-chain
FV	Factor V
FVIII	Factor VIII
FVIII:Ag	Factor VIII antigen levels
FVIII:C	Factor VIII coagulation assay
FXI	Factor XI
FXII	Factor XII
FXIII	Factor XIII
G_i	G protein Adenylyl Cyclase inhibitor
GMP	Guanosine Monophosphate
GP	Glycoprotein
GPCR	G-protein coupled receptor
GTPase	Guanosine triphosphate hydrolase enzymes
HEPES	4-(2-hydroxyethyl)-1-piperazineethanesulfonic acid
IMPACT™	Image analysis, Monitoring, Platelet, Adhesion, Cone and plate Technology
IP3	Inositol trisphosphate
K^+	Potassium ion
LDL	Low-density lipoprotein
LTA	Light Transmission Aggregometry
Na^+	Sodium ion
NO	Nitric Oxide

ORAI1	Calcium release-activated calcium channel protein 1
$P2X_1$	P2X Purinoreceptor 1
$P2Y_1$	P2Y Purinoceptor 1
$P2Y_{12}$	P2Y Purinoceptor 12
PAR1	Protease-activated receptor-1
PAR4	Protease-activated receptor-4
PDGF	Platelet derived growth factor
PDMS	Polydimethylsiloxane
Pe	Peclet number
PFA-100	Platelet Function Analyser-100
PFT	Platelet function test
PGE_1	Prostaglandin E1
PGE_2	Prostaglandin E2
PGI_2	Prostacyclin
pH	Logarithm of hydrogen ion activity
PI3K	Phosphoinositide 3-kinase
PLCβ	Phospholipase C β
PPP	Platelet poor plasma
PRP	Platelet rich plasma
PS	Phosphatidyl serine
PSI	Pounds per Square Inch
PT	Prothrombin Time
Ras-related protein	Protein superfamily of GTPases
Re	Reynold's number

rFVIIa	Recombinant activated factor VII
RIAM	Ras-proximate-1-guanine triphosphate-interacting adaptor molecule
RIPA	Ristocetin-induced platelet aggregation
ROTEM®	Rotational Thromboelastometry
STIM1	Stromal interaction molecule 1
TF	Tissue factor
TPα	Thromboxane alpha receptor
TPβ	Thromboxane beta receptor
T-Tas	Total Thrombus Formation Analysis System
TxA2	Thromboxane
UV	Ultraviolet
VASP	Vasodilator-stimulated phosphoprotein
vWD	von Willebrand Disease
vWF	von Willebrand Factor
vWF propeptide	von Willebrand factor propeptide
vWF:Ag	von Willebrand factor antigen levels
vWF:CB	von Willebrand factor collagen binding assay
vWF:FVIIIB	von Willebrand factor to FVIII assay
vWF:RCo	von Willebrand factor ristocetin cofactor assay
vWF:RCo/vWF:Ag	von Willebrand factor ristocetin cofactor assay to von Willebrand factor antigen levels assay
vWFpp/WF:Ag ratio	von Willebrand factor propeptide to von Willebrand factor antigen level assay
WPB	Weibel-Palade bodies

Chapter one: Introduction

1. Introduction

Cardiovascular disease is the leading cause of morbidity and mortality worldwide and the current depth and breadth of research into diagnostics, cures and physiology reflects the seriousness of this global pandemic.(1, 2) Platelets, anucleate cell fragments that arise as a result of megakaryocyte fragmentation, play a key role in the thrombus development that causes the disease state.(3, 4) Virchow's triad delineates the major factors that determine thrombus formation: i) blood coagulability, ii) blood flow, and iii) vessel wall damage.(5) Knowledge of the impact of blood coagulability and vessel wall damage is well-established.(6-8) However, only recently has there been interest and advances in knowledge of how haemodynamic and rheologic parameters, in particular shear forces, affect platelet function and other aspects of thrombus formation. New studies demonstrating receptor shedding and von Willebrand factor (vWF) and platelet receptor unfolding in areas of high shear have made clear the importance of understanding how haemodynamics affects platelet function.(9)

Despite these discoveries, devices to assess platelet hypo and hyperfunction are poorly optimised, as they are currently low throughput, time consuming and demonstrate significant variability in diagnostic outcomes.(9-11) Further, current devices are poor physiologic mimics, often failing to incorporate physiologically-accurate flow conditions.(12) Currently, no consensus has been reached regarding a 'gold standard' platelet function diagnostic device because no single device achieves both diagnostic accuracy and practicality in use.

Microfluidic devices are increasingly seen as potential alternatives to current devices as they operate on the micro scale and utilise the manipulation of small fluid

volumes.(13, 14) They have many advantages in the field of platelet diagnostic assay development: they use smaller blood volumes and reagent volumes, are low-cost, and afford greater capacity for control of haemodynamic variables.(15) Additionally, it is their capacity to provide rapid, physiologically-accurate, simple detection methods that makes them of especial interest in medical diagnostics, and their potential is largely untapped.(16, 17)

The introduction to this thesis presents an overview of the current understanding of mechanisms underlying platelet adhesion, activation and aggregation, and the impact of haemodynamic conditions on these processes. In addition, this review will discuss the current state of platelet function diagnostics and potential applications for microfluidic devices to fill niches in sensitivity, rapidity and portability in the field.

1.1. Review: platelet function

1.1.1. Introduction

Platelets typically circulate at concentrations between 150-400x10^9/L in human blood for an average of 10 days.(18) They arise from megakaryocytes in the final stages of their development and have a variety of functions within circulation, including haemostasis and thrombosis, leukocyte recruitment through chemical and physical signal transduction, vascular integrity maintenance, wound healing, and release of pro- and anti-inflammatory and angiogenic factors.(19-21)

1.1.2. Platelet cytoplasmic organisation

Platelets have a complex microstructure that facilitates their function.(3, 22) They have several distinct zones, found at successively greater distance from the platelet surface: i. the Peripheral Zone, which consists of the plasma membrane and

cytoskeleton, ii. The Sol-Gel zone, containing the contractile microtubular system, and iii. The Organelle Zone, which contains all other organelles facilitating platelet function *(see Fig 1.1)*.(23)

The Peripheral Zone consists of a fuzzy glycocalyx coat on the surface of the plasma membrane.(24) Within this zone, receptors for Adenosine Diphosphate (ADP), thrombin, von Willebrand Factor (vWF), collagen, fibrinogen, fibrin, fibronectin, Platelet Activating Factor, thrombospondin, thromboxane A2 (TxA2), prostacyclin, epinephrine, serotonin and glycosyl transferase act to mediate platelet function.(25, 26)

The Sol-Gel zone contains a microtubular contractile system composed of actin and myosin and assists in platelet shape change upon activation and aggregation.(26) Myosin controls organelle distribution within platelets and plays an important role in motility within the organelle zone.(27) Actin tubules play a role in mediating morphological change upon platelet activation.(27)

Interspersed between these zones sits the canalicular system, which is a series of tubes arising from invagination of the platelet cytoplasm.(28) The canalicular system acts as a secretory organ for exocytosis from the platelet. A second tubular network, the dense tubular system (DTS), is found at the centre of the platelet, and stores and regulates platelet cytoplasmic calcium concentration.(29)

Within the organelle zone, granules act primarily to facilitate thrombogenesis. Dense granules contain ADP, adenosine triphosphate (ATP), serotonin (5-HT), polyphosphates, and calcium.(30) The more abundant alpha granules store vWF, fibrinogen, P-selectin, thrombospondin, platelet derived growth factor (PDGF), Factor

V (FV) and Factor XII (FXIII).(25, 31, 32) Once released, these stored molecules either participate in formation of the platelet plug, or fibrin formation. Of the molecules stored in the alpha granules, only vWF is produced endogenously - all others are endocytosed from plasma.(33) The platelet cytoplasm also contains lysosomes: small, membrane-bound, fluid-filled sacs containing degradative enzymes.(29)

1.1.3. Platelet aggregation and thrombosis

Blood in circulation is in a constant homeostatic balance between bleeding and thrombosis, and platelets play an important role mediating this equilibrium.(34) Broadly, damage to the endothelial lining of blood vessels exposes the pro-aggregatory subendothelium, which acts as the primary site for platelet binding.(35) Various platelet agonists promote adhesion, which triggers platelet shape change, release of further pro-aggregatory molecules, and expression of more receptors for platelet aggregation.(36, 37)

Primary haemostasis is this process by which the initial aggregate is formed, and is defined by the following phases:(38)

I. **Platelet adhesion**, wherein tethering to sub-endothelial surfaces reduces platelet velocity, allowing surface translocation at the site of vascular injury;
II. **Platelet activation**, wherein platelets activate through intracellular calcium signalling, resulting in granule release, platelet shape change, integrin activation and externalisation of a procoagulant surface;
III. **Platelet aggregation**, wherein platelet-platelet adhesion results in thrombus formation.

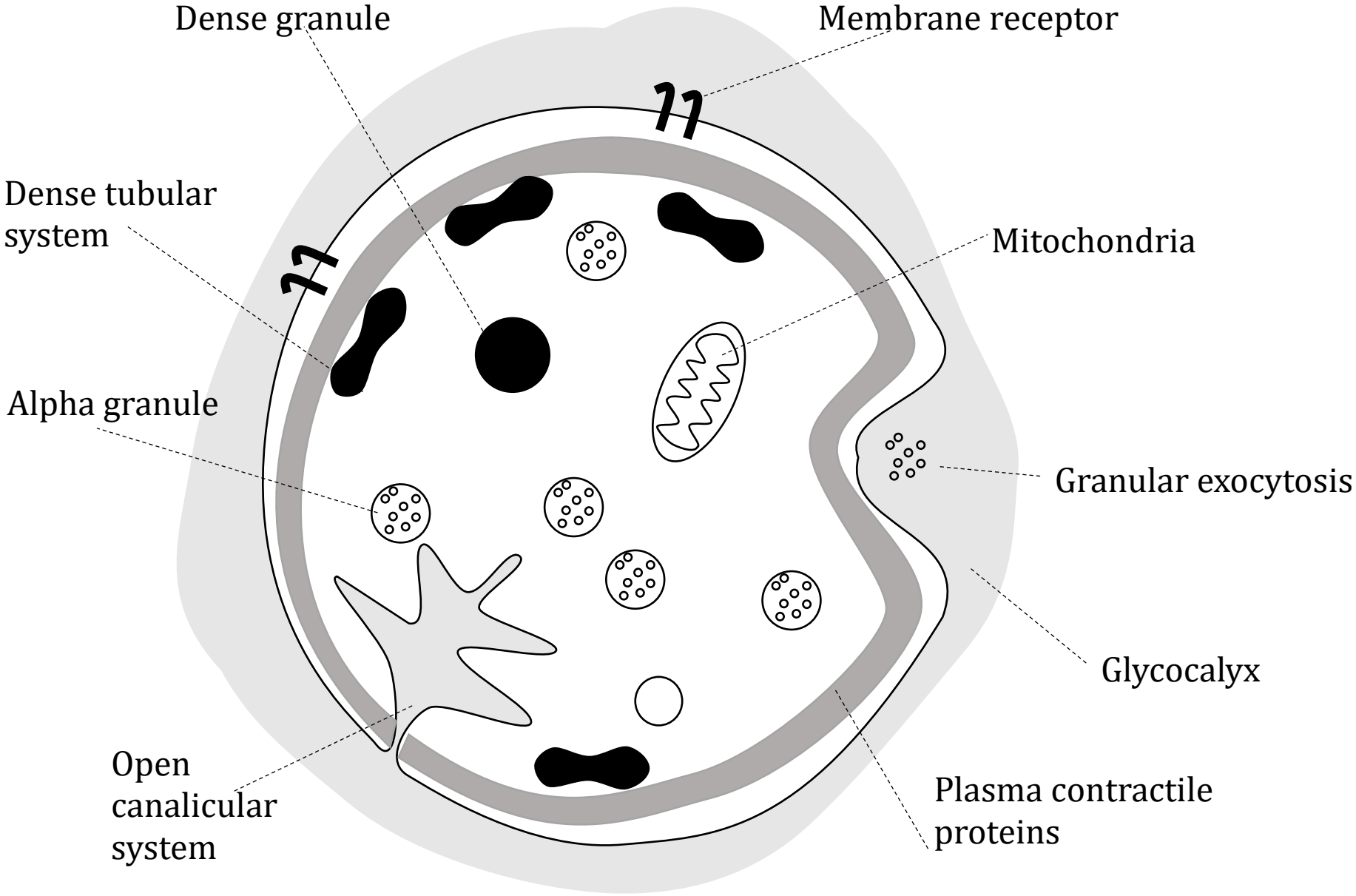
Dense granule
Membrane receptor
Dense tubular system
Mitochondria
Alpha granule
Granular exocytosis
Glycocalyx
Open canalicular system
Plasma contractile proteins

Figure 1. 1 Platelet cytoplasmic organisation

Platelets demonstrate complex intracellular organisation. They contain a number of well-characterised granules: the dense granules contain ADP, ATP, 5-HT, polyphosphates, and calcium,(3, 31) while alpha granules are more common, and contain vWF, fibrinogen, P-selectin, thrombospondin, PDGF and FV.(26) As platelets are cell fragments from megakaryocytes, they notably do not contain a nucleus.

Secondary haemostasis then follows, characterised by the formation of fibrin and aggregate stabilisation.(39)

1.1.3.1. Platelet adhesion

Platelet adhesion involves the initial platelet interaction with the subendothelium. Binding is contingent on the interaction between glycoprotein membrane receptors and adhesive proteins on the subendothelial surface. Upon disruption of the endothelial lining of blood vessels, the subendothelium becomes exposed.(40) Presentation of structural collagens enables capture of plasma vWF and shear then transforms the vWF to an open conformation, exposing platelet binding sites.(41) The endothelium also releases vWF from Weibel Palade bodies to the surface upon vessel injury.(42) Resting discoid platelets then bind to these adhesive proteins, becoming spherical.(43)

The binding profile of the platelet-ligand interactions at the subendothelium is dependent on local shear. In low shear areas (<1,000s^{-1}), fibrinogen-platelet capture predominates.(36) However, under conditions of high shear, binding is dependent on interactions between the platelet receptor GPIb/V/IX and sub-endothelial bound vWF (*see Fig 1.2*).(44) GPIb-vWF binding induces the platelets to extend long, thin membrane extensions, or 'tethers', assisting platelets to bind to each other and the membrane surface, and increasing the efficiency at which the aggregate forms.(45)

1.1.3.1.1. Proteins of the adhesion phase

1.1.3.1.1.1. von Willebrand Factor

1.1.3.1.1.1.1. von Willebrand Factor physiology

vWF is a multimer of varying polymeric size and is important in both platelet adhesion and aggregation.(46) It also has an indirect role in the clotting pathway, protecting factor VIII from proteolytic degradation.(47) It exists in two states: as a closed configuration when circulating, or as an open structure with exposed platelet binding sites.(48) In the circulating, soluble form, it may bind to either collagen or platelet-bound, immobilised vWF (self-association), a process which is more pronounced in high-shear environments.(49) In the event of injury to the vessel wall following low-density lipoprotein (LDL) oxidation, exposure of the subendothelium, especially collagen binding sites, will initiate vWF binding and platelet adhesion and thrombogenesis.(50-52)

vWF transformation into an open conformational state allows binding to the GPIb/IX/V receptor on the surface of platelets.(52, 53) vWF-platelet bonds have fast on-rates of association, making them a crucial step in the formation of a platelet monolayer in high shear environments. Primarily, this initial binding allows bonds with slower on-rates – such as platelet-GPVI and platelet-integrin $\alpha_{IIb}\beta_3$ bonds – to form.(54) While these receptors have slower binding kinetics, their bonds have greater cohesive strength and stability, and promote growth of the aggregate.(55) Disassociation rates of this bond are also quick, resulting in rapid platelet cycling between a tethered state and rolling phases.(56, 57) Functionally, vWF binding initiates platelet signalling to alter platelet conformation from a discoid to a spherical morphology facilitating rolling.(29)

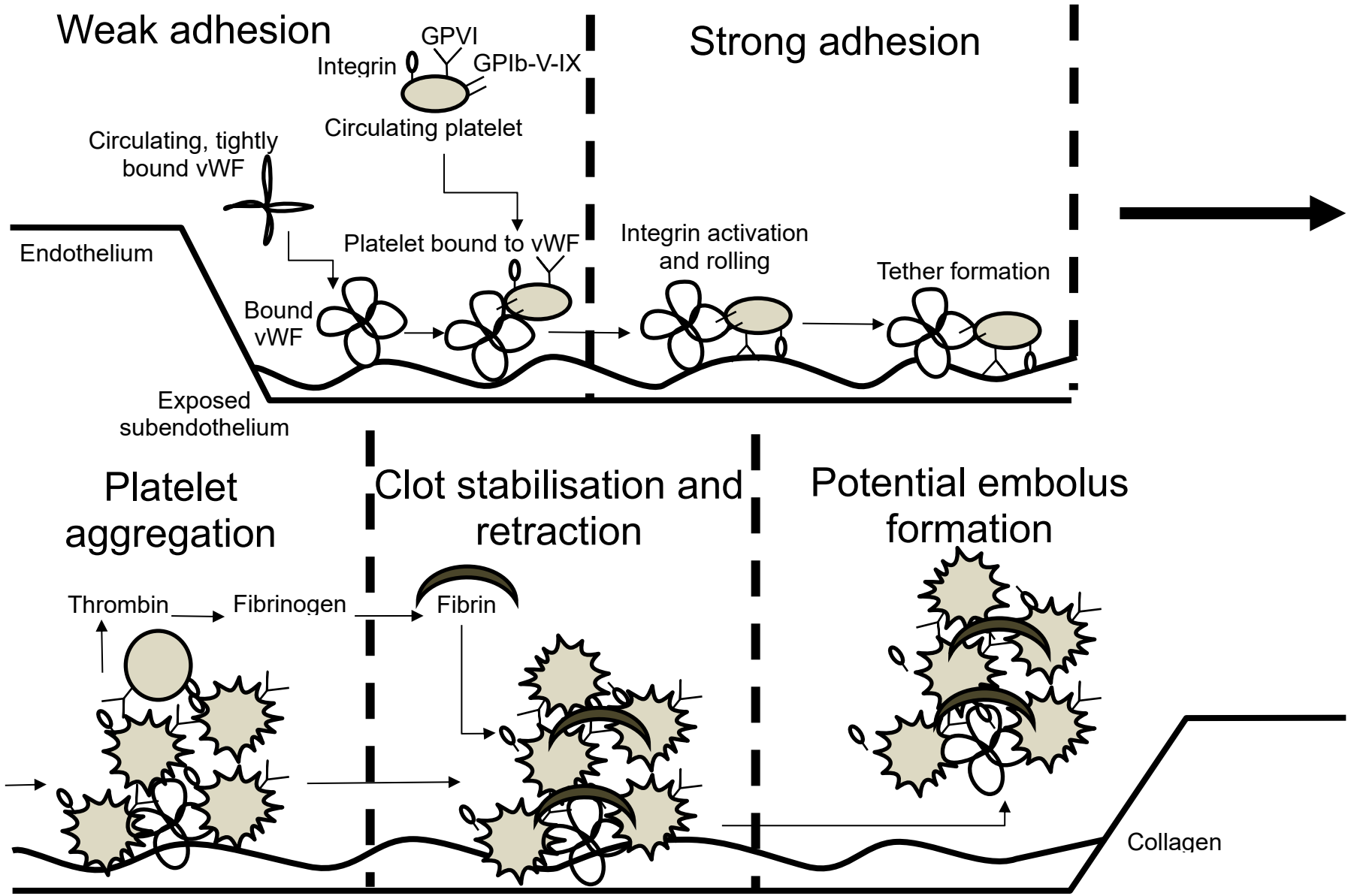
Weak adhesion
GPVI
Integrin
GPIb-V-IX
Circulating platelet
Strong adhesion
Circulating, tightly bound vWF
Endothelium
Platelet bound to vWF
Integrin activation and rolling
Tether formation
Bound vWF
Exposed subendothelium
Platelet aggregation
Clot stabilisation and retraction
Potential embolus formation
Thrombin
Fibrinogen
Fibrin
Collagen

Figure 1. 2 Platelet adhesion and aggregation

The initial platelet-ligand adhesion profile depends on the shear experienced by the platelet. In high-shear environments, adhesion is dependent on vWF. vWF may be captured from the plasma and bind to collagen on the exposed subendothelium or be expressed from the subendothelium.(58) The open conformational state of the vWF state allows exposure of additional platelet binding sites. After initial vWF binding, the platelet is slowed enough to enable longer-lasting bonds to be made with integrins, GPVI and collagen (which require longer contact times to bind).(59) The platelet alters its shape to aid translocation across the subendothelium and facilitate new bond substrates contacting. New platelets then aggregate around the initial platelet monolayer, sealing the site of injury to prevent further monolayer formation.(60) They also produce thrombin, which acts via the clotting cascade to provide stabilisation to the clot in the form of fibrin. If the shear forces are large enough, or the thrombus reaches a large size, an embolus may form.(61)

1.1.3.1.1.1.2. von Willebrand Factor production

After pre-pro-vWF is transcribed in the nucleus, it is translocated in the rough endoplasmic reticulum (ER), where post-translational modification occurs, including glycosylation dimer formation (which protects it from proteolysis). *(see Fig 1.3)*.(62) It is then transported to the Golgi apparatus for sulphation, carbohydrate processing, multimerisation and propeptide cleavage from the mature vWF structure. The final destination of the vWF subunit is dependent on the production location: if synthesised in endothelial cells, multimers may be stored in Weibel-Palade Bodies (WPB) or be constitutively secreted. If produced in megakaryocytes, it is stored in platelet alpha granules.(26, 31, 32)

1.1.3.1.1.2. Fibrinogen

Fibrinogen binds to platelet integrin $\alpha_{IIb}\beta_3$, resulting in platelet cross-linking and aggregation.(63) Although all platelets express integrin $\alpha_{IIb}\beta_3$ on their surface, aggregation is prevented in inactivated platelets through regulated fibrinogen affinity to integrin $\alpha_{IIb}\beta_3$.(6) Once platelet activation occurs, integrin $\alpha_{IIb}\beta_3$ undergoes a conformational change.(64, 65) Fibrinogen then acts as a bridging molecule between integrin $\alpha_{IIb}\beta_3$ receptors on different platelets.(66)

1.1.3.1.1.3. Collagen

The triple-helical conformation of collagen is critical for platelet binding.(75, 76) Though more than 28 collagen molecules have been identified, platelets bind

Exon origin:

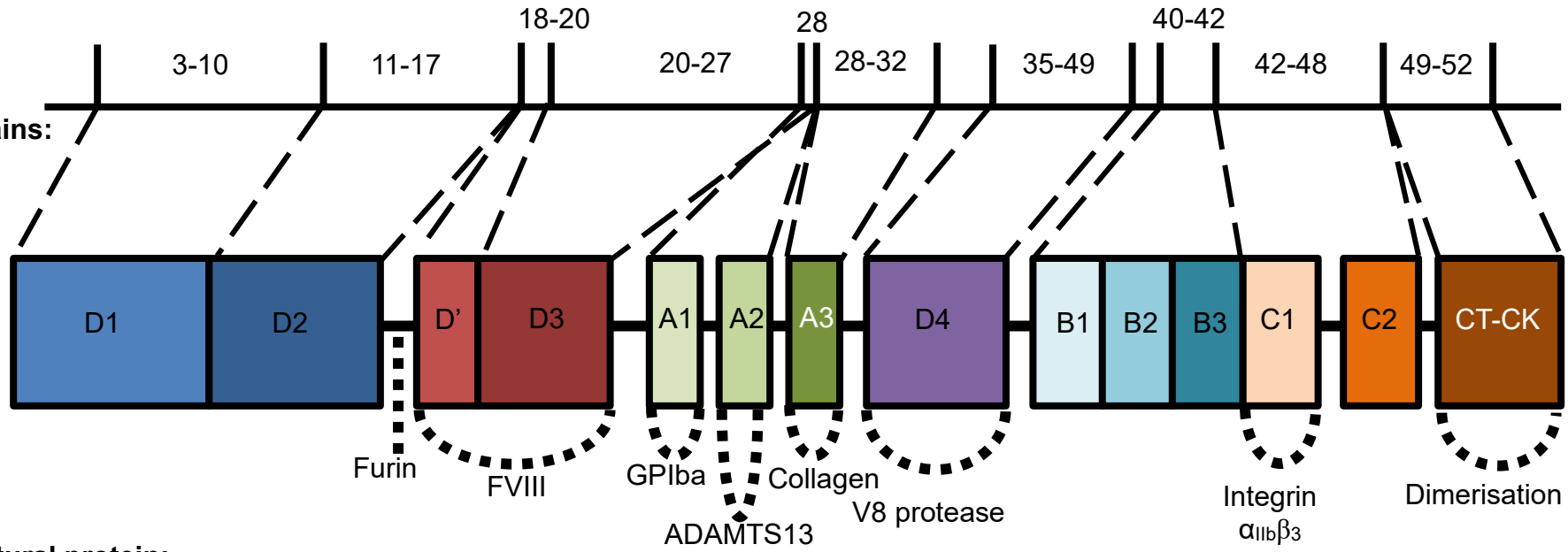

Structural protein:

Figure 1. 3 vWF genetic domains

The domains expressed in the vWF protein generate specific ligand binding sites: A1 is the binding site for collagen and the GPIb/IX/V peptide complex and A3 binds to collagen.(67, 68) β3 integrin binding is mediated by the C1 domain, and D' and D3 mediate FVIII binding.(69) Conversely, ADAMTS-13, the vWF cleavage protease, cleaves at the A2 domain. Structurally, the domains are ordered in the sequence: D1-D2-D'-D3-A1-A2-A3-D4-B1-B2-B3-C1-C2-CK.(70)

One of the determinants of vWF reactivity is multimeric size.(71) It is known that larger multimers of vWF are more effective in inducing platelet adhesion and aggregation due to increased responsiveness to shear stress. This is due to the greater degree of unfolding, and thus greater exposure of binding sites.(59, 72, 73) However, this greater degree of unfolding also has the converse effect: exposure of binding sites allows exposure of ADAMTS-13 binding sites, leading to more rapid proteolytic cleavage.(51, 73, 74)

predominantly to type I collagen.(75) Platelet binding to type I collagen occurs through either integrin α2β1 or the GPVI receptor. Additionally, indirect platelet binding can occur through vWF binding to collagen, exposing binding sites on the A1 domain of the vWF molecule.(61)

1.1.3.1.2. Receptors of the adhesion phase

Upon injury to blood vessel walls, the subendothelium becomes exposed.(77) Collagen is a major structural component of the subendothelium, and acts as a binding site for vWF in the plasma *(see Fig 1.4)*.(78) Collagen, vWF and other expressed ligands bind to glycoprotein and integrin receptors on the surface of platelets (*see Table 1.1*). The first of the platelet receptors to bind to subendothelial ligands is the GPIb/IX/V complex.(79)

1.1.3.1.2.1. Glycoprotein Ib/IX/V

GPIb/IX/V is a glycoprotein that predominately binds to vWF, though it may also bind to collagen and coagulation factors on the surface of the subendothelium.(80) GPIb-IX-V is critical to platelet capture in areas of high shear. In high-shear environments, GPIb-IX-V will bind to A1 domain in the vWF protein, inducing a platelet shape change from biconcave disc to spherical, and the formation of tethers.(79, 80) Tethers allow a greater binding strength and range of binding of platelets to each other and the endothelial surface.(45) Upon GPIb-IX-V binding and tether formation, platelets are slowed to less than 2% of their initial velocity.(37) This causes platelets to slowly translocate along the surface of the subendothelium, allowing receptors with slower on-rates of association to bind.(81) As shear increases, aggregation becomes more dependent on vWF binding to the GPIb receptor on the platelet

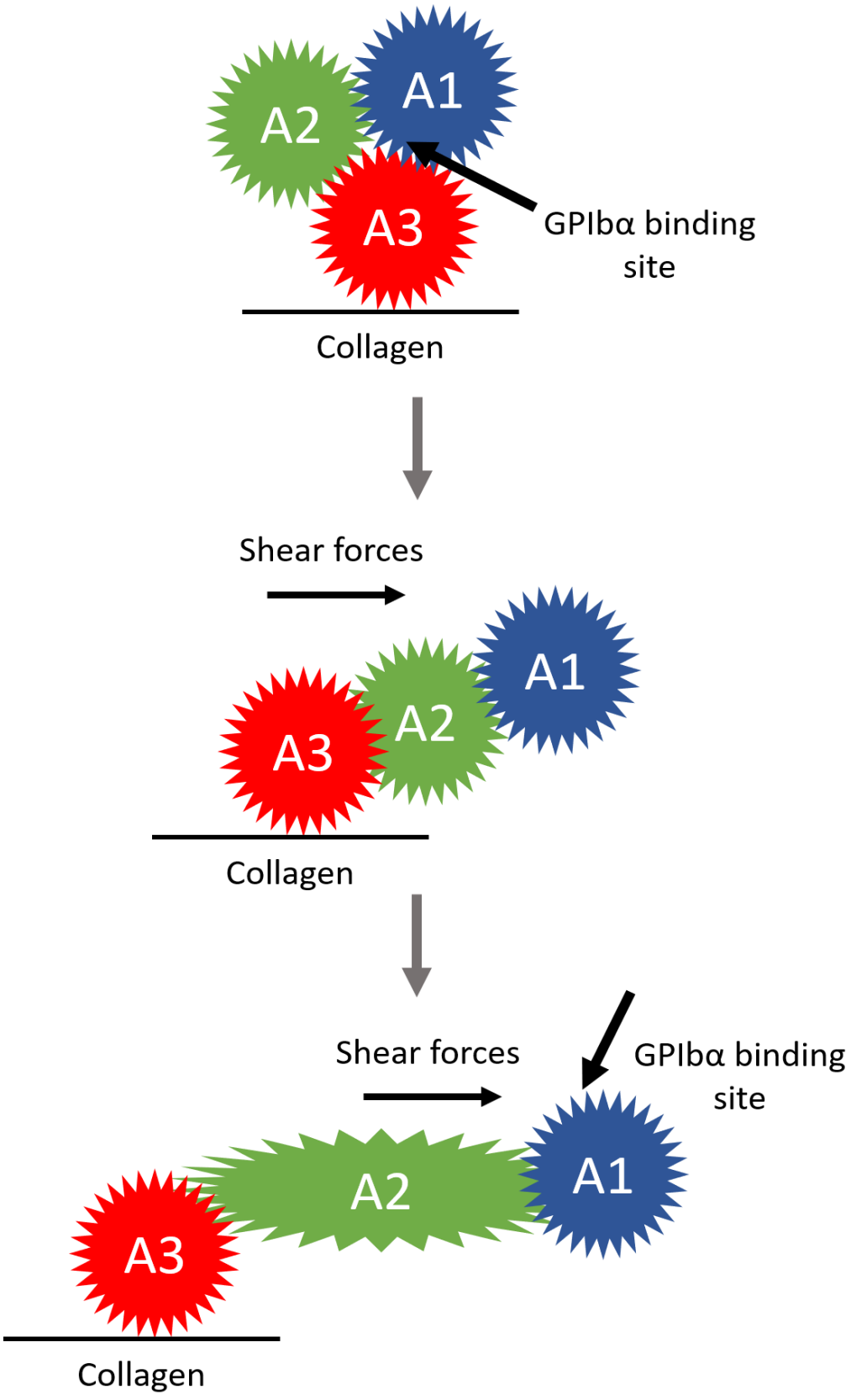
A1
A2
A3
GPIbα binding site
Collagen
Shear forces
A1
A2
A3
Collagen
Shear forces
GPIbα binding site
A1
A2
A3
Collagen

Figure 1. 4 von Willebrand Factor

vWF circulates in a tightly-folded state within the plasma, and is stored in the WPB within the subendothelium for release upon vessel wall injury.(52) Damage to the subendothelium exposes collagen on its surface, which can capture the circulating vWF and transform it into an open conformation, exposing binding sites. In high-shear environments, the GPIb/IX/V complex on the platelet surface will bind to the A1 domain of the vWF, thereby capturing platelets from the blood flow.(45)

Shear has an important impact on platelet function through impacting platelet distributions and vWF function. A greater shear force will cause unfolding of the tightly-bound vWF conformation, resulting in greater exposure of the A1 vWF domain.(41) This region has been extensively characterised as the area of platelet binding to vWF.(44)

surface.(36, 37) In areas of pathological shear (>10,000s^{-1}, as in the case of vessel stenosis), aggregation becomes almost completely dependent on vWF-binding without requiring prior platelet activation.(82)

1.1.3.1.2.2. Glycoprotein VI

In low shear environments, platelet GPVI receptors can bind directly to collagen, initiating thrombus formation.(75) However, in high-shear environments, vWF-mediated platelet capture is additionally necessary for GPVI binding and subsequent platelet activation.(83) Upon collagen binding, tyrosine phosphorylation of the tyrosine activation motif of the Fc receptor γ-chain (FcRγ) dimer induces a platelet activation cascade.(77) The action of GPVI appears to be to elicit platelet activation rather than to facilitate adhesion, and it only exhibits low affinity to collagen.

1.1.3.1.2.3. Integrins

Integrins are glycoproteins that act as transmembrane receptors, mediating adhesion-dependent signalling pathways.(37, 38) Generally, their two main functions are to induce attachment of the cell to the extracellular matrix and provide a mechanism for signal transduction from the external environment inside the cell.(84) Structurally, they are transcellular heterodimers with α and β subunits, and small cytoplasmic domains.(84) The β subunits further classify the integrins into either β1 or β3 subgroups.(85) Broadly, integrins mediate bidirectional signalling. All platelet integrins enable outside-in signalling through adhesion-dependent signalling events during platelet aggregation.(36, 86, 87) Outside-in signalling pathways act to induce a cellular response to ligand-integrin binding, resulting in platelet responses of

spreading and migration.(84) Inside-out signalling events conversely activate integrins to increase integrin response to ligand binding.(88)

1.1.3.1.2.3.1. Integrin α2β1

Integrin α2β1 is a collagen receptor and acts in areas of low shear.(40) It requires vWF-GPIbα binding prior to activation and preferentially binds to fibril-forming collagen, especially collagen I and III.(89) Unlike integrin $\alpha_{IIb}\beta_3$, integrin α2β1 does not undergo conformational change prior to ligand binding.(90) Binding of integrin α2β1 to collagen causes platelet immobilisation and allows a second platelet collagen receptor, GPVI, to bind to the collagen molecule. Both collagen receptors then act synergistically to trigger phosphorylation and dimerisation of collagen, leading to inside-out integrin $\alpha_{IIb}\beta_3$ conversion to a high-affinity state. High-affinity conversion of integrin $\alpha_{IIb}\beta_3$ occurs more quickly when collagen acts as the ligand, compared to vWF.(65)

1.1.3.1.2.3.2. Integrin $\alpha_{IIb}\beta_3$

Integrin $\alpha_{IIb}\beta_3$ is the most abundant surface-expressed platelet integrin, and binds to many ligands of importance in haemostasis, including vWF and fibrinogen.(64, 65, 91) Platelet adhesion to collagen, vWF or other subendothelial proteins initiates affinity modulation through induction of a conformational change in the integrin $\alpha_{IIb}\beta_3$ receptor through inside-out signalling. In the low-affinity state, it has a highly-bent structure concealing the ligand binding site.(91) Upon platelet activation due to soluble agonists of platelet aggregation, a conformational switch occurs within the integrin molecule, and the high affinity state with the platelet binding site is now revealed.(36) These changes induce arachidonic acid metabolism, intracellular

calcium release from stores and activation of phosphoinositide 3-kinase (PI3K).(91) In this state, affinity of binding towards vWF and fibrinogen is vastly increased.(65) Further ligand binding to the integrin $\alpha_{IIb}\beta_3$ receptor causes outside-in signalling, leading to alterations in platelet morphology and activation of tyrosine kinases.(92) During the outside-in signalling process, integrin $\alpha_{IIb}\beta_3$ receptors demonstrate clustering and incorporation into larger signalling complexes in the cytoskeleton.(65)

1.1.3.1.3. Factors preventing platelet-endothelial adhesions

Nitric Oxide (NO) acts to increase intracellular cyclic-guanosine monophosphate (GMP) to induce vasodilation decreasing shear stress in the vessel.(93) It is also one of the most powerful inhibitors of platelet adhesion and activation through both cyclic GMP-dependent and independent pathways, though specific mechanisms are yet to be defined.(94) Studies have suggested that interactions with reactive oxygen species or production of NO may directly decrease platelet recruitment in thrombus formation.(95, 96)

Prostacyclin (PGI_2) also acts to reduce arterial muscle tone and increase vessel diameter, and is a potent inhibitor of platelet aggregation.(97) It has a synergistic action with NO and is released by endothelial cells in response to similar stimuli that induce release of NO, including high shear.(97)

1.1.3.2. Platelet activation

The activation process follows platelet adhesion to the subendothelial matrix. This process causes a variety of changes in platelets through intracellular calcium signalling, including inside-out signalling, degranulation, and phosphatidylserine

exposure.(37, 41) It is an intermediate step between initial platelet adhesion and thrombus stabilisation.

1.1.3.2.1. Calcium signalling

Platelet interactions with adhesive proteins promote outside-in signalling through intracellular calcium mobilisation (*see Fig 1.5*).(40, 98, 99) Following platelet activation through either primary adhesion or soluble agonist interaction with G-protein coupled receptors (GPCRs), phospholipaseC β (PLCβ) is activated, generating inositol triphosphate (IP3) and diacylglycerol (DAG).(100) IP3 mobilises calcium from the intracellular DTS, and this net movement of calcium out of the DTS is sensed by the Stromal Interaction Molecule-1 (STIM1), which then activates the calcium channel Calcium release-activated calcium channel protein 1 (ORAI1).(101) This generates an extracellular calcium influx, acting to amplify platelet activation through further increasing cytosolic calcium.(102) Actions of increased calcium concentration within the platelet include integrin receptor clustering and avidity change, acting as a positive feedback mechanism for further integrin interactions.(103) The collagen receptor primarily exists in a resting conformation, but when calcium signalling is initiated, integrin-proximal intacellular signalling mechanisms induce changes in the extracellular binding domain, altering it to an open conformation.(77) Calcium signalling also induces release of alpha and dense granules, which release molecules which act via paracrine signalling to induce activation of nearby platelets.(104) Finally, intracellular calcium signalling causes phospholipase A2 externalisation, causing both clot retraction and platelet morphological alteration.(45)

Table 1.1: Platelet receptors(3, 61)

RECEPTOR TYPE	RECEPTOR	LIGAND
Integrins	Integrin α2β1	Collagen
	Integrin α5β1	Fibronectin
	Integrin α6β1	Laminin
	Integrin $\alpha_{IIb}\beta_3$	Fibrinogen, vWF, fibronectin, vitronectin
	Integrin αvβ3	Fibronectin, vitronectin, fibrinogen, vWF
Glycoprotein complexes	GPVI	Collagen, laminin
	GPIb/IX/V	vWF, collagen, thrombospondin-1
Receptors of soluble agonists	P2Y Purinoceptor 1 ($P2Y_1$), P2Y Purinoceptor 12 ($P2Y_{12}$)	ADP
	Protease-activated receptor-1 (PAR1), Protease-activated receptor-4 (PAR4)	Thrombin
	TP	TXA2
	5HT2a	5HT
	α2A	Adrenaline

1.1.3.2.2. Granular secretion

Soluble agonists are molecules released from platelet granules that activate GPCRs, playing a crucial role in platelet aggregation.(105) They include ADP, ATP, TxA2, thrombin, adrenaline and 5H-T.(60) Upon calcium signalling, granule release is initiated from both alpha and dense granules. Soluble agonists act to amplify platelet aggregation and adhesion responses by autocrine or paracrine outside-in signalling on the platelet surface (*see Fig 1.5*).(36) Receptors of soluble agonists are G-protein coupled and consist of several subtypes: G_q, G protein Adenylyl Cyclase inhibitor (G_i) and G_z, all of which act through inside out signalling.(100) G_q receptors are the most common, and act as receptors for ADP, thrombin, TxA2 and 5-HT.(106)

1.1.3.2.3. Soluble agonist receptors

1.1.3.2.3.1. $P2Y_1$

The $P2Y_1$ receptor predominantly acts as a receptor for ADP.(107) There are approximately 150 $P2Y_1$ receptors on each platelet surface, and $P2Y_1$ receptors are also found in alpha granules and the canalicular system of platelet microtubules.(100)

$P2Y_1$ activation activates two coupled G-protein receptors: G_i and G_q.(108) The G_q receptor stimulates PLCβ isoforms, which hydrolyse membrane phospholipids.(100, 109) Membrane hydrolysis generates IP3 and DAG, important calcium-regulatory molecules.(110) DAG acts to induce integrin activation through acting on the calcium and diacylglycerol-regulated guanine exchange factor 1 (CalDAG-GEF1) GTPase, which produces the Rap1 effector molecule Ras-proximate-1-guanine triphosphate-

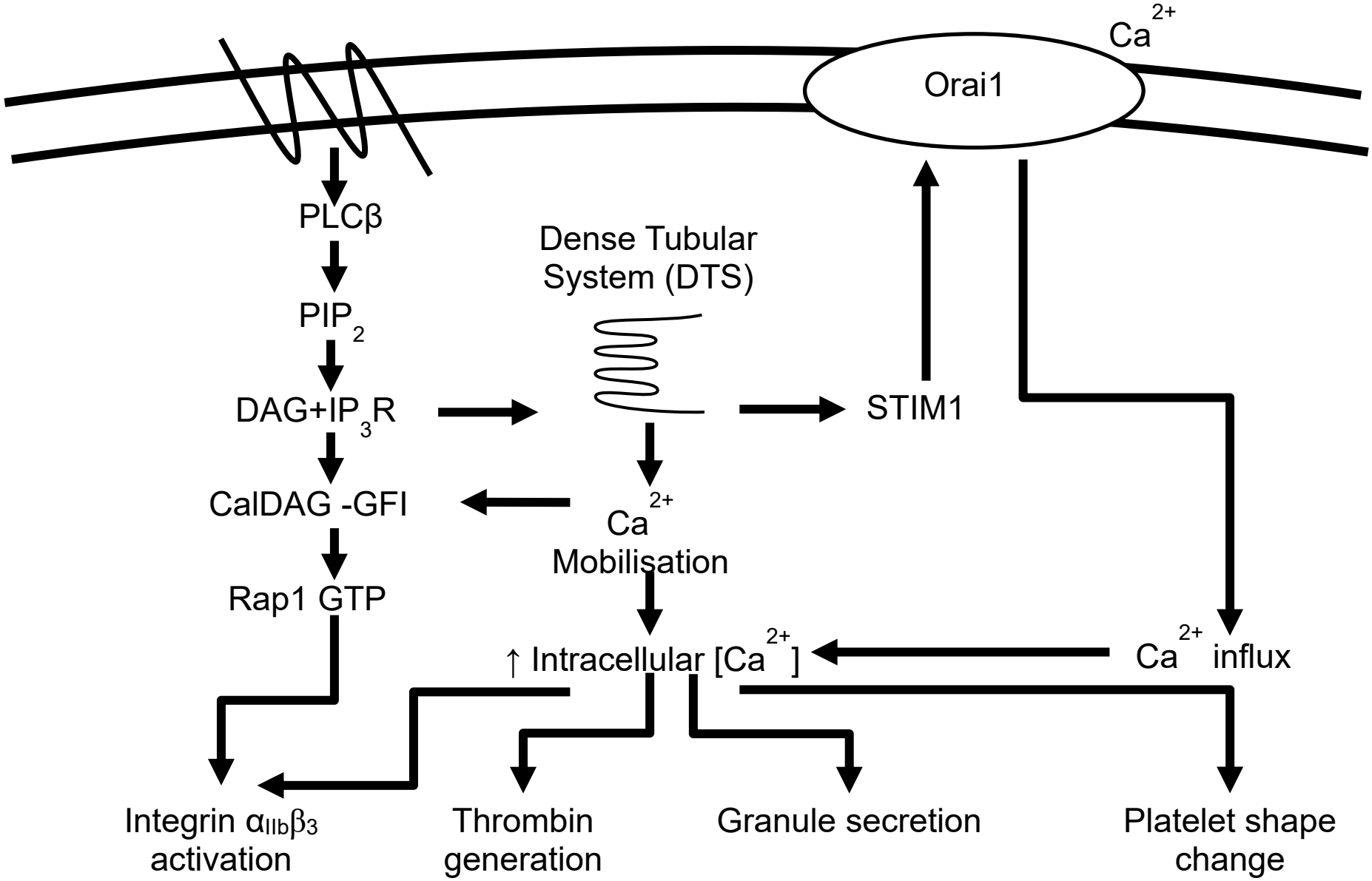
Ca2+
Orai1
PLCβ
PIP2
DAG+IP3R
CalDAG -GFI
Rap1 GTP
Dense Tubular System (DTS)
STIM1
Ca2+ Mobilisation
↑ Intracellular [Ca2+]
Ca2+ influx
Integrin αIIbβ3 activation
Thrombin generation
Granule secretion
Platelet shape change

Figure 1. 5 Calcium signalling pathways

After platelet interaction with soluble agonists, platelet activation state is increased through intracellular calcium signalling.(64, 111) After GPCR activation, IP3 and DAG are released through activation of the PLCβ. The IP3 acts to move calcium out of the intracellular DTS. STIM1, sensing a net calcium increase, activates the calcium channel Orai1, increasing Ca^{2+}, thereby further increasing platelet activation.

interacting adaptor molecule (RIAM), causing activation.(91) IP3 increases intracellular calcium concentration through interaction with the DTS (an organelle which stores calcium).(38) STIM-1 receptors within the DTS sense calcium depletion and open ORAI1 calcium channels, inducing platelet shape change and further integrin activation.

The G_i receptor acts through PI3K to induce Protein kinase B (Akt) activation and phosphorylation, which produces RIAM, leading to integrin activation.(112) The G_i receptor also inhibits Adenyl Cyclase (AC) function, decreasing cyclic adenosine monophosphate (cAMP). This reduces phosphorylation of vasodilator-stimulated phosphoprotein (VASP), which otherwise inhibits platelet activation.(111)

1.1.3.2.3.2. $P2Y_{12}$

$P2Y_{12}$ acts as a receptor for ADP, though conversely to $P2Y_1$, ATP acts as an antagonist.(108) Like $P2Y_1$, $P2Y_{12}$ is coupled to G_i receptors, though it induces a slower response.(113) Activation of $P2Y_{12}$ results in consequent inhibition of AC. Concurrent PI3K activation leads to integrin $\alpha_{IIb}\beta_3$ activation through activation of a protein kinase serine-threonine protein kinase B and Ras-related proteins. AC inhibition decreases cAMP levels, leading to a reduction of phosphorylation of VASP, initiating integrin $\alpha_{IIb}\beta_3$ receptor activation. Ultimately, $P2Y_{12}$ activation results in platelet activation, platelet conformation alteration, granulation secretion and stabilisation of the thrombus.(114)

1.1.3.2.3.3. $P2X_1$

P2X Purinoreceptor 1 ($P2X_1$) is a ligand-gated ion channel which acts as an ATP receptor.(115) ADP is an antagonist to the receptor. Three ATP molecules may bind to the $P2X_1$ extracellular domain, triggering opening of the cationic core.(115) This core allows movement of the mono and divalent cations Ca^{2+}, Na^{+} and K^{+}, which then induce platelet shape change from discoid to spherical.(107)

Hechler *et al.* demonstrated $P2X_1$ to be shear sensitive. Mouse knockout models demonstrated that at low shear rates (800 s^{-1}), the degree of aggregation on a collagen substrate did not differ between $P2X_1$ knockout models and wild type mice.(58) However, in higher shear conditions (2,000-6,000 s^{-1}), thrombus formation from knockout mice blood samples was significantly decreased. This indicated that the $P2X_1$ knockout phenotype may confer resistance to thrombus formation in high-shear *in vivo* conditions.(58)

1.1.3.2.3.4. PAR1 and PAR4

PAR1 is the primary mediator for thrombin-platelet activity and activates platelets at low thrombin concentrations. It is activated by interaction with tethered ligand loops upon irreversibly cleavage by thrombin.(115) This activates G_q, G_{13} and G_i G-protein receptors, among others, which activate PLC-β isoforms, which through a signal transduction pathway results in alteration of platelet shape, and induces thrombin production and granule release.

1.1.3.2.3.5. TP

The prostanoid Thromboxane A_2 receptor (TP) is a G_q and $G_{12/13}$-protein coupled receptor. It exists in two isoforms: α and β, which differ in their cytoplasmic conformations.(116) Only Thromboxane alpha receptor (TPα) is found in platelets, while Thromboxane beta receptor (TPβ) is found in endothelial cells. Binding of TxA2 induces a calcium and granule release, integrin activation and platelet shape change.(100)

1.1.3.2.3.6. PGE_2 receptor

PGE_2 has a biphasic dose-dependent effect on platelet aggregation. At low concentrations aggregation is enhanced, but higher concentrations have an inhibitory action.(117) The proaggregatory effects of PGE_2 have been ascribed to the PGE_2 receptor EP3, which inhibits cAMP, thereby increasing calcium mobilisation and elevating P-selectin levels which increases cell-cell adhesion and platelet recruitment.(118)

1.1.3.2.3.7. PGI_2 receptor

The Prostacyclin I_2 receptor (PGI_2) is a glycosylated protein-coupled receptor that has wide distribution around the body.(3) This receptor can bind to Prostacyclin (PGI_2), Prostaglandin E1 (PGE_1) and Prostaglandin E2 (PGE_2). Upon receptor activation, membrane-bound AC catalyses formation of cAMP, which inhibits platelet aggregation.

1.1.3.3. Platelet aggregation

Platelet aggregation refers to the process by which platelets interact to form the haemostatic plug. Monolayer formation rapidly induces further platelet recruitment, forming a thrombus. This process occurs primarily through fibrinogen-integrin $\alpha_{IIb}\beta_3$ binding, though is mediated to a smaller extent by many other receptors.(56) This resultant platelet plug stops bleeding in most small blood vessels, but stabilisation is required in the event of larger bleeds. The third stage comprises platelet aggregation, wherein vWF and fibrinogen binding to integrin $\alpha_{IIb}\beta_3$ and GPIbα receptors leads to 3D thrombus growth.(77)

Release of granular contents is stimulated in activated platelets by interaction with soluble agonists, which activate heterotrimeric G-protein-couple receptors (GPCRs).(32) This release reinforces other prothrombotic events that arise from the activation phase, including integrin up-regulation and platelet shape change.

1.1.3.4. Primary haemostasis summary

Primary haemostasis, or the formation of the primary platelet plug, is one of the processes by which blood loss is controlled in times of injury. The initial platelet adhesion profile is characterised by shear experienced by the platelet, and in high-shear environments is dependent on vWF bound to the collagen on the exposed subendothelium, or to the vWF that is constitutively expressed.(56, 119) The open conformational state of the vWF allows the exposure of additional binding sites.(55) After initial vWF binding in areas of non-pathological shear, the platelet is slowed enough to enable longer-lasting bonds to be made with integrins, GPVI and collagen. The platelet alters its shape to aid rolling across the subendothelium and facilitation

of new bond substrates contacting.(27, 120) Platelets then aggregate around the initial platelet monolayer, sealing the site of injury to prevent further monolayer formation and produce thrombin.(121)

1.1.3.5. Secondary haemostasis

Thrombin is produced in the liver as prothrombin, which is then converted to thrombin through interaction with the prothrombinase complex.(122, 123) Thrombin then itself acts as a protease and cleaves fibrinogen to form fibrin, which stabilises the thrombus.(124) Generally, thrombin formation is initiated via the binding of activated FVIIa to Tissue Factor (TF) upon exposure of the subendothelium, or activation of platelets or peripheral red blood cells, which then results in prothrombin production though the coagulation cascade.(125) Activated platelets play a role in this process through expression of a surface that induces prothrombin cleavage. The resting plasma membrane is orientated so Phosphatidyl Serine (PS) is normally located on the cytoplasmic surface, but upon activation, transfers to the plasma-oriented side.(110) The negatively-charged PS surface on platelet membranes enhances the rate of conversion of prothrombin to thrombin in the clotting cascade.(126)

The final product of the coagulation cascade, fibrin (the cross-linked insoluble polymer of fibrinogen), helps stabilise the platelet thrombus.(63) Shear is an important consideration in this process, as it facilitates increased cross-linking of platelets through fibrin.(17)

1.2. Haemodynamics and thrombosis/haemostasis

Adhesion of platelets to a damaged vessel wall is not only dependant on adhesive receptors and the exposed subendothelial matrix, but by the local haemodynamic conditions.(51) Rheology - the study of physical properties of blood - and haemodynamics - the study of the characteristics of blood flow - have a complex interplay which alters thrombogenesis and platelet function.(127, 128)

1.2.1. Fundamental physics of blood flow

Forces that operate at the macroscale often become less dominant as the scale of the system decreases.(13) These changes are utilised in microfluidic devices to manipulate fluid behaviour. Many distinct fluid behaviours help to define flow conditions, including descriptions of laminarity and turbulence.(129) Laminar flow is ordered flow, best exemplified by a system in which there are two running parallel fluids with minimal mixing occurring.(130) In contrast, turbulent fluids constantly undergo changes in direction and velocity, and display a highly disordered motion. The high momentum in turbulent flow results in greater frictional forces. Reynold's number (Re) (*see Equation 1.1*) provides the ratio of inertial to viscous forces within the fluid system and quantifies the degree of chaos.(131) Flow systems with Re less than 2000 are considered laminar, and those above 2000 are considered turbulent.(132) Due to the small scale of system operation and the difficulty in inducing turbulence, most microfluidic flows have a Re of 1 or less, indicating flow is laminar.(133)

Equation 1.1 – Reynold's number

$$Re = \frac{\rho u L}{\mu} = \frac{ul}{v}$$

Where:

Re is the Reynold's number (unitless)

ρ is the fluid density (kg/m^3)

u is the viscosity of the fluid (kg/m·s)

L is the characteristic length (the scale of the system) (m)

v is the fluid velocity (m/s)

μ is the velocity of the fluid, relative to the other fluid or object (m/s)

1.2.2. Laminar flow and the concept of shear

Theoretically, fluid flow through a straight channel is characterised as having a laminar parabolic fluid velocity profile (Poiseuille flow) *(see Fig 1.6)*.(134) Fluid towards the centre of the vessel lumen flows faster than fluid at the edges, creating layers flowing at different speeds.(135) Layers closer to the vessel walls experience friction from interactions with the wall, and thus flow slower. It is the resulting different velocities of these layers that creates a frictional shear force.(136) In areas of greater velocity, such as in stenotic regions, the overall fluid pressure increases, and differences in velocities between layers increase exponentially, thereby increasing frictional, or shear, stress between layers.(137) Four parameters may be used to define simplified stenotic geometries in terms of shear (*see Fig 1.7*):

I. The degree of shear acceleration. This may be altered through changing the angle of acceleration to peak shear.
II. The peak shear. This may be altered by changing the width of the stenotic gap itself.
III. Time spent at peak shear. This may be predicted by the length of the stenosis.
IV. The degree of shear deceleration. This is a measurement of how quickly particles may return to the area of low shear from the peak shear.

However, the theoretical model of blood flow is not a true representation of fluid behaviour - whole blood is a non-Newtonian fluid, and as such its viscosity is not constant, but rather changes dependant on applied stress.(136) The true representation of fluid layers is less parabolic due to this compressibility.(138) Additionally, areas of circulation with branching and tortuosity introduce turbulence to the flow as the layers mix and combine, and cell-cell interactions will also alter flow profiles.(139) Finally, the vascular tree is mutable and adaptive to changes in pressure – in the short term, shunting vessels may alter blood flow through small arteries, and in the longer term, areas of the vasculature with slow-growing occlusive thrombi may develop a collateral circulation supply, lowering shear forces platelets experience as they travel through the region.(140)

1.2.3. Shear stress

Shear stress is caused by differences in velocities of adjacent blood layers in a laminar flow system.(141) Shear stress of a Newtonian fluid flowing with laminar flow in an ideal world is modelled as a function of flow, lumen radius and viscosity (*see*

Equation 1.2). As the radius of the tube increases or flow decreases, or flow increases, shear stress increases proportionally.(142) Quantification of the velocity differential between adjacent fluid layers is termed the shear rate and is another component of shear to be addressed in platelet function analytic design.(143) Greater velocities result in greater drag from friction between adjacent blood cells and vessel walls. Due to this force, the speed of the fluid is zero (essentially, fluid in this layer is stuck to the boundary). However, at some distance from the boundary, flow rates must equal fluid flow speeds. This area is termed the 'boundary layer' and has important applications in flow-based microfluidics, particularly involving platelets, as cell capture in platelet aggregation has a direct correlation with shear rate.(144, 145) Mathematical modelling explains the correlation between velocity and wall shear stress (*see Equation 1.2*).(50, 102, 113)

Equation 1.2 Shear stress(17, 46, 68)

$$\tau = \frac{4\eta q}{\pi r^3}$$

where:

τ = Wall shear stress (Pa)

η = blood viscosity ($N \cdot s/m^2$)

q = flow rate (µl/min)

r = vessel radius (m)

1.2.4. Shear rate

Shear rate is another expression of shear forces experienced by particles.(119) It is a measure of the velocity gradient between fluid layers measured in inverse seconds. Shear rate in veins and large arteries are generally accepted to be 20-2,000s^{-1} but may be greater than 50,000s^{-1} at points of severe stenosis in coronary arteries.(38, 146)

1.2.4.1. Modelling blood flow behaviour in microfluidic systems

Approaches to flow considerations involve numerical analysis methods. These include consideration of the Péclet number (Pe, *see Equation 1.3*). This refers to the ratio of the rate of advection (active movement) of a substance to the rate of diffusion. Microfluidic devices under laminar flow have low Péclet numbers, indicating mixing predominantly occurs through diffusion.(147, 148)

Equation 1.3 – Péclet number

$$Pe = \frac{Convection\ time}{Diffusion\ time} = \frac{L \times u}{D}$$

Where:

Pe = Péclet number (unitless)

L= length (m)

D=mass diffusion coefficient (m^2/s)

u= flow velocity (m/sec)

The other equation of importance is the Navier-Stokes equation (*see Equation 1.4*).

Equation 1.4 - Navier-Stokes equation

$$\rho\left(\frac{\partial u}{\partial t} + u \cdot \nabla u\right) = -\nabla p + \nabla \cdot \left(\mu(\nabla u + (\nabla u)^T) - \frac{2}{3}\mu(\nabla \cdot u)I\right) + F$$

Inertial forces | Pressure | Viscous forces | External forces

Where:

u is the fluid velocity (m/s)

p is the fluid pressure (Pa)

ρ is the fluid density (kg/m^3)

μ is the fluid dynamic viscosity (g/cm^3)

t is the time (seconds)

F is the sum of the external forces per unit mass which sustain the motion (N)

T is the temperature (K)

I is the unit tensor

The Navier-Stokes equation describes the impact of temperature, density and pressure on a moving Newtonian fluid.(149, 150) It arises from the application of Newton's second law to fluid motion. Linearisation of the Navier-Stokes equation provides the equation of motion for creeping, or ‘Stokes’, flow which describes the

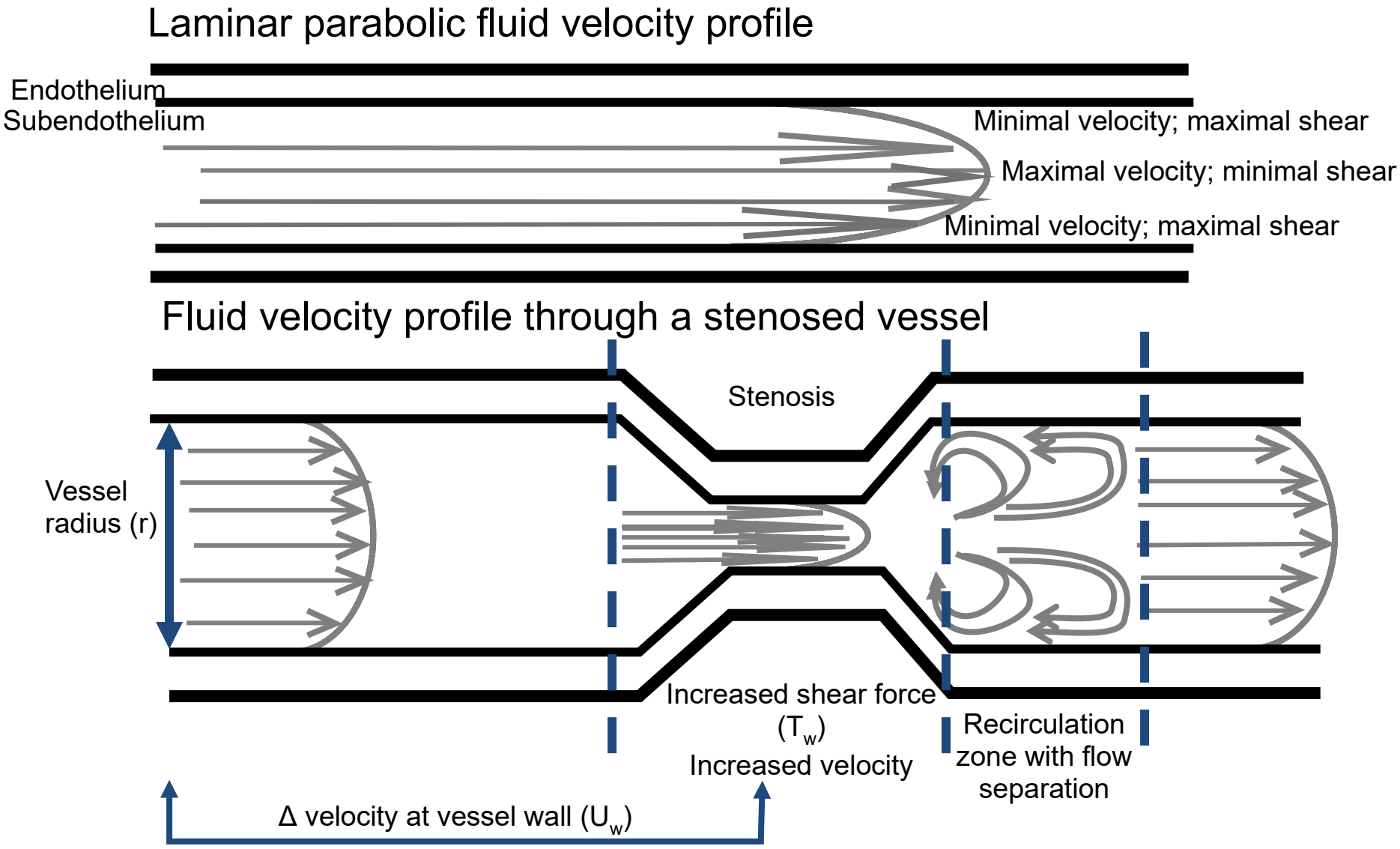
Laminar parabolic fluid velocity profile
Endothelium
Subendothelium
Minimal velocity; maximal shear
Maximal velocity; minimal shear
Minimal velocity; maximal shear
Fluid velocity profile through a stenosed vessel
Stenosis
Vessel radius (r)
Increased shear force (T_w)
Increased velocity
Recirculation zone with flow separation
Δ velocity at vessel wall (U_w)

Figure 1. 6 Laminar parabolic fluid velocity profile

Theoretically, flow in blood vessels displays a laminar parabolic profile where flow close to the walls is slower than flows towards the centre of the lumen.(152) Differences in velocities results in friction between layers. This friction, or shear, is influenced by: i) shear rate, or the difference between adjacent velocities, ii) shear stress, or the degree of force between the layers, and iii) blood viscosity, or the internal resistance in flow arising from intrinsic properties in the fluid.(119) In reality, blood demonstrates a flatter parabolic profile than expected due to its high viscosity, and cell-cell interactions within the fluid may also alter fluid dynamics.

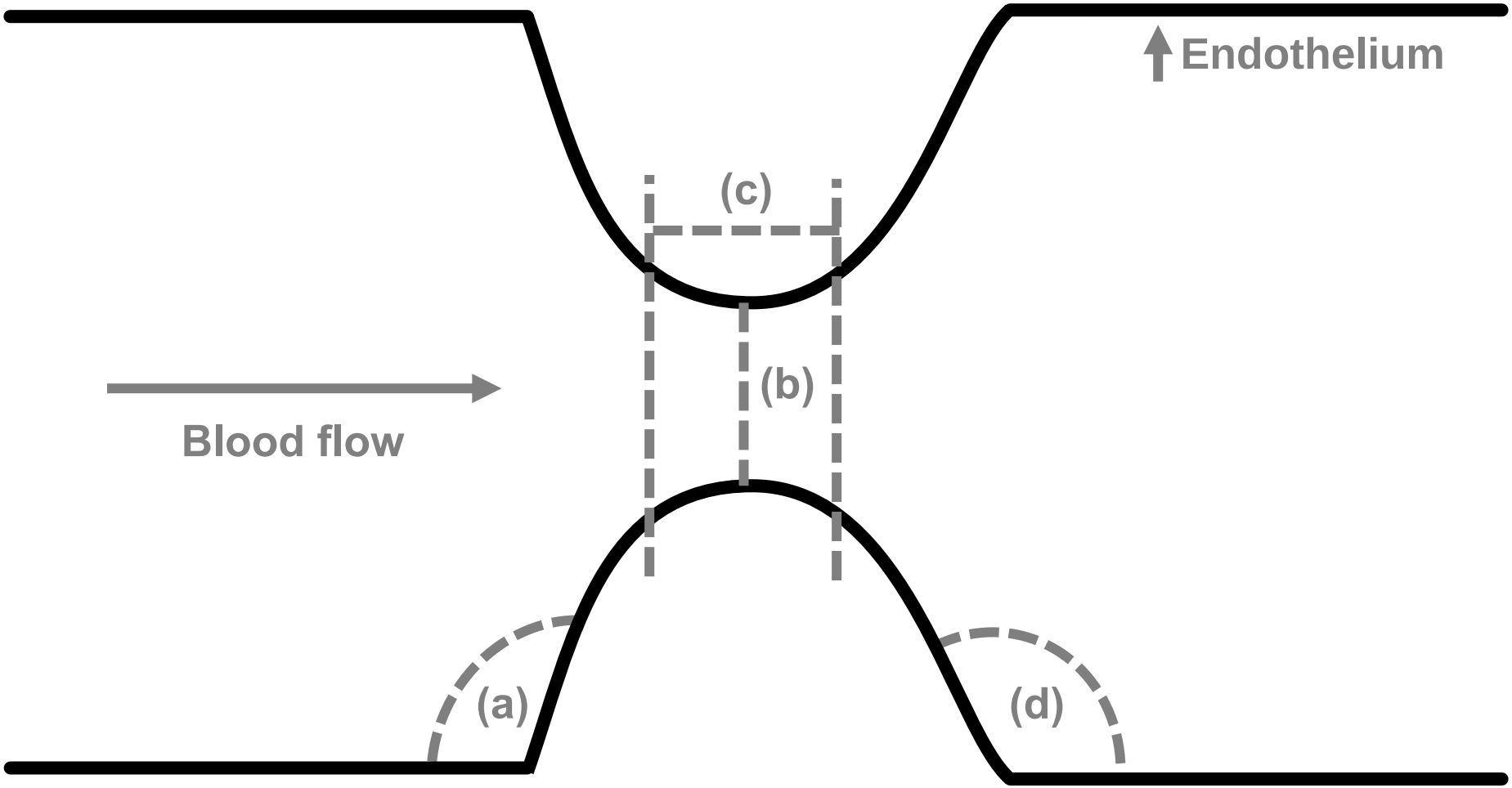
Endothelium
(c)
(b)
Blood flow
(a)
(d)

Figure 1. 7 Simplified stenotic geometry parameters

In a simplified stenotic environment, four main factors can be used to describe stenotic architecture. These are: the rate of change of shear stress into the stenosis, which may be altered by changing the degree of stenotic angle arising from the endothelium (a); the degree of peak shear (b), which is determined by the size of the stenotic width; the time spent at peak shear (c), which is determined by the length of the stenosis in the direction of blood flow; and the rate of deceleration away from the area of peak shear (d), which is altered by the angle the stenosis makes with healthy endothelium.(82, 153) In reality, the model is complicated by an uneven endothelium, the presence of multiple stenotic regions, cell-cell interactions, blood being a non-Newtonian fluid, and tortuosity and branching of the blood vessels.

fluid flow in micro-scale devices where the Reynolds number is less than one.(151) This flow is characterised by low inertial forces, and viscous forces predominate. Both the Navier-Stokes equation and the Péclet number assists in the computational fluid dynamic analysis necessary in the modelling phase of device design.

1.2.5. The role of shear in the adhesion phase

Experimental studies have demonstrated higher shear forces cause unfolding of the tightly-bound vWF, allowing greater exposure of the active (A1) domain on vWF.(59) This results in greater platelet binding and activation. Haemodynamic studies have also demonstrated that greater shear in blood vessels results in axial displacement of the smaller, non-deformable platelets towards vessel walls by erythrocytes, which results in a greater chance of platelet exposure to thrombogenic exposed subendothelium.(154, 155) This process of platelet displacement is termed platelet margination and plays an important role in aggregate growth at the vessel wall.(156, 157)

Shear has also been shown to play a role in integrin activation: supraphysiological shear stress alone can activate integrin $\alpha_{IIb}\beta_3$ expression in the platelet via inside-out signalling.(56) It has been established that the degree of activation of the $\alpha_{IIb}\beta_3$ expression increases with increasing the shear stress level and exposure time.(158) However, in areas of extreme pathological shear ($> 10{,}000\ s^{-1}$), integrin $\alpha_{IIb}\beta_3$ is not required for platelet aggregation.(82, 103) Additionally, preliminary research has demonstrated shedding of integrin $\alpha_{IIb}\beta_3$ in areas of non-physiological high shear, paradoxically reducing platelet function.(146)

1.2.6. The role of shear in the aggregation phase

Generally, increasing shear promotes platelet aggregation through increasing collision efficiency frequency (due to increased reactant velocity), and activation of distinct platelet aggregation pathways.(82, 159) At low shear rates (<1,000s^{-1}), integrin $\alpha_{IIb}\beta_3$-promoted aggregation by fibrinogen-ligand binding dominates and stable aggregation occurs between shaped-changed platelets.(79) Discoid platelets then form membrane tethers mediated by both GPIb and integrin $\alpha_{IIb}\beta_3$, facilitating further aggregation.(79, 160) As shear rates increase, aggregation becomes progressively more dependent on vWF-GPIb binding. In areas of pathological shear (>10,000s^{-1}, as in the case of vessel stenosis), vWF-GPIb predominates, and binding can occur without prior platelet activation.(82) Higher shear forces also increase the chance of aggregate embolisation, further complicating binding kinetic studies and aggregate computer modelling.(119)

1.2.7. The role of shear in enzymatic activation in development of thrombus stability

The degree of shear also determines enzymatic activation profiles, including PI3K isoforms.(161) The intracellular signal-transduction family of PI3K isoforms plays important roles in platelet signalling, membrane remodelling, and cytoskeleton re-organisation.(28) PI3Kβ is mandatory for thrombus stability at high shear, though still active at physiological shear.(162) In contrast, the other major PI3K isoform, PI3Kα has no role at high shear, and only plays a major role in low-shear environments.(162)

1.2.8. Rheological factors affecting shear stress

Blood components and vascular changes may also alter shear stress independent of the physical vessel properties, and must be considered when calculating shear rates. In systems approximating laminar flow conditions, shear stress is proportional to flow rate. Increased velocity in atherosclerotic regions disturbs flow in the region immediately downstream, which then promotes protein and proinflammatory gene expression conducive to atherosclerotic growth, thrombus instability and plaque growth.(73, 119, 146) Equation 1.2 demonstrates that vessel lumen radius inversely affects shear rates, and vessel narrowing will markedly increase local shear stress.

In terms of cellular content, red cells comprise 30-60% of whole blood samples and their deformability can significantly affect shear conditions, particularly in small vessels.(156, 163) Erythrocyte deformability is determined by cholesterol content in the phospholipid bilayer, haemoglobin content and flow parameters.(164) Red blood cells have been shown to demonstrate active responses to shear stress through regulation of the membrane skeletal proteins and integral proteins with attachments to the lipid matrix.(164) These changes in deformability can then alter the degree of margination and platelet collisions.(156)

Haematocrit also influences shear stress, particularly at the vessel wall.(165) As the haematocrit increases, wall shear stress decreases, and this effect is more marked at higher flow rates. Blood viscosity also influences shear, as greater viscosity acts as inherent resistance to flow.(152) As viscosity increases, more frictional interactions between blood cells and plasma proteins increase the shear force between layers.(166, 167)

1.3. A shear-based haematological pathology: von Willebrand Disease

von Willebrand Disease (vWD) is a bleeding disorder in which patients have quantitatively or qualitatively low levels of vWF, and experience increased severity and prolongation of bleeding events, generally with a positive family history.(47) vWD is the most common inherited bleeding disorder in Western populations, with an estimated 1% population prevalence, though only 1/10,000 people have clinically significant disease.(168, 169) The female preponderance in diagnosis is thought to be due to increased likelihood of bleeding events, such as menstruation and childbirth.(170) ABO blood grouping is also epidemiologically significant, as individuals with group O blood generally have lower vWF levels than those of type A, B or AB, increasing diagnostic rates in this population.(171)

1.3.1. von Willebrand clinical classifications

vWD can be classified into three distinct categories, which are then subdivided according to results on functional assays (*see Table 1.2*).

1.3.2. Current diagnostic guidelines

The current approach to patients presenting with mucocutaneous bleeding is to collect a focused patient history (including family history), specifically considering interventions following iatrogenic bleeding events (such as dental extractions) and a general medication review.(170) There is no single diagnostic guideline, with processes varying between healthcare institutions. Attempts at questionnaire standardisation (bleeding assessment tools) lack sensitivity and specificity, particularly between sub-classification variations.(172) Additionally, several literature reviews on the diagnostic approach to vWD have found these tests lack correlation

Table 1.2: vWD classification(175-179)

Classification	Sub - classification	Pathophysiology	Inheritance pattern	Proportion of vWD cases
Type 1 Quantitative defect	-	Partial quantitative vWF deficiency.	Mutation may occur at any point in the gene but is particularly common at the D3-4 gene domains, resulting in decreased vWF secretion and increased cleavage and clearance. It generally arises as a point missense mutation and is fully penetrant with dominant inheritance.	70%
Type 2 Qualitative defect	A	Deficiency of high molecular weight vWF multimers due to a defect in assembly or increased cleavage.	Defects in multimer assembly may be caused by mutations in the CK, D1, D3 or propeptide domains, or increased sensitivity to cleavage	Most frequent subtype classification

		in the A2 domain. It is generally a missense mutation.	
B	Increased vWF affinity for platelet GPIb leads to increased platelet binding to vWF, which is then cleaved, resulting in accelerated clearance and decreased vWF function.	Caused by a mutation in the A1 domain, causing a gain-of-function missense mutation. This results in increased proteolysis and decreased size of vWF multimers.	Least frequent subtype classification
M	Decreased vWF-dependent platelet adhesion with a normal multimer distribution.	A1 and A3 domain mutation causing decreased binding of vWF to platelets or subendothelium.	Third most frequent subtype classification
N (Normandy)	Markedly decreased vWF binding affinity for FVIII.	A D’ or D3 domain missense mutation which impairs vWF binding to FVIII. It is found in	Second most frequent

		exons 18-20 with autosomal recessive inheritance.	subtype classification
Type 3 **Quantitative defect**	Near-total deficiency of vWF	Characterised by defective synthesis of vWF due to inheritance of two defective alleles (recessive inheritance). It may be found anywhere in the coding region of vWF (exons 2-52).	<5%

There are also two disease phenotypes which closely mimic vWD presentation. Acquired von Willebrand syndrome is characterised by an initial disease process, such as hypothyroidism, essential thrombocythemia or a Wilms' tumour, resulting in loss of vWF function. Additionally, pseudo-vWD arises due to mutations on exon 2 of the GPIbα gene sequence and is instead characterised by poor vWF:GPIbα binding due to platelet changes.(176)

However, vWD sub-classification diagnosis in a clinical setting is rarely straightforward; pathology is difficult to separate from normal bleeding states, as some patients may have an unremarkable bleeding history but low vWF and vice versa.(180, 181) Diagnosis is further complicated by heterozygosity of genetic variants and the impact of environmental factors on bleeding risk, such as the immutable factors of age and blood group, or transient risk factors such as exercise, stress or inflammatory states.(168)

Table 1.3: vWD-specific testing(173, 175, 182-184)

Test	Method	Detection
vWF:Ag* (levels of vWF antigen)	Enzyme-linked immunosorbent assay (ELISA) testing quantifies vWF antigen levels with a polyclonal antibody.	Detects levels of vWF and is correlated with functional testing to determine vWD classification.
vWF:RCo* (vWF to ristocetin cofactor)	In the presence of vWF, ristocetin promotes platelet agglutination, though newer techniques include an ELISA assay with recombinant GPIb fragments with or without ristocetin.	Measures vWF activity and function - measures interaction of vWF with GPIb/IX/V complex specifically.
vWF:RCo/vWF:Ag*	Ratio of values obtained from above two tests.	Differentiates type 1 and 2 vWD, as type 1 results in a concomitant depression in both and therefore the ratio stays close to 1. In type 2, the ratio decreases as vWF:RCo decrease is disproportionate to the vWF:Ag level.

vWF:CB	Measures ability of vWF to bind to collagen.	Measures vWF activity and function, quality of interaction with collagen, but not interaction with platelets.
FVIII:Ag	Immunoassay to detect FVIII levels.	Detects levels of FVIII – important in type 2N.
FVIII :C*	Measures coagulation factor VIII in the blood.	Severely decreased in type 3 vWD, moderate depression in type 1 or 2 vWD due to lack of concomitant vWF stabilisation.
vWF:FVIIIB (vWF to FVIII binding assay)	Measures interaction of recombinant FVIII with patient vWF in an in-vitro ELISA assay.	Measures capacity of vWF to bind to FVIII, diagnostic of poor FVIII binding, as seen in 2N.
Ristocetin-induced platelet aggregation (RIPA)	Aggregometry testing with ascending ristocetin concentrations.	Confirms hyperactivity of vWF as seen in type 2B if aggregation occurs at lower ristocetin concentrations.
vWF propeptide (pp)	vWF propeptide levels in serum.	Quantifies vWF propeptide levels.
vWFpp/vWF:Ag ratio	Measured ratio of propeptide to antigen levels.	Can quantify increased vWF clearance levels, as pathological vWF clearance does not also impact on propeptide clearance.

Multimer analysis*	Gel electrophoresis separation and purification of multimers.	Distinguishes different type 2 vWD subtypes by multimer size separation.

Other testing options include genetic analysis, ELISA vWF propeptide levels and a desmopressin (DDAVP) trial

*Standard laboratory diagnostics to determine broad vWD classification(175, 185)

with vWD patient laboratory results.(168, 173-175) Table 1.3 summarises the specific assays that may be requested in a patient for whom the diagnosis of vWD is being queried, following generic blood assays.

1.3.3. Treatment and management of von Willebrand Disease

Current treatment options are guided by patient disease classification and the degree and nature of bleeding. Options can be divided into indirect measures, including measures which physically halt bleeding and adjunctive therapies, and direct measures, which act to directly increase vWF and FVIII.(173, 186) Direct treatment of vWD aims to correct the dual haemostatic defects of FVIII deficiency causing abnormal coagulation, and defective platelet adhesion and aggregation due to vWF deficiency. Clinically, desmopressin may be used to increase vWF and FVIII levels.(187, 188)

1.3.3.1. Desmopressin therapy

Desmopressin is a synthetic vasopressin (ADH) analogue which increases endogenous vWF by inducing secretion from WPB in the vascular endothelium.(189) However, it is only a short-term therapeutic solution, as levels of vWF and FVIII return to deficiency in 6-8 hours, necessitating repeat dosing.(190) Treatment is further complicated by refractory responses on repeated administration of desmopressin. Choice of desmopressin administration is highly dependent on the classification of vWD patients: it is most effective in most type 1 patients and is considered ineffective in type 3 disease.(187) Patients with type 2 vWD require a more considered approach. Patients with types 2A and 2M show variable responses and require a therapeutic trial. Desmopressin is contraindicated in patients with type

2B due to the risk of transient thrombocytopenia. Desmopressin therapy induces a FVIII rise in Type 2N patients, but it has a significantly reduced half-life, so is only used in minor bleeding episodes.(188, 190)

1.4. Platelet function diagnostics in the clinical and preclinical environment

Given the epidemiological impact of bleeding disorders (such as vWD) and atherosclerosis in modern society, the need for platelet function analysers have never been greater.(116) Currently, there is no consensus regarding gold standards in many platelet function diagnoses because a threshold for diagnosing poor platelet function has not been agreed upon.(165, 191-193) Practically speaking, most of these tests also require expensive and specialised equipment and technicians with laboratory access, and use larger volumes of patient blood than is optimal.(194) Additionally, these methods have not be extensively shown to predict poor outcomes, with some patients with very low platelet function managing well in the community, and vice versa for those with near-normal levels.(195)

A key difficulty with many of these assays is that shear is not considered, meaning that samples are not tested under physiologically-accurate conditions. Development of new devices that utilise the principles of microfluidics in a physiologically-appropriate environment could provide new standard laboratory testing for coagulopathies that is more reliable and overcomes many of these issues. Current platelet function analysers rely on initiation of platelet aggregation from exogenous biochemical stimuli. Often, they fail to incorporate physiologically relevant haemodynamic parameters, and are significantly removed from the normal haemostatic environment.(196) There is therefore a critical shortfall in devices that utilise and mimic shear-dependent platelet activation processes. Development of

new devices that utilise microfluidics principles in a physiologically-appropriate environment could pave the way for a new laboratory test that demonstrates greater specificity and sensitivity in the diagnosis of platelet function disorders.

Additionally, current pharmacologic interventions in the treatment of thrombotic disease are not optimal: they are slow to act, have significant variability in efficacy and due to their narrow therapeutic window, present significant bleeding complications.(197, 198) Microfluidic devices offer the potential for rapid drug screening that can identify novel pharmacologic agents that may be better optimised to prevent cardiovascular disease.

Due to these difficulties, the International Society of Thrombosis and Haemostasis developed a list of recommendations for platelet function assays under development:(192, 193)

- Ease of performance;
- Quick;
- Highly reliable;
- Provides robust results;
- Provides accurate results regarding risk of bleeding and thrombosis; and
- Employs and allows for alteration of flow conditions, bioequivalent endothelial mimics, and environmental conditions such as pH and temperature.

Technologies that assay platelet function may be divided into flow and non-flow classifications. Non-flow assays use biochemical markers, or directly measure platelet aggregation in static conditions. Flow methods may be more physiologically

relevant, as they more accurately depict the environment in which aggregation occurs. An overview of these tests is provided in Table 1.3.

1.4.1. Shear-based assays

Currently available shear-based assays replicate physiological conditions of flow better than the other assay systems, but often they are not widely available, there is limited clinical testing and validation, and they act as poor shear mimetics of the vasculature.(165)

1.4.1.1. PFA-100

The Platelet Function Analyser-100 (PFA-100) system is the most commonly-utilised shear-based platelet function diagnostic in use clinically.(199) It is a nominally-shear based system, as it still requires the addition of exogenous agonists. The system consists of a collagen membrane with a 150 µm collagen-coated aperture through which blood flows, creating a high-shear environment.(200) Aggregation is induced through treating the blood with either ADP or adrenaline to act as a soluble agonist. Results are quantified in terms of time taken for complete occlusion of the aperture to occur and are indicative of high-shear platelet function.(201) This system is one of the most commonly used, as it requires only 800µL of blood, is rapid, cheap and fully automated.(202) However, patients must have a minimum platelet count of $80x10^9$/L, normal haematocrit and vWF levels, and cannot be prescribed integrin $\alpha_{IIb}\beta_3$ or $P2Y_{12}$ inhibitors.(205) Significantly, platelets are not assessed in true shear-based conditions in the PFA-100, and the device is not an accurate physiological mimic. Due to these reasons and the lack of correlation with bleeding severity, clinical uptake has been poor.(206)

Table 1.4: Clinical and pre-clinical platelet analysis methods(111, 195, 203-205)

Test	Assay design	Advantages	Disadvantages	Clinical applications
Platelet-platelet aggregation assays				
Turbidimetric platelet aggregometry	Platelet-Rich Plasma (PRP) is exposed to an agonist and light transmission quantifies platelet aggregation	Historical gold standard, correlates well with clinical outcomes	Variable reproducibility of findings, slow sample turn-around, large sample volume, requires a trained technician and sample preparation	Platelet disorder diagnosis, anti-platelet therapy monitoring, haemostasis, platelet hyperfunctioning
Impedance platelet aggregometry	As above but measures electrical impedance instead of light transmission	Whole blood assay, as above	Expensive, large sample volume required, slow sample turn-around, requires sample preparation	Platelet disorder diagnosis, anti-platelet therapy monitoring
Laser platelet aggregometry	As above but measures aggregation using laser light	Sensitive, detects microaggregates	Little previous clinical application	Platelet hyperfunctioning
VerifyNow®	Measures changes in light transmission in stimulated	Simple, small blood volume required, whole-blood assay (minimal	Lack of capacity for instrumental adjustment, further research on	Anti-platelet therapy monitoring

	platelets exposed to fibrinogen-coated beads	preparation), available as a point-of-care assay, can be used for anti-platelet therapy monitoring	characterisation required, limited range of testing of haematocrit and platelet count	
Ichor Plateletworks™	Detects platelet counts before and after agonist addition	Whole-blood assay, quick, simple, small blood volume required	Needs further characterisation, limited clinical application	Bleeding prediction, anti-platelet therapy monitoring
Biochemical assays				
Soluble platelet release markers	ELISA assay	Simple to use	Prone to error	In-vivo platelet activation
VASP phosphorylation	Flow cytometry-based detection of activation-dependent platelet signalling	$P2Y_{12}$-dependant, small blood volume required, whole-blood assay	Sample requires preparation, expensive, requires experienced staff and specialised equipment	Thienopyridine irreversible ADP receptor/$P2Y_{12}$ inhibitor monitoring
Serum thromboxane B2	Measures the concentration of an active metabolite of TxA_2	Simple, measures thromboxane metabolic in serum	Not platelet specific	Monitoring of aspirin, thromboxane production defect diagnosis

Urinary 11-dehydrothroboxane B2	Measures the concentration of a urinary metabolite of TxA_2	Simple, measures thromboxane metabolic in urine	Not platelet specific, impacted by renal function	Monitoring of aspirin, thromboxane production defect diagnosis
Platelet surface P-selectin and activated Integrin $\alpha_{IIb}\beta_3$, leukocyte-platelet aggregates	Uses flow cytometry to measure activation-dependent platelet surface changes via fluorescence	Low sample volume, whole blood assay, variety of testing options	Requires sample preparation, expensive, requires experienced staff and specialised equipment	Anti-platelet therapy monitoring, platelet activation detection, platelet glycoprotein defect diagnosis
Endogenous thrombin potential assay	Measures thrombin generation	Can use a range of blood products, including: whole blood, platelet rich plasma (PRP) and platelet poor plasma (PPP)	Requires specialised equipment	Prothrombotic therapy monitoring, detection of clotting defects, measurement of platelet function
Viscoelastic testing				
Clot retraction	Measures the interaction of fibrin with platelets	Simple	Not specific results	Integrin $\alpha_{IIb}\beta_3$ and fibrinogen production and qualitative defects
Thromboelastography/	Assesses the contribution of platelets to clot strength and rate of clot formation	Available as a point-of-care assay, whole blood assay	Not platelet specific, needs further characterisation	Surgical bleeding risk prediction, Integrin $\alpha_{IIb}\beta_3$ inhibitor monitoring,

Rotational Thromboelastometry (ROTEM)®				Recombinant activated factor VII (rFVIIa) therapy monitoring
Other tests				
Blood film	Microscopy of whole blood	Simple, may be diagnostic	Contamination is common	Platelet defects in number, size, or cytoplasmic organisation
Full blood examination (FBE)	Uses flow cytometry to analyse cell number and other specific parameters	Quick	May be inaccurate due to cell factors	Platelet defects in number, size, or distribution
Haemostasis analysis System	Measures the elasticity of in-vivo clots, contractile force of platelets and thrombin generation time	Quick, simple, available as a point-of-care assay	Only measures properties of in-vivo clot formation	Bleeding predictive score, thrombosis predictive score, rFVIIa therapeutic monitoring
Hemostatus device	Measures procoagulant activity of platelets	Simple, available as a point-of-care assay	Insensitive to aspirin and GPIb function	Predictive bleeding score
Bleeding time	A small incision is made in the forearm and time taken to clot is measured	Physiological, in-vivo testing, available as a point-of-care assay	Painful, produces scarring, not sensitive or	Coagulopathy screening

			specific, low reproducibility	
Bleeding score	A standardised set of questions to ask patients with a history of bleeding and deliver a grade or score to determine if the degree of bleeding is pathological.	Simple, available in-clinic, provides information regarding bleeding history	Low degree of predictive power of future bleeding events, slow to perform in clinic, clinician variation	Assessment of bleeding history
Animal models				
In-vivo models	Typically involve an induced thrombogenic environment in the vascular system, through either insertion of a shunt, electric current application, thrombotic drug injection, vessel super-cooling, laser thrombosis induction or	Murine models are low-cost, require minimal housing areas, smaller drug samples to reach physiologically-relevant concentrations, multiple experiments can be performed simultaneously, and they have greater reproductive potential than other animal models. Extensive	Differences from human anatomy and physiology must be considered: their smaller vessel area and platelet size, different genetics, life span and body size may alter the way their platelets behave and respond to external pharmacologic influence. Models that are more accurate to human	Most common form of drug screening

	introduction of a foreign body	scientific literature regarding experimental protocols to guide the investigation	physiology are more expensive and ethically fraught	
Bleeding models	Involve incision or transection of tissue (e.g. tail) and measurement of the time until bleeding cessation	Provide a physiological model	Not specific or sensitive, results demonstrate low reproducibility	Evaluate the propensity for haemorrhage upon administration of an antithrombotic agents, and the endogenous effect of these agents
Shear/flow-based assays				
Platelet function analyser 100 (PFA-100)	Measures platelet aggregation and adhesion in a high-shear environment during clot formation	Simple, quick, small blood volume required, whole-blood assay (minimal preparation), high-shear experimental conditions, available as a point-of-care assay	Dependant on vWF levels and haematocrit, insensitive to some anti-platelet therapies, lack of capacity for instrumental adjustment	Screening for defects in primary haemostasis, anti-platelet therapy monitoring, monitoring of desmopressin therapy
Image analysis, Monitoring, Platelet,	Provides quantification of platelet aggregation and adhesion onto a surface	Simple, quick, small blood volume required, high-	Requires pipetting, not widely available	Screening for defects in primary haemostasis, anti-platelet therapy

Adhesion, Cone and plate Technology (IMPACT)	in a high-shear environment	shear experimental conditions		monitoring, platelet hyperfunctioning
O'Brien filterometer	Detects platelet function in high-shear environment	Easy to use	Not an accurate physiological study, requires specialised equipment	Defects in primary haemostasis
Gorog Thrombosis Test	Platelet function and thrombolysis in high-shear environment	Easy to use, quick, available as a point-of-care assay	Not widely available	Defects in primary haemostasis

1.4.1.2. Impact™ cone and plate analyser

The cone and plate analyser systems use whole blood in near-physiologic conditions to assess platelet function by monitoring platelet adhesion on a polystyrene plate.(207) The resulting adhesion and aggregation is assessed via microscopy by the parameters of surface area coverage in shear rate ranges of 500-5000 s^{-1}.(208) This assay system is simple, rapid, requires small blood volumes and is fully automated. However, it is highly operator-dependent and strongly affected by patient haematocrit levels.(209)

1.4.1.3. VerifyNow®

The VerifyNow® system was initially developed as a means of antiplatelet therapy monitoring, for which promising research has emerged regarding data and clinical correlation.(210) There has also been limited research into applications for bleeding defect diagnosis and monitoring. The system uses citrate-anticoagulated whole blood mixed with fibrinogen-coated styrofoam beads and tests light transmission through stimulated platelets as platelet aggregation occurs.(211) However, there is a current lack of capacity for instrumental adjustment in the VerifyNow® system and further clinical characterisation is required.(195)

1.4.2. Platelet function testing and microfluidics

Microfluidics refers to precise control and manipulation of fluids on the micro scale.(14) Through miniaturisation, throughput can be dramatically increased, and fluid volumes and processing times can be reduced.(212, 213) As it is still a novel field, the potential it holds is far from being actualised. Miniaturised platforms hold

great potential in areas such as physiological research, drug discovery and point-of-care screen tools. Point-of care-testing systems are advantageous because they provide faster turnaround times than laboratory-based testing, use whole blood and thus can identify diseases arising from interactions between blood components, and provide real-time analysis and output. However, these benefits must be weighed against increased training requirements for non-haematological staff members to use these devices, potential decrease in quality control and increased costs.(214)

Microfluidic systems are advantageous due to the low sample and reagent volumes required, low cost, high portability and better physiological mimicry.(215) Possibility of integration is another key benefit. Most microfluidic chips aimed for commercial production are designed towards multifunctionality. Micro total analysis systems (μTAS) or 'Lab on a Chip' devices are microfluidic systems that encompass all functions in a contained unit.(16, 216) These systems may integrate many variations to alter flow, both active and passive, such as reservoirs, valves, micromixers, pumps and electrodes. These systems are designed to independently complete all steps of the scientific process, including sample preparation, incubation, mixing, separation and detection of results.

Development of microfluidics devices may greatly assist in the standardisation of vWD diagnosis and other shear-based platelet function disorders by providing a device which yields consistent results. When used as an adjunct with conventional assays, they may be a useful therapeutic tool to screen for the presence of a coagulopathy through testing patient blood in a variety of physiologically-matched conditions. Additionally, after administration of transfusion therapy, patients require vWF:RCo and FVIII monitoring at various time intervals, according to specific

organisational policy.(188) Microfluidic devices have the potential to reduce required blood volumes and waiting times for test results for therapeutic monitoring, and may provide greater reliability of testing.(193, 194, 217) Microfluidics may fill a critical niche in vWD diagnostics and monitoring, providing a clinical testing option that uses lower patient blood volumes, and rapid real-time monitoring with better mimicry of physiological environments.

It has been established that conditions of pathological stenosis have many implications in medicine, the most serious of which is atherosclerosis.(218, 219) It is through understanding the haemodynamic perturbations that arise in stenosed vessels that progress can be made towards effective therapeutic interventions. The microfluidic devices detailed below also offer control of biorrheological parameters such as shear rate and shear stress to a fine degree, enabling isolation of haemodynamic variables, offering opportunities for further research.(17)

1.4.2.1. Bioflux

The experimental Bioflux system can test blood in a range of shear stress up to 200 dyne/cm^2 in a physiologically relevant microfluidic, including with a pulsatile flow profile.(220) The system works with collagen-coated microchannels, which capture fluorescently labelled platelets passing over the coating.(221) An automated detection system then records thrombus formation and calculates the area and fluorescent intensity of the aggregate. Advantages of the Bioflux include its simple operation, high reproducibility, and high throughput analysis.(221) However, the system is expensive to run and has not been characterised in a range of disease states.

1.4.2.2. T-Tas

The Total Thrombus Formation Analysis System (T-Tas) is an automated flow chamber system that has been characterised in several disorders, including platelet storage pool disease, FIX and FVIII deficiencies and vWD.(222) The device simultaneously analyses platelet thrombus formation using two parallel microfluidic systems. Blood is flowed through thrombogenically-coated microchannels at shear rates between 110-2400 s^{-1} until aggregates form that are large enough to occlude channel flow.(223) the system then analyses thrombus formation through channel pressure. Recent evaluations of T-Tas correlation with standard clinical tests have revealed good correlation with Light Transmission Aggregometry (LTA) results and the PFA-100, while the VerifyNow assay demonstrated poor correlation.(222)

1.4.2.3. Microfluidic systems in development

Use of microfluidics in analysis of platelet function is not a new concept.(224) Microfluidic devices are advantageous in clinical and preclinical settings for a number of reasons: they have the potential to use much smaller blood volumes than their conventional counterparts, use smaller reagent volumes and have subsequent reduced costs. They also have the potential to achieve greater control of haemodynamic variables producing better biological mimicry. With improvements in biomimicry, these devices could potentially reduce or eliminate the requirements for costly and ethically-fraught animal models.(225) This control could also allow microfluidics to replace traditional *in vitro* cell culture processes, as they can be patterned with a variety of flow regimes and regions of analysis can be reduced to two-dimensions, simplifying results. It is also hoped that, with development, they will allow for shorter sample turnaround times, greater ease of operation, higher

resolution and sensitivity and greater design mutability than current devices in operation.(180) In terms of improvements to diagostics, lab on a chip devices may also demonstrate greater portability, though research into the miniaturisation of all components required is still in its infancy.(226)

Additionally, current platelet diagnostic devices that measure optically-based endpoints, such as aggregometry, generally require PRP, which is collected by centrifuging whole blood samples to separate the haematocrit.(227) This method requires supplementation of the sample with a reagent to prevent early platelet activation in the course of blood processing, and limits the choice of anticoagulants to those capable of maintaining cellular integrity under high force.(203) Ideally, assays under development would be designed to be used with whole blood, to increase speed and decrease artefacts from blood processing. Microfluidics devices are typically developed with whole blood applications in mind to provide better physiologic mimicry.

Due to their small size and capacity for precise manipulation of shear conditions, microfluidic devices can be utilised for research purposes into platelet physiology and pathophysiology. The microfluidics device described by Tovar-Lopez *et al*. utilised the properties of microfluidics to provide a close physiologic mimic of an *in-vitro* stenosis.(137) Through the introduction of an on-chip stenosis, shear forces were generated to induce platelet aggregation, which could then be visualised microscopically. As previously mentioned, microfluidic devices have the advantage of fine control of haemodynamic parameters, and the device detailed by Tovar-Lopez *et al.* achieved this by altering three parameters between devices: contraction angle, which altered initial blood acceleration, expansion angle, which altered blood

deceleration after the stenosis, and stenosis gap diameter and length, which acted to alter the peak shear experienced by blood components.(137) The experimental design involved computational fluid dynamic simulations and structural modelling to characterise the haemodynamic properties of the chip, providing data on the spatial and temporal quantification of flow patterns. Through joint consideration of haemodynamics and the biological environment, the device provided valuable, physiologically-relevant data regarding platelet function.

This study showed that by altering shear microgradients within vessels, stabilised discoid platelet aggregates developed independently of the presence of soluble agonists, challenging the previous belief that thrombus formation is wholly dependent on soluble agonist presence.(137) Impacts of this discovery were manifold: it provided evidence of the importance of altered flow dynamics in thrombus formation (and a potential molecular mechanism), and also provided a potential explanation for the lack of efficacy of antiplatelet therapy in some patients with vascular disease.(137)

Another benefit in the use of microfluidics is the addition of modular components, such as valves, mixers and pumps, that can provide greater control over fluid flow. Yeom *et al*'s device is an example of a microfluidic that utilised a peristaltic pump and a rotating stirrer to induce platelet aggregation. It measured platelet adhesion and blood viscosity.(228) This pump could induce controlled, pulsatile fluid flow that was a closer approximation to flow in the vasculature than the steady-state flows of current shear diagnostics such as the PFA-100. The system assessed platelet function under flow without requiring exogenous agonists of platelet aggregation, demonstrating a more physiologically-relevant model than current diagnostics.

However, this model required the use of PRP, instead of whole blood, reducing portability and ease of use of the device.

Due to the small sample volumes required, microfluidic devices can also improve throughput potential, reducing time constraints. Jain *et al.* characterised a similar device to that outlined by Tovar-Lopez *et al.*, but allowed multichannel analysis of the same sample in the same timeframe.(229) Their discoveries consolidated earlier research performed by Tovar Lopez *et al.*, demonstrating the aggregation potential when platelets were exposed to an artificial stenotic region characterised by regions of acceleration, higher shear and deceleration.(137, 229) Using a microfluidics device and computational analysis of resulting clot formation, Jain *et al.* demonstrated that it is the shear gradient of the deceleration in a stenosis that is the critical thrombogenesis activator.(229) This was hypothesised to be due to subsequent clotting factor and signalling pathway activation in areas of high shear. A microfluidics platform was chosen for the investigations because it allowed independent variation of the shear gradient, demonstrating the applications of such a device in research settings. This device had the advantages of using human whole blood and monitored time until clot formation through fluorescence microscopy of fibrinogen and platelet aggregation.

Maloney *et al*.'s microfluidic device demonstrated the potential for lab-on-a-chip device development in drug screening applications. The device measured platelet aggregation response to anti-platelet agents.(230) In this design, eight channels were connected to a single outlet port, and patterned with thrombin and fibrinogen. Perfusion of human whole blood resulted in aggregate formation. The device demonstrated differential aggregate formation in response to various inhibitors of

platelet function and demonstrated efficacy in identifying non-responders to common anti-platelet agents.(230) This device demonstrated the utility of microfluidics in terms of fast, high-throughput sample analysis with fine control of shear forces.

However, microfluidic diagnostic development is not without its challenges. Chiefly, materials constraints limit scale and replicability of production (*see Chapter 1.4.3*). Additionally, some biological processes, such as thrombus growth, are not amenable to miniaturisation, and may demonstrate significant differences when analysed in large and small-scale devices. While the low Reynold's numbers on the microscale can approximate laminar flow within the vasculature, it present difficulties with mixing and therefore, on-chip drug screening (*see Chapter 1.5.4*).(231)

Similarly, microfluidic devices demonstrate limitations in terms of establishing biomimicry through microfluidics.(232) Okorie *et al.*'s device is such an example - it used a parallel-plate arrangement microprinted with TF in which thrombosis was induced and measured. However, like many pump-based perfusion devices with induced aggregation, there was an increase in pressure in the region containing the thrombus (due to obstruction of the lumen). While this system took advantage of platelet reactivity to high-shear environments, physiologically, such a situation would result in the development of a collateral circulation supply. This neovascularisation or shunting cannot yet be mimicked in a microfluidic setting.

1.4.3. Manufacturing materials

The most common material in microfluidic fabrication is Polydimethylsiloxane (PDMS), a siloxane polymer.(13) PDMS is the foremost elastomer used in microfluidic fabrication, due to its transparent, gas and vapour-permeable properties

and capacity for lithography, as well as practical considerations such as cheap cost and easy fabrication set-up.(22, 233) Simple manufacturing processes allow multiple device iterations to be manufactured quickly and easily.(234) Additionally, PDMS fabrication processes do not require complex equipment - a benefit when future commercialisation is considered.(235) Finally, the optical transparency and low autofluorescence of PDMS allows for use with light-based detection methods.(234)

The endothelium plays a critical role mediating the balance between thrombosis and haemostasis (*see chapter 1.1.3.1.3.*).(236) Due to the complexity of its incorporation into systems, and endothelium cell culture *in-vitro*, there is no current commercially-available system that integrates an artificial representation. However, many experimental PDMS devices have been developed to facilitate endothelial cell culture and seeding to improve physiological mimicry.(237, 238) In these devices, PDMS was chosen due to its capacity for hydrophilicity with treatment and possibility of growing cells under constant physiologic flow provided improved endothelial cellular alignment and growth.(239)

However, restrictions of PDMS limit its application, as it has been shown to absorb small molecules, potentially affecting cell signalling. Additionally, chip evaporation may occur due to the relatively low transition point, and there is lack of capacity for up-scaling of throughput methods due to slow fabrication processes, reducing commercial potential.(240, 241) Production issues are also difficult to overcome - there is significant chip-to-chip variation, and complex structures are difficult to fabricate, particularly in small aspect ratio designs.(242) Experimental difficulties may also need to be overcome - due to its inherent hydrophobicity, PDMS adsorbs hydrophobic molecules from the solution phase and can allow small hydrophobic

molecules to diffuse in or out of micropores in the PDMS gel.(240) Drug screening operates within very defined micromolar ranges, especially in a microfluidic setting, and these absorption issues could adversely affect the quality of results.(243) When dealing with systems in which analyte loss may be problematic, such as low concentration blood biomarker detection/assay and handling of small molecular weight drug analogues at low concentration, the chemi-physical properties of PDMS may limit its utility for lab-on-chip fabrication. This may be critically important for drug screening and dose ranging assays where drug loss to PDMS structures may significantly effect assay accuracy and sensitivity.

Additionally, flow-based systems often require pressure to be applied to microfluidic channels to induce flow, but pressures greater than 80 Pounds per Square Inch (PSI) will delaminate PDMS if it is adhered to a glass substrate.(244, 245) The most common method to overcome this limitation is plasma bonding, which enables permanent bonding of the PDMS chip to a glass surface by generating Si-OH groups that then form Si-O-Si bonds when bonded to glass.(246) A plasma cleaner can be used to induce this plasma treatment but it will also alter the chemical structure of the PDMS surface.(234) The plasma cleaning method is also sensitive to contaminants, such as dust on glassware or air pollution within the plasma cleaner chamber. Timing is also critical: increased time will roughen the surface, while shorter exposures may reduce the functionalised capacity of the PDMS.(247) Following plasma bonding, the effectiveness of the bond may be measured by injecting a liquid at high pressure and watching for leaks, or purposively breaking the device.(247) If plasma bonding is effective, the glass should remain adhered to the PDMS, and the PDMS should break preferentially. There are two further disadvantages of plasma cleaning: it cannot be performed on protein-treated glass,

as it would damage the functionalised area, and the treated surface is only capable of bonding for approximately 10 minutes, so the process must be performed quickly.(248) An alternative to plasma bonding is Corona-triggered PDMS bonding, which is conceptually similar to oxygen plasma bonding and suffers similar disadvantages, but is cheaper.(249)

1.4.3.1. Improving PDMS biocompatibility

Unmodified PDMS is hydrophobic, and thus promotes non-specific adsorption of plasma proteins.(250) The surface fouling problem caused by protein or analyte adsorption is enhanced by the significant increase in surface to volume ratio at the microscale, resulting in poor device performance and substantial sample loss.(250, 251) Surface properties such as energy, composition and charge also directly affect platelet function.(212) Therefore, it is important to develop efficient surface modification techniques to render the PDMS surface protein-resistant. The process of passivation confers a coating upon a surface to prevent such bonding and formation of a protein layer.(212) It is particularly important in blood-based microfluidics to prevent blood cell adhesion in areas that may affect results obtained or functionality of the device. For example, an unpassivated valve system which acts to prevent and allow flow of blood may demonstrate platelet aggregation upon the valve surface, fouling the valve and thus incompletely isolating fluidic compartments. Passivation prevents integrin binding to the substrate surface, and therefore aggregates will not form.

Passivation can be achieved by several means, chiefly by flowing a fluid preparation over the bare substrate, which will bond to the substrate and prevent further protein-substrate interactions within the passivated area.(252) Passivation must be

characterised to ensure an even surface coat, but also to determine adsorption kinetics of other proteins in the system and haemocompatibility of the passivating agent.(235) Surface activation is commonly required to clean the PDMS surface prior to passivation, rendering it hydrophilic and promoting surface functionalisation through creation of reactive silanol groups.(235) Surface activation may be achieved through oxygen plasma, UV/ozone or corona discharges.(253) Passivation techniques can be generally classified as physical or chemical in nature.

Physical adsorption methods are generally simple and efficacious, and are used to prevent electroosmotic flow and non-specific binding of plasma proteins.(252) These are conventionally bovine in derivation; bovine serum albumin (BSA) and casein milk powder are easy to prepare and are effective blocking solutions. However, they denature quickly and are difficult to integrate into point-of-care devices that require long shelf-lives. They also often lack useful functional groups, limiting creation of functionalised surfaces.(254)

1.4.3.1.1. Choice of passivation technique

Passivation choices are predicated on the surface chemistry of the substrate and fabrication methods used. Physical methods are easy to apply, though they suffer from short shelf lives and lack of stability.(212) Chemical methods often require more extensive sample preparation but offer the potential for surface functionalisation and log-term storage.(212)

1.5. Microfluidic modular components

Development of an on-chip diagnostic platform would be incomplete without integration of components to control fluid handling. Integration of on-chip

microvalves, mixing, and pumping elements can improve fluidic control and sample throughput by delivering sophisticated, multiplexed, automated, and reliable haematology focused integrated microfluidic diagnostics. Improvements in these aspects make application of microfluidics in diagnostic capacities more viable. However, the effect of such dynamic microfluidic components on blood function presents significant challenges.

1.5.1. Hemocompatibility of modular components

While hemocompatibility is a recognised criterion for microfluidic development, previous design approaches for micropumps, valves and mixers have been limited by a lack of sophistication with respect to the assessment of blood function.(213) They have often relied on superficial measures such as haemolysis and gross assessment of biofouling.(213) Performance in areas such as the mechanics of blood cell handling, effects on blood plasma protein and biomarker composition, materials hemocompatibility, and hemodynamic parameters must be carefully considered in order to achieve effective blood handling.(212) In addition, blood is a non-Newtonian fluid and its viscosity may be up to an order of magnitude more viscous than water (depending on flow parameters and biochemical factors).(255) This may lead to pressure differentials that may perturb flow and impair device performance. Finally, blood plasma protein physisorption processes at microfluidic surfaces pose significant problems with regard to biomarker loss and blood cell adhesion.(212)

1.5.2. Microfluidic valves

Valves within microfluidic systems act to create a separation of interfaces until it is necessary that the two fluids should meet.(256) Microvalve integration is crucial to the automation of many biological microfluidic systems, such as immunoassays, sample processing, cell culture and protein crystallisation.(257-260) Through careful consideration of parameters such as valve shape, electrical power requirements, width or membrane thickness, these valves systems act to control separation of two or more interfaces.

The design of a microvalve must minimise mechanical interference with the sample. Repeated opening and closing of valves can crush blood cells in mechanical haemolysis.(261) Valve haemolysis can alter the sample profile by reducing the haematocrit and therefore lessen the margination effect that forces platelets towards vessel walls where they are more likely to come into contact with biosensors *(see chapter 1.2.5*).(262) Liberated ADP and ATP from the haemolysed erythrocytes can act as an agonist of platelet aggregation, furthering biofouling.(262) Additionally, RBC haemolysis causes haemoglobin release, which acts as an NO scavenger, and arginase release, which cleaves a substrate for NO production, reducing NO bioavailability and increasing platelet activation.(262)

Broad categories of microvalves include active or passive valves, depending on their need for an external power supply, and further subclassifications may be determined by the applicability of the valve to the system in question.(263) Only valves characterised in testing conditions requiring haemocompatibility will be considered in this review.

1.5.2.1. Elastomeric microvalves

Elastomeric microvalves consist of a vertical membrane attached to another pneumatically-actuated membrane (*see Fig 1.8*). This configuration prevents flow in a working channel through downwards displacement of the vertical membrane until it contacts the channel floor, occluding the channel.(264) Pneumatically-actuated valves work with a transistor-like function, and application of a vacuum to the actuation chamber lifts the valve, allowing fluid to flow.(265) Binary states enable power conservation, as energy is needed only to transition between states.

This valve system is suitable for large-scale integration, and is relatively simple to configure.(263) Pneumatically actuated valves are the most common valve types in assays requiring large-scale integration as the fabrication process is inexpensive. Given the chief material in microfluidic design is PDMS, this system is relatively cheap to fabricate, but is limited to chemicals which PDMS does not react with, and elevated temperatures may change the properties of the system.(266) Additionally, concerns about portability and reusability have prompted further research into pneumatic valve optimisation in these areas.

Elastomeric microvalves offer quicker actuation and their geometry can be adapted to induce low shear rates.(213) While further testing is needed to ascertain the impact of specific shear geometries on blood flow and cellular responses, pneumatically-actuated elastomeric microvalves provide an effective blood valving solution that has potential to minimally impact physiology.

Elastomeric microvalves have been utilised in several blood-contacting systems. Chen and Pan demonstrated a pneumatically actuated elastomeric cantilever

microvalve for integration into a system for blood typing.(267) The system utilised whole blood which only underwent a simple dilution step prior to device loading, largely preventing handling artefacts present in data analysis. While the device represented an advance in microfluidic automation, haemocompatibility was not comprehensively tested. For example, the study authors may have found it prudent to measure haemolysis, which would have otherwise interfered with the blood-typing endpoint. Additionally, shear rates in the valving region may have induced red cell Rouleaux formation.(268) Without further microscopic analysis, red cell Rouleaux formation may be mistaken for agglutination at the macroscopic level, resulting in false positives in the blood typing process. Given the qualitative nature of the device's chosen application, considerations such as protein adsorption and platelet deposition were less important, and as such the device demonstrated no measures of control for these considerations.

Similarly, Takao *et al.* presented a microvalve that was actuated through thermopneumatic means for integration into a cell counter and haemoglobin detector.(269) The device consisted of a two-channel system connected by a channel gap. The floor of the channel gap was an elastomeric membrane, which was deflected downwards upon heating of the microchamber underneath through a thermo-isolated microheater. Though the system was not characterised with blood, the system was designed with haemocompatibility in mind. It would therefore be prudent to consider the impact of aspects of the proposed system on blood samples. Raising the temperature of blood samples beyond physiologic body temperatures can denature enzymes and alter blood cell morphology.(270) Here, the authors adjusted the design for haemocompatibility concerns by incorporating sufficient space between heated elements and blood channels to prevent blood heating and

denaturation. However, the system did incorporate a small aperture between the PDMS and actuation membrane for blood to flow between the surface fluid channels. Such gaps could induce supraphysiologic shear conditions, inducing platelet and red blood cell activation, leading to biofouling and analyte alteration.(213) The authors also alluded to the slow actuation speed with increased chamber volume. This could result in longer time periods of exposure to high shear conditions when the valve is in a transient state, increasing platelet and red cell activation.(213) Such systems demonstrate the importance of testing the design with blood samples in a controlled environment, and highlight that optimal elastomeric microvalve design and testing has not been achieved.

1.5.2.2. Phase change valves

Phase change microvalves are another common valve type in biomedical devices.(264) Phase change microvalves control fluid movement through the phase change of the obstructing valve. Phase change may occur through heating or cooling, and therefore these valve types require an element to modulate temperature. This valve type can only be used in applications that do not require fast actuation.(14) Phase-change microvalves have most commonly been constructed from hydrogels due to the ease of manufacture and wide ranges of responses to stimuli, but they have also been constructed from ice, water, smart polymers and paraffin.(272, 273) Phase-change valves that respond to high and low temperatures are often easy to manufacture, but are incompatible with biological systems, and may alter properties of drugs.(274) One suggested alternative is to use phase-change materials that expand upon solidification and shrink upon cooling.

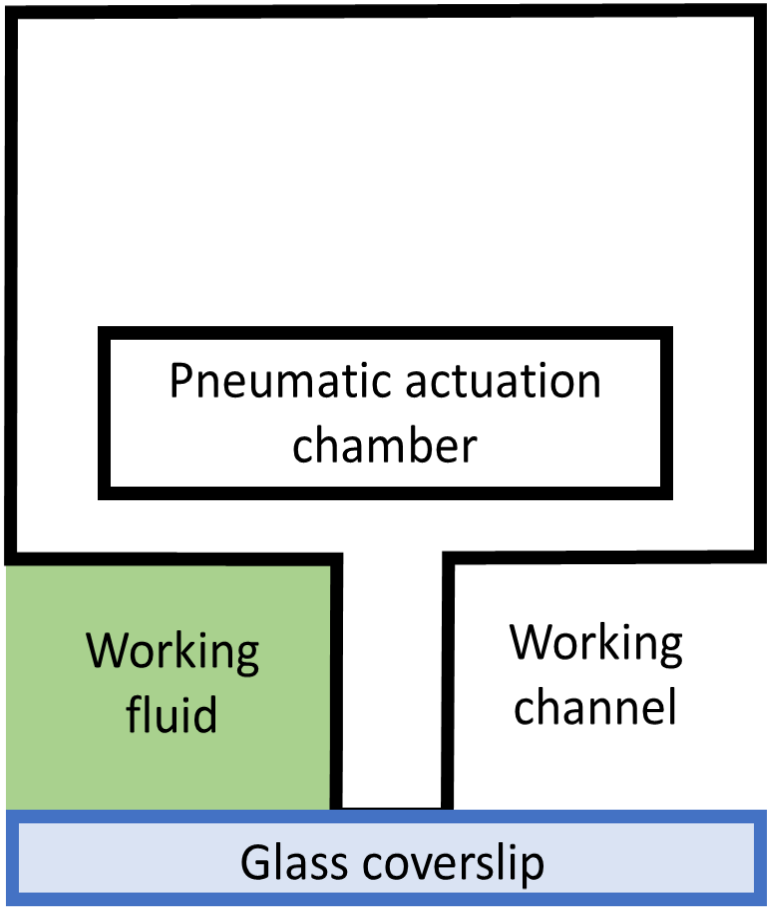

Closed configuration

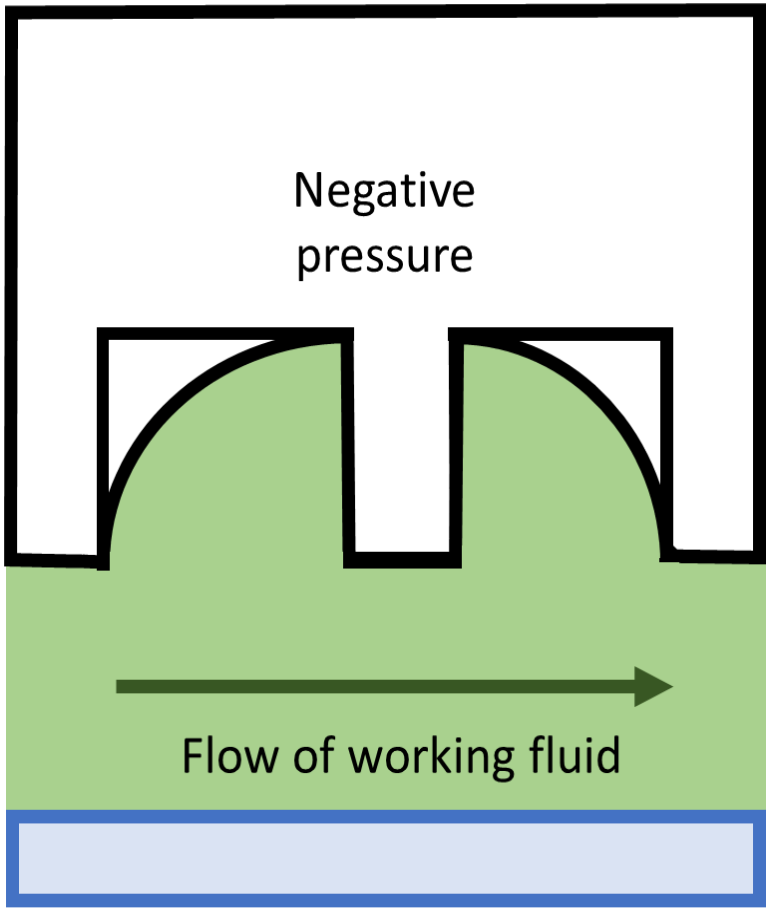

Open configuration

Figure 1. 8 Pneumatically-actuated elastomeric microvalves

Elastomeric microvalves have a pneumatic channel that sits above the fluidic layer, and provides positive closing pressure necessary to oppose the upwards displacement of the valve until the critical valve-opening pressure is reached.(271) Application of positive pressure to gated valves allow a greater pressure to be used in microfluidic channels without valve dehiscence. They are advantageous because they have low complexity in the production process without compromising valve efficacy.(264)

Alginate is a hydrogel preparation that demonstrates good biocompatibility, and Saez *et al.* have demonstrated application in a microfluidic environment.(275) Alginate is additionally low-cost and biodegradable, making it an enticing microfluidic valving alternative. In their device, the alginate was controllably injected into the working fluid channel and formed an impedance to flow. Upon dehydration, shrinkage of the hydrogel opened the channel, allowing flow. Their device demonstrated reusability through the use of Ethylenediaminetetraacetic acid (EDTA) solution to completely erase the valve, allowing for removal of damaged valve systems. However, consideration must be given to the mechanism behind valve formation and removal in the device. This valve is not optimised for testing platelet function due to the calcium ions required for valve formation, and EDTA required for valve erasure. Both these solutions would affect platelet activation, altering testing outputs.(110)

Tai *et al.* presented a phase change microvalve that utilised the properties of blood to induce a clot, thereby acting as a one-time used valve.(276) Through creating a heated valve zone to induce thermal coagulation, blood clotted in the region, preventing further flow in the channel. The system utilised a laser to induce thermal coagulation processing, potentially altering blood physiology through protein denaturation and erythrocyte transformation. While this system allowed the valve system to function, it may also have altered physiologic testing of the trapped sample, and the system may have lost specificity of diagnosis due to the supraphysiological temperatures required to induce coagulation.(270) Additionally, the sample storage at 4^{o}C prior to testing was likely to cause platelet lysis, preventing some physiologic testing of platelet parameters.(277)

1.5.2.3. Choices for haemocompatible valving

Choices in microfluidic valves depend largely on the application, and potential detriments must be considered. In the case of blood-contacting medical diagnostics, the high or low temperatures required to actuate phase-change microvalves may adversely affect blood cells and plasma proteins, causing irreversible denaturation and loss from solution.(278) Additionally, the slower actuation rates of phase-change microvalves may also be a disadvantage in flow-based devices.

1.5.3. Microfluidic pumps

Many microfluidic systems require flow of a working fluid, and it is difficult to achieve this while maintaining a micro-scale assay system. Many microfluidic systems, particularly those developed for medical applications, use passive systems that require no external energy input. In drug discovery, passive microfluidic systems are being developed as tools for identifying possible new pharmacologic agents and for use in preclinical testing.(279) The small scale, low cost of fabrication and portability makes them ideal for point-of-care applications.(280) However, in some cases, passive flow systems are simply neither fast nor powerful enough for the proposed function. In these cases, active mechanisms, such as reciprocating diaphragms, rotary displacement units or magnetohydrodynamic forces can provide the necessary pumping mechanism.(281) Active micropumps use an external signal to induce fluid flow, which generally increases the device's size, cost and complexity. However, such measures also offer greater control, and are necessary in some applications. Only micropumps with proposed or practical blood applications have been reviewed here.

Consideration must be given to the flow profile induced by the pumping mechanism in blood-based devices, as the profile of blood flow to be mimicked changes across the vasculature. In large arteries, such as the aorta, flow is pulsatile as it is pumped directly from the heart.(193) The lamina media of the muscular arteries act to dampen the flow amplitude but can become hardened over time due to atherosclerosis and ageing. In the microcirculation, flow is steadier and constant.(282) Finally, chaotic flow can occur when adjacent laminar layers of blood are disrupted, often in areas of branching, valving or pathophysiologic thrombus protrusion into the lumen.(283) This can cause blood vessel stretching, mechanically stressing vascular cells and altering integrin expression in platelets.(283) Experiments conducted on post-mortem human vasculature and studies of platelet reactivity in continuous-flow LVAD circuits concluded there was an increase in platelet activation in areas of constant flow, when compared to areas achieving pulsatility.(284, 285) Patients who have implanted pulsatile-flow LVAD device experience fewer thrombotic complications than those with continuous flow devices.

1.5.3.1. Displacement pumps

A displacement pump is one that induces fluid movement through trapping a quantity of fluid, then forcing it through a discharge channel. By their nature, they induce pulsatile flow, and the flow rate is dependent on the quantum of volume moved and the frequency at which this movement occurs.(264)

1.5.3.1.1. Reciprocating diaphragm pumps

Reciprocating diaphragm pumps generally consist of an inlet channel, pumping chamber - in which a moving planar surface is inset into a wall - and an outlet

channel (*see Fig 1.9*).(286) This planar surface is generally in the form of a diaphragm that deforms in the centre and is fixed at the edges. Movement of the diaphragm creates a pressure wave, inducing forward fluid motion.

Davies *et al.* reported design of a haemocompatible 'microthrottle' pump that utilised restrictions in flow paths to control fluid flow.(287) The pumping mechanism was similar to a reciprocating diaphragm pump, wherein upon piezoelectric actuation the membrane deflected, creating a suction effect. Upon negative application to the piezoelectric membrane, the membrane extended into the pumping chamber, forcing blood through the system. This system differed from other elastomeric micropumps because the pumping chamber itself was capable of deformation, and integrated throttles acted to seal the chamber in the suction and pumping strokes. However, conclusions regarding the pump's impact on blood function would not be made as full haemocompatibility characterisation was not conducted. While the authors measured haemolysis as an endpoint, measures such as cell activation were not measured. Additionally, it was likely that the rapid up-and down-strokes of the system induced significant shear, which may have altered blood sample physiology downstream, which was also not tested.

Hsu *et al.*'s peristaltic pump was another example of a reciprocating micropump utilised in blood handling applications. It was composed of piezoelectric discs above a fluidic channel.(289) The three piezoelectric discs could be actuated in a variety of arrangements to induce fluid flow. The system was passivated with polyethylene oxide to prevent platelet monolayer formation, plasma protein loss and biofouling. However, again, considerations of haemocompatibility were incomplete, as the impact of the different flow profiles the pump induced on blood cell activation was not

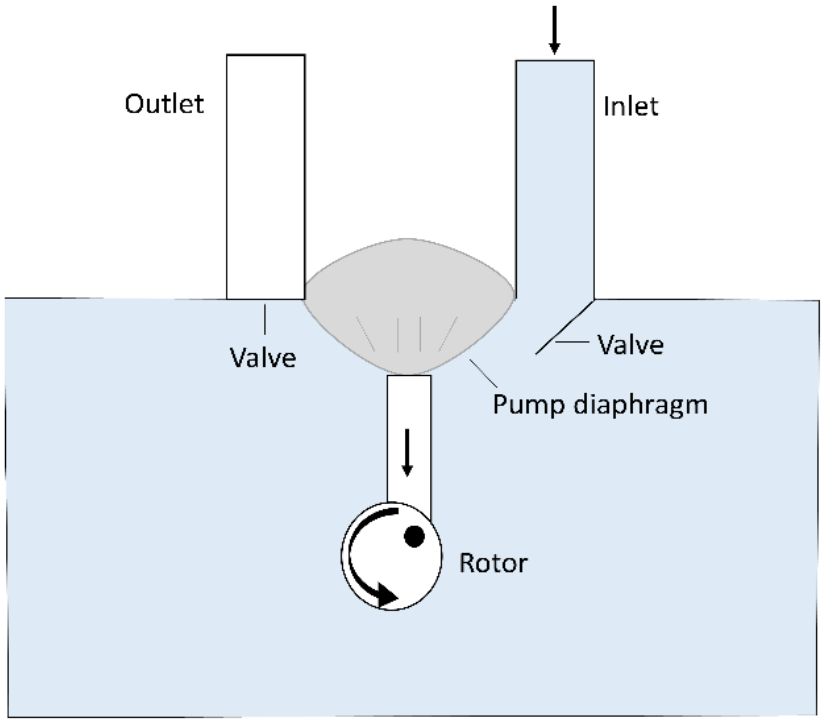

Intake phase

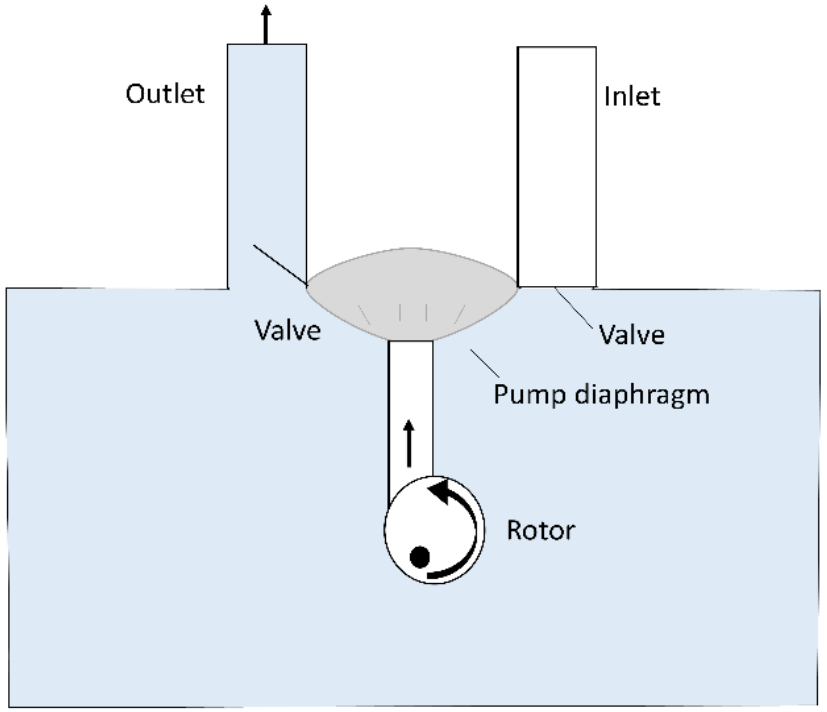

Outlet phase

Figure 1. 9 Reciprocating diaphragm pump

Diaphragmatic pumps will induce fluid movement through pressure in this pump chamber - if the chamber is under-pressured, fluid will be transferred from the inlet to the pumping chamber.(288) If the chamber is pressurised, fluid will discharge into the outlet channel. Valves in the inlet and outlet channels stop fluid flow in unwanted directions, and thus act as flow rectifiers, ensuring the working fluid only flows in the desired pathway. Choice of diaphragm material may be made on the device's intended frequency, volume delivery or flow. A low modulus material will impart a lower-frequency flow, but will maximise volume.(286) If higher frequencies or forces are required, materials with greater stiffness will generally be chosen. Conversely, if the micropump is intended for biologic application, it must be ensured that the materials in contact with the biological environment are biocompatible.

identified, and thus the haemocompatibility of the system may have been compromised.

1.5.3.1.2. Rotary displacement pumps

Rotary displacement micropumps have been used in a small number in microfluidic applications. These systems incorporate micromachined gear structures into the working fluid channel, which induce fluid movement through their rotation.(290) The major difficulty in this pump type is developing a housing system which minimises gaps between gears, through which backflow would otherwise occur.(291) As the

pressure at which pump mechanism can operate increases with an increase in working fluid viscosity, these pumps have been used in systems operating with medium-high viscosity working fluids.(292)

1.5.3.2. Dynamic pumps

Dynamic micropumps induce fluid flow through the direct transfer of energy to the working fluid without a mechanical conversion.(264) They are classified as either centrifugal, electrohydrodynamic, electroosmotic, magnetohydrodynamic, ultrasonic or miscellaneous special effect pumps.(293)

1.5.3.2.1. Centrifugal pumps

Centrifugal micropumps utilise a combined impeller-ferromagnetic unit, placed within an external magnetic field.(294, 295) The impeller is placed within the working fluid, and through its rotation, centrifugal force induces movement in the fluid. They require

high Reynold number systems to be effective, and have limited miniaturisation potential.(295)

Centrifugal pumps have predominantly been used in blood plasma extraction devices.(294-296) These devices accelerate natural sedimentation processes to achieve purified plasma with very low cellular contamination. On-chip plasma extraction is an attractive prospect from a diagnostic perspective, as it improves on-chip processes which are traditionally highly operator dependant, use large blood volumes and require specialised laboratories.(195, 297) *Haeberle et al.*'s work characterising a novel centrifugal pump to extract plasma from whole blood demonstrates application of this principle to obtain purified plasma with a residual cell concentration of 0.11%.(294) However, this pump configuration was not tested for its effects on blood. It is possible that centrifugation process such as those detailed in *Haeberle et al.*'s work poses risks of vWF polymerisation, and platelet activation and subsequent release of soluble agonists, altering the plasma composition.(294)

1.5.3.2.2. Magnetohydrodynamic pumps

Magnetohydrodynamic micropumps are utilised when the working fluid is conductive, and act to induce flow by subjecting these fluids to electric and magnetic fields placed perpendicularly to the microchannel to induce Lorentz force and thus, flow.(298) These pumps are useful because they contain no moving parts. However, by their nature this design may induce electrolysis, generating bubbles, which may affect platelet activation and flow precision.(299) Developments to overcome this problem have been proposed, but the amounts of energy required result in heating of the working fluid.(298) Magnetohydrodynamic pumps display utility with biological

applications, as most biological fluids are highly-conductive, and therefore suitable for induced flow. They have only been applied to hypothetical blood-pumping devices to date.(300)

1.5.3.2.3. Electrolytic micropumps

Electrolytic pumps rely on the use of trapped air bubbles in side-channels, the expansion or collapse of which can direct fluid flow. Electrolytic micropumps are useful because they do not require use of mechanical parts, such as valves.(301) Several electrolytic micropumps have been developed for integration into blood-based microfluidic devices. For example, electrolytic processes in Chiu and Liu's device was used to generate an air bubble.(299) Electrolysis occurred in a side channel to generate a bubble that created a forward momentum within the blood channel. Chiu and Liu chose electrochemical pumping in preference to electrostatic or piezoelectric actuation due to the low power, low voltage and low temperatures required for operation. While these are useful benefits, this pumping system may adversely affect blood due to the disadvantageous contact of blood with air, which can cause platelet activation.(302)

1.5.3.3. Choices for haemocompatible pumping

Having the capacity to manipulate and pump fluids on-chip would be a crucial step forward in the world of microfluidic engineering for blood diagnostics. Few current microfluidic pumps in the literature have been comprehensively tested for haemocompatibility, and virtually none have been tested for platelet-specific applications. Some pumps, such as rotary displacement pumps, centrifugal pumps and magnetohydrodynamic systems require use of external fluids or machinery that

would adversely affect blood composition or cells.(212) Others, such as electrolytic micropumps, would expose blood to air or electrical currents and cause inappropriate platelet activation.(302) Due to the capacity to engineer the system to suit specific requirements, reciprocating diaphragm pumps have the potential to be useful in situations requiring hemocompatibility. Additionally, due to their pulsatile flow, they can mimic cardiovascular motion and have applications in research regarding physiological flow profiles. A microfluidic micropump that has been fully characterised in terms of haemocompatibility has not been reported.

1.5.4. Microfluidic mixing

Many microfluidics aim to miniaturise large-scale processes to cause mixing, but difficulty is encountered in the design process because of the inherently low Reynold's number of microfluidic systems.(303) Mixing refers to the migration of molecules from one source transversely to another, eventually reaching a homogenous state.(304) The high surface area to volume ratio present in microfluidic scales results in a relatively low Reynold's number, decreasing turbulent mixing.(305) Specific mixing areas are therefore necessary in many microfluidic devices. These enhance the mixing efficacy so that mixing may occur in shorter channel lengths, providing economy of space.

Mixing of whole blood presents particular challenges. Blood is mostly composed of large molecules, such as haemoglobin and cellular material, and thus mixes slower than Newtonian fluids.(306) Viscosity of human blood may be up to an order of magnitude more viscous than water in pathological states, which may impede flow and affect the accuracy of detection systems (particularly optically-based systems).(307) Additionally, blood is a non-Newtonian fluid, and therefore achieving

consistent pressure in a blood-filled channel may be difficult.(279) Finally, mixing increases the likelihood of introduction of air bubbles. Air contact can activate platelets and the coagulation cascade, denature proteins and remove adhered cells from the channel surface.(212)

Mixing technologies have previously been developed for blood-based microfluidics. While these studies assess the degree of mixing, little consideration is given to the haemocompatibility of such devices. Only mixers with proposed or practical blood applications have been reviewed here.

1.5.4.1. Passive mixing

Passive mixing schemes rely on increasing the contact area between species to be mixed, or fluid flow through holes or multiple channels, thereby increasing diffusive mixing.(308) These schemes are less efficient than active mixing schemes but are generally simpler to manufacture. They are also generally more cost effective.

1.5.4.1.1. Serpentine mixers

Serpentine mixing involves introduction of a 'C-shaped' channel portion to induce chaotic advection mixing.(309) These systems typically work in systems with Reynold's numbers above one. Larger Reynold's numbers increase the folding and stretching of the fluid interfaces, increasing mixing effectiveness.(310)

Yun and Yoon’s bioreactor was designed for DNA extraction from whole blood samples and utilised a serpentine mixer.(311) The device used continuous electrowetting to propel fluids through the microchannels, with a serpentine configuration to enhance mixing. Though mixing efficiency was tested using

phenolphthalein and the mixer was found to be efficacious, it failed to assess heterogeneous fluid mixing, as is the case with blood. Additionally, little consideration was given to the shear induced in the serpentine channels which may adversely affect cellular function.

1.5.4.1.2. T and Y-shaped micromixers

T and Y-shaped micromixers use multiple input streams which then join to form one laminar stream.(312) This work as a mixer by increasing the contact surface area between the fluids, decreasing diffusion length. However, mixing with this method is slow, and long channel lengths are required. Slight modifications have been proposed, including roughening the channel wall or adding obstacles within the channel, increasing the Reynold's number and introducing chaotic advection.(313) Higher flow rates or smaller channels also increase efficacy, however these may not be appropriate in all applications, such as platelet testing devices, due to an increase in shearing forces. Parallel laminating mixers improve upon this concept with more complex designs in which the main stream is split into two or more sub-streams, then re-joined.(305) Both types of mixers typically operate at low Re values.(147, 148)

1.5.4.1.3. Micropillar array mixing

Mixing may be achieved through passage of the fluid of interest through a series of micropillars to create multiple zones of splitting and recombination. This reduces the diffusion distance, allowing for more space-efficient mixing than could be achieved with a straight channel.(314) Pillar structures have been proposed for continuous mixing of human blood, though no practical testing has been conducted.(231)

Concerns regarding haemocompatibility in micropillar array systems may arise due to the additional surface area available for protein physisorption in the blood channel.

1.5.4.2. Choices for haemocompatible mixing elements

Previous approaches to design of a microfluidic mixer have been in the context of circulating tumour cell extraction or have been tested only using non-physiological fluids such as food dye.(133) This limits extrapolation of their findings regarding both mixing efficacy and their potential impact on blood cells, flow pathways and plasma proteins. As mixers are designed to induce some degree of chaos within flow, shear environments must be carefully considered, and elements such as zigzag channels, serpentine channels and micropillar arrays potentially introduce complex, high-shear environments. Additionally, due to the high surface area of systems such as micropillar arrays and zigzag channels, dependable passivation techniques must be applied prior to contact with blood in these systems to prevent plasma protein loss. As with other microfluidic modular components, little research has been conducted into the haemocompatibility of mixing elements and little conclusion can be made regarding an optimal technique.

1.6. Conclusion

There is currently an unmet clinical need for a sensitive and highly reproducible test system that can effectively monitor platelet function across a number of clinical applications. This thesis details the development of a platelet function test (PFT) that utilises a strain rate micro-gradient that is superior to current commercial offerings in the PFT space because of its application of a combination of patho-physiological blood flow (global physiological stimulus), allowing for highly sensitive assessment of

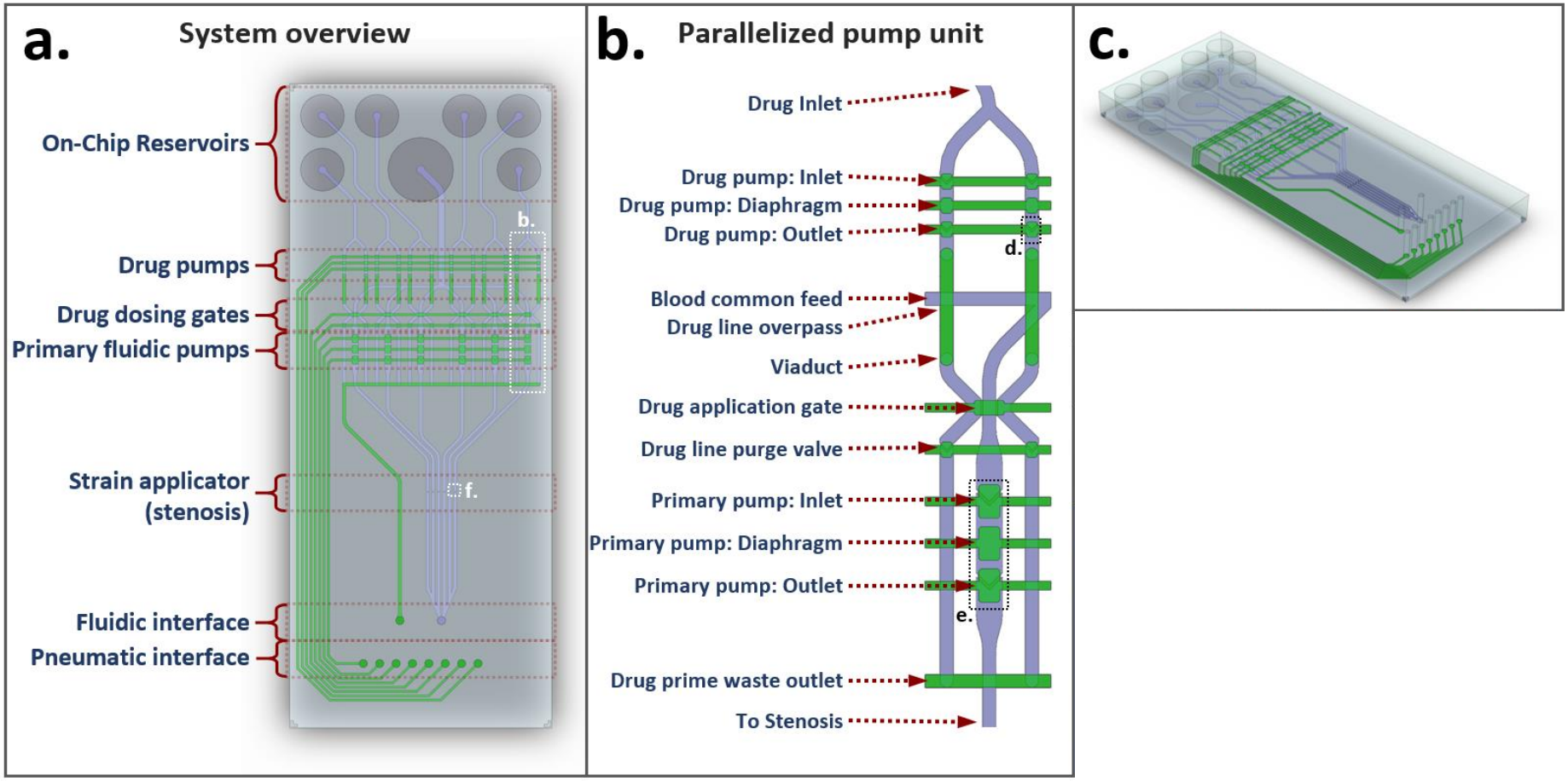
a.
System overview
On-Chip Reservoirs
Drug pumps
Drug dosing gates
Primary fluidic pumps
Strain applicator (stenosis)
Fluidic interface
Pneumatic interface
b.
f.
b.
Parallelized pump unit
Drug Inlet
Drug pump: Inlet
Drug pump: Diaphragm
Drug pump: Outlet
Blood common feed
Drug line overpass
Viaduct
Drug application gate
Drug line purge valve
Primary pump: Inlet
Primary pump: Diaphragm
Primary pump: Outlet
Drug prime waste outlet
To Stenosis
d.
e.
c.

Figure 1. 10 Automated haematology cartridge

a. System schematic showing overall "high-density" dual layer chip architecture incorporating drug/reagent pumps [b], sample pump/blood mixers [b] and parallelised strain applicator [f]. The strain applicator is of variable width and with inlet and outlet angles, depending on the required strain conditions to test. Epifluorescently-tagged human whole blood would be perfused through the device from an external syringe driver. Due to the increased shear in the stenotic region, aggregation is initiated, and the size of aggregation measured. Larger aggregates would demonstrate greater aggregation propensity, and smaller aggregates with decreased aggregation capacity. b. Schematic of micropump/mixer unit including gated drug delivery ports, and perfusion elements. c. Chip overview. Figure courtesy of Crispin Szydzik.

platelet function that will enhance clinical diagnosis of bleeding disorders and antiplatelet therapy (APT) efficacy. This substantial increase in test sensitivity over existing PFTs will fill the, as yet, unmet need for a reliable PFT that can be utilised for more tailored patient monitoring, giving the strain rate micro-gradient a significant competitive advantage in the market.

This project will detail creation of components for a fully automated PFT instrument and consumable proof of concept analyser for the assessment of congenital and acquired platelet-based bleeding (platelet hypo-function), and as a high content screening tool of new anti-platelet therapies. The system will be suitable for use in further preclinical and clinical validation of the device with the aim of developing a highly reliable, easy to use, and highly sensitive system that requires minimal operator expertise and input.

1.6.1. Microfluidic microvalves

Modular components were developed to improve automation of the device and reduce elements of handling variation. Valves in microfluidic systems enable reliable fluidic isolation, and the capacity to deliver known drug volumes to samples on-chip.(264) Previous attempts to design blood-contacting microvalves in the literature have lacked complete analysis of haemocompatibility, and often solely on superficial measures such as haemolysis or biofouling.(315) Pneumatically-actuated elastomeric microvalves were developed and comprehensively assessed to determine haemocompatibility. Characterisation of microvalves allowed determination of the elements likely to be predicative of a microfluidic component likely to impact blood. Elements under investigation included the impact of the

stationary valve on platelet activation and aggregation, red cell function and morphology, and plasma protein composition and loss. Extensive analysis of the impact of the haemodynamic environment was performed to determine the impact of local shear rate gradients and particle distribution on valve haemocompatibility. A haemocompatible valve iteration was identified that demonstrated minimal impact on blood function or composition, and observations were made that could be harnessed to further improve haemocompatible microvalve development in the future.

1.6.2. Microfluidic micropumps

Development and characterisation of a novel haemocompatible micropump was then conducted. Development of a micropump would be advantageous in the field of platelet diagnostics because it would enable the delivery of low-volume blood samples with precision and control of the haemodynamic environment.(316) On-chip micropumps offer further advantages, including rapid on-chip processing, portability, and capacity for on-chip mixing by utilising the fluid-folding effects experienced by fluid passing through on-chip pumps. Similarly to microvalves, haemocompatibility testing of micropumps in the literature has been poorly conducted. This study described the development of a pneumatically actuated elastomeric micropump and identification of elements required to improve haemocompatibility. The system took advantage of knowledge gained when characterising the microvalving components to modulate the haemodynamic environment and improve cellular handling. Scaling was demonstrated in the system through pump parallelisation, showing the system could be adapted for higher flow-rate requirements with minimal impact on cellar activation. Proof-of-concept testing demonstrated the pump acted as an effective mixer to rapidly mix anti-thrombotic drugs with human whole blood to modulate

platelet aggregate formation at defined shear conditions. This system demonstrated a significant step forward in the field of microfluidic automation as application improves on-chip functional capacity and integration of flow to diagnostic devices.

1.6.3. Microcontraction geometry

The microcontraction studies detailed in this thesis utilised prior knowledge regarding stenosis-induced aggregation in microcapillary-like devices to develop a novel microfluidic device that incorporated stenoses to introduce defined shear gradients in a microchannel.(82, 153) This was achieved through incorporation of an artificial stenosis in a microchannel designed to induce aggregation in a flowing whole blood sample. Aggregation was monitored in real-time through epifluorescence dyeing of platelets. The device was characterised in healthy donors to determine key drivers of activation and aggregation in the stenotic region, including the soluble agonists and GPIb/IX/V and integrin $\alpha_{IIb}\beta_3$ engagement. Additionally, the impact of patient-specific factors was identified, including platelet count, haematocrit and vWF levels. Device output was then correlated with standard clinical screens in patients with vWD and healthy controls to demonstrate the device's capacity to sensitively differentiate platelet function disorders. Specifically, device performance was correlated with known, commonly used tests of platelet function, including light transmission aggregometry and PFA100® within hospital pathology laboratories.

This thesis presents the development and automation a novel microfluidic device as a platelet function diagnostic platform for eventual use in high-throughput drug screening (*see Fig 1.9*). Consideration is given to fluidic isolation through integration of microfluidic microvalves (*chapter 3*), and on-chip fluid flow through micropumps (*chapter 4*). The diagnostic portion of the device utilises known and new knowledge

of platelet reactivity to offer real-time visualisation of aggregate formation in healthy controls and those with vWD (*chapter 5.2*) and provide new information regarding the impact of defined shear gradients on platelet function (*chapter 5.3*).

1.7. References

1. Finegold JA, Asaria P, Francis DP. Mortality from ischaemic heart disease by country, region, and age: statistics from World Health Organisation and United Nations. Int J Cardiol. 2013;168(2):934-45.
2. Roth GA, Huffman MD, Moran AE, Feigin V, Mensah GA, Naghavi M, et al. Global and regional patterns in cardiovascular mortality from 1990 to 2013. Circulation. 2015;132(17):1667-78.
3. Cimmino G, Golino P. Platelet biology and receptor pathways. J Cardiovasc Transl Res. 2013;6(3):299-309.
4. Berndt M, Metharom P, Andrews R. Primary haemostasis: newer insights. Haemophilia. 2014;20:15-22.
5. Wolberg AS, Aleman MM, Leiderman K, Machlus KR. Procoagulant activity in hemostasis and thrombosis: Virchow's triad revisited. Anesth Analg. 2012;114(2):275.
6. Bergmeier W, Hynes RO. Extracellular Matrix Proteins in Hemostasis and Thrombosis. Cold Spring Harbor Perspectives in Biology. 2012 February 1, 2012;4(2).
7. Broos K, De Meyer SF, Feys HB, Vanhoorelbeke K, Deckmyn H. Blood platelet biochemistry. Thromb Res. 2012 Mar;129(3):245-9.

8. Cosemans J, Angelillo-Scherrer A, Mattheij NJ, Heemskerk JW. The effects of arterial flow on platelet activation, thrombus growth, and stabilization. Cardiovasc Res. 2013 July 15;99(2):342-52.

9. Schneider SW, Nuschele S, Wixforth A, Gorzelanny C, Alexander-Katz A, Netz RR, et al. Shear-induced unfolding triggers adhesion of von Willebrand factor fibers. PNAS. 2007;104(19):7899-903.

10. Choi J-L, Li S, Han J-Y. Platelet function tests: a review of progresses in clinical application. Biomed Res Int. 2014;2014:456569.

11. Favaloro EJ, Pasalic L, Curnow J. Laboratory tests used to help diagnose von Willebrand disease: an update. Path. 2016;48(4):303-18.

12. Franchi F, Rollini F, Cho JR, Ferrante E, Angiolillo DJ. Platelet function testing in contemporary clinical and interventional practice. Curr Treat Options Cardiovasc Med. 2014;16(5):300.

13. Gravesen P, Branebjerg J, Jensen OS. Microfluidics-a review. J Micromech Microeng. 1993;3(4):168.

14. Polson N, Hayes M. Microfluidics: controlling fluids in small places. Anal Chem. 2001;73(11):312 A.

15. Wong KH, Chan JM, Kamm RD, Tien J. Microfluidic models of vascular functions. Annu Rev Biomed Eng. 2012;14:205-30.

16. Boyd-Moss M, Baratchi S, Venere MD, Khoshmanesh K. Self-contained microfluidic systems: a review. Lab Chip. 2016;16(17):3177-92.

17. Colace TV, Tormoen GW, McCarty OJ, Diamond SL. Microfluidics and Coagulation Biology. Annu Rev Biomed Eng. 2013 July 11;15(1):283-303.

18. Daly ME. Determinants of platelet count in humans. Haematologica. 2011;96(1):10-3.

19. Ware J, Suva LJ. Platelets to hemostasis and beyond. Blood. 2011;117(14):3703-4.

20. Alcaide P, Auerbach S, Luscinskas FW. Neutrophil recruitment under shear flow: it's all about endothelial cell rings and gaps. Microcirculation. 2009;16(1):43-57.

21. Franco AT, Corken A, Ware J. Platelets at the interface of thrombosis, inflammation, and cancer. Blood. 2015 July 3;126(5):582-8.

22. Broos K, De Meyer SF, Feys HB, Vanhoorelbeke K, Deckmyn H. Blood platelet biochemistry. Thromb Res. 2012;129(3):245-9.

23. Geraldo RB, Sathler PC, Lourenço AL, Saito MS, Cabral LM, Rampelotto PH, et al. Platelets: still a therapeutical target for haemostatic disorders. Int J Mol Sci. 2014;15(10):17901-19.

24. White JG. Current concepts of platelet structure. Am J Clin Pathol. 1979 Apr 1;71(4):363-78.

25. Escolar G, Clemetson K, White, JG, Persistence of mobile receptors on surface-and suspension-activated platelets. J Lab Clin Med. 1994;123(4):536-546.

26. Loftus JC, Albrecht RM. Redistribution of the fibrinogen receptor of human platelets after surface activation. J Cell Biol 1984 Sep 1;99(3):822-9.

27. Cohen I. The contractile system of blood platelets and its function. Methods Achiev Exp Pathol. 1979;9:40-86.

28. Selvadurai MV, Hamilton JR. Structure and function of the open canalicular system - the platelet's specialized internal membrane network. Platelets. 2018 Jun;29(4):319-25.

29. Heijnen HF, Korporaal SJ. Platelet morphology and ultrastructure. Platelets in thrombotic and non-thrombotic disorders: Springer; 2017. p. 21-37.

30. Ge S, Wittenberg NJ, Haynes CL. Quantitative and real-time detection of secretion of chemical messengers from individual platelets. Biochemistry. 2008;47(27):7020-4.

31. Whiteheart SW. Platelet granules: surprise packages. Blood. 2011;118(5):1190-1.

32. Thielmann I, Stegner D, Kraft P, Hagedorn I, Krohne G, Kleinschnitz C, et al. Redundant functions of phospholipases D1 and D2 in platelet α-granule release. J Thromb Haemost. 2012;10(11):2361-72.

33. Blair P, Flaumenhaft R. Platelet α-granules: basic biology and clinical correlates. Blood Rev. 2009;23(4):177-89.

34. Lapidot T, Kollet O. The brain-bone-blood triad: traffic lights for stem-cell homing and mobilization. Hematology Am Soc Hematol Educ Program. 2010;2010(1):1-6.

35. Gryglewski RJ, Ramwell PW. Prostaglandins, Platelets, And Atherosclerosi. Crit Rev Biochem. 1980 Jan 1;7(4):291-338.

36. Budnik I, Shenkman B, Savion N. Synergistic effect of signaling from receptors of soluble platelet agonists and outside-in signaling in formation of a stable fibrinogen-integrin αIIbβ3-actin cytoskeleton complex. Thromb Res. 2015;135(1):114-20.

37. Li Z, Delaney MK, O'Brien KA, Du X. Signaling during platelet adhesion and activation. Arterioscler Thromb Vasc Biol. 2010;30(12):2341-9.

38. Ruggeri ZM. Platelet adhesion under flow. Microcirculation. 2009;16(1):58-83.

39. Clemetson KJ. Platelets and primary haemostasis. Thromb Res. 2012;129(3):220-4.

40. Rivera J, Lozano ML, Navarro-Núñez L, Vicente V. Platelet receptors and signaling in the dynamics of thrombus formation. Haematologica. 2009;94(5):700-11.

41. Sing CE, Alexander-Katz A. Elongational flow induces the unfolding of von Willebrand factor at physiological flow rates. Biophys J. 2010;98(9):L35-7.

42. Valentijn K, Eikenboom J. Weibel–Palade bodies: a window to von Willebrand disease. J Thromb Haemost. 2013;11(4):581-92.

43. Hoffmeister KM. The role of lectins and glycans in platelet clearance. J Thromb Haemost. 2011;9(Suppl 1):35-43.

44. Best D, Senis YA, Jarvis GE, Eagleton HJ, Roberts DJ, Saito T, Jung SM, Moroi M, Harrison P, Green FR, Watson SP. GPVI levels in platelets: relationship to platelet function at high shear. Blood. 2003 Oct 15;102(8):2811-8.

45. Dopheide SM, Maxwell MJ, Jackson SP. Shear-dependent tether formation during platelet translocation on von Willebrand factor. Blood. 2002;99(1):159-67.

46. Wohner N, Kovács A, Machovich R, Kolev K. Modulation of the von Willebrand factor-dependent platelet adhesion through alternative proteolytic pathways. Thromb Res. 2012 Apr;129(4):41-6.

47. Terraube V, O'donnell JS, Jenkins PV. Factor VIII and von Willebrand factor interaction: biological, clinical and therapeutic importance. Haemophilia. 2010 Jan;16(1):3-13.

48. Springer TA. Von Willebrand factor, Jedi knight of the bloodstream. Blood. 2014;124(9):1412-25.

49. Yuan H, Deng N, Zhang S, Cao Y, Wang Q, Liu X, et al. The unfolded von Willebrand factor response in bloodstream: the self-association perspective. J Hematol Oncol. 2012 Oct 17;5:65.

50. van Galen KP, Tuinenburg A, Smeets EM, Schutgens RE. Von Willebrand factor deficiency and atherosclerosis. Blood Rev. 2012;26(5):189-96.

51. George JN. Platelets. Lancet. 2000;355(9214):1531-9.

52. Huck V, Schneider MF, Gorzelanny C, Schneider SW. The various states of von Willebrand factor and their function in physiology and pathophysiology. Thromb Haemost. 2014;111(4):598-609.

53. Sivaraman B, Latour RA. Delineating the roles of the GPIIb/IIIa and GP-Ib-IX-V platelet receptors in mediating platelet adhesion to adsorbed fibrinogen and albumin. Biomaterials. 2011;32(23):5365-70.

54. Maurer E, Tang C, Schaff M, Bourdon C, Receveur N, Ravanat C, et al. Targeting Platelet GPIbβ Reduces Platelet Adhesion, GPIb Signaling and Thrombin Generation and Prevents Arterial Thrombosis. Arterioscler Thromb Vasc Biol. 2013;33(6):1221-9.

55. Bryckaert M, Rosa J-P, Denis CV, Lenting PJ. Of von Willebrand factor and platelets. Cellular and Molecular Life Sciences. 2015 Jan;72(2):307-26.

56. Chen Z, Mondal NK, Ding J, Koenig SC, Slaughter MS, Griffith BP, et al. Activation and shedding of platelet glycoprotein IIb/IIIa under non-physiological shear stress. Mol Cell Biochem. 2015;409(1-2):93-101.

57. Zhu C, Yago T, Lou J, Zarnitsyna VI, McEver RP. Mechanisms for flow-enhanced cell adhesion. Ann Biomed Eng. 2008 Apr 1;36(4):604-21.

58. Hechler B, Gachet C. P2 receptors and platelet function. Purinergic Signal. 2011 Jul 27;7(3):293-303.

59. Ouyang W, Wei W, Cheng X, Zhang XF, Webb Iii EB, Oztekin A. Flow-induced conformational change of von Willebrand Factor multimer: Results from a

molecular mechanics informed model. J Nonnewton Fluid Mech. 2015 Mar;217:58-67.

60. Fuss B. Signaling pathways mediating adhesion and spreading through extracellular ADP and the P2Y12 receptor. Purinergic Signal. 2013;9(2):131-3.

61. Clemetson KJ. Platelets and Primary Haemostasis. Thromb Res. 2012 Mar;129(3):220-4.

62. Haberichter SL. von Willebrand factor propeptide: biology and clinical utility. Blood.126(15):1753-61.

63. Bennett JS. Platelet-fibrinogen interactions. Ann N Y Acad Sci. 2001;936:340-54.

64. Dai B, Wu P, Xue F, Yang R, Yu Z, Dai K, et al. Integrin αIIbβ3-Mediated Outside-in Signaling: Brake or Amplifier of Platelet Activation? Am Soc Hematology. 2014;116(5):918-30.

65. Hantgan RR, Stahle MC, Lord ST. Dynamic regulation of fibrinogen: integrin αIIbβ3 binding. Biochemistry. 2010;49(43):9217-25.

66. Lau TL, Kim C, Ginsberg MH, Ulmer TS. The structure of the integrin αIIbβ3 transmembrane complex explains integrin transmembrane signalling. The EMBO journal. 2009;28(9):1351-61.

67. Zhou Y-F, Springer TA. Highly reinforced structure of a C-terminal dimerization domain in von Willebrand factor. Blood. 2014 March 20;123(12):1785-93.

68. Bryckaert M, Rosa, J, Denis, CV, Lenting, PJ. Of von Willebrand factor and platelets. Cell Mol Life Sci. 2014 2015 Jan;72(2):307-26.

69. Gerke V. von Willebrand factor folds into a bouquet. EMBO J. 2011;30(19):3880-1.

70. James PD, Goodeve AC. von Willebrand disease. Genet Med. 2011 May;13(5):365-76.

71. Lippok S, Obser T, Müller Jochen P, Stierle Valentin K, Benoit M, Budde U, et al. Exponential Size Distribution of von Willebrand Factor. Biophys J. 2013;105(5):1208-16.

72. Schneppenheim R, Budde U. von Willebrand factor: the complex molecular genetics of a multidomain and multifunctional protein. J Thromb Haemost. 2011;9:209-15.

73. Bonazza K, Rottensteiner H, Schrenk G, Frank J, Allmaier G, Turecek PL, et al. Shear-Dependent Interactions of von Willebrand Factor with Factor VIII and Protease ADAMTS 13 Demonstrated at a Single Molecule Level by Atomic Force Microscopy. Anal Chem. 2015 Oct 20;87(20):10299-305.

74. Kragh T, Napoleone M, Fallah MA, Gritsch H, Schneider MF, Reininger AJ. High Shear Dependent von Willebrand Factor Self-assembly Fostered by Platelet Interaction and Controlled by ADAMTS13. Thromb Res. 2014;133(6):1079-87.

75. Manon-Jensen T, Kjeld N, Karsdal M. Collagen-mediated hemostasis. Journal of Thrombosis and Haemostasis. 2016;14(3):438-48.

76. Mammadova-Bach E, Ollivier V, Loyau S, Schaff M, Dumont B, Favier R, et al. Platelet glycoprotein VI binds to polymerized fibrin and promotes thrombin generation. Blood. 2015:blood-2015-02-629717.

77. Periayah MH, Halim AS, Saad AZ. Mechanism action of platelets and crucial blood coagulation pathways in hemostasis. Int J Hematol Oncol Stem Cell Res. 2017 Oct 1;11(4):319.

78. Singh I, Themistou E, Porcar L, Neelamegham S. Fluid shear induces conformation change in human blood protein von Willebrand factor in solution. Biophys J. 2009;96(6):2313-20.

79. Cosemans JM, Schols SE, Stefanini L, De Witt S, Feijge MA, Hamulyák K, et al. Key role of glycoprotein Ib-V-IX and von Willebrand factor in platelet activation-dependent fibrin formation at low shear flow. Blood. 2010;117(2):651-60.

80. Li R, Emsley J. The organizing principle of the platelet glycoprotein Ib–IX–V complex. J Thromb Haemost. 2013;11(4):605-14.

81. Skorczewski T, Griffith BE, Fogelson AL. Multi-bond models for platelet adhesion and cohesion. Society AM, editor2014. 149-72 p.

82. Nesbitt WS, Westein E, Tovar-Lopez FJ, Tolouei E, Mitchell A, Fu J, et al. A shear gradient-dependent platelet aggregation mechanism drives thrombus formation. Nat Med. 2009;15(6):665-73.

83. Jung SM, Moroi M. Platelet glycoprotein VI. Multichain Immune Recognition Receptor Signaling: Springer; 2008. p. 53-63.

84. Bennett J, Berger B, Billings P. The structure and function of platelet integrins. J Thromb Haemost. 2009;7(Suppl 1):200-5.

85. Harburger DS, Calderwood DA. Integrin signalling at a glance. Journal of cell science. 2009;122(2):159-63.

86. Varga-Szabo D, Pleines I, Nieswandt B. Cell adhesion mechanisms in platelets. Arterioscler Thromb Vasc Biol. 2008;28(3):403-12.

87. Nesbitt WS, Harper IS, Schoenwaelder SM, Yuan Y, Jackson SP. A live cell micro-imaging technique to examine platelet calcium signaling dynamics under blood flow. Platelets and Megakaryocytes: Springer; 2012. p. 73-89.

88. Shen B, Delaney MK, Du X. Inside-out, outside-in, and inside–outside-in: G protein signaling in integrin-mediated cell adhesion, spreading, and retraction. Curr Opin Cell Biol. 2012;24(5):600-6.

89. Reininger A. Platelet function under high shear conditions. Hamostaseologie. 2009;29(1):21-2.

90. Shida Y, Rydz N, Stegner D, Brown C, Mewburn J, Sponagle K, et al. Analysis of the role of von Willebrand factor, platelet glycoprotein VI-, and α2β1-mediated collagen binding in thrombus formation. Blood. 2014 Sep 11;124(11):1799-807.

91. Huang H, Vogel HJ. Structural basis for the activation of platelet integrin αIIbβ3 by calcium-and integrin-binding protein 1. J Am Chem Soc. 2012;134(8):3864-72.

92. Mehrbod M, Trisno S, Mofrad MR. On the activation of integrin αIIbβ3: outside-in and inside-out pathways. Biophysical journal. 2013;105(6):1304-15.

93. Tousoulis D, Kampoli A-M, Tentolouris Nikolaos Papageorgiou C, Stefanadis C. The role of nitric oxide on endothelial function. Curr Vasc Pharmacol. 2012;10(1):4-18.

94. Gao Y. The multiple actions of NO. Pflugers Arch. 2010;459(6):829-39.

95. Klinger JR, Abman SH, Gladwin MT. Nitric oxide deficiency and endothelial dysfunction in pulmonary arterial hypertension. Am J Respir Crit Care Med. 2013;188(6):639-46.

96. Francis SH, Busch JL, Corbin JD. cGMP-dependent protein kinases and cGMP phosphodiesterases in nitric oxide and cGMP action. Pharmacol Rev. 2010;62(3):525-63.

97. Sandoo A, van Zanten JJV, Metsios GS, Carroll D, Kitas GD. The endothelium and its role in regulating vascular tone. Open Cardiovasc Med J. 2010;4:302.

98. Furie B, Furie BC. Thrombus formation in vivo. J Clin Invest. 2005 Dec 1;115(12):3355-62.

99. Steinhubl SR, Moliterno DJ. The role of the platelet in the pathogenesis of atherothrombosis. Am J Cardiovasc Drug. 2005 Nov 1;5(6):399-408.

100. Offermanns S. Activation of platelet function through G protein–coupled receptors. Circ Res. 2006;99(12):1293-304.

101. Tsun Wong AK. Platelet biology: the role of shear. Expert Rev Hematol. 2013;6(2):205-12.

102. Park CY, Hoover PJ, Mullins FM, Bachhawat P, Covington ED, Raunser S, et al. STIM1 clusters and activates CRAC channels via direct binding of a cytosolic domain to Orai1. Cell. 2009;136(5):876-90.

103. Cosemans JM, Iserbyt BF, Deckmyn H, Heemskerk JW. Multiple ways to switch platelet integrins on and off. J Thromb Haemost. 2008;6(8):1253-61.

104. Jafarnejad M, Cromer W, Kaunas R, Zhang S, Zawieja D, Moore Jr J. Measurement of shear stress-mediated intracellular calcium dynamics in human dermal lymphatic endothelial cells. Am J Physiol Heart Circ Physiol. 2015;308(7):H697-H706.

105. Ruggeri ZM, Orje JN, Habermann R, Federici AB, Reininger AJ. Activation-independent platelet adhesion and aggregation under elevated shear stress. Blood. 2006;108(6):1903-10.

106. Cimmino G, Fischetti S, Golino P. The Two Faces of Thrombosis: Coagulation Cascade and Platelet Aggregation. J Thrombo Cir. 2017;3:117.

107. Yuan S, Chan HC, Vogel H, Filipek S, Stevens RC, Palczewski K. The Molecular Mechanism of P2Y1 Receptor Activation. Angew Chem Int Ed Engl. 2016;55(35):10331–10335.

108. Gachet C. Regulation of platelet functions by P2 receptors. Annu Rev Pharmacol Toxicol. 2006;46:277-300.

109. Jones ML, Norman JE, Morgan NV, Mundell SJ, Lordkipanidzé M, Lowe GC, et al. Diversity and impact of rare variants in genes encoding the platelet G protein-coupled receptors. Thromb Haemost. 2015;113(4):826.

110. Choo H-J, Saafir TB, Mkumba L, Wagner MB, Jobe SM. Mitochondrial calcium and reactive oxygen species regulate agonist-initiated platelet phosphatidylserine exposure. Arterioscler Thromb Vasc Biol. 2012;32(12):2946-55.

111. Fedor M, Simonova R, Fedorova J, Skornova I, Duraj L, Samos M, et al. Role of VASP Phosphorylation Assay in Monitoring the Antiplatelet Therapy. Acta Medica Martiniana. 2013;13(1):21.

112. Nieswandt B, Schulte V, Zywietz A, Gratacap M-P, Offermanns S. Costimulation of Gi-and G12/G13-mediated signaling pathways induces integrin αIIbβ3 activation in platelets. J Biol Chem. 2002;277(42):39493-8.

113. Rauch BH, Filep JG. Purinergic receptors and atherosclerosis: emerging role for vessel wall P2Y12. 2014.

114. Harrison P. Advances in the monitoring of anti-P2Y12 therapy. Platelets. 2012 2012 Nov 01;23(7):510-25.

115. Mahaut-Smith MP, Jones S, Evans RJ. The P2X1 receptor and platelet function. Purinergic Signal. 2011;7(3):341-56.

116. Fontana P, Zufferey A, Daali Y, Reny J-L. Antiplatelet Therapy: Targeting the TxA2 Pathway. J Cardiovasc Transl Res. 2013;7(1):29-38.

117. Iyú D, Glenn JR, White AE, Johnson AJ, Fox SC, Heptinstall S. The role of prostanoid receptors in mediating the effects of PGE2 on human platelet function. Platelets. 2010;21(5):329-42.

118. Iyú D, Jüttner M, Glenn JR, White AE, Johnson AJ, Fox SC, et al. PGE1 and PGE2 modify platelet function through different prostanoid receptors. Prostaglandins Other Lipid Mediat. 2011;94(1-2):9-16.

119. Bark Jr DL, Ku DN. Platelet transport rates and binding kinetics at high shear over a thrombus. Biophys J. 2013;105(2):502-11.

120. DiStasio E, DeCristofaro R. The effect of shear stress on protein conformation: Physical forces operating on biochemical systems: The case of von Willebrand factor. Biophysical Chemistry. 2010 Dec;153(1):1-8.

121. Al Dieri R, de Laat B, Hemker HC. Thrombin generation: what have we learned?. Blood Rev. 2012;26.

122. Van Der Meijden PE, Van Schilfgaarde M, Van Oerle R, Renne T, Ten Cate H, Spronk HM. Platelet- and erythrocyte-derived microparticles trigger thrombin generation via factor XIIa. J Thromb Haemost. 2012 Jul 03;10(7):1355-62.

123. Tripodi A, Chantarangkul V, Primignani M, Clerici M, Dell'Era A, Aghemo A, et al. Thrombin generation in plasma from patients with cirrhosis supplemented with normal plasma: considerations on the efficacy of treatment with fresh-frozen plasma. Intern Emerg Med. 2011 Feb 05;7(2):139-44.

124. DeLoughery TG. Basics of coagulation. Thromb Haemost. 2019 (pp. 1-9). Springer, Cham.

125. Ninivaggi M, Apitz-Castro R, Dargaud Y, de Laat B, Hemker HC, Lindhout T. Whole-blood thrombin generation monitored with a calibrated automated thrombogram-based assay. Clin Chem. 2012;58.

126. Koseoglu S, Meyer AF, Kim D, Meyer BM, Wang Y, Dalluge JJ, et al. Analytical Characterization of the Role of Phospholipids in Platelet Adhesion and Secretion. Anal Chem. 2015 Jan 06;87(1):413-21.

127. Fogelson AL, Neeves KB. Fluid Mechanics of Blood Clot Formation. Annu Rev Fluid Mech. 2015 Jan 03;47(1):377-403.

128. Nesbitt WS, Mangin P, Salem HH, Jackson SP. The impact of blood rheology on the molecular and cellular events underlying arterial thrombosis. J Mol Med. 2006;84(12):989-95.

129. Wootton DM, Ku DN. Fluid mechanics of vascular systems, diseases, and thrombosis. Annu Rev Biomed Eng. 1999;1:299-329.

130. Di Carlo D. Inertial microfluidics. Lab Chip. 2009;9(21):3038-46.

131. Loverich J, Kanno I, Kotera H. Single-step replicable microfluidic check valve for rectifying and sensing low Reynolds number flow. Microfluid Nanofluidics. 2006;3(4):427-35.

132. Pontiga F, Gaytán SP. An experimental approach to the fundamental principles of hemodynamics. Advances in physiology education. 2005;29(3):165-71.

133. Nam-Trung N, Zhigang W. Micromixers—a review. J Micromech Microeng. 2005;15(2):R1.

134. Evans J, Liepmann D, Pisano A. Planar Laminar Mixer. IEEE MEMS1997.

135. Ashinky G. Nonlinear analysis of hydrodynamic instability in laminar flames—I. Derivation of basic equations. Dynamics of Curved Fronts: Elsevier; 1988. p. 459-88.

136. Aarts PA, van den Broek SA, Prins GW, Kuiken GD, Sixma JJ, Heethaar RM. Blood platelets are concentrated near the wall and red blood cells, in the center in flowing blood. Arteriosclerosis. 1988;8(6):819-24.

137. Tovar-Lopez FJ, Rosengarten G, Westein E, Khoshmanesh K, Jackson SP, Mitchell A. A microfluidics device to monitor platelet aggregation dynamics in response to strain rate micro-gradients in flowing blood. Lab Chip. 2010;10.

138. Boileau E, Nithiarasu P, Blanco PJ, Müller LO, Fossan FE, Hellevik LR, et al. A benchmark study of numerical schemes for one-dimensional arterial blood flow modelling. International journal for numerical methods in biomedical engineering. 2015;31(10):e02732.

139. Lee J, Smith NP. The multi-scale modelling of coronary blood flow. Annals of biomedical engineering. 2012;40(11):2399-413.

140. Chakravarty S, Mandal P. Mathematical modelling of blood flow through an overlapping arterial stenosis. Mathematical and computer modelling. 1994;19(1):59-70.

141. Dewey C, Bussolari S, Gimbrone M, Davies PF. The dynamic response of vascular endothelial cells to fluid shear stress. Journal of biomechanical engineering. 1981;103(3):177-85.

142. Kroll MH, Hellums JD, McIntire L, Schafer A, Moake J. Platelets and shear stress. Blood. 1996;88(5):1525-41.

143. Casa LD, Deaton DH, Ku DN. Role of high shear rate in thrombosis. J Vasc Surg. 2015;61(4):1068-80.

144. Schuster S, Stark H. What can we learn from Einstein and Arrhenius about the optimal flow of our blood? Biochim Biophys Acta. 2014 Jan;1840(1):271-6.

145. Fitzgibbon S, Cowman J, Ricco AJ, Kenny D, Shaqfeh ES. Examining platelet adhesion via Stokes flow simulations and microfluidic experiments. Soft Matter. 2014 Nov 10;11(2):355-67.

146. Al-Tamimi M, Tan CW, Qiao J, Pennings GJ, Javadzadegan A, Yong AS, et al. Pathological shear triggers shedding of vascular receptors: a novel mechanism for downregulation of platelet glycoprotein (GP) VI in stenosed coronary vessels. Blood. 2012:blood-2011-10-386607.

147. Hamid I, Ishak M, Kamaruzzaman S, Jamil MA. Comparative Analysis of Mixing Performance of Three Types of Passive Micromixers for Laminar Blood-Reagent Mixing. J Eng Technol. 2012;2(1):6-11.

148. Zulkarnain MH, Ma'radzi AA, Jamil A, Mahadi M. Consideration of obstacles number in designing passive micromixer for laminar mixing flow. International Conference on Science and Technology; Pulau Pinang2014.

149. Formaggia L, Gerbeau J-F, Nobile F, Quarteroni A. On the coupling of 3D and 1D Navier–Stokes equations for flow problems in compliant vessels. Computer methods in applied mechanics and engineering. 2001;191(6-7):561-82.

150. Perktold K, Rappitsch G. Computer simulation of local blood flow and vessel mechanics in a compliant carotid artery bifurcation model. Journal of biomechanics. 1995;28(7):845-56.

151. Leal LG. Advanced transport phenomena: fluid mechanics and convective transport processes: Cambridge University Press; 2007.

152. Hosseinzadegan H, Tafti DK. Modeling thrombus formation and growth. Biotechnol Bioeng. 2017;114(10):2154-72.

153. Tovar-Lopez FJ, Rosengarten G, Westein E, Khoshmanesh K, Jackson SP, Mitchell A, et al. A microfluidics device to monitor platelet aggregation dynamics in response to strain rate micro-gradients in flowing blood. Lab Chip. 2010;10(3):291-302.

154. Colace TV, Diamond SL. Direct observation of von Willebrand factor elongation and fiber formation on collagen during acute whole blood exposure to pathological flow. Arterioscler Thromb Vasc Biol. 2013 Oct 25;33(1):105-13.

155. Zhao R, Kameneva MV, Antaki JF. Investigation of platelet margination phenomena at elevated shear stress. Biorheology. 2007;44(3):161-77.

156. Fitzgibbon S, Spann AP, Qi QM, Shaqfeh ESG. In vitro measurement of particle margination in the microchannel flow: effect of varying hematocrit. Biophysical journal. 2015;108(10):2601-8.

157. Gekle S. Strongly Accelerated Margination of Active Particles in Blood Flow. Biophysical journal. 2016;110(2):514-20.

158. Lee WH, Schaffner-Reckinger E, Tsoukatos DC, Aylward K, Moussis V, Tsikaris V, et al. Inhibition of αIIbβ3 Ligand Binding by an αIIb Peptide that Clasps the Hybrid Domain to the βI Domain of β3. PloS one. 2015;10(9):e0134952.

159. Tsun Wong AK. Platelet biology: the role of shear. Expert Rev Hematol. 2013 Apr 01;6(2):205-12.

160. Maxwell MJ, Westein E, Nesbitt WS, Giuliano S, Dopheide SM, Jackson SP. Identification of a 2-stage platelet aggregation process mediating shear-dependent thrombus formation. Blood. 2007 Jan 15;109(2):566-76.

161. Laurent P-A, Séverin S, Hechler B, Vanhaesebroeck B, Payrastre B, Gratacap M-P. Platelet PI3Kβ and GSK3 regulate thrombus stability at high-shear rate. Blood. 2014;125(5):588335.

162. Lian L, Wang Y, Draznin J, Eslin D, Bennett JS, Poncz M, et al. The relative role of PLCβ and PI3Kγ in platelet activation. Blood. 2005;106(1):110-7.

163. Kakouros N, Kickler TS, Laws KM, Rade JJ. Hematocrit alters VerifyNow P2Y12 assay results independently of intrinsic platelet reactivity and clopidogrel responsiveness. J Thromb Haemost. 2013;11.

164. Singh M, Shin S. Changes in erythrocyte aggregation and deformability in diabetes mellitus: a brief review. Indian J Exp Biol. 2009;47(1):7-15.

165. Brazilek RJ, Tovar-Lopez FJ, Wong AK, Tran H, Davis AS, McFadyen JD, et al. Application of a strain rate gradient microfluidic device to von Willebrand's disease screening. Lab Chip. 2017;17(15):2595-608.

166. Berndt MC, Andrews RK. Bernard-Soulier syndrome. Haematologica. 2011;96(3):355.

167. Sandrock-Lang K, Wentzell R, Santoso S, Zieger B. Inherited platelet disorders. Hämostaseologie. 2015 Feb 24;35(2):[Epub ahead of print].

168. Versteeg HH, Heemskerk JW, Levi M, Reitsma PH. New Fundamentals in Hemostasis. Physiol Rev. 2013 Jan 01;93(1):327-58.

169. Rodeghiero F, Tosetto A, Abshire T, Arnold D, Coller B, James P, et al. ISTH/SSC bleeding assessment tool: a standardized questionnaire and a proposal for a new bleeding score for inherited bleeding disorders. J Thromb Haemost. 2010;8(9):2063-5.

170. Bucciarelli P, Siboni SM, Stufano F, Biguzzi E, Canciani MT, Baronciani L, et al. Predictors of von Willebrand disease diagnosis in individuals with borderline von Willebrand factor plasma levels. J Thromb Haemost. 2015 Feb;13(2):228-36.

171. Akin M, Balkan C, Karapinar DY, Kavakli K. The Influence of the ABO Blood Type on the Distribution of von Willebrand Factor in Healthy Children With no Bleeding Symptoms. Clin Appl Thromb Hemost. 2012 Jun 01;18(3):316-9.

172. Rydz N, James PD. The evolution and value of bleeding assessment tools. J Thromb Haemost. 2012 Oct 30;10(11):2223-9.

173. Lillicrap D. von Willebrand disease: advances in pathogenetic understanding, diagnosis, and therapy. Blood. 2013 Nov 28;122(23):3735-40.

174. Branchford B, DiPaola J. Making a diagnosis of VWD. Haematology. 2012 Dec 8;2012(1):161-7.

175. Favaloro EJ. Diagnosis and classification of von Willebrand disease: a review of the differential utility of various functional von Willebrand factor assays. Blood Coagul Fibrinolysis. 2011;22(7):553-64.

176. Laffan MA, Lester W, O'Donnell JS, Will A, Tait RC, Goodeve A, et al. The diagnosis and management of von Willebrand disease: a United Kingdom Haemophilia Centre Doctors Organization guideline approved by the British Committee for Standards in Haematology. Br J Haematol. 2014;167(4):453-65.

177. Millar C. Why and how do we classify von Willebrand disease? Haemophilia. 2015;21(4):407-10.

178. Castaman G, Rodeghiero F. Advances in the diagnosis and management of type 1 von Willebrand disease. Expert Rev Hematol. 2011;4(1):95-106.

179. Sanders YV, Groeneveld D, Meijer K, Fijnvandraat K, Cnossen MH, van der Bom JG, et al. von Willebrand factor propeptide and the phenotypic classification of von Willebrand disease. Blood. 2015 May 07;125(19):3006-13.

180. Santos-Martinez MJ, Prina-Mello A, Medina C, Radomski MW. Analysis of platelet function: role of microfluidics and nanodevices. Analyst. 2011;136(24):5120-6.

181. Bolton-Maggs PH, Favaloro EJ, Hillarp A, Jennings I, Kohler HP. Difficulties and pitfalls in the laboratory diagnosis of bleeding disorders. Haemophilia. 2012;18 (Suppl 4):66-72.

182. Roberts JC, Flood VH. Laboratory diagnosis of von Willebrand disease. Int J Lab Hematol. 2015 May;37(Suppl 1):11-7.

183. Marques MB, Fritsma GA. von Willebrand Disease Laboratory Diagnosis: the Saga Continues. Am J Clin Pathol. 2011 Jun 01;135(6):818-20.

184. Campos M, Sun W, Yu F, Barbalic M, Tang W, Chambless LE, et al. Genetic determinants of plasma von Willebrand factor antigen levels: a target gene SNP and haplotype analysis of ARIC cohort. Blood. 2011;117(19):5224-30.

185. Ng C, Motto DG, Di Paola J. Diagnostic approach to von Willebrand disease. Blood. 2015 Mar 26;125(13):2029-37.

186. Tuohy E, Litt E, Alikhan R. Treatment of patients with von Willebrand disease. Journal of blood medicine. 2011 Apr 20;2:49-57.

187. Schneppenheim R. The pathophysiology of von Willebrand disease: therapeutic implications. Thromb Res. 2011;128(Supplement 1):3-7.

188. Windyga J, Dolan G, Altisent C, Katsarou O, López Fernández MF, Zülfikar B, et al. Practical aspects of DDAVP use in patients with von Willebrand Disease undergoing invasive procedures: a European survey. Haemophilia. 2016;22(1):110-20.

189. Castaman G, Goodeve A, Eikenboom J. Principles of care for the diagnosis and treatment of von Willebrand disease. Haematologica. 2013 May;98(5):667-74.

190. Svensson PJ, Bergqvist PB, Juul KV, Berntorp E. Desmopressin in treatment of haematological disorders and in prevention of surgical bleeding. Blood Rev. 2014 May;28(3):95-102.

191. Andrews RK, Arthur JF, Gardiner EE. Targeting GPVI as a novel antithrombotic strategy. J Blood Med.5:59-68.

192. Zwaginga J, Sakariassen K, Nash G, King M, Heemskerk J, Frojmovic M, et al. Flow-based assays for global assessment of hemostasis. Part 2: current methods and considerations for the future 1. Journal of Thrombosis and Haemostasis. 2006;4(12):2716-7.

193. Zwaginga JJ, Nash G, King MR, Heemskerk JW, Frojmovic M, Hoylaerts MF, et al. Flow-based assays for global assessment of hemostasis. Part 1: biorheologic considerations. J Thromb Haemost. 2006 Aug 25;4(11):2486-7.

194. Kent NJ, O'Brien S, Basabe-Desmonts L, Meade GR, MacCraith BD, Corcoran BG, et al. Shear-mediated platelet adhesion analysis in less than 100 mul of blood: toward a POC platelet diagnostic. IEEE Trans Biomed Eng. 2011;58(3):826-30.

195. Paniccia R, Priora R, Alessandrello Liotta A, Abbate R. Platelet function tests: a comparative review. Vasc Health Risk Manag. 2015 Feb 18;11:133-48.

196. Gubala V, Harris L, Ricco A, Tan M, Williams D. Point of Care Diagnostics: Status and Future. Anal Chem. 2012;84(2):487-515.

197. Harrison P, Lordkipanidzé M. Testing Platelet Function. Hematol Oncol Clin North Am. 2013 Jun;27(3):411-41.

198. Rincon L, Ammentorp B, Darius H, De Caterina R, Kirchhof P, Le Heuzey J-Y, et al. Clinical profile and cardiovascular risk factors of patients treated with novel oral anticoagulants in atrial fibrillation-patterns of use in the European PREFER in AF registry. European Heart Journal. 2013;34(suppl_1).

199. Reny JL, De Moerloose P, Dauzat M, Fontana P. Use of the PFA-100™ closure time to predict cardiovascular events in aspirin-treated cardiovascular

patients: a systematic review and meta-analysis. Journal of Thrombosis and Haemostasis. 2008;6(3):444-50.

200. Ardillon L, Ternisien C, Fouassier M, Sigaud M, Lefrançois A, Pacault M, et al. Platelet function analyser (PFA-100) results and von Willebrand factor deficiency: a 16-year 'real-world' experience. Haemophilia. 2015;21(5):646-52.

201. Hayward CP, Harrison P, Cattaneo M, Ortel TL, Rao AK. Platelet function analyzer (PFA)-100 closure time in the evaluation of platelet disorders and platelet function. J Thromb Haemost. 2006;4.

202. Favaloro E. Utility of the PFA-100® for assessing bleeding disorders and monitoring therapy: a review of analytical variables, benefits and limitations. Haemophilia. 2001;7(2):170-9.

203. Femia EA, Scavone M, Lecchi A, Cattaneo M. Effect of platelet count on platelet aggregation measured with impedance aggregometry (Multiplate™ analyzer) and with light transmission aggregometry. J Thromb Haemost. 2013;11(12):2193-6.

204. Panzer S, Jilma P. Methods for testing platelet function for transfusion medicine. Vox Sang. 2011;101(1):1-9.

205. Hintzke M, Harrington A. PFA-100 Utilization: One Institution's Experience. Am J Clin Pathol. 2015 Oct 01;144(suppl 2):131.

206. Gorog DA, Fuster V. Platelet function tests in clinical cardiology: unfulfilled expectations. J Am Coll Cardiol. 2013;61(21):2115-29.

207. Shenkman B, Savion N, Dardik R, Tamarin I, Varon D. Testing of platelet deposition on polystyrene surface under flow conditions by the cone and plate(let) analyzer: role of platelet activation, fibrinogen and von Willebrand factor. Thromb Res. 2000;99.

208. Savion N, Varon D. Impact–the cone and plate (let) analyzer: testing platelet function and anti-platelet drug response. Pathophysiology of haemostasis and thrombosis. 2006;35(1-2):83-8.

209. Varon D, Lashevski I, Brenner B, Beyar R, Lanir N, Tamarin I, et al. Cone and plate (let) analyzer: monitoring glycoprotein IIb/IIIa antagonists and von Willebrand disease replacement therapy by testing platelet deposition under flow conditions. American heart journal. 1998;135(5):S187-S93.

210. Malinin A, Pokov A, Spergling M, Defranco A, Schwartz K, Schwartz D, et al. Monitoring platelet inhibition after clopidogrel with the VerifyNow-P2Y12® rapid analyzer: the VERIfy Thrombosis risk ASsessment (VERITAS) study. Thrombosis research. 2007;119(3):277-84.

211. Godino C, Mendolicchio L, Figini F, Latib A, Sharp AS, Cosgrave J, et al. Comparison of VerifyNow-P2Y12 test and Flow Cytometry for monitoring individual platelet response to clopidogrel. What is the cut-off value for identifying patients who are low responders to clopidogrel therapy? Thromb J. 2009;7(1):1-9.

212. van Oeveren W. Obstacles in Haemocompatibility Testing. Scientifica. 2013 2013;2013:392584.

213. Szydzik C, Brazilek RJ, Khoshmanesh K, Akbaridoust F, Knoerzer M, Thurgood P, et al. Elastomeric Microvalve Geometry Affects Haemocompatibility. Lab Chip. 2018;18(12):1778-92.

214. Srivastava A, Kelleher A. Point-of-care coagulation testing. Continuing Education in Anaesthesia, Critical Care & Pain. 2012;13(1):12-6.

215. Chrimes AF, Khoshmanesh K, Stoddart PR, Mitchell A, Kalantar-zadeha K. Microfluidics and Raman microscopy: current applications and future challenges. Chem Soc Rev. 2013;42(13):5880-906.

216. Knapp MR, Kopf-Sill A, Dubrow R, Chow A, Chien R-L, Chow C, et al. Commercialized and emerging lab-on-a-chip applications. Proc Micro Total Analysis Systems; Dordrecht: Springer; 2001. p. 7.

217. Branchford BR, Ng CJ, Neeves KB, Di Paola J. Microfluidic technology as an emerging clinical tool to evaluate thrombosis and hemostasis. Thromb Res. 2015;136(1):13-9.

218. Siddiqui TI, Kumar KS, Dikshit DK. Platelets and atherothrombosis: causes, targets and treatments for thrombosis. Curr Med Chem. 2013 Apr 18;20(22):2779-97.

219. Westein E, de Witt S, Lamers M, Cosemans JMEM, Heemskerk JWM. Monitoring in vitro thrombus formation with novel microfluidic devices. Platelets. 2012;23(7):501-9.

220. Conant CG, Schwartz MA, Nevill T, Ionescu-Zanetti C. Platelet adhesion and aggregation under flow using microfluidic flow cells. J Vis Exp. 2009;(32):1644.

221. Zhou Y-J, Xiang J-Z, Yuan H, Liu H, Tang Q, Hao H-Z, et al. Neferine exerts its antithrombotic effect by inhibiting platelet aggregation and promoting dissociation of platelet aggregates. Thromb Res. 2013;132(2):202-10.

222. Yamaguchi Y, Moriki T, Igari A, Matsubara Y, Ohnishi T, Hosokawa K, et al. Studies of a microchip flow-chamber system to characterize whole blood thrombogenicity in healthy individuals. Thromb Res. 2013;132(2):263-70.

223. Ito M, Kaikita K, Sueta D, Ishii M, Oimatsu Y, Arima Y, et al. Total thrombus-formation analysis system (T-TAS) can predict periprocedural bleeding events in patients undergoing catheter ablation for atrial fibrillation. Journal of the American Heart Association. 2016;5(1):e002744.

224. Goerge T, Kleineruschkamp F, Barg A, Schnaeker EM, Huck V, Schneider MF, et al. Microfluidic reveals generation of platelet-strings on tumor-activated endothelium. Thromb Haemost. 2007;98(2):283-6.

225. Yager P, Edwards T, Fu E, Helton K, Nelson K, Tam MR, et al. Microfluidic diagnostic technologies for global public health. Nature. 2006;442(7101):412.

226. Wu J, Dong M, Rigatto C, Liu Y, Lin F. Lab-on-chip technology for chronic disease diagnosis. npj Digital Medicine. 2018;1(1):7.

227. Seyfert UT, Haubelt H, Vogt A, Hellstern P. Variables influencing Multiplate(TM) whole blood impedance platelet aggregometry and turbidimetric platelet aggregation in healthy individuals. Platelets. 2007;18.

228. Yeom E, Park JH, Kang YJ, Lee SJ. Microfluidics for simultaneous quantification of platelet adhesion and blood viscosity. Sci Rep. 2016;6:24994.

229. Jain A, Graveline A, Waterhouse A, Vernet A, Flaumenhaft R, Ingber DE. A shear gradient-activated microfluidic device for automated monitoring of whole blood haemostasis and platelet function. Nat Commun. 2016 Jan 06;7:10176.

230. Maloney JP, Silliman CC, Ambruso DR, Wang J, Tuder RM, Voelkel NF. In vitro release of vascular endothelial growth factor during platelet aggregation. Am J Physiol. 1998;275(3):H1054-H61.

231. Tran-Minh N, Karlsen F, Dong T. A simple and low cost micromixer for laminar blood mixing: design, optimization, and analysis. Biomedical Informatics and Technology: Springer; 2014. p. 91-104.

232. Okorie ON, Dellinger P. Lactate: biomarker and potential therapeutic target. Crit Care Clin. 2011;27(2):299-326.

233. Chuang H-S, Wereley S. Design, fabrication and characterization of a conducting PDMS for microheaters and temperature sensors. Journal of Micromechanics and Microengineering. 2009;19(4):045010.

234. Jo B-H, Van Lerberghe LM, Motsegood KM, Beebe DJ. Three-dimensional micro-channel fabrication in polydimethylsiloxane (PDMS) elastomer. Journal of microelectromechanical systems. 2000;9(1):76-81.

235. Wong I, Ho C-M. Surface molecular property modifications for poly (dimethylsiloxane)(PDMS) based microfluidic devices. Microfluid Nanofluidics. 2009;7(3):291.

236. Butler PJ, Weinbaum S, Chien S, Lemons DE. Endothelium-dependent, shear-induced vasodilation is rate-sensitive. Microcirculation. 2000;7(1):53-65.

237. Leclerc E, Sakai Y, Fujii T. Cell culture in 3-dimensional microfluidic structure of PDMS (polydimethylsiloxane). Biomedical microdevices. 2003;5(2):109-14.

238. Young EW, Beebe DJ. Fundamentals of microfluidic cell culture in controlled microenvironments. Chemical Society Reviews. 2010;39(3):1036-48.

239. Mata A, Fleischman AJ, Roy S. Characterization of polydimethylsiloxane (PDMS) properties for biomedical micro/nanosystems. Biomedical microdevices. 2005;7(4):281-93.

240. Zheng B, Tice JD, Roach LS, Ismagilov RF. A droplet-based, composite PDMS/glass capillary microfluidic system for evaluating protein crystallization conditions by microbatch and vapor-diffusion methods with on-chip X-ray diffraction. Angewandte chemie international edition. 2004;43(19):2508-11.

241. Toepke MW, Beebe DJ. PDMS absorption of small molecules and consequences in microfluidic applications. Lab Chip. 2006;6(12):1484-6.

242. Gale B, Jafek A, Lambert C, Goenner B, Moghimifam H, Nze U, et al. A Review of Current Methods in Microfluidic Device Fabrication and Future Commercialization Prospects. Inventions. 2018;3(3):60.

243. Hansen RR, Wufsus AR, Barton ST, Onasoga AA, Johnson-Paben RM, Neeves KB. High content evaluation of shear dependent platelet function in a microfluidic flow assay. Ann Biomed Eng. 2013;41(2):250-62.

244. Beh CW, Zhou W, Wang T-H. PDMS–glass bonding using grafted polymeric adhesive–alternative process flow for compatibility with patterned biological molecules. Lab on a Chip. 2012;12(20):4120-7.

245. Beh CW, Zhou W, Wang T-H, editors. Oxygen plasma-free microfluidic device sealing. 14th International Conference on Miniaturized Systems for Chemistry and Life Sciences; 2010.

246. Mark D, Haeberle S, Roth G, von Stetten F, Zengerle R. Microfluidic lab-on-a-chip platforms: requirements, characteristics and applications. Chemical Society Reviews. 2010 Jan 25;39(3):1153-82.

247. Szydzik C, Niego B, Dalzell G, Knoerzer M, Ball F, Nesbitt W, et al. Fabrication of complex PDMS microfluidic structures and embedded functional substrates by one-step injection moulding. RSC Advances. 2016;6(91):87988-94.

248. Waters LJ, Finch CV, Bhuiyan AMH, Hemming K, Mitchell JC. Effect of plasma surface treatment of poly (dimethylsiloxane) on the permeation of pharmaceutical compounds. Journal of pharmaceutical analysis. 2017;7(5):338-42.

249. Yang C, Wang W, Li Z, editors. Optimization of corona-triggered PDMS-PDMS bonding method. Nano/Micro Engineered and Molecular Systems, 2009 NEMS 2009 4th IEEE International Conference on; 2009: IEEE.

250. Mulvihill JN, Faradji A, Oberling F, Cazenave JP. Surface passivation by human albumin of plasmaperesis circuits reduces platelet accumulation and thrombus formation. Experimental and clinical studies. J Biomed Mater Res A. 1990;24(2):155-63.

251. Convert L, Chabot V, Zermatten P-J, Hamel R, Cloarec J-P, Lecomte R, et al. Passivation of KMPR microfluidic channels with bovine serum albumin (BSA) for improved hemocompatibility characterized with metal-clad waveguides. Sens Actuators B Chem. 2012;173:447-54.

252. Goodman S, Cooper S, Albrecht R. The effects of substrate-adsorbed albumin on platelet spreading. J Biomater Sci Polym Ed. 1991;2(2):147-59.

253. Zhou J, Ellis AV, Voelcker NH. Recent developments in PDMS surface modification for microfluidic devices. Electrophoresis. 2010;31(1):2-16.

254. Vlachopoulou M-E, Petrou P, Kakabakos S, Tserepi A, Beltsios K, Gogolides E. Effect of surface nanostructuring of PDMS on wetting properties, hydrophobic recovery and protein adsorption. Microelectronic Engineering. 2009;86(4-6):1321-4.

255. Liu B, Tang D. Influence of non-Newtonian Properties of Blood on the Wall Shear Stress in Human Atherosclerotic Right Coronary Arteries. Mol Cell Biomech. 2011;8(1):73-90.

256. Kwang WO, Chong HA. A review of microvalves. J Micromech Microeng. 2006;16(5):R13.

257. Gao X, Jiang L, Su X, Qin J, Lin B. Microvalves actuated sandwich immunoassay on an integrated microfluidic system. Electrophoresis. 2009 Jul;30(14):2481-7.

258. Baechi D, Buser R, Dual J. High-Density Microvalve Arrays for Sample Processing in PCR Chips. Biomed Microdevices. 2001 Sep;3(3):183-90.

259. Chun-Wei H, Gwo-Bin L. A microfluidic system for automatic cell culture. J Micromech Microeng. 2007 Jun 05;17(7):1266.

260. Lau BTC, Baitz CA, Dong XP, Hansen CL. A Complete Microfluidic Screening Platform for Rational Protein Crystallization. J Am Chem Soc. 2007 Jan 01;129(3):454-5.

261. Tchantchaleishvili V, Sagebin F, Ross RE, Hallinan W, Schwarz KQ, Massey HT. Evaluation and treatment of pump thrombosis and hemolysis. Ann Cardiothorac Surg. 2014 Sep;3(5):490-5.

262. Helms CC, Marvel M, Zhao W, Stahle M, Vest R, Kato G, et al. Mechanisms of hemolysis-associated platelet activation. J Thromb Haemost. 2013;11(12):2148-54.

263. Mohan R, Schudel BR, Desai AV, Yearsley JD, Apblett CA, Kenis PJA. Design considerations for elastomeric normally closed microfluidic valves. Sens Actuators B Chem. 2011;160(1):1216-23.

264. Au AK, Lai H, Utela BR, Folch A. Microvalves and Micropumps for BioMEMS. Micromachines. 2011 May 24;2(2):179-220.

265. Takao H, Ishida M, Sawada K. A pneumatically actuated full in-channel microvalve with MOSFET-like function in fluid channel networks. Journal of microelectromechanical systems. 2002;11(5):421-6.

266. Yamamoto T, Fujii T, Nojima T. PDMS–glass hybrid microreactor array with embedded temperature control device. Application to cell-free protein synthesis. Lab Chip. 2002;2(4):197-202.

267. Chen A, Pan T. Manually Operatable On-Chip Bistable Pneumatic Microstructures for Microfluidic Manipulations. Lab Chip. 2014;14(17):3401-8.

268. Robertson AM, Sequeira A, Owens RG. Rheological models for blood. Cardiovascular mathematics: Springer; 2009. p. 211-41.

269. Takao H, Miyamura K, Ebi H, Ashiki M, Sawada K, Ishida M. A MEMS microvalve with PDMS diaphragm and two-chamber configuration of thermo-pneumatic actuator for integrated blood test system on silicon. Sens Actuators A Phys. 2005;119(2):468-75.

270. Gershfeld N, Murayama M. Thermal instability of red blood cell membrane bilayers: temperature dependence of hemolysis. The Journal of membrane biology. 1988;101(1):67-72.

271. Kim J, Kang M, Jensen EC, Mathies RA. Lifting gate PDMS microvalves and pumps for microfluidic control. Anal Chem. 2012;84(4):2067-71.

272. Kwon GH, Jeong GS, Park JY, Moon JH, Lee S-H. A low-energy-consumption electroactive valveless hydrogel micropump for long-term biomedical applications. Lab Chip. 2011;11(17):2910-5.

273. Yu Q, Bauer JM, Moore JS, Beebe DJ. Responsive biomimetic hydrogel valve for microfluidics. Applied Physics Letters. 2001;78(17):2589-91.

274. Yoon HJ, Sim WY, Yang SS. The fabrication and test of a phase-change micropump. Int Mech Eng Congress Expo2001.

275. Saez J, Antoñana M, Etxebarria J, Benito-Lopez F, editors. In-situ generated biocompatible alginate actuators for flow control in microfluidics. International Conference on Solid-State Sensors, Actuators and Microsystems; 2015: IEEE.

276. Tai Y-C, Shi W, Guo L, inventors; Google Patents, assignee. Thermal blood clot formation and use in microfluidic device valving applications, 2014.

277. Reddoch KM, Pidcoke HF, Montgomery RK, Fedyk CG, Aden JK, Ramasubramanian AK, et al. Hemostatic function of apheresis platelets stored at 4 C and 22 C. Shock (Augusta, Ga). 2014;41(0 1):54.

278. Song Y, Zhao T. Modelling and test of a thermally-driven phase-change nonmechanical micropump. Journal of micromechanics and microengineering. 2001;11(6):713.

279. Kang L, Chung BG, Langer R, Khademhosseini A. Microfluidics for Drug Discovery and Development: From Target Selection to Product Lifecycle Management. Drug Discov Today. 2008;13(1-2):1-13.

280. Microfluidics-a review. J Micromech Microeng. 1993;3(4):168.

281. Xia F, Tadigadapa S, Zhang QM. Electroactive polymer based microfluidic pump. Sens Actuators A Phys. 2006;125(2):346.

282. Insull W, Bartsch G. Cholesterol, triglyceride, and phospholipid content of intima, media, and atherosclerotic fatty streak in human thoracic aorta. The Journal of clinical investigation. 1966;45(4):513-23.

283. Davies PF. Hemodynamic shear stress and the endothelium in cardiovascular pathophysiology. Nat Rev Cardiol. 2009;6(1):16.

284. Koster A, Loebe M, Hansen R, Potapov EV, Noon GP, Kuppe H, et al. Alterations in coagulation after implantation of a pulsatile Novacor LVAD and the axial flow MicroMed DeBakey LVAD. The Annals of thoracic surgery. 2000;70(2):533-7.

285. Kamdar F, Boyle A, Liao K, Colvin-adams M, Joyce L, John R. Effects of centrifugal, axial, and pulsatile left ventricular assist device support on end-organ function in heart failure patients. The Journal of heart and lung transplantation. 2009;28(4):352-9.

286. Karmozdi M, Salari A, Shafii MB. Experimental study of a novel Magneto Mercury Reciprocating (MMR) micropump, fabrication and operation. Sens Actuators A Phys. 2013;194:277.

287. Davies M, Johnston I, Tan C, Tracey M. Whole blood pumping with a microthrottle pump. Biomicrofluidics. 2010;4(4):044112.

288. Kim E, Gustenhoven E, Mescher M, Pararas E, Smith K, Spencer A, et al. A microfluidic reciprocating intracochlear drug delivery system with reservoir and active dose control. Lab Chip. 2014;14(4):710.

289. Hsu Y-C, Le NB. Equivalent electrical network for performance characterization of piezoelectric peristaltic micropump. Microfluid Nanofluidics. 2009;7(2):237-48.

290. Moghadam ME, Shafii MB. Rotary magnetohydrodynamic micropump based on slug trapping valve. J Microelectromech S. 2011;20(1):260-9.

291. Darby S, Moore M, Friedlander T, Schaffer D, Reiserer R, Wikswo J, et al. A metering rotary nanopump for microfluidic systems. Lab Chip. 2010;10(23):3218.

292. Lum P, inventor; Google Patents, assignee. Micro paddle wheel pump for precise pumping, mixing, dispensing, and valving of blood and reagents, 2003.

293. Laser DJ, Santiago JG. A review of micropumps. J Micromech Microeng. 2004;14(6):R35.

294. Haeberle S, Brenner T, Zengerle R, Ducree J. Centrifugal extraction of plasma from whole blood on a rotating disk. Lab Chip. 2006;6(6):776-81.

295. Strohmeier O, Keller M, Schwemmer F, Zehnle S, Mark D, von Stetten F, et al. Centrifugal microfluidic platforms: advanced unit operations and applications. Chem Soc Rev. 2015;44(17):6187-229.

296. Centrifugal pump theory. 3rd ed, 2010. 302 p.

297. Marx RE. Platelet-rich plasma (PRP): what is PRP and what is not PRP? Implant dentistry. 2001;10(4):225-8.

298. Jang J, Lee SS. Theoretical and experimental study of MHD (magnetohydrodynamic) micropump. Sens Actuators A Phys. 2000;80(1):84.

299. Chiu S-H, Liu C-H. An air-bubble-actuated micropump for on-chip blood transportation. Lab Chip. 2009;9(11):1524-33.

300. Lemoff AV, Lee AP, inventors; Google Patents, assignee. Magnetohydrodynamic pump with a system for promoting flow of fluid in one direction, 2010.

301. Choe Y, Kim ES. Valveless micropump driven by acoustic streaming. J Micromech Microeng. 2013;23(4):045005.

302. Warren B, Philp R, Inwood M. The ultrastructural morphology of air embolism: platelet adhesion to the interface and endothelial damage. British journal of experimental pathology. 1973;54(2):163.

303. Weng C-H, Lien K-Y, Yang S-Y, Lee G-B. A suction-type, pneumatic microfluidic device for liquid transport and mixing. Microfluid Nanofluidics. 2010;10(2):301–10.

304. Derks RJS, Frijns AJH, Prins MWJ, Dietzel A. Reversionary rotation of actuated particles for microfluidic near-surface mixing. Appl Phys Lett. 2011;99(2):024103.

305. Che-Hsin L, Chien-Hsiung T, Lung-Ming F. A rapid three-dimensional vortex micromixer utilizing self-rotation effects under low Reynolds number conditions. J Micromech Microeng. 2005;15(5):935.

306. Qin JJ, Yeo LY, Friend JR. MicroPIV and micromixing study of corona wind induced microcentrifugation flows in a cylindrical cavity. Microfluid Nanofluidics. 2009;8(10):231–41.

307. Kang YJ, Lee S-J. In vitro and ex vivo measurement of the biophysical properties of blood using microfluidic platforms and animal models. Analyst. 2018;143(12):2723-49.

308. Elwenspoek M, Lammerink TSJ, Miyake R, Fluitman JHJ. Towards integrated microliquid handling systems. J Micromech Microeng. 1994;4(4):227.

309. Song-Bin H, Min-Hsien W, Zhanfeng C, Zheng C, Gwo-Bin L. A membrane-based serpentine-shape pneumatic micropump with pumping performance modulated by fluidic resistance. J Micromech Microeng. 2008;18(4):045008.

310. Dimotakis PE, Brown GL. The mixing layer at high Reynolds number: large-structure dynamics and entrainment. Journal of Fluid Mechanics. 1976;78(3):535-60.

311. Yun K-S, Yoon E. Microfluidic components and bio-reactors for miniaturized bio-chip applications. Biotechnol Bioprocess Eng. 2004;9(2):86-92.

312. Voldman J, Gray ML, Schmidt MA. An integrated liquid mixer/valve. J Microelectromech Syst. 2000;9(3):295.

313. Chung CK, Shih TR. A rhombic micromixer with asymmetrical flow for enhancing mixing. J Micromech Microeng. 2007;17(12):2495.

314. Zhou B, Xu W, Syed AA, Chau Y, Chen L, Chew B, et al. Design and fabrication of magnetically functionalized flexible micropillar arrays for rapid and controllable microfluidic mixing. Lab on a Chip. 2015;15(9):2125-32.

315. Szydzik C, Brazilek RJ, Khoshmanesh K, Akbaridoust F, Knoerzer M, Thurgood P, et al. Elastomeric microvalve geometry affects haemocompatibility. Lab Chip. 2018;18(12):1778-92.

316. Amirouche F, Zhou Y, Johnson T. Current micropump technologies and their biomedical applications. Microsystem Technologies. 2009;15(5):647-66.

Chapter two: Methods

2.1. Introduction

Materials - *see appendix 1*

This thesis aimed to develop a novel microfluidic device as a platelet function diagnostic platform for clinical and preclinical use. Device design was predicated on the final device being used in a point-of-care environment requiring minimal space, time and expertise to operate. The choice of assays for the modular components comprised a comprehensive analysis of the impact of the device on platelet function and number, erythrocyte handling and effect on plasma proteins. Further research was conducted to determine the specific haemodynamic drivers behind platelet activation and shear rate profiles in various interactions of the micropump and microvalve through application of Computational Fluid Dynamics (CFD) and micro-Particle Image Velocimetry (μPIV).

2.2. Device design

2.2.1. Microvalve device design

The 2.2 cm x 6 cm x 0.5 cm microfluidic test platform consisted of microfluidic channels patterned onto either side of a thin injection-molded PDMS slab. The test platform included five primary fluidic channels, a control channel, and four channels containing lifting-gate valves of varied widths, allowing comparative performance assessment for multiple valve widths (300 μm, 400 μm, 500 μm and 600 μm). A thicker PDMS interface slab was plasma bonded to the top of the injection-molded slab and biopsy punched to introduce fluidic and pneumatic interfaces, while the bottom of the slab was sealed with a No. 1 borosilicate glass coverslip. The fluidic interface was achieved with small bore (750 μm) biopsy punched holes and 800 μm

stainless steel blunted needle connectors, press fitted to 5 cm medical-grade Tygon tubing (0.508 mm I.D/ 1.524 mm O.D) attached to a Harvard PHD syringe driver.

The normally closed pneumatically actuated gate valves consisted of either a 75 µm wide straight PDMS barrier or a 75 µm wide V-shaped PDMS barrier extending 45^{o} from the channel wall that completely obstructed the primary fluidic channel. The inner tip of the V-shaped valve gate was positioned at the centre of the actuation chamber, patterned on the top surface of an injection molded PDMS slab, and separated from the primary layer by a thin membrane of PDMS, with a thickness defined by the standoff distance between the molds used during fabrication. In the default “normally closed” state, the valve gates obstructed the primary fluidic channel and prevent sample flow. Evacuation of the actuation chamber caused upwards deformation of the elastomer membrane, lifting the valve gate and allowing flow in the primary fluidic channel. Valve geometry was designed such that rapid closure of the valve gates could be achieved with application of a slight positive pressure of ~5 kPa, enabling rapid switching control.

2.2.2. Micropump device design

The micropump chips were 6 cm in length, 2.2 cm in width and 5 mm thick, and consisted of two identical pumping channels per chip. Borosilicate coverslips sealed the channel undersides and acted as a viewing window for microscopy experiments. The 200 µm wide, 100 µm deep microchannels consisted of a blood inlet port, bilateral drug injection ports 3.98 mm from the inlet port, a channel widening to 600 µm to accommodate three membrane pumps 7.09 mm, 8.39 mm and 9.69 mm from the inlet port, and a ‘step up’ channel component 31 mm from the inlet port, which

reduced the channel depth to 50 µm. Above the blood channel were pneumatic actuation lines, which connected to an off-chip valve driver through 50 cm Tygon tubing connections.

2.2.3. Microcontraction device design

Microfluidic chips with microchannels of specific geometries were designed and fabricated. Channels consisted of a blood inlet reservoir, a trap zone composed of a post array to collect microaggregates and debris matter present in the blood before it reached the stenosis, symmetrical stenosis (which unless specified otherwise was 40 µm wide in all iterations and equal acceleration and deceleration angles of 80^o) and an outlet port. The microfluidic chip had a length of 60 mm, a width of 22 mm and thickness of 5 mm. The bilateral stenosis had a microchannel width of 200 µm (depth of 133.33 µm), an entry or acceleration angle into the stenosis of 80^o unless otherwise specified, apex width of 15 µm, and deceleration angle of 80^o. The outlet exhaust was connected by 50 cm of Tygon tubing to a Harvard PHD syringe driver to achieve precise flow rates.

2.3. Fabrication processes

2.3.1. Mold fabrication

The microfluidic mold was fabricated by first etching the microfluidic channel design into a high resolution chrome mask. A silicon wafer was then uniformly spin-coated with high-contrast, epoxy-based KMPR 3050 photoresist using a three-step spin program. The program consisted of a spread cycle of 300 rpm, 300 rpm/s for 10 seconds, a spin cycle of 100 0rpm, 300 rpm/s for 30 seconds and a deceleration

cycle of 300 rpm, 300 rpm/s for 10 seconds. Edge bead removal was achieved by the spraying SU8 thinner 10-15 times evenly over the wafer and resting for 10 minutes. The coated wafer was then soft-baked on a hotplate from 23^{o}C, raising the temperature by 6^{o}C/min until a temperature of 100^{o}C was held for 4 mins to ensure full solvent drying. The chip was then flood-exposed to 360 nm UV light twice for 1 minute periods each to avoid over-heating the wafer. Following this step, cross-linking was achieved by heating the chip with same heating protocol as previously described, then slowly cooling to laboratory temperature on a hotplate. The unexposed KMPR was then developed for 12 minutes and periodically agitated to eliminate unexposed materials. Finally, the mold was cleaned with isopropyl alcohol and deionised water and hard-baked at 120^{o}C for three hours to extend durability.

2.3.2. Microvalve PDMS device fabrication

Fabrication of the microvalves was completed through membrane-sandwich fabrication and injection molding. Matching molds were fabricated on glass and silicon wafers through photolithography to enable visualisation and mask alignment. PDMS was mixed in a 1:10 ratio of prepolymer to curing agent, and degassed under vacuum. The liquid polymer was then poured between the molds, which were aligned using alignment markers under microscopy, and clamped to a 2-5 mm thickness. They were then cured for 30 min at 100^{o}C. Following the curing step, the solid PDMS was extracted from separate molds, and 750 µm interface holes were cut with a biopsy punch to allow interfacing between fluidic channels. A no. 1 borosilicate coverslip was adhered to the bottom of the device and selectively plasma bonded (100% O_2, 20 seconds). To prevent valve gates being permanently

bonded to the coverslip surface, exclusion stamps were fabricated using photolithography to match the size and location of the valve gates.

2.3.3. Micropump fabrication

Complementary mold pairs were fabricated using standard multilayer photolithography techniques on silicon wafer substrates, and a combination of a membrane-sandwich fabrication and PDMS injection molding method was utilised to produce thin double sided PDMS slabs. Standard photolithography techniques were used to fabricate the required complementary mold structures, using silicon and glass wafer substrates. These molds consisted of primary fluidic channels and micro-pump diaphragms patterned onto the bottom mold, and pneumatic actuation channels and viaducts on the transparent upper mold.

PDMS pre-polymer (Sylgard 184 Silicone Elastomer - Dow Corning) was mixed with curing agent with a weight ratio of 10:1, and thoroughly degassed under vacuum. Pre-polymer was loaded between the mold pair, which was clamped and allowed to cure at 100˚C for 30 minutes. A 5 mm thick blank PDMS slab was plasma bonded to the top surface of the injection molded slab. Degassed pre-polymer was introduced between the molds, which were aligned, clamped and cured for 30 min at 100^{o}C. Following curing, the molds were separated and the PDMS slab extracted. Interface holes were biopsy punched as required, and a 5 mm thick interface slab of PDMS was plasma bonded to the upper surface of the injection molded PDMS slab (Harrick Plasma PDC-002: 100% O_2, 1 min) and fluidic reservoirs, interfaces and pneumatic interfaces biopsy punched. The interface slab, previously biopsy punched with corresponding 750 µm interface holes, acted to seal the pneumatic upper channels

while providing the fluidic and pneumatic interface. Finally, no.1 borosilicate coverslips were plasma bonded to the chip and were used to seal the bottom surface of the injection-molded slab, and acted as the imaging window for microscopy-based experiments.

2.3.4. Microcontraction chip fabrication

To fabricate the PDMS replicate chips, PDMS and curing agent were mixed in a 10:1 ratio and degassed in a vacuum system for at least 1 hour to remove dissolved gases. A polymethyl methacrylate shim was adhered to the KMPR *via* PDMS, and this solution was then carefully poured into the mold to avoid bubbles being incorporated into the prepolymer. Molds were then filled with approximately 8 g of solution and placed in pre-heated 75^{o}C ovens for 35 minutes. Once set, the PDMS was manually removed from the molds using a scalpel, and biopsy punches of 6 mm and 4 mm were made for inlet reservoir holes, and 1 mm for the outlet port to the pump system. A 65 × 25 mm ethanol/HCl-washed #1 borosilicate coverslip slide was then cleaned with isopropyl alcohol and dried with nitrogen gas under pressure, and the PDMS chip was adhered channel-side down to the chip *via* simple adhesion due to the low surface energy of the PDMS.

2.4. Whole blood collection method

Donor blood from both sample populations was collected using a 19G needle and 20 ml syringes containing 2 ml 3.2% citrate. Samples were analysed on the day of collection and were discarded after use. Following blood collection, samples were

allowed to equilibrate for 30 minutes in a 37ºC water bath to allow removal of venepuncture-induced ADP release to ADPases.

2.5. Device operation

2.5.1. Microvalve device operation

Perfusion through the valve test manifold was driven by an external Harvard PHD-200 syringe driver with a 30 ml glass syringe connected to the outlet port though 10 cm of 0.8 mm I.D. Tygon tubing, functioning in withdrawal mode. When perfusate collection was required, samples were instead loaded into 5 ml plastic syringes for use in the syringe driver, which was operated in infusion mode at the same flow rate. Actuation of valve gates was achieved through application of negative pressure by connection of a 50 ml plastic syringe with 10 cm of Tygon tubing.

2.5.2. Micropump device operation

The valve driver utilised micro-solenoid valves to switch between two pneumatic reservoirs held at either negative or positive relative pressures, acting to open or close on-chip valves. The driver was connected to the actuation chambers in the PDMS block using a 30 ml glass syringe attached to the valve driver, which was interfaced with the microfluidic chip using 10 cm of Tygon (0.8 mm I.D.) tubing, and blunt 21.5 gauge hypodermic needles. Diaphragm inflation was achieved by applying nitrogen gas at a positive pressure between 10-100 kPa, while diaphragm deflation was achieved by application of -20kPa. The valve driver was connected to a PC to enable scripted control, realised using python scripts.

2.6. Aggregation experiments

2.6.1. Microcontraction operation

Channels were derivatised with vWF (100 µg/ml), which was introduced *via* pipette into each microchannel output port, and coated the channel up to and including the stenosis. The vWF was allowed to adsorb to the microchannel surface, providing an initial ligand for platelets to bind to allow platelet recruitment to occur. After a 10 minute interval at room temperature, vWF that had not adsorbed to the microchannel was removed by pipette through the outlet port. The #1 borosilicate coverslip was removed, and a new coverslip was cleaned with 100% isopropyl alcohol and delicate task wipers in a fume hood. It was then adhered to the microfluidic chip through surface tension. 4^{o}C 2% Bovine Serum Albumin (BSA) was introduced into the microfluidic chip inlet port and intruded through the channel *via* suction from a Harvard PHD syringe driver withdrawing at 45 µl/min, and incubated for 10 minutes. The BSA was intended to act as a passivating agent, preventing non-specific platelet adhesion to the channel surface. Prior to blood flow, the syringe driver was again connected and pre-warmed 1% Tyrodes at 37^{o}C was pipetted into the inlet port and perfused through the channel to prevent blood contact with a cold, non-isotonic solution.

This system was chosen because it could visualise platelet aggregation in real-time with high-resolution microscopy, due to the use of clear PDMS materials and a clear coverslip bottom. Another advantage of this system in this application was the fact that it was relatively easy to assemble and fabrication costs are low, allowing easy repetition of experiments. Other flow-channels did not incorporate a stenotic gradient, or are technically challenging to assemble.(1)

After the period of 10 minute equilibration at 37^{o}C, citrated human whole blood was aliquotted into 1 ml Eppendorf tubes and incubated with 1 µg/ml $DiOC_6$ (a lipophilic epifluorescent membrane dye) for 10 minutes and except where indicated, three well-characterised inhibitors of soluble agonist receptors in a 37^{o}C water bath. These were: Indomethacin (10 µM), which was used to block TxA2 production, MRS-2179 (100 µM), a $P2Y_1$ antagonist, and 2-MESAMP (10 µM), a $P2Y_{12}$ antagonist.

Aggregation experiments were performed using an adhesive protein pre-coat of vWF or fibrinogen.(2, 3) The experiments were then mounted on a microscope stage, and citrated human whole blood was perfused through the device with defined flow rates controlled with an external Harvard syringe pump. The flow rate was calculated to give the desired initial wall shear rate, though this was inevitably altered as aggregate growth occurred. Flow rate was calculated through the following equation:

Equation 2.1: Flow rate calculation

$$Q = \frac{\Upsilon w h^2}{6}$$

Where:

Q is the flow rate (m^3/sec)

w is the channel width (m)

h is the height of the channel (m)

γ is the wall shear rate (s^{-1})

2.6.1.1. Optimisation of stenotic system preparations

Studies using the *in vitro* stenosis were performed to establish operational parameters. For studies describing aggregate response to shear parameters, purified vWF was used as an adhesive protein due its importance in platelet adhesion in high-shear environments.

Previous studies that have used vWF as the plasma protein responsible for platelet binding in high shear environments have identified that concentrations of greater than 100 µg/ml saturate glass surfaces.(4) It was therefore necessary to validate this finding in the proposed system using a dose-response relationship. For these studies, channels were coated with vWF concentrations of either 0, 12.5, 25, 50, 100 and 150 µg/ml (*see Fig 2.1 a,b*). After incubating channels for 10 minutes at room temperature, vWF that had not been adsorbed was washed from the channel with 2% BSA solution. The BSA solution effectively blocked the surface, preventing non-specific platelet adhesion to other adsorbed proteins from plasma in the blood sample (*see Fig 2.1 b-g*). As demonstrated in Figure 2.1a, increasing concentrations of vWF led to aggregates of greater size. Incubation with vWF concentrations about 100 µg/ml did not increase aggregate size. Thus, 100 µg/ml vWF coating concentrations were used to prevent variation in results arising from differences in vWF preparations.

Previous studies examining the device's capacity to induce platelet aggregation under flow have arbitrarily utilised devices with a 40 µm stenosis.(5, 6) To determine

whether this stenosis size was optimal to produce replicable aggregate sizes, stenoses of 20 µm and 60 µm were also trialled. Evaluation of aggregate sizes identified that maximal aggregate sizes occurred with the 40 µm stenosis (*see Fig 2.2 a-e*). The level of aggregation was lower in the 60 µm stenosis (*see Fig 2.2 a-e*).

2.6.2. Micropump platelet thrombus (perfusion) assay

Whole blood samples or reconstituted blood samples were infused through the pump test platform. 24 hours prior to blood sample loading, the microfluidic device was derivatised with purified type 1 collagen (100 µg ml^{-1}), to allow for effective platelet capture and adhesion to the glass coverslip surface. Collagen was infused 2000 µm downstream of the micropump assembly, and allowed to physisorb for one day at 4^{o}C, before removal of excess collagen solution and blocking of the microfluidic with 10% BSA for 10 min at room temperature. Thrombus formation was monitored at 37^{o}C using a Nikon A1r confocal with a Nikon Plan Fluor 40x/0.50 objective and a sCMOS camera using a 561nm laser.

2.6.3. Microvalve aggregation experiments

Blood samples were aliquotted into the input reservoir and perfused through the device by a syringe pump at a constant flow rate of 45.00 µL/min for 210 seconds. Aggregate size and density was monitored in real-time via epifluorescence using a manual TI-U Microscope with a Nikon Plan Fluor 20x/0.50 objective, and a sCMOS camera.

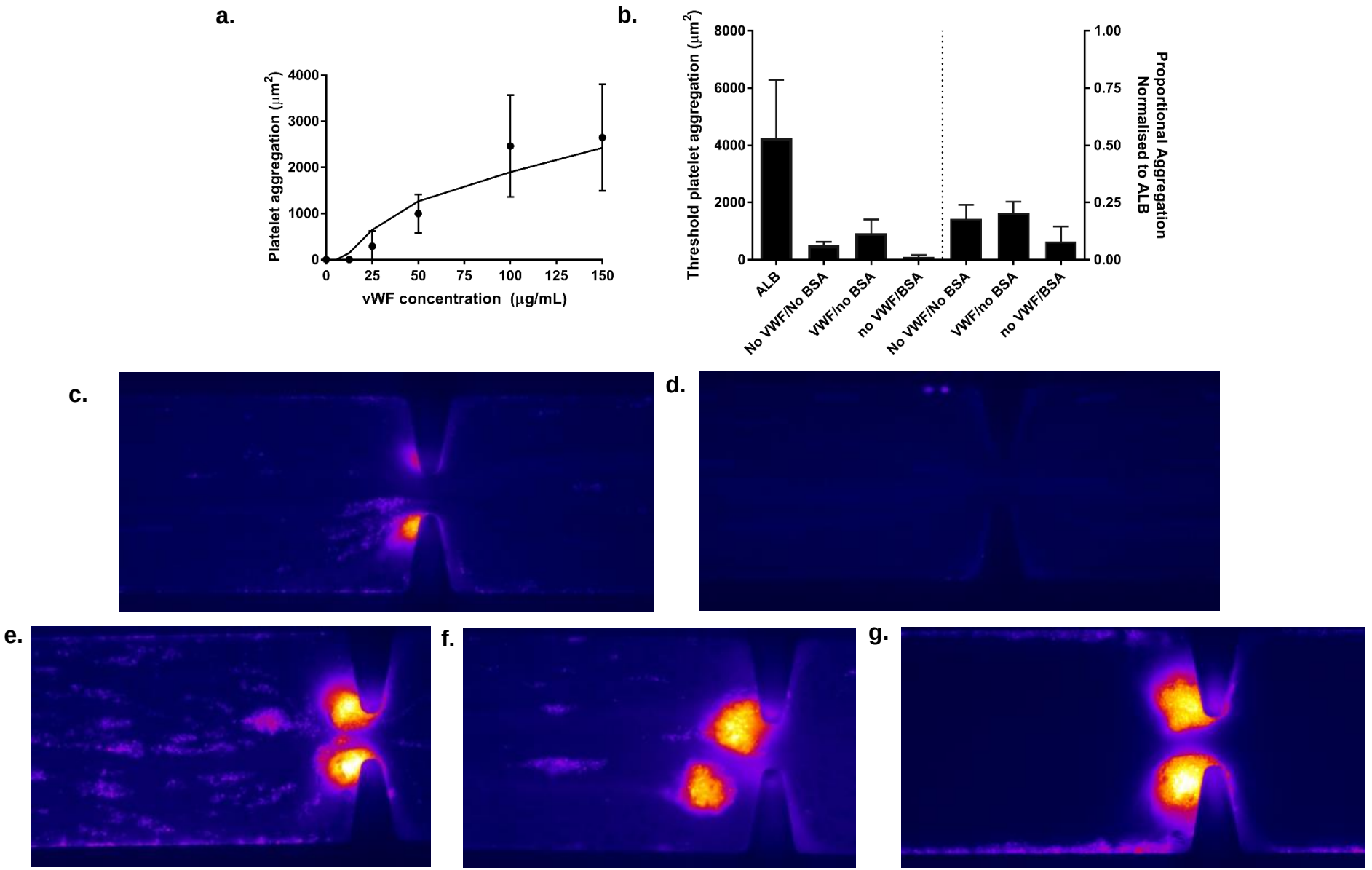
a.
Platelet aggregation (μm²)
4000
3000
2000
1000
0
0
25
50
75
100
125
150
vWF concentration (μg/mL)
b.
Threshold platelet aggregation (μm²)
8000
6000
4000
2000
0
1.00
0.75
0.50
0.25
0.00
Proportional Aggregation Normalised to ALB
ALB
No VWF/No BSA
VWF/no BSA
no VWF/BSA
No VWF/No BSA
VWF/no BSA
no VWF/BSA
c.
d.
e.
f.
g.

Figure 2.1 - BSA pre-coating vs vWF pre-coating vs no pre-coating vs pre-coating with both vWF and BSA

a. Increasing concentration of vWF concentration pre-coating from 0, 12.5, 25, 50, 100 and 150 µg/ml with a 2% BSA pre-coating, demonstrating increasing aggregate size with increasing vWF concentration. Error bars represent mean ± standard deviation. b. Representative platelet aggregation endpoint analyses of n=3 control donors demonstrating the aggregation growth response with varying pre-coating methods of: no pre-coat, pre-coating only with 2% filter-purified Bovine Serum Albumin (BSA), pre-coating only with vWF (100 µg/ml) and vWF (100 µg/ml) + 2% BSA. Error bars represent mean ± standard deviation. Results to the right side of the dotted line were normalised to the control run of: treatment with all ALBs and pre-coating with both 100 µg/ml vWF and 2% BSA, incubating each for 10 minutes. c.-g. Still images of aggregate formation at 180 seconds in microchannels treated with: c. no pre-treatment, demonstrating a small aggregate, d. 2% BSA-only pre-treatment demonstrating no aggregation, e. 100 µg/ml vWF-only pre-treatment demonstrating aggregation at the stenosis and on the coverslip, f. 100 µg/ml vWF-only pre-treatment demonstrating an aggregation occurring on the coverslip, rather than at the stenosis, g. Pre-treatment with both 100 µg/ml vWF and 2% BSA (standard treatment).

a.

40μM stenosis gap sizes vs untreated blood aggregation

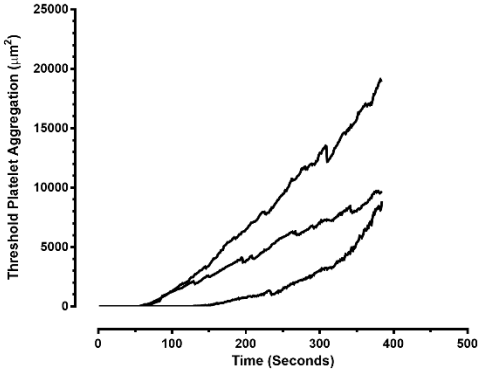

b.

20μM stenosis gap sizes vs untreated blood aggregation

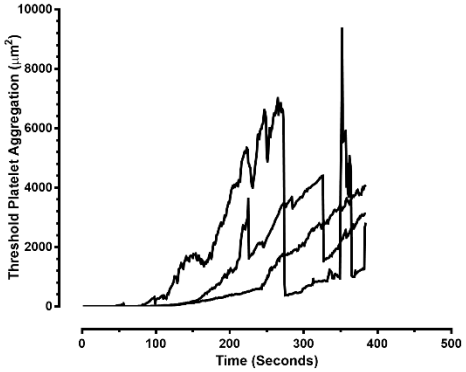

c.

Normalised aggregation vs stenosis size

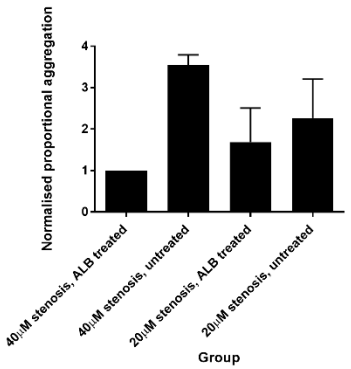

d.

40μM stenosis gap sizes vs ALB blood aggregation

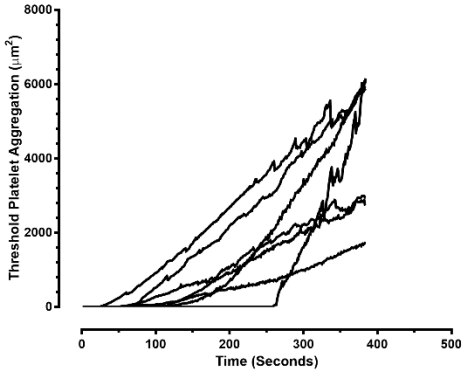

e.

20μM stenosis gap sizes vs ALB aggregation

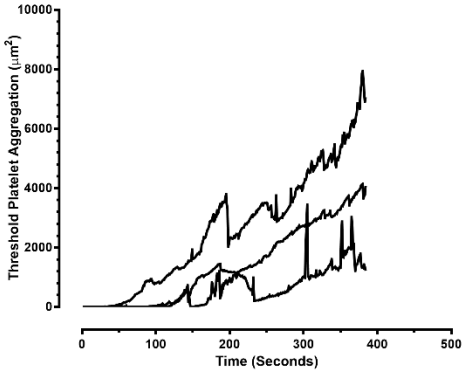

Figure 2.2 - Gap size variability - normalised maximal aggregation and platelet aggregation traces

a. Representative platelet aggregation traces demonstrating aggregation growth response with 40 µm gap size response and a 80^{o} acceleration zone stenotic iteration and 45.00 µl/min flow rate. b. Representative platelet aggregation traces demonstrating aggregation growth response with a 20 µm gap size in untreated blood and 45.00 µl/min flow rate. c. Normalised platelet aggregation measures maximal aggregate size over flows with a 20 µm or 40 µm stenosis, ± ALB pre-treatment, normalised to the 'standard' run with a 40 µm stenosis and 45.00 µl/min flow rate. Error bars represent the mean ± the standard deviation. d. Representative platelet aggregation traces demonstrating aggregation growth response with a 40 µm gap size in ALB-treated blood (Indomethacin (10 µM), MRS-2179 (100 µM), and 2-MESAMP (10 µM)) and 45.00 µl/min flow rate. e. Representative platelet aggregation traces demonstrating aggregation growth response in the 80^{o} acceleration zone stenotic iteration with a 20 µm gap size in ALB-treated (Indomethacin (10 µM), MRS-2179 (100 µM), and 2-MESAMP (10 µM)) blood and 45.00 µl/min flow rate.

a.

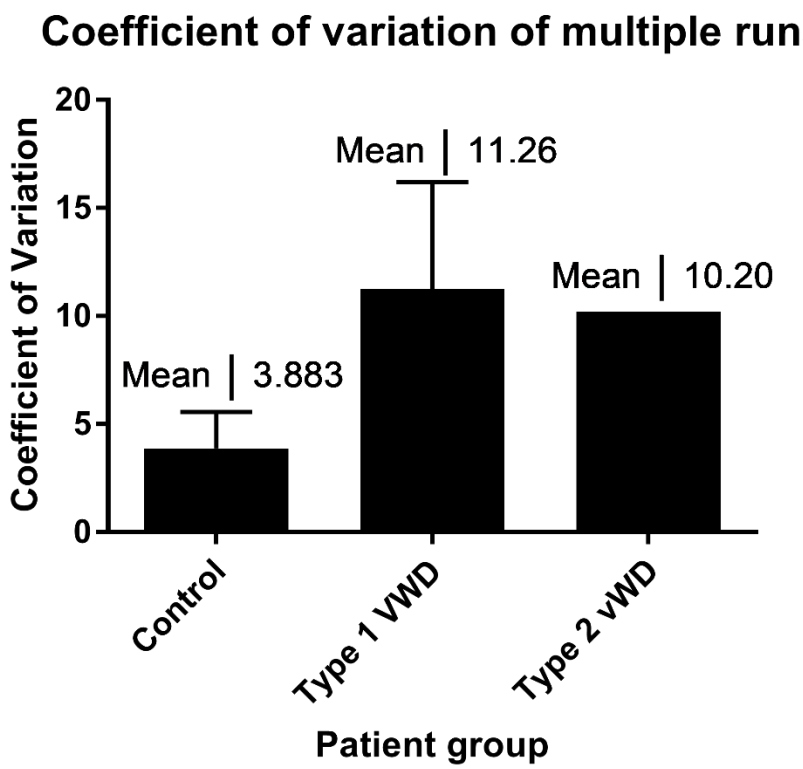
Coefficient of variation of multiple runs
Coefficient of Variation
20
15
10
5
0
Mean | 3.883
Mean | 11.26
Mean | 10.20
Control
Type 1 VWD
Type 2 vWD
Patient group

b.

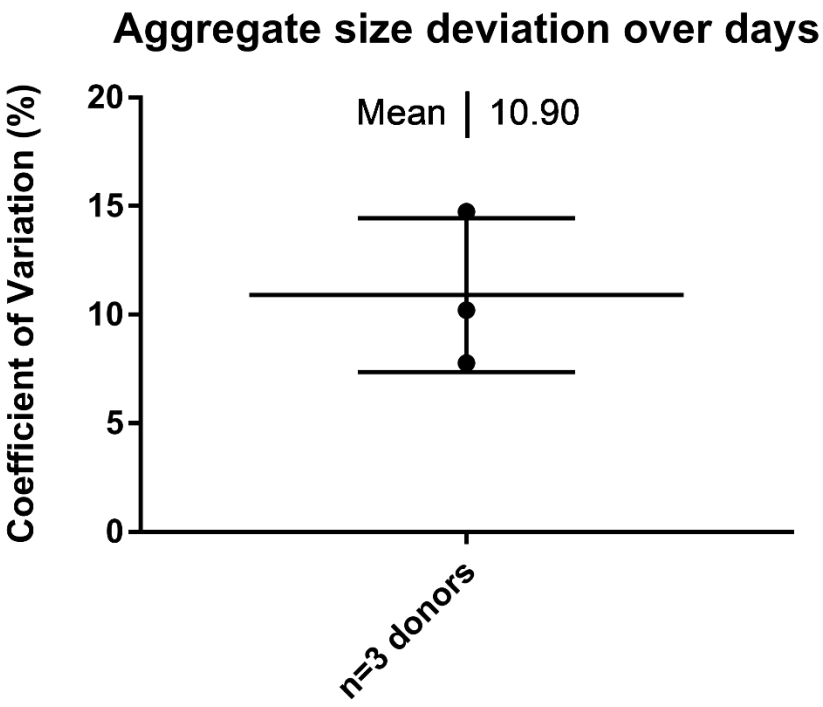
Aggregate size deviation over days
Coefficient of Variation (%)
20
15
10
5
0
Mean | 10.90
n=3 donors

Figure 2.3 - Donor variability

The coefficient of variation was calculated for n=6 control donors, 2 type 1 vWD donors, and 1 type 2 vWD donors respectively. This demonstrated the spread of aggregation of donor responses when samples of both vWD patients and control donors were tested under identical conditions within the device. Error bars represent mean ± standard deviation. The mean coefficient of variation is provided. Microchannels used had a stenosis gap width of 40 µm and a 80^{o} acceleration zone. The pre-stenosis flow rate was 45.00 µl/min. Pre-coating with both vWF and BSA was used, and patient whole blood samples were taken in 10% citrate syringes. All samples were incubated with 1 µg/ml DiOC6, 100 µM MRS-2179, 10 µM 2-MeSAMP, 10 µM indomethacin and 0.02 U/ml apyrase for 10 minutes. b. Pooled coefficients of variation for n=3 donors demonstrated a low variation in aggregate size when multiple samples were tested from the same patients on different days, under identical conditions. Microchannels used had a stenosis gap width of 40 µm. The pre-stenosis flow rate was 45.00 µl/min. Pre-coating with both vWF and BSA was used, and patient whole blood samples were taken in 10% citrate syringes. All samples were incubated with 1 µg/ml DiOC6, 100 µM MRS-2179, 10 µM 2-MeSAMP, 10 µM indomethacin and 0.02 U/ml apyrase for 10 minutes.

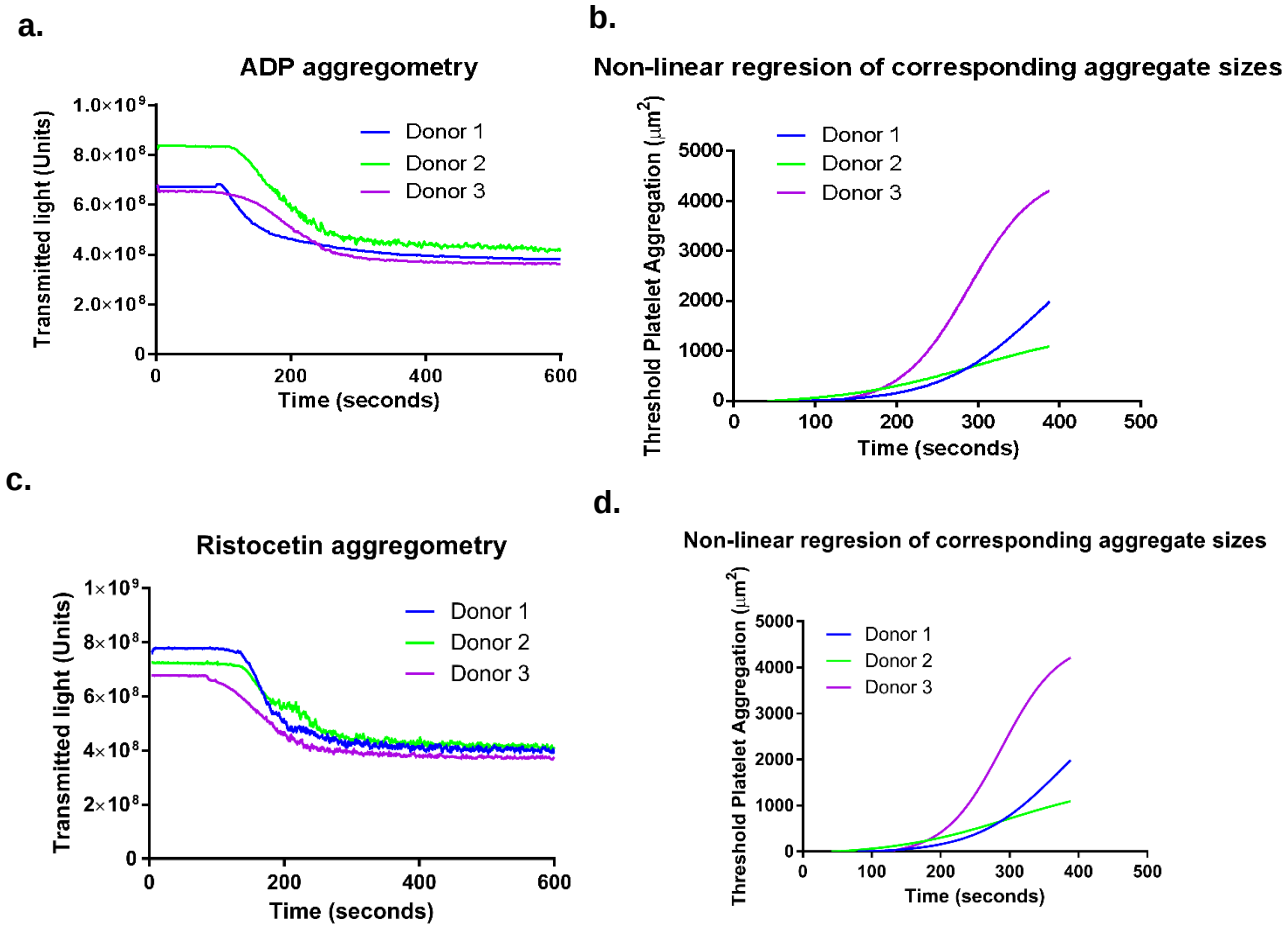
a.
ADP aggregometry
Transmitted light (Units)
1.0×10⁹
8.0×10⁸
6.0×10⁸
4.0×10⁸
2.0×10⁸
0
0
200
400
600
Time (seconds)
Donor 1
Donor 2
Donor 3
b.
Non-linear regresion of corresponding aggregate sizes
Threshold Platelet Aggregation (μm²)
5000
4000
3000
2000
1000
0
0
100
200
300
400
500
Time (seconds)
Donor 1
Donor 2
Donor 3
c.
Ristocetin aggregometry
Transmitted light (Units)
1×10⁹
8×10⁸
6×10⁸
4×10⁸
2×10⁸
0
0
200
400
600
Time (seconds)
Donor 1
Donor 2
Donor 3
d.
Non-linear regresion of corresponding aggregate sizes
Threshold Platelet Aggregation (μm²)
5000
4000
3000
2000
1000
0
0
100
200
300
400
500
Time (seconds)
Donor 1
Donor 2
Donor 3

Figure 2.4 – Aggregometry studies

a. *Representative platelet aggregation endpoint analyses of n=3 control donors demonstrating the aggregometry traces for treatment with ADP. Donors displayed normal aggregometry results and thus normal platelet responses response to ADP.* ***b.*** *Sigmoidal regression curves demonstrating the same donors' platelet aggregation traces.* ***c****. Representative platelet aggregation endpoint analyses of n=3 control donors demonstrating aggregometry traces for treatment with ristocetin. Donors displayed normal aggregometry results and thus normal platelet responses response to ristocetin, which may have otherwise confounded results.* ***d.*** *Nonlinear regression analysis of the same donors' platelet aggregation traces. A greater degree of response to ristocetin on aggregometry (as indicated by a greater decrease in transmitted light across the run) correlated with a greater aggregate size in the device response in the 80^{o} acceleration zone stenotic iteration. There appeared to be a negative correlation between vWF/GPIb binding and aggregate size in the device.*

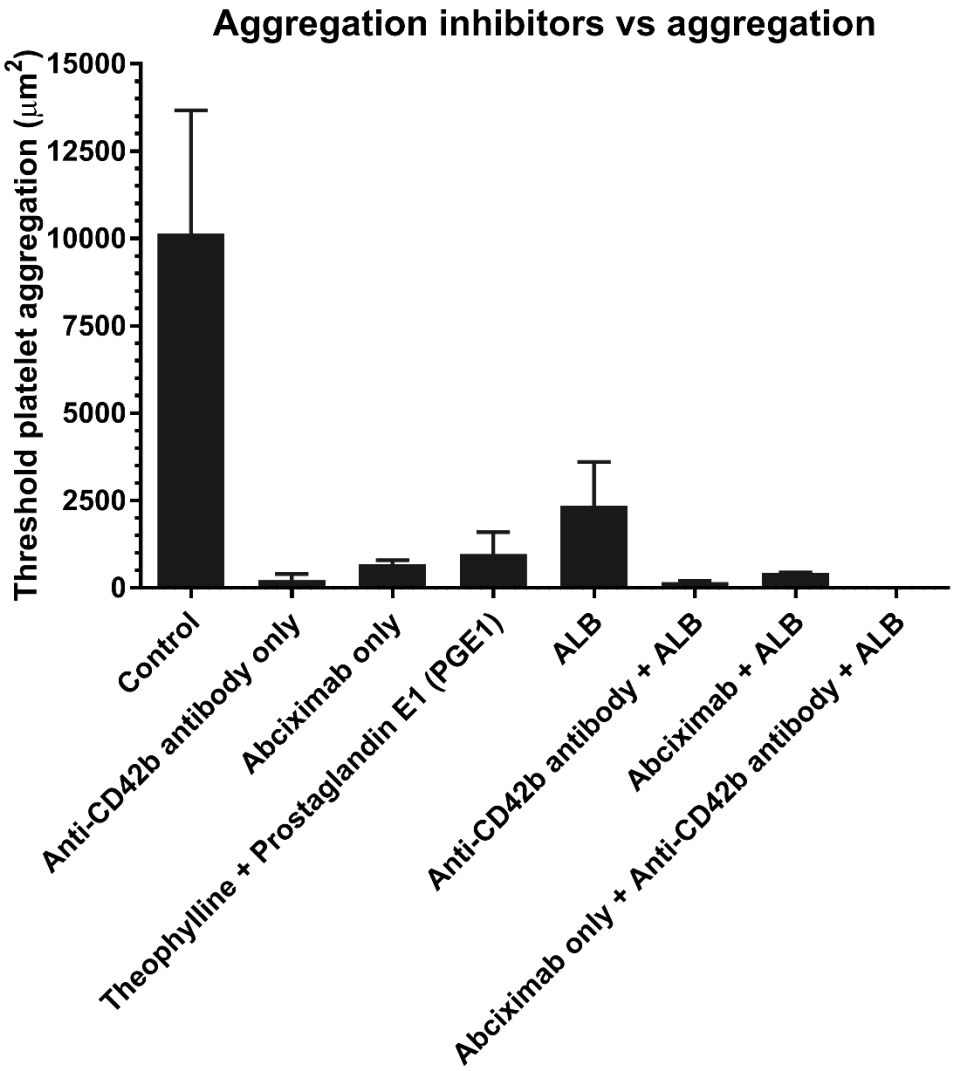
Aggregation inhibitors vs aggregation
Threshold platelet aggregation (μm²)
15000
12500
10000
7500
5000
2500
0
Control
Anti-CD42b antibody only
Abciximab only
Theophylline + Prostaglandin E1 (PGE1)
ALB
Anti-CD42b antibody + ALB
Abciximab + ALB
Abciximab only + Anti-CD42b antibody + ALB

Figure 2.5 - Effect of activation inhibitors on platelet aggregation

Representative platelet aggregation endpoint analyses of n=3 control donors demonstrating the aggregation growth response in the 80^{o} acceleration zone stenotic iteration with exposure to aggregation inhibitors at the following concentrations: Abciximab (20 µg/L), Anti-CD42b antibody (10 µg/ml), Theophylline (10 mM) and Prostaglandin E1 (PGE1) (1 µg/ml). Error bars represent the mean ± the standard deviation. Antagonism of the integrin $\alpha_{IIb}\beta_{III}$ or GPIb receptors or upregulation of cAMP production produced marked decreases in activation. Samples treated with Anti-CD42b antibody demonstrated a slower rate of growth without reaching a plateau in aggregate size.

2.6.4. Aggregate data analysis

Aggregate area data was collected in real-time by measuring epifluorescence of $DIOC_6$-labelled platelets in the stenosis using the NIS-elements BR program. All image analyses were performed off-line with ImageJ using Huang's fuzzy image thresholding. The fluorescent aggregates were thresholded to ensure inclusion of the earliest aggregates in analysis. Surface area was quantified in a 2-dimensional cross-section (μm^2) at a fixed distance approximately 30μm from the channel floor.

Raw data derived from the replicate channels were fitted to a sigmoidal (variable slope) non-linear regression in GraphPad Prism according to:

Equation 2.2: Aggregate growth curve-fitting calculation

$$Y = Bottom\ value + \frac{(Top\ value - Bottom\ value)}{1 + 10^{(logEC_{50} - X) \times Hill\ Slope}}$$

Maximal (endpoint) aggregation was extrapolated from the plateau of the regression analysis.

2.7. Physiological validation of the Microcontraction system

In order to determine the variation of device preparation, identical samples from the same donor were tested in the system. Samples were tested on the same day to prevent differences arising from haematocrit or platelet reactivity variation. The

amount of variation in aggregate size between identical samples was found to be low with a coefficient of variation of 10.9% (*see Fig 2.3 a*).

2.7.1. Blood reconstitution

Citrated whole blood from healthy control donors was dispensed into 10 ml falcon tubes and equilibrated at 37^{o}C for 30 minutes. Apyrase (0.005 U/ml) was added to remove ADP released in the venepuncture process and samples were then centrifuged at 200xg for 15 minutes with 5 acceleration and no brake. The PRP and Hct were then divided into separate falcon tubes. Apyrase (0.01 U/ml) was added the PRP, which was then was centrifuged at 1700 x g for 7 minutes with 5 acceleration and 5 brake to ensure platelet pelleting. Following a 10 minute rest period, the resulting pellet was then reconstituted in an equal volume of Platelet Washing Buffer (PWB) and apyrase (0.01 U/ml) added, before again being rested for 10 minutes. The solution was then centrifuged at 1500 x g for 7 minutes with 5 acceleration and 5 brake. Platelet concentration in the PWB was then tested in a haemogram, and using this value, standardised solutions were then suspended in Tyrode's supplemented with apyrase (0.02 U/ml) reconstituted to a standard 200 x 10^9/l ± 45 platelet count, with a varying HCT of 20 - 50%, or a standard HCT of 40% ± 9, with varying platelet counts of 50 - 300 x 10^9 in Eppendorf tubes. The Hct was then centrifuged at 1700 x g for 7 minutes with 5 acceleration and 0 brake, suspended in PWB and re-centrifuged at 1500 x g for 7 minutes with 5 acceleration and 0 brake.

Reconstitution measures determining the impact of vWF and fibrinogen on stenotic device function were also performed by obtaining platelets and packed red blood

cells. The concentration of platelets in washed buffer was then determined in a haemogram, and solutions were resuspended in 600 ml 1 x Tyrodes solution with a 40% HCT and a platelet count of 200 x 10^9/l. Solutions were then supplemented with vWF of concentrations of 0 (as a negative control), 10, 20 and 50 µg/l or fibrinogen at 50, 100, 150 and 200 µg/l concentrations.

2.7.2. Aggregometry

Due to the determination that the device was sensitive to $P2Y_{12}$ binding, it was important to ensure all control patients had normal functioning of these receptors. Additionally, one of the key deficiencies in studies in this thesis was that control donor medical history was unavailable. Thus, it was possible that some control donors may have had a platelet function disorder such as vWD. Due to these concerns, it was important to ensure all control patients had no pathologies in their aggregatory processes. This was achieved through measurement of ADP and ristocetin aggregometry.

2.7.2.1. ADP aggregometry

Citrated blood from normal donors was separated into 10 ml falcon tubes and allowed to equilibrate for 30 minutes in a 37^{o}C water bath before being spun in a centrifuge at 2000xg for 15 minutes with 5 acceleration and no brake. Platelet-rich plasma (PRP) was then collected from each falcon tube, analysed in a haemogram, then aliquotted into cuvettes at a concentration of 200 x 10^9/l before being rested for a further 30 minutes. 495 µl samples of the PRP was then aliquotted into cuvettes,

and aggregation over a 10 minute course *via* light transmission was analysed after the addition of 5 µl aliquots of Tyrode's solution as a control, and ADP in a 1% Tyrode's buffer of escalating concentrations of 0.625, 1.25, 2.5, 5 and 10 µM, standardised against 1% Tyrode's solution.

2.7.2.2. Ristocetin assay

Whole healthy donor blood was centrifuged for 15 minutes at 200 x g with 5 acceleration and no brake to obtain PRP, analysed in a haemogram, then aliquotted into cuvettes at a concentration of 200 x 10^9/l. It was then allowed to equilibrate for 30 minutes. PRP was aliquotted in 490 µl volumes, and 10 µl ristocetin was added. This assay was also standardised against 1% Tyrode's solution, and the degree of aggregation was measured over a 10 minute period. Ristocetin aggregation was performed to determine if there was any deficiency of vWF-GPIb binding that may confound results. All healthy donor blood was therefore tested for response to ristocetin and ADP with platelet aggregometry. All patients showed normal responses to ristocetin and ADP stimulation (*see Fig 2.4*).

2.7.3. Assessment of integral platelet activating pathways

The specificity of platelet adhesion to the vWF was assessed through 10 minute pre-treatment of the blood samples with antibodies to various receptors. The role of the integrin $\alpha_{IIb}\beta_{III}$ and GPIba receptors was elucidated by using reagents to antagonise their function (*see Fig 2.5*). The impact of integrin $\alpha_{IIb}\beta_{III}$/fibrinogen and vWF binding was tested by antagonising the integrin $\alpha_{IIb}\beta_{III}$ receptor with Abciximab (20 µg/l). The

impact of GPIba/vWF binding was tested by antagonising the receptor with the anti-CD42b antibody, AK2 10 µg/ml. Antagonism of the integrin $\alpha_{IIb}\beta_{III}$ or GPIb receptors or upregulation of cAMP production produced marked decreases in activation. Samples treated with Anti-CD42b antibody demonstrated a slower rate of growth without reaching a plateau in aggregate size. Upregulation of cAMP with PGE1 (1 µg/ml) and theophylline (10 mM) resulted in complete inhibition of aggregation (*see Fig 2.5*). There also appeared to be a synergistic reduction in aggregation when both receptors were blocked, as use of multiple inhibitors demonstrated more aggregate reduction than the sum of the reduction when used individually.

2.8. Ethics and patient recruitment

2.8.1. Ethics approval

The ethics application for consenting human control blood donors was granted by Monash University Standing Committee on Ethics in Research Involving Humans under application CF07/0141-2007/0025 - Investigation of new approaches to prevent and/or treat blood diseases (heart attack, stroke and haematological malignancies) (*see appendix 2*). Patients with vWD were approved for inclusion in this project by The Alfred Hospital Ethics committee, for which the project was judged 'Low Risk' (project number: 627/15).

2.8.2. Donor identification

To comply with the ethics application approval, all blood donors were between the ages of 18 to 75 and could personally consent to blood collection. Control patients

were recruited from the regular donor registry from the Australian Centre for Blood Disease, and were without known bleeding disorders. Patients with known or suspected vWD were recruited from the Ronald Sawyer Haemophilia Centre at the Alfred hospital.

2.8.3. Recruitment procedure

The recruitment process involved the patient's clinician identifying them as a likely study participant, and initiating a conversation regarding study aims and potential involvement. If they agreed, the patient was then referred to the researcher and provided with written information concerning possible risks and benefits, as well as methods to access study results and their patient data and a consent form (*see appendix 3*).

2.8.4. Privacy and confidentiality

Patient details were de-identified by assigning all donors a study number, and recording all personal data under this identifier. A master log containing all patient details was maintained in a secure soft-copy version that was password protected and accessible only to investigators who required access. No identifying patient details appeared in the final manuscript or associated publications. Potential vWD patients recruited from Ronald Sawyer Haemophilia Centre additionally consented to the inclusion of pathology results and patient notes relevant to device

characterisation, including bleeding history, a full blood examination, fibrinogen levels, FVIII levels, blood group, coagulopathy screening, and vWD-specific assays (when available) such as RIPA, vWD:Ag, vWF:CB, vWF:RCo and multimer analysis. Patients could access their personal information at any time, and disclosure of personal information to outside parties did not occur unless specifically requested or consented to. This information was collected to assess correlation of the device output with clinically-used pathology tests.

2.8.5. von Willebrand Disease patient adjunct data collection

Adjunct data collected included past pathology results and clinical history from patient notes, such as a family bleeding history. Permission for data collection was verbally obtained from patients when they consented to be included in the study, and recorded in writing on the consent form. A bleeding history was taken according to the ISTH bleeding scoring guidelines in the same meeting using information from the clinical notes with supplemental information provided by the patient. This bleeding questionnaire assessed the presence and degree of severity of bleeding symptoms such as epistaxis and treatment required. The bleeding score was assessed against device output to determine correlation.

2.9. Full blood examination

Whole blood collected from patients was analysed using the Abbott CellDyn Emerald Haemogram prior to equilibration. This was performed to provide information

regarding haematocrit and platelet count, which were independently evaluated to determine effect on resulting aggregate size.

2.10. Experiments measuring platelet activation

2.10.1. Erythrocyte and platelet FACS analysis

Blood samples were obtained in 3.2% Anticoagulant Citrate Dextrose Solution (ACD) using the venepuncture method detailed above, and 5 µl samples were then collected following perfusion through valve manifolds. The samples and 20 µl CD61 PerCP, 20 µL PAC-1 FITC or 5 µl PE-P selectin conjugated monoclonal antibodies were added to 12 x 75 mm Falcon® capped polystrene test tubes. To assess PAC-1 and P-selectin binding, 5 µl of unprocessed blood and a single antibody were added to assess voltages, and channel compensation was achieved through assessment of $2x10^{-5}$ M ADP stimulated samples. Positive control tubes were prepared using 0.45 ml of whole blood incubated with 50 µl ADP (2×10^{-4} M) for 120 seconds at room temperature then stained immediately. Tubes stained with only CD-61 were used to obtain isotype control forward and side scatter buffers. Samples containing PAC-1 antibodies also contained RGDS to prevent non-specific binding. Assessment of Annexin-V binding followed the same protocol, but positive controls instead consisted of 5 µl whole blood and calcium ionophore A23187 (1 µmol/l). All samples were assessed within a two hour window and incubated at 37^{o}C. Sample acquisition was performed on CellQuest flow analysis software using a Beckson Dickson FACSCalibur flow cytometer. Logarithmic amplification was used in both forward and side scatter parameters, and the flow rate was set to ‘low’ to maximise platelet event capture. Data analysis was performed on two-colour plots to first gate only platelet

events using CD-61 binding, then samples were assessed for relative expression of PAC-1 or P-selectin specific fluorescence, and 10,000 events were captured per datapoint. Binding and expression was recorded as a geomean, as analysed in FlowJo© software.

2.10.2. Ratiometric visualisation of calcium signalling

Platelets and red cells were isolated according to reconstitution procedures outlined in Chapter 2.8. 1 ml aliquots of platelets suspended in 1 x PWB at $3x10^8$/ml were incubated for 30 mins at 37ºC with Fura-Red-AM (2.5 µM) and Oregon Green BAPTA-1-AM (1.25 µM). The platelet suspension was then centrifuged at 2000 x g for 60 seconds, and the pellet was resuspended in 1 x PWB with 0.02 U/ml apyrase. Platelets were then centrifuged again at 2,000 x g for 60 seconds, and resuspended at $3x10^8$/ml in 1 x PWB for a 30 minutes. The suspension was then centrifuged at 2,000 x g for 60 seconds, and resuspended in 600 ml 1 x Tyrode's buffer and 400 ml Hct. Samples for analysis were supplemented with 1 mM $CaCl_2$, 1 mM $MgCl_2$ and 0.5% BSA. Samples used to calibrate maximal fluorescence (R_{max}) were suspended in Tyrodes Buffer supplemented with 5 µM A23187 + 10 mM $CaCl_2$. Samples used to calibrate minimal fluorescence (R_{min}) were probe-loaded, then resuspended in 600 ml 1 x Tyrode's buffer, 400 ml Hct and supplemented with 5 mM EGTA and 50 µM dimethyl BAPTA-AM (DM-BAPTA-AM), and incubated for 30 minutes at 37ºC. R_{min} samples were then centrifuged at 2000 x g for 60 seconds and washed with 1 x PWB. Final R_{min} samples were reconstituted with 600 ml 1 x Tyrodes buffer, 400 ml Hct and 2 mM EGTA. Samples were allowed to equilibrate for 10 minutes prior to use. Calcium signal transduction was monitored at 37ºC using a Nikon A1r confocal

at 10 msec exposure time with a Nikon Plan Fluor 60x/0.50 objective and a sCMOS camera using both a 561nm and 640 nm laser.

Fluorescence values were obtained using ImageJ software. Thresholding was applied to demarcate platelets from surrounding fluid, and background fluorescence was detected and subtracted before analysis. Fluorescence values were calculated for samples, and applied to the following equation to determine relative cytosolic Ca^{2+} concentration:

Equation 2.2 – Calcium concentration calculations – dual dye method

$$\Delta[Ca^{2+}]_c = \frac{170 \times (R - R_{min})}{(R_{max} - R) \times \frac{F_{max}}{F_{min}}}$$

Where:

R was the fluorescence ratio of sample fluorescence of the Oregon Green BAPTA-1-AM channel divided by the fluorescence of the Fura-Red-AM channel.

R_{min} was ratio of the Oregon Green BAPTA-1-AM channel divided by the fluorescence of the Fura-Red-AM channel of the R_{min} sample.

R_{max} was ratio of the Oregon Green BAPTA-1-AM channel divided by the fluorescence of the Fura-Red-AM channel of the R_{max} sample.

F_{min} was the mean fluorescence of the R_{min} sample in the Oregon Green BAPTA-1-AM channel.

F_{max} was the mean fluorescence of the R_{max} sample in the Oregon Green BAPTA-1-AM channel.

2.10.3. Cal520 Calcium signalling assay

Washed platelets (1×10^9/ml) were loaded with Cal520 (2-aminophenoxy)ethane-N,N,N′,N′-tetraacetic acid tetra(acetoxymethyl)ester (1.25 μM) for 30 min at 37^{o}C. Dye-loaded platelets (final platelet count = 200×10^9/l) were then reconstituted with washed red blood cells (below) prior to perfusion through the device.

Blood perfusion and platelet $[Ca^{2+}]_c$ dynamics were acquired on an inverted Nikon TiU microscope (Nikon Plan Fluor 60x/0.50 objective) using an Andor Zyla sCMOS camera at 50 msec exposure time using a 561nm laser. All image analysis was performed off-line in ImageJ. Background corrected fluorescence images were thresholded using Huang's fuzzy image thresholding. The corrected fluorescence values (F) for each cell were converted into pseudo-ratio values by normalising for Ca^{2+} chelated control platelet flows (F_{min}), as described elsewhere. The pseudo-ratio value was calculated as $F' = F/F_{min}$, where F_{min} was derived for independent platelet flow experiments in which Cal520 loaded platelets were treated with 50 μM DM-BATPA and resuspended in Tyrodes buffer supplemented with 2 mM EGTA/$MgCl_2$. $[Ca^{2+}]_c$ in nM was derived according to the following equation.

Equation 2.3 - Calcium flux – single dye method

$$[Ca^{2+}]_c = K_d \times \frac{F'}{(F'max - F')}, K_d = 320nM$$

The maximal pseudo-ratio fluorescence F'max was determined for each set of flow conditions following incubation of washed platelets with 1.25 mM A23187 in Tyrodes buffer supplemented with 10 mM $CaCl_2$. For mean bulk flow, $[Ca^{2+}]_c$-defined regions of interest were analysed relative to pump components.

2.10.4. PFA100 analysis

As PFA-100 data was collected off-site at Monash Medical Centre, donors whose samples were tested in this device signed a separate pathology request form. PFA-100 analysis was conducted on citrated blood collected in 3 ml Vacutainer tubes with a 10 µg epinephrine bitartrate and 2 µg equine type 1 collagen cartridge, and a 50 µg ADP and 2 µg equine type 1 collagen cartridges. 800 µl aliquots of blood were pipetted into the test cartridges, and the samples were then tested in the machine. Samples from both healthy donors and vWD patients were tested concurrently in the microfluidic device and the PFA-100 within the required four-hour window.

2.11. Experiments assessing platelet margination

To investigate margination within microchannels, platelets and red cells were isolated according to the method outlined in section 2.8. Washed red cells (2% HCT) were incubated with Vyrbrant DiL (1 µg/ml) for 60 minutes at 37^{o}C. Concurrently,

platelets (400 x 10^9/l) were incubated with Fluo-4 (1 µg/ml) at the same conditions. The red cells and platelets were then centrifuged on a benchtop centrifuge for 60 seconds at 2000 x g. Red cell and platelet samples were then reconstituted in 300 µl 1 x Tyrodes, and subsequently added to 400 µl packed red cells, to make up a sample of 1% labelled red cells, 200 x 10^9/l platelets and 40% HCT. Fluorescence images were acquired on an inverted Nikon TiU microscope (Nikon Plan Fluor 60x/0.50 objective) using an Andor Zyla sCMOS camera at 100 msec exposure time using both a 561nm and 640 nm laser.

All image analysis was performed off-line in ImageJ. Images were split into their .nd2 files were uploaded and images were split into colour channels. ‘Z project’ was applied to obtain an averaged sample. Mean fluorescence was plotted on a line scan across the width of the channel and graphed on GraphPad Prism.

2.12. Haemolysis Assay

When assessing haemolysis in the valve platform, valves were actuated at a rate of 1Hz, and whole blood samples in 3.2% ACD were perfused through the manifold *via* an external syringe driver. Samples were collected following perfusion and centrifuged at 500 x g for 5 minutes to collect the supernatant. The supernatant was then centrifuged at 500 x g for 5 minutes and 15 µl of supernatant was aliquotted in 185 µl 1% Tyrodes (4.3 mM K_2HPO_4, 4.3 mM Na_2HPO_4, 24.3 mM NaH_2PO_4, 113 mM NaCl, 5.5 mM D-glucose, pH 7.2) at 35^{o}C. 15 µl of non-perfused supernatant was mixed with 10 µl Triton-X and 185 µl Tyrodes buffer to represent a positive control with 100% haemolysis. Non-perfused plasma from the same patient was used as a

negative control. 100 µl of each sample was transferred to a clear, flat-bottom, 96-well plate absorbance was measured in a plate reader at 495 nm. Background fluorescence was corrected for by determining the average absorption of negative control samples.

When assessing haemolysis in the micropump platform, actuation pressures were alternatively set to 50, 75 and 100 kPa, and frequency varied at 3, 6, 9, 12 and 15 Hz. Samples were analysed according to the method described previously.

2.13. Plasma protein assays

2.13.1. Assessment of vWF physisorption

Assessment of vWF loss was conducted by perfusing human whole blood in 3.2% ACD through valve manifolds. Samples were then centrifuged in 500 µl aliquots at 2000 x g for 120 seconds and plasma was extracted. Plasma vWF % was determined through use of a vWF ELISA kit (Helena Laboratories). Samples were analysed in triplicate. Reference plasma provided in the kit was used to generate a reference range between 0-150%. Each sample and control plasma was prepared using a 1:26 dilution in provided diluent containing buffers, salts and sodium azide. 100 µl of diluted samples were then added to separate wells of the provided 96-microwell plate coated with anti-human vWF antibody, and an additional well was kept blank to act as a negative control. Wells were incubated for 15 mins at room temperature, then inverted and decanted thoroughly, while preventing adjacent samples from mixing. The wells were then washed four times with provided 33X PBS solution with 0.01% Tween 20, ensuring wells did not dry out between washes. 100

µl vWF-specific antibody solution conjugated with horseradish peroxidase was then added to each well except the assigned blank well, and wells were incubated for a further 15 minutes at room temperature. Wells were then dried and washed again with PBS using the method outlined previously. 100 µl substrate containing 3,3',5,5'-tetramethylbenzidine and hydrogen peroxide was then added to each well except the blank, and incubated for another 10 minutes at room temperature. 100 µl stopping solution (0.36 N Sulfuric Acid) was then added to all wells except the blank. The O.D. of wells were analysed using a plate reader at 450 nm within five minutes of the addition of stopping solution. The mean O.D. for each control was calculated. A concentration curve and regression analysis was generated to determine mean O.D. by multiplying sample values by the assigned value from the ELSIA reference plasma curve.

2.13.2. Assessment of fibrinogen physisorption

To assess fibrinogen loss, whole blood samples in 3.2% ACD were perfused through valve manifolds and collected. Samples were then centrifuged at 2000 x g for 120 seconds and the plasma fraction was decanted. 20 µl plasma samples from perfused blood and two 20 µl samples from unprocessed blood (to act as controls) were diluted 1:10 with Imidazole Buffer from a Technoclone Fibrinogen Reagent kit and incubated for 60 seconds at 37^{o}C. 0.2 ml supplied fibrinogen reagent was then added. Time until coagulation was then assessed at room temperature. A fibrinogen coagulation reference provided by Technoclone was prepared separately to determine a calibration curve from which sample fibrinogen concentrations could be calculated using linear regression.

2.14. Fluid dynamic experiments

2.14.1. Microvalve high-speed camera analysis

To image platelet streamlines across microvalve gate surfaces, isolated platelet suspensions (200x10^9/l) in platelet washing buffer (4.3 mM K_2HPO_4, 4.3 mM Na_2HPO_4, 24.3 mM NaH_2PO_4, 113 mM NaCl, 5.5 mMD-glucose, and 10 mM theophylline, pH 6.5) + Integrillin (20 mg/ml) were labelled with the lipophilic membrane dye DiOC6 (1µg/ml) (Molecular Probes) and 0.02U/ml apyrase for 10 min at 37^{o}C and subsequently perfused through the device at constant flow rate of 24 µl/min. Fluorescent platelet streamlines were acquired on an inverted Nikon TiU microscope (Nikon Plan Fluor 20x/0.50 objective) using a Phantom v1610 (Vision Research) CMOS camera attached to an Olympus IX83 microscope (UPLSAPO 60×/NA1.260 obj) with Spectra 4 light source, at 1100 fps (1280 × 1024). Time-lapse tiff imaging stacks were processed to remove background fluorescence and filtered using a median filter (2x2 kernel). Tiff stacks were subsequently processed *via* average z-projection to create average heat map distributions of platelet trajectories using a 16-color LUT.

2.14.2. High speed platelet imaging across the micropump

Washed platelets were loaded with $DiOC_6$ (2ug/ml) for 10 mins at 37^{o}C. Dye-loaded platelets (final platelet count = 200 × 10^9/l) were then reconstituted with isolated RBC prior to perfusion through the device. Reconstituted blood samples were flowed through the micropump at the described actuation pressures and duty cycle. Epifluorescence (488ex/510em) Images were acquired at 1,100 fps (1280x1024)

using a Phantom v1610 (Vision Research) CMOS camera attached to an Olympus IX83 microscope (UPLSAPO60X/NA1.260 obj) with Spectra 4 light source. Images were compiled as maximum Z-projections off-line in ImageJ.

2.14.3. Computational fluid dynamic analysis

In order to compute the relationship between the flow rate (Q), the shear rate at the entry and exit segments of the test platform and the geometric variables of the valve structure, the analytical solution of the velocity profile for a Newtonian fluid was used. To carry out CFD analysis at the microvalve assembly, the valve and microfluidic geometry was extracted from 3-dimensional reconstructions of confocal imaging of valve assemblies perfused with Tetramethylrhodamine ($488/532_{nm}$) in mQ H_2O. Confocal images were exported as a StereoLithograpy (stl) files using the software ImageJ. The stl file was further optimized using surface reconstruction algorithms in MeshLab. The mesh was constructed using snappyhexmesh resulting in a total of 16136 cells (12340 hexahedra and 3796 polyhedra). To determine the local shear conditions for human whole blood at the micro-valve structure the Navier Stokes equations over the geometry domain were solved using OpenFOAM and SIMPLE algorithms, using a viscosity of 0.00345 Pas and a density of 1050 kg/m^3.

2.14.4. Microvalve µPIV analysis

Micro-PIV was employed to validate CFD analysis. Measurement planes were taken halfway between the bottom of the blood channel and the valve tip. Experimental data was obtained through use of an inverted TI-U Eclipse Nikon microscope with an

air-immersion CFI S Plan Fluor ELWD 20× objective lens was coupled with a high-speed camera (2277 Hz at 2000 × 2000 pixels, 12 bits, PCO.dimax HS4). Flow was seeded with one-micron diameter red fluorescent polystyrene aqueous beads, with Polysorbate 20 (Tween 20) added to prevent particle-wall and particle-particle adhesion and fouling. Illumination was provided by a 532 nm Nd:YAG double-pulsed laser (EverGreen - BigSky Laser Series) pulsing at 15 Hz. Flow was achieved through connection of a Harvard PHD ULTRA syringe pump loaded with a 1000 µl glass syringe through silicon tubing. The pump was operated in withdraw mode at 24 µl/min, and valves were assessed in fully open and partially open positions (defined as the valve tip being 40 µm from the channel floor). 4000 images were captured for each measurement, and background noise was removed through subtraction of the average of 100 images of background images from the recording. The signal-to-noise ratio was improved though employment of two averaging methods: “Average Image Method” and “Average Velocity Methods”. In the Average Image Method, 20 images were overlaid to increase the number of particles per imaging window. A multigrid algorithm was then combined with a window deformation algorithm with adaptive central difference interrogation (CDI) offsetting. Using a Fast Fourier Transform based cross-correlation algorithm, the local displacements correspond to each interrogation window (32×32) were acquired. The depth of correlation and the spatial resolution of the micro-PIV measurement were 7, 8 and 9 µm, respectively. The Average Velocity Method was employed through identifying valid vectors of each realisation and using a median test to then average over the entire realisation window.

2.14.5. Micropump µPIV analysis

µPIV were carried out at the mid-plane of the micro-pump and collagen channel to measure the velocity field and the resulting shear rate. Distilled water was used that was seeded with red fluorescent polystyrene aqueous spherical particles with diameters of two-microns (ThermoFisher Scientific). Prior to the experiments, the microchannel, inlet and outlet reservoir of the micro-pump were prefilled with the seeded fluid. The microfluidic device was mounted onto a motorised stage of an inverted (Ti2, Nikon) microscope equipped with a G-2A filter cube for epifluorescence imaging. Prior to each experiment any bubbles trapped within the micro-channel was removed. The fluorescent particles were illuminated using a diode-pumped solid-state laser with a continuous wave output at 532 nm (Verdi Family, Coherent). Particle images were recorded with a high-speed PCO.dimax HS4 camera (4 Megapixels, 12 bit), capable of recording images at 2277 fps at full resolution. Images in the pump section and collagen channel were captured at 4000 Hz and 7000 Hz through a 4x and 10x objectives, respectively. Further, the optical magnification for these cases were 2.76 and 1.1 µm/pixel, respectively. In each set of measurements, 10000 images were captured. Prior to processing, the images were calibrated using a micron-sized calibration grid and pre-processed by applying a histogram equalization. PIV vector computation was performed using DAVIS (LaVision, GmbH) using a multi-pass algorithm with grid deformation with a final interrogation size was equal 6 4x 64 pixels. In order to minimize spurious vectors a 5 x 5 spatial filter and a temporal filter over 10 ms was applied to the velocity fields in post-processing. Further, due to the periodic nature of the pump, the velocity fields were phased-averaged over a pump cycle to enhance the signal-to-noise ratio.

2.15. Statistical analysis

2.15.1. Microvalve and Micropump statistical analysis

Statistical analysis was performed in GraphPad Prism using a one-way analysis of variance (ANOVA) with Dunnett's multiple comparisons test to compare means and determine significance. Error bars demonstrated standard deviations in data. Analysis of statistical significance of two means was performed through unpaired T Tests performed in Graphpad Prism with the assumption of a Gaussian distribution. Multiple regression analysis (MANOVA) was performed using SPSS Statistics. Continuous results were assessed to have a normal distribution (using a normal probability plot), linearity (using a residual plot) and constant variability (using a scatter plot). All variables were entered into the analysis. Assessment of the relationship between parameters through construction of an interactions plot in SPSS Statistics, and univariate analyses were also performed to determine the impact of parameters on blood handling.

2.15.2. Microcontraction statistical analysis

Graphpad Prism 6.0 was used to provide statistical analysis. When analysing linear correlations, linear regression was used with a 95% confidence interval. Non-linear correlates were determined with a sigmoidal dose-response curve. Determination of the coefficient of determination (R^2 value) was used to determine the degree of association. A value closer to 1 indicated a greater degree of association. Receiver-operating characteristic analysis determined the threshold for diagnosis for the device in normal donors and those with vWD, by using the borderline type 1 disease

patients to calculate the discrimination threshold. Coefficient of variation analysis determined the spread of aggregate responses. Sigmoidal curves were calculated to pool aggregate traces to identical experiments. Derivatives were provided of aggregate growth traces, to graphically represent the rate of aggregate growth.

2.16. References

1. Conant CG, Schwartz MA, Nevill T, Ionescu-Zanetti C. Platelet adhesion and aggregation under flow using microfluidic flow cells. J Vis Exp. 2009 (32):1644.
2. Brazilek RJ, Tovar-Lopez FJ, Wong AK, Tran H, Davis AS, McFadyen JD, et al. Application of a strain rate gradient microfluidic device to von Willebrand's disease screening. Lab Chip. 2017;17(15):2595-608.
3. Zhang M, Horbett TA. Tetraglyme coatings reduce fibrinogen and von Willebrand factor adsorption and platelet adhesion under both static and flow conditions. J Biomed Mater Res A. 2009 Jun;89(3):791-803.
4. Brazilek RJ, Tovar-Lopez FJ, Wong AKT, Tran H, Davis AS, McFadyen JD, et al. Application of a strain rate gradient microfluidic device to von Willebrand's disease screening. Lab Chip. 2017 Jul 25;17(15):2595-608.
5. Jain A, van der Meer AD, Papa A-L, Barrile R, Lai A, Schlechter BL, et al. Assessment of whole blood thrombosis in a microfluidic device lined by fixed human endothelium. Biomed Microdevices. 2016 Aug;18(4):1-7.
6. Nesbitt WS, Westein E, Tovar-Lopez FJ, Tolouei E, Mitchell A, Fu J, et al. A shear gradient-dependent platelet aggregation mechanism drives thrombus formation. Nat Med. 2009;15(6):665-73.

Chapter three: Development and characterisation of haemocompatible microvalves

3.1 Introduction

Microvalves can be critical modular elements within microfluidic systems, as they allow fluidic isolation, acting as a barrier to separate two fluids. In order to provide reliable fluidic isolation in blood-contacting devices, a number of valving approaches have been published in the literature. These have included pneumatically-actuated valves and phase change valves.(1) However, haemocompatibility testing of prior blood-valve designs devices has been poorly characterised, and few have been designed with consideration to their cellular handling, impact on plasma proteins, materials hemocompatibility and haemodynamics. Lack of consideration in these areas may alter aspects of the sample and interfere with the diagnostic capacity of the device.(2) One factor driving haematological incompatibility is the shear forces experienced, which can alter protein conformation and binding, platelet and red cell reactivity and the adhesion receptors involved.(3) The fluid dynamics within these systems has been poorly characterised, particularly when considering blood as the fluidic substrate. Consideration of shear rates in these systems may open avenues to improvement in design that could improve haemocompatibility.

In light of these shortcomings, this chapter presents the detailed characterisation of pneumatically actuated elastomeric haemocompatible microvalves, demonstrating investigations in platelet and red cell handling and minimisation of plasma protein loss, and a detailed investigation into the shear forces and cellular distribution driving hemocompatibility. Supplemental information is provided in chapter 3.4.

3.2 References

1. Au AK, Lai H, Utela BR, Folch A. Microvalves and Micropumps for BioMEMS. Micromachines. 2011;2(2):179-220.

2. van Oeveren W. Obstacles in Haemocompatibility Testing. Scientifica. 2013 2013;2013:392584.

3. Nesbitt WS, Mangin P, Salem HH, Jackson SP. The impact of blood rheology on the molecular and cellular events underlying arterial thrombosis. J Mol Med. 2006;84(12):989-95.

Lab on a Chip

PAPER

View Article Online
View Journal

Cite this: DOI: 10.1039/c7lc01320e

Elastomeric microvalve geometry affects haemocompatibility†

Crispin Szydzik,‡[a] Rose J. Brazilek,‡[b] Khashayar Khoshmanesh,[a] Farzan Akbaridoust,[c] Markus Knoerzer,[a] Peter Thurgood,[a] Ineke Muir,[d] Ivan Marusic,[c] Harshal Nandurkar,[b] Arnan Mitchell[a] and Warwick S. Nesbitt *[ab]

This paper reports on the parameters that determine the haemocompatibility of elastomeric microvalves for blood handling in microfluidic systems. Using a comprehensive investigation of blood function, we describe a hierarchy of haemocompatibility as a function of microvalve geometry and identify a 'normally-closed' v-gate pneumatic microvalve design that minimally affects blood plasma fibrinogen and von Willebrand factor composition, minimises effects on erythrocyte structure and function, and limits effects on platelet activation and aggregation, while facilitating rapid switching control for blood sample delivery. We propose that the haemodynamic profile of valve gate geometries is a significant determinant of platelet-dependent biofouling and haemocompatibility. Overall our findings suggest that modification of microvalve gate geometry and consequently haemodynamic profile can improve haemocompatibility, while minimising the requirement for chemical or protein modification of microfluidic surfaces. This biological insight and approach may be harnessed to inform future haemocompatible microfluidic valve and component design, and is an advance towards lab-on-chip automation for blood based diagnostic systems.

Received 11th December 2017,
Accepted 10th May 2018

DOI: 10.1039/c7lc01320e

rsc.li/loc

Introduction

There is an increasing drive toward microfluidic based blood diagnostics,[1–5] however a critical bottleneck impeding clinical translation of such devices is the ability to reliably deliver blood components to assay platforms without affecting blood composition or function.[6,7] Microfluidic performance in areas such as the mechanics of blood cell handling, effects on blood plasma protein and biomarker composition, materials haemocompatibility, and haemodynamic parameters, must be carefully considered in order to achieve effective blood handling. On-chip microvalve operated delivery, mixing, and pumping elements have the potential to deliver sophisticated, multiplexed, automated, and reliable haematology focused microfluidic diagnostics; however the effect of such dynamic microfluidic components on blood function presents significant challenges. While haemocompatibility is a recognized criterion for microfluidic development, design approaches have been limited by a lack of sophistication with respect to the assessment of blood function, and have often relied on superficial measures such as haemolysis, and gross assessment of biofouling.[8,9] Few microfluidic studies have comprehensively defined haemocompatibility and virtually none describe a detailed blood-testing regime to assess and inform microfluidic device design.[10–14]

Blood presents significant and specific challenges when working with microfluidic systems.[6,15] Blood is a non-Newtonian fluid and its viscosity may be up to an order of magnitude more viscous than water (dependent on flow parameters and biochemical factors), leading to pressure differentials that may perturb flow and impair device performance.[16,17] In addition, blood plasma protein physisorption processes at microfluidic surfaces pose significant problems with regard to blood analyte (biomarker) loss, and blood cell adhesion.[15] The plasma protein and cellular components of blood, particularly von Willebrand factor (VWF), fibrinogen, and blood platelets, have evolved to react to local changes in the hydrodynamic (haemodynamic) environment through processes of protein conformational unfolding, surface adhesion and platelet-platelet aggregation.[18] VWF binding and function is critically sensitive to the prevailing

[a]School of Engineering, RMIT University, 124 La Trobe Street, Melbourne, Victoria 3000, Australia. E-mail: warwick.nesbitt@rmit.edu.au
[b]The Australian Centre for Blood Diseases, Monash University, Alfred Medical Research and Educational Precinct, 99 Commercial Road, Melbourne, Victoria, 3004, Australia
[c]Department of Mechanical Engineering, University of Melbourne, Grattan Street, Parkville, Melbourne, Victoria 3010, Australia
[d]CSL Ltd, CSL Ltd, Bio21 Institute, Flemington Rd, Parkville, VIC 3052, Australia
† Electronic supplementary information (ESI) available. See DOI: 10.1039/c7lc01320e
‡ These authors contributed equally.

haemodynamic conditions such that shear rates >5000 s^{-1} lead to conformational unfolding and presentation of platelet binding domains.[19–21] Fibrinogen exchange at artificial surfaces is mediated by competition with proteins of the contact activation (coagulation) pathway, such as high-molecularweight kininogen, factor XII, and plasminogen, with studies demonstrating that sample flow can significantly increase initial adsorption rates and also modify exchange rates with coagulation factors (the Vroman effect).[22–24] Shear rates in relation to platelet function must be carefully considered.[25–27] Elevated shear rates on the order of 1500–10000 s^{-1} and extremes above 50000 s^{-1} can directly trigger blood platelet Ca^{2+} signalling, α-granule secretion, adhesion, and platelet aggregation through the activation and engagement of platelet adhesion receptors, such as GPIb/V/IX and the integrin $\alpha_{IIb}\beta_3$.[28,29] In addition, platelet adhesion and activation at device surfaces can trigger coagulation through the generation of "coated" procoagulant platelets expressing surface phosphatidyl serine (PS).[30] Significantly, findings from our laboratories have demonstrated that shear rate micro-gradients above a critical threshold can acutely trigger platelet aggregation in microfluidic systems.[31–33]

Pneumatically actuated microvalves are the most common valve type in assays requiring multiplexed integration, as the fabrication processes are comparatively inexpensive and simple.[34] Pneumatic valves may operate through 'normally-open' or 'normally-closed' configurations.[35] Normally-open configurations may be designed for high-density systems, but are only possible with low aspect ratio rounded channels; requiring complex fabrication methods.[36] In addition, normally open valves are limited where portability is a requirement due to the need for bulky ancillary drivers to maintain fluidic isolation.[34] In contrast, normally closed valves are able to overcome these limitations, and generally operate at lower actuation pressures (typical actuation pressures of 1–12 psi) resulting in increased performance and the capability to use relatively small footprint valve drivers.[37] Normally closed lifting gate valves consist of a vertical gate geometry patterned directly onto a membrane that deflects away from the channel floor upon actuation.[34] This valve configuration allows for reliable fluidic isolation and integration with various functional substrates,[31] with recent advances in fabrication techniques by our group significantly reducing fabrication complexity, increasing the practical integration of this valve type.[38] A key consideration for optimised lifting gate valve performance is actuation pressure, with operating pressure range in part determined by overall valve geometry.[35] A hierarchy of valve geometries as a function of actuation pressure and fluidic channel geometry has been defined, such that v-shaped valves demonstrate the lowest actuation pressures in comparison to straight or diagonal valve variants.[35] In addition, v-shaped valves are typically more reliable, as they actuate more consistently, and their actuation pressures are more reproducible across replicate devices.[35] While a number of design principles focused purely on valve mechanical performance have been identified, the specific requirements for haemocompatible blood handling microvalves and the impact of valve haemodynamics on performance have not been investigated.

In this study, we define and describe a biologically informed approach for haemocompatible microfluidic design. Using this approach, we identify a v-shaped microvalve architecture that minimally impacts blood sample integrity and function without the requirement for surface passivation (prefouling).

Experimental

Device description

The overall design of the microvalve iterations tested, the "test-manifolds", and the pneumatic actuation chamber location are shown in Fig. 1a. Valve iterations were identified by the width of the valve chamber (μm) and overall geometry as; S300, S400, S500 and S600 (straight valves) and V300, V400, V500 and V600 (v-shaped valves) (Fig. 1a). Details of valve manifold dimensions are given in Table S1.† Under normal operation sample perfusion through the valve test-manifold was driven via an external Harvard PHD-2000 syringe driver, operating in withdraw mode, connected to the outlet channel in the PDMS block using a 30 ml glass syringe attached to 10 cm of Tygon (0.8 mm I.D.) tubing. In the case of FACS based assays or assays requiring perfusate collection, blood samples were loaded into sterile plastic 10 mL syringes prior to device connection and the syringe driver operated in infuse mode. Pneumatic gate operation was achieved by applying negative pressure through connection of a 50 ml plastic syringe to the actuation chambers by 10 cm of Tygon tubing.

Device fabrication

Fabrication of microfluidic devices was achieved using a previously described method.[38] In brief, a combination of a membrane-sandwich fabrication method and PDMS injection moulding, was utilised to produce thin double sided PDMS slabs.[38] Standard photolithography techniques[33] were used to fabricate the required complementary mould structures, using silicon and glass wafer substrates. These moulds consisted of primary fluidic channels and valve gates patterned onto the bottom mould, and pneumatic actuation channels and viaducts on the transparent upper mould. Polydimethylsiloxane (PDMS) pre-polymer (Sylgard 184 Silicone Elastomer – Dow Corning) was mixed with curing agent with a weight ratio of 10: 1, and thoroughly degassed under vacuum. Degassed pre-polymer was introduced between the moulds, which were aligned, clamped and cured for 30 min at 100°C. Following curing, the moulds were separated and the PDMS slab extracted. Interface holes were biopsy punched as required, and a 5 mm thick interface slab of PDMS was plasma bonded to the upper surface of the injection moulded PDMS slab (Harrick Plasma PDC-002: 100% O_2, 1 min). The interface slab, previously biopsy punched with corresponding 750 μm interface holes, acted to seal the pneumatic upper channels while providing the fluidic and

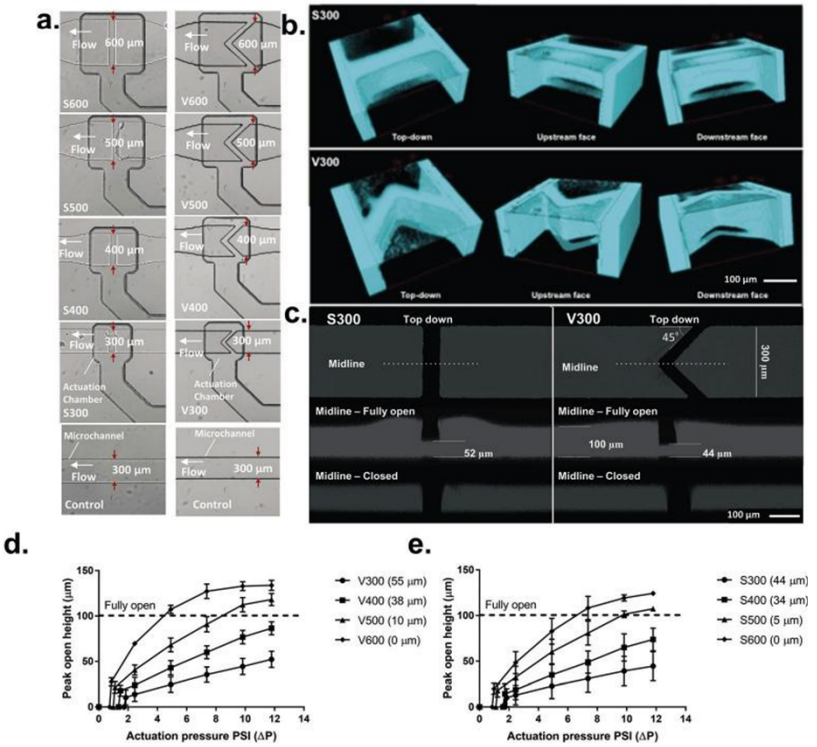

Fig. 1 Test device description and microvalve mechanical testing. a. DIC micro-image showing the straight and v-gate test-manifolds. The microfluidic test-manifolds consisted of five primary fluidic channels; a control (no-valve) channel, and four channels containing lifting-gate valves differing by the width of the valve chamber and channel expansion, including 300 µm, 400 µm, 500 µm and 600 µm. b. Confocal imaging of S300 and V300 microvalves in partially open state following perfusion with TRITC (1 µg mL^{-1}). Views show 3-dimensional reconstructions of S300 and V300 valve cases. Note the overall deformation of the valve gates under negative pressure resulting in microchannel clearance. c. Confocal imaging showing top down and lateral (midline) views of S300 and V300 gates in fully open and closed states. Note that opening heights were taken from the lateral midline. d. Valve opening height (midline) as a function of actuation pressure for v-gate valve manifolds. Numbers in brackets represent gate projection into the microchannel at a maximal actuation pressure of 7.37 psi. e. Valve opening height (midline) as a function of actuation pressure for straight valve manifolds. Numbers in brackets represent gate projection into the microchannel at a maximal actuation pressure of 7.37 psi.

pneumatic interface. A no. 1 borosilicate coverslip sealed the bottom of the injection-moulded slab and acted as the imaging window for microscopy-based experiments. Selective plasma bonding was achieved in a manner similar to those previously described for normally closed PDMS microvalves. In order to selectively prevent permanent plasma bonding of the valve gates, PDMS exclusion stamps were fabricated using photolithography to define a block with raised 150 µm tall pillars with geometry to match the location and size of all valve gates on the bottom of the injection moulded PDMS slab.[39] This exclusion stamp is aligned and placed over the valve gates prior to plasma treatment (100% O_2, 20 seconds) and allows plasma access to all PDMS surfaces with exception of the areas in contact with the exclusion stamp.

Computational fluid dynamic analysis

To conduct CFD analysis at the actuated microvalve assembly, the valve and microfluidic geometry were simplified and reconstructed from 3-dimensional confocal imaging data of valve assemblies perfused with TRITC (1 µg mL^{-1}) in mQ H_2O. Confocal images were exported as StereoLithograpy (stl) files using the open source software Fiji. The stl file was further optimized using surface reconstruction algorithms in MeshLab. Simplified reconstructions of the open valve geometry were then constructed based on these optimized stl files, using the CAD software, Solidworks (Dassault Systèmes). The mesh was constructed using snappyhexmesh resulting in a total of 16136 cells (12340 hexahedra and 3796 polyhedra). Grid convergence analysis was performed at the valve gate wall, using centerline flow profiles (Fig. S2†). To determine the local shear rate conditions for human whole blood at the microvalve structure the Navier Stokes equations over the geometry domain were solved using OpenFOAM and SIMPLE algorithm, using a viscosity of 0.00345 Pa s and a density of 1050 kg m^{-3}. Blood can be approximated as Newtonian fluid at high shear rates.[39] Non-slip at the wall was considered.

μPIV analysis

μPIV analysis was performed in order to verify and support CFD models. Detailed methodology is supplied in ESI.†

High speed platelet imaging

Washed platelets (200 × 10^9/L) were loaded with $DiOC_6$ (2 μg ml^{-1}) for 10 min at 37 °C. Dye-loaded platelets (final platelet count = 200 × 10^9/L) were then reconstituted with isolated RBC prior to perfusion through the device. Platelet adhesion and activation were blocked with theophylline (10 mM) and eptifibatide (Integrilin-20 μg mL^{-1}). Reconstituted blood samples were per-fused across the valve surface at a rate of 24 μl min^{-1} for 16 s. Epifluorescence ($_{488ex/510em}$) images were acquired at 1100 fps (1280 × 1024) using a Phantom v1610 (Vision Research) CMOS camera attached to an Olympus IX83 microscope (UPLSAPO 60X/NA1.260 obj) with Spectra 4 light source. Images were compiled as maximum z-projections off-line in ImageJ.

Blood collection and handling

Ethics approval was obtained from the Alfred Hospital and Monash University Standing Committees on Ethics in Research involving Humans. All experiments were performed in compliance with relevant laws and guidelines and followed Monash Universities policies regarding the handling of human blood samples. Whole blood samples were obtained from consenting subjects via venesection into 2% w/v citrate. Samples were allowed to rest for 10 min at 37 °C prior to device perfusion. Full blood examination was routinely conducted using a Haemogram (Abbott Diagnostics) blood analyser prior to experimentation and blood haematocrit and platelet count recorded.

Assessment of valve dependent platelet aggregation

To assess platelet aggregation as a function of valve architecture human whole blood samples were incubated with the lipophilic membrane dye $DiOC_6$ (1 μg mL^{-1}) (Molecular Probes) and 0.02 U mL^{-1} apyrase (to eliminate released ADP during blood collection) for 10 min at 37 °C and subsequently perfused through the device at constant flow rates of 24 or 108 μL min^{-1}. Blood perfusion and platelet aggregation dynamics were acquired on an inverted Nikon TiU microscope (Nikon Plan Fluor 20X/0.50 objective) using an Andor Zyla sCMOS camera at 1 fps for 210 s. All image analysis was performed off-line in ImageJ using Huang's fuzzy image thresholding. $DiOC_6$ labelled fluorescent platelet aggregates were auto-thresholded such that the earliest micro-aggregates were included in the analysis window. Platelet aggregate size was expressed as either 2-dimensional cross section (μm^2) or integrated intensity as a function of time (s).

Platelet isolation

Washed human platelets were isolated from human whole blood as described.[40] Whole blood was collected into acid citrate dextrose (ACD) anticoagulant at a ratio of 6:1 (blood/ ACD), to which 20 U ml^{-1} enoxaparin (Clexane) was added before being allowed to incubate at 37 °C for 15 min. Separation of platelet-rich plasma (PRP) and red blood cells (RBC) was achieved by centrifugation at 300 × g for 16 min. Platelets were isolated from PRP by centrifugation at 1700 × g for 7 min, followed by resuspension in an equal volume of platelet washing buffer (4.3 mM K_2HPO_4, 4.3 mM Na_2HPO_4, 24.3 mM NaH_2PO_4, 113 mM NaCl, 5.5 mMD-glucose, and 10 mM theophylline, pH 6.5). Platelets were washed by centrifugation at 1500 × g for 7 min, followed by a final resuspension at a concentration of 200 × 10^9/ml in Tyrode's buffer (10 mM Hepes, 12 mM $NaHCO_3$, 137 mM NaCl, 2.7 mM KCl, and 5 mM glucose, pH 7.3) containing bovine serum albumin (5 mg ml^{-1}), calcium (1 mM), and apyrase (0.02 units per ml) (ADPase activity).

Reconstituted blood sample preparation

Reconstituted blood was prepared from human whole blood as described.[40,41] RBC were isolated by centrifugation at 200 × g for 15 minutes, and the PRP fraction collected. The remaining RBC fraction was washed 2× with Tyrode's buffer pH 7.2 via centrifugation at 1700 × g for 7 minutes. The final RBC fraction was re-suspended in Tyrodes pH 7.2 supplemented with 0.5% w/v BSA + apyrase (0.02 U mL^{-1}) and carried through a final centrifugation at 1700 × g for 7 minutes. Packed RBC were stored at 37 °C for later use. Reconstituted blood samples were prepared using either isolated platelet suspensions in Tyrodes buffer pH 7.2 or autologous PRP at a final haematocrit (Hct) of 40% and a platelet count of 200 × 10^9/L. Hct and platelet counts were verified by full blood analysis.

Platelet and erythrocyte Ca^{2+} assay

Platelet cytosolic calcium levels $[Ca^{2+}]_c$ were monitored according to published methods.[40] Briefly, washed platelets (1 × 10^9/mL) were loaded with Oregon Green BAPTA 488 1,2-bis (2-aminophenoxy)ethane-N,N,N′,N′-tetraacetic acid tetralJacetoxymethyl) ester (1 μM), and Fura-Red/AM (1.25 μM) for 30 min at 37 °C. Dye-loaded platelets (final platelet count = 200 × 10^9/L) were then reconstituted with washed red blood cells prior to perfusion through the device. Reconstituted blood samples were perfused through the test-manifold at Q = 24 or 108 μL min^{-1}.

RBC used for monitoring intracellular calcium changes in response to shear stress were washed with modified Tyrodes pH 7.2 + 2 mM $CaCl_2$ and 10 mmol l^{-1} glucose then re-suspended in this buffer at a haematocrit of 0.002%. Fluo-4/AM dissolved at 2 mM in dimethyl sulfoxide was added to the RBC suspensions to obtain 3 μM and the suspensions were incubated with mild shaking for 1 hour at 37 °C. RBC were washed three times with supplemented Tyrodes following the incubation period and then suspended in supplemented Tyrodes. To examine changes in calcium flux, sequential confocal images of platelets or RBC were captured at a scan rate of 0.586 frames per s for 37.5 s over the 3.5 min perfusion time course at positions upstream, at the valve, immediately downstream and 1000 μm downstream of the valve structure. Standard image thresholding was used to demarcate RBC or platelets from the background and determine calcium dye

fluorescence. In the case of RBC Fluo4 fluorescence was monitored and fluorescence change normalised against resting (no perfusion) controls. In the case of platelets, the fluorescent ratio of Oregon Green BAPTA 488 to Fura Red was then calculated. Real time platelet calcium flux was calculated from ratiometric fluorescence measurements and converted to intracellular calcium concentrations (nM) as described previously.[42]

Haemolysis assay

Whole blood samples in 3.2% ACD collected following perfusion through the valve test platform were centrifuged at 500 × g for 5 minutes, and the resulting supernatant collected. The supernatant was subsequently centrifuged at 500 × g for 5 minutes, to pellet any intact RBC. 15 μL of each supernatant was then suspended in 185 μl 1% Tyrodes (4.3 mM K_2HPO_4, 4.3 mM Na_2HPO_4, 24.3 mM NaH_2PO_4, 113 mM NaCl, 5.5 mM D-glucose, pH 7.2) at 35 °C. A positive control was made by adding 15 μL of non-haemolysed haematocrit and 10 μl Triton X-100 to 185 μl of Tyrodes buffer. A negative control consisted of the collected supernatant of an unprocessed sample. 100 μl of each sample was then transferred to a clear, flat-bottomed 96-well plate and absorbance (495 nm) was measured. Background correction was determined from the average absorbance of the negative control samples. All samples were normalised with the positive control representing 100% haemolysis.

Plasma protein assay

To assess plasma VWF loss as a function of valve performance whole blood samples (500 μL) in 3.2% ACD were collected following perfusion through the valve test platformIJs). Blood samples were centrifuged at 2000 × g for 2 min and the plasma fraction retained. Plasma VWF antigen (%) was determined via von Willebrand factor ELISA (Helena laboratories) as per the manufacturers instructions. To determine the effect of valve architecture on VWF multimer profile samples were collected as per ELISA and subsequently run on an agarose multimer gel and multimer range assessed via densitometry.

Erythrocyte and platelet FACS analysis

Whole blood samples in 3.2% ACD following perfusion through the valve test platform were collected. 5 μl samples from each valve iteration were immediately transferred to 12 × 75 mm Falcon® capped polystyrene test tubes containing 20 μL CD61 PerCP, 20 μL PAC-1 FITC or 5 μL PE-P selectin conjugated monoclonal antibodies. Tubes containing only one of each antibody were prepared using inactivated blood to act as voltages, tubes containing blood activated with 2×10^{-5} M ADP were used for channel compensation, and tubes stained only with CD-61 were used to obtain isotype control forward and side scatter buffers. For all samples containing PAC-1 antibodies, RGDS was also added to the solution to exclude non-specific binding. Data was then analysed in two-colour plots.

Statistical analysis

Statistical analysis was performed in GraphPad Prism using a one-way analysis of variance (ANOVA) with Dunnett's multiple comparisons test to compare means and determine significance.

Multiple regression analysis was performed using SPSS statistics. All variables were coded as continuous except the valve type, which was coded as an ordinal variable. Continuous results were assumed to have a normal distribution (using a normal probability plot), linearity (using a residual plot) and constant variability (using a scatter plot). All variables were entered into the analysis. The R^2 for this multivariate analysis was 0.780, showing the regression explained 78.0% of the variance in the data. F-Test demonstrated a high degree of significance ($F = 116.218$), allowing the assumption that the model explained a significant degree of variation in the data. All groups demonstrated statistical significance ($p < 0.05$). Non-multicollinearity was confirmed. Standardised coefficients were compared to determine the impact of variables.

Results

Valve gate mechanical performance

To characterise micro-valve performance as a function of actuation pressure we conducted scanning confocal microscopy experiments in which valve manifolds were perfused with a tetramethylrhodamine (TRITC) solution (1 μg mL^{-1}) and valve opening recorded in 3-dimensions (Fig. 1b and c; Video S1t). Fig. 1b and c demonstrate that application of negative pressure in the actuation chamber results in the upward deformation and expansion of the actuation membrane, lifting and asymmetrically stretching the valve gates resulting in an "arched" opening profile. Valve opening efficiency (measured at mid-line) as a function of actuation pressure directly correlated with valve geometry such that S600 and V600 valves demonstrated the greatest opening efficiency, with full gate clearance (100 μm) occurring at an actuation pressure of ≃4.9 psi (Fig. 1d and e). Significantly, overall valve chamber width appeared to be a direct effector of opening efficiency, with valves in the range of 300–500 μm only partially opening at an applied pressure of ~4.9 psi (Fig. 1d and e). It should be noted by the standard deviation that valve-to-valve variance was evident due both to batch-to-batch differences in fabrication and also the inherent tolerances of PDMS based elastomeric micro-valves. Head-to-head comparison of straight versus v-shaped valves demonstrated that the v-shaped design more reliably actuated at low pressures, with the v-shaped design displaying a lower overall minimum actuation pressure (Fig. 1d and e). Furthermore, as evidenced by the variance in replicate measurements the v-gate geometry typically actuated more consistently across the applied pressure range (Fig. 1d and e). Confocal imaging demonstrated that at an opening pressure of −7.37 psi the 300–500 μm wide valve gates projected up to ~5–55 μm into the microfluidic channel, increasing the likelihood of valve gate interactions with perfused blood components (Fig. 1d and e).

Effect of valve architecture on platelet aggregation and fouling

A key problem associated with microfluidic blood handling performance is fouling due to adhesion and/or aggregation of blood cells, particularly platelets, with component systems. To investigate the effects of valve architecture on platelet adhesion and aggregation we perfused both straight and v-shaped test-manifolds with citrated whole blood for up to 5 minutes. Fig. 2a and b demonstrate that for fully open and partially open states, platelet aggregation inversely correlates with valve gate size, such that 300 µm valves show the highest levels of platelet adhesion/aggregation. Head-to-head comparison of straight versus v-shaped valves demonstrated that straight valves are significantly more pro-aggregatory than v-shaped in fully open and partially open (40 µm) states (Fig. 2a and b). The V600 geometry demonstrated limited platelet adhesion/aggregation above that observed for no-valve controls in the fully open state (Fig. 2a). Epi-fluorescence imaging of the early platelet adhesion response demonstrated that platelet aggregation was initiated at the upstream edge and bottom face of valve gates (Video S2†). Furthermore, early aggregates formed as distinct "platelet strings" that in the case of straight gates were distributed across the entire bottom face (Video S3†). In the case of v-gates, "platelet strings" formed lateral to the v-gate apex, which was free of formed aggregates (Video S2†).

3-Dimensional confocal imaging of platelet recruitment at the valve gate geometries following prolonged (5 min) blood perfusion demonstrated that platelet fouling was localised primarily at the bottom face of the valve gates with consolidated aggregates extending freely away from both the upstream and downstream faces (Fig. 2d—g). Quantitation of the time to complete fouling in the fully open and 40 µm states demonstrated that straight valve designs were more prone to occlusion as a function of valve size compared to v-gates (Fig. 2c). A 5-fold increase in flow rate ($Q = 128\ \mu L\ min^{-1}$) led to an approximate doubling in overall platelet aggregation at the v-gates across the size range tested (Fig. 3a and S3a†). Increasing haematocrit (Hct) from 40—60% led to an overall increase in platelet aggregation dependent on geometry and inversely with valve size (Fig. 3b and S3b†). Increasing platelet count led to an overall increase in platelet aggregation that scaled inversely with valve size (Fig. 3c and S3c†). Taken together these data suggest that, as for laminar flow systems, platelet margination (increased density at the wall) and mass transport effects due to red blood cell interactions may contribute to the aggregation response. There was no effect of anticoagulant (citrate versus hirudin) on the observed platelet response (Fig. S4†). Multivariate regression to predict aggregate size from; valve geometry (categorical), and open state, valve size, Hct, platelet count, and flow rate (continuous) demonstrated that all variables statistically significantly

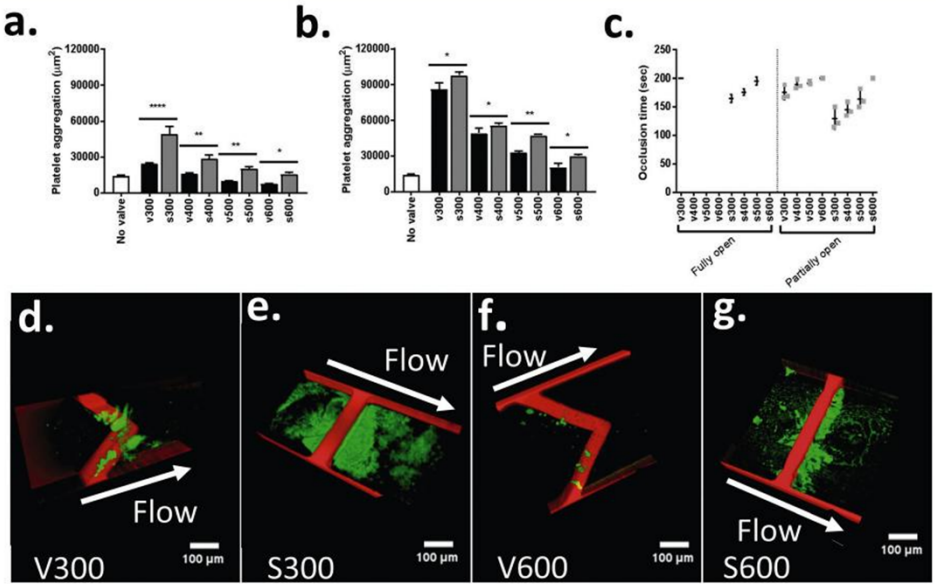

Fig. 2 Platelet aggregation and biofouling as a function of microvalve geometry. a. Platelet aggregation at straight versus v-gates in fully open states; $Q = 24\ \mu l\ min^{-1}$. b. Platelet aggregation at straight *versus* v-gates in partially open (40 µm) states; at $Q = 24\ \mu l\ min^{-1}$. Black horizontal bars indicate comparative valve shapes and sizes (e.g. V300 and S300) for which a significance significant difference was tested for using a paired t-test. * $p \leq 0.05$, ** $p \leq 0.01$, *** $p \leq 0.001$, **** $p \leq 0.0001$. c. Occlusion times of straight versus v-gates in fully open or partially open (40 µm) states; $Q = 24\ \mu l\ min^{-1}$. d—g. 3-Dimensional reconstructions of confocal microscopy epifluorescence images of representative aggregate formation, imaged after 5 minutes of blood flow. Aggregates are represented in green and the valve geometries in red. Scale bar represents 100 µm. d. V300 partially open valve with aggregate. e. S300 partially open valve with aggregate. f. V600 partially open valve with aggregate. g. S600 partially open valve with aggregate.

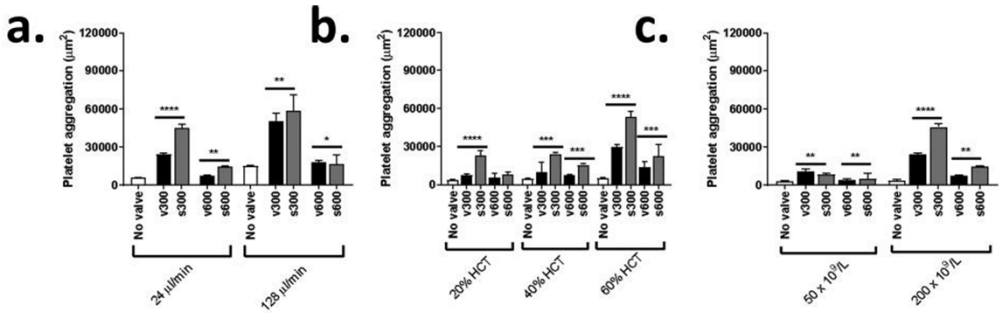

Fig. 3 Platelet aggregation in bulk flow as a function of microvalve geometry. a. Platelet aggregation at straight *versus* v-fully open gates at Q = 24 µl min^{-1} and 128 µl min^{-1}. b. Platelet aggregation at straight *versus* v-fully open gates (Q = 24 µl min^{-1}) as a function of hematocrit. c. Platelet aggregation at straight versus v-fully open gates (Q = 24 µl min^{-1}) as a function of platelet count. All data shows n = 3 independent experiments normalized to valve surface area (µm²). Error bars indicate standard deviation. Black horizontal bars indicate comparative valve shapes and sizes (*e.g.* V300 and S300) for which a significance significant difference was tested for using a paired t-test. * $p \leq 0.05$, ** $p \leq 0.01$, *** $p \leq 0.001$, **** $p \leq 0.0001$.

affected aggregate size [$F(7,236) = 79.593$, $p < 0.05$, $R^2 = 0.780$] (Table S2†). This analysis demonstrated that valve category was a significant effector of haemocompatibility (Table S2†) ($\beta = 1.041$ for straight valves, 0.750 for v-shaped valves). Taken together this data suggests that near wall platelet adhesion and aggregation and hence fouling can be significantly modulated by changes in valve geometry.

Effect of valve architecture on platelet activation

An important consideration for microvalve performance is the effect that valve haemodynamics have on platelet activation in bulk flow, particularly where downstream cell and biomarker assay are required. To investigate the impact of micro-valve design on platelet activation we examined the impact of valve architecture on platelet Ca^{2+} signal transduction in bulk flow (Fig. 4a and S5a†). Maximal platelet $[Ca^{2+}]_c$ (a global marker of platelet activation status) inversely correlated with valve size, with the straight valve architecture more reactive than v-shaped, in both fully open and partially open (40 µm) states (Fig. 4a and S5a†). Fig. 4b–d (Fig. S5b–d†) demonstrate that as per platelet $[Ca^{2+}]_c$ distinct markers of platelet function; platelet integrin $\alpha_{IIb}\beta_3$ activation (PAC1 binding), α-granule secretion (P-selectin expression), and platelet procoagulant function (phosphatidyl serine exposure) mapped to valve size and shape, suggesting that global platelet function in the bulk flow is significantly affected by valve geometry.

Effect of valve architecture on blood plasma VWF and fibrinogen

Platelet adhesion and aggregation is critically driven by the shear dependent binding and unfolding of plasma VWF and

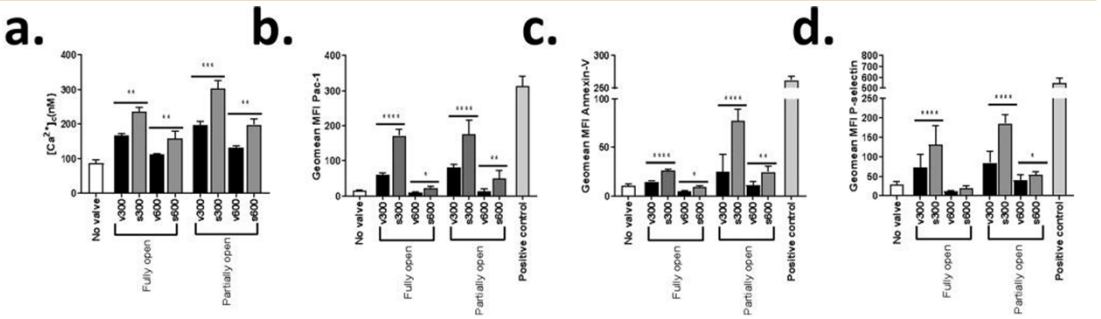

Fig. 4 Platelet activation in bulk flow as a function of microvalve geometry. a. Maximal platelet cytosolic calcium flux $[Ca^{2+}]_c$ (nm) under perfusion at Q = 24 µl min^{-1} in the fully open and partially open (40 µm) states (n = 3 independent experiments). b. Fluorescence activated cell sorting (FACS) analysis showing mean fluorescence intensity (MFI) geomean distribution of FIT-C PAC-1 antibody binding (integrin $\alpha_{IIb}\beta_3$ activation) to platelets in human whole blood following perfusion through V300, S300, V600 and S600 gates (Q = 24 µl min^{-1}) in the fully open and partially open (40 µm) states. c. FACS analysis showing MFI geomean distribution of FITC-annexin-v binding to platelets in human whole blood following perfusion through V300, S300, V600 and S600 gates (Q = 24 µl min^{-1}) in the fully open and partially open (40 µm) states. d. FACS analysis showing MFI geomean distribution of expression of P-selectin antibody binding to platelets in human whole blood following perfusion through V300, S300, V600 and S600 gates (Q = 24 µl min^{-1}) in the fully open and partially open (40 µm) states. All data indicates n = 3 independent experiments normalized to valve surface area. Error bars indicate standard deviation. Black horizontal bars indicate comparative valve shapes and sizes (*e.g.* V300 and S300) for which a significance significant difference was tested for using a paired t-test. * $p \leq 0.05$, ** $p \leq 0.01$, *** $p \leq 0.001$, **** $p \leq 0.0001$.

the surface immobilisation of fibrinogen.[42] To investigate the effect of valve design on plasma VWF and fibrinogen, valve test manifolds were perfused with whole blood or platelet poor plasma (PPP) and VWF or fibrinogen concentration in the flow-through assessed pre- and post-perfusion. Fig. 5a demonstrates that perfusate VWF antigen loss directly correlated with valve gate size, such that the 300 μm valves show the highest levels of loss. Head-to-head comparison of straight versus v-shaped valves demonstrated that straight valve designs led to significantly more VWF loss than v-shaped (Fig. 5a). VWF multimer analysis demonstrated no preferential loss of higher molecular weight multimers (data not shown). PPP experiments demonstrated that VWF loss was not dependent on the presence or absence of platelets or erythrocytes (Fig. 5a). Fig. 5b demonstrates that while perfusate fibrinogen loss did not correlate with valve gate size, loss was significantly greater (~2-fold) for straight valve geometries in comparison to v-gate. Treatment of the valve test manifolds with BSA to block the PDMS surface completely blocked both VWF antigen and fibrinogen loss demonstrating that both are driven by competitive surface physisorption mechanisms (Fig. 5a and b).

Effect of valve architecture on erythrocyte handling

Erythrocyte (red blood cell — RBC) stability in the context of microfluidic systems is critical, particularly where platelet assays are concerned, due to the propensity of RBC's to secrete potent platelet activators such as ADP and ATP upon mechanical activation and haemolysis. Subtle changes in RBC $[Ca^{2+}]_c$ and PS exposure have been demonstrated to correlate with increasing RBC mechanical fragility and overall reduction in RBC deformability.[43] To investigate the overall mechanical stability of RBCs as a function of valve design, isolated RBC at a Hct = 40% were perfused through the test manifolds and haemolysis assessed for an actuation duty cycle of 1 Hz over 200 s. Fig. 6a demonstrates that the straight valve design shows poorer RBC mechanical handling, while v-shaped designs demonstrated no increase in haemolysis over no-valve controls. Increasing the overall size of the straight valve case completely eliminated valve-dependent haemolysis (Fig. 6a). RBC echinocyte formation was inversely correlated with valve size, with v-shaped valves displaying less echinocyte formation in comparison to straight valves (Fig. 6b). Fig. 6c demonstrates a marginal but significant increase in RBC $[Ca^{2+}]c$ that was gate-size dependent, with the S300 valve in the 40 μm open state showing a significant increase in RBC $[Ca^{2+}]_c$ in comparison to the V300 case. Measurement of correlated RBC PS exposure demonstrated RBC procoagulant function is dependent on valve geometry and size, with the S300 gate at 40 μm opening showing a significant increase in RBC PS expression (Fig. 6d). Taken together this data demonstrates that RBC mechanical stability and activation status is sensitive to valve gate architecture and overall valve size; significantly v-shaped valves were superior across the tested size range.

Valve geometry effects predicted blood shear rate exposure

Previously published studies from our laboratories and others demonstrate that shear rate (both peak shear rate and potentially shear rate gradients) significantly affect blood platelet function and VWF structure, particularly at microfluidic step geometries.[31–33] Based on our blood assay findings we therefore hypothesised that shear rate magnitude (both at the wall and bulk flow) and/or shear rate gradients may play a role in determining the observed effects on blood function. To examine this hypothesis while isolating the variables of microvalve geometry from opening height we conducted a series of computational fluid dynamic (CFD) simulations in which gate-opening height was fixed at 40 μm. Valve mesh generation for CFD was derived from simplified 3-dimensional reconstructions of confocal imaging data (see

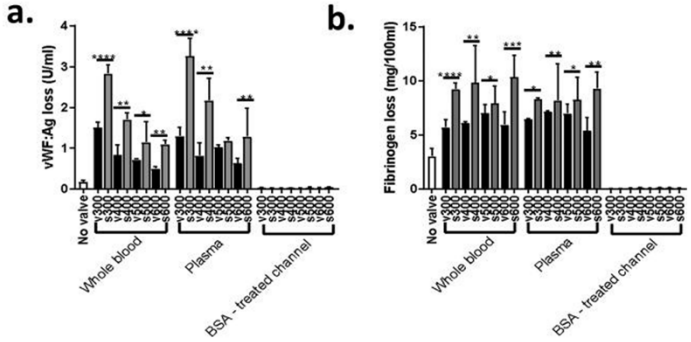

Fig. 5 Plasma protein physisorption and composition as a function of microvalve geometry. a. VWF antigen activity loss (μ ml^{-1}) in whole blood and PPP samples following perfusion through valve manifolds at 24 μl min^{-1}, compared to no-valve control. b. Plasma fibrinogen loss (mg/100 ml) in whole blood and PPP samples following perfusion through the valve manifolds at 24 μl min^{-1}, compared to no-valve controls. All data indicates n = 3 independent experiments normalized to valve surface area. Error bars indicate standard deviation. Black horizontal bars indicate comparative valve shapes and sizes (e.g. V300 and S300) for which a significance significant difference was tested for using a paired t-test. * $p \leq 0.05$, ** $p \leq 0.01$, *** $p \leq 0.001$, **** $p \leq 0.0001$.

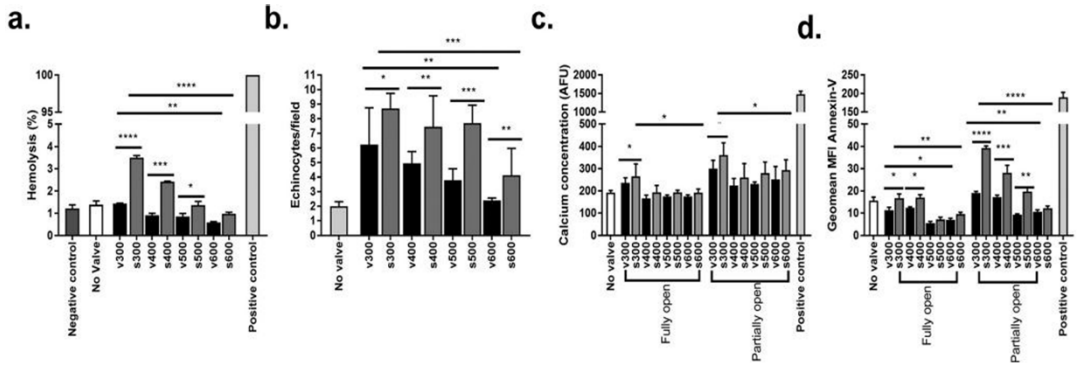

Fig. 6 Erythrocyte mechanical stability and activation as a function of microvalve geometry. a. Erythrocyte (RBC) hemolysis (% of lysed +ve control) for straight and v-shaped valve cases at an opening duty cycle of 1 Hz (Q = 24 µl min^{-1}). b. RBC echinocyte formation (total number of echinocytes per field) in blood films taken following isolated RBC (40% Hct) perfusion for V300, S300, V600 and S600 cases in the fully open state (Q = 24 µl min^{-1}). c. Maximal RBC cytosolic $[Ca^{2+}]_c$ (arbitrary fluorescence units — AFU) as a function of human whole blood perfusion through valve gates (Q = 24 µl min^{-1}) in full open and partially open (40 µm) states. d. FACS analysis showing MFI geomean distribution of FITC-annexin-v binding to isolated RBC (40% Hct) following perfusion through straight and v-gates (Q = 24 µl min^{-1}) in the fully open and partially open (40 µm) states. All data indicates n = 3 independent experiments normalized to valve surface area. Error bars indicate standard deviation. Black horizontal bars indicate comparative valve shapes (*e.g.* V300 and S300) for which a significance significant difference was tested for using a paired t-test. Longer error bars at the top of the figure indicate comparative valve sizes (e.g. V300 and V600) for which a significance significant difference was tested for using a paired t-test. * $p \leq 0.05$, ** $p \leq 0.01$, *** $p \leq 0.001$, **** $p \leq 0.0001$.

Methods) and was in part validated using µPIV (Fig. S1a–d†). CFD demonstrated that shear rate contours both at the microvalve gate walls but also within the cross-section of the gate are distinct for straight versus v-shaped valves (Fig. 7a and b and S6a and b†). High wall shear rates (wsr) were found to be distributed relatively uniformly (in the flow direction) across the S300 gate surface (wsr maxima >8750 s^{-1}) [Fig. 7a]. In contrast, v-shaped valves displayed a narrow band of high wsr (>10 000 s^{-1}) only at the upstream edge of the valve gate that rapidly reduced across the gate surface (Fig. 7b). In both cases wsr was reduced where the microvalve gates met the side walls (Fig. 7a and b). Examination of the shear rate contours in cross-section of the gate predicted a relatively larger region of reduced shear rate for the v-gate cases in comparison to straight (Fig. 7a and b insets), suggesting that blood components passing through this region of bulk flow will experience overall lower shear rate exposure at the v-gates in comparison to the straight valve geometry. CFD analysis of 600 µm valve cases showed a similar trend to that of the 300 µm cases but with a reduction in overall wsr and bulk flow shear rate magnitude (Fig. S6a and b†).

Valve geometry effects predicted platelet (particle) trajectories

To model the potential impact of gate geometry on individual platelet trajectories and shear rate exposure, we simulated the trajectories of 15 particles of 2 µm diameter (representative of 2 µm discoid platelets). These particles were released along discrete horizontal planes at incremental distances from the upstream microchannel wall, with particle 1 at the centreline and particle 15 at the lateral margin (Fig. 7c and d and S6c and d†). Analysis of particle trajectories across the gate geometries with particles released at planes of 40 µm and 3 µm from the gate ceiling suggested a rough equivalence of peak shear rate as a function of height for both straight and v-gate cases (Fig. 7c and d and S6c and d†). However, while trajectories were uniformly distributed across the straight gate at 40 and 3 µm release heights; with some trajectory convergence due to the arched open valve geometry, v-gate cases demonstrated marked divergence of trajectories across the gates at 40 µm and significant convergence at 3 µm (Fig. 7c and d and S6c and d†). This effect was predicted to initiate across the vertical upstream aspect of the v-gates (Fig. 7c and d and S6c and d†). High-speed epifluorescence imaging (see Methods) of platelet trajectories in whole blood (Q = 24 µL min^{-1}) at mid-plane (approximately 40 µm) from straight and v-shaped valves supported our CFD modelling results and demonstrated that in the presence of normal Hct, plasma, and cellular components discoid free-flowing platelets display marked divergence across the v-gate surface, in contrast platelet trajectories diverged downstream of the straight gate margin (Fig. 7e and f and S6e and f; Video S4†).

Our CFD modelling results, in conjunction with our platelet adhesion/aggregation experiments, led us to hypothesise that the v-gate geometry may alter platelet trajectories and shear rate exposure over time, increasing haemocompatibility by limiting both the duration of exposure to elevated shear rate and contact with the gate surface. To explore this hypothesis further we extrapolated platelet (particle) shear rates v time and platelet distribution as a function of z (distance

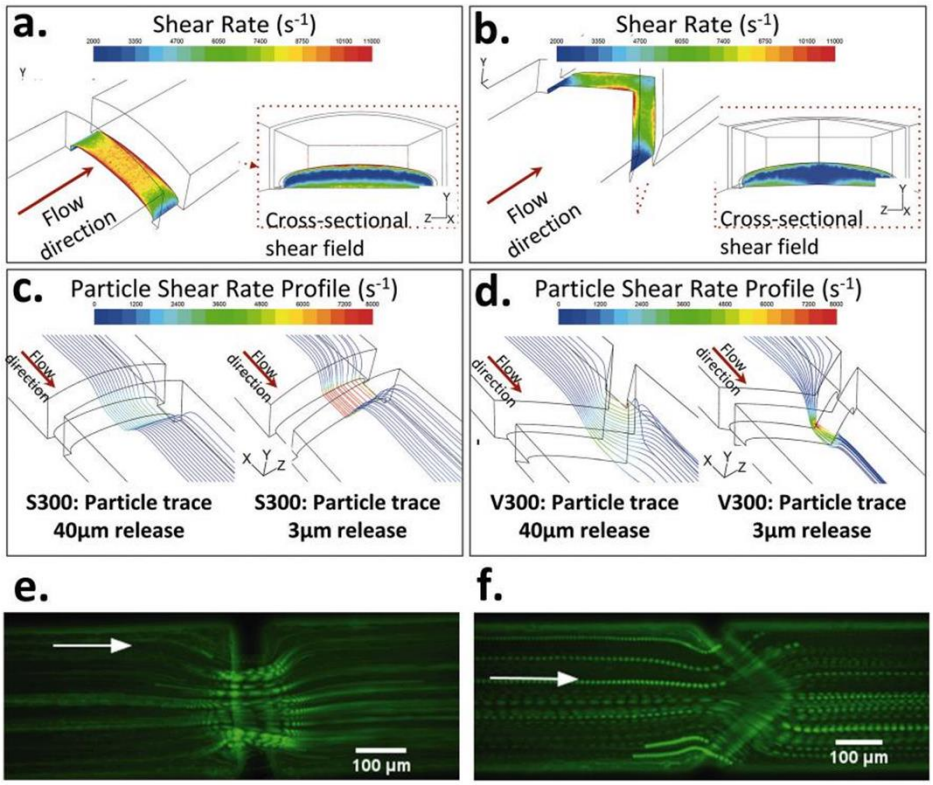

Fig. 7 Computational fluid dynamic (CFD) analyses of 300 µm straight versus v-gate geometries. a. 3-Dimensional shear contour profiles of S300 gate geometry at Q = 24 µl min^{-1} and opening height of 40 µm. Note the peaks in shear rate at the upstream and downstream edges of the straight gate and the overall elevation in shear rate across the straight gate surface. b. 3-Dimensional shear contour profiles of V300 gate geometry at Q = 24 µl min^{-1} and opening height of 40 µm. Note the initial peak in shear rate at the midline upstream face of the gate surface and overall reduced shear rates. Note the generation of a low shear rate pocket that extends across the microchannel cross-section. c. Particle shear rate for fifteen 2 µm particles released 40 µm and 3 µm from the microchannel ceiling for the straight gate case. Note the parallel particle trajectories across the gate surface. d. Particle shear rate for fifteen 2 µm particles released 40 µm and 3 µm from the microchannel ceiling for the v-gate case. Note the "funneling" for particles released at 3 µm towards the valve gate midline. Note the loss of funneling at 40 µm from the microchannel ceiling and divergent particle trajectories across the v-gate surface. e. Superimposed image of particle trajectories taken from 16 seconds of flow in partially open S300 valves. f. Superimposed image of particle trajectories taken from 16 seconds of flow in partially open V300 valves.

from the gate surface) for particles released 3 µm from the upstream microfluidic ceiling. Our modelling demonstrated that for two sample particles released (particle 1 at centreline—particle 15 at the lateral margin) the shear rate v time profiles in the straight gate case is relatively symmetric in the flow direction with shear rate peaks at the upstream and downstream edges of the gate surface (Fig. 8a and c and S7a and c†). In contrast, the v-gate cases demonstrated asymmetric shear rate v time profiles with rapid peaks at the upstream gate edge followed by a steady reduction in shear rate across the gate surface (Fig. 8b and d and S7b and d†). This difference was reflected in the shear gradient data (shear rate v time plots) (Fig. 8a—d and S7a—d†). Mapping of platelet aggregate distribution as a function of predicted gate wsr, for straight and v-gate cases, demonstrated a direct correspondence of overall platelet recruitment with shear rate distribution, with peak recruitment occurring towards the centreline for straight gate cases while translated laterally for v-gates (Fig. 8e and f and S7e and f).

To investigate the effect of gate geometry on particle trajectories in the z-plane (relative to the gate surface) we extrapolated particle trajectories from CFD analysis for equidistantly spaced particles released in a horizontal plane 3 um from the upstream channel ceiling. Fig. 8g and h demonstrate that for the v-gate cases, particles released 3 µm from the upstream ceiling are displaced between 3—8 µm from the v-gate surface while converging toward the v-gate apex in the x, y, while in the straight gate case particles were predicted to remain 3 µm from the gate surface, with minimal convergence. This indicates that the v-gate geometry may effect

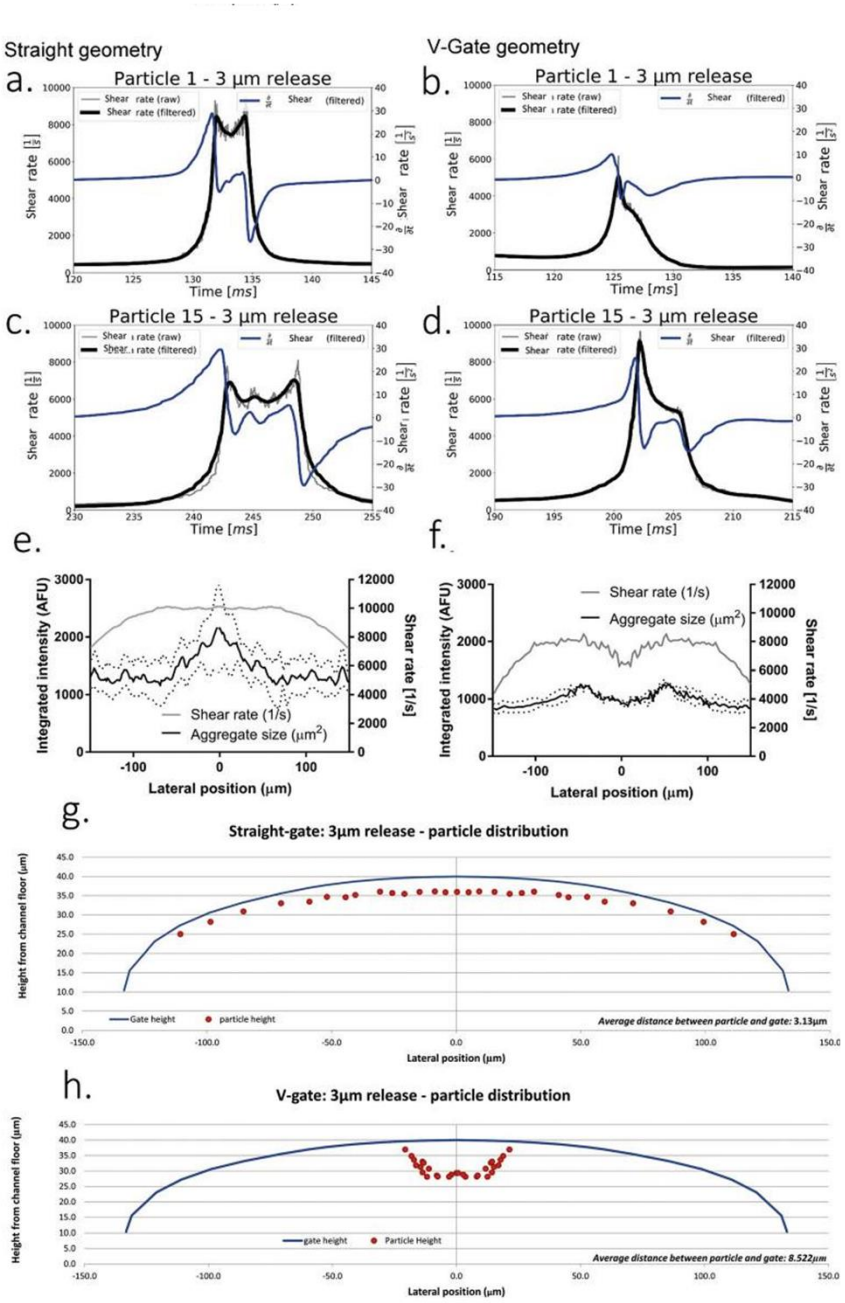

Fig. 8 Shear analyses of 300 µm straight versus v-gate geometries. a–d. Particle shear rate (s^{-1}) *v* time (black line) and shear rate gradient (s^{-1}/s) (blue line) plots for particles released 3 µm from the microchannel ceiling. Particle 1, released at the channel midlines is shown in the straight geometry (a) and v-gate (b), while particle 15, released at the lateral margin, close to the channel sidewall, is shown for the straight geometry in (c) and the v-gate in (d). Note the symmetric shear rate and shear rate gradient profiles for the straight case versus the asymmetric distribution and the overall reduction in peak shear rate for the v-gate. Particle 15 in both cases displayed extended shear profiles due to sidewall effects and the overall upward deformation of the valves in the open state. e and f. Plots of maximal platelet aggregation (black line) and wall shear rate (grey line) across the S300 partially open (40 µm) (e) and V300 partially open (f) as a function of distance from the valve midpoint. All data shows $n = 3$ independent experiments. Error bars indicate standard deviation. g and h. Cross sectional particle distribution for particles released 3 µm from the microchannel ceiling, plotting valve open height at a vertical cross-section along the centre of the valve gate (blue) and particle location at this given plane (red dots) for the v-gate (g) and straight valve geometry (h). Note the lateral convergence and vertical displacement away from the gate surface present in the v-gate case, while the straight geometry experiences only minor convergence and particles remain within 3 µm.

overall platelet distribution relative to the gate surface, and therefore the likelihood of platelet-gate surface interactions. Comparison of platelet aggregate distribution as a function of predicted z-position from the gate surfaces (Fig. 8e–h), for straight and v-gate cases, demonstrated an inverse correlation of overall aggregate position with z-displacement, with minimal aggregation occurring at the centreline apex where the predicted z-displacement was highest (Fig. 8e and f).

Discussion

Published findings from our laboratories and others demonstrate that initial platelet aggregation at both in vivo and in vitro stenosis geometries is initiated by local shear rate gradients and elevated wsr.[31–33] Based on these findings we hypothesised that micro-valve geometry with its impact on the local haemodynamic environment is a key factor contributing to microvalve haemocompatibility. Investigation of platelet surface aggregation and bulk flow activation following blood perfusion through straight and v-gate valve iterations demonstrated that v-shaped valves display less overall platelet activation and aggregation than straight valve architectures. We demonstrate that for either design, the degree of Ca^{2+} flux, α-granule secretion (P-selectin expression), integrin $\alpha_{IIb}\beta_3$ activation, PS exposure, and platelet aggregation are affected by the overall valve geometry. The consistent impact of valve geometry on a range of distinct platelet functional outputs suggests that valve geometry needs to be carefully considered with respect to downstream assay requirements, particularly where specific aspects of platelet function are under investigation.

Confocal imaging following 5 min of blood perfusion demonstrated that gate fouling was the result of consolidated platelet aggregate formation extending both up and downstream of gate surfaces (Video S3†). The propensity of valve gates to undergo fouling appeared to be initiated by, and highly dependent on, the rapid formation of discrete "platelet jets". (Video S3†). Imaging of early stage platelet aggregation at valve gate surfaces demonstrated that fouling initiated at the upstream margins of the gates where acceleration in shear rates were predicted. These observations correlate with previously published observations from our laboratories that have shown that microfluidic step geometries significantly modulate platelet aggregation through the generation of shear gradients that drive discoid platelet to platelet cohesion events.[33] The early stage "platelet jets" observed at valve gate surfaces appear to be composed of strings of tethered platelets reminiscent of observations made by our laboratories and others that have demonstrated that at elevated shear rates, or in the presence of significant shear rate gradients, platelet recruitment is driven by discrete discoid platelet membrane tethering, primarily driven by platelet GP1b/V/IX– VWF binding events and the high shear unfolding and self-association of VWF multimers.[26,32,44] While it is not possible to limit shear rate magnitude at operational gates due to flow restriction during valve closure (under constant pressure conditions), our current findings in conjunction with previously published observations lead us to posit that further modification of the overall shape of the upstream face of gate surfaces (shallower entry angles), changes in the surface profile of the bottom gate surface, and/or improved control of the rate of gate closure and thereby modification of the overall shear rate change, may further reduce or eliminate valve effects on blood platelet function. Exploration of these design concepts, while outside the scope of the current work, is under current investigation.

Our CFD modelling suggests a significant shift in the shear rate distribution across the v-gate surface in comparison to the straight valve case. Specifically, peak wsr was biased at the upstream edge of the v-gate apex; in contrast wsr maxima were distributed relatively uniformly across the straight gate surface. In addition our CFD modelling in conjunction with our platelet flow and adhesion/aggregation studies suggest that platelet path lines diverge across the v-gate surface towards regions of overall lower wsr. Furthermore, our CFD modelling suggests that for the v-gate case platelet trajectories may undergo displacement, away from the gate surface, by up to 2.5× the average discoid platelet diameter (3–8 μm from the gate surface) that may have the additional effect of limiting platelet to v-gate surface interactions during blood perfusion. This limitation on gate surface contact may be a key determinant of the increased haemocompatibility of the v-gate geometry as platelet aggregate formation, and therefore fouling, is critically dependent on the frequency and ability of platelets to interact with surface immobilised adhesive substrates.

Surface passivation through chemical modification or protein blocking of PDMS based microfluidics has been the "go to" method to limit blood dependent fouling. Physisorption of serum albumin, Pluronic block copolymers, or more sophisticated PEGylation and silanization techniques have been used to limit fouling,[45,46] however the efficacy of these approaches is application specific.[47,48] A key limitation of physisorption based blocking techniques is the relatively labile nature of these surface modifications limiting both device reliability and shelf life. Furthermore, while bulk protein physisorption methods may limit some blood-surface interactions in microfluidic systems, surface exchange of protein species such as fibrinogen (the Vroman effect) is still possible, dependent on perfusion rates and exposure times.[23] A chief aim of the present study was therefore to identify a microvalve design that minimises the requirements for surface modification steps (pre-fouling) to achieve haemocompatibility. Our experimental findings in combination with CFD modelling suggest that the haemodynamic profile of valve surfaces may be a significant contributor to both plasma protein adsorption and platelet surface interactions. By controlling both valve gate haemodynamics and therefore surface binding events it may be possible to develop microfluidic blood-handling systems that do not require surface passivation, greatly simplifying the number of device dependent steps and fabrication processes, and improving device shelf life.

Haematology based assays in the microfluidic context require a diverse range of flow rates dependent on assay requirements ranging from rates as low as <1 μl min^{-1} to several ml h^{-1}.[49–54] In the context of devices that require complex switching control, rapid blood sample delivery and flow rates have the potential to minimise sample handling times and increase assay throughput. Relatively high flow rates become increasingly important where relatively high shear rates are required for test development, such as platelet functional assays.[55] In combination with our previously published findings, our data support the concept that upstream microvalved blood handling systems be designed in such a way that they minimise both the overall applied shear rate (at a given flow rate), but also seek to eliminate acute changes in shear rate within valved components.[31] We posit that this may be of particular relevance during microvalve actuation, where dynamically changing valve-gate geometry and therefore haemodynamic profile may significantly impact blood function. In particular, the haemodynamic profile of valve gates under conditions of partial actuation or during opening-closing cycles where gates may transiently project into blood flow is a key consideration. The ability of valve gates to completely clear the microfluidic channel in the fully open state is particularly critical, given our findings that microvalves below a size cut-off of 400 μm^2 may obstruct up to 55% of microchannel height, leading to significant effects on the haemodynamic profile and platelet function, irrespective of gate geometry. This concept is supported by our findings that at a fixed clearance height of 40 μm, where shear rate gradients are acute, all valve types were found to elicit increased levels of platelet aggregation and activation. Critically, valves in the size range from 300–500 μm at a partial opening height of 40 μm experienced complete occlusion over a 200 s time frame, demonstrating that dynamic changes in valve haemodynamics may play a critical role in microfluidic fouling. This may be compounded by the duty cycle of valve opening with repeated closure leading to increased blood sample modification due to the repeated application of transiently high shear rates.

Erythrocytes (RBC) may be damaged during flow in non-physiological environments and under extreme shear stress, such as that generated within microfluidic systems. Shear-induced damage of RBC may result in haemolysis, echinocyte formation (morphology change), or in altered mechanical properties of RBC that in turn reduce their ability to withstand further damage by shear stress.[56,57] Significantly, subthreshold shear stress that is applied over multiple cycles has been shown to have a cumulative effect on RBC mechanical stability.[58] RBC mechanical stability (haemolysis) and morphology (echinocyte formation) were significantly impacted by valve size and geometry at a duty cycle of 1 Hz. Significantly, v-shaped valves across the tested size range showed no RBC haemolysis above no-valve controls, while for straight valve designs haemolysis correlated inversely with valve size at a duty cycle of 1 Hz. The echinocyte data suggest that RBC deformability and membrane elasticity are significantly influenced by valve geometry. Decrease in RBC deformability, changes of cell volume, increased cellular rigidity, increased levels of haemolysis, and changes in plasma membrane structure, such as phosphatidyl serine exposure correlate with increases in RBC $[Ca^{2+}]_c$.[43,59] Both RBC $[Ca^{2+}]_c$ and PS exposure showed a generalised inverse trend with respect to valve size and geometry. The marginal increase in PS, while not statistically significant, may be problematic where blood coagulant function (contact activation) is a consideration, particularly under conditions where blood samples have not been adequately anti-coagulated. Our findings suggest that a v-shaped valve design is superior as a single pass device, with respect to RBC handling, but may also represent a suitable design for serial valve systems, such as micropumps, where RBC's may experience repeated exposure to elevated shear rates.

A key limitation of this study is the use of an idealised CFD model to describe a complex elastomeric microvalve system and dynamic blood flow effects. The CFD mesh was derived from confocal imaging of operational valves (free of platelet aggregates) in both the partially and fully open (static) states and CFD then carried out on these fixed states. However, it should be noted that this CFD modelling approach is limited by the overall resolution limits of the confocal system and does not account for transient or dynamic deformations of the elastomeric valves during actuation. Furthermore, the CFD modelling carried out in this study does not consider dynamic changes in valve geometry as a result of platelet binding and aggregation events. It is undoubtedly the case that platelet aggregation will feedback on local haemodynamics and modify both peak shear rates and shear rate gradients that are imposed on blood flow. These limitations highlight the critical need for more complex and dynamic non-Newtonian and mechanical CFD models to more accurately inform blood handling microfluidic development in the future. Our interpretation of the overall haemodynamics of valve iterations and the effects on blood interactions therefore need to be qualified with these limitations in mind. Secondly, while we have endeavoured to incorporate a battery of blood based functional assessments to characterise valve performance these assays by no means address all of the complex blood functions that may be important for haemocompatibility. In this context, functional outputs to a large degree need to take into consideration the flow rate requirements of the specific downstream assay in use. Indeed, the flow rate range utilised across the blood based microfluidic literature demonstrates the diversity in possible assay conditions. Therefore the limitations of the present study need to be considered in this broader context.

Conclusion

In conclusion, we demonstrate a hierarchy of elastomeric microvalve design that demonstrates that v-shaped valves display the highest degree of haemocompatibility. Significantly, this valve geometry minimises the requirements for surface

chemical modification to reduce biofouling. Taken together with previously published studies examining the impact of shear rate and shear rate gradients on platelet and blood function, this study highlights the importance of considering the overall haemodynamic profile of microfluidic components when designing blood-handling systems. We believe that the approach defined in this study is a step toward rational, biologically focused, blood handling microfluidic design, with the potential to be extended to a range of microfluidic components.

Author contribution

The manuscript was written through contributions of all authors. All authors have given approval to the final version of the manuscript. CS designed, fabricated, and ran mechanical testing of the microfluidic device and co-wrote the manuscript. RJB carried out biological experiments and co-wrote the manuscript. KK developed and ran the CFD simulations. FA developed and ran the UPIV experiments. MK developed and built the ancillary valve drivers and carried out mechanical testing. PT contributed to the design of the test manifolds. IM carried out VWF experiments and multimer analysis. IM developed the UPIV experiments and imaging system. HN contributed to biological experimental design. AM designed the microfluidic device and fabrication methods and contributed to experimental design. WSN developed the experimental design, supervised the study and wrote the manuscript.

Conflicts of interest

There are no conflicts to declare.

Acknowledgements

We would like to acknowledge Robert Andrews, Justin Hamilton, and Elizabeth Gardner for helpful discussions and technical advice. We thank the staff and students at the Australian Centre for Blood Diseases for help with blood collection. The authors acknowledge the facilities and expertise of Monash Micro Imaging (MMI), Monash University, CSL Ltd, The Department of Clinical Haematology – Alfred Hospital, and Monash Statistical Services Alfred Hospital. Devices were fabricated at the Micro Nano Research Facility (MNRF) – RMIT University. CS is a recipient of a Professor Robert and Josephine Shanks Scholarship. RJB is a recipient of an Australian Research Training Program Scholarship. WSN is a recipient of an RMIT Vice Chancellor's Senior Research Fellowship.

Notes and references

1 C. Rivet, H. Lee, A. Hirsch, S. Hamilton and H. Lu, *Chem. Eng. Sci.*, 2011, **66**, 1490-1507.
2 B. Weigl, G. Domingo, P. Labarre and J. Gerlach, *Lab Chip*, 2008, **8**, 1999-2014.
3 C. Briggs, S. Kimber and L. Green, Br. *J. Haematol.*, 2012, **158**, 679-690.
4 S. K. Vashist, P. B. Luppa, L. Y. Yeo, A. Ozcan and J. H. T. Luong, *Trends Biotechnol.*, 2015, **33**, 692-705.
5 Y. Song, Y.-Y. Huang, X. Liu, X. Zhang, M. Ferrari and L. Qin, *Trends Biotechnol.*, 2014, **32**, 132-139.
6 W. Van Oeveren, *Scientifica*, 2013, **1**, 392584.
7 R. J. Gilbert, H. Park, M. Rasponi, A. Redaelli, B. Gellman, K. A. Dasse and T. Thorsen, *ASAIO J.*, 2007, **53**, 447-455.
8 L. Tingjie, Z. Limin, L. Kar Man and Y. Jun, *J. Micromech. Microeng.*, 2010, **20**, 105024.
9 B. S. Lee, J. N. Lee, J. M. Park, J. G. Lee, S. Kim, Y. K. Cho and C. Ko, *Lab Chip*, 2009, **9**, 1548-1555.
10 C. G. Conant, M. A. Schwartz, T. Nevill and C. Ionescu-Zanetti, *J. Visualized Exp.*, 2009, **1644**.
11 K. Miura and S. Shoji, *in Micro Total Analysis Systems '98: Proceedings of the uTAS '98 Workshop*, held in Banff, Canada, 13-16 October 1998, ed. D. J. Harrison and A. van den Berg, Springer Netherlands, Dordrecht, 1998, pp. 85-88, DOI: 10.1007/978-94-011-5286-0_20.
12 H. Takao, K. Miyamura, H. Ebi, M. Ashiki, K. Sawada and M. Ishida, *Sens. Actuators*, A, 2005, **119**, 468-475.
13 Y. Oimatsu, K. Kaikita, M. Ishii, T. Mitsuse, M. Ito, Y. Arima, D. Sueta, A. Takahashi, S. Iwashita, E. Yamamoto, S. Kojima, S. Hokimoto and K. Tsujita, *J. Am. Heart Assoc.*, 2017, **6**, e005263.
14 H. Takao, K. Miyamura, H. Ebi, M. Ashiki, K. Sawada and M. Ishida, *Sens. Actuators*, A, 2005, **119**, 468-475.
15 L.-C. Xu, J. W. Bauer and C. A. Siedlecki, *Colloids Surf., B*, 2014, **124**, 49-68.
16 Y. Jun Kang and S.-J. Lee, *Biomicrofluidics*, 2013, **7**, 054122.
17 Y. J. Kang, S. Y. Yoon, K. H. Lee and S. Yang, *Artif. Organs*, 2010, **34**, 944-949.
18 K. Broos, S. F. De Meyer, H. B. Feys, K. Vanhoorelbeke and H. Deckmyn, *Thromb. Res.*, 2012, **129**, 245-249.
19 W. Ouyang, W. Wei, X. Cheng, X. F. Zhang, E. B. Webb Iii and A. Oztekin, *J. Non-Newtonian Fluid Mech.*, 2015, **217**, 58-67.
20 S. W. Schneider, S. Nuschele, A. Wixforth, C. Gorzelanny, A. Alexander-Katz, R. R. Netz and M. F. Schneider, *Proc. Natl. Acad. Sci. U. S. A.*, 2007, **104**, 7899-7903.
21 C. E. Sing and A. Alexander-Katz, *Biophys. J.*, 2010, **98**, L35-L37.
22 A. L. Fogelson and K. B. Neeves, *Annu. Rev. Fluid Mech.*, 2015, **47**, 377-403.
23 S. L. Hirsh, D. R. McKenzie, N. J. Nosworthy, J. A. Denman, O. U. Sezerman and M. M. M. Bilek, *Colloids Surf., B*, 2013, **103**, 395-404.
24 M. Zhang and T. A. Horbett, *J. Biomed. Mater. Res., Part A*, 2009, **89**, 791-803.
25 L. D. Casa, D. H. Deaton and D. N. Ku, J. *Vasc. Surg.*, 2015, **61**, 1068-1080.
26 S. M. Dopheide, M. J. Maxwell and S. P. Jackson, *Blood*, 2002, **99**, 159-167.
27 D. Varga-Szabo, I. Pleines and B. Nieswandt, *Arterioscler., Thromb.*, Vasc. Biol., 2008, **28**, 403-412.
28 T. A. Springer, *Blood*, 2014, **124**, 1412-1425.
29 T. V. Colace, G. W. Tormoen, O. J. McCarty and S. L. Diamond, *Annu. Rev. Biomed. Eng.*, 2013, **15**, 283-303.
30 H.-J. Choo, T. B. Saafir, L. Mkumba, M. B. Wagner and S. M. Jobe, *Arterioscler., Thromb., Vasc. Biol.*, 2012, 32, 2946-2955.

31 R. J. Brazilek, F. J. Tovar-Lopez, A. K. T. Wong, H. Tran, A. S. Davis, J. D. McFadyen, Z. Kaplan, S. Chunilal, S. P. Jackson, H. Nandurkar, A. Mitchell and W. S. Nesbitt, *Lab Chip*, 2017, **17**, 2595-2608.

32 W. S. Nesbitt, E. Westein, F. J. Tovar-Lopez, E. Tolouei, A. Mitchell, J. Fu, J. Carberry, A. Fouras and S. P. Jackson, *Nat. Med.*, 2009, **15**, 665-673.

33 F. J. Tovar-Lopez, G. Rosengarten, E. Westein, K. Khoshmanesh, S. P. Jackson, A. Mitchell and W. S. Nesbitt, *Lab Chip*, 2010, **10**, 291-302.

34 A. K. Au, H. Lai, B. R. Utela and A. Folch, *Micromachines*, 2011, **2**, 179-220.

35 R. Mohan, B. R. Schudel, A. V. Desai, J. D. Yearsley, C. A. Apblett and P. J. A. Kenis, *Sens. Actuators, B*, 2011, **160**, 1216-1223.

36 J. Kim, M. Kang, E. C. Jensen and R. A. Mathies, *Anal. Chem.*, 2012, **84**, 2067-2071.

37 H. Kazuo and M. Ryutaro, *J. Micromech. Microeng.*, 2000, **10**, 415.

38 C. Szydzik, B. Niego, G. Dalzell, M. Knoerzer, F. Ball, W. S. Nesbitt, R. L. Medcalf, K. Khoshmanesh and A. Mitchell, *RSC Adv.*, 2016, **6**, 87988-87994.

39 S. S. Shibeshi and W. E. Collins, *Appl. Rheol.*, 2005, **15**, 398-405.

40 W. S. Nesbitt, I. S. Harper, S. M. Schoenwaelder, Y. Yuan and S. P. Jackson, in *Platelets and Megakaryocytes: Volume 3, Additional Protocols and Perspectives*, ed. J. M. Gibbins and M. P. Mahaut-Smith, Springer New York, New York, NY, 2012, pp. 73-89, DOI: 10.1007/978-1-61779-307-3_6.

41 W. S. Nesbitt, F. J. Tovar-Lopez, E. Westein, I. S. Harper and S. P. Jackson, *Methods Mol. Biol.*, 2013, **1046**, 39-58.

42 S. Gogia and S. Neelamegham, *Biorheology*, 2015, **52**, 319-335.

43 E. Meram, B. D. Yilmaz, C. Bas, N. Atac, O. Yalcin, H. J. Meiselman and O. K. Baskurt, *Biorheology*, 2013, **50**, 165-176.

44 M. J. Maxwell, E. Westein, W. S. Nesbitt, S. Giuliano, S. M. Dopheide and S. P. Jackson, *Blood*, 2007, **109**, 566-576.

45 L. Convert, V. Chabot, P.-J. Zermatten, R. Hamel, J.-P. Cloarec, R. Lecomte, V. Aimez and P. G. Charette, *Sens. Actuators, B*, 2012, **173**, 447-454.

46 S. Mukherjee, T. G. Kang, Y. Chen and S. Kim, *Crit. Rev. Biomed. Eng.*, 2009, **37**, 517-529.

47 B. Ziaie, A. Baldi, M. Lei, Y. Gu and R. A. Siegel, *Adv. Drug Delivery Rev.*, 2004, **56**, 145-172.

48 I. Wong and C.-M. Ho, *Microfluid. Nanofluid.*, 2009, **7**, 291.

49 S. Tripathi, Y. V. B. Kumar, A. Agrawal, A. Prabhakar and S. S. Joshi, *Sci. Rep.*, 2016, **6**, 26749.

50 V. VanDelinder and A. Groisman, *Anal. Chem.*, 2007, **79**, 2023-2030.

51 A. I. Rodríguez-Villarreal, M. Arundell, M. Carmona and J. Samitier, *Lab Chip*, 2010, **10**, 211-219.

52 R. D. Jäggi, R. Sandoz and C. S. Effenhauser, *Microfluid. Nanofluid.*, 2007, **3**, 47-53.

53 A. Kummrow, J. Theisen, M. Frankowski, A. Tuchscheerer, H. Yildirim, K. Brattke, M. Schmidt and J. Neukammer, *Lab Chip*, 2009, **9**, 972-981.

54 K. Loutherback, J. D'Silva, L. Liu, A. Wu, R. H. Austin and J. C. Sturm, *AIP Adv.*, 2012, **2**, 042107.

55 W. S. Nesbitt, E. Westein, F. J. Tovar-Lopez, E. Tolouei, A. Mitchell, J. Fu, J. Carberry, A. Fouras and S. P. Jackson, *Nat. Med.*, 2009, **15**, 665-673.

56 M. Kersaudy-Kerhoas and E. Sollier, *Lab Chip*, 2013, **13**, 3323-3346.

57 C. Szydzik, K. Khoshmanesh, A. Mitchell and C. Karnutsch, *Biomicrofluidics*, 2015, **9**, 064120.

58 M. Diez-Silva, M. Dao, J. Han, C.-T. Lim and S. Suresh, *MRS Bull.*, 2010, **35**, 382-388.

59 M. C. Wesseling, L. Wagner-Britz, F. Boukhdoud, S. Asanidze, D. B. Nguyen, L. Kaestner and I. Bernhardt, *Cell. Physiol. Biochem.*, 2016, **38**, 2414-2425.

3.4 – 'Elastomeric microvalve geometry affects haemocompatibility' - supplemental information

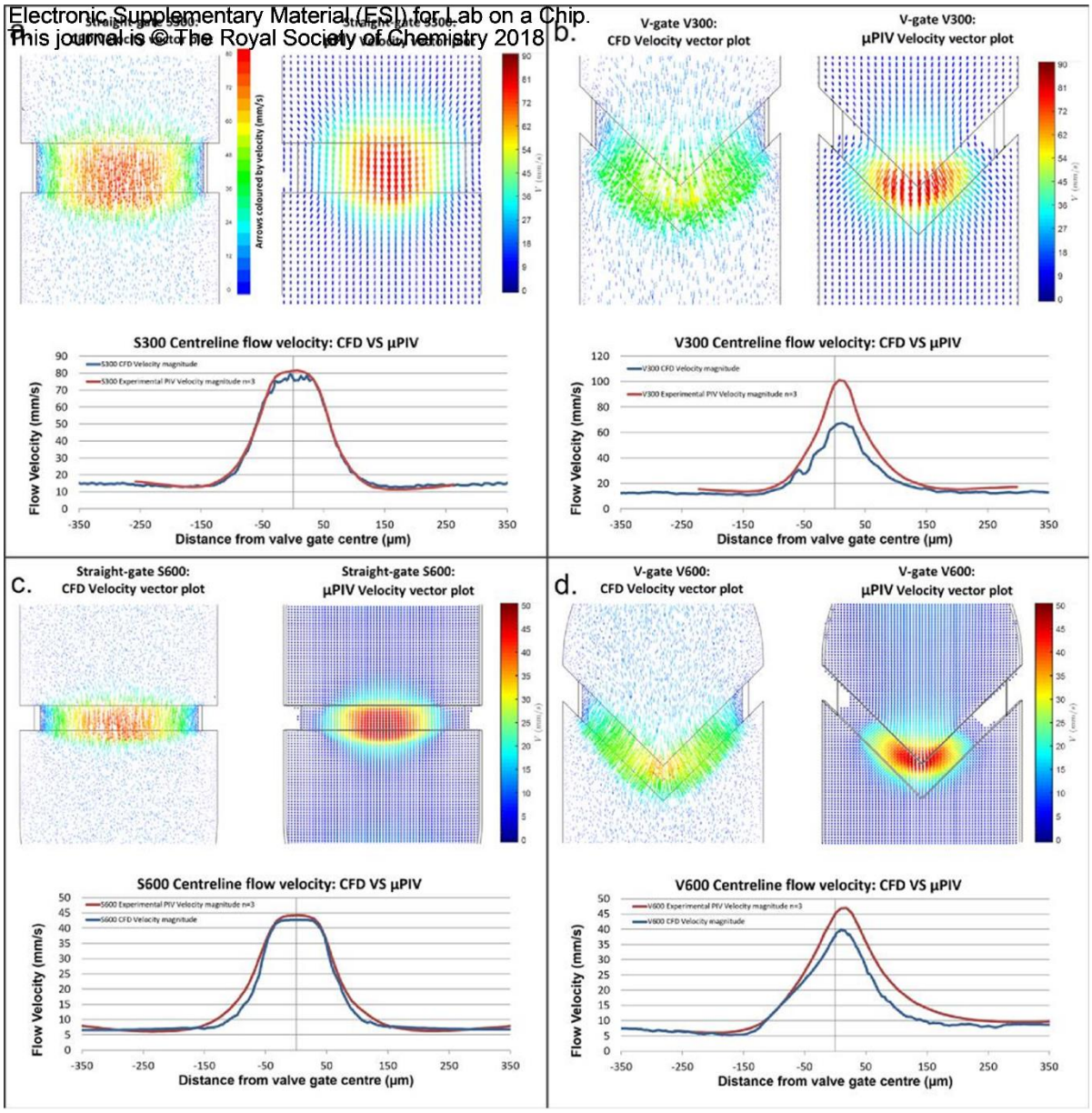

Supp fig 1 a. Direct comparison between velocity fields derived through computational fluid dynamic simulations (CFD), and corresponding experimental micro particle image velocimetry (µPIV) results, shown for 300µm straight **(a)** and v-shaped **(b)** valve gates and 600µm straight **(c)** and v-shaped **(d)**. This data is shown as velocity vectors with arrows scaled in size and coloured by magnitude, as well as centreline velocity plots superimposing longitudinal velocity along the centreline of the channel for both CFD and µPIV data. All data presented is representative of valves open to a height of 40µm at the centre of the valve gate, at Q=24 µl/min, with data shown for a central plane taken at 20µm, halfway between the valve gate and channel floor. All CFD results shown in this figure are simulated for water, in order to match µPIV conditions. CFD data is shown to match well to experimental results, with slight discrepancies most likely due to variances in individual valve actuation heights, potentially due to differing levels of delamination at the valve gate at low actuation pressures. Note the significant lateral component to fluid passing under V-shaped gates in b and d, as opposed to the relatively straight flow in a and c.

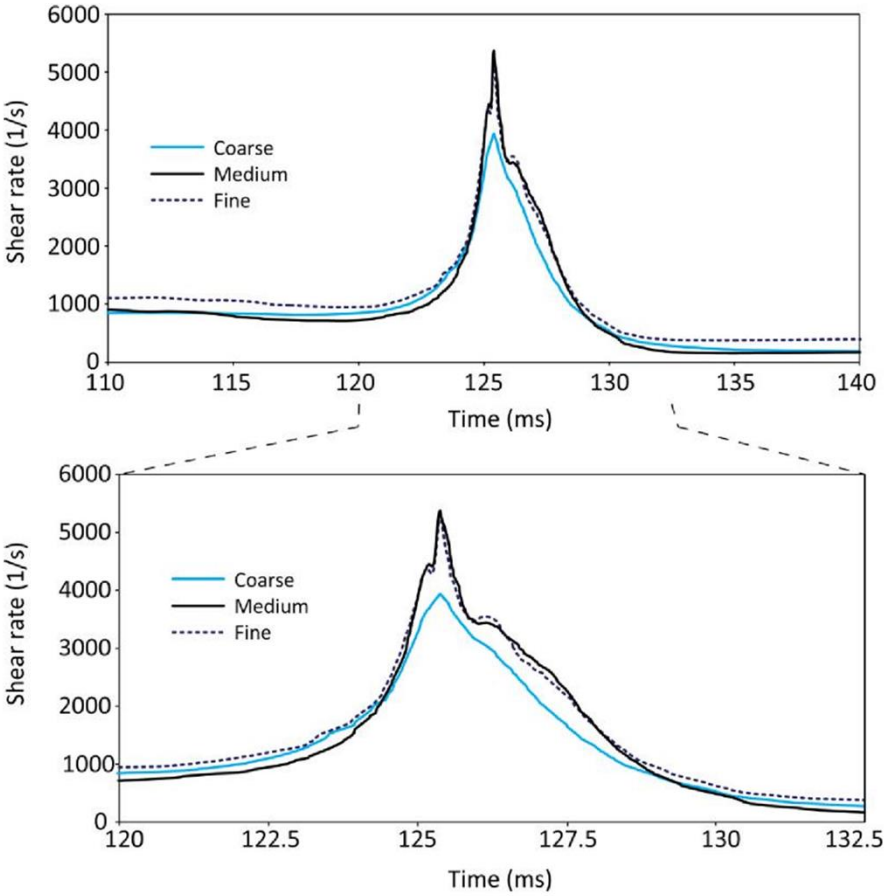

Supp fig 2. Grid convergence analysis of V-shaped gate, shear rate *v* time for a particle released 3 µm from the upstream of the V-300 gate and travelling along the middle of the gate. Simulations were conducted using three mesh densities, which are referred to as 'coarse', 'medium' and 'fine'. These mesh densities correspond to 90×15, 150×25, and 200×35 elements across the gate, respectively. A maximum shear rate of 3960 1/s was obtained using the 'coarse' mesh. Using the 'medium' mesh, the maximum shear rate increased to 5294 1/s. Applying the 'fine' mesh, the maximum shear rate only reduced to 5278 1/s with similar profiles observed before and after the gate, indicating grid convergence. Similar trends were obtained for the S300, S600 and V600 gates.

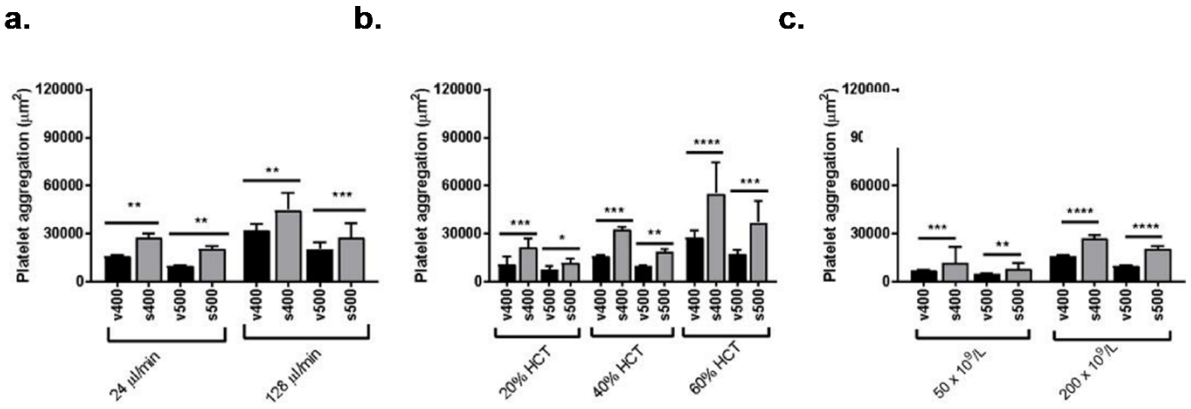

Supp fig 3 a. Platelet aggregation at straight versus v-gates at Q = 24 µl/min and 128 µl/min. **b.** Platelet aggregation at straight versus v-gates (Q = 24 µl/min) as a function of hematocrit. **c.** Platelet aggregation at straight versus v-gates (Q = 24 µl/min) as a function of platelet count. All data shows n=3 independent experiments normalized to valve surface area (µm^2). Error bars standard deviation. Black horizontal bars indicate comparative valve shapes and sizes (e.g. V300 and S300) for which a significance significant difference was tested for using a paired t-tests. * P ≤ 0.05, ** P ≤ 0.01, *** P ≤ 0.001, **** P ≤ 0.0001. * P ≤ 0.05, ** P ≤ 0.01, *** P ≤ 0.001, **** P ≤ 0.0001.

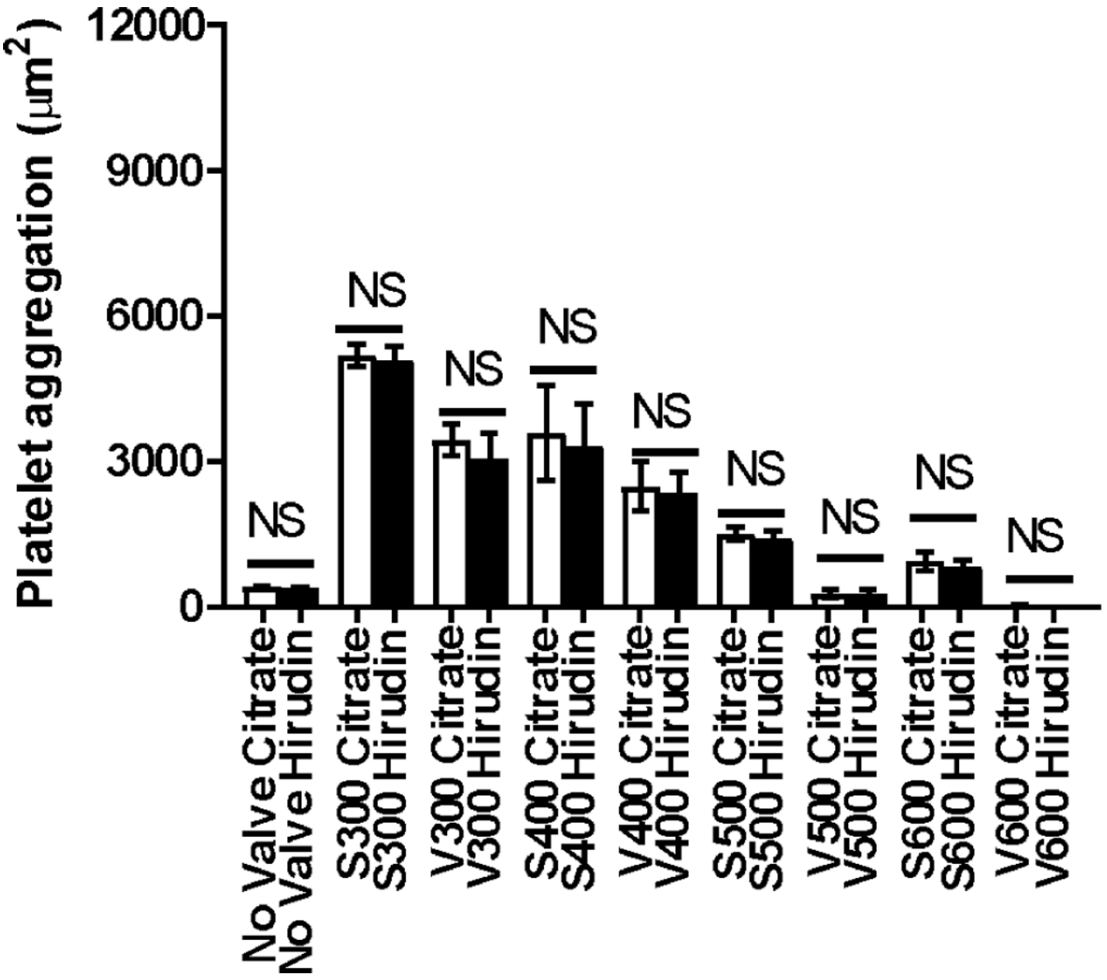

Supp fig 4 Comparison of aggregate sizes with blood collection into Hirudin (0.02% w/v) and Citrate (2% w/v) anticoagulants. Platelet aggregation was measured at Q = 24 µl/min and all valves were fully actuated. Data shows n=3 independent experiments normalized to valve surface area (μm^2). Error bars indicate standard deviation. Black horizontal bars indicate comparative valve shapes and sizes (e.g. V300 and S300) for which a significance significant difference was tested for using a paired t-tests. NS = no statistically significant difference, * $P \leq 0.05$, ** $P \leq 0.01$, *** $P \leq 0.001$, **** $P \leq 0.0001$.

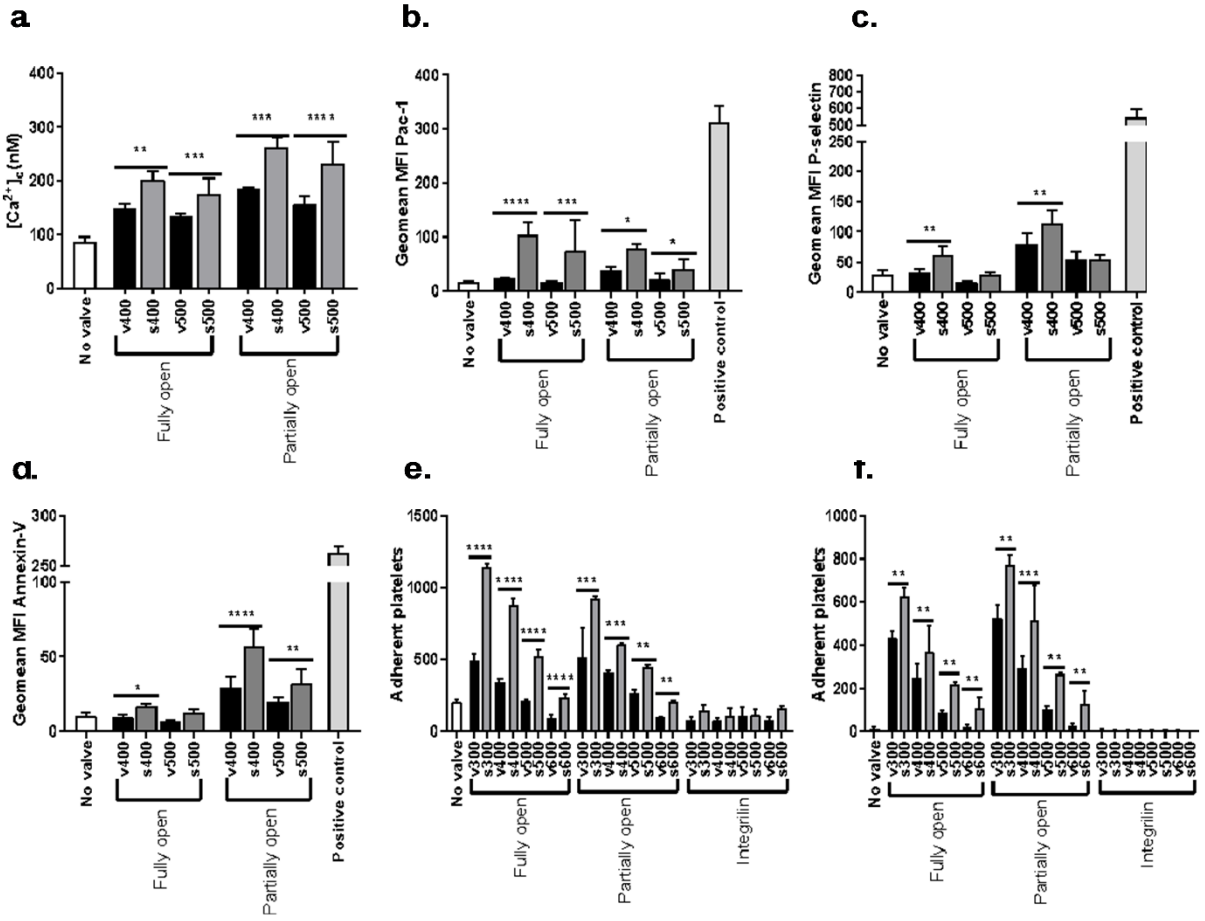

Supp fig 5 a. Maximal platelet cytosolic calcium flux $[Ca^{2+}]_c$ (nM) under perfusion at Q = 24 µl/min in the fully open and partially open (40 µm) states. (n=3 independent experiments). **b**. Fluorescence Activated Cell Sorting (FACS) analysis showing Mean Fluorescence Intensity (MFI) GeoMean distribution of FIT-C PAC-1 antibody binding (integrin $\alpha IIb\beta 3$ activation) to platelets in human whole blood following perfusion through S400, S500, V400 and V500 gates (Q = 24 µl/min) in the fully open and partially open (40 µm) states. **c**. FACS analysis showing MFI GeoMean distribution of expression of P-selectin antibody binding to platelets in human whole blood following perfusion through S400, S500, V400 and V500 gates (Q = 24 µl/min) in the fully open and partially open (40 µm) states. **d**. FACS analysis showing MFI GeoMean distribution of FITC- Annexin-V binding to platelets in human whole blood following perfusion through S400, S500, V400 and V500 gates (Q = 24 µl/min) in the fully open and partially open (40 µm) states. **e.** Total number of adherent (captured) platelets in a vWF-coated (10 µg/ml) microchannel 1,000 µm post valve passage at t=130 seconds following perfusion at a straight channel shear rate of 1,800.s^{-1}. **f.** Total number of adherent (captured) platelets in a fibrinogen-coated (13 µg/ml) microchannel 1,000 µm post valve passage at t=130 seconds following perfusion at a straight channel shear rate of 300.s^{-1}. All data indicates n=3 independent experiments normalized to valve surface area. Error bars indicate standard deviation. Black horizontal bars indicate comparative valve shapes and sizes (e.g. V300 and S300) for which a significance significant difference was tested for using a paired t-tests. * $P \leq 0.05$, ** $P \leq 0.01$, *** $P \leq 0.001$, **** $P \leq 0.0001$. * $P \leq 0.05$, ** $P \leq 0.01$, *** $P \leq 0.001$, **** $P \leq 0.0001$.

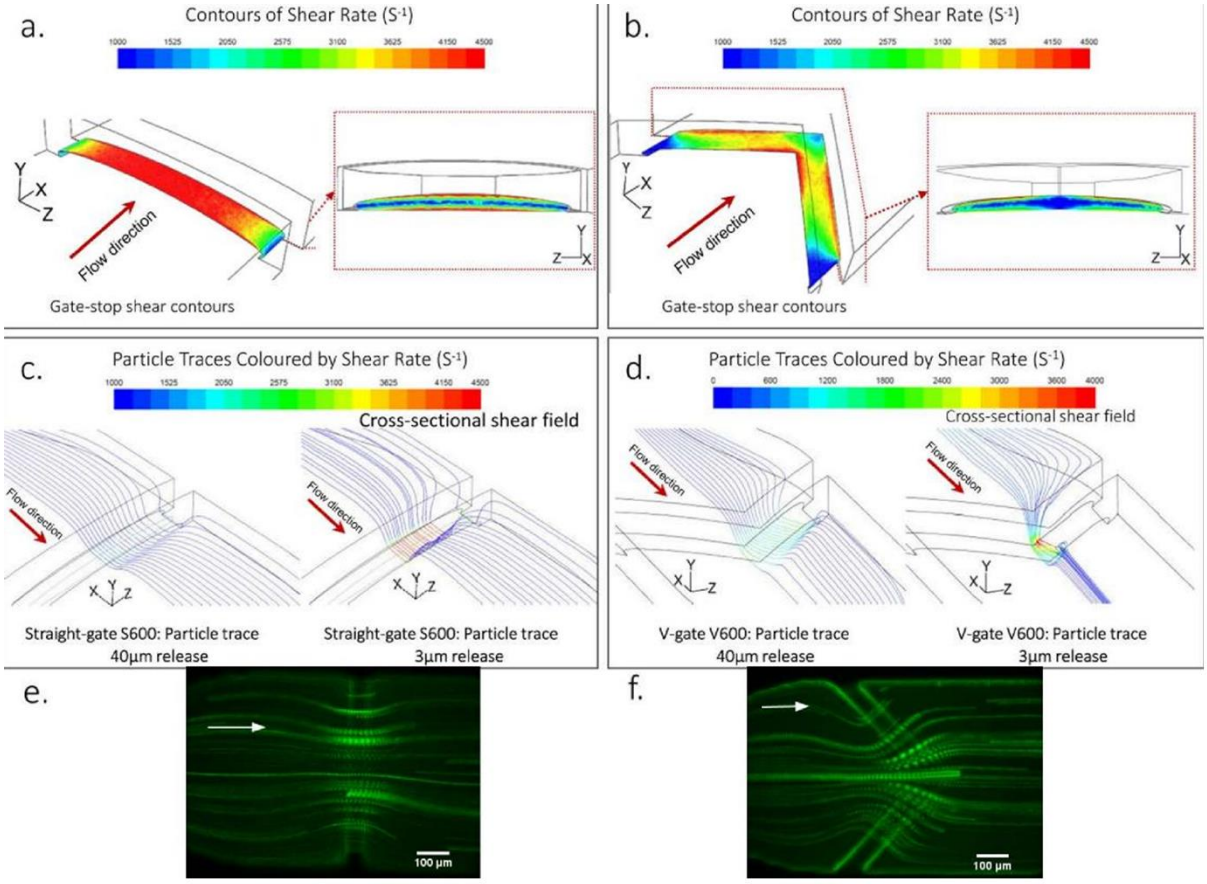

Supp fig 6. a. 3-dimensional shear contour profiles of S600 gate geometry at Q=24 ml/min and opening height of 40mm. Note the peaks in shear rate at the upstream and downstream edges of the straight gate and the overall elevation in shear rate across the straight gate surface. b. 3-dimensional shear contour profiles of V600 gate geometry at Q=24 ml/min and opening height of 40mm. Note the initial peak in shear rate at the midline upstream face of the gate surface and overall reduced shear rates. Note the generation of a low shear rate pocket that extends across the microchannel cross-section. c. Particle shear rate streamlines for fifteen 2mm particles released 40mm and 3mm from the microchannel ceiling for the straight gate case. Note the parallel particle trajectories across the gate surface. d. Particle shear rate streamlines for fifteen 2mm particles released 40mm and 3mm from the microchannel ceiling for the v-gate case. Note the streamline "funneling" for particles released at 3mm towards the valve gate midline. Note the loss of funneling at 40mm from the microchannel ceiling and divergent particle trajectories across the v-gate surface. e. Superimposed imaged of particle streamline flows taken from 16 seconds of flow in partially open S600 valves f. Superimposed imaged of particle streamline flows taken from 16 seconds of flow in partially open V600 valves.

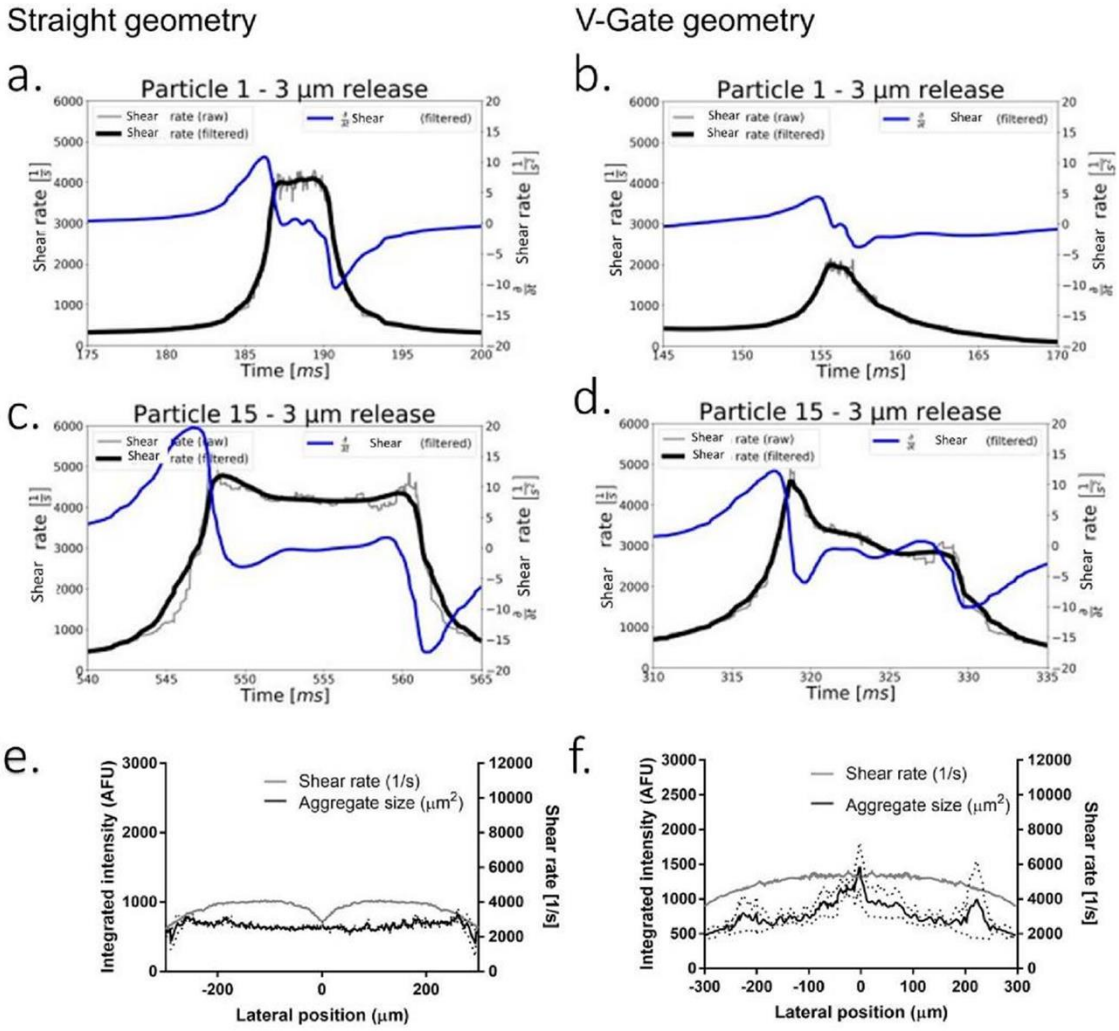

Supp fig 7 a-d. Particle shear rate (s^{-1}) v time (black line) and shear rate gradient (s^{-1}/s) (blue line) plots for particles released 3µm from the microchannel ceiling. Particle 1, released at the channel midlines is shown in the straight geometry (a) and v-gate (b), while particle 15, released at the lateral margin, close to the channel sidewall, is shown for the straight geometry in (c) and the v-gate in (d). Note the symmetric shear rate and shear rate gradient profiles for the straight case versus the asymmetric distribution and the overall reduction in peak shear rate for the v-gate. Particle 15 in both cases displayed extended shear profiles due to sidewall effects and the overall upward deformation of the valves in the open state. e-f. Points of maximal platelet aggregation and shear across the V600 partially open (40 µm) (e) and S600 partially open (f) as a function of distance from the valve midpoint. All data shows n=3 independent experiments. Error bars indicate standard deviation.

Valve Dimensions: V-600 Example case

Valve name	Valve gate geometry	Fluidic Channel height	Primary Channel width	Valve chamber width	Actuation chamber size	Actuation chamber Depth	Actuation membrane thickness	Valve Gate Thickness	Fully actuated Gate clearance	Opening area	Gate tip surface area: Closed	Gate tip surface area: Open
S 300	Straight	100 µm	300 µm	300 µm	500 X 500 µm	150 µm	30-50 µm	50 µm	44 µm	0.01184 mm^2	0.0135 mm^2	0.01599 mm^2
S 400	Straight	100 µm	300 µm	400 µm	600 X 600 µm	150 µm	30-50 µm	75 µm	73 µm	0.01932 mm^2	0.02877 mm^2	0.03207 mm^2
S 500	Straight	100 µm	300 µm	500 µm	700 X 700 µm	150 µm	30-50 µm	75 µm	107 µm	0.0363 mm^2	0.03609 mm^2	0.04228 mm^2
S 600	Straight	100 µm	300 µm	600 µm	800 X 800 µm	150 µm	30-50 µm	75 µm	124 µm	0.05171 mm^2	0.04288 mm^2	0.05006 mm^2
V 300	V - Gate	100 µm	300 µm	300 µm	500 X 500 µm	150 µm	30-50 µm	50 µm	52 µm	0.01398 mm^2	0.01856 mm^2	0.02183 mm^2
V 400	V - Gate	100 µm	300 µm	400 µm	600 X 600 µm	150 µm	30-50 µm	75 µm	86 µm	0.02496 mm^2	0.0485 mm^2	0.05539 mm^2
V 500	V -Gate	100 µm	300 µm	500 µm	700 X 700 µm	150 µm	30-50 µm	75 µm	118 µm	0.04072 mm^2	0.04871 mm^2	0.05508 mm^2
V 600	V -Gate	100 µm	300 µm	600 µm	800 X 800 µm	150 µm	30-50 µm	75 µm	133 µm	0.0642 mm^2	0.06013 mm^2	0.06775 mm^2

Supp table 1 Valve dimensions

Dimensions of valve geometries used in this study. Valve name is the name each valve type is referred to throughout the manuscript, valve gate geometry classifies the two types of valve investigated. Fluidic channel height is the height of the fluidic channels, while primary width is the width of the primary channel leading to the individual gates. Valve chamber width refers to the width of the expanded channel area at the valve gate, or length of the valve, while actuation chamber size defines the size of the pneumatic actuation chamber situated above each valve, and actuation chamber depth is the depth of this chamber. Actuation membrane thickness is the thickness of the PDMS membrane separating the valve channel roof and actuation chamber, gate thickness is the thickness of the gate itself. Fully actuated gate clearance refers to the opening height at the centre of the valve gate under minimum pressure, or fully open conditions, while opening area is the cross sectional area of the gate when fully open. Gate tip surface area when closed refers to the area of the valve gate in contact with the channel floor in the closed configuration, while gate tip surface area open refers to the area of the valve gate tip when fully expanded in the open configuration

Coefficients[a]

Model		Unstandardized Coefficients		Standardized Coefficients	t	Sig.
		B	Std. Error	Beta		
1	(Constant)	-22596.135	3484.757		-6.484	.000
	V_shaped_valve	28136.695	2530.866	.750	11.117	.000
	Straight_valve	39075.299	2530.866	1.041	15.439	.000
	Valve_size	-8202.348	542.401	-.563	-15.122	.000
	HCT	449.107	60.642	.229	7.406	.000
	Plt_count	11903.215	1855.466	.202	6.415	.000
	Flow_rate	13763.773	1855.466	.234	7.418	.000
	Open_state	31936.131	1961.298	.515	16.283	.000

a. Dependent Variable: Aggregate_size

Supp table 2 Multifactorial analysis

A multiple regression was run to predict aggregate size from valve geometry, size, patient Hct, platelet count, flow rate and open state. These variables statistically significantly predicted aggregate size, $F(7, 236) = 116.218$, $p < 0.0005$, $R2 = 0.780$. All six variables added statistically significantly to the prediction, $p < 0.0005$. The unstandardised coefficients demonstrate effect size.

Supplementary Materials & Methods

Micro particle image velocimetry (μPIV)

Micro-PIV was used to Verify and Support CFD models. Velocity field was assessed at measurement planes located halfway between the bottom surface of the channel and the tip of the valve stop. An inverted TI-U Eclipse Nikon microscope equipped with an air-immersion CFI S Plan Fluor ELWD 20× objective lens was coupled with a high-speed camera (2277 Hz at 2000 × 2000 pixels, 12 bits, PCO.dimax HS4) to record the particle images. One micron diameter red fluorescent polystyrene aqueous beads (ThermoFisher Scientific) were used to seed the flow. Polysorbate 20 (Tween 20) was added to flow to avoid particle-wall adhesion to and to prevent particle agglomeration. Illumination was provided by a 532 nm Nd:YAG double-pulsed laser (EverGreen - BigSky Laser Series) able to double-pulse at 15 Hz. A syringe pump (Harvard PHD ULTRA) and a gas-tight glass syringe (1000 μL, Hamilton) were used to deliver fluid into the microchannel via a silicon tube.

Measurements were taken at flow rates of 24 μL/hr in all channels with V-type and Straight-type valves at two different valve positions (fully opened and 40 μm open). In each set of measurements, 4000 images were captured. The common background noise in micro-PIV recordings were removed by subtracting the background image (acquired by averaging 100 images) from each recording. In micro- PIV usually low seeding density is used to reduce the background noise due to the out-of-focus particles, thereby reducing the signal to-noise ratio in correlation maps. Two averaging method ("Average Image Method" and "Average Velocity Methods") were employed to enhance the signal-to-noise. In the first method 20 images were overlaid to increase the number of particle per interrogation window (Average Image Method). Then a multigrid algorithm combined with window deformation algorithm with adaptive central difference interrogation (CDI) offsetting was implemented. Using a Fast Fourier Transform based cross-correlation algorithm, the local displacements correspond to each interrogation window (32×32) were acquired. The depth of correlation and the spatial resolution of the micro-PIV measurement were 7, 8 and 9 μm, respectively. The valid vectors of each realisation were identified using a median test and were then averaged over all realisation window (Average Velocity Method).

Assessment of platelet streamline flow

To image platelet streamlines across microvalve gate surfaces isolated platelet suspensions ($200x10^9$/L) in platelet washing buffer (4.3 mM K_2HPO_4, 4.3 mM Na_2HPO_4, 24.3 mM NaH_2PO_4, 113 mM NaCl, 5.5 mMD-glucose, and 10 mM theophylline, pH 6.5) + Integrillin (20mg/mL) were labelled with the lipophilic membrane dye DiOC6 (1μg/mL) (Molecular Probes) and 0.02U/mL apyrase (to eliminate released ADP during blood collection) for 10 min at 37°C and subsequently perfused through the device at constant flow rate of 24 μL/min. Fluorescent platelet streamlines were acquired on an inverted Nikon TiU microscope (Nikon Plan Fluor 20x/0.50 objective) using an Andor Zyla sCMOS camera at 10msec exposure time, 15fps for 60sec. Time-lapse tiff imaging stacks were processed to remove background fluorescence and filtered using a median filter (2x2 kernel). Tiff stacks were subsequently processed via average z-projection to create average heat map distributions of platelet trajectories using a 16-color LUT.

Chapter four: Design of elastomeric reciprocating micropumps

4.1 Introduction

In addition to development of a reliable fluidic isolation system, independent microfluidic systems require a system to induce fluid flow. On-chip microfluidic pumps can induce flow in a pulsatile or constant profile, including in cell-capture devices and plasma extractors.(1, 2) The literature has demonstrated a number of microfluidic pumps that have been utilised in blood-based devices, but few have demonstrated a comprehensive review of the impact of the pump on blood physiology. Chapter 3 indicated the importance of considering shear conditions and particle distribution in determining haemocompatibility. Previous studies have demonstrated that the “haemodynamic history” of platelets as they pass through a complex geometry significantly modulates platelet activation and aggregation. Modulation of the geometry of the distended membrane was therefore hypothesized to alter shear conditions and cellular activation. Taken together, the work demonstrated that platelet distribution must be mapped to shear conditions in the area to accurately predict activation. Micropump development was informed by the valve work to develop a pumping configuration that induced minimal shear while still maintaining a minimum flow rate, to prevent platelet platelet activation and impaired red cell integrity.

This chapter describes a proof-of-concept application of a pneumatically-actuated micropump design that demonstrates controllable hemocompatible on-chip blood handling. We demonstrate that factors affecting shear rate and overall flow dynamics significantly affect platelet and red blood cell handling. The following paper details the application of this knowledge in the development of a multiplexed micropump in the assessment of novel PI3-Kinase C2α inhibitors.

4.2 References

1. Haeberle S, Brenner T, Zengerle R, Ducree J. Centrifugal extraction of plasma from whole blood on a rotating disk. Lab Chip. 2006;6(6):776-81.

2. Furdui VI, Kariuki JK, Harrison DJ. Microfabricated electrolysis pump system for isolating rare cells in blood. Journal of Micromechanics and Microengineering. 2003;13(4):S164.

4.3 – 'A Scalable Micropump-reactor for Rapid Haemodynamically Controlled Platelet Function Testing'

Rose J. Brazilek[a], Crispin Szydzik[b*], Farzan Akbaridoust[c], Charitha de Silva[c], Markus Knoerzer[b], Leon Chan[c], Eric K. W. Poon[c], Andrew S. H. Ooi[c], Ivan Marusic[c], Justin R. Hamilton[a], Harshal H. Nandurkar[a], Arnan Mitchell[b], and Warwick S. Nesbitt[a,b*]*

This paper reports on the development and characterisation of a scalable haemodynamically controlled "micropump-reactor" for preclinical and clinical platelet function testing. Using a reciprocating elastomeric micropump architecture we take advantage of the flexible structural and actuation properties of this framework to manage the haemodynamics for on-chip platelet function testing. Using a battery of platelet function analyses in combination with haemodynamic analysis, we define the key mechanical parameters of micropump architecture, actuation pressure and duty cycle that affect haemocompatibility of the micropump-reactor design. Employing a system of modular parallel micropumps, we demonstrate that blood flow and shear rates can be incrementally scaled without effect on haemocompatibility. By harnessing the complex 3-dimensional haemodynamics of micropump operation in conjunction with a micro-valved reagent injection system we demonstrate a modular system that exhibits rapid reagent-to-blood mixing, allowing for the assessment of short time-scale anti-platelet drug pharmacokinetics under blood flow. In a proof-of-concept application we utilise this system to investigate the way in which dosing of human whole blood with isoform selective inhibitors of platelet Phosphatidylinositol 3-kinase modulate platelet thrombus dynamics. This modular system is a step toward the

development of new high-content systems for application in preclinical and clinical haematology screening and diagnostics.

Introduction

The International Society for Thrombosis & Haemostasis has highlighted the critical need for reliable blood-flow based platelet function tests (PFT) that can be used across the preclinical and clinical haematology settings.[1, 2] There is therefore a significant driver for effective analytical systems that facilitate the control of, and recapitulate the blood flow mechanics (haemodynamics) that are key to determining both physiological and pathological platelet function in thrombosis and haemostasis.[1-3] The ability to develop integrated, automated high-content haematology screening tools that incorporate hemodynamic control coupled to sensitive bioassays in whole blood is key to the wider development of more targeted anti-thrombotic and coagulation therapies, and more reliable clinical diagnostic systems.

Experimental flow-based assays have been extensively utilized to explore and define the shear dependent signalling (mechanotransduction) and adhesion mechanisms underlying platelet function, and have been utilized for the preclinical screening of new anti-platelet therapies.[4-10] These experimental assays have historically harnessed parallel plate or micro-capillary architectures.[4-9] A number of more recent microfluidic devices have been described for the assessment of the shear dependent activation processes underpinning platelet haemostatic function, and the hemodynamic dependencies of platelet thrombosis, with some of these applied in proof-of-

concept clinical applications.[11-22] While potentially useful, many of these microfluidic systems do not easily translate to high-throughput screening and require significant operator expertise and manual handling/setup steps as part of the typical workflow. To facilitate reliable high-content flow-based screening of platelet function there is a key requirement for integrated, scalable microfluidic lab-on-chip systems that are capable of handling large numbers of independent blood samples in combination with automated drug and reagent delivery. These systems should ideally incorporate the control interfaces necessary to deliver multiple blood samples with regulated haemodynamics, and to facilitate the titratable introduction (dilution series) of blood agonists and antagonists across replicate runs with a high degree of parallelization, automation, and reproducibility. Complex integrated microfluidic bioreactor systems have the potential to meet all of the requirements for low volume, rapid, automated blood and blood component manipulation, however the development of such platforms is in its infancy and significant research and development is required to actualize such systems in the clinical and preclinical haematology settings.[23]

A key bottleneck to the advancement of complex integrated blood bioreactor systems is the ability to manipulate small blood volumes (≤200 μL) over controllable and fast time-scales while minimizing the impact on blood composition and function. This requirement for “functional hemocompatibility” is particularly critical where platelet based assays are to be employed due to the acute sensitivity of these blood cells to micro-scale changes in shear rate and shear stress.[5, 24-28] Flow based PFT typically require the capacity to perfuse

blood samples at relatively high wall shear rates (τ_w = 300 – 50,000 s^{-1}) while minimizing the impact on platelet function prior to delivery to downstream thrombogenic substrates or assay systems; such as type 1 collagen, fibrinogen, and von Willebrand factor.[5, 24-29] To achieve this, most microfluidic assays have typically utilized large-footprint external syringe drivers, peristaltic pumps, or pressure driven pumping systems to achieve controlled blood flow rates and τ_w.[4, 30] These external pump-based systems suffer significant limitations with respect to multiplexed high-throughput screening. These limitations include: restricted ability to control relatively small blood volumes (≤200 μL) due to large dead volumes; limited facility for rapid time-varying fluidic control, due to flow resistance across connecting tubing and within high resistance microchannels; little to no control over pump hemocompatibility; and no capacity for on-chip integration to achieve complex sample switching control and reagent mixing. Integrated pneumatically actuated micropumps offer significant potential as on-chip blood perfusion and sample handling elements in blood focused microfluidic systems due to their micro-scale size, flexibility, scalability, facility for on-chip integration and automation, and the capacity for multiplexing in complex microfluidic circuits that allow for tight control over key hemodynamic parameters and concomitant reagent delivery and mixing control.[31]

Reciprocating diaphragm micropumps have several features that make them potentially useful for on-chip hemodynamic control.[32-34] Reciprocating diaphragm micropumps consist of a series of pump-chambers, in which a thin planar membrane surface or surfaces is inset into the microfluidic wall or walls. The pumping chamber is generally in the form of a deformable elastomeric

diaphragm.[33, 34] Pneumatic actuation/inflation of the diaphragm creates a peristaltic pressure wave that induces unidirectional or bidirectional fluid displacement; contingent on upstream fluidic resistance and actuation mode.[34] The pressure capacitance, duty cycle, and degree of diaphragm actuation determine overall flow rates and pulsatility.[34] While the key mechanical parameters that dictate reciprocating micropump performance with respect to generalized perfusion of Newtonian fluids such as water have been described,[34] none have addressed the specific design considerations for effective functional blood handling. Significantly, while reciprocating micropumps offer potential for platelet-based flow assays, the imposition of elevated average τw, transient τw due to pulsatility, complex flow recirculation at relatively high duty cycles, and the direct mechanical effects of pump diaphragm actuation on blood cells (erythrocytes and platelets) present potential challenges with respect to micropump hemocompatibility.

In this study we describe the development and characterization of a modular “micropump bioreactor” (micropump-reactor) design that utilizes a system of multiplexed pneumatically actuated reciprocating micropumps and define an actuation regime as part of a proof-of-concept design that satisfies the requirements for a scalable, functionally hemocompatible, blood flow-based platelet test platform.

Results

Device description & mechanical characterization

The main text of the article should appear here with headings as appropriate. The overall micropump-reactor design is shown (Figures 1 & S1). Hemodynamic control was achieved through the development and integration of reciprocating elastomeric micropump(s) consisting of three valved pump chambers [V1, V2 & V3] each incorporating a 50 µm thick diaphragm, and superimposed pneumatic actuation chamber (Figure 1a). Three micropump valve iterations were tested and identified by the surface area (mm^2) and thickness of their valve diaphragms as; 0.26/50, 0.41/50, and 2.40/50 (Table S1). Micropump-reactor prototypes consisting of 1, 2 or 3 multiplexed micropumps were structured according to Figure S1. For multiplexed iterations, parallel micropump chambers were separated by 150 x 100 µm side wall baffles with each set of parallel valves actuated by a coupled set of pneumatic actuation chambers (Figure S1). Three actuation channels provided independent positive and negative pressure control of the three-way pump cycle and were connected to a custom built pneumatic valve driver/control unit.[35] The micropump actuation cycle is depicted in Figure 1b, with peristalsis achieved using a standard 120° cycle.[34] In brief, each valve or valve set was actuated in a cyclic pattern with a phase offset of 120°, where ↓ represents a closed valve, or application of positive pressure (1 - 100 kPa) and ↑ an open valve, or application of negative pressure (-20 kPa): ↓↑↓, ↓↑↑, ↓↓↑, ↓↑↓, ↓↑↑, ↓↓↑ (Figure 1b & Video S1). The integrated micropump-reactor prototype is depicted in Figure 1c. Reagent/drug delivery was achieved

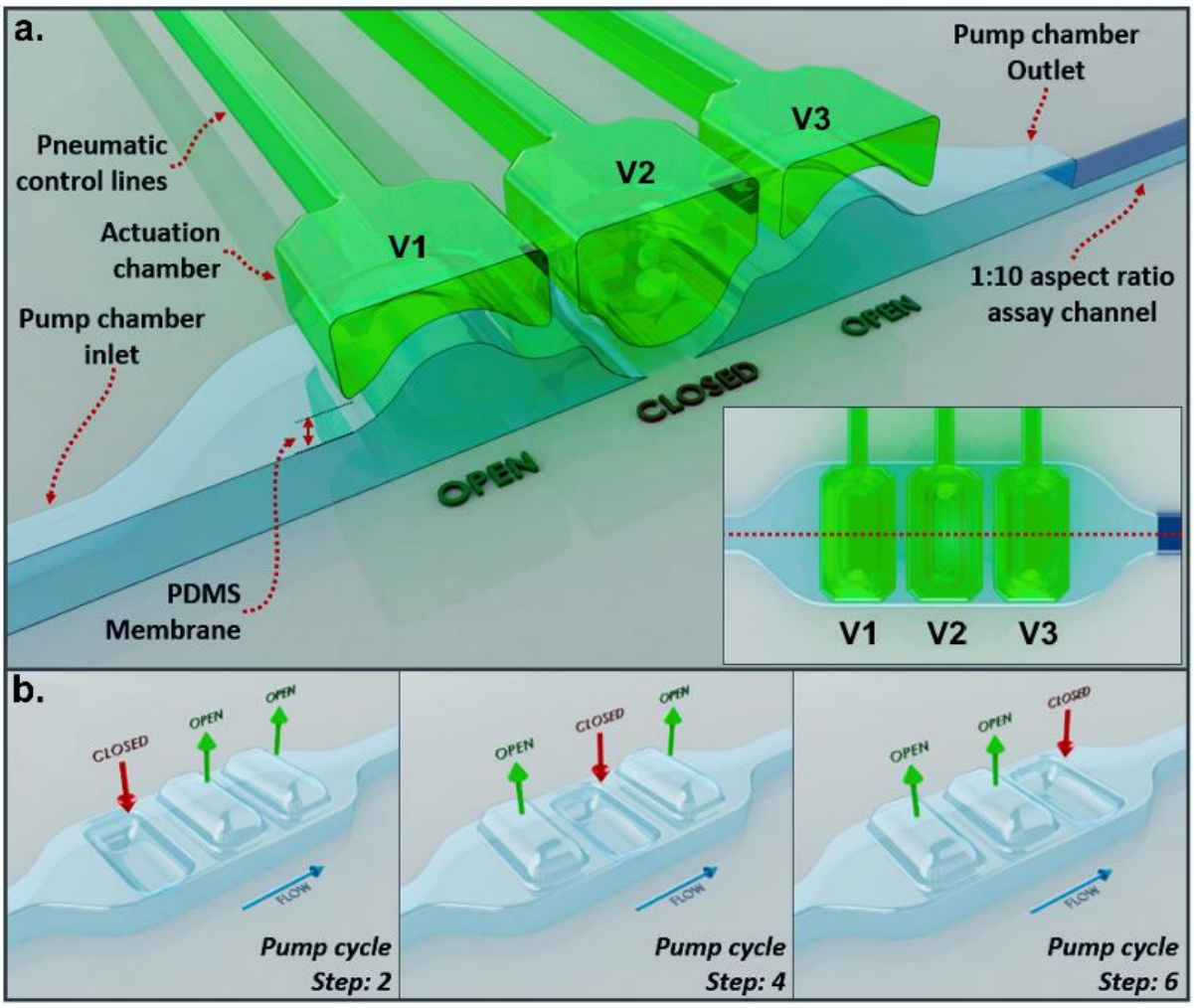
a.
Pump chamber Outlet
Pneumatic control lines
V3
V2
V1
Actuation chamber
1:10 aspect ratio assay channel
Pump chamber inlet
OPEN
CLOSED
OPEN
PDMS Membrane
V1 V2 V3
b.
CLOSED OPEN OPEN
FLOW
Pump cycle Step: 2
OPEN CLOSED OPEN
FLOW
Pump cycle Step: 4
OPEN OPEN CLOSED
FLOW
Pump cycle Step: 6
Pump Cycle: Step: 1 Step: 2 Step: 3 Step: 4 Step: 5 Step: 6
c.
(1)
(2)
(3)
(4)
(5)
(6)
(7)
(8)
VP BLOOD PUMP - 2.4 mm^2 - DUEL DRUG
OUTLETS
Top Layer
Bottom Layer

Figure 1. Micropump-reactor architecture

a. *Schematic showing micropump valve chambers (V1, V2, V3) and pneumatic actuation chambers (midline cross-section). Pneumatic control lines lead to the external valve driver.* ***b****. Schematic showing 3-dimensional view and arrangement of micropump valve chambers and operating pump cycle. Green arrows denote valve opening due to -20 kPa pressure actuation, red arrows denote valve closure (inflation) due to +ve pressure actuation, blue arrow denotes overall direction of fluid flow.* ***c****. Schematic of integrated micropump-reactor showing the arrangement of:* ***(1)*** *Pneumatic actuation micropump interfaces,* ***(2)*** *Pneumatic actuation drug gate interfaces,* ***(3)*** *Bilateral drug channel inlets,* ***(4)*** *Blood sample reservoir (200 µL),* ***(5)*** *Bilateral drug gate valves,* ***(6)*** *Micropump,* ***(7)*** *Type 1 collagen coated microchannel,* ***(8)*** *Sample collection reservoir. Note the duplicate micropump-reactor arrangement controlled through a single driver interface.*

by incorporation of laterally placed dual straight-gate-valved injection ports positioned laterally 3.98 mm downstream of the blood sample reservoir (Figure 1c). Straight gate valve design and operation was as per Szydzik et. al., (2018).[36] The thrombosis assay segment of the micropump-reactor consisted of a downstream 500(w) x 50(h) x 14,750(l) µm (10:1 aspect ratio) microchannel coated with 100 µg/mL type 1 fibrillar collagen.

Micropump dynamic performance

The main text of the article should appear here with headings as appropriate. To characterize the blood handling performance of the micropump iterations, flow rates with human citrated whole blood were assessed as a function of valve size, actuation pressure, and frequency (Figures 2a & S2). Pump performance increased with actuation pressure, with maximal flow rates for whole blood achieved at the maximum achievable actuation pressure of 100 kPa (the upper safety limit of the pneumatic valve driver) (Figures 2a & S2). Univariate analysis demonstrated there was a statistically significant effect of actuation pressure on output flow rate ($F(3, 2884.016) = 2214.575$ $p < 0.0005$; partial $\eta^2 = 0.994$), with overall micropump performance scaling with micropump valve size (Figures 2a & S2; Table S2). Examination of the relationship between actuation duty cycle (frequency) at constant pressure demonstrated a nonlinear (bell-shaped) relationship such that peak pump flow rates were achieved within a frequency range of 6 – 9 Hz (Figures 2a & S2), with univariate analysis demonstrating a statistically significant effect of actuation frequency on output flow rate ($F(4,434.88) = 333.935$; $p < 0.0005$; partial $\eta^2 = 0.971$). A significant but minor interaction (frequency*pressure) effect was observed ($F(12,135.047) = 103.700$, $p < 0.0005$; partial $\eta^2 = 0.969$).

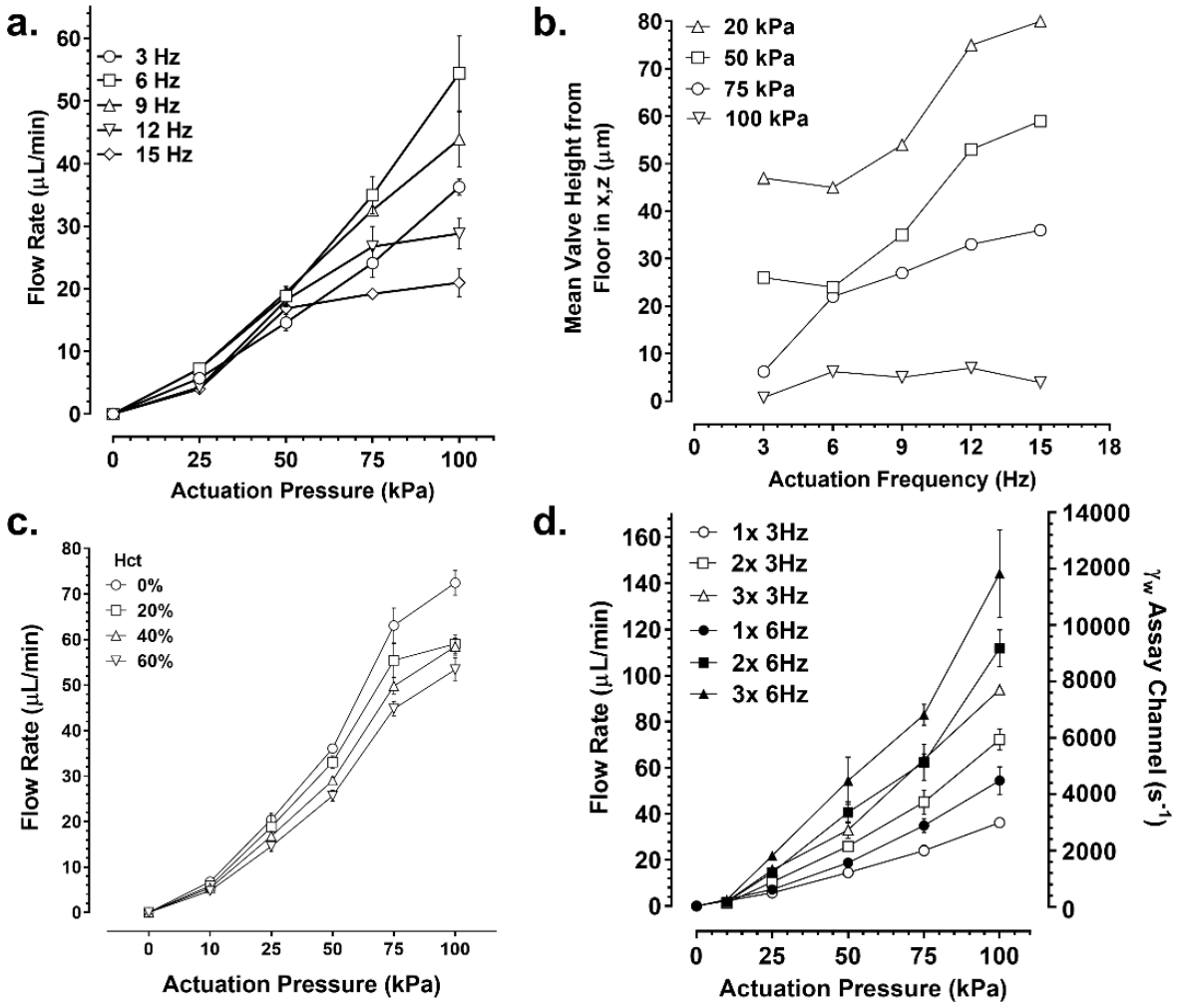
a.
Flow Rate (µL/min)
3 Hz
6 Hz
9 Hz
12 Hz
15 Hz
Actuation Pressure (kPa)
b.
Mean Valve Height from Floor in x,z (µm)
20 kPa
50 kPa
75 kPa
100 kPa
Actuation Frequency (Hz)
c.
Flow Rate (µL/min)
Hct
0%
20%
40%
60%
Actuation Pressure (kPa)
d.
Flow Rate (µL/min)
1x 3Hz
2x 3Hz
3x 3Hz
1x 6Hz
2x 6Hz
3x 6Hz
γw Assay Channel (s-1)
Actuation Pressure (kPa)

Figure 2. Micropump-reactor mechanical performance

a. *Micropump flow rate (µL/min) for citrated human whole blood (6 independent donors) as a function of actuation pressure (kPa) and duty cycle (Hz).* ***b.*** *Micropump (2.40/50) dynamic valve closing height as a function of duty cycle (Hz) and actuation pressure (kPa).* ***c.*** *Micropump performance as a function of blood hematocrit (Hct %) and actuation pressure (kPa). Note 0% Hct represents platelet rich plasma (PRP) in the absence of erythrocytes.* ***d.*** *Multiplexed 2.40/50 micropumps and resultant output flow rate (µL/min) and resultant output wall shear rate (τ_w s^{-1}) within the downstream collagen assay channel at a duty cycle of 3 and 6 Hz as a function of actuation pressure. Each data set represents N = 3 - 6 independent experiments.*

Line-scanning confocal microscopy experiments in which 2.40/50-micropump valve operation was recorded in a single cross-sectional x,z plane as a function of time demonstrated that, with the exception of 100 kPa actuation, the overall extent of valve actuation decreased with increasing duty cycle (Figure 2b). To determine the impact of the major blood cell constituent, erythrocytes, on micropump performance we conducted experiments in which reconstituted human blood samples at fixed haematocrits (Hct) of 0, 20, 40, and 60% were perfused by the 2.4/50-micropump at a duty cycle of 6 Hz. Figure 2c demonstrates that Hct within the physiological to supraphysiological range has limited impact on micropump performance compared to platelet rich plasma (PRP) alone. Significantly, while peak pump performance with whole blood was limited to a maximum of ~54.4 µL/min, multiplexed 2.4/50-micropump configurations in which two (2x) or three (3x) micropumps were combined in parallel demonstrated that step-wise scaling of peak blood flow rates and therefore shear rates within the micropump-reactor were achievable across the actuation pressure and frequency range tested (Figure 2d). Maximal estimated wall shear rates (τ_w) within the downstream collagen assay channel of the micropump-reactor approaching ~12, 000 s-1 could be achieved using the 3x 2.4/50 micropump configuration operating at 100kPa/6Hz (Figure 2d).

Effect of micropump operation on blood cell function

The main text of the article should appear here with headings as appropriate. An essential criterion identified for micropump-reactor design was the capacity to deliver blood samples at a defined τ_w while limiting the effect of pumping mechanics on blood cell function. To investigate the effect of micropump

operation on blood platelet function we conducted a factorial analysis in which the canonical platelet activation markers of, integrin $\alpha_{IIb}\beta_3$ activation (Pac1 binding), α-granule secretion (P-selectin expression), and platelet pro-coagulant function (membrane phosphatidyl serine exposure – Annexin V binding) were assessed as a function of micropump actuation pressure and frequency (Figures 3a – c). Factorial analysis demonstrated a statistically significant effect on the combined platelet activation markers based on actuation pressure ($F(9, 92.633) = 30.226$, $p < 0.0005$; Wilk's $\Lambda = 0.036$, partial $\eta^2 = 0.671$) and frequency ($F(12, 100.830) = 57.665$, $p < 0.0005$; Wilk's $\Lambda = 0.004$, partial $\eta^2 = 0.838$) (Figure S3 & Table S3) but no significant interaction (frequency*pressure) effect ($F(36, 113.003) = 1.413$, $p > 0.005$; Wilk's $\Lambda = 0.334$, partial $\eta^2 = 0.307$) (Figure S3 & Table S3). A statistically significant effect of micropump output flow rate on combined platelet activation markers ($F(4, 112.000) = 31.215$, $p < 0.005$; Wilk's $\Lambda = 0.000$, partial $\eta 2 = 0.999$) was also evident (Figure S3 &Table S3). Overall, while 2.40/50-micropump operation at 100 kPa/6Hz yielded maximal blood flow rates of ~54.4 µL/min (Figure 2a), this actuation regime led to the highest levels of platelet activation in bulk flow (Figures 3a – c; Figure S3; Table S3). Assessment of 2x or 3x multiplexed 2.40/50-micropump variants at 100kPa/6Hz demonstrated that bulk flow platelet activation was a function of single (1x) component pump dynamics, rather than combined flow rate and demonstrates that micropump control can be incrementally scaled without additional effects on hemocompatibility (Figure 3d). Investigation of the role of

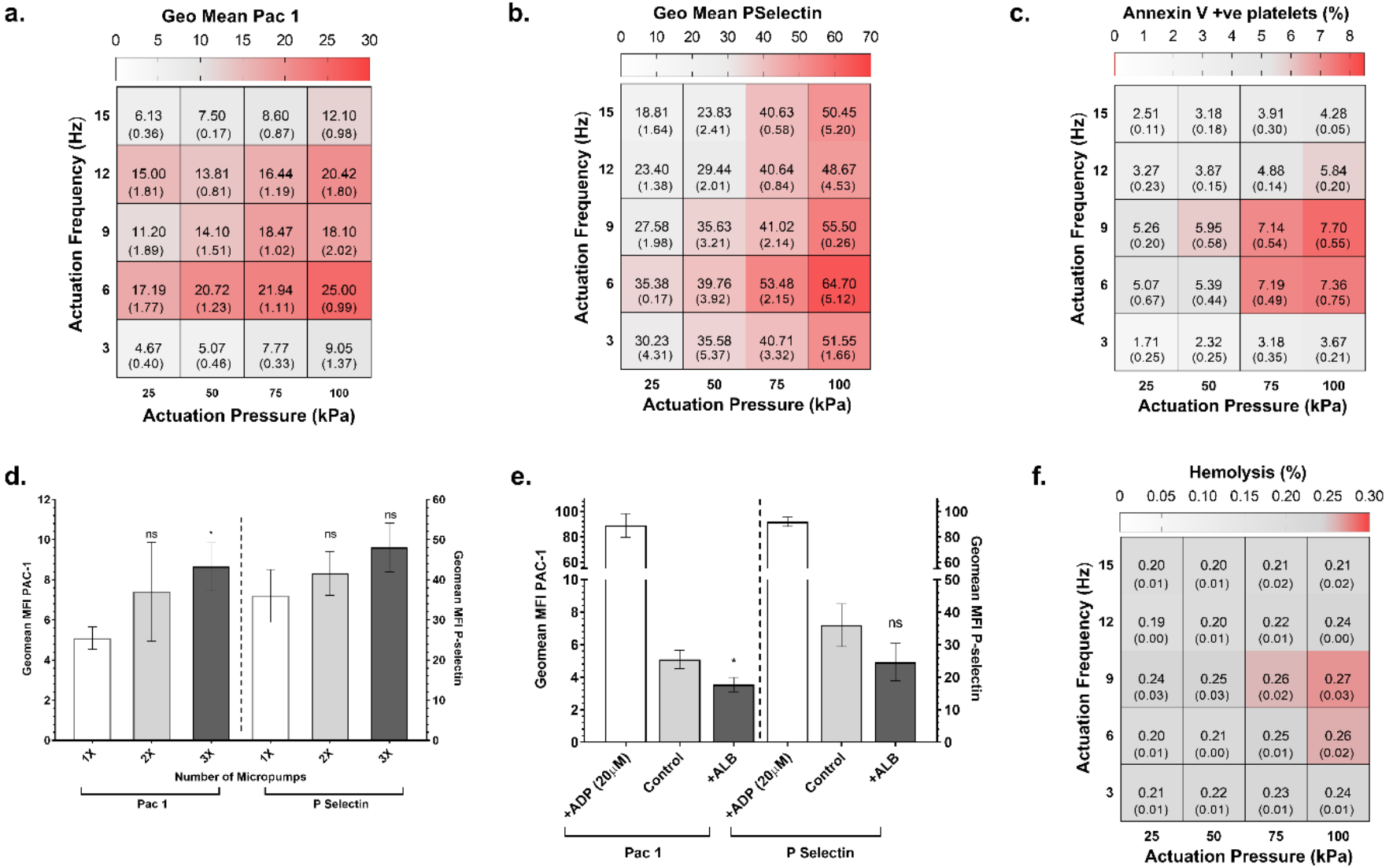
a.
Geo Mean Pac 1
0 5 10 15 20 25 30
Actuation Frequency (Hz)
15 6.13 (0.36) 7.50 (0.17) 8.60 (0.87) 12.10 (0.98)
12 15.00 (1.81) 13.81 (0.81) 16.44 (1.19) 20.42 (1.80)
9 11.20 (1.89) 14.10 (1.51) 18.47 (1.02) 18.10 (2.02)
6 17.19 (1.77) 20.72 (1.23) 21.94 (1.11) 25.00 (0.99)
3 4.67 (0.40) 5.07 (0.46) 7.77 (0.33) 9.05 (1.37)
25 50 75 100
Actuation Pressure (kPa)
b.
Geo Mean PSelectin
0 10 20 30 40 50 60 70
Actuation Frequency (Hz)
15 18.81 (1.64) 23.83 (2.41) 40.63 (0.58) 50.45 (5.20)
12 23.40 (1.38) 29.44 (2.01) 40.64 (0.84) 48.67 (4.53)
9 27.58 (1.98) 35.63 (3.21) 41.02 (2.14) 55.50 (0.26)
6 35.38 (0.17) 39.76 (3.92) 53.48 (2.15) 64.70 (5.12)
3 30.23 (4.31) 35.58 (5.37) 40.71 (3.32) 51.55 (1.66)
25 50 75 100
Actuation Pressure (kPa)
c.
Annexin V +ve platelets (%)
0 1 2 3 4 5 6 7 8
Actuation Frequency (Hz)
15 2.51 (0.11) 3.18 (0.18) 3.91 (0.30) 4.28 (0.05)
12 3.27 (0.23) 3.87 (0.15) 4.88 (0.14) 5.84 (0.20)
9 5.26 (0.20) 5.95 (0.58) 7.14 (0.54) 7.70 (0.55)
6 5.07 (0.67) 5.39 (0.44) 7.19 (0.49) 7.36 (0.75)
3 1.71 (0.25) 2.32 (0.25) 3.18 (0.35) 3.67 (0.21)
25 50 75 100
Actuation Pressure (kPa)
d.
Geomean MFI PAC-1
Geomean MFI P-selectin
ns
ns
ns
1X 2X 3X 1X 2X 3X
Number of Micropumps
Pac 1
P Selectin
e.
Geomean MFI PAC-1
Geomean MFI P-selectin
ns
+ADP (20μM) Control +ALB +ADP (20μM) Control +ALB
Pac 1
P Selectin
f.
Hemolysis (%)
0 0.05 0.10 0.15 0.20 0.25 0.30
Actuation Frequency (Hz)
15 0.20 (0.01) 0.20 (0.01) 0.21 (0.02) 0.21 (0.02)
12 0.19 (0.00) 0.20 (0.01) 0.22 (0.01) 0.24 (0.00)
9 0.24 (0.03) 0.25 (0.03) 0.26 (0.02) 0.27 (0.03)
6 0.20 (0.01) 0.21 (0.00) 0.25 (0.01) 0.26 (0.02)
3 0.21 (0.01) 0.22 (0.01) 0.23 (0.01) 0.24 (0.01)
25 50 75 100
Actuation Pressure (kPa)

Figure 3. Platelet activation in bulk flow as a function of micropump operation

a. *Heat map showing FACS analysis of geomean fluorescence intensity (SD) distribution of FITC PAC-1 antibody binding (integrin $\alpha_{IIb}\beta_3$ activation) to platelets in human whole blood following perfusion by the 2.40/50 micropump as a function of actuation duty cycle (Hz) and pressure (kPa).* ***b.*** *Heat map showing FACS analysis of geomean fluorescence intensity (SD) distribution of expression of α-P-selectin antibody binding to platelets in human whole blood following perfusion by the 2.40/50 micropump as a function of actuation duty cycle (Hz) and pressure (kPa).* ***c.*** *Heat map showing FACS analysis of geomean fluorescence intensity (SD) of FITC-Annexin-V binding to platelets in human whole blood following perfusion by the 2.40/50 micropump as a function of actuation duty cycle (Hz) and pressure (kPa).* ***d.*** *FACS analysis of Pac1, and α-P-selectin binding to platelets in whole blood for 2.40/50 single (1x), double (2x), and triple (3x) micropump iterations actuated at 50kPa/3Hz.* ***e.*** *FACS analysis of Pac1, and α-P-selectin binding to platelets in whole blood +/- platelet amplification loop blockers (ALB: indomethacin (10 μM) 2-MeSAMP (10 μM) and MRS2179 (100 μM) for 2.40/50 single (1x) micropump actuated at 50kPa/3Hz. +ADP (20 μM) – control in which whole blood was stimulated with 20 μM ADP. All data indicates n = 3 independent experiments. Error bars indicate standard deviation. Black horizontal bars indicate comparative analysis for which a significant difference was tested for using a paired t-test. * p ≤ 0.05, ** p ≤ 0.01, *** p ≤ 0.001, **** p ≤ 0.0001, ns – not significant.* ***f.*** *Heat map showing % hemolysis (SD) in human whole blood following perfusion by the 2.40/50 micropump as a function of actuation duty cycle (Hz) and pressure (kPa). All data indicates n = 3 independent experiments.*

platelet soluble agonist (ADP/ATP, and TXA2) pathways (inside-out signalling) in mediating the overall effects of micropump actuation on platelet activation demonstrated that while observed levels of integrin $\alpha_{IIb}\beta_3$ activation were partially dependent on agonist secretion, overall platelet activation was not significantly driven by canonical platelet amplification loops, suggesting that a direct adhesion independent mechanotransduction mechanism underlies the effects of micropump dynamics on platelet activation (Figure 3e). The mechanical effects of micropump operation on erythrocyte handling was negligible, with minimal levels of haemolysis observed across the actuation range tested (Figure 3f; Table S4). Taken together, this analysis demonstrates that while micropump function does affect platelet activation status in bulk flow, modulation of both pressure and frequency of actuation can be harnessed to attenuate this effect and that a “sweet spot” actuation regime of 50kPa/3Hz for the 2.4/50-micropump iteration minimizes platelet activation while maintaining serviceable flow rates of 14.6 µL/min (1x), 25.9 µL/min (2x), and 33.1 µL/min (3x).

Local micropump haemodynamics and platelet function

Micropump haemodynamics. Our observations of bulk flow platelet activation as a function micropump actuation led us to hypothesize that micropump hemocompatibility may be dependent on the extent to which changes in micropump valve geometry during actuation effects local haemodynamics. To investigate this hypothesis, we conducted computational fluid dynamic (CFD) modelling of human whole blood at a steady state flow rate of 14.6 µL/min (output flow rate at 50kPa/3Hz) and varying actuation pressures of 0, 1, 5 and

10 kPa (Figures 4a - c). CFD demonstrated that τw within 3μm (equivalent to 1.5x platelet diameters) of the valve surfaces was a function of valve actuation pressure and therefore shape (Figures 4a – c). Increases in τw was predicted at the perimeter of the micro-valves with increasing pressure (due to their inflated shape), with maximal τw approaching 300 s^{-1} at the lateral valve margins at 10kPa (Figures 4a & c). Direct comparison with bulk flow platelet activation (Pac1 and α-P-selectin binding) under equivalent conditions of 14.6 μL/min constant flow rate (external pump) and static valve actuation demonstrated a direct correlation of platelet activation with the overall increase in local τw, approaching that of dynamic micropump actuation at 50kPa/3 Hz (Figures 4d & e). Platelet activation was a function of single valve geometry with no significant additive effect when all valves were actuated simultaneously at 10 kPa (Figures 4d & e).

To investigate the time varying effects of micropump actuation we conducted experimental μ-PIV. Snapshots of the instantaneous streamwise shear rate field (τ) and instantaneous velocity vectors at the six valve positions in one cycle of the micropump is shown in Figures 5a & b (Videos S2 & 3). Unlike CFD modelling, and despite the fluid flow being ostensibly laminar, complex flow behaviours were apparent, such as the presence of counter-rotating vortices (Steps 1, 2 and 5), strong shear layers (Step 6) and the presence of stagnation points (Steps 2 and 5). Additionally, nodes of elevated τ were observed at the interface between V2 and V3 during Steps 2 and 4, with significant τ increases

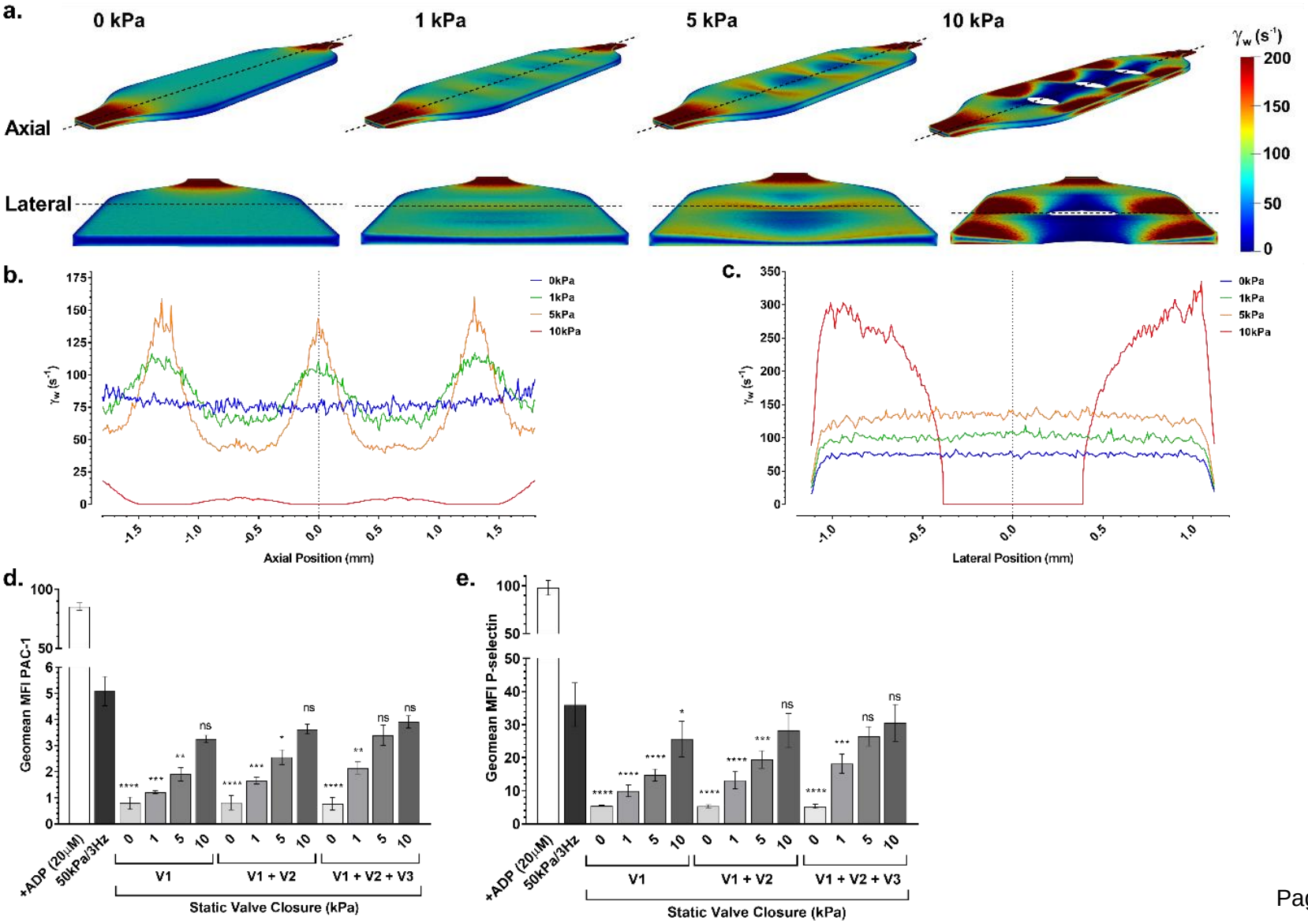
a.
0 kPa
1 kPa
5 kPa
10 kPa
Axial
Lateral
γw (s-1)
200
150
100
50
0
b.
0kPa
1kPa
5kPa
10kPa
γw (s-1)
Axial Position (mm)
c.
Lateral Position (mm)
d.
Geomean MFI PAC-1
e.
Geomean MFI P-selectin
+ADP (20μM)
50kPa/3Hz
V1
V1 + V2
V1 + V2 + V3
Static Valve Closure (kPa)
ns

Figure 4. Static micropump valve geometry and local hemodynamics

a. *CFD of a single 2.40/50-micropump valve at 0, 1 5 and 10 kPa. 3-dimensional wall shear rate (τ_w) contour profiles were determined for blood at Q = 14.6 µL/min constant flow rate.* ***b.*** *CFD modeling of a single streamline trajectory 3µm from the micropump valve surface, axially bisecting the valve geometries at centerline at static actuation pressures of 0, 1, 5, & 10 kPa at Q = 14.6 µL/min.* ***c.*** *CFD modeling of a single streamline trajectory laterally bisecting the valve geometries 3µm from the valve surface at centerline at static actuation pressures of 0, 1, 5, & 10 kPa at Q = 14.6 µL/min.* ***d. & e.*** *FACS analysis of Pac1, and α-P-selectin binding to platelets in whole blood for 2.40/50 (1x) micropump in which perfusion was controlled via an external syringe driver at Q= 14.6 µL/min and V1, V1 + V2 and V1 + V2 + V3 statically held at 0, 1, 5, and 10 kPa. Micropump – actuated micropump at 50kPa/3Hz. +ADP (20µM) – control in which whole blood was stimulated with 20 µM ADP. One-way ANOVA comparing actuation pressure v 50kPa/3Hz dynamic micropump actuation; * p ≤ 0.05, ** p ≤ 0.01, *** p ≤ 0.001, **** p ≤ 0.0001, ns – not significant. N = 3 independent experiments.*

primarily occurring during the filling phase (Step 6), cantered under and between V1 and V2, with peak τ observed at the midpoint of V2 (Figures 5a & b; Videos S2 & S3). Micropump operation at both 100kPa/6Hz and 50kPa/3Hz demonstrated predominantly similar flow features per cycle, despite the difference in operating frequency (Figures 5a & b; Videos S2 & S3). Nevertheless, the 100kPa/6Hz configuration produced a higher flow rate by virtue of the higher frequency, however this in turn lead to larger flow accelerations and higher instantaneous strain rates (Figures 5a & b; Videos S2 & S3). Overall, micropump operation at either 100kPa/6Hz or 50kPa/3Hz resulted in a pulsatile instantaneous flow rate waveform within the collagen assay segment of the device (Figures 5c & d).

Spatial and time varying effects of micropump operation on blood platelets.

To investigate the way in which spatially and time varying haemodynamics correlated with platelet flow behaviour, we conducted epifluorescence imaging of DiOC6 labelled human whole blood at V1, V2 and V3 under dynamic micropump operation. Examination of the axial distribution (at centreline) of platelets during pump cycling demonstrated a relative increase in platelet distribution cantered under the microvalves during valve upstroke due to downstream valve closure and the negative pressure of valve opening (Figure 6a). A relative increase in platelet density was observed immediately downstream of V3 upon concomitant closure of V2 and V3 (Step 4) leading to positive displacement of the platelet population in the flow direction (Figure 6a).

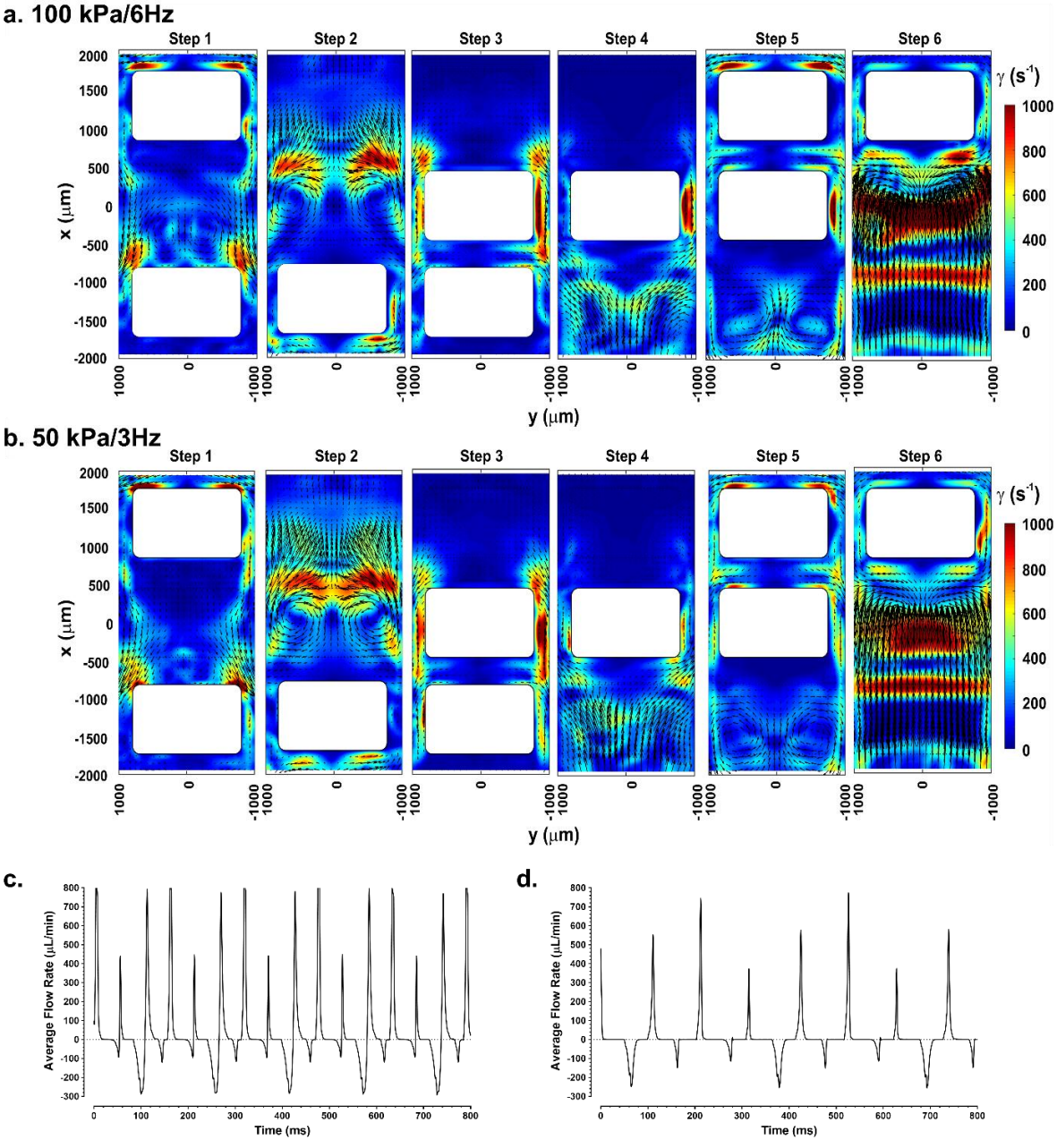
a. 100 kPa/6Hz
Step 1
Step 2
Step 3
Step 4
Step 5
Step 6
γ (s-1)
1000
800
600
400
200
0
x (μm)
y (μm)
b. 50 kPa/3Hz
c.
d.
Average Flow Rate (μL/min)
Time (ms)

Figure 5. μ-PIV of dynamic micropump operation

a. *μ-PIV contour maps showing planar shear rate magnitude (τ) and instantaneous velocity vectors for 1x 2.4/50 micropump operation at 100kPa/6Hz (Video S2).* ***b.*** *μ-PIV contour maps showing planar shear rate magnitude (τ) and instantaneous velocity vectors for 1x 2.4/50 micropump operation at 50 kPa/3Hz (Video S3). Note that panels approximate Steps 1 - 6 of micropump operation. Dotted marques denote opening microvalves; solid marques denote fully closed microvalves. Overall flow direction is bottom-to-top. Representative of n = 2 independent experiments for each case.* ***c.*** *μ-PIV analysis of instantaneous flow rate (μL/min) across the collagen assay channel component of the micropump-reactor at 100kPa/6Hz actuation.* ***d.*** *μ-PIV analysis of instantaneous flow rate (μL/min) across the collagen assay channel component of the micropump-reactor at 50kPa/3Hz actuation. Note the overall pulsatile nature of the flow with positive and negative flow transients with intervals of approximately 20ms. Also note that peak flow was biased towards the positive direction. N = 2 independent experiments.*

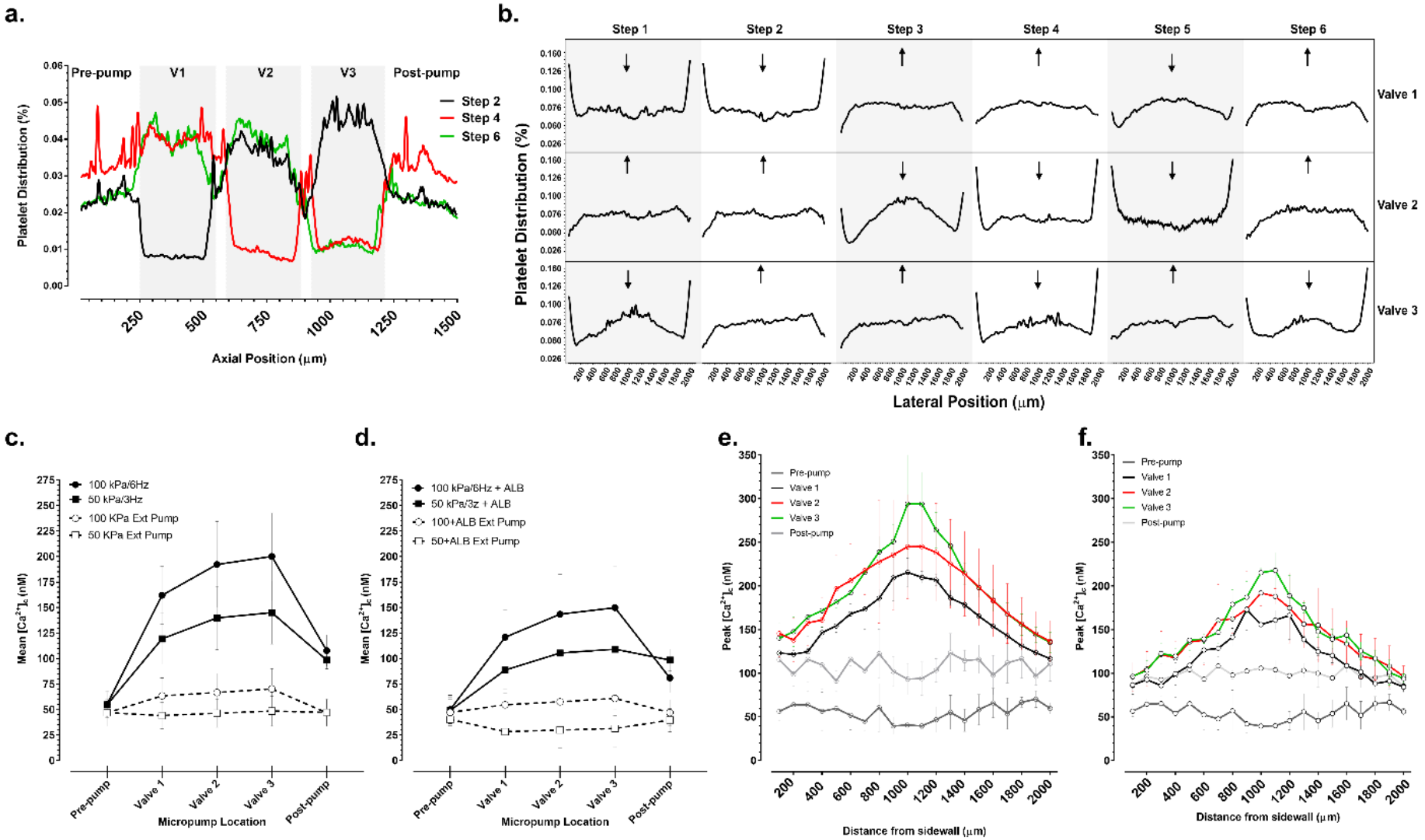
a.
Pre-pump
V1
V2
V3
Post-pump
Step 2
Step 4
Step 6
Platelet Distribution (%)
Axial Position (μm)
b.
Step 1
Step 2
Step 3
Step 4
Step 5
Step 6
Valve 1
Valve 2
Valve 3
Platelet Distribution (%)
Lateral Position (μm)
c.
100 kPa/6Hz
50 kPa/3Hz
100 KPa Ext Pump
50 KPa Ext Pump
Mean [Ca2+]c (nM)
Pre-pump
Valve 1
Valve 2
Valve 3
Post-pump
Micropump Location
d.
100 kPa/6Hz + ALB
50 kPa/3z + ALB
100+ALB Ext Pump
50+ALB Ext Pump
Mean [Ca2+]c (nM)
Micropump Location
e.
Pre-pump
Valve 1
Valve 2
Valve 3
Post-pump
Peak [Ca2+]c (nM)
Distance from sidewall (μm)
f.
Pre-pump
Valve 1
Valve 2
Valve 3
Post-pump
Peak [Ca2+]c (nM)
Distance from sidewall (μm)

Figure 6. Dynamic platelet distribution and activation as a function of micropump operation

a. *Proportional axial distribution of $DiOC_6$ labeled platelets in human whole blood as a function of micropump actuation step. Grey shaded blocks indicate the relative position of V1, V2 and V3.* ***b.*** *Proportional lateral distribution of $DiOC_6$ labeled platelets in human whole blood as a function of micropump actuation step. Note that platelet distribution is centered over each valve midpoint. Arrows indicate valve upstroke ↑or downstroke ↓ phase.* ***c.*** *Mean platelet cytosolic calcium flux $[Ca^{2+}]_c$ (nM) for the 2.40/50 micropump iteration under 100 kPa/6Hz and 50 kPa/3Hz actuation regimes at; pre-pump (2060 µm from V1), valve 1 (apex), valve 2 (apex), valve 3 (apex), post-pump (15.8 mm downstream of V3).* ***d****. Mean platelet cytosolic calcium flux $[Ca^{2+}]_c$ (nM) for the 2.40/50 micropump iteration under 100 kPa/6Hz and 50 kPa/3Hz actuation regimes +ALB (indomethacin (10 µM), 2-MeSAMP (10 µM) and MRS2179 (100 µM)); at; pre-pump (2060 µm from V1), valve 1 (apex), valve 2 (apex), valve 3 (apex), post-pump (15.8 mm downstream of V3). n = 3 independent experiments.* ***e.*** *Peak platelet cytosolic $[Ca^{2+}]_c$ (nM) for the 2.40/50 micropump iteration under 100k kPa/6Hz. Data represents lateral line scans (100µm bins) of peak $[Ca^{2+}]_c$ in reconstituted blood at; pre-pump (2060 µm from V1), valve 1 (apex), valve 2 (apex), valve 3 (apex), post-pump (15.8 mm downstream of V3).* ***f.*** *Peak platelet cytosolic $[Ca^{2+}]_c$ (nM) for the 2.40/50 micropump iteration under 50 k kPa/3Hz. Data represents lateral line scans (100 µm bins) of peak $[Ca^{2+}]_c$ in reconstituted blood at; pre-pump (2060 µm from V1), valve 1 (apex), valve 2 (apex), valve 3 (apex), post-pump (15.8 mm downstream of V3). All data indicates n = 3 independent experiments*.

Observation of platelet lateral distribution bisecting V1, V2 and V3 demonstrated distinct behaviours, dependent on the phase of micropump actuation, with redistribution of platelets to the valve margins during down-stroke and centralization of the platelet population during valve upstroke (Figure 6b). To correlate these dynamic platelet redistribution effects with localized effects on platelet activation, we monitored real-time platelet Ca^{2+} signalling as a function of position. Analysis of platelet $[Ca^{2+}]_c$ at 100 kPa/6Hz, demonstrated that mean $[Ca^{2+}]_c$ (averaged over the complete pump cycle) increased 3-fold to ~150 nM (Baseline $[Ca^{2+}]_c \approx 50$ nM) at V1, with further progressive increases at V2 and V3 resulting in an overall mean $\Delta[Ca^{2+}]_c$ of ~150 nM (Figure 6c). An actuation regime of 50 kPa/3Hz led to an overall reduction in $\Delta[[Ca^{2+}]_c \approx 75$ nM (Figure 6c). Blockade of platelet amplification loops (ALB) only partially reduced overall $\Delta[Ca^{2+}]_c$ under all actuation conditions, further demonstrating that local platelet activation is in part driven by a direct mechanotransduction effect (Figure 6d). A more detailed analysis correlating platelet $[Ca^{2+}]_c$ with lateral position (across valves) and axial position within the micropump demonstrated that peak $[Ca^{2+}]_c$ occurred at the centreline of the individual micropump valves (Figures 6e & f); where the inflated diaphragms extended maximally into the sample flow during downstroke and the highest platelet densities were observed during upstroke (Figures 6e & f). Peak $[Ca^{2+}]_c$ progressively increased from V1 to V3, suggesting that valve effects on platelet Ca^{2+} signalling are progressive (Figures 6e & f). Platelet $[Ca^{2+}]_c$ remained moderately elevated at ~80 - 90nM 15.9 mm downstream of V3, correlating with the bulk flow platelet activation identified by FACS analysis (Figures 6e & f and Figure 3).

Integrated micropump-reactor

Micropump as an active in-line reagent mixer.

Given the marked flow recirculation effects revealed by μPIV we posited that our micropump may act as an effective active mixing system. To investigate this, we conducted a series of experiments in which FITC conjugated polyethylene glycol (PEG) species with M of 350 Da, 2000 Da, and 20 kDa were injected continuously into the micropump-reactor circuit via the lateral injection ports. Confocal imaging was conducted at the following micropump locations, with mixing time (tmix) calculated based on flow velocities measured by μ-PIV relative to the drug injection ports: [1] Drug-port (tmix = 0 sec, d = 0 mm); [2] Pre-pump (tmix = 0.74 sec, d = 2.1 mm); [3] Post-pump (tmix = 8.8 sec, d = 7.8 mm); [4] Collagen-assay channel (tmix = 10.9 sec, d = 23.6 mm) (Figures 7a – c). Quantitation of the extent of mixing as a function of PEG-FITC fluorescence standard deviation (σPEG-FITC) at cross-section, according to the method of Stroock et. al., (2002),[37] demonstrated that under 2.40/50-micropump control (50kPa/3Hz) significant mixing was achieved immediately downstream of V3 (tmix = 5.09 sec), with complete homogeneity achieved (relative to premixed controls) 15.9 mm downstream of V3 (at the collagen assay channel - tmix = 10.9 sec), across the M range tested (Figures 7a – c). Experiments in which blood flow was controlled by an external syringe driver and micropump valves held in the neutral (0 kPa) position, demonstrated that diffusive mixing, in the absence of micropump actuation, was negligible across the microfluidic circuit (Figures 7a – c).

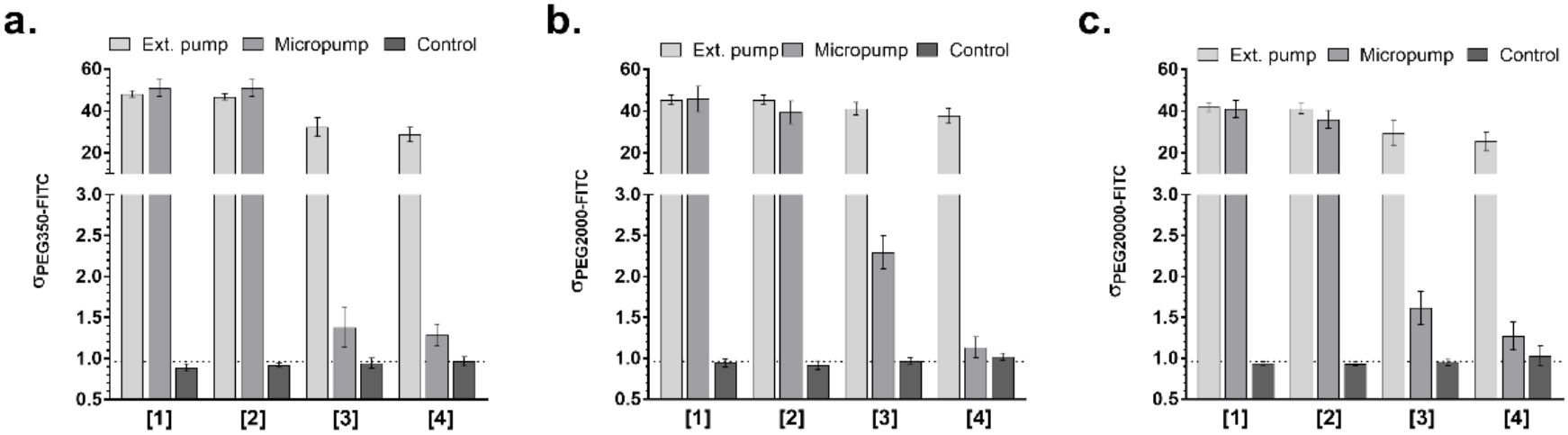
a.
Ext. pump
Micropump
Control
σPEG350-FITC
60
40
20
3.0
2.5
2.0
1.5
1.0
0.5
[1]
[2]
[3]
[4]
b.
Ext. pump
Micropump
Control
σPEG2000-FITC
60
40
20
3.0
2.5
2.0
1.5
1.0
0.5
[1]
[2]
[3]
[4]
c.
Ext. pump
Micropump
Control
σPEG20000-FITC
60
40
20
3.0
2.5
2.0
1.5
1.0
0.5
[1]
[2]
[3]
[4]

Figure 7. Micropump mixing efficiency as a function of molecular weight

a. *Confocal image analysis showing pixel x pixel fluorescence standard deviation (σ) of PEG-350-FITC in cross sectional flow under 2.40/50 micropump control (50k Pa/3Hz) or external syringe pump perfusion (Q = 13.5 µL/min)* ***b.*** *Pixel x pixel fluorescence standard deviation of PEG-2000-FITC (in cross sectional flow.* ***c.*** *Pixel x pixel fluorescence standard deviation of PEG-20,000-FITC in cross sectional flow. Control – premixed PEG-FITC perfused through the device;* ***[1]*** *cross-section at drug injection port (t_{mixing} =0 sec, d=0 µm);* ***[2]*** *cross-section pre-pump (t_{mixing} =0.74 sec, d =2.1 mm);* ***[3]*** *cross-section post-pump (t_{mixing} =8.8 sec, d =7.8 mm);* ***[4]*** *cross-section at the collagen assay channel (t_{mixing} =10.9 sec, d =23.6 mm). n = 3 independent experiments.*

Micropump-reactor as an effective platelet function and drug testing platform. Given the demonstrated effectiveness of the micropump-reactor prototype as both a hemocompatible blood perfusion and active mixing system, we next examined it's effectiveness as a preclinical test system of platelet function and as a screening tool for antiplatelet/anti-thrombotic drug candidates. One caveat to our micropump design is its peristaltic behaviour which leads to a degree of pulsatile flow within the collagen assay component of the micropump-reactor (Figures 5c & d). To investigate the effectiveness of the system to drive platelet thrombus formation at the surface of type 1 collagen (a standard in vitro measure of platelet function and thrombus formation) we compared the micropump-reactor protype with a well published microcapillary flow assay that utilized non-pulsatile laminar flow.[4, 9] Figure 8a shows experiments with citrated human whole blood comparing platelet thrombus growth dynamics for micro-capillary with the micropump-reactor demonstrating equivalency with respect to thrombus growth rate and extent at a τw = 1,100 s^{-1} (2.40/50 micropump at 50kPa/3Hz).

To explore the potential of the micropump-reactor as an efficient and rapid anti-platelet drug testing platform we conducted a series of experiments in which citrated human whole blood was treated with a series of isoform selective small molecule inhibitors of platelet Phosphatidylinositol 3-kinase (PI 3-K): AS 2524224 (M = 305.28 Da – PI 3-Kγ selective); TGX221 (M = 364.44 Da – PI 3-Kβ selective); LY294002 (M = 343.81 Da – reversible non-selective); Wortmannin (M = 428.44 Da – irreversible pan-selective).[8, 38, 39] To monitor

drug dilution and control drug-to-blood concentrations within the micropump-reactor, drug samples were spiked with TRITC (1 µg/mL) and integrated fluorescence intensities monitored in the drug channels (prior to injection) and within the collagen test channel concomitant with confocal imaging of platelet thrombus formation. Drug-to-blood dilution within the bioreactor (expressed as D = [TRITC]Drug-port/[TRITC]Blood) was equal to 2.77 ± 0.52-fold, across all drug titrations and replicate runs. Drugs were continuously infused via the drug injection ports to achieve final blood concentrations known to be inhibitory to platelet function.[8, 38, 39] Comparison of the micropump-reactor system with the standard micro-capillary system demonstrated equivalency with respect to inhibitor kinetics and demonstrated a hierarchy of inhibitor efficacy of Wortmannin >LY294002 >TGX221 >AS 2524224 over dimethyl sulfoxide (DMSO - vehicle) controls; which correlated with the known anti-platelet effects of these inhibitors (Figures 8b – d).[8, 38, 39] The effectiveness of the micropump-reactor with respect to dose ranging experiments was also examined for PI 3-K isoform selective inhibitors. Figures 8e – h show that the micropump-reactor demonstrated equivalency to the standard micro-capillary system with respect to its ability to perform inhibitor titrations. Significantly, these data demonstrate the effectiveness of the micropump-reactor to perform rapid in-flow drug dosing experiments, with a drug incubation time of ~10.9 sec (time from injection to the collagen assay window); in comparison to the standard micro-capillary system where drugs were manually mixed in an Eppendorf tube and incubated for ~10 min prior to sample perfusion.

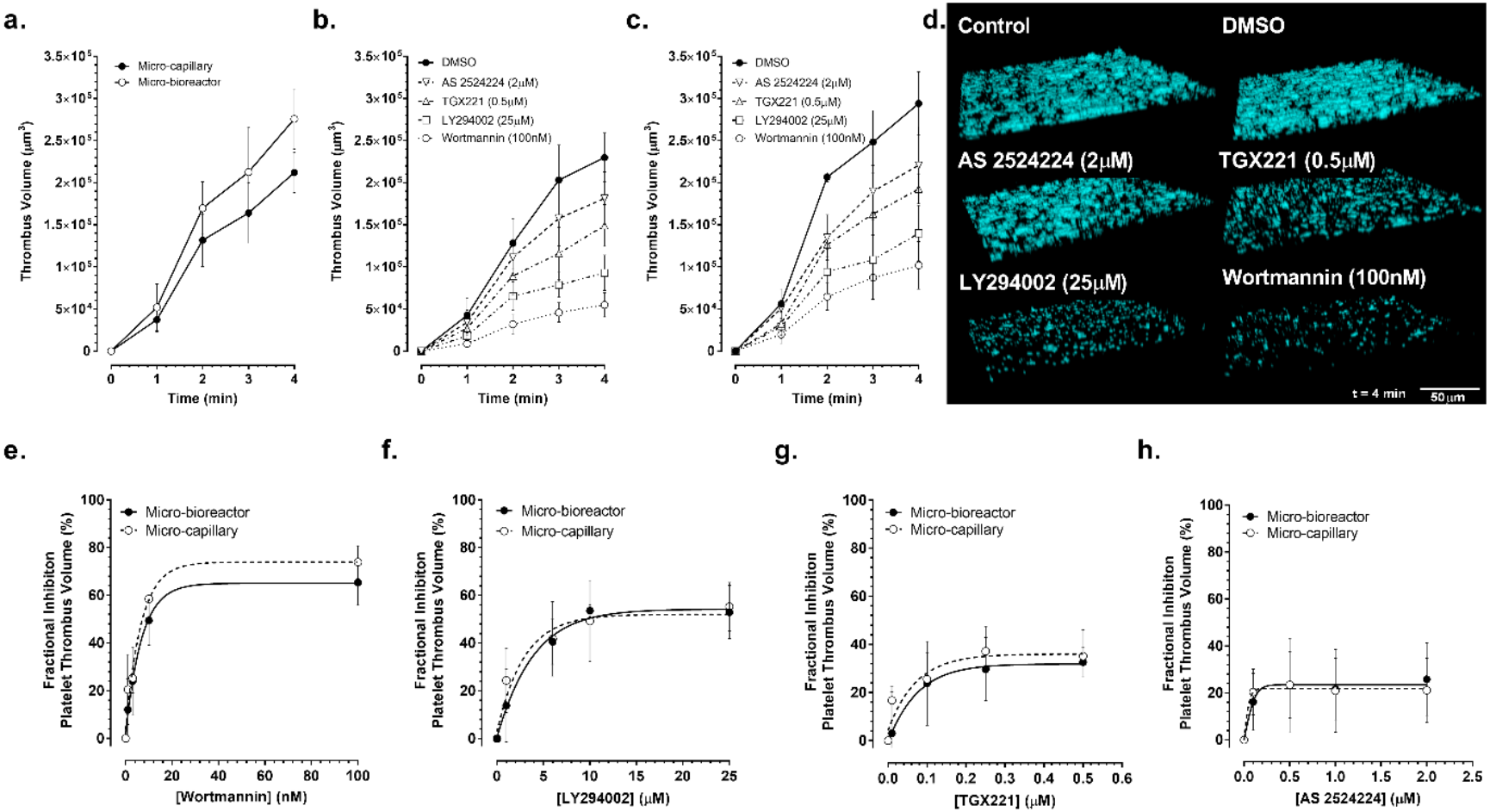
a.
b.
c.
d.
Micro-capillary
Micro-bioreactor
DMSO
AS 2524224 (2μM)
TGX221 (0.5μM)
LY294002 (25μM)
Wortmannin (100nM)
Thrombus Volume (μm³)
Time (min)
Control
DMSO
AS 2524224 (2μM)
TGX221 (0.5μM)
LY294002 (25μM)
Wortmannin (100nM)
t = 4 min
50 μm
e.
f.
g.
h.
Fractional Inhibiton Platelet Thrombus Volume (%)
[Wortmannin] (nM)
[LY294002] (μM)
[TGX221] (μM)
[AS 2524224] (μM)

Figure 8. Micropump-reactor application to platelet thrombus dynamics and drug screening

a. *Micro-capillary v micropump-reactor based whole blood flow at* $\tau_w = 1100s^{-1}$ *showing thrombus volume v time at the surface of Type 1 collagen. n = 3 independent experiments****. b.*** *Micro-capillary based drug dosing under flow at* $\tau_w = 1100\ s^{-1}$ *showing thrombus volume v time at the surface of Type 1 collagen. All reagents were premixed in Eppendorf 10 min prior to sample perfusion.* ***c.*** *Micropump-reactor-based drug dosing under flow at* $\tau_w = 1100\ s^{-1}$ *showing thrombus volume v time at the surface of Type 1 collagen. All reagents were continuously injected into the sample stream with a mixing time at homogeneity of ~30.9 sec* ***d.*** *Confocal reconstructions of micropump-reactor whole blood flow experiments t = 4 min at* $\tau_w = 1100\ s^{-1}$*. Control – citrated whole blood; DMSO – whole blood + 0.025% w/v dimethyl sulfoxide; Wortmannin – 100nM; LY294002 – 25 µM; TGX221 – 0.5 µM; AS 2524224 – 2 µM. n = 3 independent experiments.* ***e - h.*** *Dose response curves showing % inhibition of thrombus growth following injection of Wortmannin (final [Wortmannin] after micropump mixing – incubation t = 30.9 sec); LY294002 (final [LY294002] after micropump mixing – incubation t = 30.9 sec); TGX221 (final [TGX221] after micropump mixing – incubation t = 30.9 sec); AS 2524224 (final [AS 2524224] after micropump mixing – incubation t = 30.9 sec)into the prototype micropump-reactor v micro-capillary blood flow experiments (Wortmannin mixed and incubated for 10 min prior to perfusion). N = 3 independent experiments.*

Discussion

The main text of the article should appear here with headings as appropriate. A relatively large number of microfluidic based approaches to investigate platelet function and thrombosis have been described, however few have explored the way in which increased on-chip automation, reagent delivery, and mixing can be utilized to develop true lab-on-chip functionality.[11-22] We posit that the increased automation offered by the micropump-reactor described in the present work has the potential to greatly improve the reliability of platelet function assays but also lends itself to the demands of high-content screening of new, more hemodynamically targeted, anti-platelet therapies. We present this micropump-reactor system as a modular component blood handling microfluidic that has the flexibility and scalability to be incorporated into an array of haematology focused assay systems.

Characterization of the mechanical performance of the micropump-reactor design demonstrated a significant correlation between actuation pressure and duty cycle, with increases in either leading to an overall improvement in flow output. However, investigation of platelet activation in bulk flow demonstrated that functional micropump operation was restricted to a relatively narrow pressure and frequency range, with pressures above 50 kPa and frequencies above 3Hz leading to significant levels of platelet integrin activation, P-selectin expression, and to a lesser degree, procoagulant function. While this actuation range fell within the lower end of mechanical flow rate performance it was enough to allow for the generation of relatively high shear rates within the

downstream collagen assay. This limitation puts an upper ceiling on flow rates achievable with a single micropump prototype. Significantly however, parallel multiplexing of this single pump iteration (2x and 3x) allowed for a progressive (quasi-digital) increase in flow output and therefore shear rates without a concomitant increase in platelet activation. Thus, in principle the micropump-reactor architecture described allows for step-wise increases in flow rate; limited only by the overall device footprint.

A fundamental criterion for any blood handling microfluidic system is its ability to control blood sample haemodynamics while minimizing any negative impact on blood cell function. Our detailed analyses of micropump-reactor fluid dynamics demonstrated significant complexity in blood/sample flow behaviour, typified by regions of eddy formation and flow reversal, along with rapid transient peaks in micro-pump shear rates dependent on the phase of the pumping cycle. While this complexity may be advantageous with respect to sample mixing it may also be a key affecter of platelet activation. While, elevated τ on the order of 300 – 10,000.s^{-1} can directly trigger blood platelet Ca^{2+} signalling, α-granule secretion, adhesion, and platelet aggregation through the activation and engagement of platelet adhesion receptors, such as GPIb/V/IX and the integrin $\alpha_{IIb}\beta_3$, the cumulative impact of more complex flow regimes, in the absence of classical adhesion mechanisms is less well understood. Findings from our laboratories have demonstrated that τ micro-gradients can acutely trigger platelet aggregation in microfluidic systems.[12, 36, 40, 41] Our investigations of localized platelet density and Ca^{2+} signalling within the micropump-reactor suggest that both platelet distribution and Ca^{2+} activation may be affected by

the extant spatial and temporal τ gradients. Our fluid dynamic investigations in concert with platelet function experiments suggest that modification of micropump diaphragm geometry through altered actuation pressure and changes in pump output and frequency modulation, directly influence localized τ gradients and therefore the overall hemocompatibility of the device. Transient changes in diaphragm geometry in combination with the formation of recirculation zones leads to a relative displacement of platelets to the valve margins during downstroke which may expose them to sharp τ gradients. In addition, centralization of the platelet population during valve upstroke may transiently expose platelets to equivalent τ gradients at centreline flow. Our Ca^{2+} imaging studies showing peak $[Ca^{2+}]_c$ at centreline flow suggests that peak τ transients during valve upstroke may be a major affecter of platelet activation during micropump operation. Significantly, while local Ca^{2+} activation was observed this effect was substantially down-regulated post micropump, suggesting that this platelet activation mechanism may form part of a highly labile mechano-sensing function (independent of the canonical platelet activation pathways). Although outside the scope of the current study, a more detailed investigation of the time-dependency of micropump haemodynamics and platelet function may lead to further insights and modifications of micropump-reactor design. In addition, newer microfabrication approaches to allow for modification of diaphragm surface geometry at a given actuation pressure, by varying the diaphragm thickness, may allow for more precise control of inflated diaphragm shape and therefore local τ gradients, that may further improve overall blood handling performance.

While the complex fluid dynamics observed in our μ-PIV experiments may be a key limiter of overall platelet handling performance, a key benefit of the transient flow recirculation across the micropump valve chambers and the propensity for transient flow reversal is the utility of the micropump as an efficient in-line active reagent-blood mixer. Indeed, our experiments utilizing FITC-PEG species, across a Mw range that models that of small molecule inhibitors and larger Mw anticoagulant species such as high Mw Heparins, demonstrate that homogenous reagent-blood mixing can be achieved rapidly (over a time-frame of approximately ~10.9 secs). This ability to deliver drugs/reagents to blood flow over very short but controllable time-scales is unique and opens the door to the investigation of fast drug pharmacokinetic interactions not currently achievable with existing blood-flow based assay systems. In addition, this characteristic opens the door to rapid on-chip anticoagulant reversal through the introduction of a molar excess of free [Ca^{2+}], greatly expanding the scope of future applications and allowing for the investigation of the impact of haemodynamics and shear rate on coagulation factors.

Due to the peristaltic nature of our micropump-reactor design micropump output is pulsatile. In addition, μ-PIV analysis demonstrates that downstream flow exhibited a pulse frequency reflective of micropump actuation duty cycle. While not having an overt effect on the rate and extent of platelet thrombus formation on type 1 collagen (when compared with a constant flow microcapillary system) the effects of this pulsatile waveform on platelet and blood function in the context

of alternate downstream assays cannot be overlooked. While the functional effects of time varying shear on platelet function are less well described than the constant flow case, several studies suggest that shear rate transients, flow acceleration, and flow deceleration can influence platelet signalling dynamics and therefore platelet aggregation.[24, 25, 42, 43] While outside the scope of the present study, the observed ability to control pulsatile flow with rapid temporal resolution (msec time-scale) the present device may have significant utility in further exploring the effects of time varying haemodynamics on platelet function, primary haemostasis, and thrombosis.

The proof-of-concept drug screening trial described in this study effectively demonstrates the utility of the micropump-reactor to perform as a reliable and rapid preclinical assay system. Direct head to head comparison of this system with an established laminar microcapillary flow assay (well represented in the preclinical platelet literature) demonstrated equivalency, if not superiority, of the micropump-reactor system. Significantly, by integrating drug/reagent delivery on-chip and harnessing the rapid active mixing attributes of the micropump design we were able to achieve drug-blood incubation times ~55-fold shorter than that of the standard assay. Taken together these data demonstrate the potential of the micropump-reactor module for rapid on-chip anti-platelet drug titration and functional blood-flow based assessment of anti-thrombotic potential. Future developments are focused on the incorporation of on-chip drug/reagent titration under independent micropump control, and an

addressable gain-valved control system, facilitating true high-throughput lab-on-chip drug screening functionality.

While a key aim of this study was to apply both computational and experimental measures of fluid dynamics and blood function to better understand the key parameters that affect device operation, these analyses need to be qualified with respect to the underlying simplifications and limitations of both the numerical and experimental approaches used. Due to the complexity of modelling time varying flow our CFD analysis of blood τw was carried out on the micro-pump under conditions where the micropump diaphragms were progressively actuated statically; in order to explore the effects of experimentally defined diaphragm geometries on platelet function. While this analysis showed good agreement between predicted τw and platelet activation under equivalent conditions it must be recognized that the simulations are not directly predictive of dynamic micropump operation. This limitation is reflected in the complex flow behaviour revealed by μ-PIV. Interpretation of theses μ-PIV experiments also needs to be considered with respect to the use of seeding particles in an aqueous medium (not blood), the inability to resolve velocity vectors within close proximity to the microfluidic walls; limiting observation to bulk fluid shear rates, and the use of planar 2-dimensional μ-PIV which limited the observation window to a relatively thin volume at the centre plane. Finally, while we have endeavoured to incorporate a battery of blood based functional assessments to characterize valve performance these assays by no means address all the complex blood functions that may be important for hemocompatibility, such as

effects on soluble plasma proteins and effects on cellular components such as leukocytes and monocytes. In this context, the range and scope of usage of the device needs to take into consideration the specific biochemical, cellular, and hemodynamic requirements of the coupled downstream assay(s).

Current preclinical and clinical platelet function testing can still ostensibly be grouped into biochemical and aggregometry based assays.[45-47] However, despite their wide-spread use, there are several inherent limitations associated with these tests, including that they often require technically demanding plasma and platelet isolation steps, and utilize relatively large volumes of patient blood. A major shortfall of all these tests is that they do not consider the key role of haemodynamics in platelet function; a factor that is specifically relevant to the preclinical development of new more targeted APTs and is critical to clinical bleeding diatheses associated with current APTs, cardiac surgery, platelet function defects such as von Willebrand Disease (VWD), and platelet related thrombosis. We propose that the novel micropump-reactor here described is a significant step towards modular microfluidic rector design that can be applied to the development of more reliable and sensitive, hemodynamically active platelet function assay(s). This component system offers significant flexibility with respect to on-chip automation of blood handling and provides the capacity for high density multiplexed blood circuits for high-content anti-platelet drug screening. Further advancement of this novel system will see the development of a fully resolved blood platelet bioreactor for preclinical and clinical development.

Experimental

Device fabrication and operation.

The main text of the article should appear here with headings as appropriate. Fabrication of micro-pump manifolds was achieved using a previously described method.[48, 49] Micropump diaphragm actuation was driven via a custom external valve driver similar to that described in.[35] The driver utilized micro-solenoid valves to switch between two pneumatic reservoirs held at either negative or positive relative pressures, acting to open or close on-chip valves. The valve driver was interfaced with the microfluidic chip using 40 cm of Tygon (0.8 mm I.D.) tubing, and blunt 21.5 gauge hypodermic needles. The valve driver was connected to a PC to enable scripted control, realized using python scripts.

Blood collection and handling

Ethics approval was obtained from the Alfred Hospital and Monash University Standing Committees on Ethics in Research involving Humans. All experiments were performed in compliance with relevant laws and guidelines and followed Monash Universities policies regarding the handling of human samples. Whole blood samples were obtained from consenting subjects via venesection into 2% w/v citrate. Samples were allowed to rest for 10 min at 37oC prior to device perfusion. Full blood examination was routinely conducted using a Hemogram (Abbott Diagnostics).

Platelet isolation

Washed human platelets were isolated from human whole blood as described previously.[36, 50]

Reconstituted blood

Reconstituted blood was prepared from human whole blood as described.[36, 50] Reconstituted blood consisted of washed platelets in Tyrodes buffer pH 7.2 or autologous PRP with a final haematocrit (Hct) of 40% (except where indicated) and a platelet count of 200 x 10^9/L. Hct and platelet counts were verified by full blood analysis using a Hemogram (Abbott Diagnostics).

FACS analysis

Whole blood samples in 3.2% ACD following perfusion through the micropump-reactor were collected. 5 µL samples from each micro-pump condition were immediately transferred to 12 x 75mm Falcon® capped polystyrene test tubes containing 20 µL CD61 PerCP, 20 µL PAC-1 FITC or 5 µL PE-P selectin conjugated monoclonal antibodies. Tubes containing only one of each antibody were prepared using inactivated blood to act as voltages, tubes containing blood activated with $2x10^{-5}$ M ADP were used for channel compensation, and tubes stained only with CD-61 were used to obtain isotype control forward and side scatter buffers. For all samples containing PAC-1 antibodies, RGDS was also added to the solution to exclude non-specific binding. Data was then analysed in two-colour plots.

Haemolysis Assay

Whole blood samples in 3.2% ACD collected following perfusion through the micropump-reactor were centrifuged at 500 x g for 5 minutes, and the resulting supernatant collected. The supernatant was subsequently centrifuged at 500 x g for 5 minutes, to pellet any intact RBC. 15 µL of each supernatant was then suspended in 185 µL 1% Tyrodes (10 mM Hepes, 12 mM $NaHCO_3$, 137 mM NaCl, 2.7 mM KCl, and 5 mM glucose, pH 7.3) at 35^{o}C. Positive control was made by adding 15 µL of non-haemolyzed haematocrit and 10 µL Triton X-100 to 185 µL of Tyrodes buffer. Negative control consisted of the collected supernatant of an unprocessed sample. 100 µL of each sample was then transferred to a clear, flat-bottomed 96-well plate and absorbance (495 nm) was measured. All samples were normalized with the positive control representing 100% haemolysis.

CFD

Details of the numerical method can be found in [51]. Tetrahedral mesh elements were used for all geometries generated from scanning confocal images of TRITC perfused replicate micropumps statically actuated at 0, 1, 5, and 10 kPa as per [36], with meshes completed in Pointwise (Pointwise, Inc., Fort Worth, Texas, USA), with a total mesh size ranging from 4.96 to 5.42 million elements. A sufficiently long development section at the inlet (>7500 µm, where h is the channel height) was included for the simulations to ensure fully developed flow before test section. The velocity profiles were verified at multiple locations to ensure independence of the stream-wise location. The

incompressible Navier–Stokes equations were solved using the finite volume methodology based on OpenFOAM (OpenCFD, Ltd., ESI group, Bracknell, UK). Blood was modelled as a non-Newtonian fluid using the Quemada equation, to account for the nonlinear stress-strain relationship.[51] The convective and diffusive terms in the governing equations were discretized using the central differencing scheme, and the fully implicit backward scheme was used for the unsteady terms. The Semi-Implicit Method for Pressure-Linked Equations (SIMPLE) method was employed to decouple the pressure term from momentum equation and a convergence criterion of 10^{-6} was used for both velocity and pressure. At the inlet, a constant velocity boundary condition was specified to match to the volumetric flow rate of the experiments (14.6 µL/min), and a zero gradient is applied at the inlet for pressure. At the outlet, a zero gradient is applied to the velocity coupled with a zero pressure.

Micron-Resolution Particle Image Velocimetry

µPIV was carried out at the mid-plane of the micro-pump and collagen channel to measure the velocity field and the resulting. Distilled water seeded with 2µm red fluorescent polystyrene aqueous spherical particles (ThermoFisher Scientific) was perfused through the system. Imaging was performed on a motorised inverted (Ti2, Nikon) microscope equipped with a G-2A filter cube for epifluorescence imaging and a high-speed PCO.dimax HS4 camera (4 Megapixels, 12bit). Fluorescent particles were illuminated using a diode-pumped solid-state laser with a continuous wave output at 532nm (Verdi Family, Coherent). Images in the micropump and collagen channel were captured at

4000Hz and 7000Hz through a 4x and 10x objectives, respectively. The optical magnification for these cases were 2.76 and 1.1 μm/pixel, respectively. 10000 images were captured. Images were calibrated using a micron-sized calibration grid and pre-processed by applying a histogram equalization. PIV vector computation was performed using DAVIS (LaVision, GmbH) using a multi-pass algorithm with grid deformation; final interrogation size = 64x64 pixels.[52] In order to minimize spurious vectors a 5x5 spatial filter and a temporal filter over 10ms was applied to the velocity fields in post-processing. Due to the periodic nature of the pump, the velocity fields were phased-averaged over a pump cycle to enhance the signal-to-noise ratio.

Platelet imaging

Washed platelets (200 x 10^9/L) were loaded with DiOC6 (2ug/mL) for 10 mins at 37^{o}C. Dye-loaded platelets (final platelet count = 200 × 10^9/L) were then reconstituted with isolated RBC prior to perfusion through the device. Platelet adhesion and activation were blocked with theophylline (10 mM) and eptifibatide (Integrilin - 20 μg mL^{-1}). Reconstituted blood samples were run through the micropump at the described actuation pressures and duty cycle. Epifluorescence (488ex/510em) images were acquired at 20 fps (1280x1024) using a Andor Zyla sCMOS camera attached to inverted Nikon TiU microscope (Nikon Plan Fluor 5×/0.50 objective). Images were compiled as maximum z-projections off-line in ImageJ.

Platelet Ca^{2+} assay

Assessment of platelet cytosolic calcium levels $[Ca^{2+}]_c$ was adapted from published methods.[50, 53] Briefly, washed platelets (1×10^9/mL) were loaded with Cal520 (2-aminophenoxy)ethane-N,N,N′,N′-tetraacetic acid tetra(acetoxymethyl)ester (50 µM) (AAT Bioquest) for 30 min at 37°C. Dye-loaded platelets (final platelet count = 200×10^9/L) were then reconstituted with washed red blood cells prior to perfusion through the device. Blood perfusion and platelet $[Ca^{2+}]_c$ dynamics were acquired on an inverted Nikon TiU microscope (Nikon Plan Fluor 60x/0.50 objective) using an Andor Zyla sCMOS camera at 0.586 frames per second. All image analysis was performed off-line in ImageJ. Background corrected fluorescence images were thresholded using Huang's fuzzy image thresholding. The corrected fluorescence values (F) for each cell were converted into pseudo-ratio values by normalizing for Ca^{2+} chelated control platelet flows (Fmin), as described elsewhere.[50] The pseudo-ratio value was calculated as F' = F/Fmin, where Fmin was derived for independent platelet flow experiments in which Cal520 loaded platelets were treated with 50 µM DM-BATPA and resuspended in Tyrodes buffer supplemented with 2 mM EGTA/$MgCl_2$. $[Ca^{2+}]_c$ in nM was derived according to Equation 1.

$$[Ca^{2+}]_c = K_d \times \frac{F'}{(F'max - F')}\ , [K_d = 320\ nM]$$

The maximal pseudo-ratio fluorescence F'max was determined for each set of flow conditions following incubation of washed platelets with 2 µM A23187 in Tyrodes buffer supplemented with 10mM $CaCl_2$. For mean bulk flow $[Ca^{2+}]_c$ defined regions of interest were analysed relative to pump components.

Mixing assay

Mixing capacity was assessed as per [37] through injection of FITC-conjugated, PEG species of M = 350 Da, 2000 Da, and 20 kDa (NANOCS Pty Ltd). Drug pre-injection concentrations were 28.6 µM (350 Da), 5.0 µM (2000 Da), and 0.5 µM (20 kDa). Confocal microscopy was performed at four locations, and incubation times: [1] Drug-port (tmix= 0 sec, d from injection port = 0 µm); [2] Pre-pump (tmix= 1.36 sec, d = 2.1 mm); [3] Post-pump (tmix = 5.09 sec, d = 7.7 mm); [4] Collagen-assay channel (tmix = 36.0 sec, d = 23.6 mm). Assessment of mixing was performed through line-scans of florescence of averaged images from 120 seconds series according to the method published in Stroock et al.[37] In brief, the method involved conducting a z-stack of the average intensity of all images, the background fluorescence was subtracted to demonstrate fluorescent platelet location, and contrast was adjusted. A line scan was performed across the width of the channel to assess fluorescence arising from the DiOC6-labelled platelets. Standard deviations in fluorescence across the channel were calculated in GraphPad Prism to assess mixing homogeneity.

Platelet thrombus assay

24 hours prior to blood sample loading, the microfluidic device was derivatized with purified type 1 collagen (100 µg mL^{-1}; Helena Laboratories), according to previously published methods, to allow for effective platelet capture and adhesion to the glass coverslip surface.[8] Collagen was infused 1400 µm downstream of the micropump assembly, and allowed to physiosorb for 24 Hrs at 4^{o}C, before removal of excess collagen solution and blocking of the

microfluidic with 10% BSA for 10 min at room temperature. Thrombus formation was monitored at 37ºC using a Nikon A1r confocal. Microcapillary collagen experiments were conducted as per [4].

Statistical analysis

Statistical analysis to determine if there was a statistically significant difference between two groups was performed in GraphPad Prism using unpaired two-tailed T-Tests, with the assumption of gaussian distribution. Error bars demonstrated standard deviations in data. Analysis of variance (ANOVA) was performed using SPSS statistics to assess the impact of pumping variables (pressure, frequency) on P-Selectin and PAC-1 binding and Annexin-V expression. An interactions plot was generated using SPSS to determine the impact of frequency and pressure on the markers of platelet activation. Analysis of the statistical effect of frequency and pressure on flow rate and on hemolysis was assessed separately through univariate analysis. Finally, a univariate analysis was performed to determine the impact of flow rate on activation markers. All variables were coded as continuous. Continuous results were assumed to have a normal distribution (using a normal probability plot), linearity (using a residual plot) and constant variability (using a scatter plot).

Conclusions

In both the preclinical and clinical settings the ideal platelet function test should: detect baseline platelet hypo- and hyperactivity; allow for rapid screening of both antiplatelet and pro-aggregatory agents; facilitate anticoagulant reversal; an predict thrombotic and bleeding risk.[44] The described micropump-reactor

module, while limited in application to a relatively simple downstream platelet function assay, has the potential to be coupled to any assay subsystem that requires controlled hemocompatible blood delivery and rapid mixing control. In effect this system could be coupled to any microfluidic circuit and blood assay system, such as a biphotonic sensor for blood biomarker detection, or our previously described strain rate gradient device.[13]

Conflicts of interest

There are no conflicts to declare.

Acknowledgements

We would like to acknowledge Prof. Robert Andrews, Dr. Francisco Tovar-Lopez, and Mr. Stephen Cody for helpful discussions and technical advice. We thank the staff and students at the Australian Centre for Blood Diseases for help with blood collection. The authors acknowledge the facilities, and technical assistance of Monash Micro Imaging (MMI), Monash University, and The Department of Haematology, Alfred Hospital. Devices were fabricated at the Micro Nano Research Facility (MNRF), RMIT University. RJB is a recipient of an Australian Research Training Program Scholarship. CS is a recipient of a Professor Robert and Josephine Shanks Scholarship. WSN is a recipient of an RMIT Vice Chancellor's Senior Research Fellowship.

References

1. Zwaginga, J.; Sakariassen, K.; Nash, G.; King, M.; Heemskerk, J.; Frojmovic, M.; Hoylaerts, M.; ISTH, B. S. o. t. S. o. t., Journal of Thrombosis and Haemostasis 2006, 4 (12), 2716-2717.
2. Zwaginga, J.; Sakariassen, K.; King, M.; Diacovo, T.; Grabowski, E.; Nash, G.; Hoylaerts, M.; Heemskerk, J.; ISTH, B. S. o. t. S. o. t., Journal of Thrombosis and Haemostasis 2007, 5 (12), 2547-2549.
3. Kulkarni, S.; Nesbitt, W. S.; Dopheide, S. M.; Hughan, S. C.; Harper, I. S.; Jackson, S. P., Methods Mol Biol 2004, 272, 165-86. DOI 10.1385/1-59259-782-3:165.
4. Maxwell, M. J.; Westein, E.; Nesbitt, W. S.; Giuliano, S.; Dopheide, S. M.; Jackson, S. P., Blood 2007, 109 (2), 566-76. DOI 10.1182/blood-2006-07-028282.
5. Nesbitt, W. S.; Giuliano, S.; Kulkarni, S.; Dopheide, S. M.; Harper, I. S.; Jackson, S. P., J Cell Biol 2003, 160 (7), 1151-61. DOI 10.1083/jcb.200207119.
6. Savage, B.; Saldivar, E.; Ruggeri, Z. M., Cell 1996, 84 (2), 289-97.
7. Jackson, S. P.; Schoenwaelder, S. M.; Goncalves, I.; Nesbitt, W. S.; Yap, C. L.; Wright, C. E.; Kenche, V.; Anderson, K. E.; Dopheide, S. M.; Yuan, Y.; Sturgeon, S. A.; Prabaharan, H.; Thompson, P. E.; Smith, G. D.; Shepherd, P. R.; Daniele, N.; Kulkarni, S.; Abbott, B.; Saylik, D.; Jones, C.; Lu, L.; Giuliano, S.; Hughan, S. C.; Angus, J. A.; Robertson, A. D.; Salem, H. H., Nat Med 2005, 11 (5), 507-14. DOI 10.1038/nm1232.

8. Kulkarni, S.; Dopheide, S. M.; Yap, C. L.; Ravanat, C.; Freund, M.; Mangin, P.; Heel, K. A.; Street, A.; Harper, I. S.; Lanza, F.; Jackson, S. P., J Clin Invest 2000, 105 (6), 783-91. DOI 10.1172/JCI7569.
9. Mountford, J. K.; Petitjean, C.; Putra, H. W.; McCafferty, J. A.; Setiabakti, N. M.; Lee, H.; Tonnesen, L. L.; McFadyen, J. D.; Schoenwaelder, S. M.; Eckly, A.; Gachet, C.; Ellis, S.; Voss, A. K.; Dickins, R. A.; Hamilton, J. R.; Jackson, S. P., Nat Commun 2015, 6, 6535. DOI 10.1038/ncomms7535.
10. Brouns, S. L. N.; van Geffen, J. P.; Heemskerk, J. W. M., Platelets 2018, 1-8. DOI 10.1080/09537104.2018.1447660.
11. Tovar-Lopez, F. J.; Rosengarten, G.; Westein, E.; Khoshmanesh, K.; Jackson, S. P.; Mitchell, A.; Nesbitt, W. S., Lab Chip 2010, 10 (3), 291-302. DOI 10.1039/b916757a.
12. Brazilek, R. J.; Tovar-Lopez, F. J.; Wong, A. K.; Tran, H.; Davis, A. S.; McFadyen, J. D.; Kaplan, Z.; Chunilal, S.; Jackson, S. P.; Nandurkar, H., Lab on a Chip 2017, 17 (15), 2595-2608.
13. Colace, T. V.; Jobson, J.; Diamond, S. L., Bioconjug Chem 2011, 22 (10), 2104-9. DOI 10.1021/bc200326v.
14. Li, R.; Fries, S.; Li, X.; Grosser, T.; Diamond, S. L., Clin Chem 2013, 59 (8), 1195-204. DOI 10.1373/clinchem.2012.198101.
15. Li, R.; Grosser, T.; Diamond, S. L., Platelets 2017, 28 (5), 457-462. DOI 10.1080/09537104.2016.1268254.
16. Neeves, K. B.; Maloney, S. F.; Fong, K. P.; Schmaier, A. A.; Kahn, M. L.; Brass, L. F.; Diamond, S. L., J Thromb Haemost 2008, 6 (12), 2193-201. DOI 10.1111/j.1538-7836.2008.03188.x.

17. Ogawa, S.; Ohnishi, T.; Hosokawa, K.; Szlam, F.; Chen, E. P.; Tanaka, K. A., British journal of anaesthesia 2013, 111 (6), 1013-23. DOI 10.1093/bja/aet229.
18. Arima, Y.; Kaikita, K.; Ishii, M.; Ito, M.; Sueta, D.; Oimatsu, Y.; Sakamoto, K.; Tsujita, K.; Kojima, S.; Nakagawa, K.; Hokimoto, S.; Ogawa, H., J Thromb Haemost 2016, 14 (4), 850-9. DOI 10.1111/jth.13256.
19. Herbig, B. A.; Yu, X.; Diamond, S. L., Biomicrofluidics 2018, 12 (4), 042201.
20. Jain, A.; Graveline, A.; Waterhouse, A.; Vernet, A.; Flaumenhaft, R.; Ingber, D. E., Nature communications 2016, 7, 10176.
21. Schoeman, R. M.; Rana, K.; Danes, N.; Lehmann, M.; Di Paola, J. A.; Fogelson, A. L.; Leiderman, K.; Neeves, K. B., Cell Mol Bioeng 2017, 10 (1), 3-15. DOI 10.1007/s12195-016-0469-0.
22. Kim, J.; Taylor, D.; Agrawal, N.; Wang, H.; Kim, H.; Han, A.; Rege, K.; Jayaraman, A., Lab Chip 2012, 12 (10), 1813-22. DOI 10.1039/c2lc21202a.
23. Goncalves, I.; Nesbitt, W. S.; Yuan, Y.; Jackson, S. P., J Biol Chem 2005, 280 (15), 15430-7. DOI 10.1074/jbc.M410235200.
24. Nesbitt, W. S.; Westein, E.; Tovar-Lopez, F. J.; Tolouei, E.; Mitchell, A.; Fu, J.; Carberry, J.; Fouras, A.; Jackson, S. P., Nat Med 2009, 15 (6), 665-73. DOI 10.1038/nm.1955.
25. Ruggeri, Z. M., Thromb Haemost 1993, 70 (1), 119-23.
26. Ruggeri, Z. M.; Orje, J. N.; Habermann, R.; Federici, A. B.; Reininger, A. J., Blood 2006, 108 (6), 1903-10. DOI 10.1182/blood-2006-04-011551.
27. Gutierrez, E.; Petrich, B. G.; Shattil, S. J.; Ginsberg, M. H.; Groisman, A.; Kasirer-Friede, A., Lab Chip 2008, 8 (9), 1486-95. DOI 10.1039/b804795b.

28. Thon, J. N.; Mazutis, L.; Wu, S.; Sylman, J. L.; Ehrlicher, A.; Machlus, K. R.; Feng, Q.; Lu, S.; Lanza, R.; Neeves, K. B.; Weitz, D. A.; Italiano, J. E., Jr., Blood 2014, 124 (12), 1857-67.
29. Nowak, A. A.; Harris, D. N.; Laffan, M.; Millar, C., Blood 2012, 120 (21), 2171-2171.
30. Jensen, E. C.; Stockton, A. M.; Chiesl, T. N.; Kim, J.; Bera, A.; Mathies, R. A., Lab Chip 2013, 13 (2), 288-96. DOI 10.1039/c2lc40861a.
31. Au, A. K.; Lai, H.; Utela, B. R.; Folch, A., Micromachines 2011, 2 (2), 179-220.
32. Kim, J.; Kang, M.; Jensen, E. C.; Mathies, R. A., Anal Chem 2012, 84 (4), 2067-71. DOI 10.1021/ac202934x.
33. Unger, M. A.; Chou, H.-P.; Thorsen, T.; Scherer, A.; Quake, S. R., Science 2000, 288 (5463), 113-116.
34. Li, B.; Li, L.; Guan, A.; Dong, Q.; Ruan, K.; Hu, R.; Li, Z., Lab Chip 2014, 14 (20), 4085-92. DOI 10.1039/c4lc00227j.
35. Szydzik, C.; Brazilek, R. J.; Khoshmanesh, K.; Akbaridoust, F.; Knoerzer, M.; Thurgood, P.; Muir, I.; Marusic, I.; Nandurkar, H.; Mitchell, A.; Nesbitt, W. S., Lab Chip 2018, 18 (12), 1778-1792. DOI 10.1039/c7lc01320e.
36. Stroock, A. D.; Dertinger, S. K. W.; Ajdari, A.; Mezić, I.; Stone, H. A.; Whitesides, G. M., Science 2002, 295 (5555), 647-651. DOI 10.1126/science.1066238.
37. Yap, C. L.; Anderson, K. E.; Hughan, S. C.; Dopheide, S. M.; Salem, H. H.; Jackson, S. P., Blood 2002, 99 (1), 151-158. DOI 10.1182/blood.V99.1.151.

38. Gilio, K.; Munnix, I. C. A.; Mangin, P.; Cosemans, J. M. E. M.; Feijge, M. A. H.; van der Meijden, P. E. J.; Olieslagers, S.; Chrzanowska-Wodnicka, M. B.; Lillian, R.; Schoenwaelder, S.; Koyasu, S.; Sage, S. O.; Jackson, S. P.; Heemskerk, J. W. M., Journal of Biological Chemistry 2009, 284 (49), 33750-33762. DOI 10.1074/jbc.M109.048439.
39. Brazilek, R. J.; Tovar-Lopez, F. J.; Wong, A. K. T.; Tran, H.; Davis, A. S.; McFadyen, J. D.; Kaplan, Z.; Chunilal, S.; Jackson, S. P.; Nandurkar, H.; Mitchell, A.; Nesbitt, W. S., Lab on a chip 2017. DOI 10.1039/C7LC00498B.
40. Nesbitt, W. S.; Westein, E.; Tovar-Lopez, F. J.; Tolouei, E.; Mitchell, A.; Fu, J.; Carberry, J.; Fouras, A.; Jackson, S. P., Nat Med 2009, 15 (6), 665-673.
41. Sheriff, J.; Bluestein, D.; Girdhar, G.; Jesty, J., Annals of biomedical engineering 2010, 38 (4), 1442-1450. DOI 10.1007/s10439-010-9936-2.
42. Shankaran, H.; Alexandridis, P.; Neelamegham, S., Blood 2003, 101 (7), 2637-45. DOI 10.1182/blood-2002-05-1550.
43. Gorog, D. A.; Fuster, V., Journal of the American College of Cardiology 2013, 61 (21), 2115-29. DOI 10.1016/j.jacc.2012.11.080
44. Michelson, A. D., Circulation 2004, 110 (19), e489-93. DOI 10.1161/01.CIR.0000147228.29325.F9.
45. Sambu, N.; Curzen, N., British journal of clinical pharmacology 2011, 72 (4), 683-96. DOI 10.1111/j.1365-2125.2011.03955.x.
46. Szydzik, C.; Brazilek, R. J.; Khoshmanesh, K.; Akbaridoust, F.; Knoerzer, M.; Thurgood, P.; Muir, I.; Marusic, I.; Nandurkar, H.; Mitchell, A., Lab on a Chip 2018.

47. Szydzik, C.; Niego, B.; Dalzell, G.; Knoerzer, M.; Ball, F.; Nesbitt, W.; Medcalf, R.; Khoshmanesh, K.; Mitchell, A., RSC Advances 2016, 6 (91), 87988-87994.
48. Nesbitt, W. S.; Harper, I. S.; Schoenwaelder, S. M.; Yuan, Y.; Jackson, S. P., Methods Mol Biol 2012, 788, 73-89. DOI 10.1007/978-1-61779-307-3_6.
49. Poon, E. K. W.; Thondapu, V.; Hayat, U.; Barlis, P.; Yap, C. Y.; Kuo, P. H.; Wang, Q.; Ma, J.; Zhu, S. J.; Moore, S.; Ooi, A. S. H., Journal of biomechanical engineering 2018, 140 (5). DOI 10.1115/1.4039306.
50. Scarano, F., Measurement Science and Technology 2002, 13 (1), R1.
51. Heemskerk, J. W.; George, M.; Rook, M. B.; Sage, S. O., The Journal of physiology 2001, 535 (3), 625-635

4.4 'A Scalable Micropump-reactor for Rapid Hemodynamically Controlled Platelet Function Testing' - supplemental information

A Scalable Micropump-reactor for Rapid Hemodynamically Controlled Platelet Function Testing

Rose J. Brazilek, Crispin Szydzik, Farzan Akbaridoust, Charitha de Silva, Markus Knoerzer, Leon Chan, Eric K. W. Poon, Andrew S. H. Ooi, Ivan Marusic, Justin R. Hamilton, Harshal H. Nandurkar, Arnan Mitchell, and Warwick S. Nesbitt

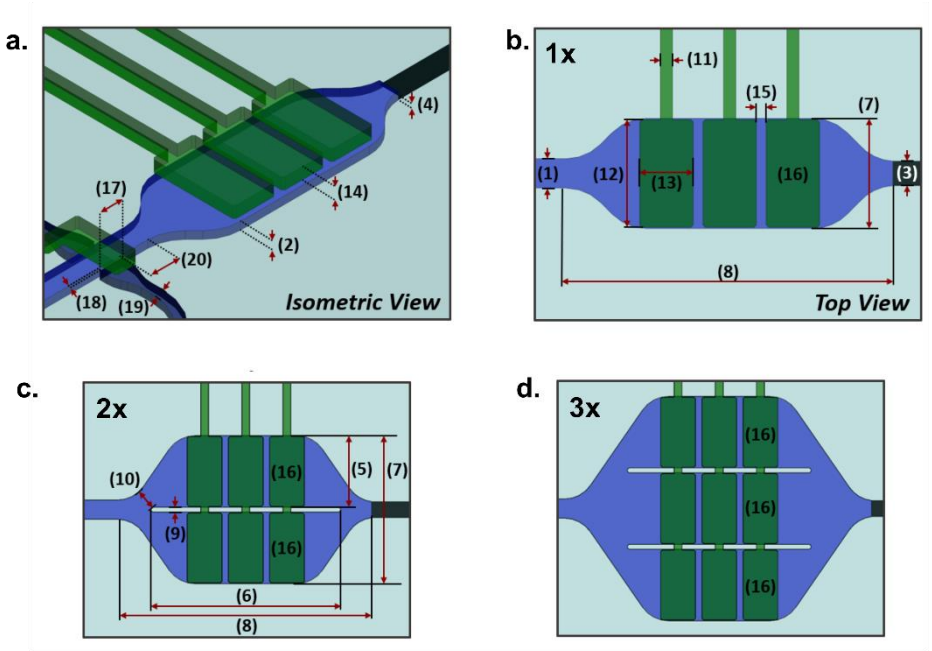

Figure S1. Multi micropump architectures
a. Isometric view of a single 2.4 mm^2 pump unit, showing the inlet, outlet, actuation channels and bilateral drug gate valves. **b.** Top-down view of single 2.4 mm^2 pump unit, excluding drug gates, for comparison with multiplexed variants of the same pump unit. **c**. 4.8 mm mm^2 duel (2x) multiplexed pump. This pump is essentially two of the single units combined with a dividing baffle and minimally spaces inlet and outlet. **d.** 7.2 triple (3x) multiplexed pump, combining three pump units.

Micropump and micropump-reactor dimensions						
		0.26	**0.41**	**2.4**	**4.8 [MP]**	**7.2 [MP]**
# (1)	***Pump chamber inlet width [μm]***	300	500	600	600	600
# (2)	***Pump chamber inlet height [μm]***	100	100	100	100	100
# (3)	***Pump chamber outlet width [μm]***	300	500	500	500	500
# (4)	***Pump chamber outlet height [μm]***	100	100	100	100	100
# (5)	***Individual pump unit width [mm]***	0.300	0.500	2.25	2.25	2.25
# (6)	***Individual pump unit length [mm]***	2.75	2.75	6.72	6.00	5.80
# (7)	***Pump chamber width [mm]***	0.300	0.500	2.25	4.65	7.01
# (8)	***Pump chamber length [mm]***	2.75	2.75	6.72	8.03	9.70
# (9)	***Baffle width [μm]***	NA	NA	NA	150	150
# (10)	***Bypass channel width [μm]***	NA	NA	NA	600	600
# (11)	***Pneumatic control line width [μm]***	NA	"	"	"	"
# (12)	***Individual actuation chamber width [mm]***	0.350	0.450	2.2	2.2	2.2
# (13)	***Individual actuation chamber length [mm]***	0.750	0.750	1.1	1.1	1.1
# (14)	***Individual actuation chamber height [μm]***	150	"	"	"	"
# (15)	***Actuation chamber spacing [μm]***	200	"	"	"	"
# (16)	***Number of multiplexed pumps***	1	1	1	2	3
# (17)	***Drug gate length [μm]***	NA	NA	600	NA	NA
# (18)	***Drug gate width [μm]***	NA	NA	75	NA	NA
# (19)	***Drug channel width [μm]***	NA	NA	250	NA	NA
# (20)	***Drug channel - distance from pump inlet [μm]***	NA	NA	750	NA	NA
# (21)	***Reservoir diameter [mm]***	5	"	"	"	"
# (22)	***Reservoir volume [μ?]***	~100	"	"	"	"
# (23)	***Device length [mm]***	35	35	50	50	50
# (24)	***Device width[mm]***	20	"	"	"	"
# (25)	***PDMS interface slab height [mm]***	~5	"	"	"	"

Table S1. Micropump and micropump-reactor dimensions. MP = Mulit-pump

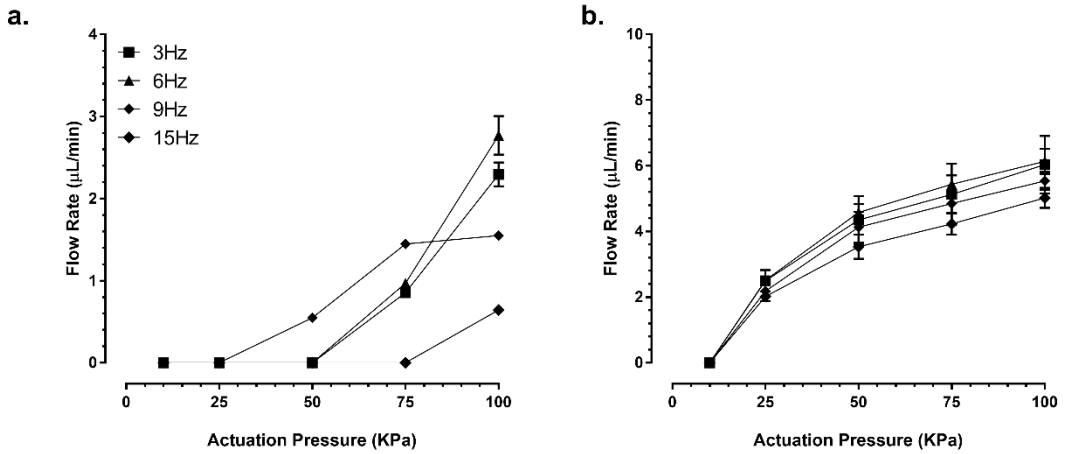

Figure S2. Micropump mechanical performance
a. 0.26/50-micropump flow rate (µL/min) output for citrated human whole blood as a function of actuation pressure (kPa) and duty cycle (Hz). **b.** 0.41/50-micropump flow rate (µL/min) output for citrated human whole blood as a function of actuation pressure (kPa) and duty cycle (Hz). Each data set represents n = 3 independent experiments.

Source	Type III Sum of Squares	df	Mean Square	F	Sig.	Partial Eta Squared	Noncent. Parameter	Observed Power[b]
Corrected Model	12012.130[a]	19	632.217	485.466	.000	.996	9223.862	1.000
Intercept	30433.939	1	30433.939	23369.581	.000	.998	23369.581	1.000
Frequency	1739.519	4	434.880	333.935	.000	.971	1335.740	1.000
Pressure	8652.048	3	2884.016	2214.575	.000	.994	6643.726	1.000
Frequency * Pressure	1620.563	12	135.047	103.700	.000	.969	1244.396	1.000
Error	52.092	40	1.302					
Total	42498.160	60						
Corrected Total	12064.221	59						

a. R^2 = .996 (Adjusted R^2 = .994)

b. Computed using alpha = .05

Table S2. Univariate analysis (Tests of Between-Subjects Effects) of the impact of pressure and frequency on flow rate.

Effect		Value	F	Hypothesis df	Error df	Sig.	Partial Eta Squared	Noncent. Parameter	Observed Power[d]
Intercept	Pillai's Trace	.998	6554.012[b]	3.000	38.000	.000	.998	19662.036	1.000
	Wilks' Lambda	.002	6554.012[b]	3.000	38.000	.000	.998	19662.036	1.000
	Hotelling's Trace	517.422	6554.012[b]	3.000	38.000	.000	.998	19662.036	1.000
	Roy's Largest Root	517.422	6554.012[b]	3.000	38.000	.000	.998	19662.036	1.000
Frequency	Pillai's Trace	2.197	27.361	12.000	120.000	.000	.732	328.328	1.000
	Wilks' Lambda	.004	57.665	12.000	100.830	.000	.838	520.638	1.000
	Hotelling's Trace	37.037	113.168	12.000	110.000	.000	.925	1358.021	1.000
	Roy's Largest Root	33.832	338.322 c	4.000	40.000	.000	.971	1353.287	1.000
Pressure	Pillai's Trace	1.087	7.576	9.000	120.000	.000	.362	68.182	1.000
	Wilks' Lambda	.036	30.226	9.000	92.633	.000	.671	188.921	1.000
	Hotelling's Trace	23.710	96.597	9.000	110.000	.000	.888	869.374	1.000
	Roy's Largest Root	23.570	314.273 c	3.000	40.000	.000	.959	942.818	1.000
Frequency * Pressure	Pillai's Trace	.899	1.427	36.000	120.000	.080	.300	51.380	.973
	Wilks' Lambda	.334	1.413	36.000	113.003	.088	.307	49.947	.966
	Hotelling's Trace	1.367	1.393	36.000	110.000	.098	.313	50.134	.966
	Roy's Largest Root	.696	2.319 c	12.000	40.000	.023	.410	27.827	.899

a. Design: Intercept + Frequency + Pressure + Frequency * Pressure

b. Exact statistic

c. The statistic is an upper bound on F that yields a lower bound on the significance level.

d. Computed using alpha = .05

Table S3. Multivariate analysis of the impact of pressure and frequency on PAC-1, P-selectin and Annexin-V binding.

Source	Type III Sum of Squares	df	Mean Square	F	Sig.	Partial Eta Squared	Noncent. Parameter	Observed Power[b]
Corrected Model	.034[a]	19	.002	4.651	.000	.688	88.375	1.000
Intercept	3.052	1	3.052	7916.581	.000	.995	7916.581	1.000
Pressure	.013	3	.004	11.129	.000	.455	33.386	.998
Frequency	.019	4	.005	12.107	.000	.548	48.426	1.000
Pressure * Frequency	.003	12	.000	.547	.870	.141	6.563	.255
Error	.015	40	.000					
Total	3.102	60						
Corrected Total	.049	59						

a. R^2 = .688 (Adjusted R^2 = .540)

b. Computed using alpha = .05

Table S4 Univariate analysis (Tests of Between-Subjects Effects) of the impact of pressure and frequency on haemolysis rates.

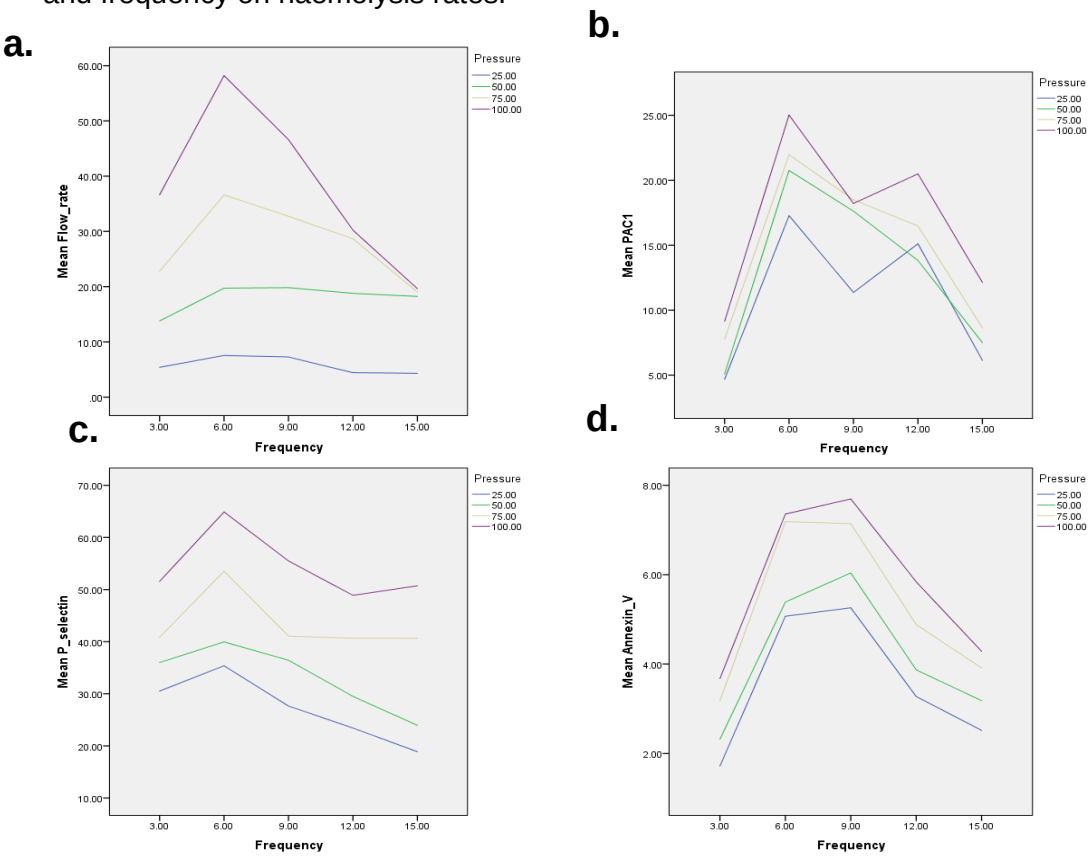

Figure S3
a. Interaction plot demonstrating the relationship between pressure, frequency and flow rate. **b.** Interaction plot demonstrating the relationship between pressure, frequency and PAC-1 expression. **c.** Interaction plot demonstrating the relationship between pressure, frequency and P-selectin expression. **d.** Interaction plot demonstrating the relationship between pressure, frequency and Annexin-V binding.

Chapter five: Investigation of the impact of spatial haemodynamic gradients on platelet function

5.1 Introduction

There is no current clinically available platelet function analyser that assess platelet function under physiologically relevant haemodynamic and rheological conditions. Blood reactivity differs markedly in static and dynamic systems, and the degree of shear distinctly alters receptor activation profiles.(1) Early experiments in our group demonstrated a relationship between localised flow changes and platelet aggregation in a murine stenosis/injury model.(1) In these experiments, stenosis in the presence of vessel wall puncture (subendothelial exposure) markedly accelerated the rate and extent of platelet aggregation. Importantly, these studies demonstrated the novel phenomenon that platelet capture and subsequent thrombus growth could occur independently of soluble agonist signaling, and could instead be driven by vWF engagement with GPIb/V/IX and integrin $\alpha_{IIb}\beta_3$ platelet receptors in areas of high shear. The degree of aggregation in these mimics of in-vivo stenoses could be assessed and correlated with known populations to determine individual aggregation propensity. The published paper in this chapter 5.2 details a pilot study of the capacity of these microstenotic channels to differentiate between healthy controls and those with the shear-defendant aggregation defect vWD.(2)

Studies into healthy donors and those with vWD demonstrated that aggregation in the device was shear-dependent and was initiated at the point of greatest shear within the stenosis. Similar investigations into haemocompatible valving in chapter 3 demonstrated that when comparing aggregation propensities of the straight valve and V-shaped valve, the straight valve had larger aggregates, despite a similar peak shear. Comparable conclusions were made in chapter 4, wherein it was shown that a faster

frequency of pump cycling (and thus, greater rate of change) correlated with greater platelet activation (as measured by flow cytometry markers and platelet intracellular calcium signaling).These findings therefore brought into question whether the stenotic geometry could be further optimised to have greater discriminatory power to differentiate between samples, particularly in borderline cases of vWD. The second part of this chapter demonstrates a small proof-of-concept study that aimed to preliminarily determine which element of the stenotic geometry promoted platelet aggregation and thrombus formation. Four key parameters may be altered in the microcontraction geometries: i. rate of flow acceleration, ii. peak shear stress, iii. duration at peak shear, and iv. flow deceleration.(1) Notably, the major difference between the straight and V-shaped valves from a haemodynamics perspective was the rate of flow acceleration, which was much higher in the straight valve. Additionally, the degree of aggregation was greater in the smaller valves, in which the rate of change was also greater. Therefore, a preliminary study of the direct impact of shear flow acceleration and extensional flow on platelet activation and function in the microcontraction devices was performed in chapters 5.4 – 5.6.

The diagnostic discriminative efficacy of this device has also been tested in PI3KC2α knock-down mice, and in the testing of novel anti-platelet therapies (*see appendices 4 and 5*. Ethics approval for the pilot study is provided in appendix 2. The patient consent form can be found in appendix 3. Supplemental information for the study '*Application of a strain rate gradient microfluidic device to von Willebrand's disease screening*' is included in chapter 5.3.

5.2 Application of a strain rate gradient microfluidic device to von Willebrand's disease screening

Lab on a Chip

PAPER

View Article Online
View Journal | View Issue

Cite this: Lab Chip, 2017, 17, 2595

Application of a strain rate gradient microfluidic device to von Willebrand's disease screening†

Rose J. Brazilek,[a] Francisco J. Tovar-Lopez,[ab] Angus K. T. Wong,[a] Huyen Tran,[ac] Amanda S. Davis,[c] James D. McFadyen,[c] Zane Kaplan,[ac] Sanjeev Chunilal,[e] Shaun P. Jackson,[d] Harshal Nandurkar,[ac] Arnan Mitchell[b] and Warwick S. Nesbitt*[ab]

Von Willebrand's disease (VWD) is the most common inherited bleeding disorder caused by either quantitative or qualitative defects of von Willebrand factor (VWF). Current tests for VWD require relatively large blood volumes, have low throughput, are time-consuming, and do not incorporate the physiologically relevant effects of haemodynamic forces. We developed a microfluidic device incorporating micro-contractions that harnesses well-defined haemodynamic strain gradients to initiate platelet aggregation in citrated whole blood. The microchannel architecture has been specifically designed to allow for continuous real-time imaging of platelet aggregation dynamics. Subjects aged ≥18 years with previously diagnosed VWD or who presented for evaluation of a bleeding disorder, where the possible diagnosis included VWD, were tested. Samples were obtained for device characterization as well as for pathology-based testing. Platelet aggregation in the microfluidic device is independent of platelet amplification loops but dependent on low-level platelet activation, GPIb/IX/V and integrin $\alpha_{IIb}\beta_3$ engagement. Microfluidic output directly correlates with VWF antigen levels and is able to sensitively detect aggregation defects associated with VWD subtypes. Testing demonstrated a strong correlation with standard clinical laboratory-based tests. Head-to-head comparison with PFA100® demonstrated equivalent, if not improved, sensitivity for screening aggregation defects associated with VWD. This strain rate gradient microfluidic prototype has the potential to be a clinically useful, rapid and high throughput-screening tool for VWD as well as other strain-dependent platelet disorders. In addition, the microfluidic device represents a novel approach to examine the effects of high magnitude/short duration (ms) strain rate gradients on platelet function.

Received 9th May 2017,
Accepted 21st June 2017

DOI: 10.1039/c7lc00498b

rsc.li/loc

Introduction

Von Willebrand's disease (VWD) is the most common inherited bleeding disorder, occurring with equal frequency among men and women, and affects up to 1% of the general population.[1–3] VWD is characterized by either quantitative (types 1 and 3) or qualitative (type 2) defects of von Willebrand factor (VWF).[4] VWD predominantly presents itself as mucocutaneous bleeding, however it can manifest as a severe bleeding diathesis following surgery, obstetric interventions or trauma.[5] Given the frequency of VWD, clinicians are often confronted by clinical uncertainty when undiagnosed patients present it in emergency settings.[6] In particular, the ability of current pathology-based tests to identify borderline defects in type 1 VWD patients is poor.[7] Currently, there is no screen with sufficient sensitivity to rapidly assess these patients.[8]

Current best practice testing for VWD includes VWF antigen analysis (VWF:Ag) and functional assays assessing platelet-VWF binding interactions [VWF collagen binding assay (VWF:CB) and VWF ristocetin cofactor assay (VWF:RCo)].[9] VWF multimer analysis, factor testing and genetic screening may also be undertaken.[10–12] These tests are limited by the fact that they are relatively labor-intensive, have relatively long turnaround times, and are often restricted to specialized laboratories.[11]

Platelet function tests (PFT) can be broadly grouped into biochemical and aggregometry-based assays. Biochemical markers include platelet surface P-selectin and vasodilator-stimulated phosphoprotein phosphorylation (VASP) measured

[a]The Australian Centre for Blood Diseases, Monash University, Alfred Medical Research and Educational Precinct, Melbourne, Victoria, Australia
[b]Microplatforms Research Group, School of Engineering, RMIT University, Melbourne, Victoria, Australia. E-mail: warwick.nesbitt@rmit.edu.au
[c]Department of Clinical Hematology, The Alfred Hospital, Melbourne, Victoria, Australia
[d]Heart Research Institute, Newtown, Sydney, NSW, Australia
[e]Haematology Department, Monash Health, Clayton, Australia
† Electronic supplementary information (ESI) available. See DOI: 10.1039/

by flow cytometry and thromboxane metabolites measured by immunoassay or mass spectrometry.[13,14] Platelet aggregometry techniques include turbidimetric and impedance aggregometry, such as the Verify-Now® and Plateletworks® systems.[15,16] There are a variety of inherent issues associated with these tests, including the requirement of technically demanding blood fractionation steps and utilization of relatively large volumes of patient blood.[17–19] Significantly, a major shortfall of many of these tests is that they do not take into account the critical role of blood flow (hemodynamic forces and gradients) in hemostasis, a factor that is specifically relevant to bleeding associated with cardiac surgery, left ventricular assist devices (LVAD), and platelet function disorders such as VWD.[20]

VWF function is critically dependent on the mechanical and adhesion receptor level effects of the prevailing hemodynamic environment.[21,22] Given this hemodynamic dependency, the International Society on Thrombosis and Hemostasis (ISTH – Biorheology SSC) recommended the development and inclusion of blood flow-incorporating assays for the detection of VWD and platelet function disorders.[19,23] The ISTH highlighted the critical need for a simple and reliable flow-based platelet diagnostic test that can accurately assess blood platelet function.[24,25] According to these recommendations, the ideal test should be simple to use, require small amounts of whole blood, and incorporate the mechanical effects of physiological blood flow.[24,25]

The nearest approximation to a flow-based assay, Siemens PFA-100/200®, is marketed as a useful global screen of platelet function and antiplatelet therapy efficacy.[26,27] However, a key limitation of the PFA-100/200® is that platelet activation is elicited by exposure of platelets to exogenous agonists, collagen, ADP or epinephrine immobilized on a solid support, rather than relying on endogenous, strain-dependent platelet secretion and adhesion mechanisms. Therefore, the PFA-100/ 200® does not fully recapitulate the synergy between mechanical and chemical drivers of strain-dependent platelet function.[27,28]

The growing application of microfluidic technologies to experimental platelet assay development provides a unique opportunity for miniaturized, flow-based, platelet diagnostic systems.[3,29–31] We describe the further development and application of a microfluidic device that exposes whole blood to precisely controlled strain rate gradients, over a millisecond time-scale, triggering focused, VWF-dependent platelet aggregation. We present detailed device characterization and a proof-of-concept clinical study demonstrating the efficacy of this device as a rapid sensitive screen for the identification of platelet aggregation defects associated with VWD and monitoring of associated clinical therapies.

Materials and methods

Device description

The device consisted of a polydimethylsiloxane (Sylgard 184® – PDMS) microfluidic flow cell composed of four replicate parallel rectangular microchannels with an aspect ratio of 2: 1. Independent microchannels were composed of a 6 mm diameter reservoir [1], a downstream sample filtration/mixing element [2], a 600 μm long and 200 μm wide entry segment [3], an "active" strain rate element consisting of symmetric steps, 15 μm in length, with an inter-step gap of 40 μm, with side-wall entry and exit angles of 80°, designed to subject blood platelets to a defined rate and amplitude of hemodynamic strain, and a 20 mm long and 200 μm wide exhaust port [4] connected to an external Harvard Apparatus PHD syringe driver (Fig. 1a and b).

Microfluidic device fabrication/functionalization

The microfluidic device was fabricated from PDMS using high-resolution chrome masks and established soft photolithography methods.[30,31] The PDMS channels were allowed to passively adhere to ethanol/HCl-washed #1 borosilicate coverslips that formed the bottom channel wall and also acted as the imaging window. 10 min prior to blood sample loading, the microfluidic device was derivatized with purified human VWF (100 μg ml^{-1}) isolated from BioState® (CSL Ltd), according to previously published methods, to allow for effective platelet capture and adhesion to the PDMS surface.[32] VWF was introduced via manual aspiration at the 1 mm exhaust port [4] (Fig. 1a) up to and including the strain rate geometry and allowed to physisorb for 10 min at room temperature, before being aspirated via the same port. The chips were subsequently perfused with bovine serum albumin (BSA – 10 μg ml^{-1}) via the sample-loading reservoir at Q = 45 μl min^{-1} for 10 min in order to passivate all non-VWF-coated upstream segments and the underlying coverslip. In this way, VWF-specific platelet adhesion was focused at the active strain geometry surface only.

Blood sample preparation

Ethics approval was obtained from the Alfred Hospital and Monash University Standing Committees on Ethics in Research involving Humans. Citrated whole blood samples were obtained from consenting subjects via venesection into citrate Vacutainers® (Becton Dickinson) according to the manufacturer's instructions. Preliminary investigation demonstrated no significant difference between citrate and the direct thrombin inhibitor lepirudin (80 U ml^{-1}) as an anticoagulant (Fig. S1†). Samples were allowed to rest for 10 min at 37 °C and subsequently incubated with the lipophilic membrane dye $DiOC_6$ (1 μg ml^{-1}) (Molecular Probes) for 10 min at 37 °C prior to device perfusion. Except where indicated blood samples were routinely treated with blockers of platelet amplification loops (ALB) in order to minimize the masking effects of soluble agonist-driven platelet activation on VWF-dependent mechanisms. In the case of platelet amplification loop blockade (ALB), blood samples were incubated for 10 min with indomethacin (10 μM) to block TXA_2 generation, 2-MeSAMP (10 μM) to block $P2Y_{12}$-dependent signaling and MRS2179 (100 μM) to block $P2Y_1$-dependent signaling.[33–35]

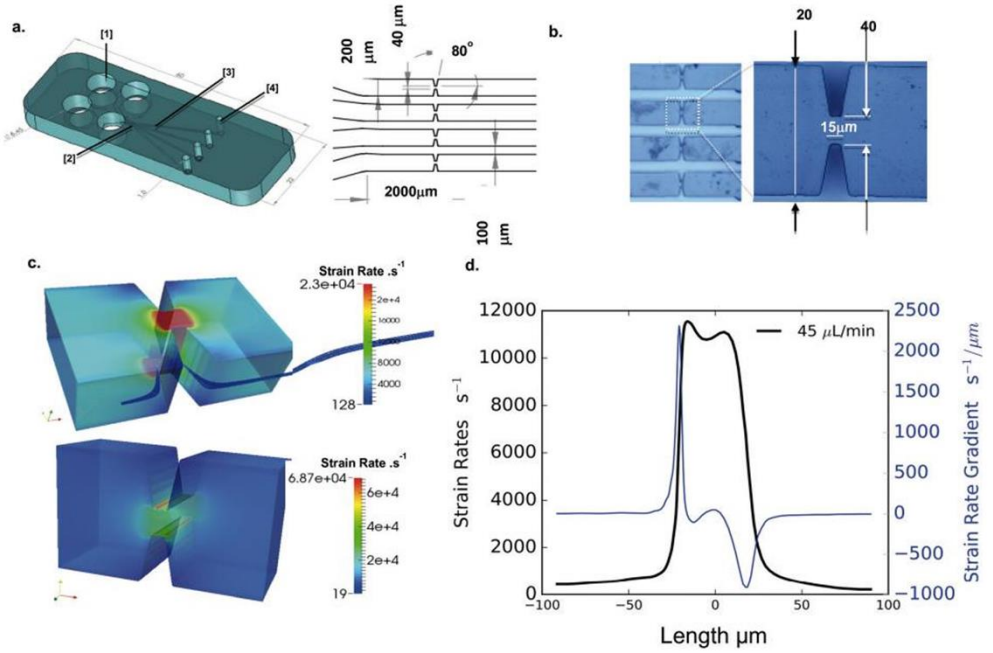

Fig. 1 a. Schematic detailing the main components of the microfluidic chip including: [1] 4 x 200 µl sample reservoirs for blood delivery, [2] post-array trap to prevent channel fouling by micro-clots in the blood sample due to inadequate anticoagulation, [3] high-resolution micro-channel with defined shear gradient geometry, and [4] exhaust channel connection to a Harvard PHD syringe driver. Schematic detailing the overall micro-contraction geometry and replicate layout and dimensions (µm). b. DIC image (20x) showing replicate active micro-contraction geometries on-chip and expanded view showing a single micro-contraction. c. CFD modeling (color map) showing the strain rate distribution in a cross-section at a single micro-contraction at the bottom wall (top panel) and a mid-plane cross-section (bottom panel). Note that the maximal strain rate at the stenosis approaches 68000 s^{-1} at the apex margins. d. CFD modeling of a single platelet particle trajectory 30 µm from the bottom wall and 10 µm from the symmetric geometry surface showing the full "strain rate history" of a platelet passing through the naïve microchannel at Q = 45 µL min^{-1}. Note the dual strain peaks at the step apex approaching ≈12 000 s^{-1} and the sharp strain rate gradient in the acceleration phase of 2315 s^{-1} $µm^{-1}$ and strain rate gradient in the deceleration phase of 935 s^{-1} $µm^{-1}$ for the platelet trajectory.

Samples for reconstitution were centrifuged at 100 x g for 2 minutes, and the Platelet-Rich Plasma (PRP) fraction was collected. The remaining red blood cell (RBC) fraction was washed 2x with Tyrode's buffer (pH 7.2) *via* centrifugation at 1700 x g for 7 minutes. The final RBC fraction was resuspended in Tyrode's buffer (pH 7.2) supplemented with 0.5% w/v BSA + apyrase (0.02 U ml^{-1}) and carried through a final centrifugation at 1700 x g for 7 minutes. Packed RBCs were stored at 37°C for later use. Platelet-Poor Plasma (PPP) was collected after the first washing step. Apyrase (0.02 U ml^{-1}) was added to the PRP, PPP and packed RBCs. RBCs, PRP and PPP were reconstituted at normalized cell counts and a full blood examination was conducted using a Haemogram (Abbott Diagnostics) blood analyser.

Platelet Ca^{2+} assay

Platelet cytosolic calcium levels $[Ca^{2+}]_c$ were monitored according to published methods.[36] Briefly, washed platelets (1 x 10^9 ml^{-1}) were loaded with Oregon Green BAPTA 488 (1,2-bis(2-aminophenoxy)ethane-N,N,N′,N′-tetraacetic acid tetra-(acetoxymethyl) ester, 1 µM) and Fura-Red/AM (1.25 µM) for 30 min at 37 °C. Dye-loaded platelets (1 x 10^7 ml^{-1}) were then reconstituted (as above) prior to perfusion through the device. To examine changes in calcium flux, sequential confocal images of platelet aggregates were captured at a scan rate of 0.586 frames per s for 37.5 s over a 3.5 min perfusion time course. Real-time platelet calcium flux was expressed as ratiometric fluorescence measurements. Platelet $[Ca^{2+}]_c$ response was categorised as high, intermediate or low based on ratiometric output.

Microscopy/image analysis

Blood perfusion and platelet aggregation dynamics were acquired on an inverted Nikon TiU microscope (Nikon Plan Fluor 20x/0.50 objective) using an Andor Zyla sCMOS camera at 1 fps for 210 or 600 s. All image analyses were performed off-line with ImageJ using Huang's fuzzy image thresholding.[37] $DiOC_6$-labeled fluorescent platelet aggregates were auto-thresholded such that the earliest micro-aggregates were included in the analysis window, and aggregate surface

area was quantitated at a fixed image plane 30 μm from the bottom coverslip wall. Platelet aggregate size was expressed as a 2-dimensional cross-section (μm²) as a function of time (s). Raw data derived from 4 replicate channels were fitted in GraphPad Prism to a sigmoidal (variable slope) non-linear regression according to:

$$Y = B + \frac{(T + B)}{1 + 10^{(log\,EC_{50} - X)X\ Hill\ Slope}}$$

Maximal (endpoint) aggregation was extrapolated from the plateau of the regression analysis.

Computational fluid dynamic analysis

Microfluidic flow rates were calculated to produce a strain rate close to the reported value for human arterioles (between 500 and 5000 s^{-1}). In order to compute the relationship between the flow rate (Q), the strain rate at the entry section, and the geometric variables of the microchannel, the analytical solution of the velocity profile for a Newtonian fluid in a rectangular geometry was used as previously reported.[30] Once the strain rate was calculated at the straight section and preliminary experimental testing was performed, the strain rates at the symmetric micro-contractions were calculated using Computational Fluid Dynamics (CFD):

Case 1. Naïve microchannel. For analysis of the naïve microchannel (no aggregation), we solved the Navier–Stokes equations over the geometry domain by means of OpenFOAM and SIMPLE algorithms, using a viscosity of 0.00345 Pa s and a density of 1050 kg m^{-3}. Blood can be approximated as a Newtonian fluid at high strain rates.[30] Non-slip at the wall was considered and relative pressure at the outlet as zero. The mesh was constructed using snappyhexmesh resulting in a total of 16136 cells (12340 hexahedra and 3796 polyhedra). After solving the Navier–Stokes equations, the strain rate history for a particle following a streamline at 10 μm from the wall was calculated. The strain rate gradient was calculated by taking the discrete derivative of the strain rates using a forward finite difference approach. A Savitzky–Golay filter was employed to smooth the representation of the derivative.

Case 2. Developing aggregate. In order to calculate the strain rates over the platelet aggregate, the geometry was extracted from confocal images at different time points (60 s, 120 s, 180 s, 240 s). The t = 240 s case was exported as a StereoLithograpy (stl) file using the software ImageJ. The stl file was further optimized using surface reconstruction algorithms in MeshLab and then combined with the naïve microchannel geometry in ICEM (Ansys Inc.). The same boundary conditions, material properties and solution algorithm were used as those for Case 1.

Clinical proof-of-concept trials

Patients aged-18 years with previously diagnosed VWD or who presented for evaluation of a bleeding disorder, where the possible diagnosis included VWD, were sampled after obtaining informed consent. Patients <18 years of age and patients who were unable to consent to involvement were excluded. The definition from Sadler *et al.* for VWD subtyping was utilized.[38] Only patients presenting type 2 VWD were routinely genotyped as part of their clinical assessment. Blood was obtained for device testing as well as for standardized VWD testing (VWF:Ag, VWF:CB, VWF:RCo), full blood examination, fibrinogen levels, FVIII levels, blood group and coagulation testing (Table 1). Patients were diagnosed as having or not having VWD and further subtyped according to accepted criteria[38] by the attending clinician. 12 patient blood samples were assessed using the prototype device (Fig. 1a). Overall, 4 patients were diagnosed with type 1 VWD, 1 patient with type 2A VWD, 2 patients with type 2N VWD, 2 patients with type 3 VWD, and 2 patients with a bleeding phenotype that was found to be not a result of VWD. The male-to-female ratio was 0.42 : 1, and the mean age was 34.4 years. Except where indicated, none of the participants had received any VWF replacement or desmopressin treatment prior to blood donation. Control blood samples $n = 33$ were taken from subjects without a known bleeding or thrombotic history, currently not taking medications known to effect platelet function. A

Table 1 Clinical subject demographics & clinical test results

	Not vWD *(n = 2)*	Type 1 (30–55%) *(n = 3)*	Type 1 (<30%) *(n = 1)*	Type 2A *(n = 1)*	Type 2B *(n = 1)*	Type 2M *(n = 1)*	Type 2N *(n = 1)*	Type 3 *(n = 2)*
Age (years)	35.5 (33–38)	21 (18–25)	18	42	55	25	30	47 (32–62)
Sex	2 ♀	3 ♀	1 ♂	1 ♂	1 ♀	1 ♀	1♀	2 ♀
Blood group O	1	2	1	0	0	1	0	2
INR (1.0–1.3)	1.05 (1–1.1)	1.3 (1–1.2)	1.2	1	1	1	1.1	0.95 (0.9–1)
PT (10.6–15.3 s)	13.45 (13.1–13.8)	13.3 (13.1–13.8)	15.1	12.8	11.2	13.4	13.8	12.9 (12.4–13.4)
APTT (26–38 s)	34.55 (30.8–38.3)	36.9 (35.6–36.9)	51.2	43.7	42.5	29.6	38.3	40.8 (32–49.6)
Fibrinogen (2–4 g L^{-1})	3.05 (2.6–3.5)	2.9 (2.2–4.2)	2.6	3.7	3.0	2.4	3.1	3.9 (3.8–4.0)
FVIII (50–200%)	110 (96.7–123.3)	78.0 (65.9–87.2)	35.3	45.6	48.2	115	35.2	70.0 (50.1–90)
vWF antigen (50–200%)	66 (65–67)	35.7 (33–40)	13	27	48	85	112	6 (3–9)
Collagen binding assay (50–200%)	94.5 (79–110)	35 (30–38)	16	11	29	94	128	2.5 (<1–4)
Ristocetin cofactor assay	65 (63–67)	33.3 (31–35)	13	12	48	14	134	5.5 (5–6)

subset of controls (n = *12*) were assessed for VWF antigen, VWF:RCo and VWF:CB levels using standardized pathology laboratory procedures.[39–41] A standardised bleeding history was also obtained.[42]

Desmopressin trial

Prior to receiving desmopressin, patients' FBE, FVIII:C, VWF:Ag and VWF:RCo levels were tested. The patients then received 0.3 μg kg^{-1} desmopressin in 50 ml 0.9% saline intravenously over 30 minutes. Citrated blood samples were then tested for aggregation response as per above. The FBE, FVIII:C, VWF:Ag and VWF:RCo levels were then measured 1 hour, 2 hours and 4 hours post administration.

Statistical analysis

Statistical analysis was performed with GraphPad Prism using a two-tailed t-test for comparison of maximal aggregate sizes. A receiver-operating characteristic (ROC) analysis was performed to determine sensitivity and specificity cut-offs for the device based on selectivity for type 1 VWD subjects.

Results

Hemodynamic characterization

To characterize the prototype microfluidic device, we carried out detailed CFD and experimental analysis of the strain rate gradient geometry used in all subsequent studies. CFD modeling of the microcontraction used in the device demonstrated that the peak strain rate (center cross-section), approaching ≈68 000 s^{-1}, occurs as two peaks at the outer margins of the 15 μm long apex (Fig. 1c). Analysis of the spatial "strain rate gradient" experienced by individual platelets passing within a streamline 10 μm from the step-wall (30 μm from the sidewall) demonstrated that individual platelets experience a near-wall gradient during a stenosis entry of 2315 s^{-1} μm^{-1}, near the contraction achieving a peak strain rate approaching 12000 s^{-1} at both margins of the apex (average peak strain rate across the apex of 1200 s^{-1}), followed by a strain rate gradient at the exit of −935 s^{-1} μm^{-1} (Fig. 1d). Epifluorescence imaging of citrated whole blood treated with amplification loop blockers (ALB) for 10 min prior to perfusion through the device demonstrated that platelet aggregation occurred exclusively at the downstream face of the symmetric step-geometry (Fig. 2a and S2at). Platelet aggregation followed a sigmoidal growth profile defined by: a lag-time to initial platelet monolayer development of ≈50 s, a linear rate of aggregation of ≈45 μm^2 s^{-1}, and a quasi-steady-state plateau phase that underwent cyclical aggregation–disaggregation (Fig. 2a). Platelet recruitment to the step geometry was strictly dependent on prior VWF coating and coating concentration (Fig. S3t). Examination of the correlation between input flow velocity (Q) and the rate and extent of platelet aggregation at the strain geometry demonstrated a linear relationship, with both initial lag time and linear aggregation rates dependent on device perfusion rates (Fig. 2b). Investigation of the proportional endpoint aggregate size at 3.5 min showed a strict linear correlation with the applied flow rate and the dependent strain rate gradient (Fig. 2c–e). To fully characterize the hemodynamic conditions present throughout platelet aggregate development, we carried out confocal imaging of aggregation as a function of time and performed CFD analysis at t = 210 s. Confocal sectioning demonstrated that the bulk of aggregate development was biased at the bottom sidewall of the device (Fig. 2f). CFD analysis demonstrated that, at maximal size, platelet aggregation led to an approximate doubling in peak strain rate at the aggregate apex, increasing from 12000 to 28000 s^{-1}, that was displaced 15–20 μm in the flow direction, distal to the secondary strain peak under initial conditions (Fig. 2f). Examination of overall platelet aggregation dynamics revealed that initial platelet recruitment occurred at the location of the secondary peak (Fig. 1c, d, S2a and b†). Subsequent semi-stable aggregation occurred preferentially at the downstream face of the symmetric step, with plateau phase aggregation extending into the low to zero strain rate zone (Fig. 2f, S2a and b†).

Soluble agonist and adhesion receptor dependency

Platelet activation under blood flow occurs through the combined effects of secreted chemical activators (soluble agonists), such as ADP and TXA_2, and mechanical drivers, such as applied strain rates. To investigate the soluble agonist dependency of platelet aggregation in the microfluidic device, perfusion experiments (Q = 45 μL min^{-1}) were conducted in the presence of amplification loop inhibitors (see Materials and methods). Fig. 3a and b demonstrate that platelet aggregation in the device is in part dependent on ADP signaling via the $P2Y_{12}$ pathway. Blockade of the $P2Y_{12}$ receptor with 2-MeSAMP (10 μM) did not significantly affect aggregation lag-time but did result in a 2-fold reduction in both the rate and extent of platelet aggregation in the device at Q = 45 μL min^{-1}. Blockade of TXA_2 generation (indomethacin) or $P2Y_1$-dependent signaling (MRS) singly or in combination (data not shown) had no significant effect on aggregation in the device (Fig. 3a and b). Combination amplification loop (ALB) blockade showed no additive effect on platelet aggregation.

To investigate the platelet adhesion receptor dependency of device function, citrated blood samples were treated with both blocking antibodies directed against GPIb/IX/V–VWF binding (AK2, 10 μg ml^{-1}) and integrin $\alpha_{IIb}\beta_3$ engagement (c7E3 Fab, 20 μg ml^{-1}). Blockade of GPIb/IX/V alone led to an ≈80% reduction in overall aggregation, with formed aggregates displaying rapid and unstable aggregation dynamics (Fig. 3c and data not shown). Blockade of integrin $\alpha_{IIb}\beta_3$ alone led to an ≈90% reduction in overall aggregation, with formed aggregates showing rapid disaggregation dynamics (Fig. 3c and data not shown). Combined blockade completely inhibited aggregation in the device (Fig. 3c). Experiments in which $DiOC_6$-labeled ALB-treated blood was chased after 1100 s with an unlabelled ALB-treated blood sample demonstrated complete turnover of $DiOC_6$-labelled platelets,

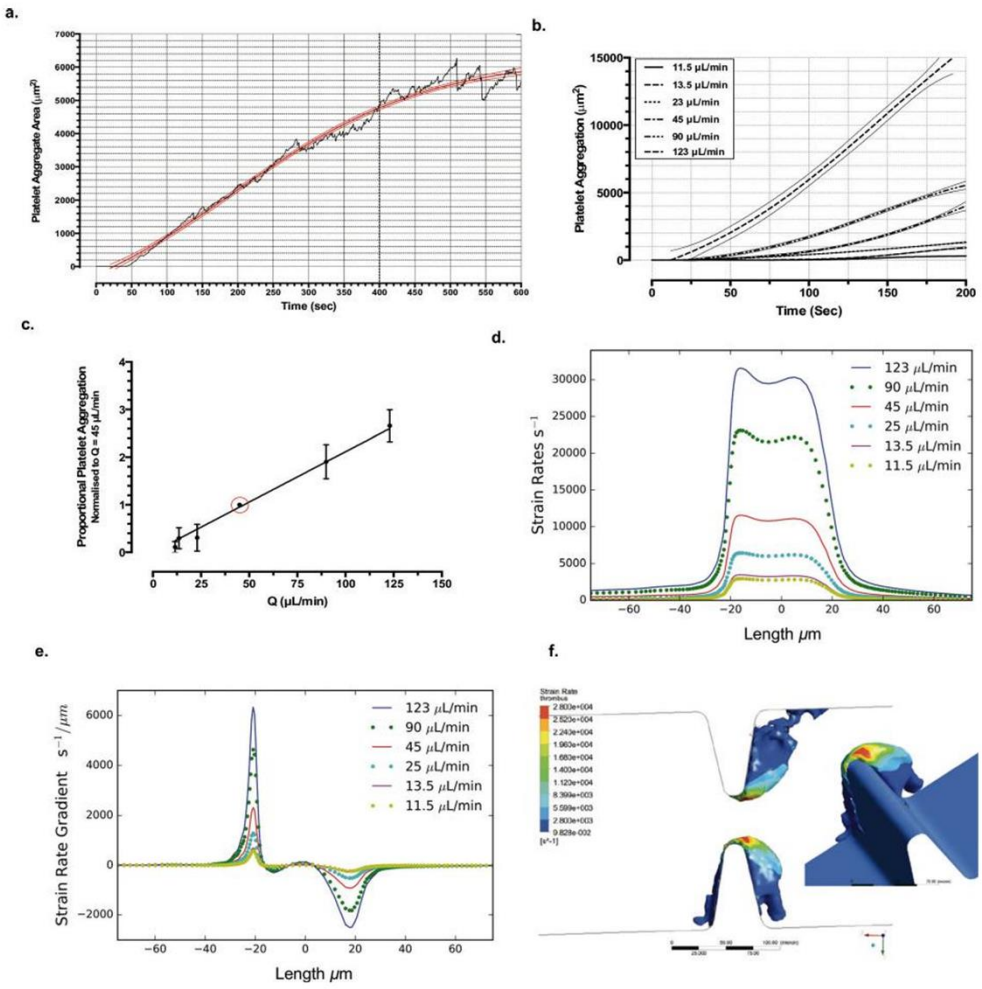

Fig. 2 a. Platelet aggregate surface area versus time graph showing platelet aggregation dynamics over 10 min of device perfusion. Red line – nonlinear curve fit and 95% confidence interval (R^2 = 0.778) to data averaged over 4 independent replicate micro-channels for a single blood donor. b. Flow rate dependency of platelet aggregation dynamics for flow rates of 11.5–123 μL min^{-1}. Note the lag time increase and overall reduction in linear aggregation rate (n = 4 independent experiments). c. Normalized plateau aggregation following perfusion for 3.5 min at the indicated flow rates. Note the linear dependency of aggregate size on the flow rate (n = 4 independent experiments). A flow rate of 45 μL min^{-1} (red circle) was chosen for all subsequent studies. d. CFD modeling of strain rate as a function of input flow rate across the symmetric step geometry. e. CFD modeling of strain rate gradient as a function of input flow rate. Note that significant platelet aggregation was only observed in the device when the acceleration phase strain rate gradient exceeded 1286 s^{-1} μm^{-1}. f. CFD model of a platelet aggregate developing in the device at t = 210 s taken from scanning confocal imaging of whole blood perfusion. Note that peak strain rates are experienced at the apex of the aggregate, which is displaced downstream from the secondary strain peak, with progressive strain rate reduction post stenosis at the trailing edge. Note that >50% of the aggregate mass sits within a shielded zone experiencing minimal to no strain.

suggesting that plateau phase aggregation is in a state of dynamic equilibrium, such that the overall rates of platelet accrual and loss are equivalent under amplification loop blockade (Fig. S4a†). Inhibition of overall platelet activation via PGE_1 + theophylline treatment completely blocked device-dependent aggregation (Fig. 3c). Preliminary data examining the overall level of platelet activation ($[Ca^{2+}]_c$ flux) within formed aggregates suggest that platelets undergo a relatively low level of activation, with the most significant levels of activation occurring proximal to the microchannel (VWF-coated) wall (Fig. S4b†). Investigation of the correlation between aggregate residence time and platelet $[Ca^{2+}]_c$ demonstrated that low to intermediate $[Ca^{2+}]_c$ responders are transiently incorporated into developing aggregates (Fig. S4c

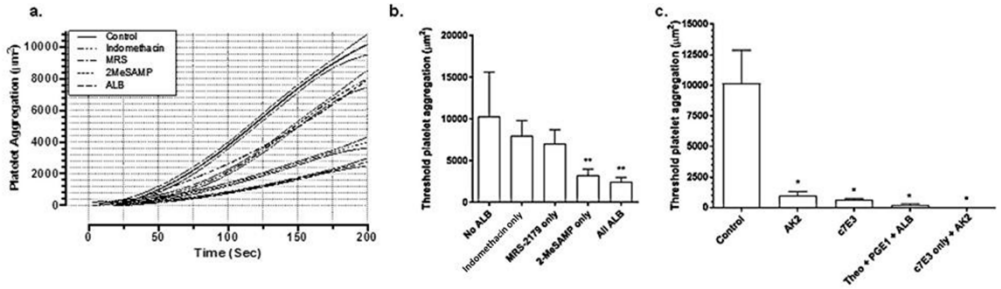

Fig. 3 a. Platelet aggregation vs. time graphs showing device sensitivity to blockade of soluble agonist signalling. Control – citrated human whole blood. Indomethacin – citrated whole blood treated with indomethacin (10 μM) for 10 min @ 37 °C prior to device perfusion ($n = 3$, $P < 0.5502$). MRS – citrated whole blood treated with MRS2179 (100 μM) for 10 min @ 37 °C prior to device perfusion ($n = 3$, $P < 0.3705$). 2MeSAMP – citrated whole blood treated with 2-MeSAMP (10 μM) for 10 min @ 37 °C prior to device perfusion ($n = 3$, $P < 0.0056$). ALB – citrated whole blood treated with MRS2179 (100 μM), 2-MeSAMP (10 μM), indomethacin (10 μM), and apyrase (1 U ml^{-1}) for 10 min @ 37 °C prior to device perfusion ($n = 3$, $P < 0.0012$). Nonlinear curve fitting and 95% CI shown. b. Maximal platelet aggregation ± SD following 3.5 min of device perfusion ($n = 3$ donors). c. Maximal platelet aggregation ± SD following whole blood treatment with anti-GP1b/V/IX IgG AK2 (10 μg ml^{-1}), $p < 0.0159$, anti-integrin $\alpha_{IIb}\beta_3$ Fab c7E3 (20 μg ml^{-1}), $p < 0.0182$, AK2 (10 mg ml^{-1}) and c7E3 (20 mg mL^{-1}), $p < 0.0316$, and theophylline (10 mM) + prostaglandin E1 (1 μg ml^{-1}), $p < 0.0149$. All blood samples were treated with the amplification loop blockers MRS2179 (100 μM), 2-MeSAMP (10 μM), indomethacin (10 μM), and apyrase (0.02 U ml^{-1}).

and dt). Taken together, these data demonstrate that platelet aggregation in the device is VWF-mediated with steady-state aggregation dependent on $\alpha_{IIb}\beta_3$ engagement and outside-in activation processes, independent of soluble agonist activation. Furthermore, these data suggest that the steady-state aggregates are in a state of dynamic equilibrium, with platelets undergoing minimal $[Ca^{2+}]_c$ flux and relatively rapid turnover rates.

Effect of hematocrit and platelet count on device function

In the non-Newtonian environment of blood flow, platelet aggregation is directly and indirectly influenced by both fluid dynamic and cellular (particle) dynamics, with red blood cell partitioning leading to platelet margination (increased density) at vessel/channel walls. To investigate the impact of cellular dynamics on device function, we conducted a series of experiments examining the impact of platelet count and hematocrit on platelet aggregation dynamics. Fig. 4a demonstrates that platelet counts in individual whole blood samples demonstrated an overall linear trend with respect to device-dependent aggregation and platelet count ($R^2 = 0.58$). Hematocrit (Hct) demonstrated a relatively poor correlation (Fig. 4b: $R^2 = 0.22$), which may be due, in part, to the uncontrolled platelet count in these whole blood experiments. To further investigate the influence of Hct on aggregation dynamics, we conducted a series of reconstituted blood (see Materials and methods) flow experiments in which isolated erythrocytes (Hct = 0.05–0.4) were reconstituted with isolated platelets at a fixed count of 200 × 10^9 L^{-1} in autologous platelet-poor plasma (PPP). By controlling platelet count, device-dependent aggregation was found to correlate linearly with Hct, such that the lag-time to initial aggregation, the linear phase of aggregation and maximal aggregation directly correlated with Hct (Fig. 4c and d). Reciprocal experiments in which isolated platelets at 25–200 × 10^9 L^{-1} were reconstituted with autologous PPP and erythrocytes at a fixed Hct of 0.4 demonstrated a tight correlation with platelet count, with a sharp drop-off in maximal aggregation below a platelet count of 100 × 10^9 L^{-1} (Fig. 4e and f). In addition, the overall lag-time to initial aggregation was significantly prolonged and mapped to platelet count (Fig. 4e). Taken together, these data demonstrate that blood cell dynamics play a key role in modulating device performance.

Clinical proof-of-concept

In order to demonstrate the potential of the device for application to von Willebrand's disease (VWD) screening, blood samples were taken from control subjects ($n = 33$) and $n = 12$ subjects presenting to the Alfred Hospital's Ronald Sawers Hemophilia Centre who had a bleeding diathesis with a suspected VWD phenotype. Patient demographics and clinical test results are presented in Table 1. Characterization of the device across multiple control subjects demonstrated a relatively broad distribution of aggregate surface area, with a range of 876–7577 μm^2 (mean = 3455 ± 2013 μm^2; 95% CI = 2913–4307) [Fig. S5a and b†]. There was a modest overall difference in aggregation magnitude between male and female subjects and type O subjects relative to other subtypes, potentially due to overall higher VWF antigen levels in this population (Fig. S5c and dt). Receiver-Operating Characteristic (ROC) analysis of control versus borderline type 1 VWD samples, where antigen levels ranged between 30–55%, resulted in an aggregate size cut-off of 1269 μm^2 yielding a threshold sensitivity of

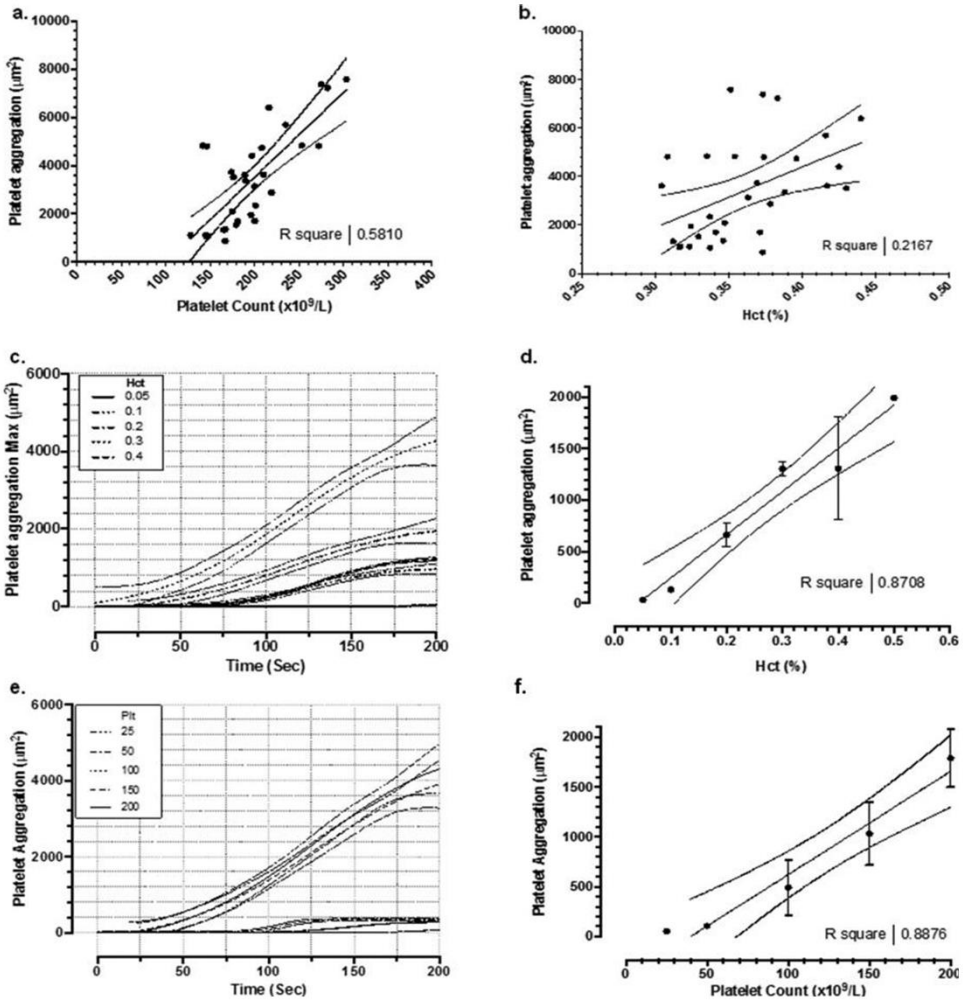

Fig. 4 a. Maximal platelet aggregation vs. platelet count ± SD following 3 minutes of device perfusion. b. Maximal platelet aggregation vs. HCT ± SD following 3 minutes of device perfusion. c. Platelet aggregation vs. time graphs showing device sensitivity to varying Hct levels. Citrated whole blood treated with MRS2179 (100 µM), 2-MeSAMP (10 µM), indomethacin (10 µM), and apyrase (1 U ml^{-1}) for 10 min @ 37 °C prior to device perfusion ($n = 3$). Nonlinear curve fitting and 95% CI shown. d. Maximal platelet aggregation ± SD following 3.5 min of device perfusion ($n = 3$ *donors*). e. Platelet aggregation vs. time graphs showing device sensitivity to varying platelet count (×10^9). Citrated whole blood treated with MRS2179 (100 µM), 2-MeSAMP (10 µM), indomethacin (10 µM), and apyrase (1 U ml^{-1}) for 10 min @ 37 °C prior to device perfusion ($n = 3$). Nonlinear curve fitting and 95% CI shown. f. Maximal platelet aggregation ± SD following 3.5 min of device perfusion ($n = 3$ *donors*).

83.3% and a specificity of 87.18% (Fig. 5). Assessment of control blood samples demonstrated that a small subset of controls tested ($n = 6$) fell below the ROC cutoff (Fig. 5). Assessment of samples taken from clinical subjects presenting with suspected or diagnosed VWD demonstrated that the device is able to identify platelet aggregation defects in patients with types 1 (VWF:Ag <30%; $p < 0.0001$), 2A ($p = 0.0238$), 2B ($p = 0.0436$) and 3 ($p = 0.0018$) VWD (Fig. 5, S2c–e and S6a–d†). Significantly, comparison of borderline (VWF:Ag = 30–50%) with severe type 1 VWD subjects (VWF:Ag <30%) demonstrated that the device is capable of differentiating these subpopulations ($p < 0.0001$), with severe type 1 subjects showing a significant reduction in maximal aggregation and lag time to initial aggregate growth (Fig. 5, S2c and S6a–c†). One of two subjects presenting with bleeding symptoms but

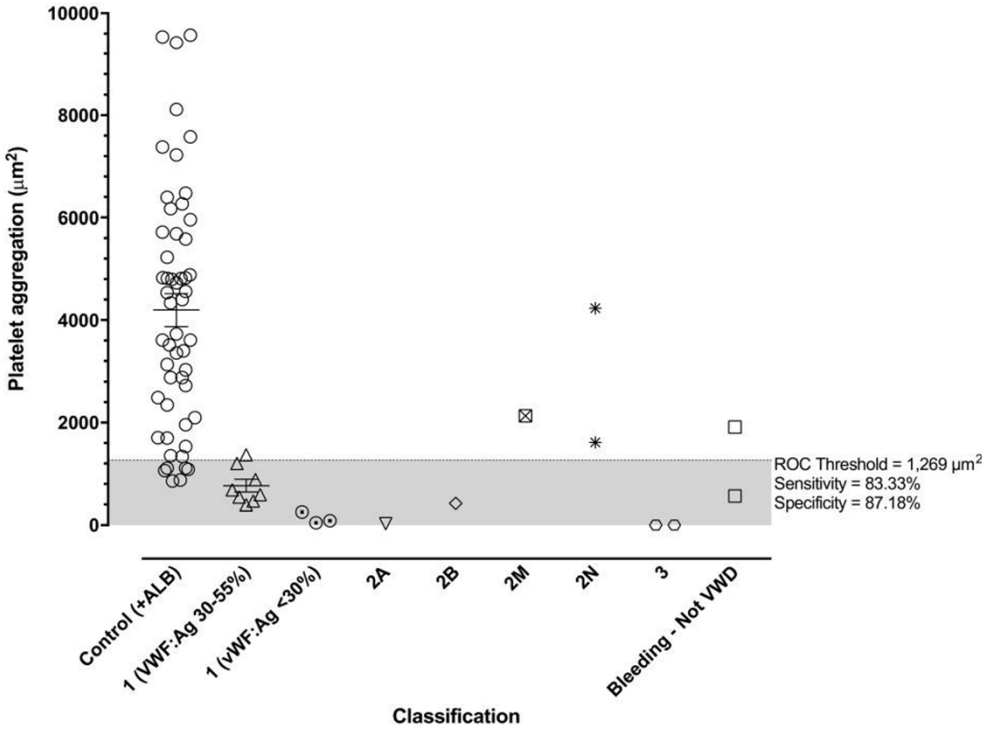

Fig. 5 Dot plot distribution of maximal platelet aggregation for controls and subjects with clinically defined VWD subtypes. Type 1 VWD subjects were further demarcated by their clinically tested VWF antigen levels into borderline type 1 (VWF:Ag = 30–55%) and severe type 1 (VWF:Ag <30%). Each data point represents n = 4 repeat experiments.

found not to have clinically defined VWD (VWF:Ag = 65%) showed a significant aggregation defect in the device (Fig. 5). Type 3 VWD subjects displayed no platelet aggregation beyond 15 min of perfusion in the device, which mapped to their VWF antigen levels (Table 1 & Fig. 5). Overall, device output for all VWD subtypes demonstrated good linear correlation with clinically assessed VWF antigen levels (Fig. 6a). Supplementation of type 3 (VWF:Ag <9%) subject samples with increasing concentrations of purified VWF (10–125 μg ml^{-1}) was able to repair the aggregation defect (Fig. 6a). Blood from two type 2N subjects displayed platelet aggregation within the normal range for the device, demonstrating that the system is not sensitive to FVIII binding defect (Fig. 5). One diagnosed type 2M subject displayed normal device-dependent aggregation (Fig. 5), with subsequent clinical testing showing that the patient's VWF:Ag levels were well within the normal range (VWF:Ag = 85%); this subject was 22 weeks pregnant at the time of testing. Significantly, this patient did not present with a bleeding phenotype demonstrating that the output of our prototype device closely correlates with clinical bleeding status. Comparison of device output with clinically assessed bleeding score, VWF:CB, and VWF: RCo demonstrated strong linear correlation (Fig. 6b–d).

Direct comparison of device performance with the PFA100 system demonstrated increased sensitivity in the ability to identify aggregation defects in type 1 VWD subjects, with 3/5 type 1 subjects (VWF:Ag = 30–55%) showing normal Coll/ADP and Coll/Epi closure times (CT), while demonstrating significantly perturbed device-dependent aggregation (Fig. 7a and b). In the case of a single type 2N subject, the PFA100 gave a false positive result (CT >300) while normal device-dependent aggregation was observed (Fig. 7a and b).

Desmopressin trials

Current first line therapy for type 1 VWD includes treatment with desmopressin (DDAVP; 0.3 μg kg^{-1}), where appropriate and where clinical testing demonstrates efficacy.[43] Currently, the monitoring sufficiency of desmopressin treatment in the clinic is problematic as no routine rapid screens are available. To assess the potential of the microfluidic device as a rapid screening tool for desmopressin monitoring, blood samples were taken from three consenting type 1 VWD subjects undergoing desmopressin trials. Samples were taken pre-desmopressin, 1 and 4 hours post desmopressin treatment. Fig. 8a and b demonstrate that device-dependent

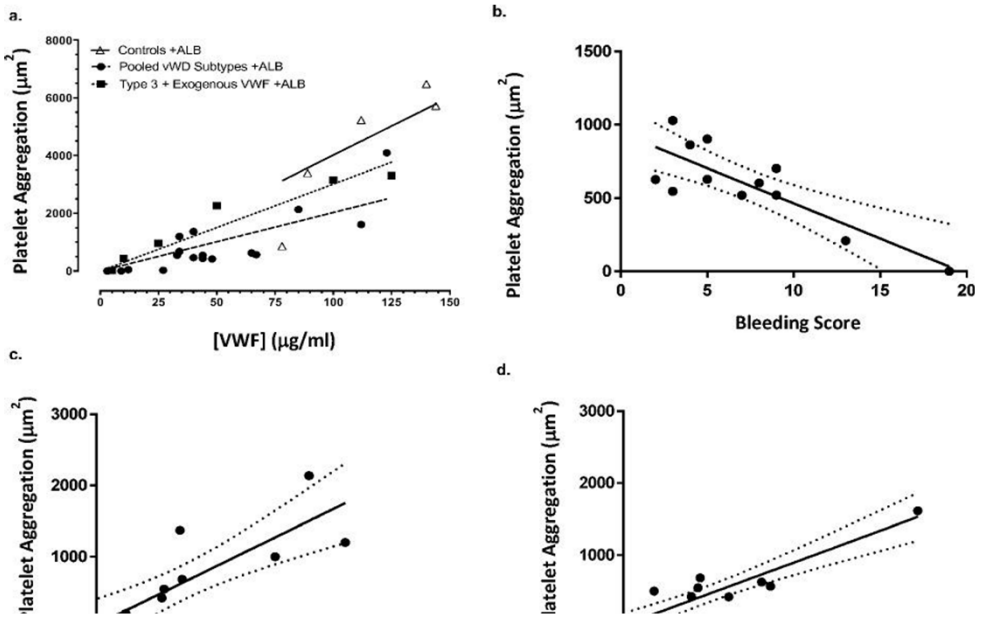

Fig. 6 a. Device-dependent aggregation vs. VWF antigen (mg mL^{-1}) for controls (open triangles) and pooled VWD subtypes (closed circles). Data for type 3 VWD subjects (closed squares) shows the response pre-VWF spiking and following spiking of type 3 samples with 10–125 μg ml^{-1} purified VWF. b. Device-dependent aggregation vs. clinical bleeding score. Note the inverse linear relationship R^2 = 0.68 (n = 12 subjects). c. Device-dependent aggregation vs. collagen binding assay (%). Note the direct linear correlation R^2 = 0.71 (n = 12 subjects). d. Device-dependent aggregation vs. ristocetin cofactor assay (%). Note the direct linear correlation R^2 = 0.85 (n = 12 subjects). Dotted lines denote 95% confidence intervals.

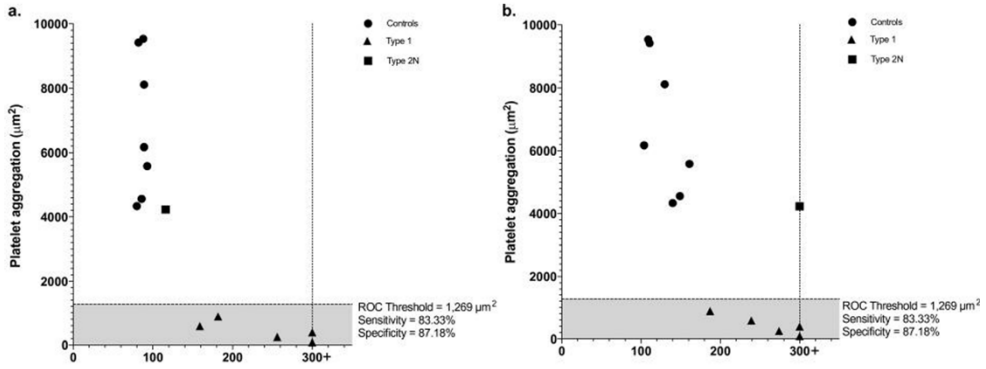

Fig. 7 a. Device-dependent platelet aggregation vs. PFA100 collagen/ADP cartridge CT (s). b. Device-dependent platelet aggregation vs. PFA100 collagen/epinephrine cartridge CT (s). Dotted vertical lines denote nonclosure (CT = 300+ s). Note that, for both PFA100 test cases, borderline type 1 VWD subjects (n = 2) achieved CTs of less than 200 s while showing minimal aggregation in the device. Horizontal dotted lines (1269 μm^2) represent the ROC-derived aggregation cutoff (sensitivity = 83.3%, specificity = 87.2%) for controls vs. type 3 VWD subjects.

aggregation correlates directly with VWF:Ag levels pre and post desmopressin treatment, and further demonstrate that desmopressin therapy effectively alleviates the VWF-dependent platelet aggregation defect in these subjects.

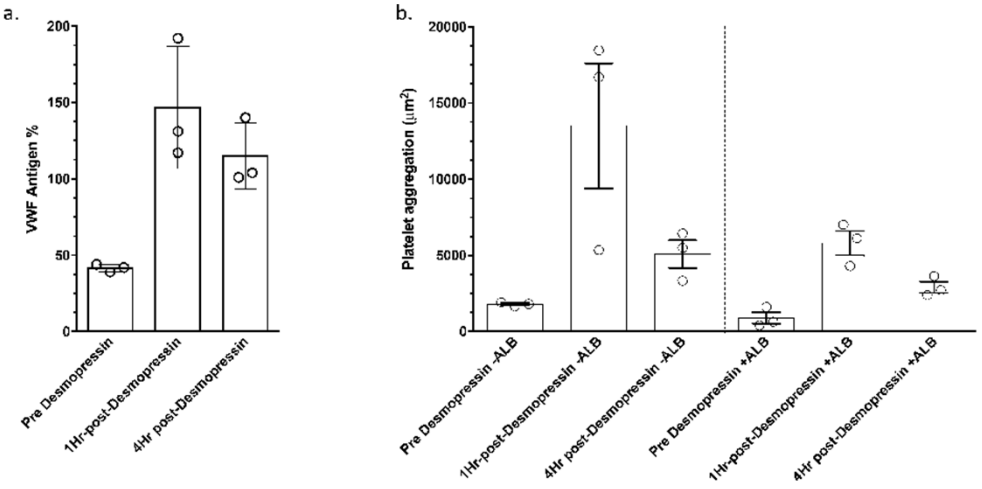

Fig. 8 a. Patient VWF antigen levels pre desmopressin (0.3 μg kg^{-1}), 1 h and 4 h post desmopressin treatment. Note the approximately 3-fold increase at 1 h and marginal decline at 4 h post treatment. b. Device-dependent platelet aggregation ± ALB, pre desmopressin (0.3 μg kg^{-1}) and 1 h and 4 h post treatment. Note the overall correlation with VWF antigen levels (n = 3 subjects).

Discussion

This study describes the refinement and clinical proof-of-concept of a prototype microfluidic screening tool that has been tailored to be an effective, rapid screen for VWF-dependent platelet aggregation defects associated with VWD. This new microfluidic device incorporates a symmetric step geometry and parallelized replicate micro-channels leading to a significant increase in device performance and reproducibility. By locally functionalizing the PDMS substrate with purified VWF, we present a novel system that allows for precise control of the location and extent of platelet aggregation, facilitating rapid continuous assessment of aggregation dynamics. In addition, through modification of key hemodynamic parameters within the active step geometry, we have been able to generate a device that is significantly more reliable and user-friendly, facilitating rapid blood sample screening. The device has the advantage of being able to reduce sample volumes to less than 150 μL and allows the rapid screening of shear-dependent platelet function in response to acute changes in strain rate.

In contrast to other commercially available flow-based assays, this new microfluidic device has the advantage of allowing for the continuous monitoring of aggregation dynamics with the capability to assess platelet function both under reversible, steady-state conditions, in which the canonical platelet activation pathways (ADP, TXA_2 signaling) are blocked, and under conditions of irreversible platelet aggregation, in which autocrine secretion mechanisms and amplification loops are allowed to proceed.[27]

Device validation studies using VWF as the adhesion substrate support our previously published observations suggesting that discoid platelet aggregation occurs immediately downstream of acute stenosis, where blood flow undergoes a rapid deceleration phase.[30,31] Significantly, aggregate remodeling appears to conform to the overall strain rate profile created by the developing aggregate and is limited to a peak strain rate at the thrombus surface of ≈28 000 s^{-1}, under the conditions present in the device.

The soluble agonist dependency of platelet aggregation is a function of the prevailing haemodynamic environment. Across the continuum of patho-physiological shear conditions, three subset environments are operative: low venous shear (100–1000 s^{-1}), intermediate arterial shear (1000–4000 s^{-1}), and high pathologic shear (≥4000 s^{-1}). Our prototype device subjects blood samples to a maximum peak strain rate >20 000 s^{-1}. At such a strain rate, the primary driver of platelet aggregation is VWF–GPIb engagement, with minimal involvement of secreted chemical drivers of platelet activation. Our validation studies demonstrate that both the rate of linear growth and final aggregate size are in part dependent on ADP secretion and signaling via the $P2Y_{12}$ G_i pathway. However, as per our previously published findings, mechanical flow is still able to drive significant platelet aggregation in the absence of $P2Y_{12}$ amplification. This partial ADP dependency may reflect the relatively short duration of high strain rate exposure at the step geometry and the requirement for $PY2Y_{12}$ signaling in stabilizing formed aggregates in the downstream deceleration component of the step geometry.

A critical consideration for any flow-based device, in the clinical setting, is the impact of altered platelet count and hematocrit on device function, particularly when dealing with anemic or thrombocytopenic patients.[3] Our device validation studies demonstrate that while the magnitude of aggregation in the device is sensitive to platelet depletion, overall device output falls well within the normal range (defined in this

study), even when platelet count falls below 100–150 × 10^9 L^{-1} (the lower limit of normal). Overall, the platelet count dependency of the device mirrors that found for the PFA100, in which platelet counts are typically adjusted to or above 100 x 10^9 L^{-1}.[27]

The phenomenon of platelet margination, as a function of red blood cell packing under the influence of high velocity flow streamlines, is a well-characterized phenomenon across a range of physiological and pathological strain rates.[44,45] The increased near-wall concentration of platelets due to margination is known to occur at hematocrits >10%.[46] This shear and particle-induced platelet diffusion has been confirmed in in vivo and in vitro experiments, and has been explained in several theoretical and numerical studies.[47] The hematocrit dependency observed for our device is consistent with these studies and that of other flow-based experimental systems, such as parallel plate flow chambers, where hematocrit plays a critical role in the margination of platelets and directly affects platelet surface density.[48] Preliminary experiments in which patient samples were corrected for hematocrit via supplementation with isolated autologous red blood cells demonstrated that this hematocrit dependency can be corrected when necessary (data not shown).

The calcium imaging studies presented here suggest that, under the prevailing conditions of our device, platelet aggregate formation is not due to large-scale platelet activation (Fig. S4†). The bulk of the aggregate forming in the device appears to be composed of platelets with low levels of $[Ca^{2+}]_c$ (Fig. S4†). This in conjunction with our receptor blocking antibody studies would suggest that aggregate formation occurs via a strictly VWF–GPIb-dependent mechanism, with potential stabilization occurring through low affinity $\alpha_{IIb}\beta_3$ engagement. A key parameter cited to drive platelet aggregation in equivalent microfluidic systems is the conformational unfolding of VWF under both the strain and elongational stresses of blood flow.[49–52] Studies by Schneider et al. (2007) point to a critical shear (strain) rate value (γ_{crit}) of ≈5000 s^{-1}, above which VWF undergoes a transition from globular to extended conformation.[49] Furthermore, studies by Sing and Alexander-Katz (2010) suggest that elongational flow may play a significant role in VWF unfolding.[50] While direct observation of the VWF conformational change falls well outside the scope of the present study, we hypothesize that the elevated strain rates (≈28 000 s^{-1}) developed within the device may lead to VWF unfolding and presentation of VWF A1 domains that drive device-dependent platelet aggregation.

A number of microfluidic-based studies describe the formation of platelet–VWF strings and/or ultra-large VWF multimers as a result of elevated applied shear rates.[53–55] While these studies share many commonalities with the device presented in this study, we did not observe the formation of ultra-large VWF species. A key difference between our device and previous studies is that platelet aggregation is restricted to the PDMS surface by selective VWF coating, while previous studies have involved adhesion to the bottom wall (glass substrate) of these differing microfluidic devices. In addition, many of these published studies involve the use of a primary type I collagen substrate or an endothelial cell monolayer that has been stimulated to express ultra-large multimeric VWF.[56,57] We hypothesize that the absence of apparent VWF self-association in our device is a function of the spatially restricted nature of the VWF coating, the use of purified VWF that does not contain ultra-large VWF multimers, the absence of type I collagen, and the relatively discontinuous spatial distribution of the VWF surface, which is restricted to the active PDMS step geometry only.

A significant feature of platelet aggregation in our prototype device is the ability to monitor platelet aggregation continuously, rather than relying on endpoint measures of occlusion or flow cessation. Our investigation of platelet dynamics within the semi-stable aggregates that form in the device demonstrates that aggregates undergo continual aggregation–disaggregation that maintains an equilibrium aggregate size for a given flow rate (Fig. S2†). A key observation underpinning this is that no apparent large embolus formation occurs but rather platelet turnover consists of the loss of 2–3 platelet microaggregates and single platelets from the growth face within the high velocity regions of the flow (data not shown). These observations parallel our previously published observations demonstrating that high shear gradient aggregation occurs via the recruitment of un-activated discoid platelets through the formation of individual membrane tethers driving platelet-on-platelet tethering interactions that comprise the unstable growth-face of thrombi both in vivo and in vitro.[31]

A key shortfall of current clinical testing for VWD is the lack of diagnostic resolution in the identification of patients with borderline type 1 VWD. Our proof-of-concept studies suggest that our device is capable of differentiating borderline type 1 VWD patients from severe type 1 VWD, based on their overall ability to undergo device-dependent aggregation. While the present study focused on a refined geometry with a defined strain rate gradient, it is possible that further modification of one or all of the identified geometric parameters defining the symmetric geometry may further enhance the ability to differentiate subtle aggregation defects. Preliminary studies suggest that modification of either the rate of flow acceleration into the micro-contraction or the peak strain and dwell time at the micro-contraction may modulate overall device performance.

Platelet aggregation in the PFA100 is due to aspiration of samples at high shear rates (5000–6000 s^{-1}) through a capillary in the instrument cartridge coupled to a 150 μm membrane aperture coated with collagen and ADP or collagen and epinephrine.[26] The membrane triggers platelet adhesion, activation and aggregate formation, leading to occlusion and blood flow cessation. Results are reported as the closure time (CT) in seconds, with values >300 s reported as non-closure.[58] Head-to-head comparison of our microfluidic device with the PFA100 system demonstrates at least equivalency with respect to the identification of VWF-dependent platelet aggregation defects. Significantly, in the case of borderline

Subcommittee of the SSC of the ISTH, *J. Thromb. Haemostasis*, 2006, **4**, 2716–2717.
26 E. J. Favaloro, *Semin. Thromb. Hemostasis*, 2008, **34**, 709–733.
27 B. Jilma, *J. Lab. Clin. Med.*, 2001, **138**, 152–163.
28 S. Panzer and P. Jilma, *Vox Sang.*, 2011, **101**, 1–9.
29 E. Westein, S. de Witt, M. Lamers, J. M. Cosemans and J. W. Heemskerk, *Platelets*, 2012, **23**, 501–509.
30 F. J. Tovar-Lopez, G. Rosengarten, E. Westein, K. Khoshmanesh, S. P. Jackson, A. Mitchell and W. S. Nesbitt, *Lab Chip*, 2010, **10**, 291–302.
31 W. S. Nesbitt, E. Westein, F. J. Tovar-Lopez, E. Tolouei, A. Mitchell, J. Fu, J. Carberry, A. Fouras and S. P. Jackson, *Nat. Med.*, 2009, **15**, 665–673.
32 R. R. Montgomery and T. S. Zimmerman, *J. Clin. Invest.*, 1978, **61**, 1498–1507.
32 B. H. Rauch and J. G. Filep, *Cardiovasc. Res.*, 2014, **102**, 339–341.
33 P. Harrison, *Platelets*, 2012, **23**, 510–525.
34 C. Gachet, *Annu. Rev. Pharmacol. Toxicol.*, 2006, **46**, 277–300.
35 W. S. Nesbitt, I. S. Harper, S. M. Schoenwaelder, Y. Yuan and S. P. Jackson, *Methods Mol. Biol.*, 2012, **788**, 73–89.
36 L.-K. Huang and M.-J. J. Wang, *Pattern Recognit.*, 1995, **28**, 41–51.
37 J. E. Sadler, U. Budde, J. C. Eikenboom, E. J. Favaloro, F. G. Hill, L. Holmberg, J. Ingerslev, C. A. Lee, D. Lillicrap, P. M. Mannucci, C. Mazurier, D. Meyer, W. L. Nichols, M. Nishino, I. R. Peake, F. Rodeghiero, R. Schneppenheim, Z. M. Ruggeri, A. Srivastava, R. R. Montgomery and A. B. Federici, Working Party on von Willebrand Disease Classification,
38 *Thromb. Haemostasis*, 2006, **4**, 2103–2114.
39 E. J. Favaloro, L. Grispo, T. Exner and J. Koutts, *Blood Coagulation Fibrinolysis*, 1991, **2**, 285–291.
40 R. Redaelli, A. R. Corno, L. Borroni, G. Mostarda, M. Nichelatti, E. Morra and F. Baudo, *J. Thromb. Haemostasis*, 2005, **3**, 2684–2688.
41 I. Tornai, P. J. Declerck, L. Smets, J. Arnout, H. Deckmyn, K. M. Caekebeke-Peerlinck and J. Vermylen, *Haemostasis*, 1991, **21**, 125–134.
42 F. Rodeghiero, G. Castaman, A. Tosetto, J. Batlle, F. Baudo, A. Cappelletti, P. Casana, N. De Bosch, J. C. Eikenboom, A. B. Federici, S. Lethagen, S. Linari and A. Srivastava, *J. Thromb. Haemostasis*, 2005, **3**, 2619–2626.
43 A. B. Federici, G. Castaman, A. Thompson and E. Berntorp, *Haemophilia*, 2006, **12**, 152–158.
44 G. J. Tangelder, D. W. Slaaf, H. C. Teirlinck, R. Alewijnse and R. S. Reneman, *Microvasc. Res.*, 1982, **23**, 214–230.
45 G. J. Tangelder, H. C. Teirlinck, D. W. Slaaf and R. S. Reneman, *Am. J. Physiol.*, 1985, **248**, H318–H323.
46 S. Fitzgibbon, A. P. Spann, Q. M. Qi and E. S. G. Shaqfeh, *Biophys. J.*, 2015, **108**, 2601–2608.
47 H. Hosseinzadegan and D. K. Tafti, *Biotechnol. Bioeng.*, 2017, DOI: 10.1002/bit.26343.
48 B. Prabhakarpandian, M. C. Shen, K. Pant and M. F. Kiani, *Microvasc. Res.*, 2011, **82**, 210–220.
49 S. W. Schneider, S. Nuschele, A. Wixforth, C. Gorzelanny, A. Alexander-Katz, R. R. Netz and M. F. Schneider, *Proc. Natl. Acad. Sci. U. S. A.*, 2007, **104**, 7899–7903.
50 C. E. Sing and A. Alexander-Katz, *Biophys. J.*, 2010, **98**, L35–L37.
51 E. Westein, A. D. van der Meer, M. J. E. Kuijpers, J.-P. Frimat, A. van den Berg and J. W. M. Heemskerk, *Proc. Natl. Acad. Sci. U. S. A.*, 2013, **110**, 1357–1362.
52 T. Goerge, F. Kleineruschkamp, A. Barg, E. M. Schnacker, V. Huck, M. F. Schneider, M. Steinhoff and S. W. Schneider, *Thromb. Haemostasis*, 2007, **98**, 283–286.
53 M. Stockschlaeder, R. Schneppenheim and U. Budde, *Blood Coagulation Fibrinolysis*, 2014, **25**, 206–216.
54 S. Gogia and S. Neelamegham, *Biorheology*, 2015, **52**, 319–335.
55 E. Di Stasio and R. De Cristofaro, *Biophys. Chem.*, 2010, 153, 1–8.
56 S. Zhu, B. A. Herbig, R. Li, T. V. Colace, R. W. Muthard, K. B. Neeves and S. L. Diamond, *Biorheology*, 2015, 52, 303–318.
57 J. Zilberman-Rudenko, J. L. Sylman, K. S. Garland, C. Puy, A. D. Wong, P. C. Searson and O. J. T. McCarty, *Platelets*, 2017, 1–8, DOI: 10.1080/09537104.2017.1280600.
58 M. Hintzke and A. Harrington, *Am. J. Clin. Pathol.*, 2015, **144**, 131.
59 L. Ardillon, C. Ternisien, M. Fouassier, M. Sigaud, A. Lefrançois, M. Pacault, O. Ribeyrol, E. Fressinaud, P. Boisseau and M. Trossaërt, *Haemophilia*, 2015, **21**, 646–652.
60 E. J. Favaloro, *Haemophilia*, 2015, **21**, 642–645.

5.3 - 'Application of a strain rate gradient microfluidic device to von Willebrand's disease screening' - supplemental information

Supplementary Figure 1

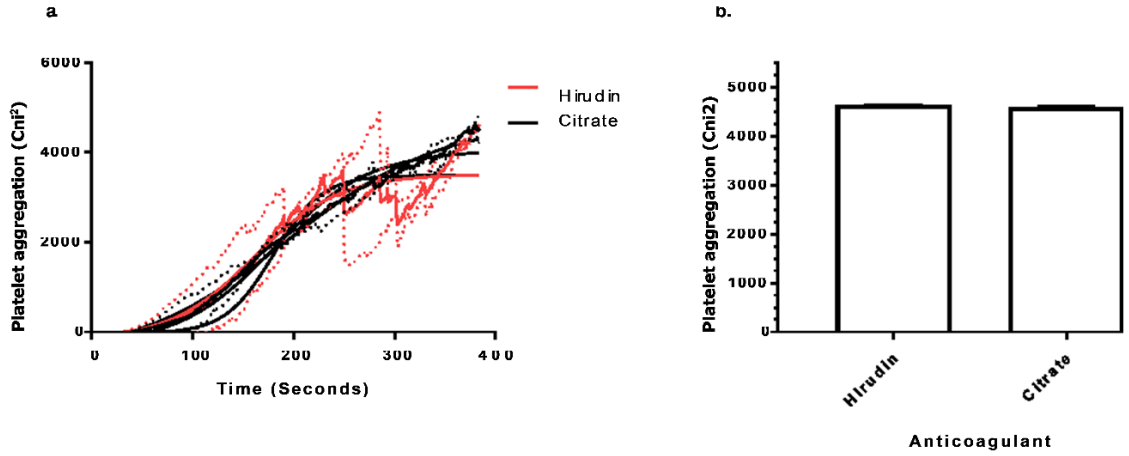

Supplementary Figure 1. Anticoagulant comparison
a. Representative aggregate growth vs time graph showing platelet aggregation after collection in 3.2% citrate (black) or hirudin (80 U/mL) (red). Whole blood treated with MRS2179 (100mM), 2MeSAMP (10mM), Indomethacin (10 mM), and apyrase (1 U/mL) for 10 min @ 37°C prior to device perfusion (n = 2). Nonlinear curve fitting and 95% CI shown. **b.** Maximal aggregate growth over 3.5 min of device perfusion (n=2 donors).

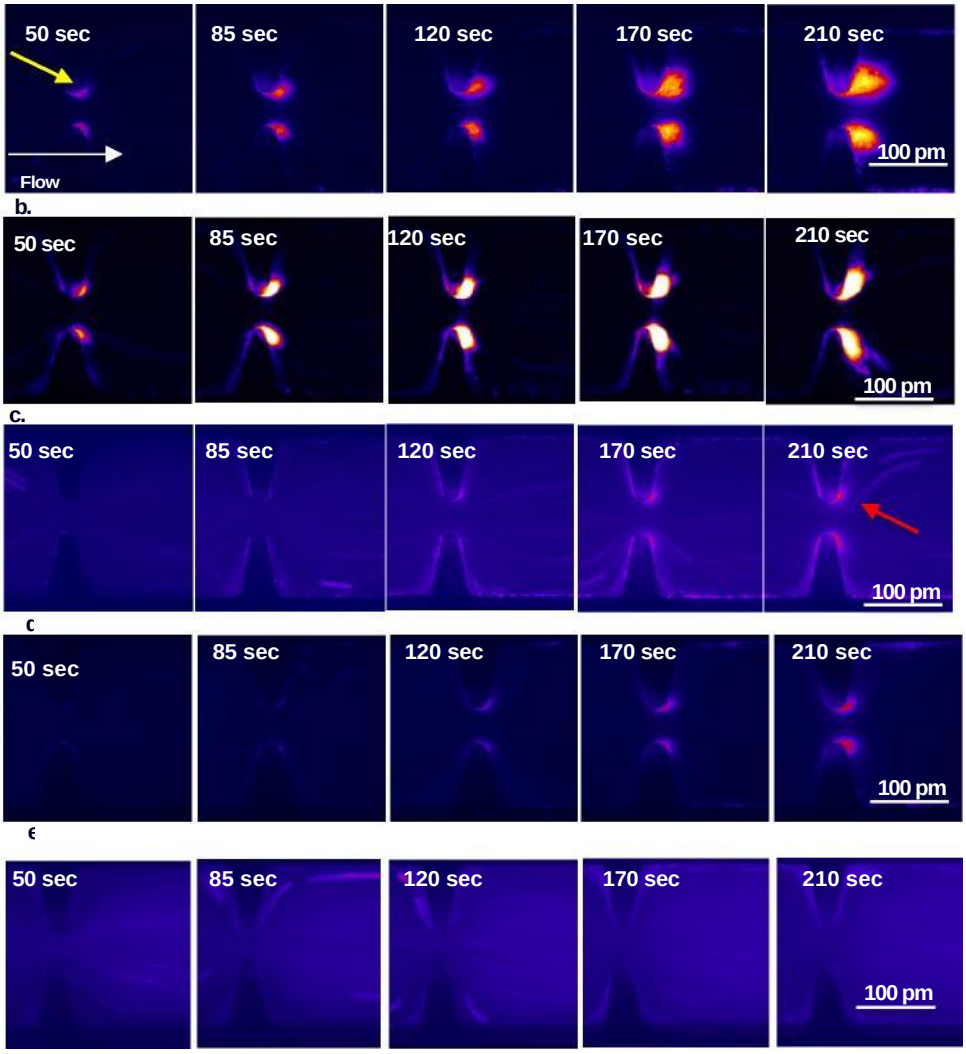

Supplementary Figure 2. Device description and characterization
a. Representative timelapse images of platelet aggregation dynamics at the axisymmetric device microcontraction showing the overall development of the platelet aggregate in citrated whole blood. Yellow arrow denotes the point of aggregate initiation at the downstream margin of the 15μm long apex. Note that semistable aggregates project into the flow deceleration zone where aggregate surface shear rates approach $0.s^{-1}$. Also note the axisymmetric aggregation. **b.** Representative timelapse images of platelet aggregation dynamics at the axisymmetric device microcontraction showing the overall development of the platelet aggregate in amplification loop blocked (ALB) blood. **c.** Representative timelapse images of platelet aggregation in a type 1 VWD patient. Red arrow denotes the decreased maximal aggregate area seen in VWD samples. **d.** Representative timelapse images of platelet aggregation in a type 2 VWD patient. **e.** Representative timelapse images of platelet aggregation in a type 3 VWD patient.

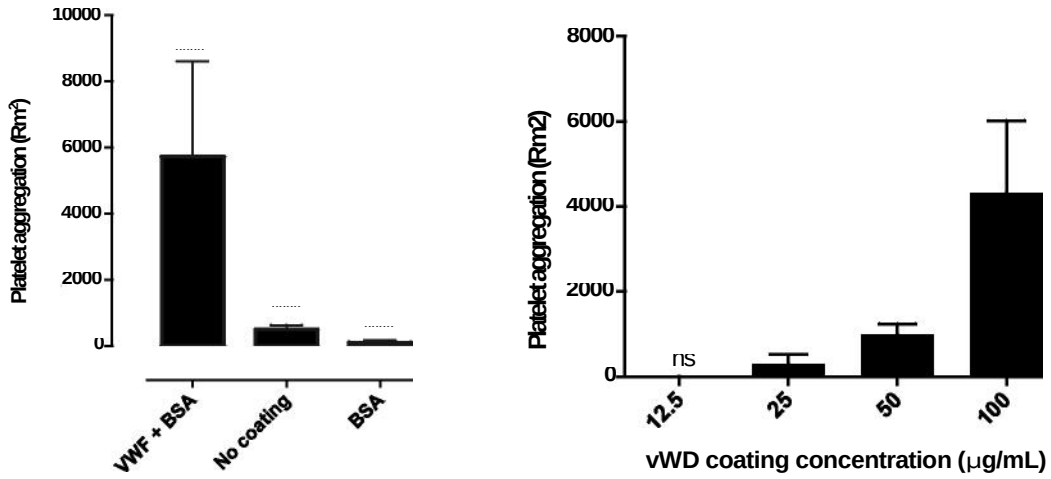

Supplementary Figure 3. Device Performance as a Function of Coating Method
a. Maximal platelet aggregation as a function of coating method. VWF + BSA - device treated with 100µg/mL VWF followed by 10µg/mL BSA (as per Materials & methods); No coating Ð whole blood perfused through naïve device without any prior protein coating; BSA Ð device coated with 10µg/mL BSA alone prior to blood perfusion (n= 5 experiments). **b**. Device performance as a function of VWF coating concentration 12.5 Ð 100µg/mL. Note that maximal aggregation maps to VWF concentration (n=3 experiments).

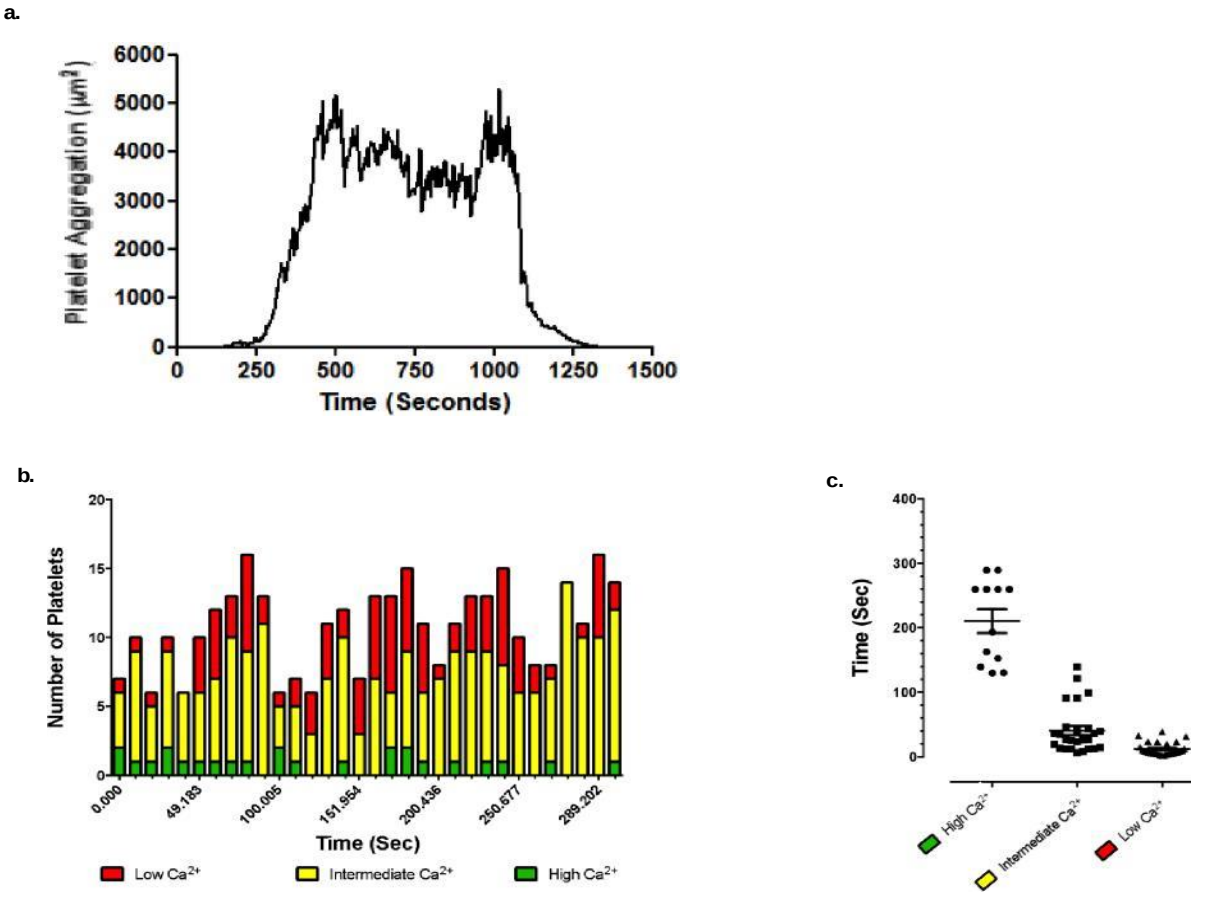

Supplementary Figure 4. Platelet activation Status & Aggregate Dynamics

a. Representative aggregation trace showing chase experiments in which ALB treated DiOC6 labelled whole blood was chased with unlabeled whole blood samples at t=1125 s (n=3). Note that complete platelet turnover is achieved post chase demonstrating that the aggregate is in a state of dynamic equilibrium. **b.** Frequency distribution of platelet $[Ca^{2+}]_c$ as a function of time in developing platelet aggregates in the device (n = 3 experiments). **c.** Dot plot showing the relationship between time in aggregate and platelet $[Ca^{2+}]_c$. Note that platelets showing significant levels of Ca2+ flux demonstrate the greatest aggregate retention time. Also note that aggregates are primarily composed of platelets in a intermediate to low activation state.

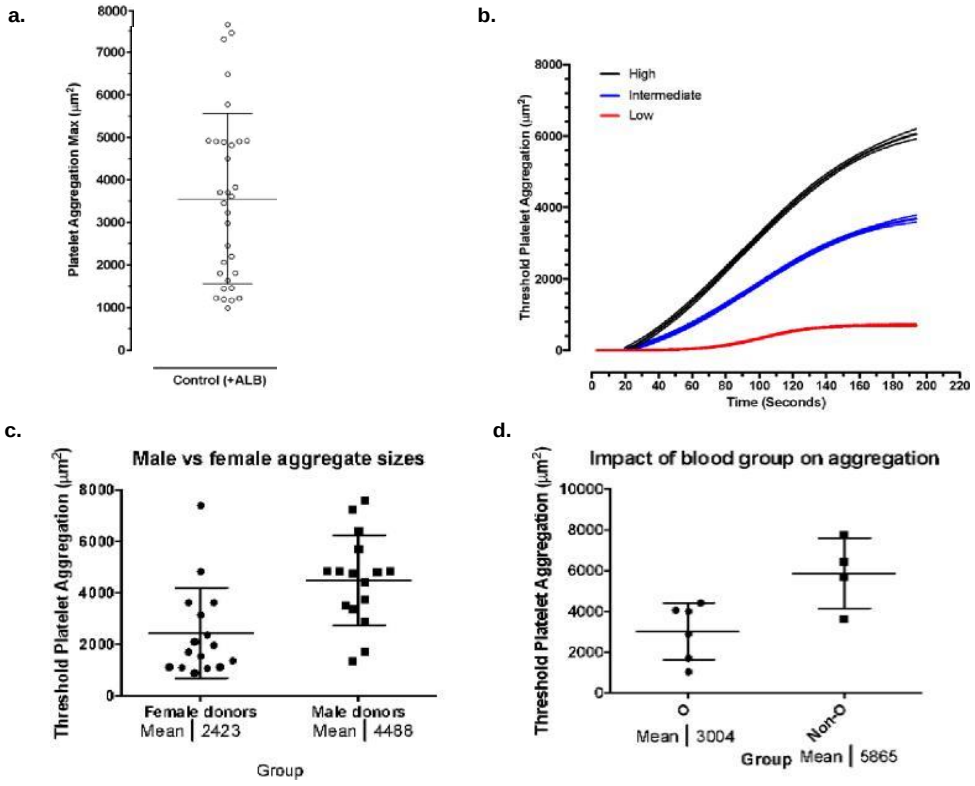

Supplementary Figure 5. Device performance

a. Platelet aggregation v time graphs showing device sensitivity to varying Hct levels. Citrated whole blood treated with MRS2179 (100mM), 2MeSAMP (10mM), Indomethacin (10 mM), and apyrase (1 U/mL) for 10 min @ 37ºC prior to device perfusion (n = 3). Nonlinear curve fitting and 95% CI shown. **b.** Maximal platelet aggregation ± SD following 3.5 min of device perfusion (n = 3 donors). **c.** Platelet aggregation v time graphs showing device

sensitivity to varying platelet count ($x10^9$). Citrated whole blood treated with MRS2179 (100mM), 2MeSAMP (10mM), Indomethacin (10 mM), and apyrase (1 U/mL) for 10 min @ 37ºC prior to device perfusion (n = 3). Nonlinear curve fitting and 95% CI shown. **d.** Maximal platelet aggregation ± SD following 3.5 min of device perfusion (n = 3 donors).

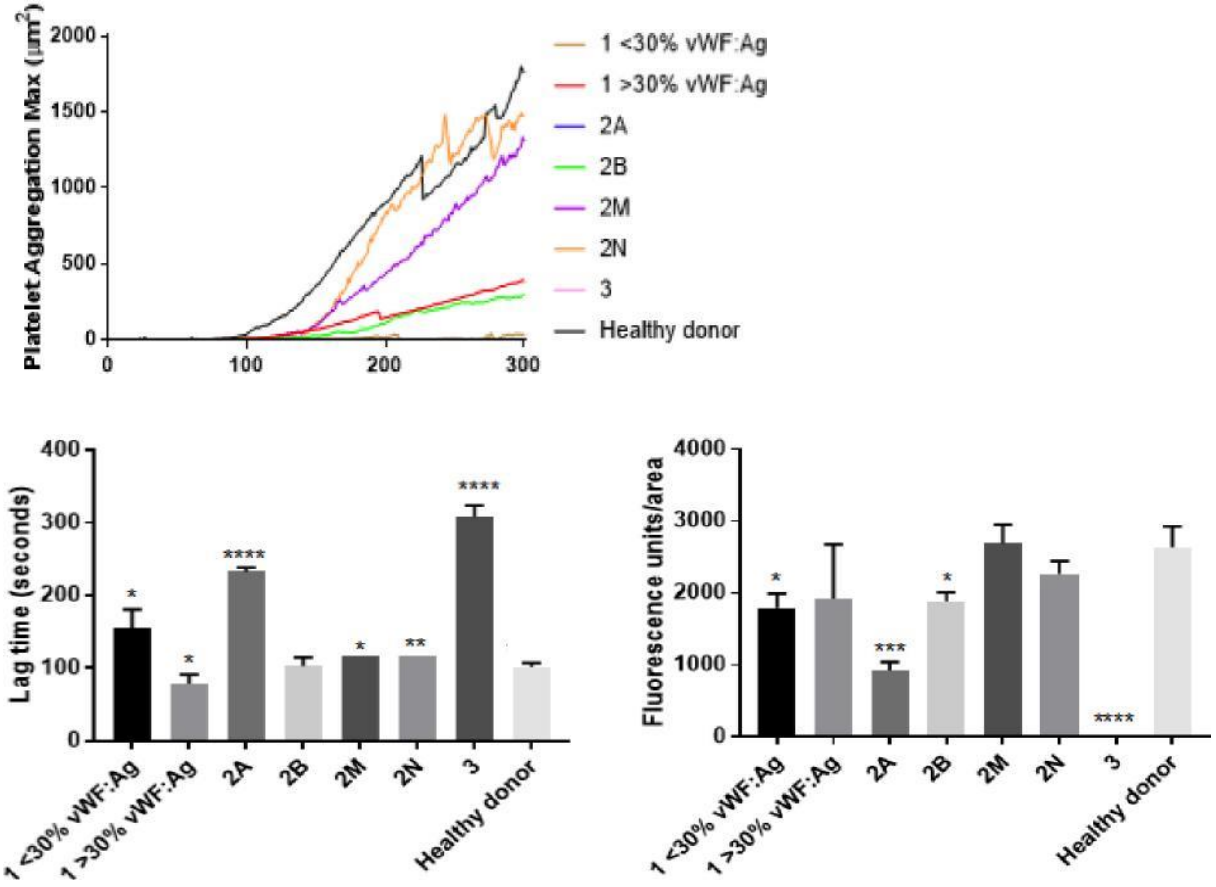

Supplementary Figure 6. Device performance across VWD subtypes

Maximal platelet aggregation ± SD following 3.5 min of device perfusion. Citrated whole blood treated with MRS2179 (100mM), 2MeSAMP (10mM), Indomethacin (10 mM), and apyrase (1 U/mL) for 10 min @ 37ºC prior to device perfusion. **b.** Lag time until initial platelet adhesion, as measured by time until first fluorescence detection vs VWD subclassification. **c.** Maximal fluorescence per unit area of aggregate vs VWD subclassification, as measured by determining maximal aggregate size and level of fluorescence at that point.

5.4. Examination of platelet aggregation under flow with variable acceleration geometries

Previous literature, including Fig. 2c in chapter 5.2, and platelet responses to varying flow rates and stenosis sizes in this study suggests that platelets are highly response to external shear environments.(3-5) It was hoped that knowledge of how the stenosis could be altered to modulate platelet reactivity could lead to better improved understanding of the diagnostic efficacy of the device. Early studies within chapter 5.4 therefore were a preliminary examination into the extent of platelet aggregation when exposed to different gradients of shear acceleration in the artificial environment of the microcontractions. To examine platelet aggregation under flow, whole blood was flowed over stenoses with acceleration angles of 7.5º, 15º, 40º and 80º with constant peak shear. These studies demonstrated that vWF-dependent platelet aggregation at the stenosis was directly proportional to entry angle magnitude (*see Fig 5.1a*). Additionally, samples tested in the 7.5º channel appeared to aggregate only to a very small degree. To this end, studies of shear gradients present in the device when entry angles were altered were conducted to quantitatively demonstrate the alterations to shear profile (*see Fig 5.1 b-e*). Finally, experimental results demonstrated platelet aggregate volumes to coverslips derivatised with type 1 collagen (100 µg/ml) downstream of the stenosis indicated no statistically significant difference between aggregates (*see Fig 5.2*).

5.5. Margination and mass transport effects do not play a role in aggregate variable across acceleration geometries

Previous haemodynamic studies have demonstrated axial displacement of the smaller, non-deformable platelets towards vessel walls by erythrocytes, which

resulted in a greater chance of platelet exposure to exposed thrombogenic subendothelium. This process was termed platelet margination.(6,7) It has been suggested in the literature that shallow acceleration geometries may result in a wider red-cell free margination layer.(6,7) A denser red-cell layer in the centre of the channel lumen would therefore decrease platelet concentration and near-wall interactions. It was hypothesised that this phenomenon may explain the smaller aggregate formation in the shallower entry angle acceleration geometries. To investigate this possibility, reconstituted human blood (HCT: 40%) was perfused through the device, and the resulting images were recorded and binarised to clearly define the red-cell core and the red-cell-free outer layers (*see Fig 5.3*). Measurement of the width of the red-cell free layer demonstrated no difference between acceleration geometries.

To further investigate the margination hypothesis, epifluorescence microscopy was conducted with reconstituted red cells (Hct 20, 40, 60%) and platelets (400 x 10^9/l). Washed platelets and red cells were treated with Fluo-4 (1 µg/ml, peak emission: 565 nm) and Vybrant DiI (1 ug/ml, peak emission: 504 nm) respectively, and reconstituted to determine if there was a clear demarcation in distribution of the cell types across the channel width. Representative averaged images from the each channel were superimposed and areas of fluorescence were compared to determine if margination was occurring and to what degree in each channel (*see Fig 5.3 a-d*). This experiment did not demonstrate noticeable platelet displacement towards the channel walls, nor increases in red cell density towards the centre of the channel (*see Fig 5.3 e-l*).

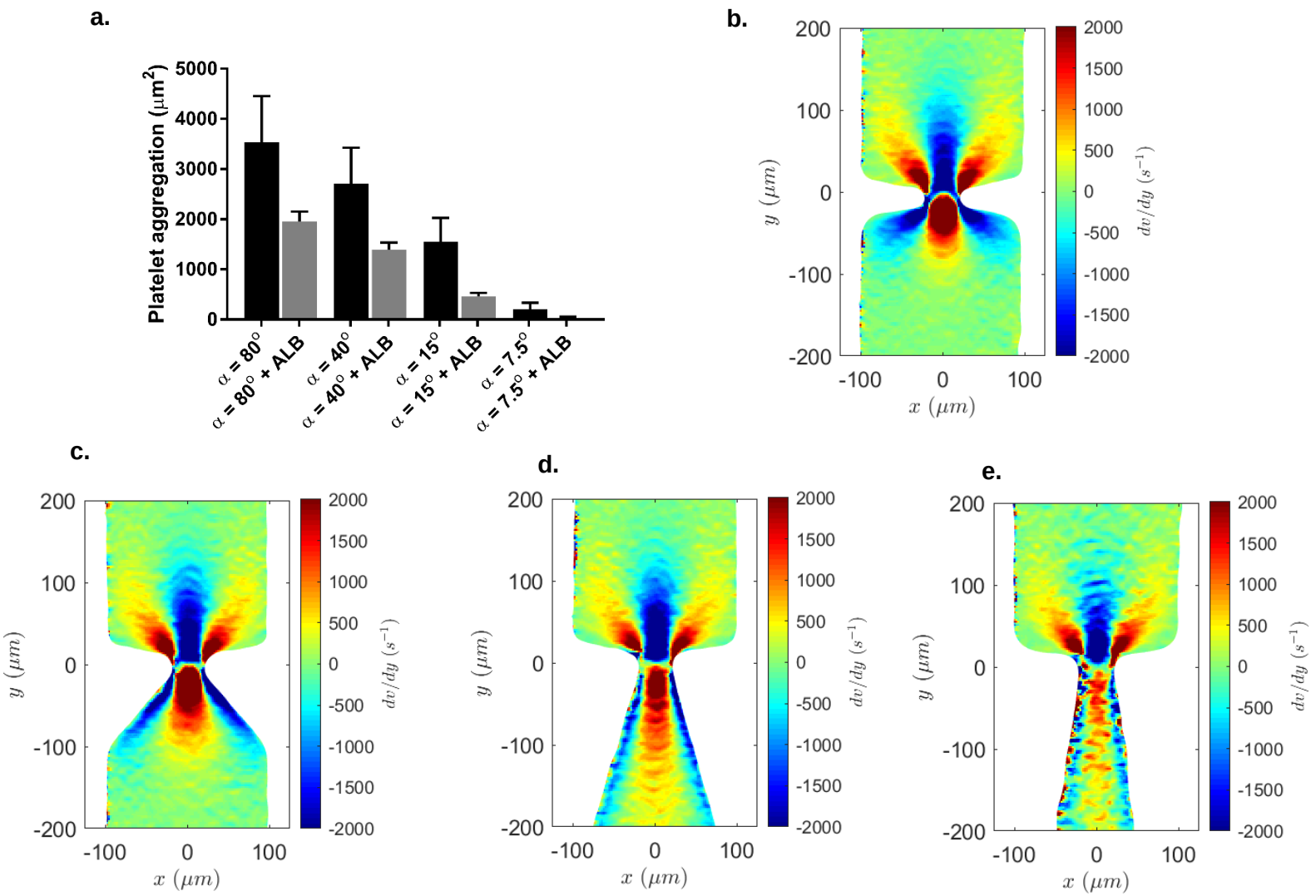
a.
Platelet aggregation (μm²)
5000
4000
3000
2000
1000
0
α = 80°
α = 80° + ALB
α = 40°
α = 40° + ALB
α = 15°
α = 15° + ALB
α = 7.5°
α = 7.5° + ALB
b.
c.
d.
e.
y (μm)
x (μm)
dv/dy (s⁻¹)
200
100
0
-100
-200
2000
1500
1000
500
-500
-1000
-1500
-2000

Figure 5.1 – Effect of acceleration angle on platelet aggregation

a) Representative platelet aggregation endpoint analysis demonstrating maximal aggregation area with varying acceleration angle. Error bars represent the mean ± the standard deviation. This graph represents results from n=6 control donors whose samples were tested in each angle. Data shows a strong relationship between increasing acceleration angle and aggregate size. An acceleration angle of 7.5^{o} demonstrated effectively no platelet aggregation. b-e) Computational fluid dynamic modelling in a stenosis with an acceleration angle of 80^{o}(b), 40^{o}(c), 15^{o}(d) or 7.5^{o}(e), demonstrates that reduction of stenosis entry angle significantly alters the duration and rate of shear rate increase experienced by platelets while not affecting maximum shear. This demonstrates that platelets respond to the rate of change in shear flow in a highly specific manner, independent of peak shear rate magnitude.

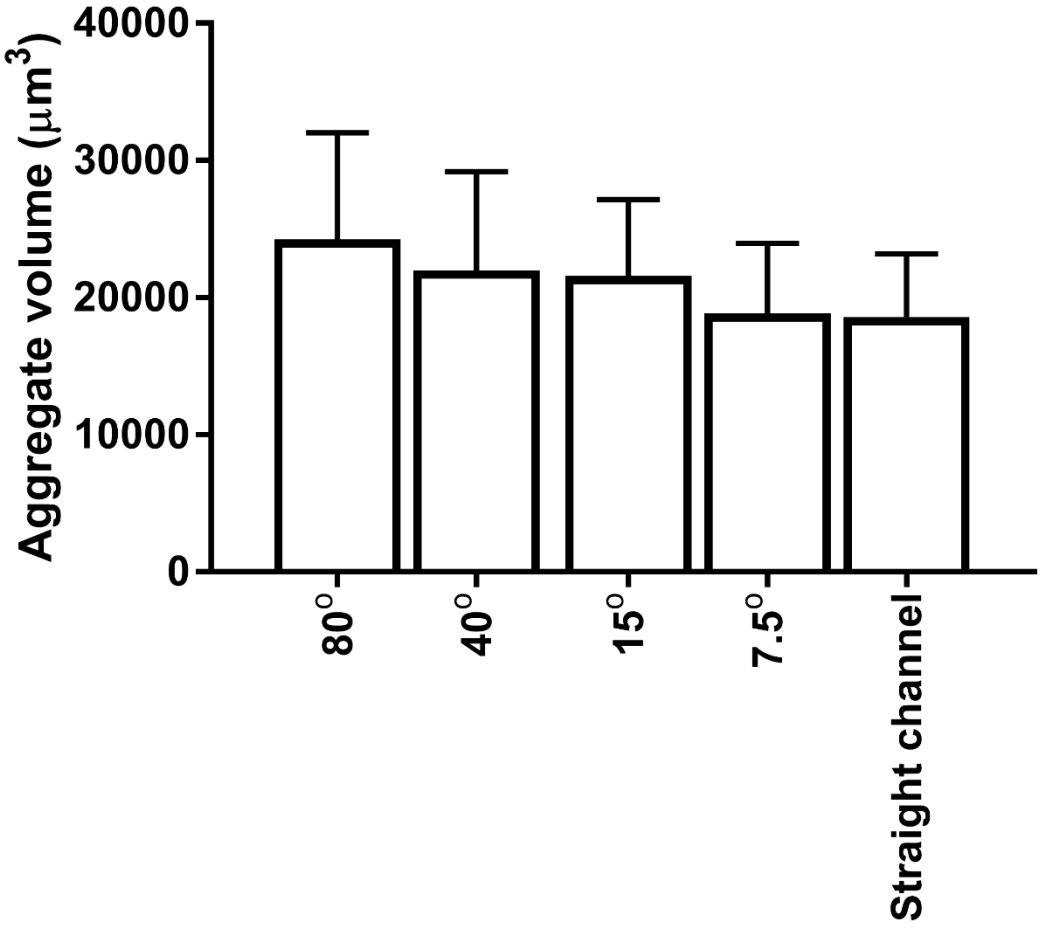
Aggregate volume (μm3)
40000
30000
20000
10000
0
80°
40°
15°
7.5°
Straight channel

Figure 5.2 – Platelet aggregation on downstream collagen

Endpoint platelet aggregation on a strip of collagen (100 µg/ml) 2000 µm downstream from the stenosis following 300 seconds of perfusion of epifluorescently-tagged human whole blood. Error bars represent the mean ± the standard deviation. No statistically significant differences in aggregate volumes were demonstrated between aggregates forming downstream of acceleration geometries of 80^{o}, 40^{o}, 15^{o} or 7.5^{o}. Data represents results from n=6 control donors.

5.6. Understanding the role of Ca^{2+} signalling in platelet response to shear conditions

Studies in the literature have demonstrated vWF binding to GPIbα in areas of high shear independent of integrin $\alpha_{IIb}\beta_{III}$ activation.(9-11) To investigate if these processes were contributing to the differential aggregate response in high-shear conditions, platelet Ca^{2+} signal transduction was measured in real-time in bulk flow. Platelet calcium signalling was measured through determination of the fluorescence of the calcium-sensitive dye Cal-520, which increases in fluorescent intensity in the 520 nm wavelength upon binding to intracellular calcium (*see chapter 4*).

Fluorescence was measured at five points: i) immediately prior to the stenotic gradient, ii) in the acceleration portion, iii) at the stenosis apex (the point of greatest shear), iv) in the immediate deceleration zone, and v) 3000 µm downstream of the stenosis. Fluorescence levels were expressed against platelets treated with A23187 (1.25 µM) and $CaCl_2$ (10 mM) to induce maximal platelet binding and act as a positive control, or the calcium chelators EGTA (2 mM) and DM-BAPTA (50 µM) to act as negative controls. To prevent aggregate formation and subsequent alteration of the acceleration angle, all channels were pre-treated with BSA (2%) to prevent plasma protein adsorption. These studies suggested a potentially important role for intracellular Ca^{2+} signalling in determining platelet response to shear gradients. Platelets passing through the stenoses with more acute acceleration angles (15^o, 20^o) demonstrated greater Ca^{2+} signalling transduction, which increased through the acceleration gradient, reached a peak at the apex, and decreased downstream of the stenosis (*see Fig 5.4*). This effect was apparent even with the addition of ALBs,

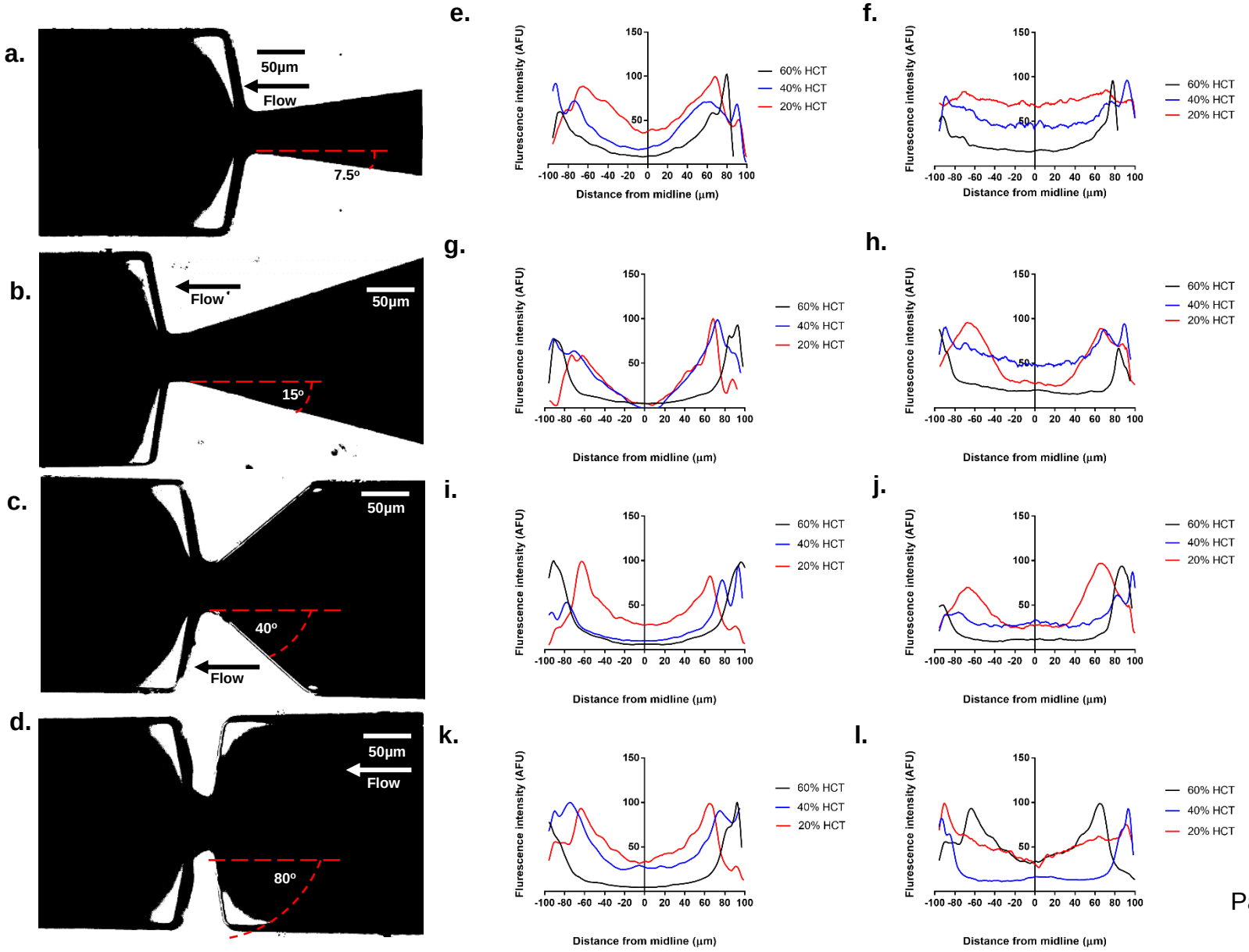
a.
50µm
Flow
7.5°
b.
Flow
50µm
15°
c.
50µm
40°
Flow
d.
50µm
Flow
80°
e.
f.
g.
h.
i.
j.
k.
l.
Flurescence intensity (AFU)
Distance from midline (µm)
60% HCT
40% HCT
20% HCT

Figure 5.3 – Margination investigations

a-d. *Thresholded, averaged transmission light microscopy images of stenotic gradients of 7.5^{o} (a), 15^{o} (b), 40^{o} (c), and 80^{o} (d) of two minutes of perfusion with human whole blood. Black regions indicate areas of red cell concentration. White areas indicate regions without red cells ('cell-free layer'), where light transmission has occurred. The images illustrate no significant differences in red cell distribution patterns or the size of red cell exclusion zones.* ***e-l****. Platelet and red cell distributions, as measured by a line scan across the channel width in the deceleration zone in reconstituted human blood at haematocrit concentrations of 20, 40 and 60%. Red cell and platelet concentration was measured through epifluorescent tagging of the cells with Vybrant DiI (1 µg/ml) and Fluo-4 (1 µg/ml) respectively.* ***e.*** *Platelet distribution after perfusion through a 7.5^{o} acceleration geometry.* ***f.*** *Red cell distribution after perfusion through a 7.5^{o} acceleration geometry.* ***g.*** *Platelet distribution after perfusion through a 15^{o} acceleration geometry.* ***h.*** *Red cell distribution after perfusion through a 15^{o} acceleration geometry.* ***I.*** *Platelet distribution after perfusion through a 40^{o} acceleration geometry.* ***j.*** *Red cell distribution after perfusion through a 40^{o} acceleration geometry.* ***k.*** *Platelet distribution across the channel width after perfusion through a 80^{o} acceleration geometry.* ***l.*** *Platelet distribution across the channel width after perfusion through a 80^{o} acceleration geometry. No differences in distribution were evident in red cell or platelet distribution across the channel. Figures represent data from n=3 individual donors.*

correlating with PAC-1 binding data (*see Fig 5.5*) and suggesting the response was soluble agonist independent.

5.7. Discussion

While the inducement of a high shear environment in the microcontraction has been established to be critical in thrombus development, the impact of specific haemodynamic parameters has not been not elucidated. Studies presented in this chapter suggest that adhesion-independent platelet activation in the artificial microcontraction can be differentially precipitated under variable extensional force conditions. These results have established the validity of using this flow assay system to examine platelet responses to differences in extensional flow, and preliminary studies to suggest potential mechanisms underlying this phenomenon. The observation that platelet aggregation is dependent on the shear rate gradient is in agreement with other published findings.(11,12) These suggest that platelets are primed to respond to extensional flow dynamics rather than just the magnitude of imposed shear rates, and furthermore that a defined shear flow acceleration threshold must be achieved to trigger platelet aggregation, independent of mass transport (margination) effects. Previous studies have aimed to demonstrate a role for margination and mass transport effects in explaining this differential response.(6,7) Experiments in this study did not demonstrate this margination effect, or a variation in the size of the erythrocyte-free layer in the geometries examined. Overall, these studies did not support an important role for platelet margination or mass transport effects in the differential platelet aggregation in stenotic geometries of variable acceleration angles. A detailed analysis of shear conditions within the

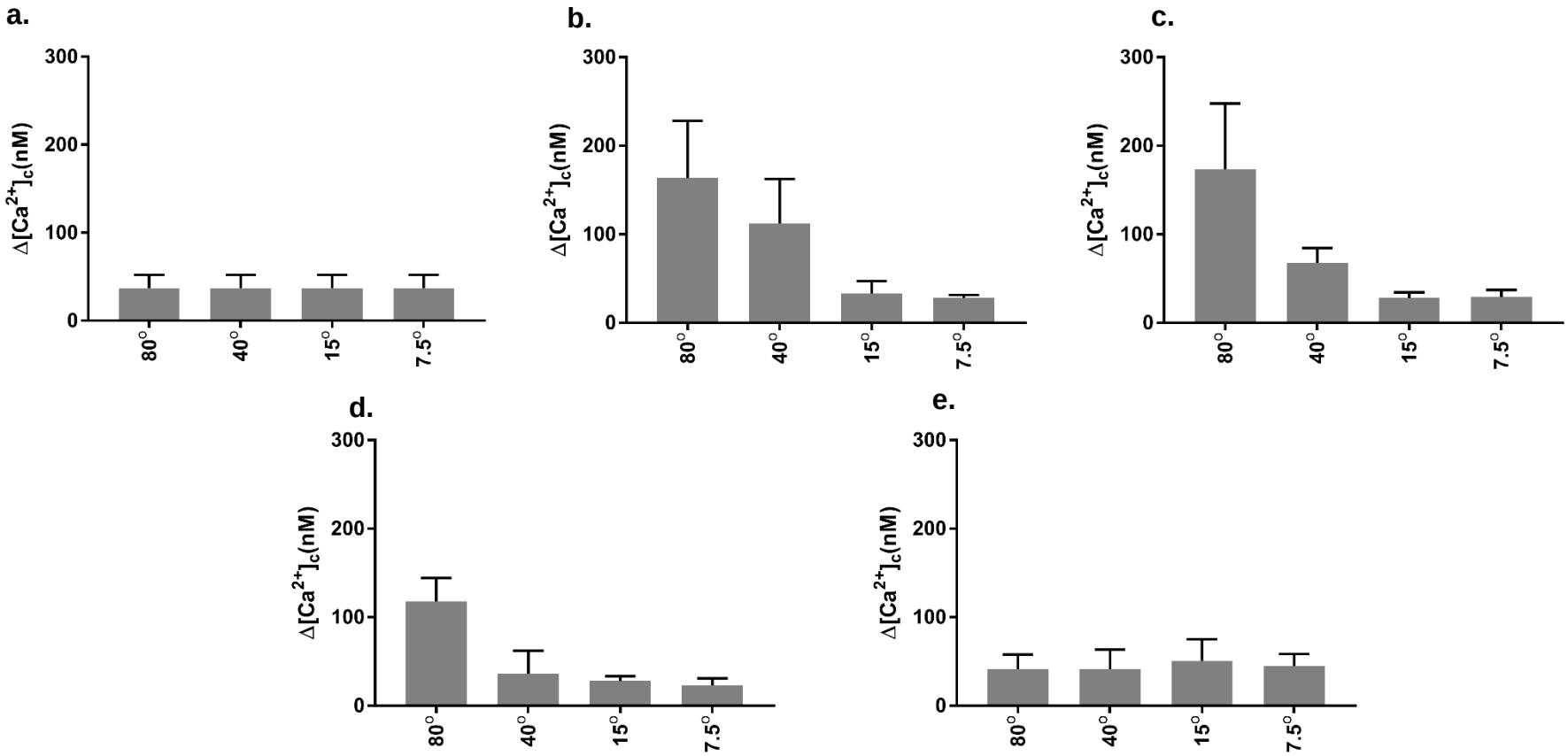
a.
b.
c.
d.
e.
300
200
100
0
Δ[Ca2+]c(nM)
80°
40°
15°
7.5°

Figure 5.4 – Real-time measurement of platelet activation in bulk flow

Maximal platelet cytosolic calcium flux $[Ca^{2+}]_c$ (nm) under perfusion at Q = 45 µl/min in stenoses with 80^o, 40^o, 15^o and 7.5^o acceleration angles. ***a.*** *Average platelet $\Delta[Ca^{2+}]_c$ 200 µm prior to the acceleration geometry, as measured by a line scan across the channel width.* ***b.*** *Average platelet $\Delta[Ca^{2+}]_c$ in the acceleration zone of the stenotic geometry, as measured by a line scan across the channel width.* ***c.*** *Average platelet $\Delta[Ca^{2+}]_c$ flux at the apex of the stenotic geometry at the point of peak shear, as measured by a line scan across the channel width.* ***d.*** *Average platelet $\Delta[Ca^{2+}]_c$ in the deceleration zone, as measured by a line scan across the channel width.* ***e.*** *Average platelet $\Delta[Ca^{2+}]_c$ 3000 µm after the acceleration geometry, as measured by a line scan across the channel width. Results represent n=3 independent samples from different patients.*

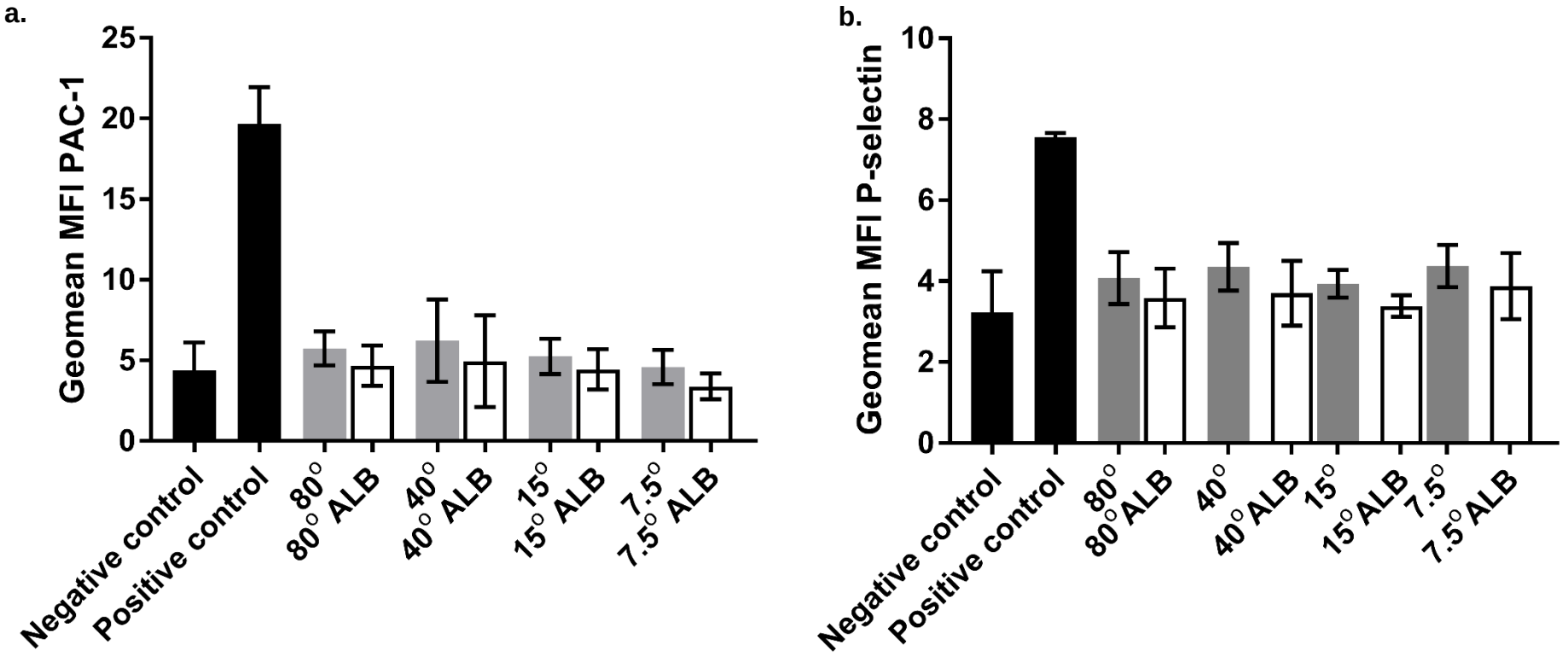
a.
Geomean MFI PAC-1
25
20
15
10
5
0
Negative control
Positive control
80°
80° ALB
40°
40° ALB
15°
15° ALB
7.5°
7.5° ALB
b.
Geomean MFI P-selectin
10
8
6
4
2
0
Negative control
Positive control
80°
80° ALB
40°
40° ALB
15°
15° ALB
7.5°
7.5° ALB

Figure 5.5 – Platelet activation in perfusate bulk flow as a function of microstenosis geometry

a. *FACS analysis demonstrating MFI geomean distribution of FIT-C PAC-1 antibody binding (integrin $\alpha_{IIb}\beta_{III}$ activation) to platelets in human whole blood following perfusion through microcontractions with acceleration geometries of 7.5^{o}, 15^{o}, 40^{o}, and 80^{o} (Q = 45 µl/min). ALB samples were treated with 100 µM MRS-2179, 10 µM 2-MeSAMP, 10 µM indomethacin and 0.02 U/ml apyrase.* ***b.*** *FACS analysis demonstrating MFI geomean distribution of FIT-C P-selectin antibody binding (α granule release) to platelets in human whole blood following perfusion through microcontractions with acceleration geometries of 7.5^{o}, 15^{o}, 40^{o}, and 80^{o}(Q = 45 µl/min). ALB samples were treated with 100 µM MRS-2179, 10 µM 2-MeSAMP, 10 µM indomethacin and 0.02 U/ml apyrase. Results represent n=3 independent samples from different patients.*

microcontraction is beyond the scope of this thesis but is explored in the published study in appendix 6.

To investigate other potential mechanisms behind this modulation of platelet reactivity, pathways of action of the canonical agonists were individually blocked.

There were several lines of evidence which suggest the shear stress response was not dependent on the presence or recognition of soluble agonists. First, differential aggregate responses still occurred despite the addition of amplification loop blockers, which inhibit reception of soluble agonists. Second, as previously discussed, despite studies demonstrating a margination of soluble agonists in microcapillaries, differences in margination were not evidenced. Finally, flow cytometry analysis demonstrated no differential binding of PAC-1 antibodies to platelets and α-granule release in the different perfusates. However, results on this point are inconclusive because this technique analyses all platelets in the sample, all of which would have encountered different shear gradients depending on their lateral position.

Importantly, studies presented in this chapter demonstrated a role for calcium-dependent signalling transduction in determining platelet activation in the artificial microstenosis. This phenomenon was found to be adhesion-independent, and occurred even in platelets that passed through in bulk flow. This activation was initiated in the acceleration zone of the geometry, indicating it was a function of the shear gradient, rather than peak shear. This activation was rapid and transient, as

calcium-dependent fluorescence levels returned almost to baseline in the downstream analysis region. If platelet response to shear gradients is secondary to intracellular calcium signalling, then the response is rapid and extremely sensitive to stimulation, as other platelet activation markers such as PAC-1 and P-selectin, were not elevated in the collected perfusate. The findings in this preliminary study could be used to explain and modulate platelet reactivity within the proposed diagnostic to improve haemocompatibility or better target diagnosis towards specific patient subgroups.

5.8. References

1. Tovar-Lopez FJ, Rosengarten G, Westein E, Khoshmanesh K, Jackson SP, Mitchell A. A microfluidics device to monitor platelet aggregation dynamics in response to strain rate micro-gradients in flowing blood. Lab Chip. 2010;10.
2. Wohner N, Kovács A, Machovich R, Kolev K. Modulation of the von Willebrand factor-dependent platelet adhesion through alternative proteolytic pathways. Thromb Res. 2012 Apr;129(4):41-6.
3. van Ryn J, Schurer J, Kink-Eiband M, Clemens A. The successful reversal of dabigatran-induced bleeding by coagulation factor concentrates in a rat tail bleeding model do not correlate with ex vivo markers of anticoagulation. 2011.
4. Jackson SP, Schoenwaelder SM, Goncalves I, Nesbitt WS, Yap CL, Wright CE, et al. PI 3-kinase p110beta: a new target for antithrombotic therapy. Nat Med. 2005 May;11(5):507-14.

5. Strony J, Beaudoin A, Brands D, Adelman B. Analysis of shear stress and hemodynamic factors in a model of coronary artery stenosis and thrombosis. Am J Physiol Heart Circ Physiol. 1993;265(5):H1787-H96.
6. Fitzgibbon S, Spann AP, Qi QM, Shaqfeh ESG. In vitro measurement of particle margination in the microchannel flow: effect of varying hematocrit. Biophysical journal. 2015;108(10):2601-8.
7. Gekle S. Strongly Accelerated Margination of Active Particles in Blood Flow. Biophysical journal. 2016;110(2):514-20.
8. Zhao R, Kameneva MV, Antaki JF. Investigation of platelet margination phenomena at elevated shear stress. Biorheology. 2007;44(3):161-77.
9. Tsun Wong AK. Platelet biology: the role of shear. Expert Rev Hematol. 2013;6(2):205-12.
10. Sing CE, Alexander-Katz A. Elongational flow induces the unfolding of von Willebrand factor at physiological flow rates. Biophys J. 2010;98(9):L35-7.
11. Colace TV, Diamond SL. Direct observation of von Willebrand factor elongation and fiber formation on collagen during acute whole blood exposure to pathological flow. Arterioscler Thromb Vasc Biol. 2013 Oct 25;33(1):105-13.
12. Tolouei E, Butler CJ, Fouras A, Ryan K, Sheard GJ, Carberry J. Effect of hemodynamic forces on platelet aggregation geometry. Ann Biomed Eng. 2011 May;39(5):1403-13.

Chapter six: Discussion

6.1. Introduction

This thesis reported on a series of developments in the characterisation of haemocompatible modular components of microfluidics systems. When integrated, these may be utilised in a comprehensive platelet diagnostic (*see Fig 6.1*). Individually, these components will contribute to increased control of flow rates and profiles through on-chip pumping capacities, fluidic isolation through valving, and detection of platelet reactivity through inducement of aggregation in high-shear or derivatised regions of pro-thrombogenic surfaces. Alternatively, the individual components represent significant breakthroughs in haemocompatible systems and may be adapted for use in other blood-handling devices. Through testing these components, advancements have been made in the standards of testing device haemocompatibility, as a battery of assays has been created and adapted to comprehensively assess the impact on platelet and red cell function and plasma protein composition. Work published from this research encompassed novel assessment of platelet function, development of novel micro-scale modular components, and a comprehensive approach to haemocompatibility testing. These findings have contributed to the breadth of knowledge that may be applied to microfluidic systems in the future to develop haemocompatible commercial systems.

6.2. Haemocompatible microvalves

Inclusion of microvalves in chapter three can vastly increase the precision of blood handling and application potentials of the proposed platelet function testing device (*Fig 6.1*), as they can prevent sample mixing, ensure delivery of precise reagent volumes, and offer sequential mixing and sample delivery.(1) A range of assays assessing haemocompatibility were developed to determine the impact of valve

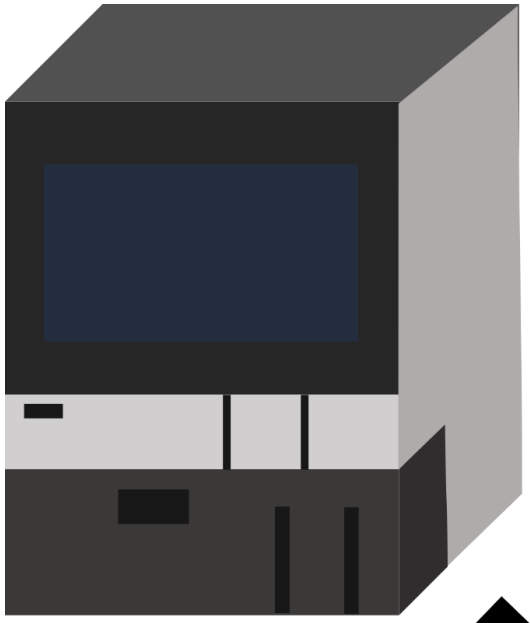

1. Final device exterior
2. Blood input port
3. Drug delivery line
4. Drug delivery reservoir
5. Pneumatic pump membrane
6. Microcontraction
7. Light receptor
8. Derivatised collagen
9. Waste container
10. Light source
11. Pneumatic reservoirs
12. Pneumatic lines

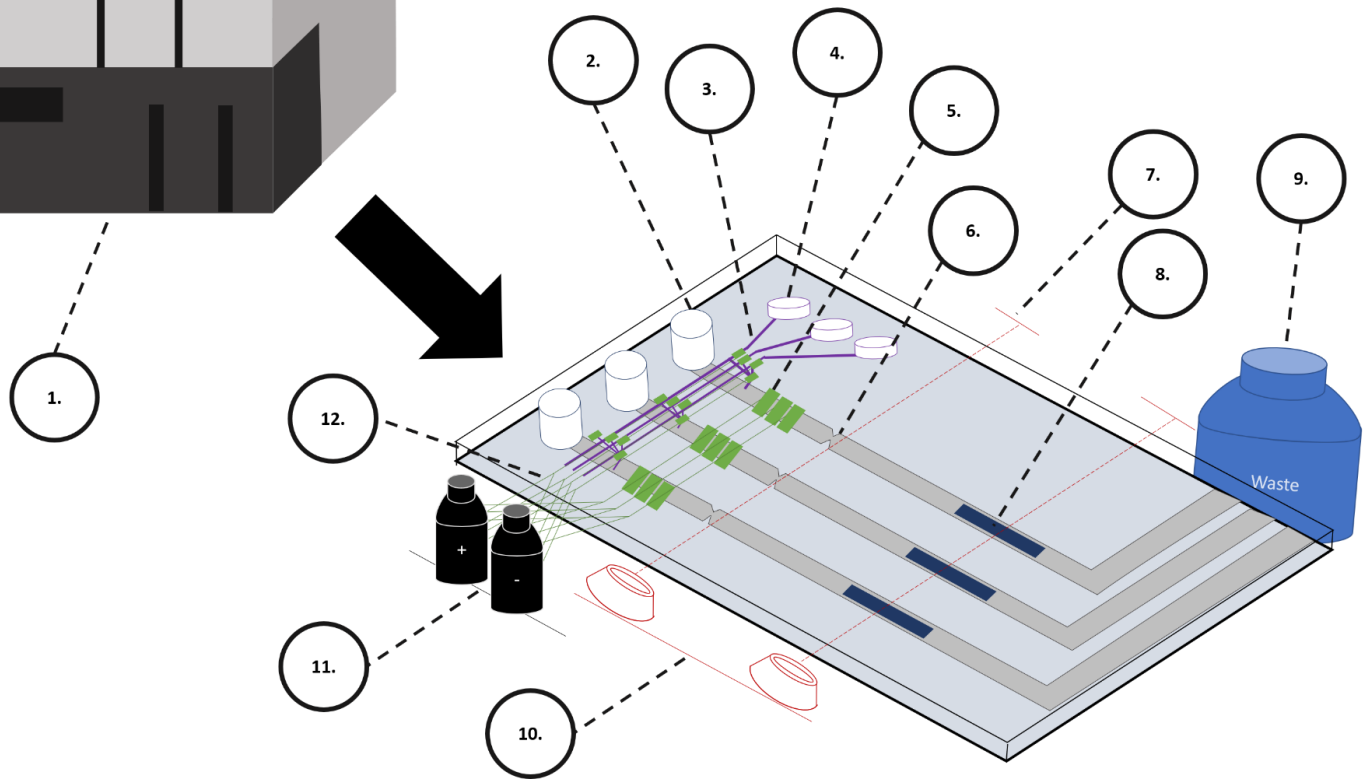

Figure 6.1 Schematic of projected final device

Automated haematology cartridge: system schematic showing overall "high-density" dual layer chip architecture incorporating drug/reagent pumps, perfusion elements, sample pump/blood mixers and parallelised strain applicator. This high-content screening system will harness on-chip automation and integration to allow potential for very small volume high-throughput screening of large chemical libraries to screen for shear selective anti-platelet drugs, assessment of congenital and acquired platelet-based bleeding (platelet hypo function), risk stratification of patients at thrombotic risk in the context of atherothrombosis and stent related thrombosis (platelet hyper-function).

The schematic represents several elements which were developed in this thesis, including the microcontraction geometries (6), pneumatic pumping membranes (5), derivatised collagen surface (8) and pneumatically actuated microvalves (not shown but expected to be integrated into drug delivery lines (3). These could be optimised through further haemocompatibility testing to reduce sample handling. Elements yet to be developed include an automated detection system (7, 10), and integrated automation of the entire device so it may be utilised clinically or in a laboratory with minimal operator input and variation.

geometry on platelet function, red cell handling and plasma protein composition. Through these assays, a haemocompatible elastomeric microvalving system was identified that minimally affected platelet function while still providing reliable fluidic control and isolation. The valves additionally lacked the need for surface passivation, improving the potential for practical integration in biosensors. Microvalve design was proposed and iterated based on knowledge from previously published studies that demonstrated local strain rate gradients are critical in determining platelet aggregation and biofouling.(2)

Findings in this chapter additionally demonstrated the importance of consideration of patient factors on diagnostic device output. Principally, platelet count, haematocrit and vWF levels and multimeric distribution were the chief parameters determined to alter device output. An increased haematocrit correlated with increased platelet aggregation in the stenotic architecture. This may have been due to the margination effect, increasing platelet density at the wall, which would result in an increase in aggregatory response. Similarly, increasing platelet count increased platelet-platelet interactions, resulting in greater thrombus growth. If these valves were used in the projected platelet function diagnostic (see *Fig 6.1*) differences in patient populations across these parameters could alter diagnostic outputs. These differences could be solved through standardisation of the platelet count and haematocrit through reconstitution if necessary. However, the clinical diagnostic device may lose some utility if reconstitution is deemed necessary, as reconstitution methods introduce additional variables and time and monetary constraints.

6.3. Haemocompatible micropump

Design of the elastomeric reciprocating micropumps in chapter four utilised the flexible architecture of PDMS to modulate the haemodynamic environment and improve haemocompatibility. Microfluidic pumping systems developed in this project offer the potential for the final device to have automated, fast, precisely controlled drug boluses with specific incubation times on-chip, before the testing zone with minimal impact on blood components, even at low fluid volumes (which other experimental micropump systems struggle to achieve).(3) The on-chip nature of the pump offered several advantages: provided capacity for rapid time-varying fluid control and complex sample switching, and offered the capacity for on-chip integration. Additionally, integration of on-chip pumps allowed for testing of the potential for on-chip mixing. On-chip mixing was found to be enhanced beyond diffusion-limited mixing due to direct contact of blood components with the pumping membranes. This was thought to be due to enhanced fluid folding arising from membrane movement after drug introduction to the blood sample.

Data presented in this chapter demonstrated compatibility was partially dependent on prevailing shear conditions. This was established through testing three parameters: assessment of the impact of actuation pressure (and intrinsically, membrane contact with the channel floor), actuation frequency and pump channel width. In all cases, higher shear conditions resulted in poorer platelet and red blood cell handling. These are important considerations for the final device, and indicate potential avenues for future improvement.

6.4. Stenotic gradient device

A key deficiency of current platelet diagnostics is that they fail to assess platelet function under physiologically relevant conditions, such as under flow.(4) Flow conditions are one of the elements of Virchow's triad which are key determinants of thrombogenic propensity.(5) Specifically, flow conditions must approximate shear parameters found in the human vasculature. Devices that do not replicate these shear conditions risk inaccurate assessments of platelet function as they do not replicate physiological conditions.(6-8)

In chapter 5 of this thesis, the influence of flow and knowledge of platelet responses to haemodynamic environments was utilised to develop the diagnostic component of the proposed device in Figure 6.1. The diagnostic device demonstrated several benefits above current diagnostics and microfluidics under development. A key feature differentiating this device from other-flow based diagnostics was its ability to closely mimic shear stresses present in the in-vivo haemodynamic environment. Specifically, the device was potentially superior to other flow-based devices in use clinically, such as the PFA-100, because it did not rely on the addition of exogenous agonists, and approximated shear levels found in the human vasculature.(9) Instead, it relied on endogenous levels of inhibitors and agonists within patient samples, providing a more physiologically-relevant output. Proof-of concept characterisation demonstrated the device was capable of differentiating between samples of patients with borderline type 1 vWD and healthy donors, which was traditionally a difficult distinction that relied on inaccurate measures.(10)

The device also offered the potential for modulation of the shear parameters depending on desired device output. In the human vasculature, as flow rates increase through a vessel stenosis, shear forces increase proportionally, contributing to greater platelet activation and aggregate size.(11) Modulation of the stenosis width, flow rate or acceleration angle was therefore performed to provide insight into platelet function under these different shear conditions. The work presented in chapter 5 demonstrated platelet aggregation was initiated on the downstream edge of a stenosis, and the aggregate grew into the downstream low-shear area. Aggregate size increased linearly with increasing flow rates, indicating aggregate size in the device was dependent on shear forces experienced by the platelets. Testing of the aggregate response in stenotic configurations with varying acceleration angles demonstrated that aggregate response at the artificial microcontractions was dependent on both peak shear and the rate of change in shear.

6.5. Limitations and future work

6.5.1. White blood cell assessment

This thesis describes the comprehensive assessment of the effect of the developed modular components on red cells, platelets and plasma proteins, but does not describe the impact on white cells, nor on the complement system. Despite their low number in non-pathologic samples of human blood, white blood cells have been shown to be responsive to shear conditions.(12) As white cell activation can alter platelet activity, this may have consequences for sensitivity of platelet diagnostics.(12,13) Sustained shear has been implicated in the prevention of leukocyte pseudopod formation and cellular adhesion, preventing spreading.(13)

White cells appear to be more sensitive to shear than red cells, and may be activated upon platelet activation.(14, 15) Platelets can release cytokines that act as chemoattractants for neutrophils and monocytes, enhancing inflammatory reactions *in-vivo*.(16) Alternatively, white cell activity may be adversely affected by biomaterial choice. Biomaterial incompatibility with leukocyte function cause the release of free radicals and cell signalling molecules such as prostaglandins, leukotrienes, interleukins and platelet activating factor.(17) Detection of these molecules in perfused blood in the device could be used in further haemocompatibility testing to provide a measure of white cell activation in the system.

The complement system is a circulating plasma protein cascade that may also be stimulated by incompatible materials.(18) It is an element of innate immunity, and plays a role in leukocyte and lymphocyte activation, inflammation and direct pathogen attack. Briefly, one of three pathways – the Classical, Alternative or Mannose Binding Lectin is activated, resulting in the activation and cleavage of C3, the fragments of which precipitate opsonisation, inflammation, cell membrane damage and further cellular activation.(18) The resulting inflammation can cause flooding of the system with inflammatory proteins or alter protein composition through cleavage reactions. Assessment of complement activation may be important in the context of studies described in this thesis because it can precipitate platelet aggregation, as platelets have receptors for elements of the coagulation cascade.(19) Complement activation is very sensitive to bioincompatibility, and studies have suggested complement activation may be used as a marker for materials incompatibility.(18) Additionally, thrombin production initiated by platelet intracellular calcium signalling can conversely initiate the complement cascade.

Measurement of complement system activation through quantification of serum C3a or C4a may provide a measure of the impact of the microfluidic systems developed in this thesis on blood components.(18)

6.5.2. Improvements in valve design

There is scope for further refinement in the design of haemocompatible microvalves to improve blood handling for the proposed device. The present V-shaped valving design was tested extensively in the third chapter and found to minimally interfere with platelet function due to the so-called ‘platelet funnelling’ effect, which drove platelets away from high shear zones, and prevented interactions with the valve surface. This effect was precipitated through the V-gate geometry itself, as the valve guided the fluid layers towards the apex, displacing platelets downwards. This effect could be further optimised through integrating more apices in the geometry – for example, by switching from a ‘V’-gate to a ‘W’ shape, providing an increased number of acute angles for the funnelling effect to occur through. This may further minimise platelet activation and induce further platelet displacement away from the valve surface. Further investigations could establish the optimum number of such zones and determine whether there is a minimum apical distance required to achieve the funnelling effect.

6.5.3. Improvements in pump design

The micropump/micromixer in chapter 4 demonstrated effective mixing of drugs with blood due to the disruption of laminar flow within the blood channel. However, the device may demonstrate practical improvements if the micromixers only require a single pump membrane, or if a shorter discharge channel was used to reduce the

device footprint. Increasing efficacy of the mixer may be achieved through micropatterning designs on the membrane surfaces to induce chaotic advection. A mixing approach commonly employed in microfluidics in the literature is integration of a herringbone pattern, wherein grooved surfaces stretch and fold the fluid layers to reduce the distance required for diffusive mixing.(20) Combination of this approach with the current membrane pumps though patterning onto the pump surface may approach sufficient homogeneity with a single membrane, while maintaining similar device flow rates.

While a micropump was identified with acceptable levels of haemocompatibility when operated under certain actuation parameters, levels of platelet activation and haemolysis rates could be further improved. Both issues could irreversibly modify analytes of interest in the blood sample, altering device output. Comparison between µPIV analysis and platelet [Ca^{2+}] results demonstrated correlation between high-shear environments and platelet activation. The impact of a high shear environment could be further decreased by simultaneously decreasing overall membrane size and increasing the number of membranes per channel. This solution would maintain similar flow rates, but decrease the overall shear applied to the sample. Alternatively, increasing fluidic resistance by increasing the length of the pneumatic actuation lines would decrease the speed of actuation, reducing the sharp ‘spikes’ seen in shear evidenced by the µPIV analysis. Another option that would maintain the small device footprint would be to integrate in-line fluidic capacitors.(20) Hydrodynamic capacitors act by creating an elastic surface that can absorb the sharp pressure spikes, thereby reducing the strain rate the blood sample would be subjected to. These could be integrated during device fabrication by adding more membranes to the blood channel

walls, reducing sharp changes in shear. This would improve final device application by reducing the shear applied blood samples tested.

6.5.4. Optimising POC device applications

Development of the device fully into a clinically useful point-of-care diagnostic would require further characterisation and improvement. Principally, the device is not portable due to the requirement of a microscope to visualise aggregate formation. Addressing this issue could involve the development of alternative optical detection devices, such as those being developed for smartphones, to enable portability.(21-23) This may also involve altering the endpoint analysis, as epifluorescent imaging detection would be difficult to achieve with smartphones while maintaining a short time frame and portability.(24) A relatively simple alternative that has been presented in the literature would be to utilise the haemoglobin contained within red blood cells to demarcate the clear growing aggregates.(25) Red cells flowing past an aggregate would create a red region directly adjacent to the clear platelet aggregate, which could be detected through machine learning for automated detection of aggregate size.

Such an alteration would require another process of characterisation to confirm similar degrees of sensitivity and specificity of detection, but would eliminate the time-sensitive dye-loading process and the requirement for lasers or alternative light sources which reduce portability and limit application. A database would be progressively defined to assist the automated detection system; containing results from normal subjects, vWD and antiplatelet therapy patients. In order to train the machine learning system, blood samples from control subjects, vWD and antiplatelet

therapy patients would be modified *ex vivo* to change key parameters such as platelet count, haematocrit, and plasma VWF and fibrinogen concentrations. In addition, blood samples would be titrated with defined doses of thrombin, ADP and TXA_2, to directly activate platelets, or treated with defined doses of anti- platelet agents to directly inhibit platelet function. The device would be validated through continual testing of blood samples taken from normal healthy donors, samples taken from patients presenting with diagnosed or suspected platelet related bleeding, patients prescribed anti-platelet therapy, and patients presenting with thrombotic episodes associated with platelet hyper-function. Experiments would be conducted on all iterations of the device in which anti-coagulated blood is treated with combinations of the platelet inhibitors; MRS2179 (100 µM), 2-MeSAMP (10 µM), and Indomethacin/aspirin (10 µM), either singly or in combination to mimic blood taken from patients on APT or blood taken from normal consenting donors given a bolus dose of clopidogrel and/or aspirin. In addition, experiments would be conducted to assess the capacity of the PFT to operate using re-calcified blood in order to reverse citrate anticoagulation and establish platelet reactivity in a closer physiological mimic.

6.5.5. Improving automation through multiplexing

Elements of the diagnostic device outlined in this thesis, including a micropump/micromixer, microvalves and high-shear microcontraction are hoped to be integrated into a coherent automated microfluidic diagnostic. However, further refinement is needed to determine the impact of all components on blood samples, and provide automation and control. Multiplexing, or the capacity to control multiple

components at once, is one avenue to increase automation. Multiplexing may be achieved through gang-valve integration, through better control of fluidic parameters. The microchip technology is planned to be further developed through integration of a series of valve-gated reagent ports and on-chip micropump/mixers that allow for the controlled introduction of blood samples, reagents (such as $CaCl_2$, to allow for assessment of thrombus formation in the presence of coagulation) and biochemical activators, as well as potential drug targets, at a precise location within the sample flow. Development of fully automated systems will simplify operation and move the device from a laboratory based system to a small footprint clinically accessible device, resulting in a highly robust and portable instrument package.

6.5.6. Materials optimisation for high volume manufacture

Current cartridge prototypes are based on low throughput standard PDMS micro-fabrication techniques suitable for rapid prototyping. While PDMS is a material well suited to numerous microfluidic applications, its suitability to mass fabrication, and thus commercial application is limited. In order to transition the microfluidic cartridge to a high volume commercial manufacturing process the current microfluidic cartridge could be replicated using industrial injection moulding methods used to fabricate the microvalve and micropump devices will be utilised. Cartridge performance could be assessed via ISO13485 standardised testing of fabrication tolerances and physical measures of sample handling and cartridge performance. Cartridge performance and overall intra- and inter-sample variability would need to be assessed again over multiple runs using control blood samples from normal donors.

6.5.7. Further haemodynamic investigations

One key consideration only briefly investigated in this thesis is the mechanism behind the variable platelet reactivity in different shear conditions (*see chapter 5.4*). Through correlation of CFD studies with platelet functional assays, a critical role for acceleration zones into regions of high shear in modulating platelet activation was noted in chapter 5 of this thesis. This finding was also prominent when investigating valving hemocompatibility in chapter 3, wherein it was demonstrated that despite a greater peak shear, the V-gated valves showed less platelet activation due to decreased extensional flow. These findings suggest haemocompatibility and platelet reactivity may be predicted by extensional flow dynamics, rather than the magnitude of imposed shear rates at stenosis. Our findings in this thesis demonstrated a critical role for flow acceleration in modulating platelet function independent of platelet adhesion events but did not determine the specific mechanism.

Future work is needed to identify the specific and potentially novel mechanisms behind this process. These mechanisms would demonstrate a new shear-sensitive detector in platelet biology, and could be elucidated through blood sample pre-treatment with inhibitors of various stages of platelet activation until the pathway can be elucidated. Previous studies have referenced this increase in platelet activation status as a function of stenotic entry angle, and have conjectured various hypotheses, including inducement of vWF self-association or unfolding, or RBC remodelling.(27-29) Understanding the precise impact of haemodynamics on platelet function may provide new diagnostic pathways and drug targets and allow development of more haemocompatible platelet processing devices. Similarly, investigation of other stenotic variants, such as stenoses with different times spent at

maximal shear, alterations in exit angle, or multiple stenoses in series may shed more light on platelet function in different shear conditions. Finally, understanding the impact of these variables in different patient populations may be critical in understanding the impact of certain pathologies on platelet function. Patients with diabetes and cardiovascular disease often demonstrate hyperreactive platelets for example, and through investigating platelet reactivity in these donor populations, the mechanism behind the increased incidence of thrombosis may be determined.(30, 31)

6.5.8. Scalable geometries

The proposed diagnostic device demonstrated potential with its capacity to discriminate between samples from healthy donors and those with shear-sensitive platelet disorders. However, it must be stressed that the events and growth of small-scale thrombi are intrinsically different to those evidenced in large-scale aggregation.(32, 33) For example, Casa *et al.* (2015) demonstrated that large thrombi are more sensitive to aspirin treatment.(34) It is therefore a limitation of the device that it may not be able to be extrapolated to investigate thrombus formation in large arteries.

6.6. Future device applications

6.6.1. Non-diagnostic device design

Findings in this thesis on the elements of stenotic geometries that influence platelet may allow for better design and overall blood handling in blood handling devices, such as microfluidics and ECMO. Such devices are very prone to thrombus generation, particularly in areas of tubing connection.(11) The tubing connection may

create a stenosis, activating platelets due to the high shear environment. Findings in the studies in this thesis suggest a reduced entry angle may reduce aggregation potential and should be considered in the design of such circuits. Additionally, knowledge of the impact of altered stenosis geometry on platelet activation may assist in the assessment of the thrombogenicity of arterial stenosis, and development of clinically useful risk stratification techniques.

6.6.2. Haemodynamic investigations

The effect of pulsatility on platelet function has been recognised for some years.(35) Increased turbulence, such as in the region of artificial valves, can trigger platelet activation and thromboembolic events, and abnormal blood flow patterns have been demonstrated *in-vitro* to induce platelet activation through imposing increased shear forces, and increasing the duration and frequency of platelet contact with stenotic regions.(36) Additionally, when compared with steady flow, pulsatile flow also generally increases platelet activation, platelet spreading and platelet adhesion.(37) However, little research has been conducted into the effect of pulsatile patterns on platelet function, particularly in regards to altered cardiac cycles. Previous attempts at characterisation of the impacts of flow profile have used a sinusoidal flow pattern, which while providing ostensible pulsatility, do not approximate physiological profiles.(38) The micropump detailed in this thesis could be used to investigate the effect of specific pulsatility parameters on platelet function by altering the degree of actuation, fluidic resistance or actuation frequency.

6.6.3. Clinical applications

Further development and characterisation of the device in various patient populations may allow testing for other platelet function disorders and responses to anti-thrombotic medication. A clinically significant example of this is in clopidogrel prescription: patients demonstrate a variable response to clopidogrel, an irreversible $P2Y_{12}$ inhibitor, and unnecessary dosing may be exposing patients to side effects and increased risk of thrombosis if it is not effective.(39) The impact of soluble agonists on platelet aggregation in the device was elucidated in this thesis through dosing with amplification loop blockers. Antagonism of the $P2Y_{12}$-ADP receptor specifically with 2-MeSAMP was found to produce the greatest decrease in aggregation, and the device was concluded to be $P2Y_{12}$-sensative.(40) Due to the demonstrated $P2Y_{12}$-ADP sensitivity, the device could therefore be characterised to determine a demarcation between patients who respond to clopidogrel by assessing aggregate size in samples that have and have not been dosed with the drug. It would be expected that patients or their samples treated with clopidogrel may have unimpeded aggregate growth in the device, and their aggregate sizes would approximate an untreated sample. Other clinical improvements include the device's capacity to diagnose vWD in borderline cases, or in subclassification diagnoses, which could be implemented through integration of other established vWD diagnostic tests on-chip, such as vWF:Ag or vWF:CB assays.(10)

6.7. Conclusion

The ability of circulating platelets to adhere to a blood vessel wall requires specialised adhesion mechanisms capable of withstanding high-shear environments.(2, 41-43) Platelets have evolved adhesion mechanisms enabling

them to form stable adhesion and aggregation under flow.(34, 44-46) Due to the differences in platelet responses in different haemodynamic environments, accurate assessment of platelet function must also be performed under physiologically relevant shear conditions. Current platelet function diagnostics are poorly optimised, and development of an-chip diagnostic with haemodynamics that mimic human vasculature has the potential to improve preclinical and clinical platelet function testing devices.(47)

In this thesis, development and characterisation of a haemocompatible microfluidic microvalve and micropump/mixer was detailed. Coupling these modular components to a diagnostic modular element would provide fluidic control while minimally impacting blood functioning and composition. The microvalving system can provide fluidic isolation, allowing for delivery of accurate blood or drug boluses at timed intervals. The micropump developed in this thesis allows for on-chip flow control, reducing the overall device footprint. Additionally, the micropump's mixing capacity provides the capacity for on-chip drug mixing and blood dosing with antithrombotic compounds with known incubation times. Further development will focus on further reducing the size of the pump driver to improve portability and allow for use in environments such as ambulances, patient's houses and at the bedside. The final component of the device developed in this thesis was the diagnostic element, which consisted of a stenotic gradient with a defined geometry. This was demonstrated to be a sensitive screen for vWD with good correlation with current platelet function tests. This stenotic gradient was also used to establish platelet response to varying shear gradients, and demonstrate early evidence of differential platelet response to

altered acceleration rates to peak shear within the artificial microstenosis environment.

Understanding the impacts of haemodynamics in terms of shear gradients and particle distribution, as demonstrated in the characterisation of the individual components, will be critical in the development of the fully integrated device. The integrated device may be characterised in patient populations with shear-sensitive platelet defects, or application may be demonstrated through testing with a novel anti-thrombotic drug library. This application would demonstrate reproducibility of device function, and improvement in processing times over existing devices.

Taken together, the developments in this thesis could make a positive impact on the diagnosis of platelet function disorders, understanding of platelet responses to haemodynamics, and in high-throughput anti-platelet drug screening. The system will be suitable for use in further preclinical and clinical validation of the device with the aim of developing a highly reliable, easy to use, and highly sensitive system that requires minimal operator expertise and input. The proposed device is superior to current commercial offerings in the platelet function testing space because of its application of a combination of patho-physiological blood flow and discrete reagent delivery (global stimulus), allowing for highly sensitive assessment of platelet function that enhances clinical diagnosis of bleeding disorders and anti-platelet therapy efficacy. It is anticipated that this substantial increase in test sensitivity over existing platelet function tests will fill the, as yet, unmet need for a reliable platelet function tests that can be utilised for more tailored patient monitoring.

6.8. References

1. Szydzik C, Brazilek RJ, Khoshmanesh K, Akbaridoust F, Knoerzer M, Thurgood P, et al. Elastomeric microvalve geometry affects haemocompatibility. Lab Chip. 2018;18(12):1778-92.

2. Nesbitt WS, Westein E, Tovar-Lopez FJ, Tolouei E, Mitchell A, Fu J, et al. A shear gradient-dependent platelet aggregation mechanism drives thrombus formation. Nat Med. 2009;15(6):665-73.

3. Woias P. Micropumps-summarizing the first two decades. Proc SPIE. 2001;4560:39.

4. Paniccia R, Priora R, Alessandrello Liotta A, Abbate R. Platelet function tests: a comparative review. Vasc Health Risk Manag. 2015 Feb 18;11:133-48.

5. Dickson B. Virchow's triad. Brit J Haematol. 2009 May;145(3):433.

6. Huck V, Schneider MF, Gorzelanny C, Schneider SW. The various states of von Willebrand factor and their function in physiology and pathophysiology. Thromb Haemost. 2014;111(4):598-609.

7. Tokarev AA, Butylin AA, Ataullakhanov FI. Platelet Adhesion from Shear Blood Flow Is Controlled by Near-Wall Rebounding Collisions with Erythrocytes. Biophysical Journal. 2011 Feb 16;100(4):799-808.

8. Tovar-Lopez FJ, Rosengarten G, Westein E, Khoshmanesh K, Jackson SP, Mitchell A, et al. A microfluidics device to monitor platelet aggregation dynamics in response to strain rate micro-gradients in flowing blood. Lab Chip. 2010;10(3):291-302.

9. Hintzke M, Harrington A. PFA-100 Utilization: One Institution's Experience. Am J Clin Pathol. 2015 Oct 01;144(suppl 2):131.

10. Marques MB, Fritsma GA. von Willebrand Disease Laboratory Diagnosis: the Saga Continues. Am J Clin Pathol. 2011 Jun 01;135(6):818-20.

11. Tsun Wong AK. Platelet biology: the role of shear. Expert Rev Hematol. 2013 Apr 01;6(2):205-12.

12. Zhang X, Hurng J, Rateri DL, Daugherty A, Schmid-Schönbein GW, Shin HY. Membrane cholesterol modulates the fluid shear stress response of polymorphonuclear leukocytes via its effects on membrane fluidity. Am J Physiol Cell Physiol. 2011;301(2):C451-C60.

13. Moazzam F, DeLano FA, Zweifach BW, Schmid-Schönbein GW. The leukocyte response to fluid stress. PNAS. 1997;94(10):5338-43.

14. Carter J, Hristova K, Harasaki H, Smith W. Short exposure time sensitivity of white cells to shear stress. Asaio Journal. 2003;49(6):687-91.

15. Dong C, Cao J, Struble EJ, Lipowsky HH. Mechanics of leukocyte deformation and adhesion to endothelium in shear flow. Annals of biomedical engineering. 1999;27(3):298-312.

16. Kral JB, Schrottmaier WC, Salzmann M, Assinger A. Platelet Interaction with Innate Immune Cells. Transfus Med Hemother. 2016 Sep 03;43(2):78-88.

17. Badylak SF, Gilbert TW, editors. Immune response to biologic scaffold materials. Semin Immunol; 2008: Elsevier.

18. Ricklin D, Hajishengallis G, Yang K, Lambris JD. Complement: a key system for immune surveillance and homeostasis. Nat Immunol. 2010;11(9):785.

19. Yun S-H, Sim E-H, Goh R-Y, Park J-I, Han J-Y. Platelet Activation: The Mechanisms and Potential Biomarkers. BioMed Research International. 2016;2016:9060143.

20. van Oeveren W. Obstacles in Haemocompatibility Testing. Scientifica. 2013 2013;2013:392584.

21. Yang K, Peretz-Soroka H, Liu Y, Lin F. Novel developments in mobile sensing based on the integration of microfluidic devices and smartphones. Lab Chip. 2016;16(6):943-58.

22. Hu J, Cui X, Gong Y, Xu X, Gao B, Wen T, et al. Portable microfluidic and smartphone-based devices for monitoring of cardiovascular diseases at the point of care. Biotechnol Adv. 2016;34(3):305-20.

23. Barbosa AI, Gehlot P, Sidapra K, Edwards AD, Reis NM. Portable smartphone quantitation of prostate specific antigen (PSA) in a fluoropolymer microfluidic device. Biosens Bioelectron. 2015;70:5-14.

24. Roda A, Michelini E, Cevenini L, Calabria D, Calabretta MM, Simoni P. Integrating biochemiluminescence detection on smartphones: mobile chemistry platform for point-of-need analysis. Analytical chemistry. 2014;86(15):7299-304.

25. Jiang Y, Lei C, Yasumoto A, Kobayashi H, Aisaka Y, Ito T, et al. Label-free detection of aggregated platelets in blood by machine-learning-aided optofluidic time-stretch microscopy. Lab Chip. 2017;17(14):2426-34.

26. Strony J, Beaudoin A, Brands D, Adelman B. Analysis of shear stress and hemodynamic factors in a model of coronary artery stenosis and thrombosis. Am J Physiol Heart Circ Physiol. 1993;265(5):H1787-H96.

27. Cosemans J, Angelillo-Scherrer A, Mattheij NJ, Heemskerk JW. The effects of arterial flow on platelet activation, thrombus growth, and stabilization. Cardiovasc Res. 2013 July 15;99(2):342-52.

28. Bray PF. Platelet hyperreactivity: predictive and intrinsic properties. Hematol Oncol Clin North Am. 2007;21(4):633-vi.

29. Puurunen Marja K, Hwang SJ, Larson Martin G, Vasan Ramachandran S, O'Donnell Christopher J, Tofler G, et al. ADP Platelet Hyperreactivity Predicts Cardiovascular Disease in the FHS (Framingham Heart Study). J Am Heart Assoc. 2018;7(5):e008522.

30. Suslova TE, Sitozhevskii AV, Ogurkova ON, Kravchenko ES, Kologrivova IV, Anfinogenova Y, et al. Platelet hemostasis in patients with metabolic syndrome and type 2 diabetes mellitus: cGMP- and NO-dependent mechanisms in the insulin-mediated platelet aggregation. Front Physiol.5:501.

31. Davies PF. Hemodynamic shear stress and the endothelium in cardiovascular pathophysiology. Nat Rev Cardiol. 2009;6(1):16.

32. Yokoyama S, Ikeda H, Haramaki N, Yasukawa H, Murohara T, Imaizumi T. Platelet P-selectin plays an important role in arterial thrombogenesis by forming large stable platelet-leukocyte aggregates. J Am Coll Cardiol. 2005;45(8):1280-6.

33. Fogelson AL, Neeves KB. Fluid Mechanics of Blood Clot Formation. Annu Rev Fluid Mech. 2015 Jan 03;47(1):377-403.

34. Casa LD, Deaton DH, Ku DN. Role of high shear rate in thrombosis. J Vasc Surg. 2015;61(4):1068-80.

35. Zhao XM, Wu YP, Cai HX, Wei R, Lisman T, Han JJ, et al. The influence of the pulsatility of the blood flow on the extent of platelet adhesion. Thromb Res. 2008;121(6):821-5.

36. Dasi LP, Simon HA, Sucosky P, Yoganathan AP. Fluid mechanics of artificial heart valves. Clin Exp Pharmacol Physiol. 2009;36(2):225-37.

37. Crow S, Milano C, Joyce L, Chen D, Arepally G, Bowles D, et al. Comparative analysis of von Willebrand factor profiles in pulsatile and continuous left ventricular assist device recipients. Asaio Journal. 2010;56(5):441-5.

38. van Breugel HH, Sixma JJ, Heethaar RM. Effects of flow pulsitility on platelet adhesion to subendothelium. Thromb Haemost. 1987;58(01):1419.

39. Yusuf S, Zhao F, Mehta SR, Chrolavicius S, Tognoni G, Fox KK. Effects of clopidogrel in addition to aspirin in patients with acute coronary syndromes without st-segment elevation. N Engl J Med. 2001;345.

40. Brazilek RJ, Tovar-Lopez FJ, Wong AKT, Tran H, Davis AS, McFadyen JD, et al. Application of a strain rate gradient microfluidic device to von Willebrand's disease screening. Lab Chip. 2017 Jul 25;17(15):2595-608.

41. Laurent P-A, Séverin S, Hechler B, Vanhaesebroeck B, Payrastre B, Gratacap M-P. Platelet PI3Kβ and GSK3 regulate thrombus stability at high-shear rate. Blood. 2014;125(5):588335.

42. O'Brien J. Shear-induced platelet aggregation. Lancet. 1990;335(8691):711-3.

43. Reininger A. Platelet function under high shear conditions. Hamostaseologie. 2009;29(1):21-2.

44. Bark Jr DL, Ku DN. Platelet transport rates and binding kinetics at high shear over a thrombus. Biophys J. 2013;105(2):502-11.

45. Conant CG, Schwartz MA, Nevill T, Ionescu-Zanetti C. Platelet adhesion and aggregation under flow using microfluidic flow cells. J Vis Exp. 2009 (32):1644.

46. Zwaginga JJ, Nash G, King MR, Heemskerk JW, Frojmovic M, Hoylaerts MF, et al. Flow-based assays for global assessment of hemostasis. Part 1: biorheologic considerations. J Thromb Haemost. 2006 Aug 25;4(11):2486-7.

47. Brazilek RJ, Tovar-Lopez FJ, Wong AK, Tran H, Davis AS, McFadyen JD, et al. Application of a strain rate gradient microfluidic device to von Willebrand's disease screening. Lab Chip. 2017;17(15):2595-608.

Appendices

Appendix one: Materials

Reagents	
Bovine serum albumin (10 % stock concentration)	Sigma Aldrich - U.S.A.
Human vWF (1 mg/ml stock concentration)	Sigma Aldrich - U.S.A.
Milli-Q water	Merck Millipore - U.S.A
Human fibrinogen (4.8 mg/ml stock concentration)	Sigma Aldrich - U.S.A.
Adenosine 5'-diphosphate sodium salt (30 mM stock concentration)	Sigma Aldrich - U.S.A.
Ristocetin (10 mg/ml stock concentration)	Helena Laboratories - U.S.A.
Refludan (Lepirudin) (800,000U/ml stock concentration)	Celgene – Aus
Calcium ionophore A23187 (2.5 mM stock concentration)	Sigma Aldrich - U.S.A.
Triton-X	Sigma Aldrich - U.S.A.
Collagen (500 µg/ml stock concentration)	Helena laboratories - U.S.A.
Fluorescent Tags	
DiOC6(3) iodide (1 mg/ml stock concentration)	ThermoFisher Scientific - U.S.A.
Cal-520-AM (1.25 mM stock concentration)	AAT Bioquest - U.S.A.
Fura Red-AM (2.5 mM stock concentration)	ThermoFisher Scientific - U.S.A.
Oregon Green BAPTA-1-AM (1.25 mM stock concentration)	ThermoFisher Scientific - U.S.A.

Tetramethylrhodamine (TRITC) dye (1 mg/ml stock concentration)	Sigma Aldrich - U.S.A.
mPEG-Fluorescein conjugates – Mw: 350 D, 2000 D, 20000 D (1 mg/ml stock concentration)	NANOCS Inc. - U.S.A.

Buffers

Acid-citrate-dextrose (ACD-7x): 85 mM sodium citrate, 72.9 mM citric acid, 10 mM d-glucose, 70 mM theophylline (pH 6.6, conductivity 12-15)

Platelet washing buffer (1x): 4.3 mM K_2HPO_4, 4.3 mM Na_2HPO_4, 11 mM NaCl, 5.5 mM glucose, 0.5% BSA, 10 mM theophylline, 0.02U/mL apyrase (pH 7.2-7.3, conductivity 13-15)

Tyrode's buffer (1x): 12 mM $NaHCO_3$, 10 mM HEPES pH 7.4, 137 mM NaCl, 2.7 mM KCl, 5.5 mM glucose (pH 7.2-7.3, conductivity 13-15)

Antibodies

AK2 (monoclonal CD42b-PE antibody) (0.1 mg/ml stock concentration)	Beckman Coulter - U.S.A.
Reopro (Abciximab) (2 mg/ml stock concentration)	Janssen Biotech - U.S.A
CD61 PerCP (RUU-PL 7F12)	B.D. Biosciences – U.S.A.
PAC-1 FITC	B.D. Biosciences – U.S.A.
Anti-human CD62P FITC conjugate	Thermo Fisher Scientific – U.S.A
Annexin V FITC conjugate	Sigma Aldrich - U.S.A.

Inhibitors

2-MESAMP (10 mM stock concentration)	Sigma Aldrich - U.S.A.
MRS-2179 (10 mM stock concentration)	Sigma Aldrich - U.S.A.
Indomethacin (10 mM stock concentration)	Sigma Aldrich - U.S.A.
Apyrase (200 U/ml stock concentration)	Sigma Aldrich - U.S.A.

Hirudin (lepirudin) (800,000 U/ml stock concentration)	Celgene - U.S.A
Enoxaparin sodium 100 mg/1 ml (anti-Xa: 10,000 IU)	Sanofi-Aventis, U.S.A
Theophylline	Sigma Aldrich - U.S.A.
PGE1	Sigma Aldrich - U.S.A.
RGDS	Sigma Aldrich - U.S.A.
Eptifibatide (2.4 x 10^{-3} M stock concentration)	Schering-Plough Pty Ltd – U.S.A.
ELISA kits	
vWF antigen kit	Helena Laboratories – U.S.A.
Fibrinogen antigen kit	Technoclone - Austria
PDMS manufacturing supplies	
PDMS Sylgard	Dow Corning - U.S.A.
KMPR 3050 photoresist	Microchem - U.S.A
SU8 Thinner	Microchem - U.S.A
Chrome mask	Microchrome Technology - U.S.A.
Silicon wafer	Micro Materials & Research Consumables - Aus
Glass wafer	Micro Materials & Research Consumables - Aus
Borosilicate glass slides (24 x 60 mm)	Menzel Glass - Aus
Punch biopsy (1.00 mm, 3.00 mm, 6.00 mm)	Harris Uni-Core - U.S.A.
2-Propanol	Merck Millipore - U.S.A
PDMS manufacturing equipment	

MA6 Mask aligner	SUSS MicroTec – Germany
Spin coater (Rotina 46)	Laurell Technologies – U.S.A.
Programmable Hotplate (MCS66)	CAT Scientific – U.S.A.
PDMS degasser	Tarsons Products - India
Vacuum oven	Thermo Scientific - Aus
Electronic scale	Digitech - U.S.A.
PDC-002 Plasma cleaner	Harrick Plasma – U.S.A.
Fume hood	Lab systems - Aus
Valve driver	
500 ml glass Pressure reservoirs	Schott Duran - Germany
1 bar valves	Burkert – U.S.A.
On-chip hard drive	Raspberry Pi – U.K.
Blood collection equipment	
19G butterfly needle	Terumo - U.S.A.
20 mL Luar-lock syringes	Terumo - U.S.A.
3 mL citrate Vacutainer	BD Vacutainer - U.S.A.
Vacutainer one-use holder	BD Vacutainer - U.S.A.
Blood storage equipment	
Eppendorf tubes (1.7 mL clear)	Eppendorf - U.S.A.
Falcon tubes	Beckton Dickinson - Australia
Disposable pipettes	Terumo - Japan
Eppendorf pipettes	Eppendorf - U.S.A.
Pipette tips (0.5-1 µL, 1-200 µL, 100-1000 µL)	Eppendorf - U.S.A.
12 x 75 mm Polystyrene test tubes	Fisher Scientific – U.S.A.
0.45 µm, 0.1 µm Filters	Sartorius – Aus
Delicate task wipers	Kimtech - Aus

Pump equipment	
Water bath	Ratek instruments - Aus
Harvard syringe Pump (PH.D. Ultra)	Harvard apparatus - U.S.A
Glass syringe (10 mL)	Top syringe - U.S.A.
Three-way stopcock	B. Braun - U.S.A
Silicon tubing	Saint Gobain - France
Needle connector	Terumo - Japan
Electrical equipment	
Centrifuge (z306 Hermle)	In Vitro Technologies - U.S.A.
Bench centrifuge (G766 HS)	Corning LSE - U.S.A.
pH meter (HI 2210)	Hanna instruments - U.S.A.
Nikon intensilight (C_HGFI)	Nikon instruments - U.S.A.
Camera (Zyla 5.5 sCMOS)	Andor - U.S.A.
High speed camera (inverted Nikon TiU microscope)	Nikon instruments - U.S.A.
v1610 (Vision Research) CMOS camera	Amtek – U.S.A
Bench scale (AG204)	Fisher Scientific - U.S.A.
Water bath	Ratek Laboratory Equipment - Australia
Microscope (Eclipse Ti-U)	Nikon instruments - U.S.A.
TIRF microscope (Olympus IX83 microscope)	Olympus – Japan
Haemogram (Cell Dyn Emerald)	Abbott Diagnostics - U.S.A.
FACSCalibur flow cytometer	Beckson Dickson – U.S.A.
FLUOstar Optima plate reader	BMG Labtech - Germany
CFD equipment and reagents	
Aqueous beads	
Polysorbate 20	

Nd:YAG double-pulsed laser	EverGreen - BigSky Laser Series – U.S.A.

Computer software

Fiji image processing software	Laboratory for Optical and Computational Instrumentation - U.S.A.
NIS-elements BR	Nikon instruments - U.S.A.
CellSens Dimension	Olympus – U.S.A.
GraphPad Prism version 5.0	GraphPad software - U.S.A.
MeshLab	Meshlab – U.S.A.
FlowJo	FlowJo LLC – U.S.A.
BD CellQuest	B.D. Sciences – U.S.A.
IBM SPSS	IBM Analytics – U.S.A.

Appendix two: Project ethics approval

ETHICS COMMITTEE CERTIFICATE OF APPROVAL

This is to certify that

Project No: 627/15

Project Title: Clinical validation of a new von Willebrand Disease (vWD) screening device

Principal Researcher: Professor Harshal Nandurkar

was considered for Low Risk Review and ***APPROVED*** *on* **09/03/2016**

It is the Principal Researcher's responsibility to ensure that all researchers associated with this project are aware of the conditions of approval and which documents have been approved.

The Principal Researcher is required to notify the Secretary of the Ethics Committee, via amendment or report,

Any significant change to the project and the reason for that change, including an indication of ethical implications (if any);
Serious adverse effects on participants and the action taken to address those effects;
Any other unforeseen events or unexpected developments that merit notification;
The inability of the Principal Researcher to continue in that role, or any other change in research personnel involved in the project;
A delay of more than 12 months in the commencement of the project; and,
Termination or closure of the project.

Additionally, the Principal Researcher is required to submit A Final Report on completion of the project.

Approval covers the project as described in the application (including any modifications made prior to approval). Low Risk projects are subject to audit and ethical approval may be withdrawn if the project deviates from that proposed and approved.

SPECIAL CONDITIONS

None

SIGNED:

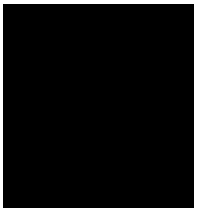

Professor John J. McNeil
Chair, Ethics Committee

Please quote project number and title in all correspondence

Appendix three: Patient consent form

The Australian Centre for Blood Diseases-Monash University

Participant Information and Consent Form
Clinical validation of a new VWD screening device

Principal Researcher:
Professor Harshal Nandurkar MBBS, PhD, FRACP, FRCPA
Director of Clinical Haematology, Alfred Health
Head, Australian Centre for Blood Diseases, Monash University
Level 1, Walkway,
via The Alfred Centre,
99 Commercial Rd
Melbourne, 3004

Phone: +61 3 990 30122

Fax: +61 3 990 30228

Email: Harshal.Nandurkar@monash.edu

Introduction

You are invited to take part in this research project. We are studying whether a new prototype blood test is useful to diagnose patient's with von Willebrand Disease (vWD). The reason for this is because the blood test currently used can be complex and may not always help in diagnosing patient's with bleeding disorders such as von Willebrand Disease (vWD). This research project will therefore compare the results of this new blood test with standard blood tests, which you normally have for your clinic appointment.

This Participant Information and Consent Form tells you about the research project. It explains the procedures involved. Knowing what is involved will help you decide if you want to take part in the research.

Please read this information carefully. Ask questions about anything that you do not understand or want to know more about. Before deciding whether or not to take part, you might want to talk about it with a relative, friend or healthcare worker.

Participation in this research is voluntary. Participation in this project will not affect your regular treatment. If you decide you want to take part in the research project, you will be asked to sign the consent section. By signing it you are telling us that you:

- Understand what you have read;
- Consent to take part in the research project;
- Consent to participate in the research processes that are described;
- Consent to the use of your personal and health information as described

You will be given a copy of this Participant Information and Consent Form to keep.

What is the purpose of this research project?

- **The aim of the project is to examine how a new research based blood test**

compares to the standard clinical blood tests in detecting patients with von Willebrand Disease (vWD).

- **Background: Patients with von Willebrand Disease (VWD) can suffer from easy bleeding and bruising. Currently employed blood tests may not always be able to detect all patient's with VWD or bleeding symptoms. We will use a new research tool (a blood test) to examine if this test can reliably detect patients with von Willebrand's Disease. We are expecting up to 50 patients with suspected, or confirmed von Willebrand Disease (vWD) to take part in this project.**
- **This project will be held at the Australian Centre for Blood Diseases, Monash University in collaboration with the The Haemophilia Clinic, Alfred Hospital. This research has been initiated by Professor Harshal Nandurkar.**
- To my knowledge, this project is the first of its type.
- The project will form part of a medical students Bachelor of Medical Science (Honours) year during which the student will gain firsthand experience and training in laboratory based research and medical device research and development. Data generated from blood samples will be used by the student to validate a research stage diagnostic system prototype and will form part of the students research thesis and final assessment. The data generated by the student and associated thesis will directly contribute to his/her Honours year grade.

What does participation in this research project involve?

- **If you agree to participate, after obtaining informed consent, we will need a maximum of 5 mls of blood to be collected only once on the day of your participation. This can be done on the same day as your clinic visit and will take not more than 10-20 minutes of your time.**

What will happen to my test samples?

- **This project involves collecting a blood sample from the participant and utilises new research techniques to assess platelet function. The blood samples are only used on the day of collection; hence no samples will be stored for future use. The samples will be individually coded, and the result will be stored in a safe and password protected database that can be accessed only by the researches involved in the project.**

What are the possible benefits?

We cannot guarantee or promise that you will receive any benefits from this research; however, possible benefits may include the future development of a new and simpler way to diagnose von Willebrand Disease (vWD).

What are the possible risks?

Possible risks or side effects include slight discomfort from blood collection - which is the same as you experience when having a regular blood test. We will ensure that the sample is collected by a person experienced in blood collection. We expect no significant consequence to occur from the procedure.

How will I be informed of the results of this research project?

If you wish to be informed of the outcome of this project, you can contact the investigators who will be happy to inform you of the research outcome.

What else do I need to know?

- **What will happen to information about me?**

Any information obtained for the purpose of this research project that can identify you will be treated as confidential and securely stored. It will be disclosed only with your permission, or in compliance with the law.

In any publication and/or presentation, information will be provided in such a way that you cannot be identified, except with your permission.

It is desirable that your local doctor be advised of your decision to participate in this research project. By signing the consent section, you agree to your local doctor being notified of your decision to participate in this research project.

- **How can I access my information?**

In accordance with relevant Australian and/or Victorian privacy and other relevant laws, you have the right to access the information collected and stored by the researchers about you. You also have the right to request that any information, with which you disagree, be corrected. Please contact one of the researchers named at the end of this document if you would like to access your information.

- **What happens if I am injured as a result of participating in this research project?**

If you suffer an injury as a result of your participation in this research project, please contact the research staff. Hospital care and treatment will be provided by the public health care system (Medicare) at no cost to you.

- **Is this research project approved?**

This research project has been approved by the Human Research Ethics Committee of the Alfred hospital.

This project will be carried out according to the *National Statement on Ethical Conduct in Human Research* (2007) produced by the National Health and Medical Research Council of Australia. This statement has been developed to protect the interests of people who agree to participate in human research studies.

If you have any further questions, you can contact Professor Harshal Nandurkar (Head, Department of Haematology, Alfred Hospital) 9903 0122, or any complaints, you can contact Ms Emily Bingle (Research Governance Officer, Alfred Health) 9076 3629 or research@alfred.org.au

Consent

I have read, or have had read to me in a language that I understand, this document and I understand the purposes, procedures and risks of this research project as described within it.

I give permission for my doctors, other health professionals, hospitals or laboratories outside this hospital to release information to the Australian Centre for Blood Diseases concerning my disease and treatment that is needed for this project. I understand that such information will remain confidential.

I have had an opportunity to ask questions and I am satisfied with the answers I have received.

I freely agree to participate in this research project as described. I understand that my participation involves collecting 5 mls of my blood once on the day of the experiment.

I understand that I will be given a signed copy of this document to keep.

Participant's name (printed) ……

Signature Date

Name of witness to participant's signature (printed) ……

Signature Date

Declaration by researcher*: I have given a verbal explanation of the research project, its procedures and risks and I believe that the participant has given me informed consent.

Researcher's name (printed) ……

Signature Date

Appendix four: ‘Disrupting the platelet internal membrane via PI3KC2α inhibition impairs thrombosis independently of canonical platelet activation’

Disrupting the platelet internal membrane via PI3KC2□ inhibition impairs thrombosis independently of canonical platelet activation

M.V. Selvadurai[1], M.J. Moon[1], Z. Zheng[2], S.J. Mountford[2], R.J. Brazilek[1], R.P. Iman[1], J.-Y. Rinckel[3] A. Eckly[3], C. Gachet[3], W.S. Nesbitt[1,4], I.G. Jennings[2], P.E Thompson[2] and J.R. Hamilton[1]*

Affiliations:

[1]Australian Centre for Blood Diseases, Monash University, Melbourne, VIC 3004, AUSTRALIA

[2]Monash Institute of Pharmaceutical Sciences, Monash University, Parkville, VIC 3052, AUSTRALIA

[3]Unité mixte de recherche S949 Institut National de la Santé et de la Recherche Médicale, Université de Strasbourg, Etablissement Français du Sang-Alsace, Strasbourg, France

[4]Microplatforms Research Group, School of Electrical & Computer Engineering, RMIT University, Melbourne, Australia

*To whom correspondence should be addressed:

Justin R. Hamilton
Australian Centre for Blood Diseases
Monash University
L1 AMREP Building
99 Commercial Road
Melbourne, VIC 3004
AUSTRALIA

Telephone: +61-3-9903-0125
Email: justin.hamilton@monash.edu

One Sentence Summary: PI3KC2α inhibition selectively impairs platelet function during thrombosis by disrupting the structure of the internal membrane and blocking platelet function independently of canonical activation.

Abstract:

Arterial thrombosis causes heart attacks and most strokes and is the most common cause of death in the world. Platelets are the cells that form arterial thrombi, and anti-platelet drugs are the mainstay of heart attack and stroke prevention. Yet current drugs have limited efficacy, preventing fewer than 25% of lethal cardiovascular events without clinically significant effects on bleeding. The key limitation on the ability of all current drugs to impair thrombosis without causing bleeding is that they block global platelet activation, thereby indiscriminately preventing platelet function in hemostasis and thrombosis. Here, we identify an approach that overcomes this limitation by preventing platelet function independently of canonical platelet activation and that appears relevant specifically in the setting of thrombosis. Genetic or pharmacological targeting of the Class II PI3-kinase, PI3KC2α, dilates the internal membrane reserve (open canalicular system) of platelets but does not affect activation-dependent platelet function. Inhibition of PI3KC2α is potently anti-thrombotic in human blood *ex vivo* and mice *in vivo*, but does not impact hemostasis. Mechanistic studies reveal this anti-thrombotic effect occurs via a unique mechanism involving the regulation of membrane-dependent platelet adhesive function in the presence of hemodynamic forces. These findings demonstrate an important role for PI3KC2α in regulating platelet structure and function via a unique membrane-dependent mechanism, and suggest that drug targeting the platelet internal membrane may be a suitable approach for novel anti-thrombotic therapies with an improved therapeutic window.

Introduction

PI3Ks are a family of broadly-expressed enzymes that catalyse the formation of the intracellular signalling molecules PI(3)P, PI(3,4)P_2, and PI(3,4,5)P_3. These membrane-bound lipids influence the location and activity of signalling complexes by scaffolding key signalling proteins *via* specialised lipid-binding domains (1). Mammals have eight PI3Ks that are separated into three classes defined by substrate specificity and use of regulatory subunits: four Class Is (p110α, p110β, p110δ, and p110γ), three Class IIs (PI3KC2α, PI3KC2α, and PI3KC2α), and one Class III (Vps34). The Class I PI3Ks are by far the most widely studied and have well-defined roles in a number of cell types (2-4). In marked contrast, the cellular functions of Class II PI3Ks have only begun to emerge in recent years, in large part due to the recent development of genetically modified mouse models and selective pharmacological inhibitors of these enzymes (5, 6).

We and others have recently reported an important role for PI3KC2α in mouse platelet function (7-9). We have shown that platelets from mice and humans express PI3KC2α and PI3KC2α, but not PI3KC2α (7). We generated mice deficient in PI3KC2α or PI3KC2α and found no platelet defect in PI3KC2α-/- mice and 100% embryonic lethality in PI3KC2α-/- mice (7). To overcome this, we developed an inducible RNAi-based approach to reduce gene expression in platelets of adult mice (10). We used a CMV-driven and tet-regulated system to induce expression of microRNA-based short hairpin RNAs (shRNAs) (11, 12) against PI3KC2α. We have shown that this system induces knockdown of target proteins in a wide range of cells and is highly effective in platelet (10). Treating these mice with doxycycline (600 mg/kg in food for ≥10 days) resulted in undetectable platelet PI3KC2α expression and led to marked protection

against arterial thrombosis without any impact on bleeding (7). These findings were confirmed using a distinct mouse model in which a kinase-inactivating point mutation was introduced into the active site of PI3KC2α (8). Intriguingly, the *in vivo* platelet dysfunction of PI3KC2α-deficient mice appears due to a novel mechanism related to the regulation by PI3KC2α of the structure of the internal membrane reserves of platelets (open canalicular system; OCS) (7-9). Together, these studies defined an unexpected role for PI3KC2α in regulating the structure of the platelet internal membrane, and provide the first evidence linking the OCS to the thrombotic function of platelets. This initial work suggests that drug targeting of platelet internal membrane structure and function via pharmacological inhibition of PI3KC2α may represent a viable approach for novel anti-platelet therapy. However, in the absence of PI3KC2α inhibitors, whether or not a similar function occurs in human platelets remained unknown.

Here, we develop a first generation PI3KC2α inhibitor and show that it reproduces in human platelets the structural and functional anti-platelet effects observed in PI3KC2α-deficient mouse platelets. Further, PI3KC2α inhibition provides potent anti-thrombotic effects in mice and humans via a mechanism involving the function of the platelet membrane. Our studies indicate PI3KC2α inhibition is a viable target for unique anti-platelet drug therapy and represents the first known approach for targeting the platelet internal membrane structure and function for therapeutic benefit.

Results

A rational drug design approach yields compounds with activity against PI3KC2α.

There are no reported isoform selective PI3KC2α inhibitors, and the literature relating to PI3KC2α inhibition in general is sparse. We drew on a report by Knight *et al*, that described "off-target" PI3KC2α inhibition induced by a range of compounds from the patent literature, among them PIK-90, which has an IC_{50} against PI3KC2α of 47 nM (versus 11 nM against PI3K p110α) (13). We also identified the analogue copanlisib as a potent inhibitor of all class I isoforms (< 10 nM for each) but substantially more moderate against PI3KC2α (> 1000 nM) (14). We confirmed those potencies in our own assays and sought to make more potent inhibitors (Table 1). The x-ray structures of PIK-90 and copanlisib bound to the Class I PI3K, p110γ, show that the C5-amide of each molecule projects into the affinity pocket (13, 14). This region is conserved across the PI3K isoforms except for PI3KC2α, where there is both a Phe for Tyr substitution and a Glu for Asp substitution in PI3KC2α. Therefore we considered that changes in structure may enhance the potency or selectivity of PIK-90 for PI3KC2α.

To this end, modification of the PIK-90 at the C5-nicotinamide yielded several compounds with comparable potency versus PI3KC2α. The 4-amino-nicotinamide, SJM-X151, was the most potent of these, with an IC_{50} against PI3KC2α of 13nM. Moreover, SJM-X151 showed a switch in the preference to the Class II isoforms over the Class I isoforms (IC_{50}s against p110α, p110β, and p110δ of 260, 41, and 444 nM, respectively; Table 1).

PI3KC2α inhibition reproduces the platelet cell biology effects of PI3KC2α-deficiency

Having uncovered a series of compounds with varying potency and specificity against PI3KC2α, we first examined whether pharmacological inhibition of

PI3KC2α reproduces the phenotypes observed in PI3KC2α–deficient mice. We have previously reported that genetic deficiency of PI3KC2α causes dilation of the open canalicular system (OCS) in platelets that appears linked to an *in vivo* platelet dysfunction sufficient to impair arterial thrombosis (7, 9). Therefore we examined whether PI3KC2α inhibition mimicked these effects. Here, SJMX-151 accurately reproduced the changes in OCS structure observed in PI3KC2α-deficient mouse platelets, both qualitatively and quantitatively, in mouse and human isolated platelets. Ultrastructure analysis by transmission electron microscopy revealed that exposure of mouse platelets to SJMX-151 (10 μM, 3 h) induced a similar pattern of OCS dilation to that observed in platelets from PI3KC2α-deficient mice (Figure 1A). Both PI3KC2α–deficient and SJMX-151–treated mouse platelets displayed regions of dilated OCS, with a cross-sectional surface area that was 30 – 40% larger than in platelets from their littermate or vehicle-treated controls respectively (Figure 1B). Importantly, the same treatment of human platelets with SJMX-151 (10 μM, 3 h) resulted in a near-identical effect (Figure 1A,B). A concentration-response curve to SJMX-151 revealed concentrations of 1 μM were sufficient to induce a significant effect in this assay (Figure 1 c).

The OCS dilation induced by SJMX-151 appeared due to the compound's activity against PI3KC2α since 1) treatment of platelets from PI3KC2α–deficient mice with SJMX-151 caused no additional effect (Figure 1A,B) and 2) the OCS dilation induced by SJMX-151 was not observed following exposure of platelets to compounds without significant activity against PI3KC2α but that are potent inhibitors of other PI3K isoforms (Figure 1D). For example, no effect on the OCS was observed following treatment with any of copanlisib (IC_{50}s [nM] against PI3KC2α>10000; PI3KC2β□>10000; p110α –=

0.5), pictilisib (IC_{50}s [nM] against PI3KC2α >10000; PI3KC2β = 590; p110δ = 7) or dactolisib (IC_{50}s [nM] against PI3KC2α = 155; PI3KC2β = 27; p110 isoforms = 4 – 10), nor with the compound SJMX-125, from the same series as SJMX-151 but with markedly different activity levels (IC_{50}s [nM] against PI3KC2α >10000; PI3KC2β = 278; p110β = 775). Together, this genetic and pharmacological evidence strongly suggests that it is inhibition of PI3KC2α that leads to dilation of the OCS in mouse and human platelets.

The OCS dilation induced by PI3KC2α inhibition occurred rapidly, with a significant increase in OCS surface area in as little as 5 min of SJMX-151 treatment and with no greater dilation occurring beyond this time out to 3 h of drug treatment (Figure 1E). In addition, the OCS effects induced by SJMX-151 were fully reversible; pretreatment of human isolated platelets for 5 min followed by drug washout resulted in a marked reduction in OCS dilation after 5 min and a return to control levels after 60 min (Figure 1E). Together, these findings indicate the regulation of OCS structure by PI3KC2α is surprisingly dynamic.

To extend on this 2-dimensional analysis of OCS dilation in response to genetic deficiency or pharmacological inhibition of PI3KC2α, we next examined the complete architecture of the OCS using focused ion bean-scanning electron microscopy (FIB-SEM) (15). Whole cell 3D reconstructions of wildtype versus PI3KC2α–deficient mouse platelets and vehicle- versus PI3KC2α inhibitor-treated human platelets revealed a similar pattern of OCS dilation as observed in our 2-dimensional analysis (Figure 2A and Supplementary videos 1 and 2). In both cases, a near-uniform OCS dilation was observed throughout the cells, without any major change in its distribution (Figure 2A). Quantitation revealed a strikingly similar ~ 40% increase in OCS volume

in PI3KC2α–deficient mouse platelets or PI3KC2α–inhibitor treated human platelets when compared with their respective control (Figure 2B). This altered OCS structure occurred without any gross changes in the structure of other organelles (Supplementary videos 1 and 2). Taken together, these studies indicate pharmacological inhibition of PI3KC2α accurately reproduces the effects of PI3KC2α–deficiency relating to the structure of the internal membrane reserves of platelets, and that this effect extends to human platelets.

PI3KC2α inhibition is anti-thrombotic in human blood ex vivo *independently of canonical platelet activation mechanisms*

Pretreatment of human platelets with SJMX-151 had no effect on thrombin-induced platelet aggregation (Figure 3A) or $\alpha_{IIb}\beta_3$ activation (Figure 3B), even at concentrations 10- to 100-fold above that required to induce marked changes in OCS structure under identical treatment conditions. The rank order of potency for inhibition of both aggregation and $\alpha_{IIb}\beta_3$ activation was copanlisib > SJMX-125 >> SJMX-151, which closely aligns with the rank order of potency of these compounds against the Class I PI3Ks and suggests inhibition of platelet activation observed here is largely dependent on Class I PI3Ks and is decoupled from PI3KC2α.

We next examined the anti-thrombotic potential of PI3KC2α inhibition. Platelet-dependent thrombus formation was examined in human blood *ex vivo* by perfusing anticoagulated whole blood over an immobilised Type I fibrillar collagen substrate (16, 17). Here, we observed that pretreatment of human whole blood with SJMX-151 (10 μM, 10 min) was sufficient to provide striking anti-thrombotic effects, markedly impairing platelet-dependent thrombus growth on a collagen surface (Figure 3 c,D). 3D reconstructions of thrombi indicated that the platelet deposition on the collagen

surface was not significantly different at its base level (platelet-collagen interaction), but that subsequent platelet-platelet interaction-dependent growth was markedly impaired (Figure 3 c). As was observed in the platelet cell biology experiments, the anti-thrombotic effects induced by SJMX-151 occurred rapidly (10 mins pre-treatment).

We next examined the effects of PI3KC2α inhibition directly against the effects of the two most commonly-used anti-platelet strategies, aspirin (50 µM acetylsalicylic acid) and P_2Y_{12} receptor inhibition (100 µM 2-MeSAMP). As previously observed, the anti-thrombotic effects of both aspirin and 2-MeSAMP were dependent on the blood shear rate present during thrombogenesis. As expected, both aspirin and 2-MeSAMP effectively impaired human thrombus formation at 1800 s^{-1}, but not at the elevated shear rate of 3000 s^{-1} (Figure 3E). In contrast, the anti-thrombotic effects of SJMX-151 were retained at 3000 s^{-1} (Figure 3E). These findings indicate that inhibition of PI3KC2α provides robust anti-thrombotic effects in human blood that occur in the absence of overt inhibition of canonical platelet activation. Further, this anti-thrombotic activity persisted in the face of elevated blood shear forces that are sufficient to overcome the anti-thrombotic effects of gold-standard approaches to platelet function inhibition.

PI3KC2α inhibition is anti-thrombotic in mice in vivo *but has no effect on hemostasis*

Having established the anti-thrombotic effects of PI3KC2α inhibition in humans *ex vivo*, we next examined the *in vivo* effects of SJMX-151 on thrombosis and hemostasis. Electrolytic-injury induced thrombosis of the mouse carotid artery was significantly impaired by pre-treatment of mice with as little as 0.1 mg/ml SJMX-151 and almost abolished by 1 mg/kg SJMX-151 (Figure 4A). Histological analyses of

thrombi formed in the damaged carotid arteries in these experiments showed occlusive platelet-rich thrombi in vehicle-treated mice, non-occlusive thrombi in mice treated with 0.1 mg/ml SJMX-151, and markedly smaller fibrin-rich thrombi with very few platelets in mice treated with 1 mg/ml SJMX-151 (Figure 4B). Similarly striking anti-thrombotic activity was observed in a distinct mouse model of occlusive thrombus formation. In the Folts' model of recurrent occlusive thrombotic events in the mouse carotid artery damaged by physical trauma (16, 18), i.v. administration of SJMX-151 (1 mg/ml) abolished the stable recurrent occlusive thromboses in this model inside 15 min (Figure 4 c). This absolute protection against thrombosis remained for the entirety of the 60 min observation period (Figure 4 c). Despite striking anti-thrombotic effects in these two models, the same dose of SJMX-151 (1 mg/kg) had no impact on bleeding when compared to vehicle-treated control mice in an *in vivo* model of hemostasis (Figure 4D). Notably, a therapeutic dose of the gold-standard anti-platelet drug, aspirin (200 mg/kg – sufficient to cause modest anti-thrombotic effects in the two *in vivo* models examined here), significantly prolongs bleeding time under these conditions (Figure 4D). These *in vivo* findings support our *ex vivo* human thrombosis studies and indicate PI3KC2α inhibition prevents *in vivo* thrombosis and affords an improved therapeutic window over that provided by the current leading anti-platelet approaches.

The anti-platelet effects provided by PI3KC2α inhibition are due to a unique impact on membrane-dependent platelet adhesion under high shear

We next examined the mechanism by which modulation of the OCS structure may link to the prothrombotic function of platelets. The OCS is the specialized internal membrane reserve of platelets and its mobilization is important for the increased platelet surface area that occurs during platelet shape change and spreading (19). Our

previous observations in mice revealed that, despite their dilated OCS, PI3KC2α-deficient platelets do not have additional membrane reserves nor cytoskeletal abnormalities, yet they fail to form robust and stable thrombi under the hemodynamic shear forces of flowing blood (7). Here, we observed the same holds true for PI3KC2α-inhibited human platelets. First, SJMX-151 pretreatment (10 μM, 10 min) had no effect on the surface area of human platelets spread on immobilized fibrinogen (Figure 5A) nor on tether-dependent platelet adhesion to von Willebrand factor (Figure 5B), despite the latter being dependent on both GPIb and $\alpha_{IIb}\beta_3$, indicated by a 3-fold increase in platelet translocation velocity with the $\alpha_{IIb}\beta_3$ inhibitor, integrilin (Figure 5B). Second, SJMX-151 had no effect on the structure of the platelet microtubule ring at rest nor on the formation of filamentous actin in activated platelets (Figure 5 c). Given 1) the similarities between PI3KC2α-deficient mouse platelets and PI3KC2α-inhibited human platelets in both structure and function and 2) that, in both cases, antithrombotic effects are observed only in the presence of hemodynamic forces, we focused on the utilization of membrane reserves under such conditions. Therefore, we next established a microfluidic system in which the prothrombotic function of platelets occurs largely independently of traditional platelet activation mechanisms (Figure 5). Specifically, we examined real time platelet aggregation in human blood perfused through a von Willebrand factor-coated microfluidic channel that incorporates a high-shear-inducing stenosis (Figure 5D,E). Under these conditions, platelet deposition is largely resistant to inhibitors of platelet activation; combined treatment with drugs to block $P2Y_1$ (10 μM MRS2179), $P2Y_{12}$ (100 μM 2-MeSAMP), ADP (2 U/ml apyrase), cyclooxygenase (COX) (10 μM indomethacin), and thrombin (800 U/ml hirudin) only partially impaired platelet deposition in these channels (ALB; Figure 5F,G). Remarkably, pretreatment of human blood with SJMX-151 alone (10 μM, 10 min)

inhibited platelet deposition to a greater extent than with this cocktail of platelet activation inhibitors, and nearly abolished the residual platelet deposition when added to the cocktail of platelet activation inhibitors (Figure 5F,G). Together, these experiments suggest PI3KC2α regulates the utilization of platelet membrane reserves that drives activation-independent platelet adhesion in the setting of pronounced hemodynamic shear stress.

Discussion

We have described here an approach to prevent thrombosis without inhibition of canonical platelet activation. We developed a small molecule inhibitor of PI3KC2α that was an effective anti-thrombotic in mice and humans but did not affect agonist-induced platelet activation in vitro – even at concentrations 100-fold greater than those required for thrombosis prevention. Intriguingly, and in contrast to all known anti-platelet approaches, this effect appears to involve a structural change in the platelet's OCS that leads to impaired platelet function only under conditions where thrombus formation is promoted independently of platelet activation.

We have previously reported that PI3KC2α-deficiency in mouse platelets results in impaired thrombus formation. Specifically, we used in inducible RNAi-based approach to deplete PI3KC2α in adult mouse platelets. These mice exhibited delayed and unstable thrombosis in an *in vivo* model, yet platelet function in standard *in vitro* function tests (aggregation, alpha and dense granule secretion, phosphotidylserine exposure, adhesion and spreading on various surfaces, etc) remained unchanged. Indeed the only change we observed in PI3KC2α-deficient platelets was a previously undescribed and marked dilation of the OCS that was apparent in circulating platelets. These previous studies led us to hypothesize a link between the OCS and in vivo prothrombotic platelet function. Our initial observations were supported by a subsequent study, using a distinct model of PI3KC2α-deficiency in mouse platelets, but in which strikingly similar effects on platelet OCS structure and prothrombotic function were reported. However, in the absence of pharmacological inhibitors of PI3KC2α, whether or not a similar mechanism existed in human platelets remained unknown. Indeed, in the studies from both us and others, a modest effect on

megakaryocyte structure was also observed, indicating the likelihood that the OCS structural abnormalities of PI3KC2α-deficient mouse platelets may have been inherited at the time of their production. However, the pharmacological studies described here not only reveal that the regulation of OCS structure by PI3KC2α in mouse platelets is conserved in human platelets, but they also indicate that the regulation of OCS structure by PI3KC2α can occur acutely and is surprisingly dynamic.

There is little information indicating it is possible to rapidly and acutely alter OCS structure. Cholesterol depletion has been suggested to collapse the OCS, presumably through a direct effect on membrane composition. To our knowledge, the only pharmacological manipulation of OCS structure reported to date involves the use of amphiphilic cationic agents, such as the calmodulin inhibitor W-7, which have been shown to dilate the megakaryocyte DMS and platelet OCS. It has been proposed that this dilation of internal membrane reserves in these cells occurs via a mechanism that may involve interference with phospholipid signaling, most likely $PI(4,5)P_2$. Our studies extend on this work to show that inhibition of Class II PI3K function can similarly dilate the OCS of mouse and human platelets, and that this can impact on platelet function. While the PI3KC2α-dependent effects observed here are unlikely to be due to a direct effect on $PI(4,5)P_2$, phospholipid signaling may still be involved. Previous studies have shown that the Class II PI3K, PI3KC2α, is responsible for producing a basal pool of PI(3)P in mouse platelets. This same study also showed reduced expression of key cytoskeletal proteins in PI3KC2α-deficient mouse platelets. The rapid effect of PI3KC2α inhibition on platelet structure observed here (< 5 min) suggests changes in cytoskeletal protein expression are unlikely causative of the structural and functional changes in PI3KC2α-inhibited platelets. However, whether or not continued PI(3)P production is necessary for the maintenance of OCS structure remains unknown, and

is certainly plausible. Using standard approaches for the analysis of phospholipid production, we have not yet observed any basal or induced changes in PI levels in PI3KC2α-deficient platelets. The rapid nature of the effects of PI3KC2α inhibition are suggestive of this mechanism, but will require approaches with improved sensitivity for detecting changes in intracellular PI levels.

Regardless of the level of involvement of PI signaling, the specificity of the effect for PI3KC2α is clear: pharmacological targeting acutely reproduced the genetic effects; PI3KC2α inhibition produced no additional effects over PI3KC2α-deficiency; and only drugs with significant activity against PI3KC2α were with effect. Together, these findings strongly suggest further drugs targeting PI3KC2α are likely to produce the potent anti-thrombotic effects observed here, and further improvements in potency and, more particularly, specificity, for PI3KC2α are keenly sought.

Finally, the translation here of previous studies in mice to humans is the first demonstration of drug targeting the OCS for anti-thrombotic benefit. It is far too early to say whether this novel approach is a viable strategy for anti-thrombotic therapy. However, it is noteworthy that the anti-thrombotic effects observed here in response to PI3KC2α inhibition occur independently of known platelet activation mechanisms. One potential advantage of such an approach is that PI3KC2α-inhibited platelets function normally in all situations we have examined – except when forming thrombi under pathological conditions. One major limitation on the efficacy of all current anti-platelet drugs is that they all block global platelet activation and thus indiscriminately prevent platelet function in the setting of hemostasis and thrombosis. Our prediction is that the unique mechanism by which PI3KC2α-deficiency or inhibition prevents platelet function underlies the lack of bleeding observed in PI3KC2α-deficient or

PI3KC2α-inhibited mice, since the platelets are not circulating in an inhibited state. Whether or not this will enable a widening of the therapeutic window between hemostasis and thrombosis remains to be seen, but is of obvious appeal. In addition, the targeting of a distinct mechanism of action within the cell provide an opportunity for additive effects over standard–of-care. Such additive effects are most readily observed in our microfluidic assay in which significant platelet deposition occurs independently of platelet activation. Much of the platelet aggregation and deposition under these conditions is not inhibited by drugs blocking global platelet activation mechanisms, and yet is highly sensitive to PI3KC2α inhibition. The ability to target this aspect of thrombosis that is relatively resistant to current therapies is appealing. It is notable this such deposition of unactivated platelets is largely favored by the presence of a region of stenosis (high shear) followed followed by a rapid expansion (low shear), with platelet accumulation occurring almost exclusively in the low shear zone immediately downstream of the stenosis. This anatomy resembles that observed in, for example, large arteries burdened with significant deposits of atherosclerotic plaque – a major site of arterial thrombosis – and it is tempting to speculate that PI3KC2α inhibition may improve thrombosis prevention in the setting of such pathologies.

Materials and Methods

Study Design

This study was designed to determine the feasibility and impact of pharmacological inhibition of PI3KC2α in the context of arterial thrombosis. Our first-in-class small molecule inhibitor of PI3KC2α, SJMX-151, was identified using a rational drug design approach, and chosen due to its high potency (IC_{50} = 13nM). The effect of SJMX-151 on human and mouse platelet membrane structure was examined using transmission electron microscopy for 2D imaging and focused ion beam-scanning electron microscopy for 3D modelling. Functional anti-thrombotic effects were examined in human blood from healthy volunteers using an *ex vivo* thrombosis assay, and in mice using the electrolytic thrombosis and Folts models.

Mouse generation and use

All animal experiments performed in this study were approved by the Alfred Medical Research and Education Precinct Animal Ethics Committee (approvals E/1465/2014 M and E/1644/2016/M). All mice used in this study were backcrossed ≥ 5 generations on a C57BL/6 genetic background (i.e., ≥ 98%) and maintained on a 12-h light/dark cycle with food and water given *ad libitum*. PI3KC2α-deficient mice were generated using our previously published shRNA-based inducible and reversible gene-silencing approach (20). To induce gene knockdown, mice were placed on a doxycycline diet (600 mg kg^{-1}, Speciality Feeds, Australia), for at least 10 days prior to experimentation.

For mouse whole blood and platelet isolation, blood was drawn from the inferior vena cava of anaesthetised mice, using a 25-gauge needle, into enoxaparin (40 U, final concentration). Platelets were isolated as previously described (20).

Human platelet preparation

All human studies were approved by the Monash University Human Research Ethics Committee.

Blood from healthy volunteers was withdrawn using a 19-gauge butterfly needle into syringes containing either acid citrate dextrose (7: 1 v/v, final concentration) for platelet isolation, or hirundine (800 U, final concentration) or enoxaparin (40 U, final concentration), for *ex vivo* whole blood flow experiments.

Platelets were isolated as previously described (17, 21). Briefly, platelet-rich plasma (PRP) was obtained by centrifuging blood at 200 *g* for 15 min. Following 10 min of rest, the PRP was centrifuged at 1700 *g*. The platelet-poor plasma was removed by aspiration, and the pellet resuspended in platelet wash buffer (4.3 mM K_2HPO_4, 4.3 mM $NaHPO_4$, 24.3 mM NaH_2PO_4, 113 mM NaCl, 5.5 mM D-glucose and 10 mM theophylline; pH 6.5; containing 0.5% BSA, 20 U total enoxaparin and 0.01 U ml^{-1} apyrase). After a second 10 min rest period, centrifugation at 1500 *g* produced a platelet pellet, which was resuspended at the required concentration in Tyrode's buffer containing 0.5% BSA, 1.8 mM Ca^{2+} and 0.02 U ml^{-1} apyrase.

Transmission electron microscopy and OCS analysis

Platelet ultrastructure was analysed via TEM as described (22). Briefly, isolated platelets were fixed in 2% glutaraldehyde and 2.5% paraformaldehyde, post-fixed in 2% osmium tetroxide, dehydrated through an ethanol series, and embedded in Spurr's resin. Ultrathin sections were cut with a diamond knife (Diatome) on an ultramicrotome (Leica) and stained with methanolic uranyl acetate and lead citrate before TEM imaging (JEOL 1011). Images were recorded with a MegaView III CCD (Soft Imaging Systems) and were analysed using FIJI software. A common threshold was applied to

all images used to quantify the surface area of the OCS, which was expressed as a percentage of the total surface area of the cell.

Focused ion beam-scanning electron microscopy

Isolated mouse and human platelets were fixed in 2.5% glutaraldehyde, postfixed in 1% osmium tetroxide and 1.5% potassium ferrocyanide, incubated in 4% uranyl acetate, then dehydrated through a series of graded ethanol concentrations before being embedded in Epon resin. Samples were imaged using a Helios NanoLab microscope (FEI). Stacks of approximately 1000 images, with a field size of 15 µm x 15 µm, were generated. 3D models were computed using the imaging software Amira (FEI).

Ex vivo *thrombosis and platelet adhesion assays*

Glass microslides (0.1 × 1.0 mm, VitroCom) were washed in nitric acid, rinsed with dH2O and coated with bovine type 1 collagen (250 µg ml−1 diluted in 10 mM acetic acid, overnight at 4 °C), or vWF (100 µg ml−1, 10 min). For thrombus formation on collagen, human whole blood collected in hirudin (800 U/mL) or enoxaparin (40U/mL) was pretreated with DiOC6 (0.1% v/v) and either dimethylsulfoxide (DMSO, 0.1% v/v), 10 µM SJMX-151, 10 µM SJMX-125, 10 µM copanlisib, 100 µM 2-MeSAMP, saline (0.009% v/v), or 50 µM aspirin (ASA). Blood was then perfused through coated microslides at 37 °C for 10 mins at 600 s-1, 1800 s-1 or 3000 s-1, and thrombus formation monitored in real time using a Nikon A1r confocal microscope with a 25x water objective. Thrombus volume was analysed using NIS-Element confocal imaging software, and was quantified by applying a constant threshold to all Z-stack images obtained and summing the resultant surface areas.

Analysis of spread platelet area was performed on acid-washed glass coverslips. Washed platelets resuspended in Tyrode's buffer at 3 x 107/mL were placed on the coverslips and allowed to spread for 15 min. Non-adherent platelets were then removed with a Tyrode's buffer wash and adherent platelets fixed using 4% PFA. Platelets were imaged using a Nikon Ti-E motorised inverted microscope with a 60x water objective, and analysed using ImageJ software.

For platelet translocation, microslides were coated with vWF (100 µg/mL, 10 min) and blocked with BSA (2%, 10 min). Enoxaparin-anticoagulated human whole blood (40U/mL) was pretreated with dimethylsulfoxide (DMSO, 0.1% v/v), 10 µM SJMX-151, or 20 µg/mL integrilin (all 10 min). Blood was then perfused through coated microslides at 1800 s-1 for 2.5 min. Platelet translocation across the substrate was monitored in real time using a Nikon Ti-E motorised inverted microscope with a 60x water objective. Videos were analysed offline using ImageJ software for platelet translocation velocity.

Cytoskeletal analyses

Isolated platelets were pretreated with dimethylsulfoxide (DMSO, 0.1% v/v), 10 µM SJMX-151, or 10 µM copanlisib (10 min). Some platelets were activated with 1U/mL thrombin (10 min) prior to fixation with 2% PFA. Fixed platelets were seeded on poly-L-lysine coated coverslips, and then permeabilised (0.1% Triton X-100, 15 min), blocked (1% BSA in 0.1% Triton X-100, 15 min), stained (α-tubulin Alexa Fluor 488 antibody, 0.5 µg/mL, and Alexa Fluor 647 phalloidin, 40U/mL, 45 min) and mounted with Dako fluorescent mounting media. Images were taken using a Nikon A1r confocal microscope with a 60x oil objective.

Microfluidic ex vivo *thrombosis assay*

Platelet aggregation was performed as described (23). Briefly, a microfluidic device consisting of 100 µm wide channels with inset 40 µm stenosis was fabricated using standard photolithography techniques. The channels were blocked with 2% BSA and human whole blood was pretreated with $DiOC_6$ (0.1% v/v). The blood was perfused through the channels at a rate of $1800s^{-1}$ and platelet aggregation at the stenosis was monitored in real time using a invert Nikon TiU microscope (Nikon Plan Fluor 20x/0.50 objective) using an Andor Zyla sCMOS camera at 1 fps for 210 s. Thrombus size was analysed using Image-J imaging processing software by applying Huang's fuzzy image thresholding method. Maximal aggregation was extrapolated from the 210 s runtime. Statistical significance was determined using one-way ANOVA where appropriate.

In vivo *thrombosis model*

The electrolytic model of thrombosis was performed essentially as described (18, 24). Mice were anaesthetised via intraperitoneal injection using a combination of ketamine (85 mg kg^{-1}) and xylazine (15 mg kg^{-1}), and a flow probe (0.5 mm inner diameter) linked to a flow meter (TS420, Transonic Systems) placed around the exposed left carotid artery to record blood flow using PowerLab Chart (v. 5.0, AD Instruments). Either DMSO, SMJX-151 (1 mg kg^{-1}, and 0.1 mg kg^{-1}) or SJMX-125 (1 mg kg^{-1}), was administered intravenously via the right jugular vein, and blood flow allowed to stabilise for 10 min prior to injury. A constant current lesion maker (53500, Ugo Basile) was used to deliver 22 mA for 2.75 min to the carotid artery via a platinum electrode—the minimal current required to reliably produce a stable occlusive thrombotic event in untreated, wild type mice. Blood flow was monitored for 30 min post-injury.

In vivo *haemostasis assay*

Tail transection bleeding times were performed as described (20). Briefly, mice were anaesthetised via intraperitoneal injection using a combination of ketamine (85 mg kg^{-1}) and xylazine (15 mg kg^{-1}). DMSO, SMJX-151 (1 mg kg^{-1}, and 0.1 mg kg^{-1}) or SJMX-125 (1 mg kg^{-1}) was administered via the right jugular vein 10 min prior to tail transection. The tail was transected 5 mm from the tip with a scalpel blade. The bleeding end was immediately immersed in warmed saline (37 °C) and time to bleeding cessation (stoppage for > 2 min) was measured.

Histological analysis

Following *in vivo* thrombosis assays, carotid arteries were excised and fixed in 4% paraformaldehyde at room temperature for at least 24 hours. Fixed tissues were embedded in paraffin and kept at room temperature until sectioning. 2µm thick transverse sections were prepared using a microtome (microTec CUT-4060) and stained with Carstairs' stain (25) for platelets, collagen, fibrin and red blood cells. Slides were imaged using a Nikon Eclipse TS100 with a 10x objective, and images captured using NIS-Elements software.

Statistical analyses

Statistical analyses were performed using GraphPad Prism. Statistical significance ($P < 0.05$) was determined with either an unpaired, two-tailed Student's *t*-test or a one-way ANOVA with Dunnett's multiple comparisons test, as indicated in the relevant figure legends.

References

1. Toker A, Cantley LC. Signalling through the lipid products of phosphoinositide-3-OH kinase. Nature. 1997;387(6634):673-6.
2. Stephens L, Williams R, Hawkins P. Phosphoinositide 3-kinases as drug targets in cancer. Curr Opin Pharmacol. 2005;5(4):357-65.
3. Hirsch E, Costa C, Ciraolo E. Phosphoinositide 3-kinases as a common platform for multi-hormone signaling. The Journal of endocrinology. 2007;194(2):243-56.
4. Hirsch E, Ciraolo E, Ghigo A, Costa C. Taming the PI3K team to hold inflammation and cancer at bay. Pharmacology & therapeutics. 2008;118(2):192-205.
5. Falasca M, Maffucci T. Regulation and cellular functions of class II phosphoinositide 3-kinases. Biochem J. 2012;443(3):587-601.
6. Maffucci T, Falasca M. New insight into the intracellular roles of class II phosphoinositide 3-kinases. Biochemical Society transactions. 2014;42(5):1378-82.
7. Mountford JK, Petitjean C, Kusuma Putra HK, McCafferty JA, Setiabakti NM, Lee H, et al. The Class II PI 3-Kinase, PI3KC2α Links Platelet Internal Membrane Structure to Shear-dependent Adhesive Function. Nat Commun. 2015;6:6536.
8. Valet C, Chicanne G, Severac C, Chaussade C, Whitehead MA, Cabou C, et al. Essential role of class II PI3K-C2alpha in platelet membrane morphology. Blood. 2015;126(9):1128-37.
9. Petitjean C, Setiabakti NM, Mountford JK, Arthur JF, Ellis S, Hamilton JR. Combined deficiency of PI3KC2alpha and PI3KC2beta reveals a nonredundant role for PI3KC2alpha in regulating mouse platelet structure and thrombus stability. Platelets. 2016;27(5):402-9.
10. Takiguchi M, James C, Josefsson EC, Carmichael CL, Premsrirut PK, Lowe SW, et al. Transgenic, inducible RNAi in megakaryocytes and platelets in mice. J Thromb Haemost. 2011;8(12):2751-6.
11. Dickins RA, McJunkin K, Hernando E, Premsrirut PK, Krizhanovsky V, Burgess DJ, et al. Tissue-specific and reversible RNA interference in transgenic mice. Nature genetics. 2007;39(7):914-21.
12. Dickins RA, Hemann MT, Zilfou JT, Simpson DR, Ibarra I, Hannon GJ, et al. Probing tumor phenotypes using stable and regulated synthetic microRNA precursors. Nature genetics. 2005;37(11):1289-95.
13. Knight ZA, Gonzalez B, Feldman ME, Zunder ER, Goldenberg DD, Williams O, et al. A pharmacological map of the PI3-K family defines a role for p110alpha in insulin signaling. Cell. 2006;125(4):733-47.
14. Scott WJ, Hentemann MF, Rowley RB, Bull CO, Jenkins S, Bullion AM, et al. Discovery and SAR of Novel 2,3-Dihydroimidazo[1,2-c]quinazoline PI3K Inhibitors: Identification of Copanlisib (BAY 80-6946). ChemMedChem. 2016;11(14):1517-30.
15. Eckly A, Heijnen H, Pertuy F, Geerts W, Proamer F, Rinckel JY, et al. Biogenesis of the demarcation membrane system (DMS) in megakaryocytes. Blood. 2013.
16. Lee H, Sturgeon SA, Jackson SP, Hamilton JR. The contribution of thrombin-induced platelet activation to thrombus growth is diminished under pathological blood shear conditions. Thrombosis and haemostasis. 2012;107(2).

17. Ono A, Westein E, Hsiao S, Nesbitt WS, Hamilton JR, Schoenwaelder SM, et al. Identification of a fibrin-independent platelet contractile mechanism regulating primary hemostasis and thrombus growth. Blood. 2008;112(1):90-9.
18. Sturgeon SA, Jones C, Angus JA, Wright CE. Adaptation of the Folts and electrolytic methods of arterial thrombosis for the study of anti-thrombotic molecules in small animals. J Pharmacol Toxicol Methods. 2006;53(1):20-9.
19. White JG, Clawson CC. The surface-connected canalicular system of blood platelets--a fenestrated membrane system. The American journal of pathology. 1980;101(2):353-64.
20. Mountford JK, Petitjean C, Kusuma Putra HK, McCafferty JA, Setiabakti NM, Lee H, et al. The Class II PI 3-Kinase, PI3KC2a Links Platelet Internal Membrane Structure to Shear-dependent Adhesive Function. Nature Communications. 2015;in press.
21. Lee H, Sturgeon SA, Jackson SP, Hamilton JR. The contribution of thrombin-induced platelet activation to thrombus growth is diminished under pathological blood shear conditions. Thrombosis and haemostasis. 2012;107(2):328-37.
22. McCormack MP, Hall MA, Schoenwaelder SM, Zhao Q, Ellis S, Prentice JA, et al. A critical role for the transcription factor Scl in platelet production during stress thrombopoiesis. Blood. 2006;108(7):2248-56.
23. Brazilek RJ, Tovar-Lopez FJ, Wong AKT, Tran H, Davis AS, McFadyen JD, et al. Application of a strain rate gradient microfluidic device to von Willebrand's disease screening. Lab on a chip. 2017.
24. Lee H, Sturgeon SA, Mountford JK, Jackson SP, Hamilton JR. Safety and efficacy of targeting platelet proteinase-activated receptors in combination with existing anti-platelet drugs as antithrombotics in mice. British journal of pharmacology. 2012;166(7):2188-97.
25. Carstairs KC. The identification of platelets and platelet antigens in histological sections. The Journal of pathology and bacteriology. 1965;90(1):225-31.

Figures and legends:

Figure 1

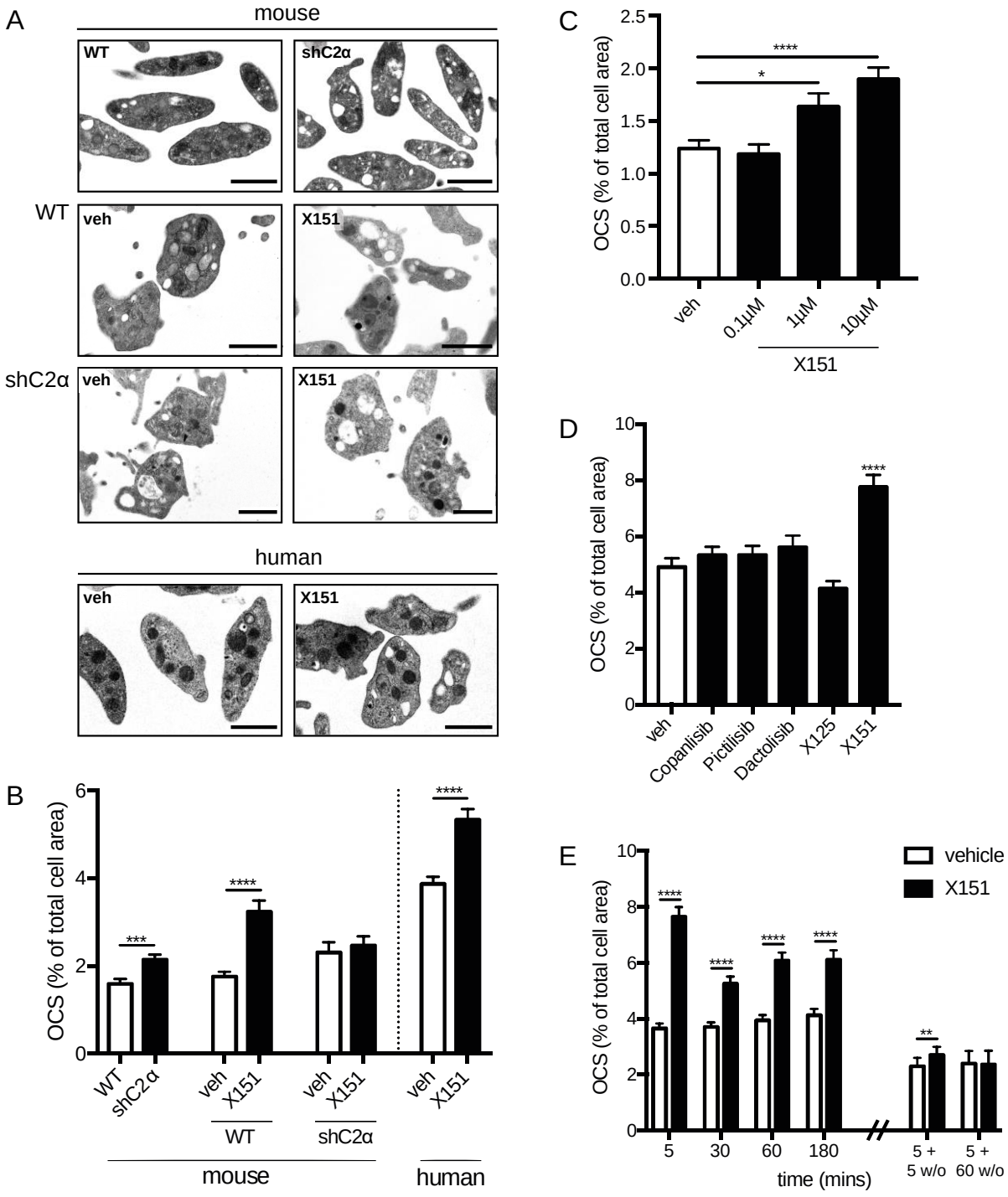

Figure 1. PI3KC2α inhibition reproduces the platelet cell biology effects of PI3KC2α deficiency. (**A**) Representative transmission electron microscopy images of platelets. Top panels: untreated platelets from wild-type (WT) or PI3KC2α-deficient (shC2α) mice. Middle panels: platelets from WT or shC2α mice treated with vehicle (0.1% v/v DMSO, 3 h) or X151 (10 μM, 3h). Bottom panels: human platelets treated with vehicle (0.1% v/v DMSO, 3 h) or X151 (10 μM, 3h). Note the dilated OCS in both PI3KC2α-deficient and X151-treated platelets (red arrows). All scale bars are 1 μm. (**B-E**) Quantification of OCS surface area from transmission electron microscopy images, showing: (**B**) Mouse and human platelets as described in (**A**); (**C**) The concentration-response of X151 in human platelets; (**D**) The specificity of the OCS dilation in human platelets to X151 over inhibitors of other PI3Ks (all at 10 μM for 3 h); (**E**) The time course of response to X151 (10 μM) in human platelets, and its reversibility in cells treated for 5 min before drug washout (w/o) for a further 5 or 60 min. All data are expressed as percentage OCS of the total cell area and are presented as mean ± SEM of n=81-455 cells from n=3-6 experiments per condition. *, P<0.05; **, P<0.01; ***, P< 0.001; ****, P<0.0001 (unpaired, two-tailed, Student's t-test versus indicated control in **B** and **E** and one-way ANOVA with Dunnett's multiple comparison test against vehicle in **C** and **D**).

Figure 2

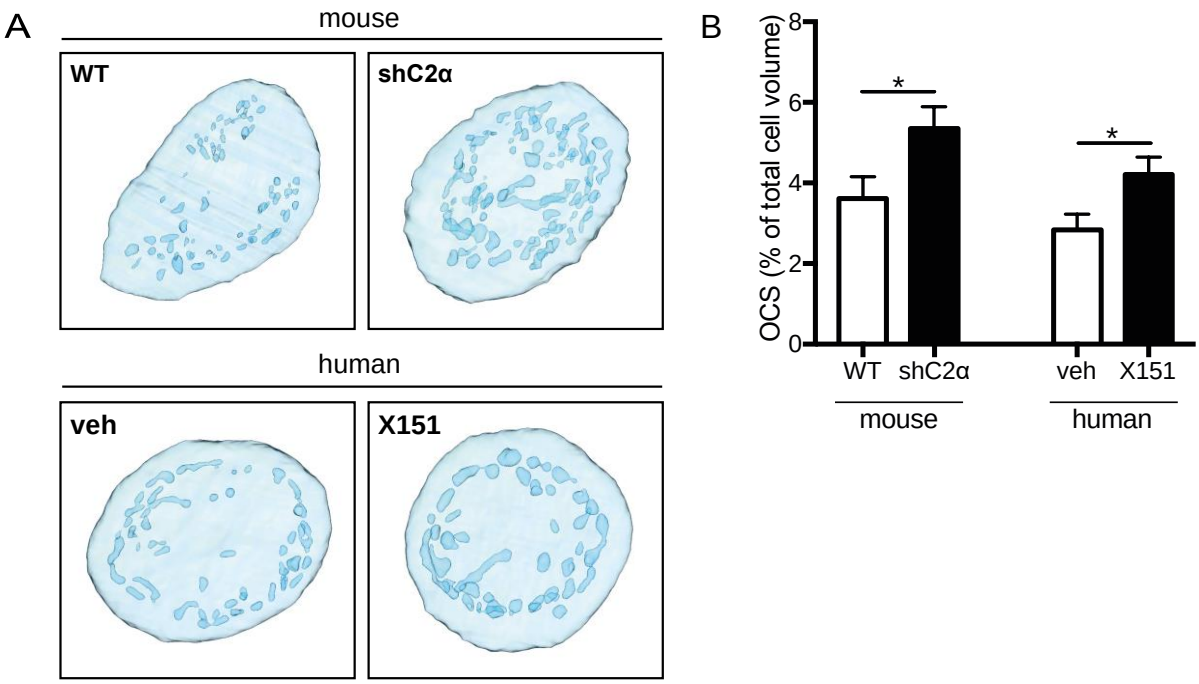
A
mouse
WT
shC2α
human
veh
X151
B
OCS (% of total cell volume)
0
2
4
6
8
*
*
WT
shC2α
veh
X151
mouse
human

Figure 2. Genetic deficiency or pharmacological inhibition of PI3KC2α similarly dilate the platelet internal membrane system throughout the entire cell. (**A,B**) FIB-SEM analyses of the whole-of-cell platelet membrane. (**A**) Representative 3D reconstructions of membranes of platelets from wild-type (WT) or PI3KC2α-deficient (shC2α) mice (top panels), and human platelets treated with X151 (10 μM, 3 h) or vehicle (0.1% v/v DMSO), showing plasma (light blue) and internal (dark blue) membrane. Note the even dilation of the OCS throughout both PI3KC2α-deficient mouse platelets and X151-treated human platelets. (**B**) Quantification of OCS volume from 3D reconstructions. Data are mean ± SEM from n=10-12 platelets per group. *, P<0.05 (unpaired, two-tailed, Student's t test). (**C,D**) SEM analyses of the platelet membrane surface. (**C**) Representative SEM images of membranes of platelets from wild-type (WT) or PI3KC2α-deficient (shC2α) mice, showing OCS surface openings (arrows). (**D**) The diameter of OCS surface openings measured from SEM images. Individual data points are shown. Bars are mean ± SEM. *, P<0.05 (unpaired, two-tailed, Student's t test).

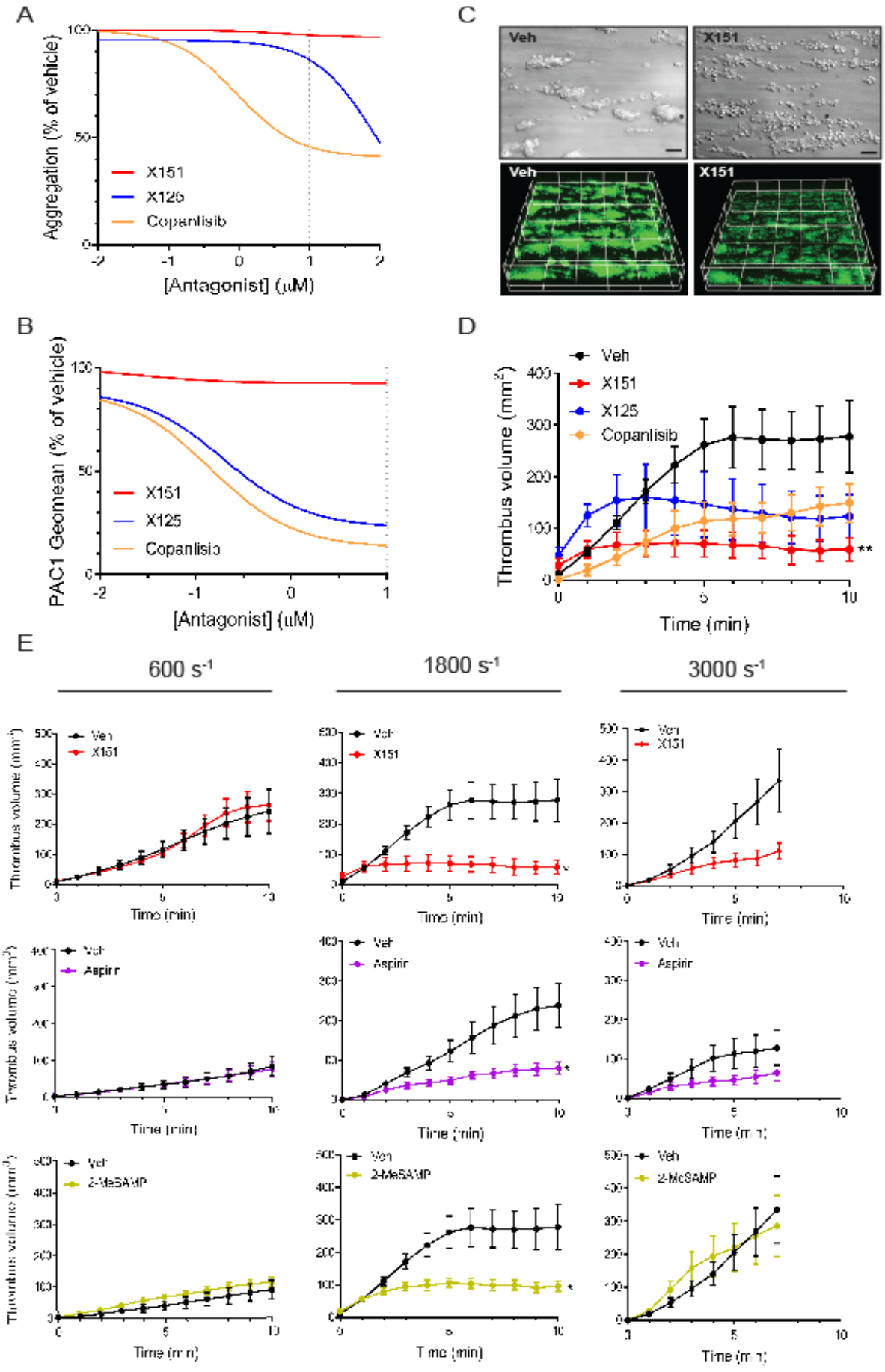
A
Aggregation (% of vehicle)
[Antagonist] (μM)
X151
X125
Copanlisib
B
PAC1 Geomean (% of vehicle)
[Antagonist] (μM)
X151
X125
Copanlisib
C
Veh
X151
Veh
X151
D
Thrombus volume (mm³)
Time (min)
Veh
X151
X125
Copanlisib
**
E
600 s⁻¹
1800 s⁻¹
3000 s⁻¹
Thrombus volume (mm³)
Time (min)
Veh
X151
Aspirin
2-MeSAMP

Figure 3. PI3KC2α inhibition is anti-thrombotic in human blood independently of canonical platelet activation. (**A,B**) Concentration-inhibition curves for X151, X125, or copanlisib against (**A**) aggregation or (**B**) $\alpha_{IIb}\beta_3$ activation (PAC-1 binding) in thrombin (1 U/ml)-stimulated human platelets. Shown are curve fits generated from mean ± SEM data expressed as a percentage of vehicle from 8 experiments (individuals) in **A** and 3 in **B**. (**C,D**) Thrombus formation in anticoagulated human blood flowed over a type I collagen surface at a shear rate of $1800s^{-1}$ in the presence of X151, X125, copanlisib (all 10 μM), or vehicle (0.1% v/v DMSO). (**C**) Representative bright field images (top, scale bars = 10 μm) and 3D reconstructions (bottom, graticules = 50 μm) at the 10 min endpoint. (**D**) Total thrombus volume determined in real time every min for 10 min. Mean ± SEM of n=6 experiments (individuals). **, P<0.01 (one-way ANOVA with Dunnett's multiple comparison test against vehicle). **(E)** Thrombus volume in anticoagulated human blood flowed over a type I collagen surface at one of 600, 1800, or 3000 s^{-1}, in the presence of X151 (10 μM, top row), aspirin (50μM, middle row), or the $P2Y_{12}$ antagonist 2-MeSAMP (100μM; bottom row) versus relevant vehicle (0.1% v/v DMSO for X151 and 2-MeSAMP; 0.9% saline for aspirin). Data are mean ± SEM from n=6-13 experiments (individuals). Data is only shown up to 7 min in experiments performed at 3000 s^{-1} because gross embolization occurred in >50% of cases after this time in these experiments. Note the data in the middle graph of the top row is taken from the experiments shown in **D**. *, P<0.05; **, P<0.01 (unpaired, two-tailed, Student's t-test).

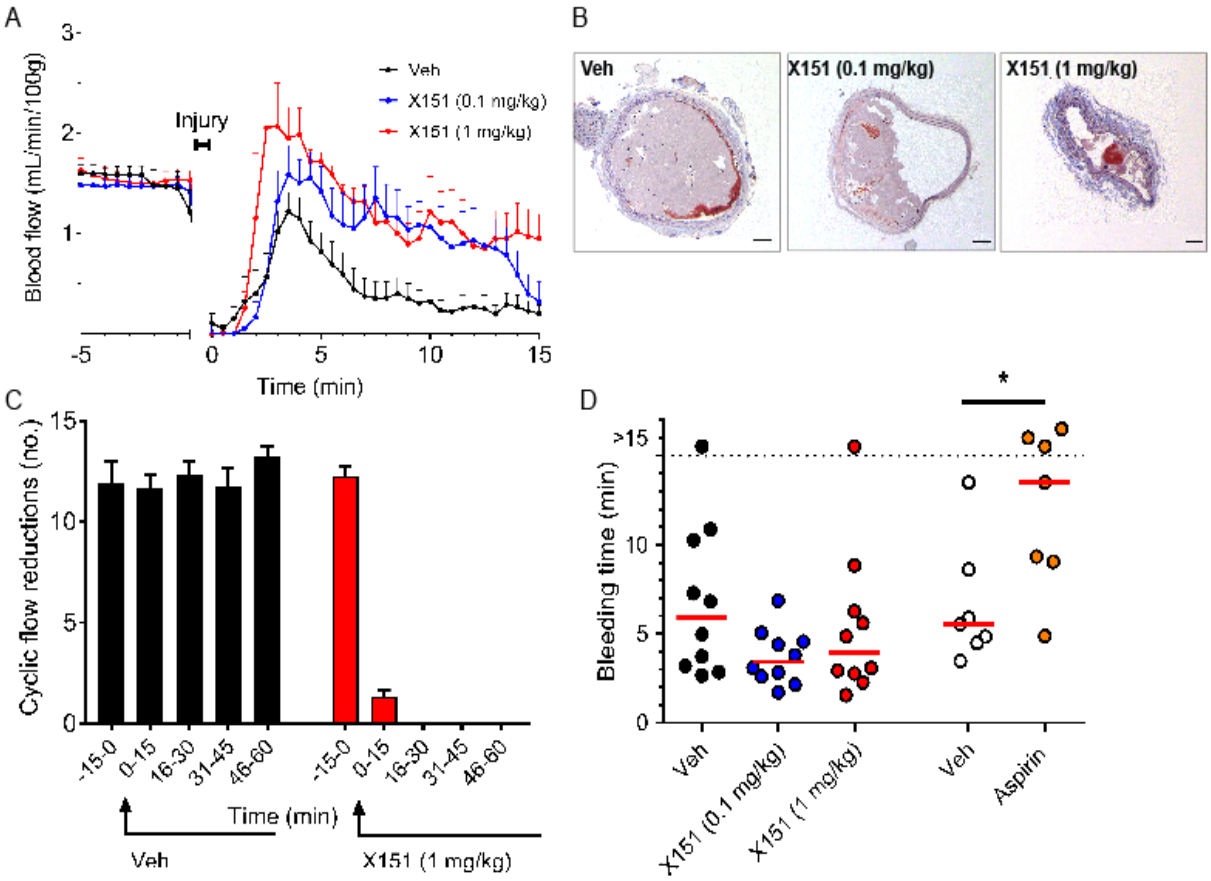
A
Blood flow (mL/min/100g)
Injury
Veh
X151 (0.1 mg/kg)
X151 (1 mg/kg)
Time (min)
B
Veh
X151 (0.1 mg/kg)
X151 (1 mg/kg)
C
Cyclic flow reductions (no.)
-15-0
0-15
16-30
31-45
46-60
Time (min)
Veh
X151 (1 mg/kg)
D
Bleeding time (min)
>15
*
Veh
X151 (0.1 mg/kg)
X151 (1 mg/kg)
Veh
Aspirin

Figure 4. PI3KC2α inhibition is anti-thrombotic in mice *in vivo* but has no effect on hemostasis. (**A-C**) Thrombosis and (**D**) hemostasis in *in vivo* mouse models in the absence and presence of PI3KC2α inhibition. (**A**) Carotid artery blood flow before and after electrolytic injury of the vessel in wild-type mice treated with X151 (0.1 or 1 mg/kg; n=8 each) or vehicle (DMSO; n=11). Mean ± SEM. **(B)** Representative histological images of transverse sections of carotid arteries containing Carstair's-stained thrombi from experiments in **A**, showing platelets (purple), fibrin (red), and collagen (blue). Scale bar = 50 μm. **(C)** Cyclic flow reductions in carotid arteries of mice in a Folts'-like model of recurrent occlusive thrombosis in the absence and presence of X151 (1 mg/kg; n=4) or vehicle (DMSO, n=3). Five pinches of the carotid artery induced an occlusive thrombosis which was then manually embolized. Shown are the number (mean ± SEM) of reformed occlusive thrombi (cyclic flow reductions) per 15 min period before and after drug administration (arrow). **(D)** Tail bleeding time in wild-type mice treated with X151 (0.1 or 1 mg/kg) or vehicle (DMSO), or aspirin (200 mg/kg) or vehicle (0.9% saline). Data points represent time to cessation of bleeding in an individual mouse. Experiments were terminated after 15 minutes and mice still bleeding at this time are shown above the dotted line. Red bars are medians. (*, $P<0.05$ with significance determined by plotting the data as Kaplan-Meier survival curves and analyzing by log-rank test versus the relevant vehicle).

FIGURE 5

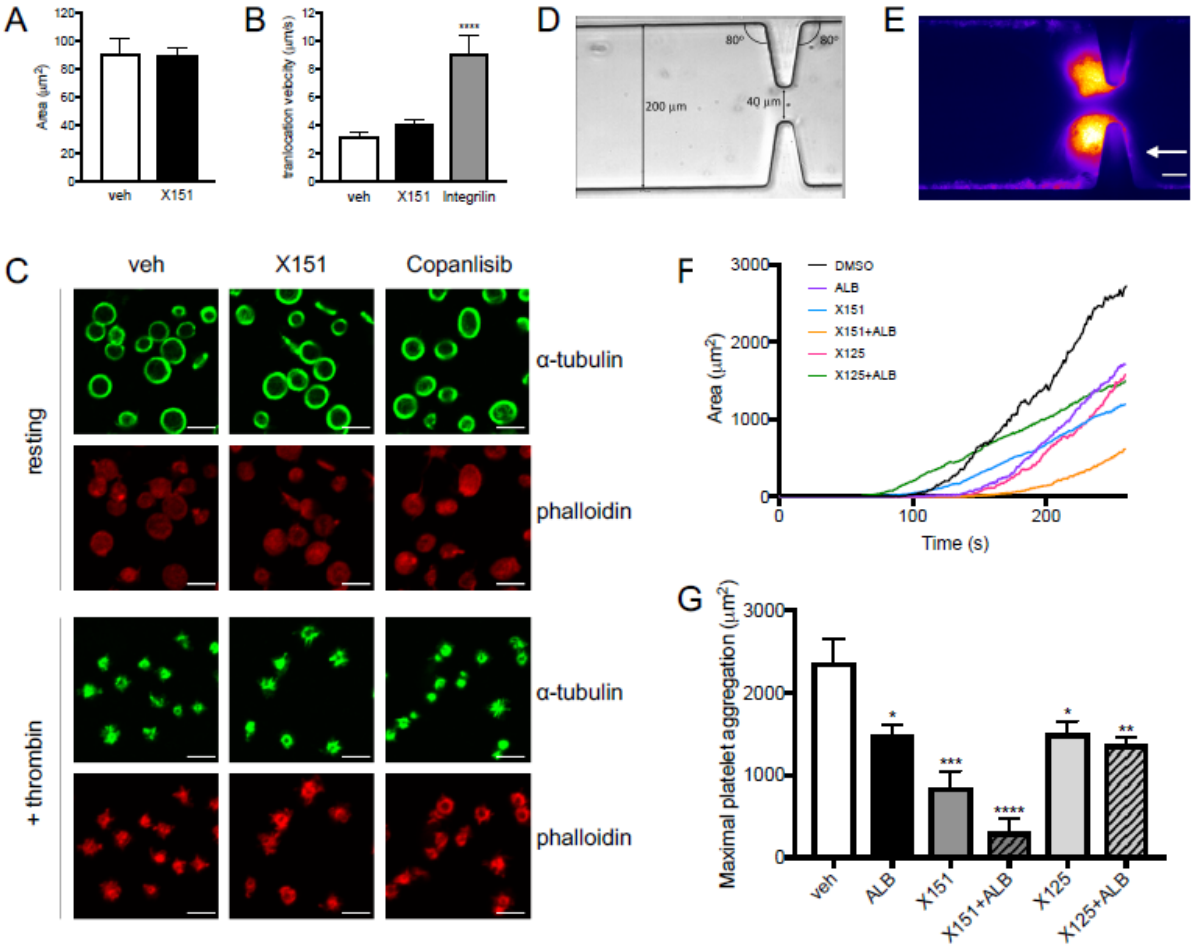
A
Area (µm²)
veh
X151
B
translocation velocity (µm/s)
****
veh
X151
Integrilin
D
80°
80°
200 µm
40 µm
E
C
veh
X151
Copanlisib
resting
α-tubulin
phalloidin
+ thrombin
α-tubulin
phalloidin
F
DMSO
ALB
X151
X151+ALB
X125
X125+ALB
Area (µm²)
Time (s)
G
Maximal platelet aggregation (µm²)
veh
ALB
X151
X151+ALB
X125
X125+ALB

Figure 5. The anti-platelet effects provided by PI3KC2α inhibition are due to a unique impact on membrane-dependent platelet adhesion under high shear. (A) Surface area of human platelets pre-treated for 10 min with vehicle (0.1% DMSO) or X151 (10 μM) and spread on glass for 15 min. Data are mean ± SEM of n=60 cells from n=3 independent experiments. **(B)** Translocation velocity of platelets in human blood flowed over vWF at a shear rate of 1800 s^{-1} in the presence of vehicle (0.1% DMSO), X151 (10 μM) or integrilin (20 μg/mL). Data are mean ± SEM of n=35-89 cells from n=3-6 independent experiments. ****, P<0.0001 (one-way ANOVA with Dunnett's multiple comparisons test against vehicle). **(C)** Representative immune-fluorescence images (n=3) of human platelets treated with vehicle (0.1% DMSO), X151 (10 μM) or copanlisib (10 μM) and stained with an α-tubulin antibody (green) or phalloidin (red). Platelets were either unactivated (top panels) or activated in suspension with thrombin (1 U/mL; bottom panels). Scale bars are 5 μm. **(D)** DIC image (20 X) showing the geometry of the PDMS microfluidic flow channel used in the microfluidic thrombosis assay. The channel has a width of 200 μm narrowing to 40 μm at the stenosis, with entry and exit angles of 80°. **(E)** Representative fluorescence image during blood perfusion through the channel in (D), showing platelet aggregation downstream of the stenosis. Arrow indicates direction of blood flow. Scale bar is 25 μm. **(F)** Real time platelet aggregation in the microfluidic thrombosis assay from one individual and **(G)** group data of maximal platelet aggregation following device perfusion with human blood for 260 s. Blood was pretreated for 10 min with vehicle (0.1% DMSO), amplification loop blockers (ALB: 10 μM MRS2179, 100 μM 2-MeSAMP, 2 U/ml apyrase, 10 μM indomethacin and 800 U/ml hirudin), X151 (10 μM), X151 + ALB, X125 (10 μM), or X125 + ALB. Data in (G) are mean ± SEM of n=3 experiments (individuals).

*, P<0.05; **, P<0.01; ***, P<0.001; ****, P<0.0001 (one-way ANOVA with Dunnett's multiple comparisons test against vehicle).

Appendix five: ‘The PI 3-kinase PI3KC2α regulates mouse platelet membrane structure and function independently of membrane lipid composition’

FEBS Letters

FEBS PRESS science publishing by scientists

The PI 3-kinase PI3KC2α regulates mouse platelet membrane structure and function independently of membrane lipid composition

Maria V. Selvadurai[1], Rose J. Brazilek[1], Mitchell J. Moon[1], Jean-Yves Rinckel[2], Anita Eckly[2], Christian Gachet[2], Peter J. Meikle[3], Harshal H. Nandurkar[1], Warwick S. Nesbitt[1,4] and Justin R. Hamilton[1]

1 Australian Centre for Blood Diseases, Monash University, Melbourne, Australia
2 INSERM, EFS GEST, BPPS UMR_S1225, FMTS, Universit¨e de Strasbourg, France
3 Metabolomics Laboratory, Baker IDI Heart and Diabetes Institute, Melbourne, Australia
4 Microplatforms Research Group, School of Engineering, RMIT University, Melbourne, Australia

Correspondence
J. R. Hamilton, Australian Centre for Blood Diseases, Monash University, L1 AMREP Building, 99 Commercial Road, Melbourne, Vic. 3004, Australia
Fax: +61 3 9903 0228
Tel: +61 3 9903 0125
E-mail: justin.hamilton@monash.edu

(Received 31 October 2018, accepted 7 November 2018)

doi:10.1002/1873-3468.13295

Edited by Michael Bubb

PI3KC2α is a phosphoinositide 3-kinase with a recently reported function in platelets; PI3KC2α-deficient mouse platelets have altered membrane structure and impaired function. Yet, how these membrane changes cause platelet dysfunction remains unknown. Here, focused ion beam-scanning electron microscopy of PI3KC2α-deficient platelet ultrastructure reveals a specific effect on the internal membrane structure, while liquid chromatography-tandem mass spectrometry profiling of 294 lipid species shows unaltered lipid composition. Functionally, PI3KC2α-deficient platelets exhibit impaired thrombosis specifically under conditions involving membrane tethering. These studies indicate that the structural changes in PI3KC2α-deficient platelets are limited to the membrane, occur without major changes in lipid composition, and selectively impair cell function during thrombus formation. These findings illustrate a unique mechanism that may be targetable for anti-thrombotic benefit.

Keywords: open canalicular system; phosphoinositide 3-kinase; platelets; thrombosis

The phosphoinositide 3-kinases (PI3Ks) are a family of lipid kinases that catalyse the phosphorylation of the 3' hydroxyl group of the inositol ring of phosphoinositides to produce the 3-phosphorylated phosphoinositides – important second messengers for a wide range of processes in cells [1,2]. There are eight mammalian PI3K isoforms, divided into three classes based on structural and functional similarities: four class I, three class II, and one class III PI3K. The class I PI3Ks are comfortably the most widely studied and have well-defined roles in range of cells, including platelets [3]. More recently, mouse genetic models have been used to uncover the importance of the sole class III PI3K, Vps34 [4,5], and one of the class II PI3Ks, PI3KC2α [6-8], in platelet function. PI3KC2α in particular regulates the thrombotic function of mouse platelets by a unique and as-yet-undefined mechanism that may involve the structure of the cell membrane. Specifically, we used an inducible shRNA-based approach to deplete PI3KC2α protein in the platelets of adult mice to show that PI3KC2α regulates the structure of the platelet internal membrane system (the

Abbreviations
FIB-SEM, focused ion beam-scanning electron microscopy; OCS, open canalicular system; PI3K, phosphoinositide 3-kinase; TEM, transmission electron microscopy.

open canalicular system; OCS) [6,7]. Here, transmission electron microscopy (TEM) revealed that PI3KC2α-deficient platelets exhibit dilatations of the channels of the OCS. Perhaps surprisingly, platelets from PI3KC2α-deficient mice displayed normal function in all in vitro function tests performed (aggregation, granule secretion, integrin activation, and adhesion and spreading on activating surfaces), yet have impaired platelet thrombotic function in both in vitro and in vivo models [6,7]. A subsequent study confirmed this role for PI3KC2α in platelet structure and function in a distinct mouse model involving heterozygosity of a kinase-inactivating point mutation in the PI3KC2α active site [8]. These intriguing findings suggest PI3KC2α links regulation of the platelet internal membrane structure to the cell's prothrombotic function. However, the mechanism by which this occurs remains unknown.

One potential mechanism by which alterations in the platelet membrane structure might impair platelet function is provided by the observation that PI3KC2α-deficient platelets exhibit reduced cytoskeletal co-localization of key proteins that link the cell membrane with the cytoskeleton, most notably spectrin and myosin [8]. If the reduction in these proteins is sufficient to impair communication between the membrane and cytoskeleton, one prediction is that this may lead to impaired filopodia formation in activated platelets. Yet how such an impact would result in the observed selective impairment of platelet function in the setting of thrombosis – and not a global impairment of platelet function in, for example, standard assays of aggregation, granule secretion, or platelet spreading [6], remains unclear.

Given this uncertainty regarding the mechanism by which PI3KC2α regulates platelet membrane structure and function, we have further examined the structural changes to the platelet membrane induced by PI3KC2α-deficiency and have investigated how these structural changes affect the function of the platelet membrane. Here, we use focused ion beam-scanning electron microscopy (FIB-SEM) [9], as well as traditional SEM, to perform a detailed, three-dimensional ultrastructural analysis of platelets from PI3KC2α-deficient mice. This analysis indicates PI3KC2α-deficient platelets exhibit specific changes to the structure of the OCS. These changes occur without major alterations in the lipid composition of these platelets. Surprisingly, the structural changes to the platelet OCS membrane have no impact on the formation of filopodia by platelets activated in suspension, yet markedly impacts on the ability of these platelets to form thrombi in a blood flow environment involving a prominent shear gradient that produces membrane tether formation [10.12]. Together, these findings indicate that PI3KC2α modulates the structure of the platelet internal membrane (OCS) independently of changes to membrane composition. These structural changes to the OCS appear to compromise platelet membrane function specifically in the setting of thrombus formation. If this regulation of membrane structure by PI3KC2α is acute, these studies reveal the potential for a novel approach toward thrombosis-specific anti-platelet therapy.

Materials and methods

Mice

All animal experiments were approved by the Alfred Medical Research and Education Precinct Animal Ethics Committee (approvals E/1465/2014/M and E/1644/2016/M). Mice were backcrossed ≥ 5 generations on a C57BL/6 genetic background (i.e. ≥ 98%) and maintained on a 12 h light/dark cycle with food and water ad libitum. All genetic studies were littermate controlled and were performed with mice at 6–20 weeks of age of either sex. Mice deficient in PI3KC2α (CMV-rtTA;TRE-GFP-shPI3KC2α) were generated using an inducible shRNA-based gene-silencing approach, as reported previously [6]. Control mice consisted of either pooled wild-type and monotransgenic litter-mates or were mice with similar transgenes but with a control shRNA targeting Renilla luciferase (CMV-rtTA; TRE-GFP-shControl). To induce shRNA-based knockdown of PI3KC2α expression, mice were placed on a doxycycline diet (600 mg·kg^{-1}; Speciality Feeds, Glen Forrest, Australia), for at least 10 days prior to experimentation.

Platelet isolation

Blood was drawn from the inferior vena cava of anaesthetized mice into enoxaparin (40 U·mL^{-1}, final concentration), using a 25-gauge needle. Platelets were isolated as previously described [6]. Briefly, blood was treated with acid-citrate-dextrose and platelet wash buffer (4.3 mM K_2HPO_4, 4.3 mM Na_2HPO_4, 24.3 mM NaH_2PO_4, 113 mM NaCl, 5.5 mM D-glucose and 10 mM theophylline; pH 6.5; containing 0.5% BSA, 20 U·mL^{-1} enoxaparin and 0.01 U·mL^{-1} apyrase), platelets isolated via centrifugation, and resuspended in Tyrode's buffer containing 0.5% BSA, 1.8 mM Ca^{2+} and 0.02 U·mL^{-1} apyrase.

Focused ion beam-scanning electron microscopy

Isolated mouse platelets were fixed in 2.5% glutaraldehyde, postfixed in 1% osmium tetroxide and 1.5% potassium ferrocyanide, incubated in 4% uranyl acetate, and then

dehydrated through a series of graded ethanol concentrations before being embedded in Epon resin. Samples were imaged using a Helios NanoLab microscope (FEI, Tokyo, Japan). Stacks of approximately 1000 images with a field size of 15 µm x 15 µm were generated. Samples were milled with the FIB (20 kV) at a thickness of 20 nm per section. Three-dimensional models were computed using the imaging software AMIRA (FEI).

Scanning electron microscopy

Isolated mouse platelets were activated with ADP under constant stirring in the presence of eptifibatide (40 lg.mL^{-1}) and then fixed with the addition of glutaraldehyde (2.5%, final concentration). Fixed platelets were seeded on glass coverslips precoated with 0.01% poly-L-lysine; coverslips were then rinsed, dehydrated, and coated with a 10 nm layer of platinum/palladium or gold using a sputter coater (Cressington 208-HR; Cressington, Watford, UK). Imaging was performed, using a Nova NanoSEM 450 scanning electron microscope (FEI) at 5 kV, and analysis completed using FIJI software (open source).

Platelet lipid composition

Platelet lipid composition analyses were performed as previously described [13,14]. Briefly, lipids were extracted using a single-phase chloroform : methanol extraction. Isolated mouse platelets in suspension were added to equal volumes of internal standard mix, comprising known concentrations of all lipid classes measured. A 2 : 1 ratio of chloroform : methanol was added to each sample. Samples were mixed with a rotary mixer for 10 min, sonicated for 30 min, and rested for 20 min at room temperature. Samples were then centrifuged at 16 000 ***g*** for 10 min and the resulting supernatant removed and dried with nitrogen gas at 40 °C. Samples were dissolved in water-saturated butanol and sonicated for 10 min prior to addition of an equal volume of methanol with 10 mM ammonium formate. The lipid extracts were centrifuged at 3350 ***g*** for 5 min and the supernatant removed for analysis.

Lipid analysis was performed using liquid chromatography electrospray ionization – tandem mass spectrometry, as previously described in detail [13,14], using an Agilent 1200 UHPLC coupled to an AB Sciex Q/TRAP 4000 mass spectrometer (SCIEX, Framingham, MA, USA) with a turbo-ionspray source (350 °C) and Analyst 1.5 and Multiquant data systems (SCIEX). Separation by liquid chromatography was performed on a Zorbax C18 column (1.8 µm, 50 9 2.1 mm; Agilent Technologies, Santa Clara, CA, USA), again as previously described [13,14]. In total, 294 lipids were detected and quantitated.

The total lipid concentration for each class measured was determined by summing the concentrations of individual species in that class. Univariate comparisons were conducted comparing lipid classes between PI3KC2α-deficient (CMV-rtTA;TRE-GFP-shPI3KC2α) and littermate control mice, using Welch's *t*-test followed by Bonferroni correction to account for multiple comparisons.

Microfluidic assay

Platelet aggregation was performed using a previously described method modified for use in this study with mouse whole blood [11]. Briefly, a microfluidic device consisting of 200 µm wide channels with inset 40 µm stenosis was fabricated using standard photolithography techniques [10]. Microchannels were selectively coated at the stenosis geometry with human vWF (10 µg·mL ı – isolated from Biostate® CSL Ltd, Melbourne, Australia) for 10 min, blocked with BSA (2 µg.mL^{-1}) for 10 min, then coated with botrocetin (2.5 µg.mL^{-1}) for 10 min, before being flushed with Tyrode's buffer prior to sample perfusion. Hirudin-anticoagulated mouse whole blood was perfused through the microfluidic at 45 µL·min ^{1} (equating to a shear rate at the stenosis geometry of 11,500 s^{1}) and platelet deposition at the stenosis monitored in real time via epifluorescence (Nikon Ti-U microscope – Plan Fluor 20x/0.50 (Nikon, Melville, NY, USA) objective with Andor Zyla sCMOS detector, Andor, Belfast, UK). Mid-plane platelet aggregate size was analysed in IMAGEJ (open source) following thresholding (Huang's fuzzy image thresholding method). Maximal aggregation, expressed as cross-sectional area µm^2), was extrapolated from nonlinear curve fitting following 300 s perfusion time.

Analyses

Statistical analyses were performed using GRAPHPAD PRISM (Graphpad, La Jolla, CA, USA). Statistical significance was defined at $P < 0.05$ and was determined with an unpaired, two-tailed Student's t-test, followed by Bonferroni correction to account for multiple comparisons where appropriate and as indicated in the figure legends.

Results

PI3KC2α regulates platelet membrane structure

We have previously used two-dimensional TEM imaging to demonstrate that PI3KC2α-deficiency results in a dilation of the channels of the OCS within mouse platelets [6]. In order to examine this and any other potential ultrastructural change caused by PI3KC2α-deficiency in more detail, we used FIB-SEM to create whole-cell, three-dimensional reconstructions of PI3KC2α-deficient mouse platelets. These reconstructions allow for visualization and quantitation of

various intracellular compartments, which in this case comprised the OCS and plasma membrane, as well as alpha and dense granules. In agreement with our previous two-dimensional findings, we observed dilation of the OCS in platelets from PI3KC2α-deficient mice when compared with platelets from littermate controls (Fig. 1A). Areas of OCS dilation in PI3KC2α-deficient platelets were more evident at certain points in a given cell (Fig. 1A, red arrows) and the total volume of OCS in platelets isolated from PI3KC2α-deficient mice was 48% greater than in platelets from littermate control mice (3.6 ± 0.5 vs 5.4 ± 0.6% of total cell volume for control and PI3KC2α-deficient cells, respectively; Fig. 1B). Despite this OCS dilation, no obvious differences were observed in the spatial distribution of the OCS throughout the cell (Fig. 1A). In contrast to the OCS, the total volume of either alpha or dense granules was not different between control and PI3KC2αdeficient platelets (Fig. 1C).

Given the OCS dilatation observed here and previously [6,7], we next examined the external aspect of the OCS – its openings at the plasma membrane – via SEM (Fig. 2A). There were similar numbers of OCS openings in the visible plasma membrane of cells examined in these studies (Fig. 2B). However, in a near-identical finding to the OCS measurements inside platelets, the diameter of OCS openings at the plasma membrane were significantly increased by 46% in platelets from PI3KC2α-deficient mice versus littermate controls (37 ± 4 vs 54 ± 3 nm, respectively; Fig. 2C).

PI3KC2 does not regulate platelet membrane lipid composition

One of the most important contributors to membrane structure is the lipid content of the membrane. Therefore, we next examined whether the observed structural changes to the OCS were caused by or associated with alterations in the lipid profile of the platelet. We performed a detailed analysis of 294 lipids across the 22 most abundant lipid classes and subclasses, using liquid chromatography electrospray ionization-tandem mass spectrometry. This analysis revealed an unchanged lipid profile in PI3KC2α-deficient when compared with littermate control platelets (Fig. 3), with no significant differences in molar abundance observed in any of the lipid classes analysed.

PI3KC2 does not regulate filopodia formation in platelets

We next examined whether the structural alteration in the platelet internal membrane impacts on platelet

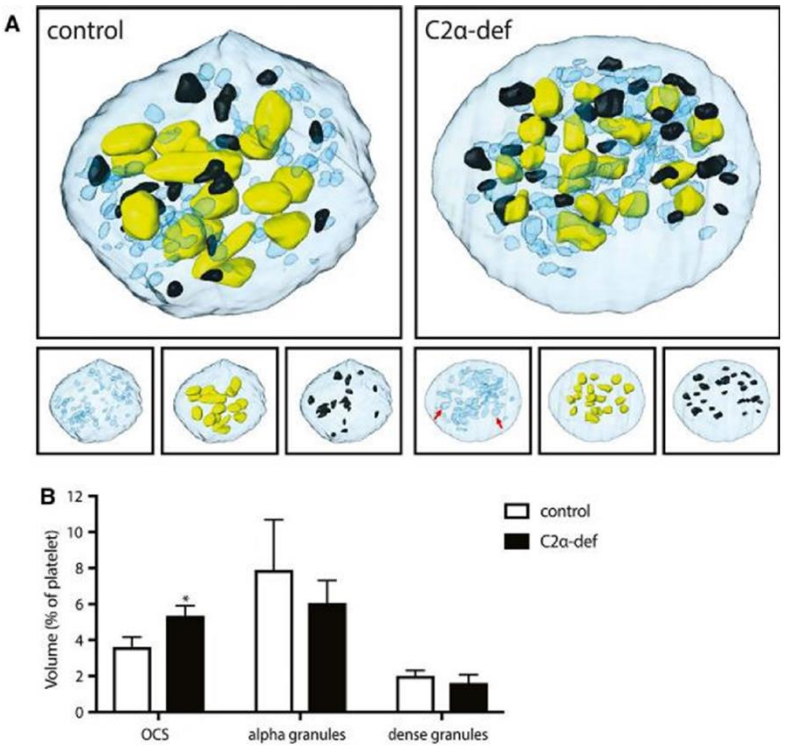

Fig. 1. PI3KC2α regulates internal platelet membrane structure. (A) Representative three-dimensional whole-cell FIB-SEM reconstructions of a platelet from a CMV-rtTA;TRE-GFP-shPI3KC2α bi-transgenic mouse (C2a-def) and a monotransgenic littermate (control) mouse, showing the OCS (blue), alpha granules (yellow), dense granules (black), and plasma membrane (light blue). Bottom panels show reconstructions with individual components only for clarity. Note dilation of the OCS in the PI3KC2α-deficient platelet (red arrows). (B) Quantitation of the volume of each organelle measured (as a percentage of the total platelet volume). Data are mean ± SEM from n = 6 platelets. *D < 0.05 (unpaired, two-tailed, Student's t-test).

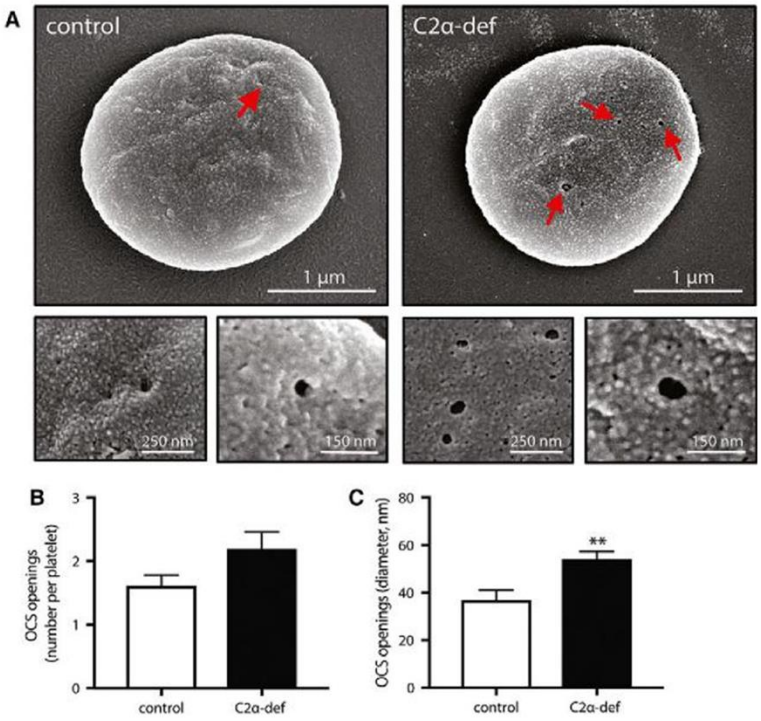

Fig. 2. PI3KC2α regulates external platelet membrane structure. (A) Representative SEM images of resting platelets isolated from CMV-rtTA;TRE-GFP-shPI3KC2α bitransgenic mice (C2α-def) or their wild-type and monotransgenic littermates (control), showing OCS surface openings (red arrows and the focus of the increased magnification images). (B) Number and (C) size of OCS openings. Data are mean ± SEM from $n = 112$ to 116 platelets from $n = 4$ mice per genotype. **$P < 0.01$ (unpaired, two-tailed, Student's t-test).

membrane function by imaging filopodia formation in platelets activated in suspension or in the presence of shear forces. First, isolated platelets were stimulated with ADP (in the presence of eptifibatide to prevent aggregation), then fixed and imaged by SEM (Fig. 4A). No differences were detected in either the number or length of filopodia between platelets isolated from PI3KC2α-deficient or littermate control mice (Fig. 4B,C). In addition, filopodia formed by platelets flowed over a monolayer of activated platelets were also examined. Again, no differences in tether length or stability (total time of attachment) were observed (Fig. 4D,E).

PI3KC2 regulates platelet adhesion and thrombus formation

Given the impaired arterial thrombus formation previously observed in PI3KC2α-deficient mice, we examined platelet function in a microfluidic whole blood flow assay known to be dependent on membrane tether formation [10-12]. Mouse blood was perfused through a von Willebrand factor-coated microfluidic channel incorporating a shear force gradient-inducing stenosis [10-12]. Platelet aggregation occurred downstream of the stenosis and the size of these platelet aggregates was quantified, using the epifluorescent signal of the GFP-positive platelets (Fig. 5). The extent of platelet deposition was significantly lower in blood from PI3KC2α-deficient mice (838 ± 314 μm^2) versus that in blood from control mice (2194 ± 485 μm^2) – a 62% reduction (Fig. 5).

Together, these findings suggest loss of PI3KC2α leads to a specific structural change in the platelet membrane that occurs independently of membrane lipid composition. This membrane modification is sufficient to selectively impact upon platelet function in the setting of thromboses formed downstream of a shear gradient-inducing stenosis and dependent on membrane tethering.

Discussion

We performed an analysis of the structural and functional consequences of the loss of PI3KC2α in mouse platelets in order to gain insights into the mechanism by which PI3KC2α deficiency leads to the previously observed anti-thrombotic phenotype. We showed that PI3KC2α deficiency leads to an ultrastructural change in platelets that is limited to the internal membrane (OCS) of these cells. Specifically, the OCS in platelets from PI3KC2α-deficient mice was dilated throughout the cell, including at the plasma membrane. This structural change in the platelet membrane occurred

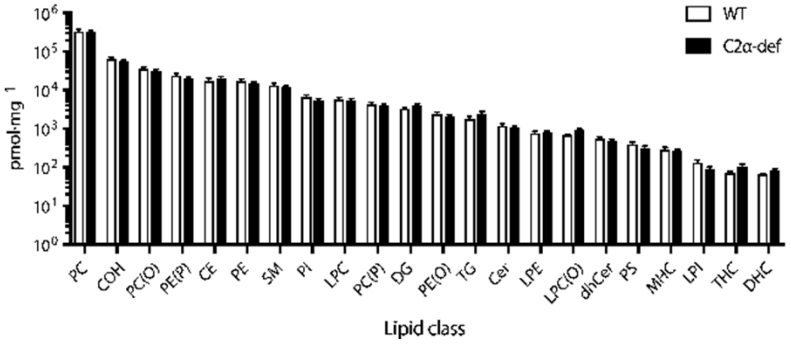

Fig. 3. PI3KC2α does not regulate platelet lipid composition. Concentration of the 22 most abundant lipid classes in platelets isolated from CMV-rtTA;TRE-GFP-shPI3KC2α bitransgenic mice (C2a-def) or their wild-type and monotransgenic littermates (control), via LC-ESI-MS/MS. Lipid classes are phosphatidylcholine (PC), free cholesterol (COH), alkylphosphatidylcholine (PC(O)), alkenylphosphatidylethanolamine (PE(P)), cholesterol ester (CE), phosphatidylethanolamine (PE), sphingomyelin (SM), phosphatidylinositol (PI), lysophosphatidylcholine (LPC), alkenylphosphatidylcholine (PC(P)), diacylglycerol (DG), alkylphosphatidylethanolamine (PE(O)), triacylglycerol (TG), ceramide (Cer), lysophosphatidylethanolamine (LPE), lysoalkylphosphatidylcholine (LPC(O)), dihydroceramide (dhCer), phosphatidylserine (PS), monohexosylceramide (MHC), lysophosphatidylinositol (LPI), trihexosylceramjde (THC) and dihexosylceramide (DHC). Molar abundance of each class is the total of the individual species within each class. Data are mean ± SEM from $n = 10$ to 13 mice per genotype. No significant differences were observed ($P > 0.05$ by unpaired, two-tailed, t-test with Bonferroni correction for multiple comparisons).

independently of the cell's lipid composition. Yet inspection of platelet membrane function revealed PI3KC2α deficiency had selective effects under pro-thrombotic conditions: filopodia formation was unaffected, but platelet deposition and aggregation was significantly impaired in an ex vivo whole blood flow thrombosis model.

We and others have previously shown that platelets from PI3KC2α-deficient mice exhibit an increased surface area occupied by the channels of the OCS in TEM images [6,8]. Here, we add to those findings to show that the enlargements previously reported in 2D TEM images are reflective of a widespread and largely uniform dilation of membrane channels throughout the cell, including at the plasma membrane. Our detailed three-dimensional analysis of PI3KC2α-deficient platelets revealed this structural change was specific to the OCS: its volume was significantly increased in PI3KC2α-deficient platelets while the volumes of alpha and dense granules were unaffected, despite the occasional change in granule number or shape between individual cells. Furthermore, the size of the openings of the OCS at the plasma membrane were significantly larger in PI3KC2α-deficient platelets. Despite this OCS dilation throughout the cell, no gross change in the spatial distribution of the OCS across the cell was observed.

Despite these obvious changes in the structure of the cell's membrane, it remains unclear how PI3KC2α-deficiency leads to such changes. It has previously been shown that PI3KC2α-deficiency reduces the basal levels of PI(3)P in platelets [8]. Yet, this small change in a low abundance lipid appears unlikely to directly cause the structural changes in the platelet membrane observed here. Given that the biggest predictor of any membrane structure is its lipid composition, here we expanded on these previous studies by performing a comprehensive analysis of the lipidome of both PI3KC2α-deficient and wild-type platelets. This more broad-based analysis included all of the most abundant membrane lipid species and revealed the gross lipid profile of PI3KC2α-deficient platelets was indistinguishable to that of wild-type platelets. These studies indicate the observed internal membrane dilatation is unlikely driven by compositional changes to the membrane. This is, to our knowledge, the most comprehensive lipidomic analysis of the mouse platelet. On this, it is interesting to note some potential differences in the relative abundance of some lipids between mouse platelets and similar lipidomic analyses of human platelets [15]. For example, while phospholipids are the predominant component in both mouse and human platelet membranes, there is a notably higher abundance of sterol lipids and a relative paucity of glycerolipids in mouse platelets when compared with human [15]. Whether these differences are important in terms of membrane function remains to be determined.

Previous studies have demonstrated an in vivo antithrombotic phenotype conferred by loss of PI3KC2α [6,8]. Given that platelets from these PI3KC2α-deficient mice have a structural defect that is specific to the OCS - a reserve of membrane thought to be utilized for platelet shape change and spreading

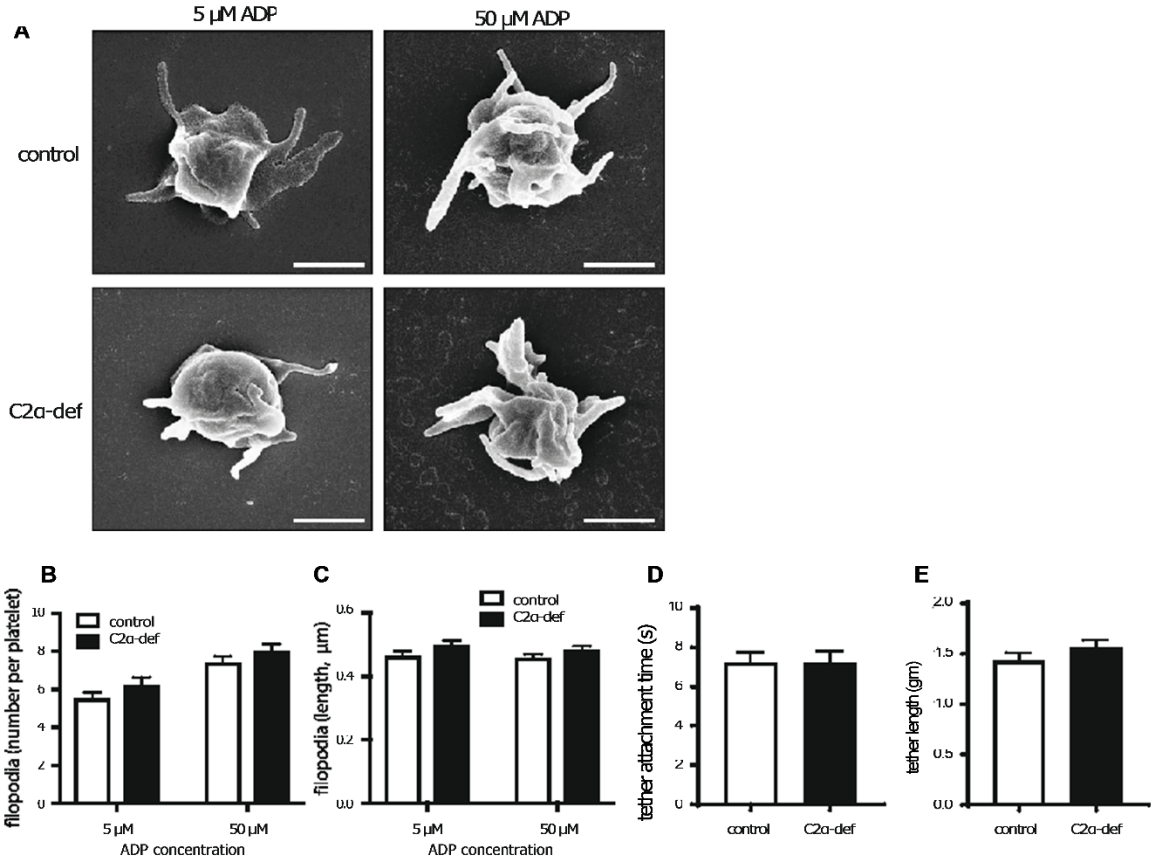

Fig. 4. PI3KC2α does not regulate filopodia formation. (A) Representative SEM images of platelets isolated from CMV-rtTA;TRE-GFP-shPI3KC2α bitransgenic mice (C2a-def) or monotransgenic littermates (control) and activated in suspension with 5 or 50 μM ADP (in the presence of eptifibatide to prevent aggregation). All scale bars are 1 μm. (B) Number and (C) length of filopodia per platelet. Data are mean ± SEM from $n = 119$ to 122 platelets from $n = 6$ mice per genotype. No significant differences were observed in any comparison ($P > 0.05$ by unpaired, two-tailed, *t*-test). (D) Length and (E) stability (total adhesion time) of filopodia from C2a-def or control platelets flowed over a monolayer of wild-type mouse platelets. Data are mean ± SEM from $n = 100$ platelets from $n = 5$ mice per genotype. No significant differences were observed in any comparison ($P > 0.05$ by unpaired, two-tailed, t-test).

during activation and aggregation [16] we examined platelet membrane function in both static and blood flow environments. We found that platelet membrane function is affected specifically in the setting of thrombus formation. Here, filopodia production in suspension-activated platelets or under flow were unaffected by loss of PI3KC2α, yet in a microfluidic assay incorporating a high shear gradient-inducing stenosis, PI3KC2α-deficiency led to a marked reduction in platelet deposition. We utilized this microfluidic blood flow assay because of its incorporation of a pronounced stenosis that has been shown to cause a substantial shear gradient (from very high at the point of stenotic narrowing, to very low immediately downstream of the stenosis) [10-12]. Importantly, in vivo studies of platelet behaviour following exposure to such a shear gradient environment (via a vascular stenosis) have shown that initial platelet deposition occurs largely independently of cellular activation by soluble agonists [12]. Indeed, such shear gradients appear to drive initial platelet deposition via the formation of membrane tethers [10-12]. As a result, the significant reduction in platelet deposition in this system using blood from PI3KC2α mice may suggest that PI3KC2α is important for the earliest stages of platelet adhesion, where membrane tethers, presumably derived from the OCS, are pulled from platelets without detectable cell activation via an interaction between von Willebrand factor and the platelet adhesion receptor GPIbα [17]. This hypothesis fits our

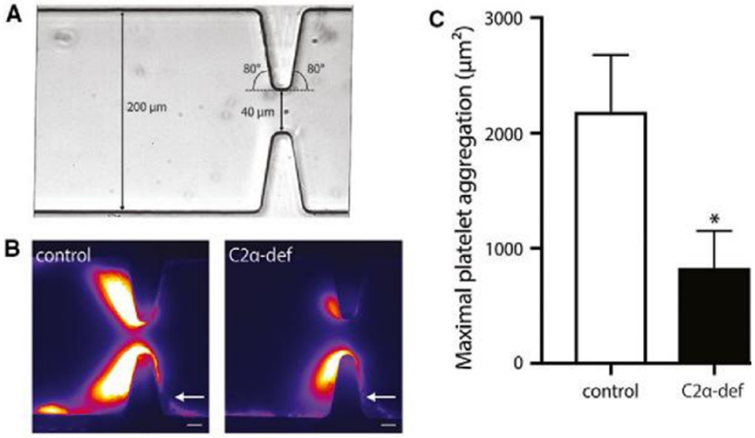

Fig. 5. PI3KC2α regulates platelet adhesion and deposition driven by a shear gradient. (A) DIC image showing the geometry of the microfluidic flow cell used in the whole blood flow assay. The channel has a width of 200 µm narrowing to 40 µm at the stenosis, with side-wall entry and exit angles of 80°. (B) Representative fluorescence images following perfusion of blood taken from CMV-rtTA;TRE-GFP-shPI3KC2α (C2a-def) or CMV-rtTA;TRE-GFP-shControl (control) mice through the flow cell shown in (A), with platelet aggregates seen forming downstream of the stenosis. Arrows indicate direction of flow. Scale bars, 10 µm. (C) Maximal platelet aggregation measured in these experiments (expressed as aggregate area). Data are mean ± SEM from $n = 5$ to 6 mice per genotype. *P < 0.05 (unpaired, two-tailed, Student's *t*-test).

previous observations in which PI3KC2α-deficient platelet adhesion and thrombus formation is differentially affected under conditions in which platelet activation is substantial, that is, on a collagen-coated surface upon which marked platelet activation occurs [6]. Alternatively, PI3KC2α may be involved in the subsequent propagation of platelet aggregates, since incoming platelets that tether to the surface of forming thrombi are discoid and demonstrate low levels of activation markers and minimal calcium flux, in sharp contrast to the initial core of the thrombus where platelets are generally fully activated [12,18]. The lack of effect of PI3KC2α deficiency on platelet filopodia production in response to cell activation may suggest that the involvement of PI3KC2α is most prevalent where changes in shear stress sustain and drive thrombus propagation, potentially in the absence of conspicuous agonist-induced activation. The surprising lack of effect of PI3KC2α deficiency in standard assays of agonist-induced in vitro platelet function [6,8] supports this hypothesis.

The intriguing link between the PI3KC2α-dependent modulation of platelet internal membrane structure and impaired platelet function specifically in the setting of blood flow suggests targeting PI3KC2α and/or the platelet internal membrane system may have utility as an anti-thrombotic strategy. However, it remains unknown whether this function of PI3KC2α translates to human platelets. In addition, the relevance of changes in platelet membrane structure to human platelet function are completely unexplored. There are a number of clinical syndromes in which abnormalities in the OCS are observed, including some with either bleeding or thrombotic consequences [19-21]. Yet platelets from patients with these conditions demonstrate a number of structural abnormalities in addition to OCS changes, making it difficult to determine how much, if any, contribution the OCS defect has to the clinical phenotype. The development of PI3KC2α inhibitors would be a useful step forward in determining the role of this enzyme in human platelets and in addressing any validity of this target as an antithrombotic approach. If PI3KC2α function is conserved in human platelets and acute inhibition of this enzyme is able to reproduce the phenotype observed in mouse platelets, this opens the possibility of manipulating the platelet membrane structure via PI3KC2α as a novel, thrombosis-specific, antiplatelet strategy.

Acknowledgements

Microfluidic devices were fabricated within the Micro Nano Research facility, RMIT University. We thank Monique Freund, Catherine Strassel, Fabienne Proamer and Neslihan Ulas for technical support; the staff of AMREP animal services for animal husbandry and care; staff of the Ramaciotti Centre for Cryo-Electron Microscopy and Monash Micro Imaging (Monash University) for assistance with microscopy; Jacqui Weir and Natalie Mellett for assistance with LC-MS;

and Andrew Yett for interesting insights. This work was supported by grants to JRH from the National Health Medical Research Council of Australia (1047295 and 1120522), Australian Research Council (FT130100540), and CASS Foundation (SM/16/7334).

Author contributions

MVS performed research, analysed data and wrote the manuscript; RJB, MJM and J-YR performed research; AE, CG, PJM, HHN and WSN contributed to study design, data analysis and interpretation of results; JRH designed the study, interpreted results and wrote the manuscript.

References

1 Jean S and Kiger AA (2014) Classes of phosphoinositide 3-kinases at a glance. *J Cell Sci* **127**, 923-928.

2 Vanhaesebroeck B, Stephens L and Hawkins P (2012) PI3K signalling: the path to discovery and understanding. *Nat Rev Mol Cell Biol* **13**, 195-203.

3 Valet C, Severin S, Chicanne G, Laurent PA, Gaits-Iacovoni F, Gratacap MP and Payrastre B (2016) The role of class I, II and III PI 3-kinases in platelet production and activation and their implication in thrombosis. *Adv Biol Regul* **61**, 33-41.

4 Valet C, Levade M, Chicanne G, Bilanges B, Cabou C, Viaud J, Gratacap MP, Gaits-Iacovoni F, Vanhaesebroeck B, Payrastre B et al. (2017) A dual role for the class III PI3K, Vps34, in platelet production and thrombus growth. *Blood* **130**, 2032-2042.

5 Liu Y, Hu M, Luo D, Yue M, Wang S, Chen X, Zhou Y, Wang Y, Cai Y, Hu X et al. (2017) Class III PI3K positively regulates platelet activation and thrombosis via PI(3)P-directed function of NADPH oxidase. *Arterioscler Thromb Vasc Biol* **37**, 2075-2086.

6 Mountford JK, Petitjean C, Putra HW, McCafferty JA, Setiabakti NM, Lee H, Tonnesen LL, McFadyen JD, Schoenwaelder SM, Eckly A et al. (2015) The class II PI 3-kinase, PI3KC2alpha, links platelet internal membrane structure to shear-dependent adhesive function. *Nat Commun* **6**, 6535.

7 Petitjean C, Setiabakti NM, Mountford JK, Arthur JF, Ellis S and Hamilton JR (2016) Combined deficiency of PI3KC2alpha and PI3KC2beta reveals a nonredundant role for PI3KC2alpha in regulating mouse platelet structure and thrombus stability. *Platelets* **27**, 402-409.

8 Valet C, Chicanne G, Severac C, Chaussade C, Whitehead MA, Cabou C, Gratacap MP, Gaits-Iacovoni F, Vanhaesebroeck B, Payrastre B et al. (2015) Essential role of class II PI3K-C2alpha in platelet membrane morphology. *Blood* **126**, 1128-1137.

9 Eckly A, Heijnen H, Pertuy F, Geerts W, Proamer F, Rinckel JY, Leon C, Lanza F and Gachet C (2014) Biogenesis of the demarcation membrane system (DMS) in megakaryocytes. *Blood* **123**, 921-930.

10 Tovar-Lopez FJ, Rosengarten G, Westein E, Khoshmanesh K, Jackson SP, Mitchell A and Nesbitt WS (2010) A microfluidics device to monitor platelet aggregation dynamics in response to strain rate micro-gradients in flowing blood. *Lab Chip* **10**, 291-302.

11 Brazilek RJ, Tovar-Lopez FJ, Wong AKT, Tran H, Davis AS, McFadyen JD, Kaplan Z, Chunilal S, Jackson SP, Nandurkar H et al. (2017) Application of a strain rate gradient microfluidic device to von Willebrand's disease screening. *Lab Chip* **17**, 2595-2608.

12 Nesbitt WS, Westein E, Tovar-Lopez FJ, Tolouei E, Mitchell A, Fu J, Carberry J, Fouras A and Jackson SP (2009) A shear gradient-dependent platelet aggregation mechanism drives thrombus formation. *Nat Med* **15**, 665-673.

13 Weir JM, Wong G, Barlow CK, Greeve MA, Kowalczyk A, Almasy L, Comuzzie AG, Mahaney MC, Jowett JB, Shaw J et al. (2013) Plasma lipid profiling in a large population-based cohort. *J Lipid Res* **54**, 2898-2908.

14 Giles C, Takechi R, Mellett NA, Meikle PJ, Dhaliwal S and Mamo JC (2016) The effects of long-term saturated fat enriched diets on the brain lipidome. *PLoS One* **11**, e0166964.

15 Slatter DA, Aldrovandi M, O'Connor A, Allen SM, Brasher CJ, Murphy RC, Mecklemann S, Ravi S, Darley-Usmar V and O'Donnell VB (2016) Mapping the human platelet lipidome reveals cytosolic phospholipase A2 as a regulator of mitochondrial bioenergetics during activation. *Cell Metab* **23**, 930-944.

16 Escolar G, Leistikow E and White JG (1989) The fate of the open canalicular system in surface and suspension-activated platelets. *Blood* **74**, 1983-1988.

17 Savage B, Saldivar E and Ruggeri ZM (1996) Initiation of platelet adhesion by arrest onto fibrinogen or translocation on von Willebrand factor. *Cell* **84**, 289-297.

18 Stalker TJ, Traxler EA, Wu J, Wannemacher KM, Cermignano SL, Voronov R, Diamond SL and Brass LF (2013) Hierarchical organization in the hemostatic response and its relationship to the platelet-signaling network. *Blood* **121**, 1875-1885.

19 Maldonado JE, Gilchrist GS, Brigden LP and Bowie EJ (1975) Ultrastructure of platelets in Bernard-Soulier syndrome. *Mayo Clin Proc* **50**, 402-406.

20 Dayal S, Pati HP, Pande GK, Sharma P and Saraya AK (1995) Platelet ultra-structure study in Budd-Chiari syndrome. *Eur J Haematol* **55**, 294-301.

21 White JG, Krumwiede MD and Escolar G (1999) Glycoprotein Ib is homogeneously distributed on external and internal membranes of resting platelets. *Am J Pathol* **155**, 2127-2134.

Appendix six: ‘Examining flow dynamics of platelet function in micro-contractions using micro-PIV’

21st Australasian Fluid Mechanics Conference
Adelaide, Australia
10-13 December 2018

Examining flow dynamics of platelet function in micro-contractions using micro-PIV

F. Akbaridoust[1], C. M. de Silva[1], R. J. Brazilek[2], X. Chen[1], F. J. Tovar-Lopez[3] , E. Poon[1], A. Ooi[1], A. Mitchell[3], H. Nandurkar[2], W. S. Nesbitt[2,3] and I. Marusic[1]

[1]Department of Mechanical Engineering
University of Melbourne, Victoria 3010, Australia

[2]Australian Centre for Blood Diseases
Monash University, Victoria 3004, Australia

[3]School of Engineering
RMIT University, Victoria 3000, Australia

Abstract

This study examines the flow field in the near-vicinity of micro-contraction-expansion geometries in microfluidic devices designed to specifically examine the impact of flow acceleration on platelet function. To this end, a set of Micron-resolution Particle Image Velocimetry (micro-PIV) measurements is conducted under a specific set of shear flow gradient conditions with both Newtonian (water) and non-Newtonian (blood analog solutions) fluids. These experiments are complemented by numerical simulations and a set of measurements at matched conditions using blood platelets labelled with DiOC6 (1μg/mL), introduced into the citrated human whole blood. Preliminary results reveal a good agreement between the experiments and numerical simulations at matched flow conditions. However, the experiments with blood analog solutions appear to exhibit different flow patterns both downstream and upstream of the micro-contractions. Furthermore, comparisons between the micro-PIV and blood flow experiments reveal that platelet aggregation appears to coincide with regions of high strain rate and wall shear stress. Collectively, these findings provide a better understanding of the appropriate simplifications that can be made in numerical and experimental work and provides a platform for future works to better understand the impact of flow acceleration on platelet activation.

Introduction

The blood flow in our body is complex and rich with fluid dynamics and is influenced by a number of factors which include: the vessel geometry, tissue properties associated with vessel compliance, and the physical properties of the blood. Of particular interest has been the examination of the flow dynamics that lead to platelet activation, which usually occurs where blood flow is disturbed for example after a vascular injury or stenosis. More specifically, blood-flow strain rate and its gradients play a critical role in initiating platelet activation at sites of arterial stenosis. Platelets can experience significant peak shear stresses/rates and elongation forces during flow accelerations at stenosis [9, 4]. A large body of work to date has focused on the key biological effects of elevated wall shear rates and stress under constant laminar flow regimes. However, the impact of shear flow stresses and its gradients on platelet function are less understood.

Early works, both numerical and experimental have highlighted the critical role played by the vessel geometry/stenosis on platelet activation and thrombus formation. More recently, (see [6]) it has been shown that the flow dynamics in the near-vicinity of a stenosis is an important factor in determining the rate of platelet activation, particularly in regions of flow decelerations at sites of stenosis and downstream of formed thrombi.

Based on these observations, Tovar-Lopez et al [9] measured the platelet aggregation based on the local strain rate micro-gradients in different micro-contraction geometries, mimicking the strain rates conditions of blood vessel geometries with a stenosis.

Blood as a fluid has shear-thinning and viscoelastic non-Newtonian characteristics. Therefore, unless experiments are conducted with blood samples careful consideration has to be given to the chosen fluid properties, in particular when studying small diameter vessels such as capillaries and arterioles. Despite this, several works still opt to use Newtonian fluids for both numerical and experimental investigations [5]. To overcome these challenges, a few studies [8] have reported some success using blood analog solutions by matching the shear rheology to blood samples. However, they conclude that different blood analog solutions can exhibit markedly different flow patterns, particularly near abrupt changes in geometry such as a stenosis.

Accordingly, in the present study, we aim to provide a platform to study the impact of shear flow acceleration and extensional flow on blood platelet activation in a set of micro-contraction-expansion channel geometries. More specifically, we conduct a series of micro-PIV measurements, which are complemented by a set of experiments using whole blood at matched flow conditions. Preliminary comparisons are also drawn with numerical simulation results and blood analog solution experiments, providing us with a comprehensive set of data and tools to quantitatively examine the flow dynamics.

Experimental details

For the present study a set of microfluidic devices, each including four micro-contraction-expansion channels with different contraction angles of θ =7.5, 15, 40 and 80 degrees are fabricated using a soft-lithography technique (see figure 1). The micro-channels are fabricated with a width of 200 μm and a height of 100 μm and are composed of a micro-contraction (~stenosis) with a nominal width of 40 μm and maximum surface roughness of ±300nm.

The microfluidic device is mounted onto the stage of a mo-

Figure 1: Micrograph of the fabricated micro-contraction-expansion geometries in a microfluidic device with different contraction angles of 7.5, 15, 40 and 80 degrees.

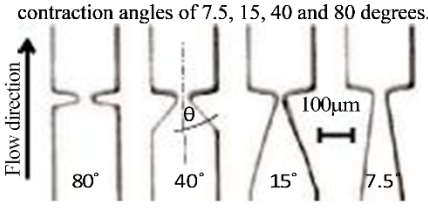

torised inverted Nikon Ti2 microscope containing a G-2A filter cube for epifluorescence imaging. For the first set of experiments, the four different micro-contraction geometries are tested primarily using distilled water (Newtonian fluid) at a flow rate of 45 μL/min using micro-PIV. The flow is seeded with one-micron diameter red fluorescent polystyrene aqueous spherical particles (ThermoFisher Scientific). A programmable syringe pump (Harvard PHD ULTRA) is used to withdraw the fluid from a reservoir through silicon tubes (0.020 in ID, 1/16in OD) to a 1000 μL gas-tight glass syringe (Hamilton).

The micro-PIV setup consists of a 15 Hz double-pulsed laser (70 mJ per 9 ns pulse, EverGreen - BigSky Laser Series) coupled with an external motorised attenuator module for illumination and a PCO.dimax HS4 camera (2000 x 2000 pixels, 12 bits) capable of capturing images at 2277 fps at full resolution. The microscope is equipped with a 40x objective lens (CFI Super Plan Fluor ELWD, N.A.=0.6) providing an optical magnification of 0.27 μm/pixel and a depth of correlation of approximately 5.5 μm, which is estimated using the technique outlined in [7].

For the present experiments, micro-PIV measurements for all of the contractions are carried out in four different microfluidic chips to investigate the repeatability of experiments. In each set of measurements, 2000 pairs of images were recorded at 15 Hz. Each set of image pairs are processed using DAVIS (LaVision, GmbH) using standard PIV processing algorithms. More specifically, images are scaled based on a calibration grid and are then pre-processed using background image subtraction and by applying a histogram equalisation (see [2, 3, 1]). Further, to minimise interference from out-of-focus particles due to the reduced seeding density in micro-PIV measurements [10], two averaging methods, namely, 'Average Image Method' and 'Average Correlation Method' are employed to enhance the signal-to-noise ratio. Specifically, in Average Image Method, we overlay 20 images to increase the number of particles per interrogation window and the correlation between image pairs for the whole dataset (1000 image pairs per dataset) are averaged.

Velocity vector evaluation is performed based on a cross-correlation algorithm using multi-grid with window deformation applied at each pass. Two multigrid passes are performed in all measurements, with the final window sizes of 32x32 pixels (8.5 μm). A 75% overlap is employed for all images at the final interrogation window size, and any spurious vectors are identified using a median test [11] in a post-processing step.

Biological experiments

A set of experiments with blood are conducted at matched flow conditions (45 μL/min) to micro-PIV experiments to monitor platelet aggregation (see [6] for blood properties). For these experiments, the PDMS channels were allowed to passively adhere to ethanol/HCl-washed #1 borosilicate coverslips that formed the bottom channel wall and also acted as the imaging window. Ten minutes prior to blood sample loading, the microfluidic device is derivatized with purified human von Willebrand Factor (VWF) (100 μg.ml^{-1}) isolated from BioState ~R (CSL Ltd), according to previously published methods [4], to allow for effective platelet capture and adhesion to the PDMS surface. VWF is introduced via manual aspiration up to and including the micro-contraction apex and allowed to physisorb for 10 minutes at room temperature, before being aspirated via the same port. The chips are then subsequently perfused with bovine serum albumin (BSA- 10 μg.ml^{-1}) for a further 10 minutes in order to passivate all non-VWF-coated upstream segments and the underlying coverslip.

To assess platelet aggregation as a function of micro-contraction architecture human whole blood samples is incubated with the lipophilic membrane dye DiOC6 (1 μg/mL) (Molecular Probes) and 0.02 U/mL apyrase (to eliminate released ADP during blood collection) for 10 minutes at 37°C and subsequently perfused through the device at constant flow rates of 45 μL/min. Blood perfusion and platelet aggregation dynamics are monitored on an inverted Nikon TiU microscope (Nikon Plan Fluor 20x/0.50 objective) using an Andor Zyla sCMOS camera at 1fps for 210 seconds.

Numerical simulations

To compliment the experimental databases, a set of computational fluid dynamics (CFD) simulations of water are performed in the four channels shown in figure 1. These simulations solve the incompressible Navier–Stokes equations using the finite volume methodology in OpenFOAM (OpenCFD, Ltd., ESI group, Bracknell, UK). Further, the convective and diffusive terms are approximated by the central differencing scheme, and the fully implicit backward scheme is used for the unsteady term. The Pressure Implicit with Splitting of Operator (PISO) method is employed to decouple the pressure term from momentum equation and a convergence criterion of 10^{-6} is used for both velocity and pressure. The velocity-inlet boundary condition is matched to the volumetric flow rate of the experiments (45 μL/min), and a zero gradient is applied at the inlet for pressure. At the outlet, a zero gradient is applied to the velocity coupled with a zero pressure.

Tetrahedral mesh elements are used for all four channel geometries and the meshes are completed in Pointwise (Pointwise, Inc., Fort Worth, Texas, USA), with a total mesh size ranging from 1.7 to 2.5 million elements. We note, the surface mesh resolution in the near vicinity of the constriction is refined to accurately capture any possible chaotic flow in this region. Further, in order to attain a fully developed statistically converged channel flow profile at the inlet similar to the experiments, a sufficiently long development section was included for the simulations. The development length for all cases was at least 20w, where w is the width of the channel. The velocity profiles were verified at multiple locations prior to the contraction to ensure they are independent of the stream-wise location.

Results

To examine the differences in flow patterns at different contraction angles, θ, figure 2 presents the ensemble-averaged stream-wise velocity contours in the mid-plane (channel half-height) of the micro-contractions. Results are presented for the experiments at $\theta = 40^{\circ}$ and $\theta = 7.5^{\circ}$ using water at a flow rate of

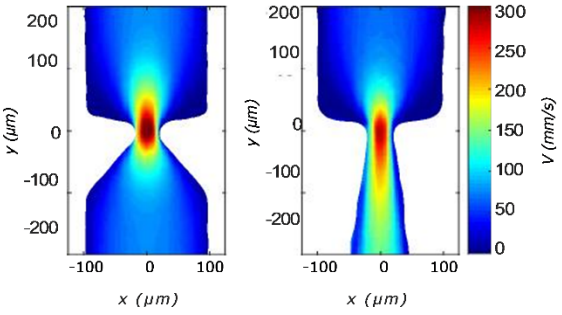

Figure 2: The ensemble-averaged stream-wise velocity contours at the mid-plane of micro-channels with a contraction angle of 40° (left) and 7.5° (right). Results are presented at a flow rate of 45 μL/min.

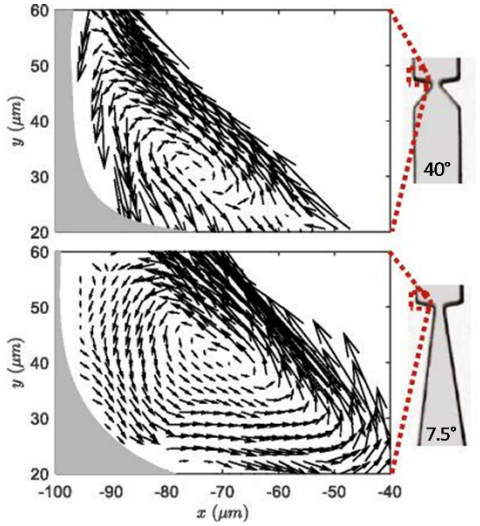

Figure 3: Magnified view of the velocity vector field of the expansion corners for the two micro-contraction configuration shown in figure 2. (top) $\theta = 40°$ and (bottom) $\theta = 7.5°$.

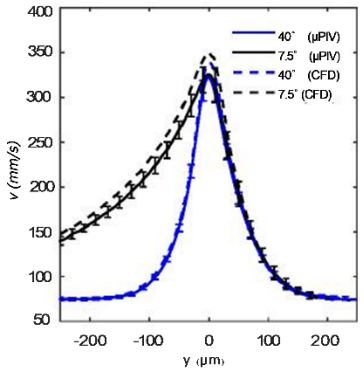

Figure 4: Profiles of stream-wise velocity at the centreline of the channel from the micro-PIV (solid lines) and numerical simulations (dashed lines). Results are presented for contraction angles of $\theta = 40°$ and $\theta = 7.5°$ at the flow rate of 45 μL/min. The error bars (± standard deviation) show the repeatability of experiments and is computed from four independent experiments for each case at matched conditions.

45 μl/min. Qualitatively, the high-speed region is more pronounced prior to the contraction at smaller θ due to the narrower inlet geometry. In contrast, immediately after the contraction the downstream flow patterns only have a subtle difference between the two cases compared, due to the similar channel geometry after the contraction. However, upon closer inspection, we observe two recirculation regions in the expansion corner after the micro-contraction at both $\theta = 7.5°$ and $\theta = 40°$ (c.f. figure 3). Upon closer inspection, at smaller θ (figure 3 bottom) the results appear to exhibit larger/stronger recirculation zones, which might be a consequence of the slightly higher velocity on the centre plane at the contraction, which in turn leads to stronger decelerations immediately after the contraction (c.f. figure 4).

To quantify the velocity profile at different contraction angles, θ, figure 4 shows the stream-wise velocity profile at the centreline of the micro-channels. The solid and dashed lines correspond to results from the micro-PIV experiments and the numerical simulations, respectively, which appear to be in good agreement with a maximum discrepancy of 5% at the velocity peak. We note the error bars on the solid lines corresponds to the repeatability of experiments for the measurements carried out in different microfluidic chips, which shows a maximum deviation of 4.5%. This discrepancy is primarily due to the subtle difference in the channel height (maximum 2.5%), which is primarily caused by the accuracy in precisely locating the channel half height. Future experiments are planned to minimise these discrepancies across a wider range of contraction angles.

In order to visualise blood platelet activation at the micro-contractions, figures 5(a-c) present snapshots from epifluorescence imaging. The results are presented for the case $\theta = 80°$ on a wall-parallel slice at the channel centreline in z-direction. The colour contours reveal that a strong region of platelet aggregation is present on the side-walls immediately after the contraction. To visualise the underlying flow patterns and acceleration figure 5(d) presents the strain rate (dv/dy) at matched flow conditions from the micro-PIV experiments. The results show that initial platelet recruitment (aggregate formation) appears to occur in regions where the flow strain is high at the wall at the apex of step geometry. Moreover, through the numerical simulation results, we observe that the shear stress (see figure 5e) is also at its highest on the side walls in this region.

Blood analog solution experiments

The results presented in the preceding discussions from the micro-PIV experiments are from a set of experiments using a Newtonian fluid (water). However, blood as a fluid exhibits shear-thinning and viscoelastic non-Newtonian characteristics, therefore in this section, we present preliminary findings from a set of micro-PIV experiments using a non-Newtonian solution. For the present case, we have chosen to use a solution of Xanthan gum (500 ppm w/w) based on works by [8]. However, as pointed out in their study, although the fluid exhibits shear thinning behaviour the fluid still differs from whole blood and results should be interpreted with caution. Further, due to limitations of the experimental setup, a lower flow rate of 4.5 μL/min is employed and results are only shown for a micro-contraction with an angle of $\theta = 40°$.

Figure 6 shows the ensemble-averaged stream-wise velocity contours in the mid-plane (channel half-height) of the micro-contractions at matched conditions with water and the blood analog solution. The results show clear evidence of different flow patterns arising from the two fluids examined, albeit at a low flow rate. More specifically, the Xanthan gum solution appears to exhibit large recirculation zones prior to the micro-contraction (see figure 7), which is absent from the experiments using water at matched conditions. These results highlight the significance of employing fluids that have closer properties to whole blood, in future works.

Conclusions

This study employs micro-PIV measurements and numerical simulations to examine the effect of flow acceleration and deceleration at a stenosis on platelet function in a set of micro contraction-expansion channels. The micro-channels tested are constructed with a width of 200 μm and a height of 100 μm with a symmetric micro-contraction of 40 μm with different contraction inlet angles that applies an extensional flow at the stenosis entry. To complement these measurements an independent set of biological experiments are conducted using blood platelets labelled with DiOC6 introduced into citrated human whole blood. Our results reveal good agreement between the

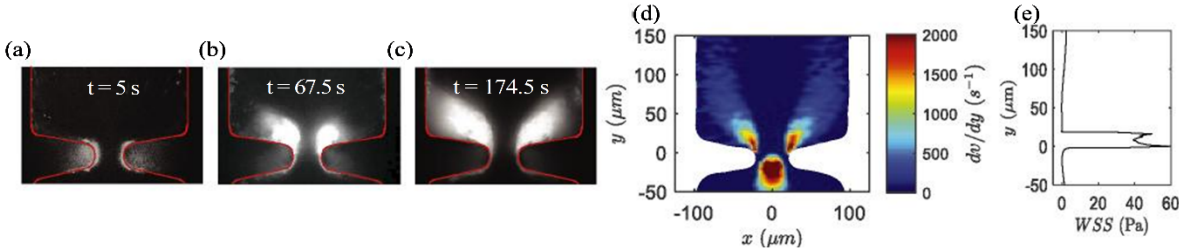

Figure 5: Snapshots from confocal imaging experiment, where colour contours correspond to blood platelets which have been labelled with DiOC6 (1μg/mL). (a) t = 5 s, (b) t = 67.5 s and (c) t = 174.5 s. (d) Flow strain rate (dv/dy) at the mid-plane from micro-PIV experiments and (e) shows the wall shear stress from the numerical simulations. All results are presented for a contraction angle of 80° at a flow rate of 45 μL/min.

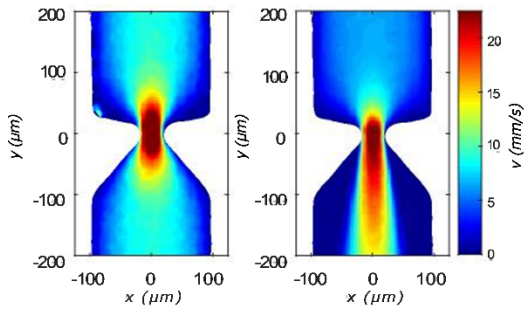

Figure 6: The ensemble-averaged stream-wise velocity contours at the mid-plane of micro-channels with a contraction angle of 40° for water (left) and xanthan gum solution (right). Results are presented at a flow rate of 4.5 μL/min.

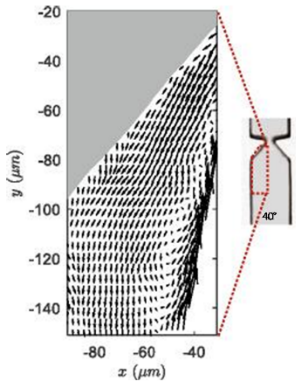

Figure 7: Xanthan gum flow recirculation in the contraction corner of micro-channel with the contraction angle degree of 40°at the flow rate of 4.5 μL/min.

micro-PIV and numerical simulations at matched flow conditions. Further, a comparison to the biological experiments appear to provide support that the initiation of platelet aggregation coincides with high strain rate zones near the wall that also coincide with increased wall shear stress. Collectively, these findings can be used to improve numerical models and also provide a platform for future works to better understand the impact of flow acceleration at stenosis on platelet activation.

Acknowledgements

The authors wish to gratefully thank the financial support of the Australian Research Council.

References

[1] Akbaridoust, F., *Characterisation of a microfluidic hydro-trap to study the effect of straining flow on waterborne microorganisms*, Ph.D. thesis, University of Melbourne, 2017.

[2] Akbaridoust, F., Philip, J. and Marusic, I., A miniature high strain rate device, *Proc. 20th AFMC. Conf.*.

[3] Akbaridoust, F., Philip, J. and Marusic, I., Assessment of a miniature four-roll mill and a cross-slot microchannel for high-strain-rate stagnation point flows, *Meas. Sci. Tech.*, **29**, 2018, 045302.

[4] Brazilek, R. J., Tovar-Lopez, F. J., Wong, A. K., Tran, H., Davis, A. S., McFadyen, J. D., Kaplan, Z., Chunilal, S., Jackson, S. P., Nandurkar, H. et al., Application of a strain rate gradient microfluidic device to von willebrand's disease screening, *Lab Chip*, **17**, 2017, 2595–2608.

[5] Cherry, E. M. and Eaton, J. K., Shear thinning effects on blood flow in straight and curved tubes, *Phys. Fluids*, **25**, 2013, 073104.

[6] Nesbitt, W. S., Westein, E., Tovar-Lopez, F. J., Tolouei, E., Mitchell, A., Fu, J., Carberry, J., Fouras, A. and Jackson, S. P., A shear gradient–dependent platelet aggregation mechanism drives thrombus formation, *Nat. Med.*, **15**, 2009, 665.

[7] Olsen, M. G. and Adrian, R. J., Out-of-focus effects on particle image visibility and correlation in microscopic particle image velocimetry, *Exp. Fluids*, **29**, 2000, S166–S174.

[8] Sousa, P., Pinho, F., Oliveira, M. and Alves, M., Extensional flow of blood analog solutions in microfluidic devices, *Biomicrofluidics*, **5**, 2011, 014108.

[9] Tovar-Lopez, F. J., Rosengarten, G., Westein, E., Khoshmanesh, K., Jackson, S. P., Mitchell, A. and Nesbitt, W. S., A microfluidics device to monitor platelet aggregation dynamics in response to strain rate micro-gradients in flowing blood, *Lab Chip*, **10**, 2010, 291–302.

[10] Wereley, S. T., Gui, L. and Meinhart, C. D., Advanced algorithms for microscale particle image velocimetry, *AIAA*, **40**, 2002, 1047–1055.

[11] Westerweel, J. and Scarano, F., Universal outlier detection for PIV data, *Exp. Fluids*, **39**, 2005, 1096–1100.